transactions of the ASME

Published Quarterly by
The American Society of
Mechanical Engineers
Volume 95 • Series C • Number 1
FEBRUARY 1973

journal of heat transfer

EDITED and PUBLISHED quarterly at the offices of The American Society of Mechanical Engineers, United Engineering Center, 345 E. 47th St., New York, N. Y. 10017. Cable address, "Mechaneer," New York. Second-class postage paid at New York, N. Y., and at additional mailing offices.

CHANGES OF ADDRESS must be received at Society headquarters seven weeks before they are to be effective. Please send old label and new address.

PRICES: To members, $15.00, annually; to nonmembers, $30.00. Single copies, $10.00 each. Add $1.50 for postage to countries outside the United States and Canada.

INDEXED by the Engineering Index, Inc.

(Contents continued on page 119)

CONTENTS

(CONTINUED)

E. MARSCHALL
R. S. HICKMAN
Department of Mechanical Engineering,
University of California,
Santa Barbara, Calif.

Laminar Gravity-Flow Film Condensation of Binary Vapor Mixtures of Immiscible Liquids

The condensation of a binary vapor mixture of immiscible liquids has been studied. The general formulation of this condensation problem includes the application of the conservation laws to both liquid and vapor phase, along with the boundary and interface conditions. The results indicate that only for small condensation rates, that is, for small temperature differences across the liquid film, do transport processes in the vapor boundary layer play an important role. For large condensation rates, heat and mass transfer can be calculated without the solution of the boundary equations of the vapor flow as long as the condensate film is laminar.

Introduction

LAMINAR film condensation of a single vapor or vapor mixtures both in the presence and absence of noncondensable gases has been the subject of detailed analytical and empirical investigations. A predictive theory for condensation of a binary vapor mixture has been formulated by Sparrow and Marschall [1].[1] This theory is based on the assumption that the condensed vapors are completely miscible, thus permitting one to formulate descriptions of the condensate flow with the help of classical Nusselt theory [2]. The condensation of vapors of immiscible liquids has been the subject of limited experimental study. A recent literature review on this special condensation problem conducted by Bernhardt and Westwater [3] shows that experimental data are always fitted into empirical or semiempirical equations. All of these equations, including the one proposed by Bernhardt and Westwater, contain only properties of the condensate flow. Effects of transport processes in the vapor boundary layer on condensation heat and mass transfer are generally neglected.

The theoretical treatment of the condensation of vapors of immiscible liquids has not been formulated. The present paper is concerned with the formulation of a laminar theory to allow conservative prediction for at least this flow regime.

The analytical formulation of the problem requires the application of the conservation laws to both the liquid film and the vapor phase. The present study deals with film condensation on a cooled vertical isothermal plate. The condensate consists of two immiscible liquids flowing downward along the plate under the action of gravity. All motion in the vapor phase is induced by the motion of the condensate or by free convection due to concentration differences; effects of forced convection are neglected.

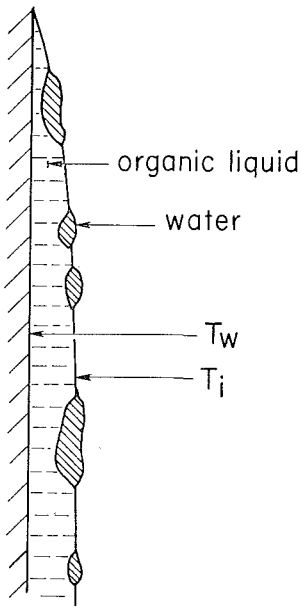

Fig. 1 Condensate film of immiscible liquids

As Tobias and Stoppel [4] have discussed, the two-phase condensation is quite irregular. In the case of a mixture of water and an organic liquid it has been observed that the organic liquid adheres to the cooled wall while the water condenses as drops on the film of organic liquid. The water drops often flow together, thereby covering large areas of the organic-liquid film, Fig. 1. A similar observation has been made by Akers and

[1] Numbers in brackets designate References at end of paper.

Contributed by the Heat Transfer Division and presented at the Winter Annual Meeting, New York, N. Y., November 26–30, 1972, of The AMERICAN SOCIETY OF MECHANICAL ENGINEERS. Manuscript received by the Heat Transfer Division August 8, 1971. Paper No. 72-WA/HT-8.

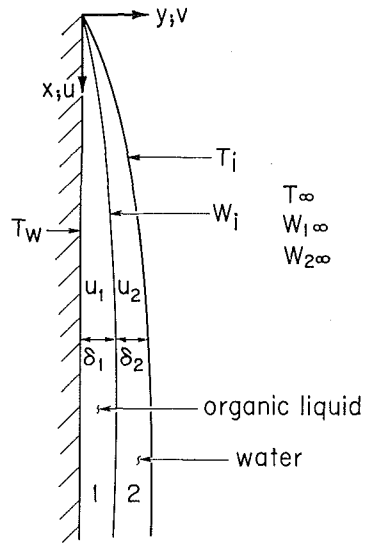

Fig. 2 Model for the description of the flow characteristics of the condensate film

Turner [5]. At low or moderate heat fluxes water will condense as drops or lenses on the wetting or organic films. At high heat fluxes water will condense in distinct channels or as a more or less continuous film on the wetting organic phase. From a consideration of spreading coefficients and static equilibrium, Akers and Turner conclude that in no case could water be in contact with the cooled wall. New experiments carried out by Bernhardt and Westwater [3] lead to a different result. It was found that the organic liquid forms a film on the heat-transfer surface. Water forms small mobi e drops which move with the organic film. It forms also large standing drops which are in contact with the metal surface. The last observation clearly contradicts the results obtained by Tobias and Stoppel and by Akers and Turner.

The present experimental evidence does not allow an exact mathematical description of this particular condensation phenomenon. Therefore, to make the problem tractable, appropriate assumptions must be made. There are two basic analytical models which can be applied to the two-phase film flow. In the first model the components are treated as a pseudofluid with average properties. The description of the flow pattern is thus reduced to the Nusselt theory with modified transport properties. In the second flow model the phases are assumed to flow side by side [6]. Separate equations are written for each phase and coupled by equations for the behavior at the interface.

Since the evaluation of average properties, especially of viscosity and thermal conductivity, is again based on a number of assumptions and simplifications, the second model has been used. The model of the condensate has been treated as two film flows composed of the two materials. This simplification together with the omission of the wavy character of the liquid film leads to a straightforward solution of the problem under study.

A schematic diagram of the condensation problem is presented in Fig. 2. The cooled vertical plate is at the uniform temperature T_w. The temperature at the liquid–vapor interface is the eutectic temperature T_i which controls the interfacial concentrations of the component vapors and the pressure P of the system; however, T_i is independent of the interfacial concentrations W_i of the component liquids. Far away from the surface the vapors have the prescribed concentrations W_∞ and a prescribed temperature T_∞. The total film thickness δ at each vertical position x is the sum of thickness δ_1 and thickness δ_2 measured in the horizontal y direction.

Mathematical Formulation and Solution

The formulation involves the description of the liquid film and the vapor phase which are connected through the conditions at the liquid–vapor interface.

Condensate Film. The film by film flow is treated using the Nusselt model. Denoting the liquids with 1 and 2 as shown in Fig. 2, the momentum equations are

$$\mu_1 \frac{\partial^2 u_1}{\partial y^2} = -\rho_1 g_a \qquad \mu_2 \frac{\partial^2 u_2}{\partial y^2} = -\rho_2 g_a \tag{1}$$

with the boundary conditions at

$$\begin{aligned} y &= 0 & u_1 &= 0 \\ y &= \delta_1 & u_1 &= u_2 \\ & & \mu_1 \frac{du_1}{dy} &= \mu_2 \frac{du_2}{dy} \\ y &= \delta & \frac{du_2}{dy} &= 0 \end{aligned} \tag{2}$$

The solution of equations (1) and (2) gives

$$u_1 = \frac{g_a \rho_1}{2\mu_1}\left[\left(\frac{\delta_2}{\rho} + \delta_1\right) 2y - y^2\right] \tag{3}$$

and

$$u_2 = \frac{g_a \rho_2}{2\mu_2}\left[\left(\frac{\rho}{\mu} - 1\right)\delta_1^2 + 2\delta_1\delta_2\left(\frac{1}{\mu} - 1\right) + 2(\delta_1 + \delta_2)y - y^2\right] \tag{4}$$

where $\rho = \rho_1/\rho_2$, $\mu = \mu_1/\mu_2$, and $\delta_2 = \delta - \delta_1$. From equations (3) and (4) the mass flow rates m_1 and m_2 are found by simple integration to be

$$m_1 = \frac{g_a \rho_1^2 \delta^3}{3\mu_1}\left[\frac{3}{2\rho\Phi} + 1\right] \tag{5}$$

and

Nomenclature

c = constant
D = binary diffusion coefficient
f = dimensionless stream function
g = mass-fraction variable
g_a = gravitational acceleration
h = heat-transfer coefficients
k_1, k_2 = thermal conductivities (liquid)
K_δ = constant
m = mass flow ratio (liquid)
m_1, m_2 = local mass flow rates in liquid film
$\dot{m}, \dot{m}_1, \dot{m}_2$ = local condensation rates
M_1, M_2 = molecular weights
q = heat flux
Sc = Schmidt number
T_i = eutectic temperature
T_w = wall temperature
u_1, u_2, u = velocities in x direction
v_1, v_2 = volume fraction
W_1, W_2 = mass fractions in vapor
x, y = coordinates
$\delta, \delta_1, \delta_2$ = liquid-film thickness
η = similarity variable
$\lambda_1, \lambda_2, \lambda$ = latent heats
μ_1, μ_2, μ_v = viscosities
μ = viscosity ratio (liquid)
ν = kinematic viscosity (vapor)
ρ_1, ρ_2, ρ_v = densities
ρ = density ratio (liquid)
Φ = film thickness ratio
ψ = stream function

Subscripts

i = interface (liquid–vapor)
v = vapor
w = wall
1, 2 = component fluids
∞ = bulk

$$m_2 = \frac{g_a \rho_2^2 \delta_2^3}{3\mu_2}\left[\frac{3}{2}\frac{\rho}{\mu}\Phi^2 + \frac{3}{\mu}\Phi + 1\right] \tag{6}$$

where $\Phi = \delta_1/\delta_2$. Denoting the ratio $m_1/m_2 = m$, equations (5) and (6) yield

$$\Phi^3 + \Phi^2 \frac{3}{2}\frac{1}{\rho}(1 - m) - \Phi\frac{3m}{\rho^2} - \frac{m\mu}{\rho^2} = 0 \tag{7}$$

Equation (7) combines the film thickness ratio Φ with the ratios of the mass flow rate m, the densities ρ, and the viscosities μ. Assuming $d^2T/dy^2 = 0$, the local heat-transfer rate q is

$$q = \frac{k_1 k_2}{k_1\delta_2 + k_2\delta_1}(T_i - T_w) \tag{8}$$

For the local mass-transfer rate it follows that

$$\frac{q}{\lambda} = \frac{k_1 k_2}{\delta_1\left(k_1\frac{1}{\Phi} + k_2\right)}\frac{1}{\lambda}(T_i - T_w)$$

$$= \frac{dm_1}{dx} + \frac{dm_2}{dx} \tag{9}$$

where

$$\lambda = \frac{1}{1 + \frac{1}{m}}\lambda_1 + \frac{1}{1 + m}\lambda_2 \tag{10}$$

is the latent heat of the condensate. Since

$$m = \frac{m_1}{m_2} = \frac{dm_1/dx}{dm_2/dx} \tag{11}$$

equation (9) can be written as

$$\frac{q}{\lambda} = \frac{dm_1}{dx}\left(1 + \frac{1}{m}\right) \tag{12}$$

From equations (5), (9), and (12) it follows

$$\delta_1(x) = \left(\frac{4\mu_1}{g_a\rho_1^2}\frac{k_1k_2}{\left(k_1\frac{1}{\Phi} + k_2\right)}\frac{T_i - T_w}{\left(\frac{3}{2\rho\Phi} + 1\right)}\frac{x}{\left(1 + \frac{1}{m}\right)}\right)^{1/4} \tag{13}$$

Since the film thickness δ is

$$\delta = \delta_1 + \delta_2 \tag{14}$$

it is readily derived that

$$\delta = \delta_1 + \frac{\delta_1}{\Phi} = \delta_1\left(1 + \frac{1}{\Phi}\right) \tag{15}$$

and

$$\delta_2 = \frac{\delta_1}{\Phi}$$

An inspection of the foregoing equations shows that for given surface temperature T_i and wall temperature T_w the velocity u_{2i} at the film surface, film thickness δ, heat flux q, and condensation rate $\dot{m}$ could be determined provided that the film thickness ratio Φ were known. The ratio Φ, however, is not known a priori but is one result of the calculations which in general have also to be based on the behavior of the vapor phase. Therefore consideration is now to be given to the processes in the vapor phase.

Vapor Phase

The vapor boundary layer is fully described by the equations for momentum, energy, and mass conservation. Assuming a small temperature variation across the boundary layer, the set of boundary-layer equations is

$$\frac{\partial u}{\partial x} + \frac{\partial v}{\partial y} = 0 \tag{16}$$

$$u\frac{\partial u}{\partial x} + v\frac{\partial u}{\partial y} = g_a\left(1 - \frac{\rho_{v\infty}}{\rho_v}\right) + \nu\frac{\partial^2 u}{\partial y^2} \tag{17}$$

$$u\frac{\partial W_1}{\partial x} + v\frac{\partial W_1}{\partial y} = D\frac{\partial^2 W_1}{\partial y^2} \tag{18}$$

The equations may be reduced by the following well-known similarity transformation:

Similarity Variable

$$\eta = c(y - \delta)/x^{1/4}$$

$$c = \frac{g_a(M_1 - M_2)(W_{1i} - W_{1\infty})}{4\nu^2[M_1 - W_{1\infty}(M_1 - M_2)]} \tag{19}$$

Dependent Variables

$$f(\eta) = \frac{\psi}{4cx^{3/4}} \qquad g(\eta) = \frac{W_1 - W_{1\infty}}{W_{1i} - W_{1\infty}} \tag{20}$$

where ψ is the stream function. The transformation yields

$$f''' + 3ff'' - 2(f')^2 + g = 0 \tag{21}$$

$$g'' + 3\,\mathrm{Sc}\,fg' = 0 \tag{22}$$

The velocity components u and v follow directly by differentiation of the stream function.

$$u = 4\nu c^2 x^{1/2} f' \tag{23}$$

$$v = \frac{\nu c}{x^{1/2}}\left[\frac{cy}{x^{1/4}}f' - 3f'\right] \tag{24}$$

Next the mass flux at the condensate–vapor interface due to convection and diffusion is obtained for both components:

$$\dot{m}_1 = \left[g'_{(0)} + 3f_{(0)}\mathrm{Sc}\frac{W_{1i}}{W_{1i} - W_{1\infty}}\right]\rho_v D(W_{1i} - W_{1\infty})cx^{-1/4} \tag{25}$$

and

$$\dot{m}_2 = \left[-g'_{(0)} + 3f_{(0)}\mathrm{Sc}\frac{1 - W_{1i}}{W_{1i} - W_{1\infty}}\right]\rho_v D(W_{1i} - W_{1\infty})cx^{-1/4} \tag{26}$$

The total mass flux crossing the interface is obtained by summing $\dot{m}_1$ and $\dot{m}_2$:

$$\dot{m} = 3\mu_v c x^{-1/4} f_{(0)} \tag{27}$$

The ratio of the mass fluxes $\dot{m}_1$ and $\dot{m}_2$ at the interface must be equal to the ratio m of the components in the condensate film, and therefore

$$\frac{\dot{m}_1}{\dot{m}_2} = m = \frac{g'_{(0)} + 3f_{(0)}\mathrm{Sc}\left(\frac{W_{1i}}{W_{1i} - W_{1\infty}}\right)}{-g'_{(0)} + 3f_{(0)}\mathrm{Sc}\left(\frac{1 - W_{1i}}{W_{1i} - W_{1\infty}}\right)} \tag{28}$$

The ratio m is not known but is also one result of the calculations.

Boundary Conditions for the Vapor Phase. To solve the system of differential equations consisting of equations (21) and (22), five boundary conditions must be known. From equations (27) and (9) it follows

$$f_{(0)} = \frac{k_1k_2}{(k_1/\Phi + k_2)\lambda}\frac{(T_i - T_w)}{(3\mu_v c x^{-1/4})}\frac{1}{\delta_1} \tag{29}$$

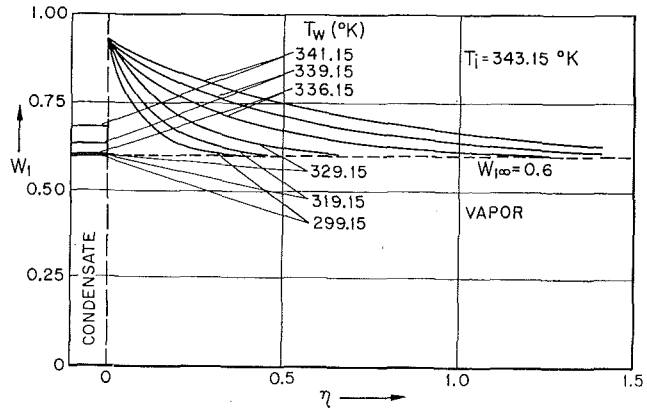

Fig. 3 Representative mass-fraction profiles for benzene

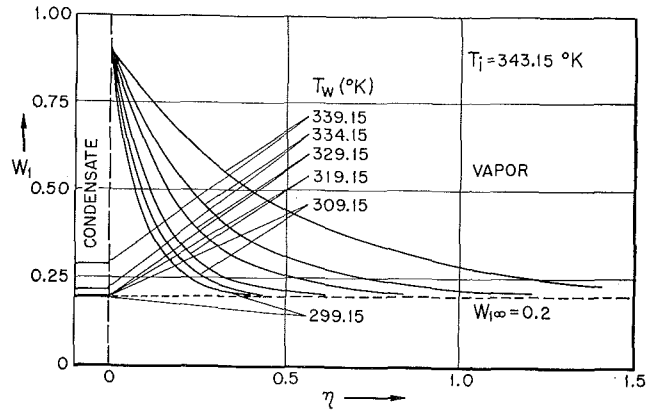

Fig. 4 Representative mass-fraction profiles for benzene

Equations (23) and (4) yield

$$f'_{(0)} = \frac{g_a \rho_2}{2\mu_2} \cdot \frac{1}{4\nu c^2} K_\delta^2 \left[\left(\frac{\rho}{\mu} - 1 \right) + \frac{2}{\Phi} \left(\frac{1}{\mu} - 1 \right) + \left(1 + \frac{1}{\Phi} \right)^2 \right] \quad (30)$$

Equation (20) gives

$$g_{(0)} = 1 \quad (31)$$

and

$$g_{(\infty)} = 0 \quad (32)$$

Finally, the condition that $u = 0$ *in the bulk of vapor determines along with equation* (23)

$$f'_{(\infty)} = 0 \quad (33)$$

Solutions

In order to demonstrate the use of the developed theory, the foregoing equations and concepts will now be applied to the condensation of mixtures of water and benzene vapor. All thermodynamic and transport properties of benzene and water required for the calculation were taken from [7] or determined according to [8] and were fitted with algebraic equations for use in a computer program.

As a first step in the calculations, the wall temperature T_w and the total pressure P were specified. The surface temperature T'_i of the condensate film was then determined by the pressure–temperature relations of saturated water vapor and benzene vapor. Next a trial-and-error method was used to find the mass ratio m. A value for m was selected and with this Φ was found from equation (7). Then the boundary conditions for the vapor phase, equations (29) to (33), were evaluated and finally equations (21) and (22) were solved. Equation (28) was then used

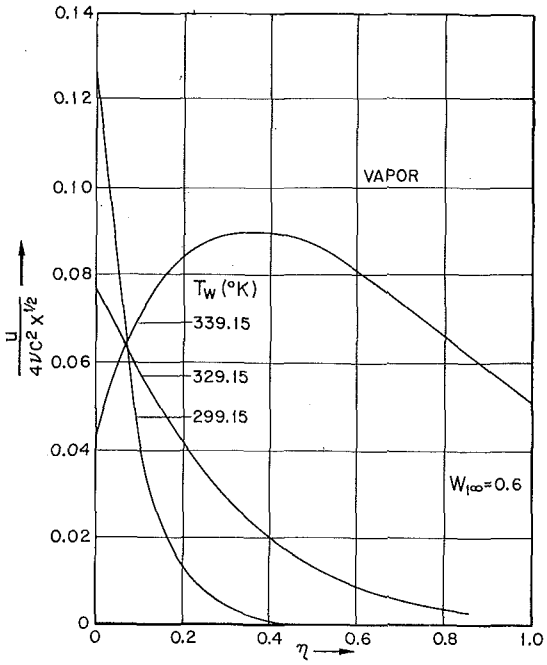

Fig. 5 Representative velocity profiles

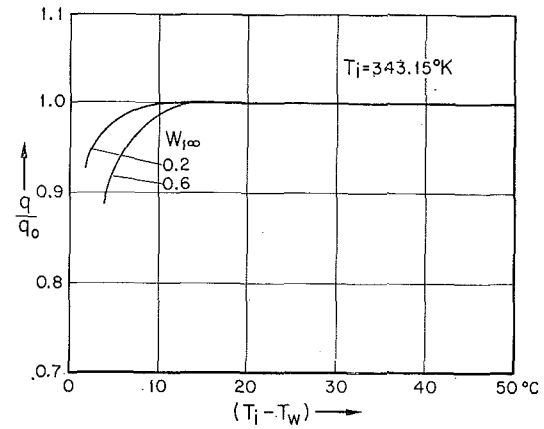

Fig. 6 Heat-transfer results

to check the guessed value of the mass ratio m. If the equality was fulfilled the selected value for m was validated.

Results

Calculations have been carried out for a variety of different temperatures, pressures, and mass fractions.

Mass-fraction profiles of benzene for values of $T_i - T_w$ ranging from 2 to 44 deg C for an interface temperature $T_i = 343.15$ deg K and for benzene mass fractions in the bulk of $W_{1\infty} = 0.2$ and 0.6 are shown in Figs. 3 and 4. An inspection of the figures reveals that for an increasing temperature difference across the liquid film, the vapor boundary-layer thickness decreases. This can be explained with the increasing condensation rates and therefore stronger suction of the condensate film, coupled with increasing temperature drops across the condensate film. A second and more important observation is that in this particular case only for temperature differences $T_i - T_w \leq 15$ deg C are the component mass fraction in the liquid film and the bulk of the vapor different. For higher temperature differences the strong suction of the condensate film controls the transport process in the vapor boundary layer, free convection becomes negligibly small, Fig. 5, and a detailed analysis of the vapor boundary layer can be bypassed for the heat-transfer calculation, as is shown below.

In Fig. 5 velocity profiles are plotted for fixed values of T_i = 343.15 deg K and $W_{1\infty}$ = 0.6. The curves are for wall temperatures of 299.15, 329.15, and 339.15 deg K. The strong maximum in the curve for $T_i - T_w$ = 4 deg C indicates the presence of free convection in the vapor boundary layer, while at the large temperature difference of $T_i - T_w$ = 44 deg C the curve is monotonic decreasing, suggesting that free convection is negligibly small.

Results of heat-transfer calculations are reported in the form q/q_0, where q is the local heat flux across the liquid film (as determined by this analysis) to given values of T_w, T_i, and W, and q_0 is the reference heat flux calculated under the assumption that the component mass fractions are the same in the liquid film and the bulk of vapor. As is shown in Fig. 6, the ratio of q/q_0 is essentially equal to one for values of $T_i - T_w > 15$. Heat-transfer calculations in this range are reduced to an analysis of the liquid film. For smaller temperature differences the ratio differs from one, indicating that the heat-transfer calculation has to include the analysis of both liquid film and vapor boundary layer.

In order to confront the calculation method with experimental data, the recently reported empirical correlation [3]

$$h = v_1 h_1 + v_2 h_2 \tag{34}$$

has been used for comparison. For pure benzene and for pure water, heat-transfer results obtained with the help of the presented method and with equation (34) are identical. Very small deviations in the heat-transfer results were found up to a water content of about 20 percent in the condensate. For higher water contents, the presented method predicts up to 35 percent lower heat-transfer coefficients than equation (34). Therefore the calculation procedure will allow the prediction of conservative heat-transfer coefficients.

The above-mentioned simplified method of calculating heat transfer, bypassing the analysis of the vapor boundary layer, is, however, of limited value. In many applications of technical interest large condensation rates will lead to turbulent film flow with a quite different heat-transfer characteristic than the laminar film flow assumed in this paper. For these cases it is advisable to use correlations of experimental data such as are reported in [3].

It should be emphasized that the simplified computation procedure for q is applicable only at large condensation rates, that is, at large differences of T_i and T_w, and at laminar film flow. Therefore a complete heat-transfer analysis of the condensation of a binary vapor mixture of immiscible liquids must employ the complete solution procedure to find the smallest value of $T_i - T_w$ for which the simplified procedure is valid, as well as to check the Reynolds number of the condensate film in order to make sure that the film flow is laminar.

References

1 Sparrow, E. M., and Marschall, E., "Binary, Gravity-Flow Film Condensation," JOURNAL OF HEAT TRANSFER, TRANS. ASME, Series C, Vol. 91, No. 2, May 1969, pp. 205–211.

2 Nusselt, W., "Die Oberflächenkondensation des Wasserdampfes," Z. *VDI*, Vol. 60, 1916, pp. 541–546, 568–575.

3 Bernhardt, S. H., and Westwater, J. W., "Condensation of Immiscible Mixtures," presented at the 12th National Heat Transfer Conference, Tulsa, Okla., Aug. 15–18, 1971.

4 Tobias, M., and Stoppel, A. E., "Condensation of Vapor of Water and Immiscible Organic Liquids," *I&EC*, Vol. 46, 1955, pp. 1450–1455.

5 Akers, W. W., and Turner, M. M., "Condensation of Vapors of Immiscible Liquids," *AIChE Journal*, Vol. 8, 1962, pp. 587–589.

6 Sykes, J. A., and Marchello, J. M., *Ind. Eng. Chem. Process Res. Develop.*, Vol. 9, 1970, pp. 63–71.

7 Landolt-Börnstein, ed., *Zahlenwerte und Funktionen*, Bd. 2, Bd. 4, Springer-Verlag, New York, N. Y.

8 Reid, R. C., and Sherwood, T. K., *The Properties of Gases and Liquids*, McGraw-Hill, New York, N. Y., 1966.

R. H. TURNER
Research Assistant.
A. F. MILLS
Associate Professor.
Assoc. Mem. ASME
V. E. DENNY
Associate Professor.

University of California,
Los Angeles, Calif.

The Effect of Noncondensable Gas on Laminar Film Condensation of Liquid Metals[1]

The effect of noncondensable gas on laminar film condensation of a liquid metal on an isothermal vertical surface with forced vapor flow is analyzed. Where necessary the interfacial resistance due to thermodynamic nonequilibrium is included for a condensation coefficient $\sigma = 1$. A computer program has been developed to solve a finite-difference analog of the governing partial differential equations and is applied here to the mercury–air and sodium–argon systems. Heat-transfer results are presented for vapor velocities in the range 1 to 100 fps with mass fraction of gas varying from 10^{-5} to 3×10^{-2}. The overall temperature difference ranged from 0.1 to 30 deg F while the temperature levels were 1200 and 900 deg R for mercury–air and 2000 and 1500 deg R for sodium–argon. The effect of noncondensable gas is most marked for low vapor velocities and high gas concentrations. At the lower pressure levels the interfacial resistance plays a dominant role, causing maxima in the curves of q/q_{Nu} versus x. For the mercury–air system the adverse buoyancy force causes vapor boundary-layer separation when the free-stream vapor velocity is low.

Introduction

THE PRESENCE of a small amount of noncondensable gas in a vapor results in a markedly reduced condensation heat-transfer rate. The magnitude of the reduction is very much dependent on the vapor flow pattern in the vicinity of the condenser surface; high vapor velocities past the surface tend to alleviate the problem. For laminar film condensation on a vertical surface the limiting case of zero forced vapor flow was analyzed for constant properties (Boussinesq approximation) by Sparrow and Lin [1],[2] while Minkowycz and Sparrow [2] extended the work to include variable properties and interfacial resistance due to thermodynamic nonequilibrium for the water-vapor–air system. For forced vapor flow vertically downward, the water-vapor–air system was analyzed by Denny, Mills, and Jusionis [3]; this work has been extended by Denny and Jusionis [4] to other high-Prandtl-number liquids including ammonia, Freon-12, ethanol, butanol, and carbon tetrachloride. The objective of the present study is to complete the picture for forced vapor flow by considering the low-Prandtl-number liquids, i.e., metals.

The noncondensable-gas problem for liquid metals has a number of unique features: (*a*) The high thermal conductivity of liquid metals implies that in most cases the temperature drop across the liquid film is very small compared to that in the vapor phase, (*b*) the low pressures typical of technological applications require that the interfacial resistance due to thermodynamic nonequilibrium be included in the model, and (*c*) some important systems, e.g., mercury–air, may exhibit boundary-layer separation due to an adverse buoyancy force. These features lead to a more complex physical problem than that considered in [3, 4]; on the other hand, the characteristic low temperature drop across the liquid film can be exploited to simplify the calculation procedure.

Technological applications of liquid-metal condensation include binary power cycles such as mercury–steam central power plants and use of a metal such as sodium as the working fluid of a power-generation cycle in a space vehicle. Thus the systems chosen for the present study are (*a*) mercury–air (here we envisage an air leak into a mercury condenser) and (*b*) sodium–argon (here there may possibly be residual gas after purging the equipment with argon). The results of our study will also be pertinent to a number of experimental investigations of liquid-metal condensation, e.g., [5, 6] where unexpectedly low condensation rates were measured, suggesting the presence of noncondensable gas.

Laminar film condensation on a vertical surface with forced vapor flow parallel to the surface is a boundary-layer problem for which a self-similar solution cannot be obtained. An exact

[1] This work was supported by NASA on research grant NSG 237-62. Computer time for the numerical calculations was supplied by the Campus Computing Network and the School of Engineering and Applied Science of the University of California, Los Angeles, Calif.

[2] Numbers in brackets designate References at end of paper.

Contributed by the Heat Transfer Division and presented at the Winter Annual Meeting, New York, N. Y., November 26–30, 1972, of THE AMERICAN SOCIETY OF MECHANICAL ENGINEERS. Manuscript received by the Heat Transfer Division June 28, 1971. Paper No. 72-WA/HT-9.

analytical result requires solution of two sets of coupled boundary-layer conservation equations, one set describing the liquid-film flow and the other the vapor flow. A previous result of Denny, Mills, and Gardiner [7] does permit a significant simplification of the solution procedure. In [7] it is shown that the behavior of the liquid film may be accurately analyzed using the Nusselt assumptions, whereby liquid acceleration and energy convection are neglected and physical properties are assumed constant. Due to the typically small temperature drop across the liquid film, the properties may conveniently be evaluated at the wall temperature. Thus the set of parabolic partial differential equations governing conservation of momentum, species, and energy in the vapor phase can be solved by finite-difference methods using a forward marching technique, extracting the necessary boundary conditions at the interface from a locally applied Nusselt analysis. Further simplifications are made when warranted. For example, when the temperature drop across the liquid film is negligible the liquid–vapor-interface temperature may be set equal to the wall temperature in the calculation procedure. Also, when the free-stream velocity is large the liquid-surface velocity can be set equal to zero when solving the vapor-phase momentum equation. The exploitation of such simplifying assumptions greatly reduces the cost of the final numerical computations while maintaining an acceptable level of accuracy in the data.

The problem parameters are mass fraction of noncondensable gas in the free stream $m_{2,e}$, free-stream velocity u_e, overall temperature difference $T_e - T_w = \Delta T$, temperature level T_e, and length of condensing surface L. The problem domain was restricted by choosing parameter values so as to (*a*) insure the absence of a rippled or turbulent film and (*b*) limit the heat flux to values attainable in practice. Thus the film Reynolds number ($\mathrm{Re} = 4\Gamma/\mu_l$) will not be allowed to exceed 30, and the heat flux will not exceed 300,000 Btu/ft²-hr at $x = 0.1$ ft.

Analysis and Calculation Procedure

Physical Model and Coordinates. The coordinates along and normal to the surface are x and y respectively, and the corresponding velocity components are u and v. In the free stream the vapor has velocity u_e and temperature T_e, and the concentration of noncondensable gas is $m_{2,e}$. The system total pressure P is determined from T_e and $m_{2,e}$ by imposing the requirement that the free-stream vapor be saturated. The condenser wall is at a uniform temperature T_w. The condensate film has thickness δ, which is a function of x and must be determined as part of the solution. At the liquid–vapor interface the temperature T_i and the vapor partial pressure $P_{1,i}$ are also unknown and are determined in the course of the analysis.

Conservation Equations and Boundary Conditions. For the vapor phase the equations governing conservation of mass, momentum, species, and energy, in boundary-layer form, are

$$\frac{\partial}{\partial x}(\rho_v u) + \frac{\partial}{\partial y}(\rho_v v) = 0 \tag{1}$$

$$\rho_v u \frac{\partial u}{\partial x} + \rho_v v \frac{\partial u}{\partial y} = \frac{\partial}{\partial y}\left(\mu_v \frac{\partial u}{\partial y}\right) + g(\rho_v - \rho_{v,e}) \tag{2}$$

$$\rho_v u \frac{\partial m_1}{\partial x} + \rho_v v \frac{\partial m_1}{\partial y} = \frac{\partial}{\partial y}\left(\rho_v \mathfrak{D}_{12} \frac{\partial m_1}{\partial y}\right) \tag{3}$$

$$\rho_v u \frac{\partial T}{\partial x} + \rho_v v \frac{\partial T}{\partial y} = \frac{\partial}{\partial y}\left(\frac{k_v}{C_{pv}} \frac{\partial T}{\partial y}\right) + \frac{k_v}{C_{pv}} \frac{\partial T}{\partial y} \frac{\partial \ln C_{pv}}{\partial y} + \frac{\rho_v \mathfrak{D}_{12}}{C_{pv}} (C_{p1} - C_{p2}) \frac{\partial m_1}{\partial y} \frac{\partial T}{\partial y} \tag{4}$$

Viscous dissipation and compressibility effects are ignored in the energy equation since low-velocity flow is to be considered. In addition, thermal diffusion and diffusional conduction (Dufour effect) are ignored in view of the results obtained in [2]. Under the Nusselt assumptions with the physical properties assumed constant at the wall values, the equations governing conservation of momentum and energy for the liquid phase are respectively

$$0 = \mu_l \frac{d^2u}{dy^2} + g(\rho_l - \rho_{v,e}) \tag{5}$$

$$0 = \frac{d^2T}{dy^2} \tag{6}$$

Equations (1)–(6) must be solved subject to the boundary conditions:

vapor at infinity, $y \to \infty$

$$u \to u_e \qquad m_1 \to m_{1,e} \qquad T \to T_e \tag{7}$$

liquid at the wall, $y = 0$

$$u = 0 \qquad T = T_w \tag{8}$$

interface continuity, $y = \delta$

$$u_{l,i} = u_{v,i} = u_i \tag{9}$$

$$T_{l,i} = T_{v,i} = T_i \tag{10}$$

$$\mu_l \left.\frac{\partial u}{\partial y}\right|_{l,i} = \mu_v \left.\frac{\partial u}{\partial y}\right|_{v,i} = \tau_i \tag{11}$$

Nomenclature

$\mathfrak{G}$ = mass-transfer driving force
C_p = heat capacity (Btu/lb-deg R)
$\mathfrak{D}_{12}$ = binary diffusion coefficient (ft²/sec)
g = normal gravity (ft²/sec), also conductance (lb/ft²-sec)
k = thermal conductivity (Btu/ft-sec-deg R)
L = length of condensing surface (ft)
M = molecular weight
m = mass fraction
$\dot{m}$ = condensation rate (lb/ft²-sec)
Nu_m = Nusselt number for mass transfer, $gx/\rho\mathfrak{D}_{12}$
P = pressure (atm)
q = wall heat flux (Btu/ft²-hr)
q_{Nu} = Nusselt heat flux defined by equation (24), (Btu/ft²-hr)
$\mathfrak{R}$ = universal gas constant (atm-ft³/lb-mole-deg R)
R = specific gas constant (atm-ft³/lb-deg R)
Re = film Reynolds number, $4\Gamma/\mu_l$
Sc = Schmidt number, $\mu_e/\rho_e\mathfrak{D}_{12}$
T = absolute temperature (deg R)
u, v = velocity components (ft/sec)
x, y = boundary-layer coordinates (ft)
Γ = liquid flow rate per unit width (lb/ft-sec)
δ = condensate film thickness (ft)
δ_v = vapor boundary-layer thickness (ft)
λ = latent heat of vaporization (Btu/lb)
μ = absolute viscosity (lb/ft-sec)
ρ = density (lb/ft³)
σ = condensation (mass-accommodation) coefficient
τ = shear stress (lb/ft-sec²)
ψ = stream function (lb/ft-sec)
$\omega = (\psi - \psi_i)/(\psi_e - \psi_i)$

Subscripts

e = in the vapor free stream
i = at the interface
l = in the liquid phase
v = in the vapor phase
w = at the wall
1 = of vapor
2 = of noncondensable gas

Superscript

* = zero mass transfer

$$\frac{d}{dx}\int_0^\delta \rho_l u dy = \frac{\sigma}{1 - 0.523\sigma}\sqrt{\frac{M_1}{2\pi \mathcal{R} T_i}}\,[P_{1,i} - P_{1,\mathrm{sat}}(T_i)]$$

$$= \frac{\rho_v \mathfrak{D}_{12}}{1 - m_1}\frac{\partial m_1}{\partial y}\bigg|_i = -\dot{m} \quad (12)$$

$$k_l \frac{\partial T}{\partial y}\bigg|_{l,i} = -\dot{m}\lambda + k_v \frac{\partial T}{\partial y}\bigg|_{v,i} \quad (13)$$

In addition there is the equation of state for an ideal mixture, $P = \rho_v RT$. The treatment of the interfacial resistance due to thermodynamic nonequilibrium follows Schrage [8] as presented in [9]. Since Schrage's theory is of doubtful validity for significant departures from equilibrium, the simple linearized form, equation (12), was chosen for use in all situations. The condensation coefficient σ will be taken equal to unity in accordance with the recent experimental data of Wilcox and Rohsenow [10]. As discussed in [9] the velocity and temperature jumps at an interface with phase change are essentially the usual jumps of low-density flow in the slip regime and are usually negligible even when the interfacial resistance described by equation (12) is appreciable. Such is the case in the present study and hence the simple continuity relations, equations (9) and (10), may be employed. Closure of the problem is effected through a heat balance on the liquid film which determines its thickness δ, namely

$$\int_0^x k_l \frac{\partial T}{\partial y}\,dx\bigg|_{y=0} = \int_0^\delta \rho_l u[\lambda + C_{pl}(T_i - T)]dy\big|_x + \int_0^x k_v \frac{\partial T}{\partial y}\,dx\bigg|_{v,i} \quad (14)$$

For the range of parameter values of relevance to the condensation of metals, a number of further assumptions can be made.

1 Since $\rho_{v,e} \ll \rho_l$, equation (5) becomes

$$0 = \mu_l \frac{d^2u}{dy^2} + g\rho_l \quad (15)$$

2 Since $k_v \dfrac{\partial T}{\partial y}\bigg|_{v,i} \ll -\dot{m}\lambda$, equation (13) becomes

$$k_l \frac{\partial T}{\partial y}\bigg|_{v,i} = -\dot{m}\lambda \quad (16)$$

3 Also, $C_{pl}(T_i - T_w) \ll \lambda$, so equation (14) becomes

$$\int_0^x k_l \frac{\partial T}{\partial y}\,dx\bigg|_{y=0} = \int_0^\delta \rho_l u\lambda dy \quad (17)$$

4 The only way the temperature profile in the vapor now affects the problem is via the vapor transport and thermodynamic properties. It is therefore legitimate to simplify equation (4) and solve

$$\rho_v C_{pv} u\frac{\partial T}{\partial x} + \rho_v C_{pv} v\frac{\partial T}{\partial y} = \frac{\partial}{\partial y}\left(k_v \frac{\partial T}{\partial y}\right) \quad (18)$$

where essentially we have assumed that the specific heats of gas and vapor are equal.

Thermophysical Properties. The properties ρ_l, μ_l, k_l, and λ were obtained directly from [11]. The saturation vapor pressure P_{sat} was used in the form of curve fits to the data in [11], locally linearized for specific problems. The vapor-phase density was calculated according to the ideal-gas law, while gas-species transport properties were calculated following the Chapman–Enskog kinetic theory of gases with the Lennard–Jones potential model. The required force constants were taken from Svehla [12]. The vapor–gas-mixture viscosity was calculated following Wilke [13] and the mixture thermal conductivity following Mason and Saxena [14].

Rearrangement of the Mathematical Problem. The major analytical task is the solution of the vapor-phase conservation equations, (1)–(3) and (18). However, the techniques for accomplishing this task have been established in previous work [3] so that it is convenient to pose the problem as if $(\partial u/\partial y)_{v,i}$ and $(\partial m_1/\partial y)_i$ are known. In this manner the overall closure of the problem is clarified. Also, the simple forms of the differential equations governing conservation of momentum and energy in the liquid film, equations (15) and (6) respectively, allow analytical integration. After so doing, the equations to be solved may be written as

$$-\dot{m} = \frac{\rho_v \mathfrak{D}_{12}}{1 - m_1}\frac{\partial m_1}{\partial y}\bigg|_i \quad (19)$$

$$-\dot{m} = \frac{k_l(T_i - T_w)}{\lambda\delta} \quad (20)$$

$$-\dot{m} = \frac{1}{1 - 0.523}\sqrt{\frac{M_1}{2\pi \mathcal{R} T_i}}\,[P_{1,i} - P_{1,\mathrm{sat}}(T_i)] \quad (21)$$

$$-\int_0^x \dot{m}dx = \frac{\rho_l \delta}{2}\left[u_i + \frac{\rho_l g}{6\mu_l}\delta^2\right] \quad (22)$$

$$u_i = \frac{\rho_l g}{2\mu_l}\delta^2 + \frac{\mu_{v,i}}{\mu_l}\delta\left(\frac{\partial u}{\partial y}\right)_{v,i} \quad (23)$$

which are five equations in the five unknowns T_i, $m_{1,i}$ (or equivalently $P_{1,i}$), $\dot{m}$, u_i, and δ.

Solution Procedure. The numerical procedure used to solve the vapor-phase conservation equations follows [3]. Briefly, the transformation of independent variables $x, y \rightarrow x, \omega$, suggested by Patankar and Spalding [15], is introduced; ω is a nondimensional stream function defined as $\omega \equiv (\psi - \psi_i)/(\psi_e - \psi_i)$. The partial differential equations are then approximated by fully implicit finite-difference forms, and the resulting set of algebraic equations is solved at each step of the overall solution procedure as it is advanced in the x direction. The procedure used to solve the set of equations (19)–(23) depended on the simplifying assumptions that could be invoked. For example, when the gas concentration was high the resulting low condensation rates allowed the assumptions $T_i = T_w$, $P_{1,i} = P_{1,\mathrm{sat}}(T_w)$, and $u_i = 0$; for this situation the overall solution procedure was quite straightforward. Also, even with low gas concentrations the characteristically small temperature drop across the liquid film allowed a simple explicit calculation of the temperature difference $T_i - T_w$ [16].

Initial conditions for the parabolic problem were obtained from solutions valid in the limit $x \rightarrow 0$, where both u_i and the gravitational forcing go to zero. For negligible interfacial resistance the overall problem is self-similar and was solved using the iterative methods of Wortman [17]. With interfacial resistance, $-\dot{m}$ approaches a finite upper bound as $x \rightarrow 0$, given by equation (21) with $P_{1,i} = P_{1,e}$ and $T_i = T_w$. Furthermore, a reasonable value of $x > 0$ could be found for which $\dot{m} \cong \dot{m}|_{x=0}$; the associated vapor profiles were obtained from the self-similar solution by assuming local self-similarity.

Results and Discussion

Numerical solutions for condensation heat transfer from mercury–air and sodium–argon mixtures were obtained, and comprehensive data in the form of q/q_{Nu} versus x are presented in [16]. Here q_{Nu} is the classical Nusselt result based on overall temperature drop $T_e - T_w$ and assuming zero vapor drag

$$q_{\mathrm{Nu}} = \left[\frac{g\rho_l^2 \lambda k_l^3 (T_e - T_w)^3}{4\mu_l x}\right]^{1/4} \quad (24)$$

The parameter values studied included $m_{2,e} = 10^{-5}$, 10^{-4}, 10^{-3}, 10^{-2}, 3×10^{-2}; $u_e = 1$, 3, 10, 30, 100 fps; $\Delta T = T_e - T_w = 0.1$, 0.2, 0.3, 0.5, 1.0, 3, 10, 30 deg F; for mercury–air $T_e = 1200$

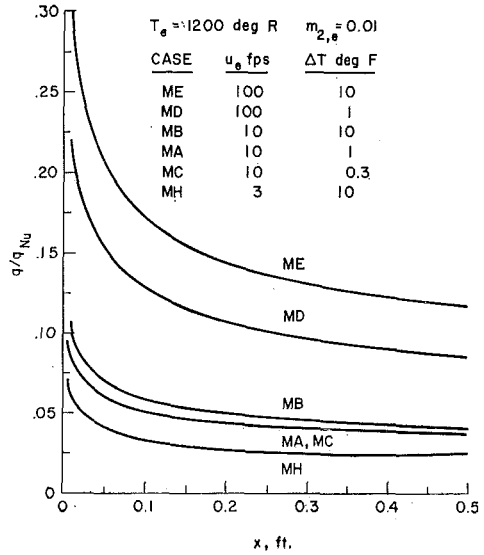

Fig. 1 Condensation heat transfer: mercury–air, T_e = 1200 deg R, $m_{2,e}$ = 0.01; effect of u_e and ΔT

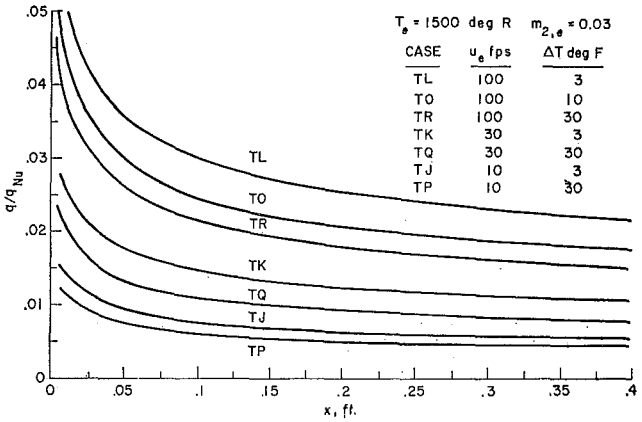

Fig. 2 Condensation heat transfer: sodium–argon, T_e = 1500 deg R, $m_{2,e}$ = 0.03; effect of u_e and ΔT

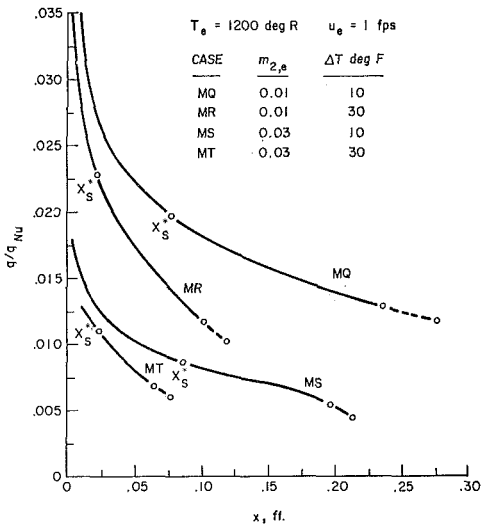

Fig. 3 Condensation heat transfer: mercury–air, T_e = 1200 deg R, u_e = 1 fps; effect of $m_{2,e}$ and ΔT on vapor boundary-layer separation

and 900 deg R, while for sodium–argon T_e = 2000 and 1500 deg R. The length of condenser wall was 0.5 ft; the estimated accuracy of the data for q/q_{Nu} in the range $0.1 \leq x \leq 0.5$ ft is 5 to 10 percent. The average computer cost per case was about $2.50 (IBM 360/91 system). Selected data will be presented here to illustrate (*a*) the effects of the problem parameters, (*b*) the onset of buoyancy-induced vapor boundary-layer separation, and (*c*) the role played by the interfacial resistance.

Results for High Gas Concentration. Figures 1 and 2 show the effect of vapor velocity u_e and overall temperature difference ΔT for mercury–air and sodium–argon respectively. At these high gas concentrations ($m_{2,e}$ = 0.01 and 0.03 respectively) the interfacial resistance and temperature drop across the liquid film are negligible. The main features of the data are (*a*) the heat flux decreases with increased gas concentration, (*b*) the heat flux increases with vapor velocity, and (*c*) the heat flux increases as $x \to 0$. These features are explained using the governing equation for mass transfer across the vapor-phase boundary layer; following Spalding [18] we write

$$\dot{m} = g\mathcal{B} = g\frac{m_{1,e} - m_{1,i}}{m_{1,i} - 1} \tag{25}$$

where $\mathcal{B} = (m_{1,e} - m_{1,i})/(m_{1,i} - 1)$ is the mass-transfer driving force and $g = \rho\mathcal{D}_{12}\mathrm{Nu}_m/x$ is the mass-transfer conductance. As $m_{1,e} \to 1$, $\mathcal{B} \to -1$ and $\dot{m} \to -\infty$; thus the noncondensable-gas problem involves a strongly nonlinear coupling between the factors $\mathcal{B}$ and g. Nevertheless equation (25) gives a qualitative appreciation of the behavior of $\dot{m}$, and hence q ($= \dot{m}\lambda$). An increased gas concentration simply serves to decrease the driving force $\mathcal{B}$ by decreasing the free-stream vapor concentration $m_{1,e}$. In the limit of zero mass transfer, and for negligible buoyancy forcing, the mass-transfer conductance has the usual dependence for flat-plate boundary-layer flow, namely

$$g \propto u_e^{1/2}\rho_e^{1/2}x^{-1/2} \tag{26}$$

The observed dependence of q on u_e and x follows directly from equation (26). The effect of overall temperature drop ΔT is more complex. In Fig. 1 q/q_{Nu} is seen generally to increase with ΔT, although at 10 fps q/q_{Nu} is identical for ΔT = 1 and 0.3 deg F; in Fig. 2 q/q_{Nu} is seen to decrease with increasing ΔT. The effect of ΔT is usually small, but an exception is noted for cases ME and MD in Fig. 1; as ΔT increases from 1 to 10 deg F, q/q_{Nu} increases about 25 percent. The anomaly is explained as follows. The mercury–air system at 1200 deg R has a high vapor density (~0.4 lb/ft³), some fortyfold higher than for sodium–argon at 2000 deg R. Equation (26) shows that the mass-transfer conductance, and hence the condensation rate $-\dot{m}$, will be correspondingly high. At $x \cong 0.3$ ft the values of $-\dot{m}$ are 0.075 and 0.010 lb/ft²-sec for cases ME and MD respectively. Both cases are for the highest vapor velocity, u_e = 100 fps, and vapor drag on the liquid film has a significant effect on q/q_{Nu}. In the limit of strong suction, $\tau_i = -\dot{m}u_e$, which indicates that the higher values of q/q_{Nu} for case ME should be attributed to vapor drag.

Figure 3 illustrates the phenomenon of buoyancy-induced boundary-layer separation. In contrast to the sodium–argon system, the mercury–air system is characterized by a noncondensable gas lighter than the vapor. Thus gas buildup at the interface gives rise to a buoyancy force directed opposite to the external flow, causing the vapor boundary layer to separate at some distance down the wall x_s. Figure 3 shows typical results for u_e = 1 fps. Since the solution is advanced in discrete x-steps, the exact separation point cannot easily be determined; the dashed lines in Fig. 3 represent the steps in which the velocity gradient at the interface goes negative. Combined forced- and free-convection flow on a vertical wall has been analyzed by Acrivos [19] for the situation of zero suction. With condensation the suction rate can be quite high and separation is significantly delayed. From Fig. 7 of [19] for a Schmidt number of 0.32 the distance to separation in the absence of suction is

$$x_s^* = \frac{0.21\rho_i u_e^2}{g(\rho_e - \rho_i)} \tag{27}$$

The values of x_s^* are shown on the curves in Fig. 3. In view of

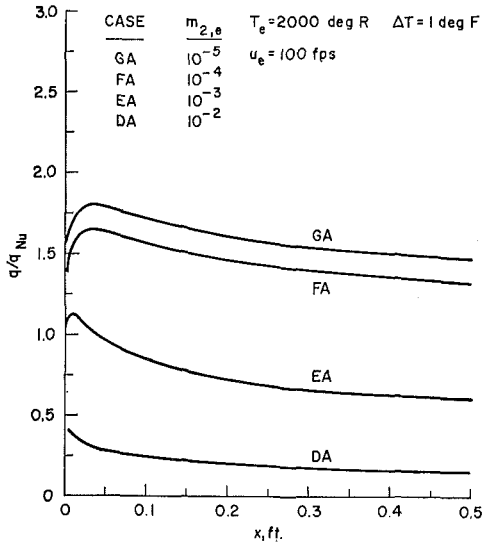

Fig. 4 Condensation heat transfer: sodium–argon, T_e = 2000 deg R, ΔT = 1 deg F, u_e = 100 fps; effect of gas concentration

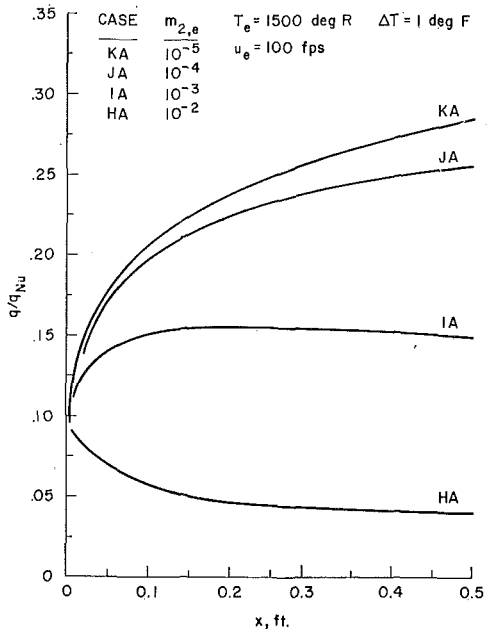

Fig. 5 Condensation heat transfer: sodium–argon, T_e = 1500 deg R, ΔT = 1 deg F, u_e = 100 fps; effect of gas concentration

equation (27) we would expect a fourfold increase in x_s as u_e is increased from 1 to 2 fps. The actual increase was slightly greater due to higher mass-transfer conductances, and hence higher condensation and suction rates associated with increased velocity. The computed vapor velocity profiles were found to assume the characteristic S-shape at separation as the gradient $(\partial u/\partial y)_i$ approached zero. The behavior of the mass-transfer conductance g and hence the interface concentration gradient $(\partial m_1/\partial y)_i$ as separation is approached is also shown by Fig. 3. In general g remains relatively large at separation, though a falling off is in evidence, especially for cases MR and MS.

Results for Lower Gas Concentrations. When the interfacial resistance is included the basic shape of the curves of q/q_{Nu} versus x changes character. Since $-\dot{m}$ now has a maximum value, given by equation (21) with $P_{1,i} = P_{1,e}$ and $T_i = T_w$, and q_{Nu} varies as $x^{-1/4}$, the ratio q/q_{Nu} must approach zero as $x \to 0$. In general q/q_{Nu} increases rapidly with x to attain a maximum value; thereafter the character of the curves is similar to that of the curves of Figs. 1 and 2, due to the decreased interfacial resistance accompanying the lower values of heat flux. In some cases the

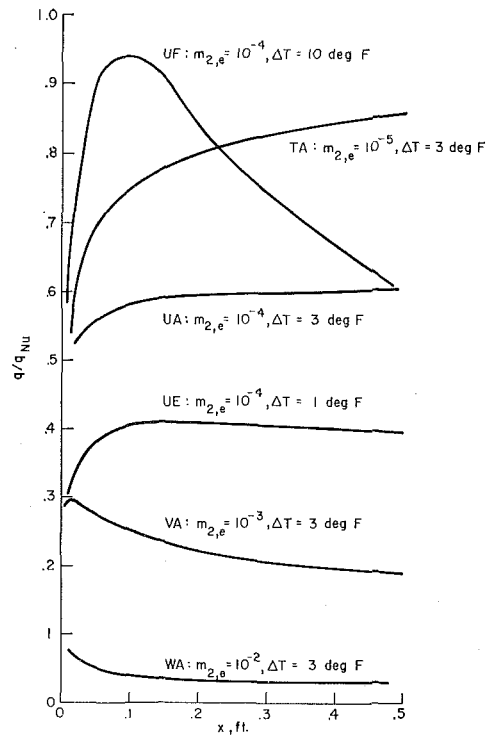

Fig. 6 Condensation heat transfer: mercury–air, T_e = 900 deg R, u_e = 100 fps; effect of ΔT and gas concentration

expected maximum in q/q_{Nu} is not attained before x = 0.5 ft, the location at which computing was usually stopped; in other cases the maximum occurs at too small a value of x to be shown in the figures.

Figure 4 shows the effect of gas concentration for the sodium–argon system at T_e = 2000 deg R; the marked sensitivity of q/q_{Nu} to $m_{2,e}$ is readily seen. Figure 5 shows the effect of gas concentration at T_e = 1500 deg R; comparing Figs. 4 and 5 demonstrates that the q/q_{Nu} levels are much lower at the lower temperature. This feature is a result of the marked temperature-level-dependence of the interfacial resistance; the saturation vapor pressure increases exponentially with temperature and the interfacial resistance is roughly inversely proportional to vapor pressure. Figure 5 also shows that for the lowest gas concentrations $m_{2,e} = 10^{-5}$ and 10^{-4} (cases KA and JA respectively) the maximum value of q/q_{Nu} is not attained before x = 0.5 ft.

Results for the mercury–air system are shown in Fig. 6; since the temperature level is low (900 deg R) and vapor velocity high (100 fps), the interfacial resistance can be expected to have a significant effect on q/q_{Nu}. The delayed maxima for cases UA and TA confirm this expectation. A comparison of cases UF and UA indicates a reversal in the influence of ΔT on q/q_{Nu} at $x \cong 0.5$ ft, a further illustration of the complex manner in which ΔT enters the problem. Perhaps the most striking feature of Figs. 4–6 is that the variation of q/q_{Nu} with x shows marked differences from case to case as the vapor velocity, temperature level, overall temperature difference, and gas concentration are varied.

References

1 Sparrow, E. M., and Lin, S. H., "Condensation Heat Transfer in the Presence of a Noncondensable Gas," JOURNAL OF HEAT TRANSFER, TRANS. ASME, Series C, Vol. 86, No. 3, Aug. 1964, pp. 430–436.

2 Minkowycz, W. J., and Sparrow, E. M., "Condensation Heat Transfer in the Presence of Noncondensables, Interfacial Resistance, Superheating, Variable Properties and Diffusion," *International Journal of Heat and Mass Transfer*, Vol. 9, 1966, pp. 1125–1144.

3 Denny, V. E., Mills, A. F., and Jusionis, V. J., "Laminar Film Condensation From a Steam-Air Mixture Undergoing Forced Flow Down a Vertical Surface," JOURNAL OF HEAT TRANSFER, TRANS. ASME, Series C, Vol. 93, No. 3, Aug. 1971, pp. 297–304.

4 Denny, V. E., and Jusionis, V. J., "Effects of Noncondensable

Gas and Forced Flow on Laminar Film Condensation," *International Journal of Heat and Mass Transfer*, Vol. 15, 1972, pp. 315–326.

5 Wilhelm, D. F., "Condensation of Metal Vapors: Mercury and the Kinetic Theory of Condensation," Argonne National Laboratory Report 6948, 1964.

6 Sukhatme, S. P., and Rohsenow, W. M., "Heat Transfer During Film Condensation of a Liquid Metal Vapor," JOURNAL OF HEAT TRANSFER, TRANS. ASME, Series C, Vol. 88, No. 1, Feb. 1966, pp. 19–28.

7 Denny, V. E., Mills, A. F., and Gardiner, J. R., "Nonsimilar Solutions for Laminar Film Condensation of Liquid Metals," *Proceedings of the Fourth International Heat Transfer Conference*, Elsevier, Amsterdam, The Netherlands, 1970, paper Cs2.1.

8 Schrage, R. W., *A Theoretical Study of Interphase Mass Transfer*, Columbia University Press, New York, N. Y., 1950.

9 Mills, A. F., and Seban, R. A., "The Condensation Coefficient of Water," *International Journal of Heat and Mass Transfer*, Vol. 10, 1967, pp. 1815–1827.

10 Wilcox, S. J., and Rohsenow, W. M., "Film Condensation of Potassium Using Copper Condensing Block for Precise Wall-Temperature Measurement," JOURNAL OF HEAT TRANSFER, TRANS. ASME, Series C, Vol. 92, No. 3, Aug. 1970, pp. 359–371.

11 Weatherford, W. D., Jr., et al., "Properties of Inorganic Energy Conversion and Heat-Transfer Fluids for Space Applications," WADD Technical Report 61-96, Nov. 1961.

12 Svehla, R. A., "Estimated Viscosities and Thermal Conductivities at High Temperatures," NASA TR R-132, 1962.

13 Wilke, C. R., "A Viscosity Equation for Gas Mixtures," *J. Chem. Phys.*, Vol. 18, 1950, pp. 517–519.

14 Mason, E. A., and Saxena, S. C., "Approximate Formula for the Thermal Conductivity of Gas Mixtures," *Phys. Fluids*, Vol. 1, 1958, pp. 361–369.

15 Patankar, S. V., and Spalding, D. B., "A Finite Difference Procedure for Solving the Equations of the Two-dimensional Boundary Layer," *International Journal of Heat and Mass Transfer*, Vol. 10, 1967, pp. 1389–1411.

16 Turner, R. W., "Forced Flow Condensation of Liquid Metals on a Vertical Wall with a Noncondensable Gas," *PhD dissertation*, School of Engineering and Applied Science, University of California, Los Angeles, Calif., June 1971.

17 Wortman, A., "Mass Transfer in Self-Similar Boundary-Layer Flows," PhD dissertation, School of Engineering and Applied Science, University of California, Los Angeles, Calif., 1969.

18 Spalding, D. B., *Convective Mass Transfer*, McGraw-Hill, New York, N. Y., 1963.

19 Acrivos, A., "Combined Laminar Free and Forced Convection Heat Transfer in External Flow," *AIChE Journal*, Vol. 4, 1968, pp. 285–289.

CHARLES J. HURST
Associate Professor,
Department of Mechanical Engineering,
Virginia Polytechnic Institute
and State University,
Blacksburg, Va.
Mem. ASME

DONALD R. OLSON
Professor,
Department of Mechanical Engineering,
Pennsylvania State University,
University Park, Pa.
Mem. ASME

Conduction through Droplets during Dropwise Condensation

An experimental investigation was undertaken in which dropwise condensation was caused to occur on the upper side of a 0.001-in-thick horizontal copper condensing surface. The lower side of the condensing wall was convectively cooled, and the cooled-side temperatures under growing droplets were measured using infrared-radiation techniques. Temperature measurements showed good agreement with the results of a finite-element analysis of the droplet and condensing surface. Both experimental and analytical results pointed to the existence of an area of very high heat transfer right around the droplet perimeter, and to the importance of the condensing wall as a heat-diffusing mechanism in dropwise condensation.

Introduction

THE SUBJECT of dropwise condensation has received a considerable amount of attention since its discovery as a separate entity by Schmidt, Schuring, and Sellschopp [1][1] in 1930 and the confirmation of its existence by Spoelstra [2] in 1931. Subsequent investigations into dropwise condensation can be considered within the framework of three essentially separate categories.

First, there have been a number of strictly experimental investigations undertaken to determine the magnitudes of heat-transfer rates possible with dropwise condensation [3–8]. The purely experimental approach, however, has had relatively little success. The only general conclusion that has been reached is that dropwise condensation can allow much higher heat-transfer rates than even the comparatively effective filmwise condensation. One of the major problems with the experimental approach has been the large number of factors which can influence dropwise condensation.

The second category of investigations concerning dropwise condensation has been in the area of finding suitable "promoters" which would cause dropwise condensation to occur on clean metal surfaces. The classical papers in this area were published in 1933 and 1935 by Nagle and Drew [9] and by Drew, Nagle, and Smith [10]. More recent papers [11–14] have discussed the theoretical requirements for a good promoter: It should consist of a long-chain hydrophobic hydrocarbon molecule with a radical on one end which can be strongly adsorbed onto the metal surface. Recent advances in the application of very thin plastic films to metal have opened additional possibilities for producing long-lasting surfaces giving dropwise condensation.

The third category of investigation has been into the basic mechanism of dropwise condensation. Explanations of the physical processes occurring during dropwise condensation polarized around two conflicting ideas. On the one hand, several attempts have been made to explain dropwise condensation by starting with the assumption that the droplets must pose a large resistance to heat flow, and thus all condensation of importance must occur directly on the condensing surface or on a very thin liquid layer between droplets [15–20]. Heat transfer through the droplets was assumed to be negligible. The opposing school of thought has held that the free-surface-energy relationships which must be satisfied before dropwise condensation can occur preclude either the condensation of vapor directly onto a bare condensing surface between droplets or the formation of any thin liquid films.

A review of the experimental and analytical evidence presently available in the literature has led most observers to the conclusion that the important phenomena occurring during dropwise condensation involve the droplets themselves rather than anything between the droplets. The bulk of the evidence for this has centered around studies of droplet nucleation and droplet growth rate. However, the exact mechanism of heat transfer through the droplet has still not been conclusively determined. Nearly all the analytical studies which have been done have been based on conduction, and have analyzed the heat transfer for a hemispherical droplet with known, fixed temperatures on the outer boundaries. In most studies, the hemispherical surface of the droplet has been assumed to be at the saturation temperature of the condensing vapor and the flat base of the droplet has been assumed to be at some other uniform temperature. This has led to an anomaly at the perimeter of the droplet where the two surfaces intersect and where two boundary temperatures have thus been assigned. Since the length of the conduction path through the droplet goes to zero as this perimeter is approached,

[1] Numbers in brackets designate References at end of paper.

Contributed by the Heat Transfer Division of THE AMERICAN SOCIETY OF MECHANICAL ENGINEERS and presented at the AIChE-ASME Heat Transfer Conference, Denver, Colo., August 6–9, 1972. Manuscript received by the Heat Transfer Division November 30, 1970; revised manuscript received July 19, 1971. Paper No. 72-HT-50.

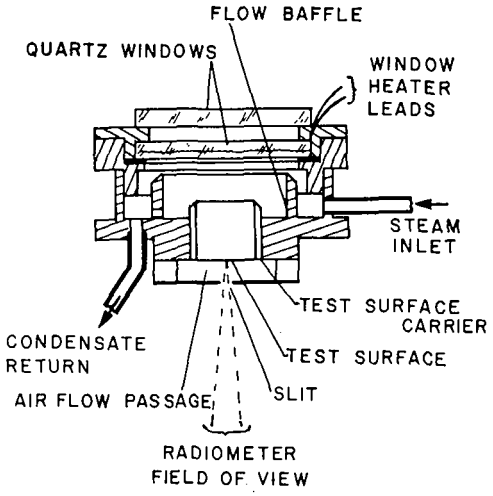

Fig. 1 Cross section of the test condenser

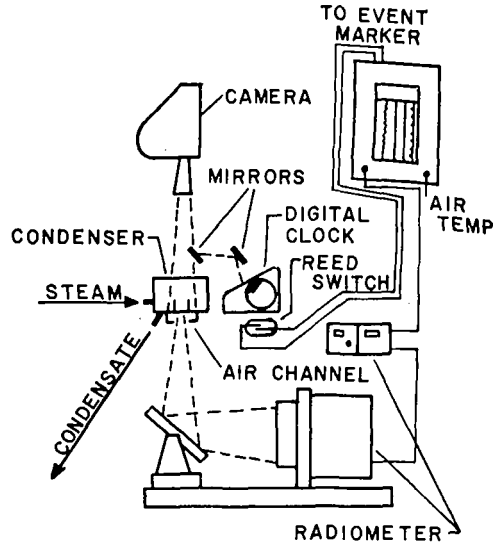

Fig. 2 Schematic arrangement of the salient test apparatus

the predicted heat-transfer rates have gone to infinity. This has generally been regarded as a mathematical difficulty in the method of solution, and the usual recourse has been to ignore some arbitrarily chosen region of the droplet perimeter from the final heat-transfer-rate calculations. If conduction is the appropriate mechanism of heat transfer through the droplet, however, solutions near the droplet perimeter so dominate the heat-transfer-rate calculations that the answers obtained depend strongly on just how close to the edge of the droplet one considers the temperature solutions to be valid. McCormick and Baer [21], for example, obtained a 60 percent increase in the heat-transfer rate predicted through a single droplet by moving the outer limit of their heat-transfer-rate integration from 95 to 99 percent of the droplet radius.

One of the most recent conduction analyses has been published by Umur and Griffith [13]. They studied a hemispherical droplet with an isothermal base, but used an equivalent film coefficient derived from the kinetic theory of gases to predict the coupled heat and mass transfers from the vapor to the droplet. The Legendre series they obtained for their temperature solution converges only slowly, if at all, over parts of the droplet if the condensing film coefficient gets large or the thermal conductivity of the condensate is too low. They circumvented this difficulty by integrating over the droplet to find an average temperature on the hemispherical surface.

The question of whether or not conduction is a valid mechanism on which to base single-droplet heat-transfer-rate analyses has not been conclusively settled by previous investigators. A recent analytical investigation undertaken by Lorenz and Mikic [22] has indicated that thermocapillary flow due to surface-tension effects along the droplet surface is not an important part of the problem. This conclusion was also reached by the authors of this paper from a simple experiment in which titanium dioxide particles were used to help visualize the flow within condensate droplets. Observation of the particles indicated very little flow except for a brief period following the coalescence of the droplet with a neighboring droplet. (Immediately following such a coalescence intense mixing took place.)

In the investigation described in this paper, attention was focused on the problem of heat transfer through a droplet due to conduction. If conduction is the correct mechanism, then very high heat-transfer rates should occur right near the droplet perimeter, while the heat-transfer rates through the center of the droplet should be much lower. The net result of this, for a convectively cooled condensing wall, should be a temperature gradient along the condensing surface under the droplet, with higher temperatures occurring under the droplet perimeter. This investigation was concerned with discovering whether, in fact, such a temperature gradient did exist and whether or not its magnitude could be predicted on the basis of a single droplet analysis based on conduction.

The primary thrust of this investigation was experimental. The experimental procedure employed was to measure the temperatures obtained on the cooled side of a very thin condensing wall at various points immediately under growing droplets. Copper foil having a thickness of 0.001 in. was used as the condensing surface to limit the lateral diffusion of heat under the droplet and thus to accentuate the expected temperature profile. These temperatures were then compared with those obtained from a finite-element analysis of a hemispherical droplet resting on a cylindrical condensing surface of slightly larger outside diameter.

Experimental Investigation

A preliminary analytical investigation revealed that measurable temperature gradients could be expected on the cooled side of a condensing surface only for relatively large droplets resting on very thin condensing walls. The temperature gradient was of interest because it would allow identification of areas of high heat-transfer rate under the droplet, and thus give an indication of whether or not the expected high heat-transfer rates were taking place around the edge of the droplet.

The condensing surface chosen for this investigation consisted of 0.001-in-thick copper foil. This was placed in a horizontal position to encourage the growth of the large droplets needed. The condenser was designed to allow easy interchange of the $^7/_8$-in-dia condensing surfaces and to keep the velocity of the steam over the test surface essentially zero. Heat-transfer rates on the order of 12,000 Btu/hr-ft^2 were realized with this apparatus. A cross section of the condenser is shown in Fig. 1.

A schematic diagram of the complete testing arrangement is shown in Fig. 2. The steam used as the condensing vapor was generated in a small, electrically heated boiler, using a distilled-water charge. Infrared radiometry was chosen as the means for measuring, without appreciably changing, the temperatures on the cooled side of the condensing surface. Air forced through a rectangular channel at high velocities was used as the cooling medium, as it was essentially transparent to the infrared radiation of interest. The cooling-air temperature was measured with a single, bare, unshielded thermocouple located in the center of the channel and just downstream of the condensing surface. Errors possible with this arrangement were not considered significant in view of the large temperature difference between the condensing surface and the air. A visual record of the sizes and locations of condensate droplets was obtained by a movie camera mounted above the condenser.

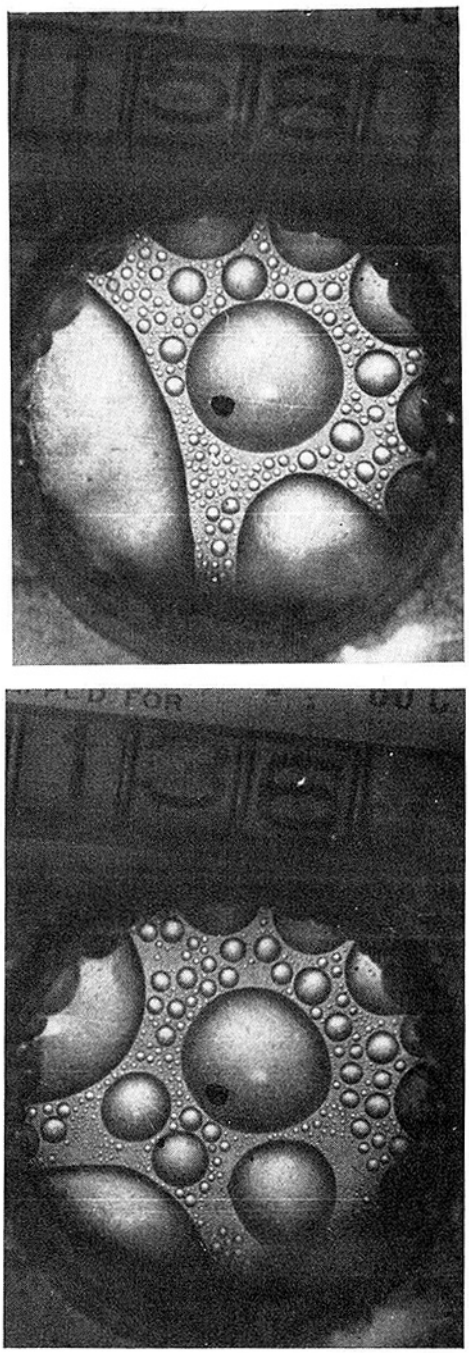

Fig. 3 Photographic record of condensation events corresponding with the radiometer record of Fig. 4; black dot in center indicates location whose temperature was being monitored

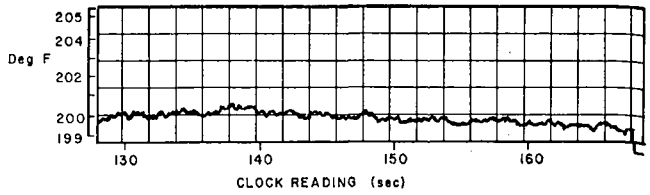

Fig. 4 Typical radiometer output record; corresponds with condensation events shown in Fig. 3

Very high air-flow rates were used through the 1/4-in. by 2-in. cross-section channel in order to obtain sufficiently high values for the air-side heat-transfer film coefficient. Calculations predicted a value of 92 Btu/hr-ft²-deg F, and measurements made using a dummy test assembly incorporating a copper rod heated on one end yielded results ranging from 96 to 115 Btu/hr-ft²-deg F. For purposes of calculation in this investigation an average figure of 105 Btu/hr-ft²-deg F was used.

Contaminants and noncondensable gases always present problems in experiments involving condensation. The precautions taken to prevent contamination began with the use of a specially constructed closed steam-supply system which was chemically cleaned after final assembly. The entire system was carefully sealed so that it could maintain a vacuum of about 28 in. of mercury for a 24-hr period without additional pumping. Prior to each experimental run the system was evacuated using a vacuum pump. The pressure within the system during evacuation was essentially equal to the saturation pressure of the water in the boiler, and equaled about 1 1/2 to 2 in. of mercury. The point for attachment of the pump was chosen such that the flow of vapor would help to flush out any noncondensable gases in the condenser or in the lines. The boiling occurring in the liquid charge during this time helped to drive out any remaining air in the triply distilled water. The water manometer used for pressure measurement during the runs could not be left connected during this time; to prevent the introduction of inert gases from this source the manometer and all connecting lines (which were deliberately kept short) were filled with water. During actual testing the vapor pressure was kept above atmospheric pressure to further insure against air leakage. While no direct measurements were made of the amount of noncondensable gases present in the vapor, the consistency of results obtained from run to run indicated very little effect on the experimental results from this cause. On those occasions when some air entered the system due to equipment malfunction, a dramatic slowing of the condensation rate occurred which was easy to detect.

It was necessary to coat the copper surface with a promoter to insure dropwise condensation. Benzyl mercaptan was chosen for this because it had contact angles near 90 deg when water vapor was condensing, so that condensate droplets were very nearly hemispherical. The promoter was swabbed onto the condensing surface following a thorough chemical cleaning. Excess promoter was then rinsed off, both before installation in the condenser and during the calibration of the radiometer which preceded each run.

The radiometer which was used to measure the temperature of the cooled side of the condensing wall was found by direct calibration to have a sensitivity of about 1 v/deg F when viewing the chemically oxidized copper test surfaces. Calibration was done with each test surface in place immediately prior to each run. It was accomplished using a length of tubing placed on the open condenser in such a way that the copper test surface formed a part of the bottom of an open container. This "container" was then filled with water which was heated and vigorously stirred. With no air flow through the channel, the downward-facing condensing surface was assumed to be at the same temperature as the stirred water with which it was in contact on its upper surface. The water-bath temperature was measured using a precision potentiometer and three copper–constantan thermocouples with an ice-bath reference.

The radiometer measured an average temperature over an area about 1/32 in. in diameter. The 98 percent response time of the instrument, as used in this investigation, was found to be 0.6 sec, which was adequate for the comparatively slow condensation events under scrutiny. Initially, it was hoped to obtain an entire temperature profile under a droplet by scanning the field of view of the radiometer across the test surface. The variations in emissivity of the test surfaces proved an insurmountable problem in this, however, since variations in emissivity were indistinguishable from changes in temperature when running. It was found necessary to fix the location of the field of view of the radiometer and then to calibrate each new test surface in place just prior to running a test. In fact, the problem of obtaining a high and reasonably uniform emissivity on the cooled

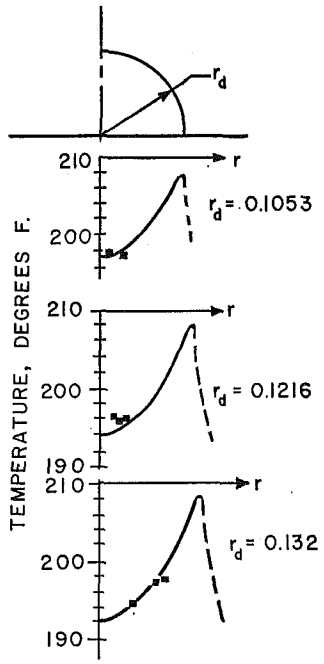

Fig. 5 Comparison of experimental results (black squares) with analytically predicted temperature profiles for several droplets; vapor temperature = 210.5 deg F; coolant temperature = 92.0 deg F

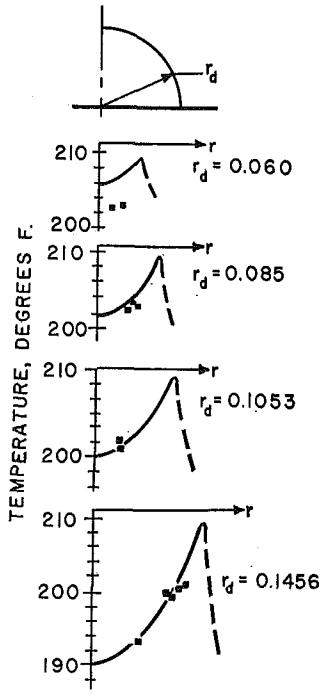

Fig. 6 Comparison of experimental results (black squares) with analytically predicted temperature profiles for several droplets; vapor temperature = 211.5 deg F; coolant temperature = 92.0 deg F

side of the test surface was one of the most difficult parts of the experimental side of this investigation. Paints and coatings were ruled out, as even a coating 1 mil thick had an appreciable insulating effect and thus upset the experiment. The desired effect was finally obtained by roughening the copper foil using fine grit and a low-pressure air gun, then oxidizing the cooled side of the copper foil after it had been mounted on its support for installation in the test condenser.

The use of a fixed field of view for the radiometer worked better than might be expected. The random coalescences between droplets served to move the droplets relative to the radiometer field of view at reasonably frequent intervals. Thus it was possible to obtain temperatures under different parts of a droplet having nearly the same diameter.

Samples of the output records obtained in this investigation are shown in Figs. 3 and 4. Fig. 3 shows a typical photographic record obtained of the condensation events, with a black dot placed on the photographs to indicate the position and relative size of the area being monitored by the radiometer for temperature. The radiometer record for the time period covered by the photographs has been shown in Fig. 4.

Further details and discussion of the experimental equipment can be found in Hurst [23].

Results of the Experimental Investigation

Some typical results from the experimental investigation are shown in Figs. 5 and 6. The experimental results are shown as squares. The temperature profiles shown came from a finite-element analysis to be discussed in the following section.

The experimental results are presented in the form given because the temperatures measured were a strong function of both the droplet diameter and of the radial location of the spot where the temperature was being measured. The information available on any one droplet size was limited by the testing method. It was necessary to sift through the data obtained from different runs and find occasions when the area within the radiometer field of view was covered with droplets having identical diameters for tests in which the saturation pressures in the condenser and the cooling-air temperatures were identical.

Since the droplet locations were somewhat random, a great deal of data had to be taken in order to find the information shown. In the process of running the tests and reviewing the data, however, a number of things became evident. The most important of these was that the surface temperature increased as the edge of the droplet was approached from the inner part of the droplet. This has been indicated in the results shown, and it was even more dramatically illustrated during a test run. Droplet movement due to coalescence often placed the radiometer field of view at a different radial location under a droplet whose diameter had been increased by a very small and often negligible amount. If the droplet perimeter were closer to the radiometer field of view, the temperature of the condensing surface increased, whereas if the radiometer field of view ended up farther from the droplet edge the temperature was found to decrease.

Further confirmation of the importance of the liquid–metal–vapor junction in the transferring of heat came from the apparently erratic temperature changes noticed toward the end of a run when the condensing surface became covered with several rather large puddles of condensate. The temperature changes were found to be associated with the movement of one of the edges of the puddles of condensate over the area where the temperature was being monitored. Markedly higher temperatures were observed around the edge of a puddle, indicating much higher heat-transfer rates in that vicinity.

Analytical Investigation

The analytical part of this investigation was undertaken to determine if the temperatures measured experimentally could be predicted on the assumption that heat transfer through growing droplets occurred primarily due to conduction. Since experimental measurements were made on the cooled side of the condensing wall, it was necessary to include a portion of the metal surface in the analysis.

The model chosen for analysis is indicated in Fig. 7. A saturated vapor was assumed to be in contact with a hemispherical condensate droplet which rested on a flat, convectively cooled condensing surface. An equivalent interfacial "film" coefficient was defined to calculate the coupled heat- and mass-transfer rates from the saturated vapor to the condensate surface as func-

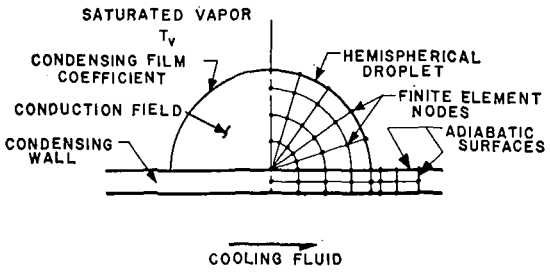

Fig. 7 Physical model considered in the analysis

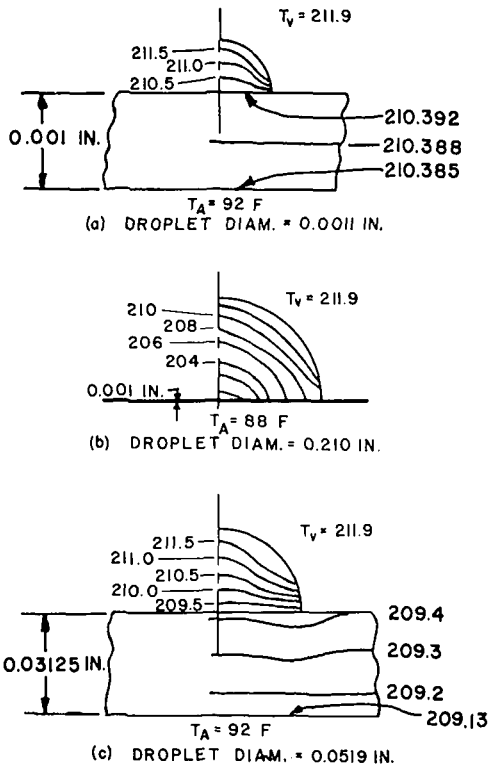

Fig. 8 Analytical results for droplets of different sizes resting on various copper condensing walls

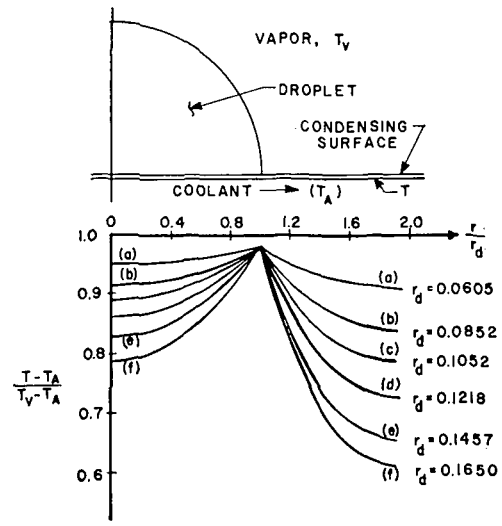

Fig. 9 Summary of analytical results shown on dimensionless coordinates; copper condensing wall 0.001 in. thick

tions of the temperature difference between the vapor and the droplet surface. The value for this film coefficient was obtained from work done by Silver [24] and Schrage [25], among others, who used the kinetic theory of gases as a starting point. Within the droplet and within the condensing surface the mechanism of heat transmission was considered to be conduction. The accumulation of condensate within the droplet necessarily implies a growth in the droplet diameter, and this was included in the analysis. This inclusion brought with it the necessity of using transient rather than steady-state conduction equations.

The part of the condensing surface which was in contact with the condensing vapor, but which was outside the area covered by the droplet, was considered to be adiabatic. Thus, one role of the promoter could be envisioned as imposing a reversible (adiabatic) barrier between the vapor and condensing surface when it is not covered by liquid droplets. Since a single droplet was to be studied, the droplet was assumed to be one of a number of similar droplets resting on the surface, and a general boundary condition was required for solution. This was approximated by a cylindrical adiabatic surface through the condensing wall at twice the droplet radius. These assumptions gave rise to the prediction of condensing-surface temperatures which were unrealistically far below the saturation temperature for the vapor with which the surface was in contact. In retrospect, the primary error in these assumptions appears to be in the choice of the maximum diameter of the condensing wall. Some subcooling should exist in that part of the condensing wall which is not covered by a droplet, but when a critical value of subcooling is reached, nucleation of a new droplet should start. McCormick and Baer [21] have estimated that 0.4 deg C might be the critical amount of subcooling for steam on a promoted surface. Based on this, the analytical results obtained should predict droplet nucleation very near the edge of most droplets. For other vapor and condensing-wall combinations, however, the situation might be quite different. For example, Koutsky, Walton, and Baer [26] report critical subcooling of 15 to 19 deg C for polyethylene condensing onto single-crystal alkali halides. This would imply a comparatively wide droplet spacing and dictate use of outer-condensing-wall diameters comparable to those used in this analysis.

The physical model which has been described leads to a coupled set of partial differential equations. These equations were written, but all attempts to find a closed-form analytical solution have proven fruitless. The approach, therefore, was through a finite-element analysis. The nodes chosen to represent the lumped thermal capacities have been indicated in Fig. 7.

The calculations required for the finite-element analysis were performed on a computer using a backward-difference approach. Backward differences in time were selected to minimize computation-stability problems, particularly in the elements near the center of the droplet. A fractional element at the droplet boundary was changed in size after each time step to account for the necessary increase in droplet size due to condensate accumulation. This necessitated changing a large number of coefficients in the finite-element equations after each time step, preventing the efficient use of any matrix-inversion technique and forcing the use of large blocks of computer time to obtain the desired answers.

Some sample results obtained from the analysis are shown in Fig. 8, where the isotherms have been shown for some droplets of different sizes on a thin condensing surface as well as for a droplet resting on a relatively thick condensing surface. Results are also shown in Fig. 9, but in that figure only the air-side condensing-wall temperature is shown for comparison with the experimental results.

As can be seen from an examination of the predicted isotherms in Fig. 8, the condensing wall, with its high thermal conductivity, had a marked effect on the temperature distributions under and within the droplet. For either very small droplets or comparatively thick condensing surfaces, the conductance of the metal was sufficiently high to cause the base of the droplet to become very nearly isothermal. For larger droplets resting on very thin condensing surfaces, however, a considerable temperature gra-

dient was predicted along the metal wall. These profiles reached a peak temperature underneath the edge of the droplet, indicating the expected region of high heat transfer from the droplet. Just how sensitive the solution was to the condensing-wall thickness was of some interest in the design of the experimental equipment; for a droplet diameter on the order of 0.1 in., a change in condensing-wall thickness from 0.001 in. to 0.005 in. was sufficient to make the base of the drop nearly isothermal.

The sensitivity of the temperature and heat-transfer solutions to the ability of the condensing wall to transfer heat laterally underneath and around droplets is one of the interesting results from this investigation. Apparently the condensing wall acts very much like an extended surface in convective-cooling situations. It receives heat from the droplet perimeter, where very high heat-transfer rates are possible, and diffuses this heat laterally over a larger area so that it can be transferred into the coolant across a comparatively high thermal resistance.

A detailed study of the temperature predicted throughout the droplet and condensing wall at successive times in the calculation indicated that transient thermal effects were of very little consequence in the model as defined. It now appears evident that a steady-state-temperature solution assuming an isothermal droplet base is justified for most practical applications. Of course, in this investigation the experimental conditions were chosen so as to obtain large temperature gradients under droplets, so the results from the finite-element analysis were necessary for comparison with experimental information.

Finally, an attempt was made to use the temperature results to calculate the rate of heat transfer through a droplet [23]. The limitations of a finite-element analysis became evident here, as it was found that from 83 to 98 percent of the calculated total heat transfer through a droplet was coming in through the "corner" element where the hemispherical surface of the droplet intersected the condensing surface, even for very small droplets. Droplet growth rates obtained represented primarily the increase in the hemispherical liquid-surface area of this element, and thus were not considered reliable. It appears that a good solution to the heat- and mass-transfer problem considering just the area very near the perimeter of the droplet could predict the overall heat-transfer rate to within about 15 percent or better even if the contributions of the upper part of the droplet were ignored.

The results of McCormick and Westwater [27] also support this view. Assuming a hemispherical droplet, constant thermal properties, and a heat-transfer rate proportional to an exponent of the droplet diameter, $q = Cd^n$, it can be shown that [23] the droplet radius is a function of time according to the expression

$$r^{(3-n)} = \frac{2^{(n-1)}(3-n)c}{\pi \rho_c L} t + r_0^{(3-n)}$$

where r is droplet radius, ρ_c is condensate density, L is latent heat of vaporization, r_0 is initial droplet radius, and t is time. If the heat-transfer rate is proportional to droplet diameter, $n = 1$, and the expression becomes

$$r^2 = (\text{const})\, t + r_0^2$$

On the other hand, if the heat-transfer rate through a droplet is proportional to the hemispherical surface area of the droplet, it would be expected that $q = Cd^2$ ($n = 2$), and the expression shows that the droplet growth rate should be constant. The experimental results of McCormick and Westwater, when examined closely, show the apparent relationship to be

$$r^{1.75} = (\text{const})\, t + r_0^{1.75}$$

giving $q = Cd^{1.25}$. Apparently, even for the microscopically small droplets investigated by McCormick and Westwater, the heat-transfer rate into a droplet is much more closely related to its diameter than to its hemispherical surface area.

Observations on the Results of This Investigation

The first and most obvious observation is that there was very good agreement between the predicted temperatures and those measured in the experiments, despite some of the restrictive assumptions made in setting up the analysis and the approximations inherent in the finite-element approach. This is particularly true in areas near the droplet center line.

Because of the finite diameter of the area where the temperature was being measured by the radiometer, it was impossible to determine experimentally the temperature right under or just outside of the edge of a droplet. This was unfortunate, since it was at these locations that the accuracy of the finite-difference solution and the assumptions was the least. However, the trend in the experimental results unmistakably bore out the results obtained analytically: A significantly higher temperature did exist right under the edge of the droplet, which indicated a very high heat-transfer rate in that vicinity. The droplet thus becomes, in effect, a mechanism for producing a very "thin" cooled liquid perimeter onto which the vapor can readily condense.

A conclusion of engineering importance then emerges from examination of the mean temperatures under different-sized droplets: It can be seen that the mean temperature under a small droplet is higher than the mean temperature under a large droplet. Since the controlling thermal resistance in a dropwise-condensation situation is usually on the coolant side of the wall, a higher condensing-surface temperature implies that the overall heat transfer will be greater. Thus small droplets will be more "active" in transferring heat than large droplets, and the most desirable situation is to have the condensing surface covered with a population of droplets which are as small in diameter as possible. This conclusion was verified experimentally during the early stages of a run, when the condensing surface was covered by a rather uniform population of small droplets. During this period, the average temperature being measured by the radiometer dropped steadily as the average droplet diameter increased. Temperatures measured were consistent with the mean temperatures predicted for very small droplets. Similar results were observed when droplet coalescence suddenly swept the area where the temperature was being measured free of condensate: The temperature of this area quickly rose to a value consistent with the nucleation and growth of a population of very small droplets.

The next important observation has to do with the way in which the droplet reacts with the condensing surface. So far as the condensing surface is concerned, the droplet could be replaced with a ring heat source of the appropriate intensity. This is a useful concept, because it then becomes obvious that one of the primary roles of the condensing surface is to take this relatively concentrated heat input and diffuse it laterally so that it can be transferred out of the condensing surface across a comparatively high heat-transfer resistance into the coolant stream. It operates in a manner entirely analogous to a fin in a forced-convection situation. This is an important conclusion, as it implies that there must be some sort of minimum condensing-wall thickness below which its function as a fin cannot be efficiently carried out. In other words, the minimum condensing-wall thickness may not be best for use with dropwise condensation. Calculations done in designing the experimental apparatus, for example, predicted lower heat-transfer rates when very thin condensing surfaces were tried.

The role of the condensing wall in dropwise condensation has been recognized by other investigators, and in particular by Mikic [28]. Mikic pointed out that nonuniform temperatures could be expected on condensing walls during dropwise condensation due to the varying sizes of the droplets in an assumed population. He then proceeded to discuss this effect in terms of a "constriction resistance" which was a pseudo–thermal resistance introduced into the analysis to account for the fact that the surface area of the condensing wall available for small "active"

droplets was reduced because of the presence of neighboring large "inactive" drops. The latter he assumed to be adiabatic because of their relative inefficiency in transferring heat to the condensing wall in terms of the surface area they covered.

The ring-heat-source concept advanced and the experimental evidence presented in this investigation lead to very nearly the same conclusions advanced by Mikic, even though this investigation was based on consideration of a single droplet and Mikic's work was based on some assumptions about the droplet population as a whole. For example, a very small ring heat source (small droplet) placed on a surface of high lateral conductance (due either to a very high thermal conductivity or a relatively thick surface) would be expected to yield very little temperature variation in the condensing wall. This was predicted by the finite-element analysis. In Mikic's terminology, the "constriction resistance" for this individual droplet would be negligible. For many engineering situations this would certainly be the case. This investigation gives some basis for deciding when such an assumption would be justifiable by considering condensing-wall temperatures under a single droplet. Mikic also postulated that growth rates of neighboring "active" drops would be reduced by the presence of other active droplets. It is evident that a number of ring heat sources placed close together on a surface of high lateral conductance would interact to raise the mean surface temperature, particularly if the controlling resistance were on the cooled side. Thus a population of small droplets would give a higher heat-transfer rate. This analysis also indicates (as Mikic's did not) that the spacing between such active droplets could be affected by the conductance of the condensing wall. If, as postulated in this investigation, the heat-transfer rate into a droplet is proportional to its perimeter, then the net heat-transfer rate per unit of condensing surface covered by the drop is inversely proportional to its diameter. Mikic's assumption that large droplets contribute little to the total heat transfer can then be justified on the basis that a droplet one order of magnitude larger in diameter would transfer one order of magnitude less heat per unit of condensing surface covered. This analysis, again, gives some basis for deciding the degree of accuracy involved in Mikic's assumptions.

In summary, the results of this investigation show clearly that the lateral conductance of the condensing wall is a very important parameter in dropwise condensation.

The nonuniformity of the wall temperature becomes a serious problem in the attempt to define and measure a heat-transfer film coefficient for dropwise condensation. Use of such a film coefficient assumes the existence of a specific temperature difference between the vapor and the wall surface. As postulated by Mikic, and as demonstrated experimentally in this investigation, appreciable temperature variations may occur on a condensing wall. In the experimental work undertaken in this investigation, for instance, conditions were chosen to obtain temperature variations on the surface of 10 deg F. About the best that can be done, therefore, is to talk about a mean temperature difference based on an average temperature over the condensing-wall surface. If the population of droplets on the wall is not stationary, in the statistical sense, then the mean temperature must also be a time average. The problems in trying to measure such a time and space average are formidable, and doubtless account for much of the spread reported in experimental dropwise-condensation film coefficients.

Conclusion

It has been shown in this investigation that condensing-surface temperatures in dropwise condensation can be predicted by assuming that all heat is transferred through a droplet by conduction. The conduction analysis also indicated a very large heat-transfer rate right around the droplet perimeter, and experimental observations have borne this out as well. The finite-element analysis used to predict temperatures did not consider elements small enough to allow accurate prediction of heat-transfer rates in the sensitive droplet-perimeter area, but it did indicate rates of the right order of magnitude. The analysis clearly points to the importance of the condensing wall in diffusing heat laterally underneath and around a droplet, and gives a logical explanation for the interaction between growth rates for neighboring droplets which has been observed by other investigators. The action of the condensing wall is thus shown to be analogous to an extended surface in convective-cooling applications, in that it receives heat from a very narrow ring around the droplet perimeter and diffuses it laterally so that it can be transferred out of the condensing wall into a cooling-fluid stream across a comparatively high thermal resistance. The presence of a neighboring droplet limits the condensing-surface area which can be used as a "fin" by a droplet, and thus reduces the growth rate of each.

References

1 Schmidt, E., Schuring, W., and Sellschopp, W., "Versuche über die Kondensation von Wasserdampf in Film- und Tropfenform," *Techn. Mech. Thermodynamik*, Vol. 1, 1930, p. 53.

2 Spoelstra, H. J., "Effects of Deposits on the Steam Side of Evaporator Tubes upon the Heat Transmission," *Arch. Suikerlind. in Nederl. Indie*, Part 3, No. 23, 1931, p. 905.

3 Hebbard, G. M., and Badger, W. L., "Steam-Film Heat Transfer Coefficients for Vertical Tubes," *AIChE Transactions*, Vol. 30, 1933–1934, pp. 194–214.

4 Nagle, W. M., Bays, G. S., Blenderman, L. M., and Drew, T. B., "Heat Transfer Coefficients during Dropwise Condensation of Steam," *AIChE Transactions*, Vol. 31, 1935, pp. 593–604.

5 Fitzpatrick, J. P., Baum, S., and McAdams, W. H., "Dropwise Condensation of Steam on Vertical Tubes," *AIChE Transactions*, Vol. 35, 1939, p. 97.

6 Shea, F. L., and Krause, N. W., "Dropwise and Film Condensation of Steam," *AIChE Transactions*, Vol. 36, 1940, p. 463.

7 Hampson, H., "The Condensation of Steam on a Tube with Filmwise or Dropwise Condensation and in the Presence of a Non-Condensable Gas," *International Developments in Heat Transfer, Proceedings of the 1961–62 International Heat Transfer Conference*, ASME, New York, N. Y., 1963, p. 310.

8 Selin, Gunnar, "Condensation of Water Vapor in Droplets," *Dechema Monograph*, Vol. 40, Nos. 616–641, 1962, pp. 149–154.

9 Nagle, W. M., and Drew, T. B., "The Dropwise Condensation of Steam," *AIChE Transactions*, Vol. 30, 1934, pp. 217–225.

10 Drew, T. B., Nagle, W. M., and Smith, W. D., "The Conditions for Dropwise Condensation of Steam," *AIChE Transactions*, Vol. 31, 1935, pp. 605–621.

11 Blackman, L. C. F., Dewar, M. J. S., and Hampson, H., "An Investigation into Compounds Promoting Dropwise Condensation of Steam," *Journal of Applied Chemistry*, Vol. 7, 1957, pp. 160–171.

12 Osment, B. D. J., and Tanner, D. W., "Promoters for the Dropwise Condensation of Steam," *Dechema Monograph*, Vol. 42, Nos. 781–804, 1963, pp. 145–174.

13 Umur, A., and Griffith, P., "Mechanism of Dropwise Condensation," JOURNAL OF HEAT TRANSFER, TRANS. ASME, Series C, Vol. 87, No. 2, May 1965, pp. 275–282.

14 Reisbig, R. L., "Dropwise Condensation of Water Vapor on a Horizontal Polytetrafluoroethylene Coated Aluminum Condenser Tube," unpublished master's thesis, University of Washington, Seattle, Wash., June 1963.

15 Jakob, M., "Heat Transfer in Evaporation and Condensation—II," *Mechanical Engineering*, Vol. 58, No. 11, Nov. 1936, pp. 729–739.

16 Welch, J. F., and Westwater, J. W., "Microscopic Study of Dropwise Condensation," *International Developments in Heat Transfer, Proceedings of the 1961–62 International Heat Transfer Conference*, ASME, New York, N. Y., 1963, p. 302.

17 Eucken, A., "Energy and Material Exchange on Boundary Surfaces," *Naturwissenschaften*, Vol. 25, 1937, p. 209.

18 Kast, W., "Heat Transfer in Dropwise Condensation," *Chem. Ing. Tech.*, Vol. 35, Jan. 1963, pp. 163–168.

19 Silver, R. S., "An Approach to a General Theory of Surface Condensers," *Proc. Inst. Mech. Eng.*, Vol. 178, Part 1, No. 14, 1963–1964.

20 Emmons, H., "Mechanism of Dropwise Condensation," *AIChE Transactions*, Vol. 35, 1939, pp. 109–125.

21 McCormick, J. L., and Baer, E., "Dropwise Condensation on Horizontal Surfaces," *Developments in Mechanics*, Pergamon Press, 1965, pp. 749–775.

22 Lorenz, J. J., and Mikic, B. B., "The Effect of Thermocapil-

lary Flow on Heat Transfer in Dropwise Condensation," JOURNAL OF HEAT TRANSFER, TRANS. ASME, Series C, Vol. 92, No. 1, Feb. 1970, pp. 46–52.
23 Hurst, C. J., "Transient Droplet Growth during Dropwise Condensation," Acc. No. AD-633702, available from Clearinghouse for Federal and Scientific Information, U.S. Department of Commerce.
24 Silver, R. S., "Heat Transfer Coefficients in Surface Condensers," *Engineering*, Vol. 161, 1946, p. 505.
25 Schrage, R. W., *A Theoretical Study of Interphase Mass Transfer*, Columbia University Press, New York, N. Y., 1953.
26 Koutsky, J. A., Walton, A. G., and Baer, E., "Heterogeneous Nucleation of Polyethylene Melts on Cleaved Surfaces of Alkali Halides," *Journal of Polymer Science*, Polymer Letters, Part B, Vol. 5, No. 2, Feb. 1967, pp. 185–190.
27 McCormick, J. L., and Westwater, J. W., "Drop Dynamics and Heat Transfer during Dropwise Condensation of Water Vapor on a Horizontal Surface," *Chem. Engr. Progress Symp. Ser.*, Vol. 62, No. 64, 1966.
28 Mikic, B. B., "On Mechanism of Dropwise Condensation," *International Journal of Heat and Mass Transfer*, Vol. 12, 1969, pp. 1311–1323.

lary Flow on Heat Transfer in Dropwise Condensation," JOURNAL OF HEAT TRANSFER, TRANS. ASME, Series C, Vol. 92, No. 1, Feb. 1970, pp. 46–52.
23 Hurst, C. J., "Transient Droplet Growth during Dropwise Condensation," Acc. No. AD-633702, available from Clearinghouse for Federal and Scientific Information, U.S. Department of Commerce.
24 Silver, R. S., "Heat Transfer Coefficients in Surface Condensers," *Engineering*, Vol. 161, 1946, p. 505.
25 Schrage, R. W., *A Theoretical Study of Interphase Mass Transfer*, Columbia University Press, New York, N. Y., 1953.
26 Koutsky, J. A., Walton, A. G., and Baer, E., "Heterogeneous Nucleation of Polyethylene Melts on Cleaved Surfaces of Alkali Halides," *Journal of Polymer Science*, Polymer Letters, Part B, Vol. 5, No. 2, Feb. 1967, pp. 185–190.
27 McCormick, J. L., and Westwater, J. W., "Drop Dynamics and Heat Transfer during Dropwise Condensation of Water Vapor on a Horizontal Surface," *Chem. Engr. Progress Symp. Ser.*, Vol. 62, No. 64, 1966.
28 Mikic, B. B., "On Mechanism of Dropwise Condensation," *International Journal of Heat and Mass Transfer*, Vol. 12, 1969, pp. 1311–1323.

DISCUSSION

D. G. Wilkins[2]

The authors are to be congratulated on their interesting and innovative experimental technique.

Issue is taken with the authors' analytical investigation and observations. First, the assumption of an adiabatic area surrounding the growing drop is not justified. In light of the results of Welch and Westwater [29] for drop populations and the photographs of the authors which show large drops surrounded by numerous smaller drops, it would seem more reasonable to assume constant heat flux or even constant temperature over the area outside the growing drop. In fact, one would expect the temperature of the underside of the foil to be nearly the steam temperature for areas outside the edge of the drop.

Secondly, the authors do not state the value of the steam-condensation coefficient they employed. If they used the value 0.04 recommended by Silver [19] instead of unity as found by recent workers [30], this would reduce the temperature gradients at the edge of a drop.

Thirdly, the effect of having a low coefficient on the cooled side of the foil does not appear to have been recognized by the authors. With such a low (105 Btu/hr-ft²-deg F) coefficient on the cooled side, lateral conduction is much more important than conduction through the foil for high-thermal-conductivity metals like copper. Thus it is not surprising that the authors found that the base of the drop can be considered isothermal except for large drops on thin foils, but it is not realistic for practical application of dropwise condensation.

With such a low coefficient on the cooled side of the wall there is little advantage in having dropwise condensation. Typically, processes where dropwise condensation might be considered practical, such as sea-water conversion, have cooled-side coefficients 2 to 3 orders of magnitude higher. In such cases the base of drops large enough to be considered inactive cannot be taken as isothermal. The experimental results of Griffith and Lee [31] support this view. Griffith and Lee measured steam-side dropwise heat-transfer coefficients for specimens of varying thermal conductivity that were plated with 0.005 in. of gold in a horizontal position facing down. They reported a coefficient of 10,000 Btu/hr-ft²-deg F for copper and 2000 Btu/hr-ft²-deg F for stainless steel. The authors predict that for a drop diameter of 0.1 in. a wall thickness of 0.005 in. is sufficient to make the base of the drop nearly isothermal. In a horizontal position facing down one would not expect drops much larger than 0.25 in. in diameter. Clearly, if the authors' model were valid, there should be little variation in the observed steam-side coefficient of specimens with 0.005 in. of gold plate. The authors' analytical model does not appear to be valid for practical applications of dropwise condensation, and the base of the inactive drops cannot be considered isothermal. Further evidence for the magnitude of the dependence of the steam-side heat-transfer coefficient upon the condensing-wall thickness is contained in the PhD dissertation of Wilkins [32].

[2] Research Assistant, Department of Chemical Engineering, University of California, Berkeley, Calif. Assoc. Mem. ASME.

Authors' Closure

The authors wish to thank Mr. Wilkins for his thoughtful comments. There appear to be several items which need clarification, and a few on which there appears to be some disagreement between the authors and Mr. Wilkins.

First, with regard to the condensation events outside the droplet: It is still the authors' contention that the area immediately adjacent to any droplet is very nearly, if not truly, adiabatic. Assumptions of either constant heat flux (without condensation occurring) or constant temperature would appear to be arbitrary assumptions without basis in physical reasoning. The question which needs to be resolved is the extent of the adiabatic area. The relationship among the extent of the adiabatic area, the amount of subcooling necessary to cause droplet nucleation, and the resulting droplet spacing has been discussed in the paper and will not be repeated here. It will simply be noted that the small amount of subcooling required for nucleation of a steam droplet together with the rapid temperature drop expected in a practical condensing surface under the adiabatic area would lead to the conclusion that steam droplets should grow very close together. As Mr. Wilkins has correctly noted, this is what is observed in practice. It is also exactly what the authors would expect, based on their hypothesized model.

In determining which value of the steam condensation coefficient to use in the analysis, the authors consulted a number of references, including the paper of Navabian and Bromley [30]. This paper was of particular interest because of the determination of the steam condensation coefficient from condensing vapor rather than evaporating liquid. For several reasons, however, see Hurst [23], it was decided initially to use a value of 0.045 as recommended by Knacke and Stranski [33]. When results were obtained it was immediately apparent that even order-of-magnitude changes in the value of the steam condensation coefficient would not have any appreciable effect on the results for the set of conditions under study. All of the droplet surface temperatures (except for the "average" corner temperature predicted right at the droplet perimeter) were predicted to be within 0.003 deg F of the vapor saturation temperature. The heat-transfer rates were controlled by the conduction and cooled-side-convection heat-transfer restrictions for this case. Consequently it was not felt to be necessary to redo the analysis with different condensation-coefficient values. Of course, for cases where extremely high thermal conductivities in the condensate and condensing wall were encountered along with a very high heat-transfer coefficient on the cooled side of the wall, the value of the steam condensation coefficient might become of sufficient importance to warrant further study.

The third comment of Mr. Wilkins is puzzling, particularly in view of the fact that the central idea of this work was that the determination of the nonuniform condensing-wall temperatures is a *system* problem involving not only the vapor and droplet but also the properties of the condensing wall and the cooling mechanism. In designing the experimental apparatus it was clearly necessary to consider all of these in the attempt to obtain a surface with large temperature gradients on it. For a much higher cooling rate the condensing wall could have been made thicker without making it effectively isothermal. The use of a cooling coefficient of 105 Btu/hr-ft²-deg F was dictated by the necessity of using air to have a cooling medium transparent to infrared radiation.

The authors agree with Mr. Wilkins that the use of dropwise condensation is certainly not called for in practice if the heat-

transfer rate is limited by a relatively low heat-transfer coefficient in some other part of the heat flow path. The parameters used in the analysis were chosen to model the events being observed experimentally, which, in turn, were deliberately chosen to learn something about the mechanism of dropwise condensation.

The authors feel that Mr. Wilkins has taken the statement about a 0.005-in. condensing-wall thickness being sufficient to cause the droplet base to become effectively isothermal out of context. That statement applied only to the set of conditions being studied, and in particular to the use of a cooled-side heat-transfer coefficient of 105 Btu/hr-ft^2-deg F for steam condensing at atmospheric pressure on a copper wall. It is impossible to take that piece of information and conclude anything from the work of Griffith and Lee [31], as their conditions on the cooled side of the 0.005-in-thick gold plate were vastly different. The authors concluded that a droplet acts much like a ring source of heat with a diameter equal to the droplet diameter so far as the condensing surface is concerned. Thus it is clear that only a complete conduction and convection analysis of the condensing wall and its coolant could determine whether or not a wall could be considered isothermal under a droplet. In many cases of engineering significance the condensing walls are thick enough and the cooling rates low enough that areas under the droplets will turn out to be nearly isothermal, but it is not too difficult to specify a situation where the condensing wall is far from isothermal. Finally, the authors' model does not depend in any way on an assumption of constant temperature under the droplet. Conclusions concerning wall temperature gradients are of interest primarily in trying to assess the validity of the static droplet conduction studies of several previous investigators, and the information given was presented for that reason.

The authors and Mr. Wilkins appear to have a considerable amount of common ground in believing that conductivity within a condensing wall is of considerable importance in the study of dropwise condensation. The authors look forward to reading Mr. Wilkins' thesis and/or paper when it becomes available.

Additional References

29 Welch, J. F., and Westwater, J. W., "Microscopic Study of Dropwise Condensation," *International Developments in Heat Transfer, Proceedings of the 1961–62 International Heat Transfer Conference*, ASME, New York, N. Y., 1963, p. 302.

30 Navabian, K., and Bromley, L. A., "Condensation Coefficient of Water," *Chem. Eng. Sci.*, Vol. 18, 1963, p. 651.

31 Griffith, P., and Lee, M. S., "The Effect of Surface Thermal Properties and Finish on Dropwise Condensation," *International Journal of Heat and Mass Transfer*, Vol. 10, 1967, p. 697.

32 Wilkins, D. G., "Dropwise Condensation Phenomena," PhD thesis, University of California, Berkeley, Calif., 1972.

33 Knacke, O., and Stranski, I. N., "The Mechanism of Evaporation," *Progress in Metal Physics*, B. Chalmers and R. King, eds., Pergamon, Elmsford, N. Y., 1956, p. 181.

J. D. CARY
Student Mem. ASME

B. B. MIKIC
Mem. ASME

Massachusetts Institute of Technology, Cambridge, Mass.

The Influence of Thermocapillary Flow on Heat Transfer in Film Condensation

The influence of fluid flow—induced by surface-tension forces—on heat transfer through a condensate film broken by non-wetting strips was considered. The film was modeled as a two-dimensional layer on an isothermal, vertical flat surface; the layer has a flat midsection with circular arcs at the edges. The solution was obtained by a finite-difference technique for several values of the Marangoni number (Nm) *which provides a relative measure of the surface-tension forces and of the Biot number* (Bi) *which provides a relative measure of the heat transfer at the liquid–vapor interface. The range of parameters covered by this work transcends the limits of most practical interest for water. The results show that internal thermocapillary circulation causes modest increases in heat transfer. It is concluded that thermocapillary flow might be an important factor in determining the geometry of channeled condensate films.*

Introduction

THIS WORK is an attempt to show the effect of thermocapillary flows on the heat transfer in film condensation. These flows are induced by breaking the condensate layer to cause a nonuniform surface-temperature distribution.

Flows induced by nonuniform surface tension at a liquid–vapor interface were first reported by C. G. M. Marangoni in 1871. Surface tension is a thermodynamic property of a liquid dependent only upon its temperature and composition. Hence variations in either property can influence the transport of heat, mass, and momentum near an interface, especially in small-scale systems [1].[1] Surface-tension-induced flows are grouped collectively under the "Marangoni effect." Thermocapillary flows are those induced by thermal gradients; these have been considered by various authors [1–6].

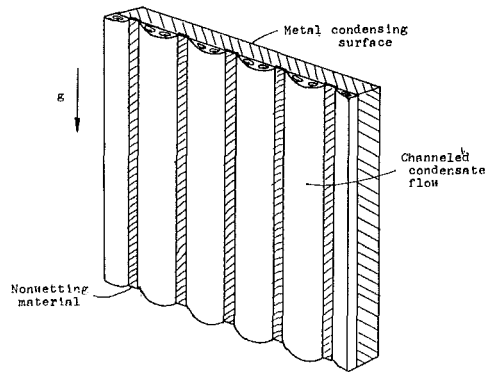

Fig. 1 Hypothetical scheme for channeled film condensation

Model Description

The model is illustrated in Figs. 1 and 2. It is two-dimensional with symmetry about the y axis. The condensate layer is considered to be running down a vertical flat surface between parallel strips of a non-wetting material. The shape of the model was arbitrarily determined to facilitate the writing of linearized finite-difference equations. No consideration was made of free surfaces determined from the interaction between surface tension and pressure. The model is quasi-steady, inertial terms in the momentum equation are neglected, and constant properties and parameters are assumed. For a complete discussion of the modeling process, see [8].

The solution domain is the interior of the condensate layer depicted in Fig. 2. The physics of the energy and momentum transport within this domain, subject to the above assumptions, are specified by the following dimensionless governing equations [4, 6–8]. All symbols are explained in the Nomenclature.

$$\nabla'^2\omega' = 0 \tag{1}$$

$$\omega' = -\nabla'^2\psi \tag{2}$$

$$\nabla'^2\theta = \frac{\partial\psi}{\partial y'}\frac{\partial\theta}{\partial x'} - \frac{\partial\psi}{\partial x'}\frac{\partial\theta}{\partial y'} \tag{3}$$

The dimensionless boundary conditions are:

at boundary I

[1] Numbers in brackets designate References at end of paper.

Contributed by the Heat Transfer Division for publication (without presentation) in the JOURNAL OF HEAT TRANSFER. Manuscript received by the Heat Transfer Division December 29, 1971. Paper No. 72-HT-H.

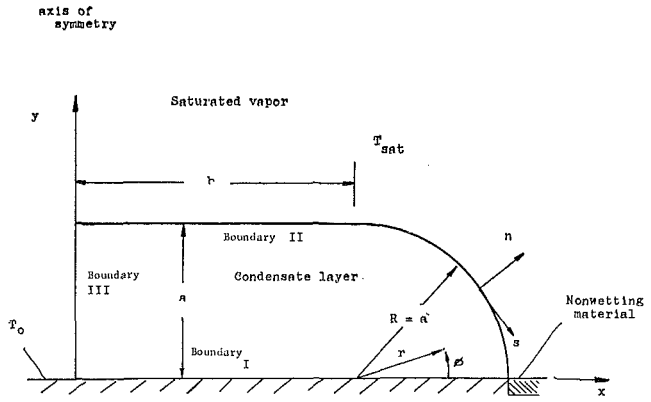

Fig. 2 Model for solution domain

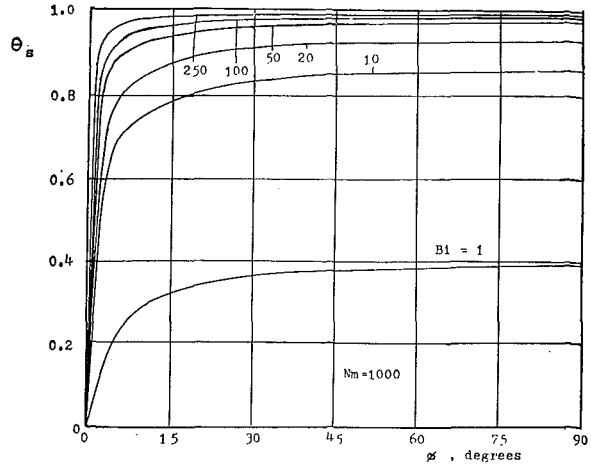

Fig. 3 Dimensionless surface temperature for several values of Bi; $b = 0$

$$\theta = 0, \quad \psi = 0, \quad \frac{\partial \psi}{\partial n'} = 0 \tag{4}$$

at boundary II

$$\frac{\partial \theta}{\partial n'} = -\mathrm{Bi}(\theta - 1), \quad \psi = 0 \tag{5}$$

$$\omega' + \frac{1}{R}\frac{\partial \psi}{\partial n'} = -\mathrm{Nm}\frac{\partial \theta}{\partial s'}$$

at boundary III

$$\frac{\partial \theta}{\partial n'} = 0, \quad \psi = 0, \quad \omega' = 0 \tag{6}$$

Method of Solution

Numerical Procedures. Governing equations (1)–(3) with boundary conditions (4)–(6) were expressed as linear finite-difference equations written at each node of a finite-difference grid network. The radius and angle distributions of the network were selected to crowd nodal points in the region of greatest change of the problem variables.

The problem, as formulated, is not, of course, completely linear. There are coupling and nonlinearity between the problem variables in the governing equations and boundary conditions. This was handled by breaking the difference equations into two separate linear sets and solving iteratively between the two until the change between iterations in the heat flux conducted through the liquid–vapor interface was less than 1 percent.

Range of Parameters. The two parameters which completely specify the solution for a given condensate-layer geometry are Bi and Nm. Their range covered in this work determined from consideration of a vertical-flat-plate analysis is $1 \leq \mathrm{Bi} \leq 250$ and $0 \leq \mathrm{Nm} \leq 5000$.

For $\mathrm{Bi} \geq 1$, the conduction resistance for water films is greater than or equal to 20 percent (for small b) and 50 percent (for large b) of the total resistance [8]. For lower values of Bi the interfacial (liquid–vapor) resistance becomes the controlling resistance, and the overall heat-transfer coefficient is not significantly affected by strong thermocapillary circulation within the liquid. In the above, the term "conduction resistance" refers to the thermal resistance from the surface of the condensate film at the liquid–vapor interface through the layer to the condensing surface. For a complete discussion of the orders of magnitude of h and a, which determine the magnitudes of the interfacial and conduction resistances respectively in the condensation of water, see references [8–13].

Nomenclature

a = radius of curvature of the end of the broken condensate film layer, and thickness of the layer
b = half-width of region of constant thickness a
Bi = ha/k, Biot number
c_p = specific heat of the condensate liquid
h = heat-transfer coefficient at the liquid–vapor interface
k = thermal conductivity of the condensing surface
n, s = curvilinear coordinate system at the boundary
Nm = $-(T_{sat} - T_0)a\beta/\mu\alpha$, Marangoni number
p = pressure
Pr = $\mu c_p/k$, Prandtl number
q = heat flux
q_{cond} = pure conduction heat flux (Nm = 0)
r, ϕ = polar coordinate system
$r', n', s',$ x', y' = dimensionless coordinates
R = radius of curvature of the liquid–vapor interface
Re = $\rho|\mathbf{V}|a/\mu$, Reynolds number
t = time
T = temperature
T_0 = temperature of the condensing surface
T_{sat} = saturation temperature of the vapor
$\mathbf{V}$ = velocity vector
$\mathbf{V}'$ = $\mathbf{V}a/\alpha$, dimensionless velocity vector
$V_n, V_s,$ $V_r, V_\phi,$ V_x, V_y = velocity components in the various coordinate directions
$V_n', V_s',$ $V_r', V_\phi',$ V_x', V_y' = dimensionless velocity components
x, y = cartesian coordinate system
α = $k/\rho c_p$, thermal diffusivity of the liquid
β = $\partial\sigma/\partial T$, derivative of surface tension with respect to temperature
σ = surface tension
μ = absolute viscosity of the condensate liquid
ω = $\nabla \times \mathbf{V}$, vorticity
ω' = $\omega a^2/\alpha$, dimensionless vorticity
ρ = density of the condensate liquid
τ_{ns} = shear stress on the liquid-vapor surface
ψ = dimensionless stream function, $V_x' = \partial\psi/\partial y'$ and $V_y' = -\partial\psi/\partial x'$
$\theta = \dfrac{T - T_0}{T_{sat} - T_0}$, dimensionless temperature
θ_s = dimensionless surface temperature
∇' = $a\nabla$, dimensionless vector operator

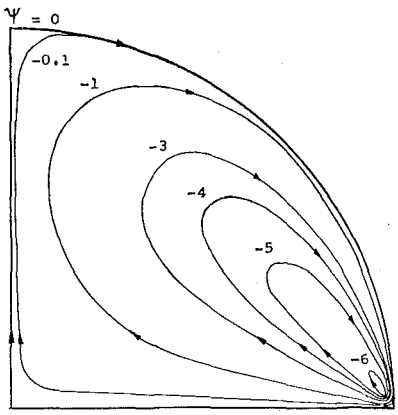

Fig. 4 Flow field inside condensate layer, $b = 0$; Bi = 20, Nm = 5000

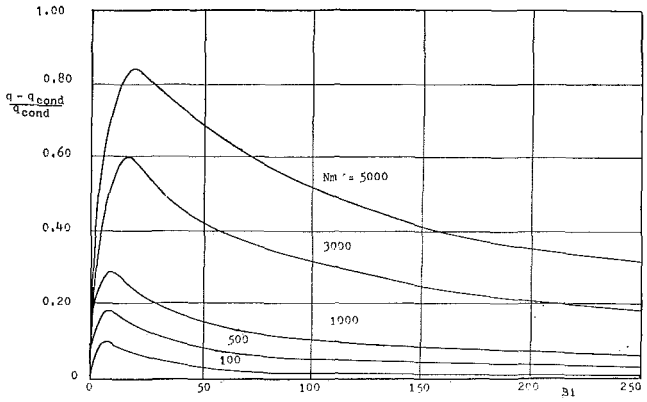

Fig. 6 Augmentation over conduction solution, $b = 0$

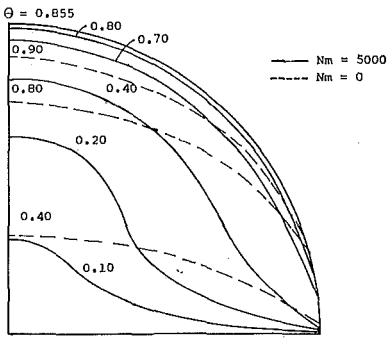

Fig. 5 Temperature field inside condensate layer, $b = 0$; Bi = 20

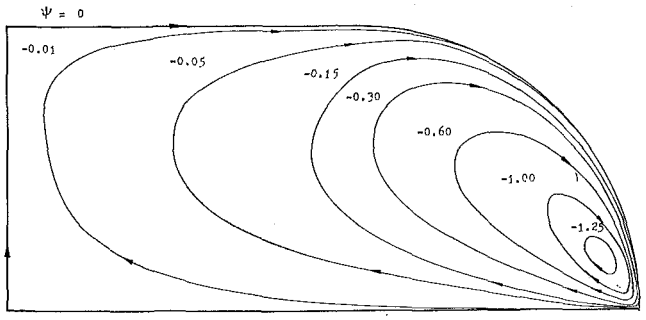

Fig. 7 Flow field inside condensate layer, $b = 1.25a$; Bi = 20, Nm = 500

The upper limit on Nm ($= 5000$) was determined by setting an upper bound on $[a(T_{sat} - T_0)]$ for cases of practical interest.

Results and Discussion

Case I. $b = 0$ (layer of semicircular cross section). Nonuniform temperature distributions on the liquid–vapor surface, which are the indirect cause of thermocapillary flows, are a consequence of the presence of a finite heat-transfer coefficient h at the interface. The results shown in Fig. 3 illustrate this point.

Figs. 4 and 5 illustrate the case where the thermocapillarity is strong. Fig. 4 is a plot of the stream function ψ (i.e., the flow field) for Bi = 20 and Nm = 5000. The nondimensional thermocapillary driving force $\mathrm{Nm}(\partial\theta/\partial s')$ pulls the liquid down toward the corner, resulting in the flow pattern observed. Fig. 5 illustrates the temperature field within the same film; the dotted lines are the conduction solution (i.e., Nm = 0). In general the thermocapillary flow acts to decrease temperatures from the conduction solution at any given point except near the corner, where the opposite occurs.

The augmentation, defined as $(q - q_{cond})/q_{cond}$, was employed to measure the increase in heat transfer due to thermocapillarity. It measures the increase (due to thermocapillary flow) in heat flux, or overall heat-transfer coefficient, over the conduction flux with no thermocapillary flow. The flux through the liquid–vapor boundary integrated over that surface is represented by q. A cross-plot of the augmentation as a function of Bi and Nm is provided in Fig. 6. For the range of Nm explored in this work, the maximum augmentation occurs for $10 < \mathrm{Bi} < 20$. For small Bi, it appears that since the rate of increase of the augmentation decreases with increasing Nm, either the interfacial resistance is controlling or the Marangoni effect is self-limiting.

Case II. $b = 1.25\,a$. A run was made for $b = 1.25a$ (see Fig. 2), Bi = 20, and Nm = 500. It was thought that extending the layer (i.e., making $b > 0$) would lessen constrictions on the flow caused by the tight loop around which it was forced to circulate when $b = 0$. The flow field for the given values of b, Bi, and Nm is illustrated in Fig. 7. The flow around the corner is about twice as great as for the nonextended case (when $b = 0$). However, the surface temperatures on the top of the layers are about the same for the two cases. The augmentation decreases slightly in the extended case. The flow in the extended parts is weak and does not contribute much to the augmentation, although the flow in the region $|x| > b$ is approximately doubled. It is believed that the augmentation would not be significant for wide thin layers.

Case III. $b = 0$ (finite condensing-surface resistance). This case was explored by assuming the condensing surface to be of thickness a and thermal conductivity 10 Btu/hr-ft-deg F. A constant temperature was impressed on the bottom of the surface, and the sides at $x = \pm a$ were considered to be insulated. The conduction-solution temperature field is shown in Fig. 8 for Bi = 20. Setting Nm = 500, the augmentation decreased slightly from the value in the previous case. Since $k_s = 10$ Btu/hr-ft-deg F represents a lower limit on any metal-condensing-surface thermal conductivity, other surfaces will have less effect on the heat transfer.

Summary and Conclusions

The Effect of Thermocapillary Flows on Heat Transfer. The maximum increase in heat transfer due to thermocapillarity is found to be 83 percent (for Bi = 20 and Nm = 5000). For Bi = 250 and Nm = 5000 the augmentation is only 32 percent. It appears that thermocapillarity is an important mechanism in heat transfer only for cases with large thickness a and small heat-transfer coefficient h. However, these conditions are the opposite of what is desired, and their occurrence within a total system would be in regions which do not contribute much to the overall heat transfer. Also, the results for the augmentation are calculated for the layer of half width a. Extension of the layer re-

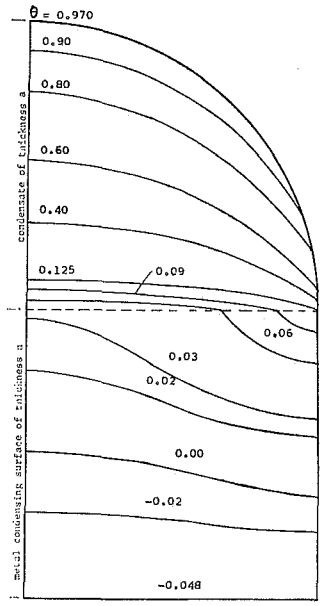

Fig. 8 Conduction temperature field with finite condensing-surface resistance, $b = 0$; $k_s = 10$ Btu/hr-ft-deg F, Bi = 20

duces the relative effect of the thermocapillary flows, since all of the action occurs at the ends. Therefore, it appears that within the restriction of the model formulation, thermocapillary flows cause at best modest increases in the heat transfer in film condensation.

Influence of Modeling Approximations and Assumptions on the Results. After the fact, it appears that inclusion of the inertia terms in the problem model would have the net effect of decreasing the augmentation of the heat transfer due to thermocapillary flow. Along a given streamline, the magnitude of the velocity changes drastically; adding inertia would have the effect of reducing the maximum velocity, because the energy associated with accelerating the fluid has not been accounted for, and the effect of raising the minimum velocity, because it would not be slowed as much by viscous friction. Lorenz [6] found in dropwise condensation heat transfer (Bi = 100 and Nm = 450 with Pr = 1) that the inclusion of inertia in the problem model slightly reduced the surface velocity.

It can be shown that the Reynolds number based on the thickness a is $|\mathbf{V}'|/\mathrm{Pr}$. At atmospheric pressure for saturated water $\mathrm{Pr} \cong 2$; Pr increases as the pressure decreases. Therefore, for low-pressure systems, or away from the corner where velocities are small, or for small Nm, the Reynolds number is small, and the influence of the inertia terms with respect to the viscous terms can be neglected.

The model geometry was assumed for ease in writing the finite-difference equations. No account was made of the effect of the thermocapillary flows on the shape of the condensate layer. The very large radial accelerations due to the tangential velocity found at the interfacial surface would require unrealistically large pressure gradients to balance them. One would expect that a large radius of curvature at the free surface would be caused by thermocapillary flows to reduce pressure gradients there.

Summary. For the model considered it appears that the direct effect of thermocapillary flows on augmentation of the heat transfer in film condensation is modest. Thermocapillary flows might be important in determining condensate-layer geometries due to the relatively large velocities induced in the broken condensate layer, and thus indirectly affecting the heat transfer.

References

1 Kenning, D. B. R., "Two-Phase Flow with Nonuniform Surface Tension," *Applied Mechanics Reviews*, Vol. 21, No. 11, 1968, p. 1101.

2 Berg, J. C., Boudart, M., and Acrivos, A., "Natural Convection in Pools of Evaporating Liquids," *Journal of Fluid Mechanics*, Vol. 24, 1966, p. 721.

3 Scriven, L. E., and Sternling, C. V., "The Marangoni Effects," *Nature*, Vol. 187, 1960, p. 186.

4 Gaddis, E. S., "The Thermal Equilibrium of a Vapour Bubble on a Heated Surface," PhD thesis, The Victoria University of Manchester, 1968.

5 Kao, Y. S., "Two-Phase Flow with Heat Transfer," PhD thesis, University of Oxford, St. Edmund Hall College, 1970.

6 Lorenz, J. J., and Mikic, B. B., "The Effect of Thermocapillary Flow on Heat Transfer in Dropwise Condensation," JOURNAL OF HEAT TRANSFER, TRANS. ASME, Series C, Vol. 92, No. 1, Feb. 1970, pp. 46–52.

7 Larkin, B. K., "Thermocapillary Flow around a Hemispherical Bubble," *AIChE Journal*, Vol. 16, No. 1, 1970, p. 101.

8 Cary, John D., "The Influence of Thermocapillary Flow on Heat Transfer in Film Condensation," SM thesis, M.I.T., Cambridge, Mass., 1971.

9 Nabarian, K., and Bromley, L. A., "Condensation Coefficient of Water," *Chemical Engineering Science*, Vol. 18, 1963, pp. 651–660.

10 Umur, A., and Griffith, P., "Mechanism of Dropwise Condensation," JOURNAL OF HEAT TRANSFER, TRANS. ASME, Series C, Vol. 87, No. 2, May 1965, pp. 275–282.

11 Citakoglu, E., and Rose, J. W., "Dropwise Condensation—Some Factors Influencing the Measurements," *International Journal of Heat and Mass Transfer*, Vol. 11, 1968, pp. 523–537.

12 Silver, R. S., "An Approach to a General Theory of Surface Condensers," The Institution of Mechanical Engineers, Steam Plant Group (London), 1963.

13 Rohsenow, W. M., and Choi, H., *Heat, Mass, and Momentum Transfer*, Prentice-Hall, Englewood Cliffs, N. J., 1961, p. 239.

14 Mikic, B. B., "On Mechanism of Dropwise Condensation," *International Journal of Heat and Mass Transfer*, Vol. 12, 1968, p. 1319.

R. C. PFAHL, JR.
Research Leader,
Thermal Energy Studies,
Western Electric Engineering Research Center,
Princeton, N. J.
Mem. ASME

Specular Reflectors for Prescribed Disturbed Radiant Heating from a Point Energy Source

This paper presents a mathematical model for designing a reflector shape which will produce a prescribed rotationally symmetric energy distribution on a plane workpiece using a single point energy source. The model considers spectral, directional, and polarizing effects. The necessary equations are developed and their solutions described. A reflector is designed to uniformly heat a 6-in-dia circle using a 200-w compact mercury-arc lamp. The validity of the model is demonstrated by constructing the designed reflector and experimentally confirming that the desired heat-flux distribution is achieved. It is quantitatively shown that the minor differences between the desired flux distribution and the actual distribution are due primarily to the finite source size and that a more precise distribution could be obtained by modeling the source as four point sources.

Introduction

RADIANT heating systems consisting of a single compact energy source and a reflector are used for a variety of applications including manufacturing in the electronics industry [1],[1] thermal simulation [2], and photolysis research [3]. Most of the systems use reflectors of either elliptic or parabolic cross section with the source at a focus. The elliptic reflectors concentrate the energy from the source onto a workpiece located at the second focus, while the parabolic reflectors produce a collimated beam of nonuniform intensity [4]. The goal of the present study was to develop techniques for designing and constructing a reflector system which would produce a prescribed heat-flux distribution on a workpiece, the heat-flux distribution of greatest interest being a uniform distribution over a relatively large area.

A previous paper [4] presented a mathematical model describing the radiant heating system and used the model to predict the heat-flux distribution for a known reflector shape. That study demonstrated that reflectors of conic section will not produce a uniform heat flux. The present study uses the same mathematical model to design a reflector which will produce a prescribed heat-flux distribution.[2]

The following sections of this paper discuss the assumptions of the analysis, develop the equations describing the system and discuss their solution, present the design of a reflector to produce a prescribed distribution using a specific mercury-arc lamp, discuss the construction of the reflector, and present the experimental heat-flux distribution of the reflector system. A comparison is made between experimental and theoretical findings and the differences are discussed. A second example is presented to illustrate how the present design procedure is coupled with the conduction heat transfer occurring within the workpiece.

Assumptions

The present work treats a radiant heating system consisting of a point light source, a reflector, and a plane workpiece. The system, illustrated in Fig. 1, is restricted to rotational symmetry about a central axis. Because of the simple geometry many of the restrictive assumptions commonly made in radiant-heat-transfer calculations are not required. Spectral, directional, and polarizing effects [5] are included in the model.

The assumptions of the analysis are (*a*) a spectral reflector, (*b*) a nonparticipating gas, (*c*) a point energy source, (*d*) negligible emission from the reflector, surroundings, and workpiece, and (*e*) energy transfer only along those paths illustrated in Fig. 1.

No source exactly satisfies assumption (*c*), but experimental measurements verify that many do approximate a point source. The degree to which the source used in this experiment approximates a point is discussed in depth later in the paper.

Assumption (*d*) implies that the only important radiator of

[1] Numbers in brackets designate References at end of paper.

Contributed by the Heat Transfer Division and presented at the Winter Annual Meeting, New York, N. Y., November 26–30, 1972, of THE AMERICAN SOCIETY OF MECHANICAL ENGINEERS. Manuscript received by the Heat Transfer Division May 5, 1972. Paper No. 72-WA/HT-1.

[2] A concurrent analytical study by Horton and McDermit [14] describes the design of a reflector for use with a nonuniform collimated source. The authors do not treat spectral, directional, or polarizing effects. In their conclusion they correctly note that by following the outline of their work one could design reflectors for use with nonuniform point sources. The present work is an analytic and experimental study of this case which includes the above effects.

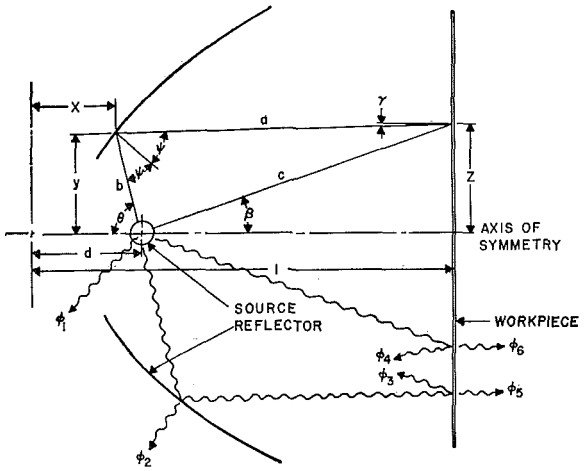

Fig. 1 System geometry

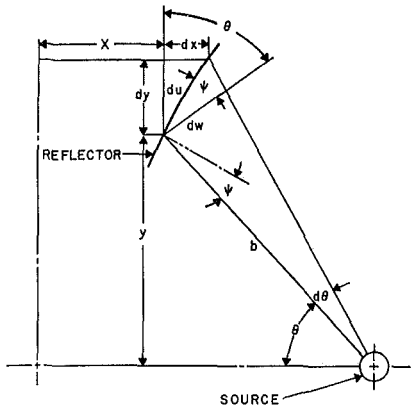

Fig. 2 Differential geometry for reflector

energy in the system is the source. In verifying the validity of this assumption one must consider the temperature, area, and emittance of each surface. The emission from the reflector can be neglected if the temperature of the reflector is sufficiently low. Reflectors normally are operated at low temperatures (often by water cooling) to maintain surface quality. The emission from room-temperature surroundings should also be small; however, the emission from the workpiece can be important if its temperature and emittance are large. In the present experiments the workpiece is a water-cooled calorimeter, and hence its emission is low.

Assumption (e) requires that the components of power reflected from the workpiece, ϕ_3 and ϕ_4 (Fig. 1), not strike the reflector. This assumption must be verified if the part is a good specular reflector. For parts which are good diffuse absorbers (such as the calorimeter used in the present study) the assumption is valid.

Derivation of Equations

Energy Equation. The objective is to design a reflector which will produce a radially symmetric heat flux of $E_w(z)$, where the subscript w indicates workpiece and the variable z indicates that this flux distribution may be a function of the radial coordinate (Fig. 1). Note that $E_w(z)$ is the radiant flux absorbed by the workpiece (not the incident radiant energy), and thus the reflector shape will depend on the surface characteristics of the workpiece. No restrictions are placed on the spectral distribution or state of polarization of the absorbed flux $E_w(z)$, since we are only concerned with obtaining a specified amount of absorbed thermal energy.

At each point z on the workpiece there will be two contributions to $E_w(z)$: the flux E_5 which is reflected by the reflector and then absorbed by the workpiece and the flux E_6 which is directly absorbed by the workpiece. Thus

$$E_w(z) = E_5 + E_6 \tag{1}$$

A differential equation describing the energy transfer in the system can be derived by tracing polarized spectral power along the two paths from the source to the workpiece using the previously discussed assumptions. These differential powers are then integrated over frequency and summed over components of polarization to obtain the total fluxes E_5 and E_6. Substitution into equation (1) yields the energy equation as a first-order ordinary differential equation. The details of the derivation are presented in [4].

$$\frac{dA}{d\theta_s} = \frac{\sum_{j=s,p} \int_0^\infty \rho_r(\nu, \Psi, j)\alpha_w(\nu, \gamma, j)I_\nu(\theta, j)d\nu}{\left[-\sum_{j=s,p} \int_0^\infty \alpha_w(\nu, \beta, j)I_\nu(\beta, j)d\nu\right](l-d)[(l-d)^2 + z^2]^{-3/2} + E_w(z)} \tag{G2}^3$$

In the energy equation ($G2$), j is the component of polarization, ν is frequency, $\rho_r(\nu, \Psi, j)$ is the spectral specular reflectance of the reflector for the j component of polarized power and Ψ is the angle of incidence of the incoming ray, $\alpha_w(\nu, \gamma, j)$ is the spectral directional absorptance of the workpiece and γ is the angle of incidence of the incoming ray, $I_\nu(\theta, j)$ is the polarized spectral radiant intensity of the ideal point source in the direction θ, and l, d, and z are geometrical distances defined in Fig. 1. The variable A is the area of the workpiece

$$A = \pi z^2 \tag{3}$$

and θ_s is the solid angle generated by rotating the plane angle θ about the x axis

$$\theta_s = 2\pi(1 - \cos\theta) \tag{4}$$

Geometrical Equations. The energy equation ($G2$) involves the independent variable θ_s and six dependent variables A, Ψ, θ, γ, β, and z. In addition there are two other dependent variables of direct concern, x and y, which specify the reflector shape. Thus seven additional equations must be determined from the geometry of the reflector system; one of these equations is a differential equation, the remainder are algebraic equations.

The differential equation is first derived. From Fig. 2

$$\frac{dy}{du} = \cos(\theta - \Psi) \tag{5}$$

$$\frac{dw}{du} = \cos\Psi \tag{6}$$

$$d\theta = dw/b \tag{7}$$

$$y/b = \sin\theta \tag{8}$$

From equations (5)–(8) and the trigonometric identity for the cosine of the difference of two angles

$$\frac{dy}{d\theta} = y(\cot\theta + \tan\Psi) \tag{9}$$

Using equation (4), equation (9) is reformulated with θ_s as the independent variable

$$\frac{dy}{d\theta_s} = y\,\frac{(\cot\theta + \tan\Psi)}{2\pi\sin\theta} \tag{H10}$$

The variable θ_s has been selected as the appropriate independent variable for the differential equations since for a source with uniform intensity equal differential solid angles $d\theta_s$ will contain

[3] Lettered equations are used in the final model.

equal amounts of power; thus uniform accuracy in the power distribution will be achieved during the numerical integration of the differential equations.

The six algebraic equations will now be derived. Rearrangement of equations (4) and (3) yields the following equations:

$$\theta = \arccos\left(1 - \frac{\theta_s}{2\pi}\right) \qquad 0 \leq \theta \leq \pi \qquad (A11)$$

$$z = (A/\pi)^{1/2} \qquad (B12)$$

From Fig. 1

$$x = d - y \cot\theta \qquad (C13)$$

Applying the law of cosines to the triangle with sides a, b, and c and solving for Ψ yields

$$\Psi = \frac{1}{2}\arccos\left(\frac{x^2 + y^2 + l(d-x) - xd - yz}{\{[(l-x)^2 + (z-y)^2][(d-x)^2 + y^2]\}^{1/2}}\right) \qquad 0 \leq \Psi \leq \pi/2 \qquad (D14)$$

From Fig. 1

$$\beta = \arctan\left(\frac{z}{l-d}\right) \qquad 0 \leq \beta \leq \pi/2 \qquad (E15)$$

Also from Fig. 1

$$\gamma = |\theta - 2\Psi| \qquad (F16)$$

To complete the model, initial values of θ_s, y, and A must be specified.

Solution of Equations

The system of equations is rewritten below in functional form.

Algebraic equations

$$\theta = \theta(\theta_s) \qquad (A)$$

$$z = z(A) \qquad (B)$$

$$x = x(y, \theta) \qquad (C)$$

$$\Psi = \Psi(x, y, z) \qquad (D)$$

$$\beta = \beta(z) \qquad (E)$$

$$\gamma = \gamma(\theta, \Psi) \qquad (F)$$

Differential equations

$$\frac{dA}{d\theta_s} = f(\Psi, \gamma, \theta, \beta, z) \qquad (G)$$

$$\frac{dy}{d\theta_s} = g(y, \theta, \Psi) \qquad (H)$$

Initial conditions

$$\theta_s = \theta_{si} \qquad y = y_i \qquad A = A_i \qquad (I)$$

Inspection of the equations reveals that the six algebraic equations have been formulated so that it is possible to substitute the algebraic equations sequentially into succeeding equations, eliminating the dependent variables θ, z, x, Ψ, β, and γ. After performing the required algebra the equations reduce to two first-order coupled ordinary differential equations which are numerically integrated using Hamming's modified predictor–corrector method [6]. At each step in the integration, after the new values of A and y are determined by integration, the corresponding values of the other dependent variables θ, z, x, Ψ, β, and γ are calculated from equations (A) through (F). This procedure yields the coordinate points x and y of the reflector as well as the point z on the workpiece to which each ray is directed. The integration is halted when $z \geq z_f$ or when it has been determined that the source has insufficient energy to produce the desired flux distribution.

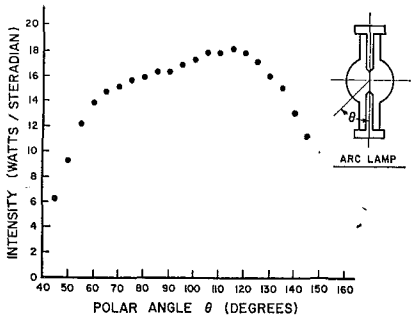

Fig. 3 Total intensity distribution of 200-w compact mercury-arc lamp

Equations (C) and (H) are both singular for $\theta = 0$ and π radians. If energy is to strike the workpiece a reflector cannot enclose a complete 4π steradians; therefore the only singular point of concern is $\theta_i = \theta = 0$. A special starting procedure which employs forward finite differences is used to integrate the equations at this singular point.

Design of Reflector

To exemplify the preceding analysis a reflector has been designed for an optical application which requires the illumination of a 6-in-dia circle with an approximately uniform flux of 0.480 w/cm² using a 200-w compact mercury-arc lamp. The reflector was vapor-deposited aluminum on an electroformed nickel shell. The workpiece was opal glass. The system was designed to operate with a vertical axis of symmetry (the axis of the lamp electrodes) with the opal glass in a horizontal plane above the lamp and reflector.

In order to design the reflector for this application the four functions E_w, I, ρ_r, and α_w must be specified; in addition d, l, θ_i, y_i, z_i, and z_f must be chosen. The selected values were $d = 0.6$ in., $l = 5.0$ in., $\theta_i = 60$ deg, $y_i = 1.039$ in., $z_i = 0$ in., and $z_f = 3.0$ in. The minimal restrictions imposed on the four functions have been outlined. Because of a lack of information on the spectral distribution of the source intensity all spectral effects have been neglected in the present application; instead, total or average values have been used. The following paragraphs describe the functional forms used in designing the reflector.

***E*$_w$(*z*).** The heat-flux distribution required for the present application was

$$E_w(z) = 0.4805/\cos^4 0.0582z \quad \text{w/cm}^2 \qquad (17)$$

where $0 \leq z \leq 3.0$ in. Thus the desired flux is essentially uniform, increasing by only 6.5 percent from the center to the outer edge of the workpiece.

***I*(θ, *j*).** The model permits the intensity of the source to vary with state of polarization, polar angle, and frequency. The chosen 200-w compact mercury-arc lamp radiates symmetrically about the axis of the two electrodes, but its energy distribution is a strong function of polar angle θ. The angular distribution of total intensity from this lamp was determined experimentally at 5-deg increments from 45 to 150 deg. The total intensity was calculated from heat-flux measurements made using a Gardon-type [7] calorimeter. At angles greater than 145 deg there is convective heating from the wake caused by the free-convective flow of air around the lamp. This heating can give erroneous heat-flux measurements. The convective heat transfer to the calorimeter was minimized by maintaining the calorimeter cooling water at the ambient temperature and by placing a closed cell with a 1-mil mylar window over the calorimeter. Figure 3 shows the measured distribution of total intensity for the lamp. The electrical power to the lamp was maintained at 183 w during the heat-flux measurements; integration of the intensity distribution indicates that 155 w was radiated. For the example reflector

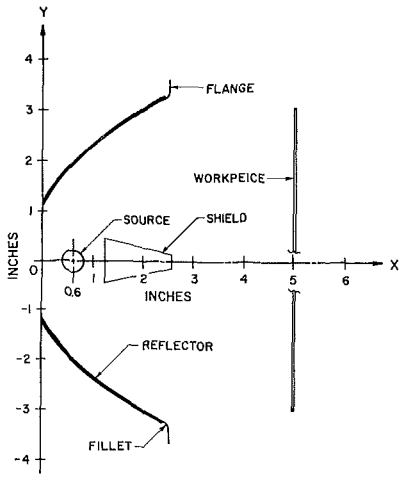

Fig. 4 Reflector design for example problem

system the intensity from 130 to 180 deg was zero, since a shield was placed over the lamp to block the direct radiation. A least-squares procedure was used to fit a polynominal to the intensity data points of Fig. 3 from 45 to 125 deg. This polynominal was used to model the intensity. It was assumed that the source was uniformly polarized

$$I(\theta, s) = I(\theta, p) = \tfrac{1}{2}I(\theta) \tag{18}$$

$\rho_r(\nu, \Psi, j)$. The only restriction on the reflector reflectance is that it be specular. The specular reflectance may be described by Fresnel's equations [8].

$$\begin{aligned} \rho(\Psi, s) &= f(n, k, \Psi) \\ \rho(\Psi, p) &= g(n, k, \Psi) \end{aligned} \tag{19}$$

where Ψ is the angle of incidence, n is the refractive index, and k the extinction coefficient. Both n and k and hence also the reflectance are functions of frequency; however, a wavelength of 0.492 μ was selected as an appropriate average for the chosen source. The appropriate values for aluminum at 0.492 μ are n = 0.64, k = 5.50 [9]. The reflectance for aluminum at this frequency is constant only for Ψ less than 45 deg. If many of the rays are reflected at angles greater than 45 deg the variation of reflectance with both Ψ and j may become significant in evaluating equation (2).

$\alpha_w(\beta, j)$. The present analysis places no restrictions on the model describing the workpiece's spectral directional absorptance. For the present application the glass was assumed to be a specular reflector; hence

$$\alpha(\beta, j) = 1 - \rho(\beta, j) \tag{20}$$

where $\rho(\beta, j)$ is defined by Fresnel's equations; n was specified based on experimental measurements of crown glass at 0.5086 μ [10].

Construction of Reflector

Figure 4 is a scale drawing of the reflector designed for the example problem. The portion of the reflector used to reflect energy to the workpiece is shown with a heavy line. The reflector has been extended at both ends; the outer extension provides a flange to mount the reflector and the central extension simplifies the construction of the reflector. This central extension is removed as the final step in construction. The shield for direct radiation is also shown.

After designing the reflector the computer program outputs the x–y coordinates of the reflector on 80-column punched cards. These cards are used to program a numerically controlled milling machine which produces a female template of the reflector cross section. A male template is cast from the female template using a metal-filled epoxy. The male template is used to generate on a

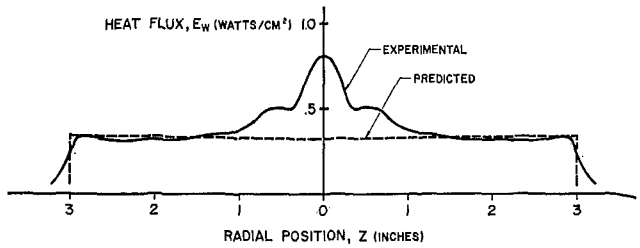

Fig. 5 Experimental and predicted flux distributions

tracing lathe a stainless-steel mandrel. The mandrel is polished to achieve an excellent surface finish. The reflector shells are constructed by electroforming nickel onto the mandrel. These shells can be either gold-plated or aluminum-coated to achieve the desired reflectance characteristics.

The dimensional accuracy of the x–y coordinates of the reflector cross section was carefully measured at each stage of manufacture using a Sheffield Cordax three-axis measuring machine. The dimensions of the polished mandrel were within ±2 mil of the desired dimensions. The electroformed reflector apparently sprang out from the mandrel near the flange so that while at x_i the value of y_i was within +0.5 mil of the desired value, at x_f the value of y_f was 12.5 mil too large.

Experimental Evaluation of Reflector System

The system has been evaluated by experimentally measuring the heat flux at the workpiece location using a Gardon-type calorimeter and a millivolt x–y chart recorder. This experimental system differs in two characteristics from the previous design problem: The electroformed nickel reflector is not coated with vapor-deposited aluminum and the workpiece is a black calorimeter instead of crown glass. Thus the system will not provide the flux distribution prescribed by equation (17). The expected flux for this modified system can be calculated using the present model to predict the flux distribution for the known reflector shape [4]. Surface characteristics of the calorimeter were assumed to be those of a black body; this assumption is consistent with the method of calibrating the calorimeter. Fresnel's equations were used to describe the reflector's reflectance. Experimental measurements of reflectance were made at 0.492 μ using a bidirectional reflectometer similar to the instrument described by Love and Francis [11]. From these measurements n and k were calculated to be 1.961 and 3.23, respectively; these values correspond to a normal specular reflectance of 0.592.

Figure 5 presents the measured flux distribution and the predicted flux distribution for the experimental system. The reflector successfully distributes the energy as desired except for a peak at the center. Integration of the experimental radial flux distribution shows that the system distributes 62.4 w over the 6-in-dia circle compared with the predicted 60.7 w.

Figure 6 is a photograph of the light intensity on an opal glass workpiece. The visible intensity appears uniform except for "rays" radiating from the center and a dark spot of 0.23-in. radius in the center. It was observed that when the reflector was rotated about its axis the ray pattern rotated on the workpiece. The ray pattern is apparently produced by imperfections in the circularity of the reflector. It is hypothesized that the imperfections are from striations on the surface of the mandrel which radiate from the axis and which are produced during turning on the tracing lathe.

The dark spot in the center of Fig. 6 appears to contradict the central peak shown in the total flux measurements of Fig. 5. This apparent contradiction is the result of the finite size of the source and quantitatively can be explained by modeling the source as four point sources instead of a single point. Figure 7 is a scale drawing of the lamp overlayed with four point sources. Each source is arbitrarily assumed to radiate the percentage of total power indicated on Fig. 7 with the angular intensity distri-

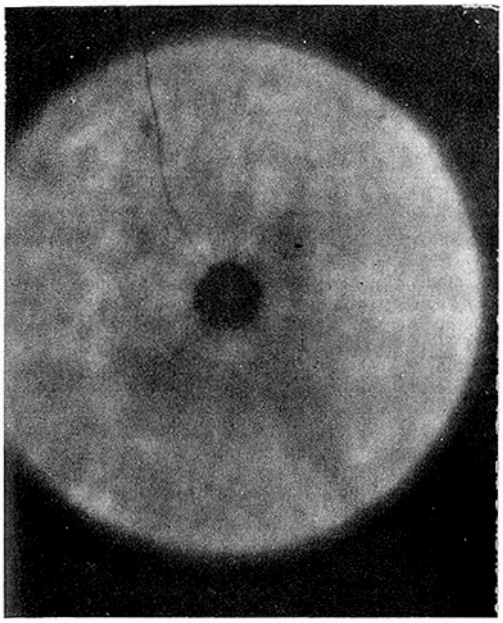

Fig. 6 Illumination on opal glass workpiece

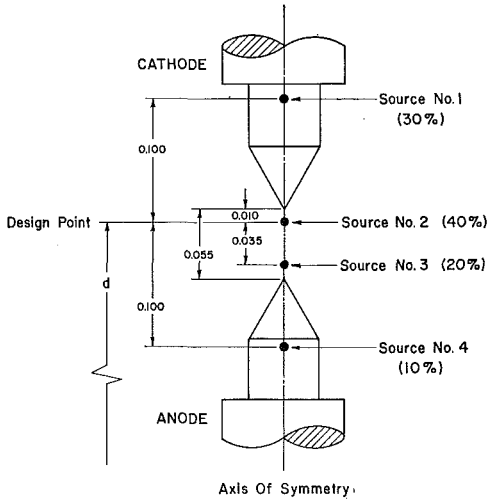

Fig. 7 Representation of lamp as four point sources

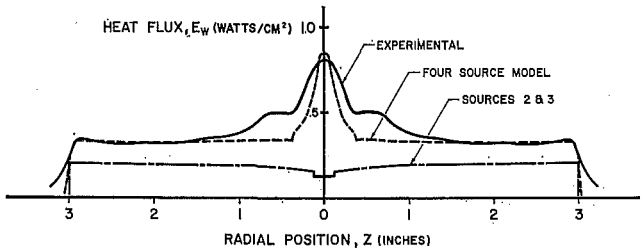

Fig. 8 Predicted flux distribution for four-source model

bution presented in Fig. 3. Source 1 models the infrared thermal emission of the hot cathode. Since this source is displaced from the source design point by 0.100 in., the rays doubly illuminate a circle of 0.367-in. radius producing a hot spot on the workpiece. Source 2 models the ultraviolet and visible emission from the hot spot [12] in the arc column near the cathode. This source is the dominant source to which the experimental system was aligned. Since the source is at the design point it will illuminate the workpiece with the flat flux distribution shown in Fig. 5. Source 3 models the ultraviolet and visible emission from the small hot spot in the arc column near the anode. Because this source is displaced from the design point it does not illuminate a small circle, thus producing a dark spot at the center of the workpiece. Source 4 models the infrared thermal emission from the anode; this source also does not illuminate a small circle at the center of the workpiece.

Figure 8 presents the flux distribution predicted using the four-source model and the experimental total flux measurements. The four-source model predicts the observed hot spot and the local minimum at a radius of 0.4 in. Also shown in Fig. 8 is the predicted flux distribution for only sources 2 and 3, which corresponds to the illumination recorded on the photographic film. The model predicts the observed central dark circle.

Mixed-Mode Problems

The accurate specification of $E_w(z)$ often requires developing a conduction, a convection, or a radiation heat-transfer model which is coupled to the model of radiant interchange in the reflector system. This section briefly illustrates the application of the model to a heat-transfer problem of this type.

Consider heating a 1-in-dia circle on the surface of a semi-infinite piece of stainless steel to a uniform temperature T_0, 360 deg F above ambient, the remainder of the surface being thermally insulated. The desired temperature distribution in the stainless steel is [13]

$$T(z, x) = \frac{2T_0}{\pi} \int_0^\infty e^{-\lambda x} J_0(\lambda z) \sin(\lambda z_f) \frac{d\lambda}{\lambda} \tag{21}$$

where $z_f = 1$ in.

Solving equation (21) for the surface heat flux in the circle of radius z_f by differentiating equation (21) with respect to x and evaluating at $x = 0$ yields the required absorbed flux

$$E_w(z) = \frac{2KT_0}{\pi(z_f^2 - z^2)^{1/2}} \tag{22}$$

where K is the thermal conductivity of the stainless steel. The required flux is singular at $z = z_f$; however, integrating the flux to determine the total required power yields a finite value

$$\phi = 4KT_0 z_f \tag{23}$$

A reflector was designed to produce the flux distribution of equation (22). It was assumed that the reflector was aluminum as in the previous design and that the stainless-steel workpiece had been coated to achieve a perfectly black surface. The energy source was assumed to be a uniform point source radiating 300 w. The geometry was $d = 2.0$ in., $l = 5.5$ in., $y_i = 1.33$ in., $\theta_i = 33.7$ deg, $z_i = 0$ in., and $z_f = 0.5$ in. Figure 9 shows the calculated reflector shape and the heat-flux distribution $E_w(z)$. Note that there are many reflector shapes that will produce this flux distribution since the shape depends on the values of d, l, y_i, and θ_i. The choice of the four variables should be based on obtaining an optimum shape which maximizes the manufacturing tolerances for the reflector.

Summary and Conclusions

A model for designing rotationally symmetric reflectors to produce prescribed flux distributions has been presented. The model has considered spectral, directional, and polarizing effects; the ability to include these effects in the model results from the simple geometry of the system. A reflector system has been constructed for a specific application and its heat-flux distribution experimentally observed. The experimental measurements demonstrate that the model is sufficiently accurate to design heating systems for most applications. Heat-flux predictions for a four-source model have been presented to show that the minor differences between the theoretical and the experimental system are due to the distributed source. The four-source model indicates that the hot spot in the total measurements and

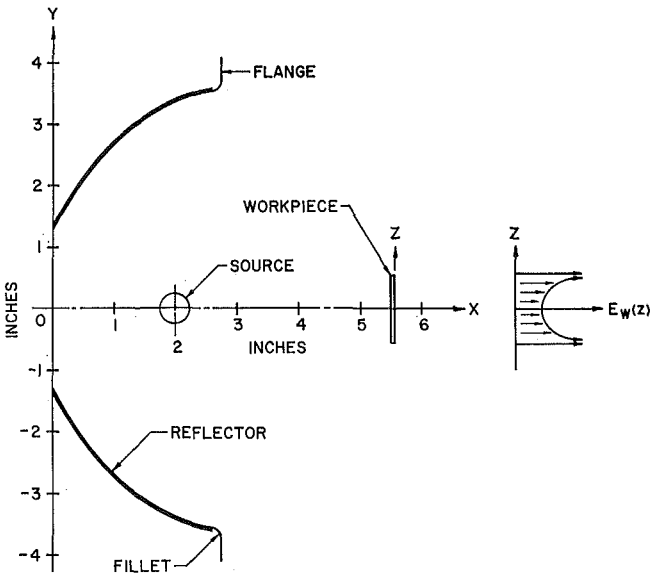

Fig. 9 Reflector design for mixed-mode problem

cold spot in the photographic observations are not contradictory but result from different portions of the source emitting at different frequencies. It is expected that an improved reflector could be designed based on the four-source model.

References

1 Schoenthaler, D., "Reflow Soldering with Radiant Heating," *Symposium Record*, Vol. 10, International Electronic Circuit Packaging Symposium, 1969.

2 Anderson, J. W., LaBlanc, E. A., and Cohan, H., "Experimental and Analytical Assessment of Space Thermal and Vacuum Environment Simulation Requirements," *Journal of Spacecraft and Rockets*, Vol. 3, No. 7, July 1966.

3 Jacob, S. M., and Dranoff, J. S., "Light Intensity Profiles in an Elliptical Photoreactor," *AIChE Journal*, Vol. 15, No. 1, Jan. 1969, pp. 141–144.

4 Pfahl, R. C., Jr., "Radiant Heat Transfer in Reflector Systems," *AIAA Progress in Astronautics and Aeronautics, Heat Transfer and Spacecraft Thermal Control*, Vol. 24, J. W. Lucas, ed., M. I. T. Press, Cambridge, Mass., 1971, pp. 361–382.

5 Edwards, D. K., and Bevans, J. T., "Effect of Polarization on Spacecraft Radiation Heat Transfer," *AIAA Journal*, Vol. 3, No. 7, July 1965, pp. 1323–1329.

6 Ralston, A., and Wilf, H. S., *Mathematical Methods for Digital Computers*, Wiley, New York, N. Y., 1969, pp. 95–109.

7 Gardon, R., "An Instrument for the Direct Measurement of Intense Thermal Radiation," *Review of Scientific Instruments*, Vol. 24, May 1953, pp. 366–370.

8 Sparrow, E. M., and Cess, R. D., *Radiation Heat Transfer*, Brooks/Cole, Belmont, Calif., 1966, pp. 63–64.

9 Hass, G., "Mirror Coatings," chapter 8 in: *Applied Optics and Optical Engineering*, Vol. III, R. Kingslake, ed., Academic, New York, N. Y., 1965, pp. 309–330.

10 Jenkins, F. A., and White, H. E., *Fundamentals of Optics*, McGraw-Hill, New York, N. Y., 1957, p. 465.

11 Love, T. J., and Francis, R. E., "Experimental Determination of Reflectance Function for Type 302 Stainless Steel," *AIAA Progress in Astronautics and Aeronautics, Thermophysics of Spacecraft and Planetary Bodies*, Vol. 20, G. B. Heller, ed., Academic, New York, N. Y., 1967, pp. 115–135.

12 Carlson, F. E., and Clark, C. N., "Light Sources for Optical Devices," chapter 2 in: *Applied Optics and Optical Engineering*, Vol. I, R. Kingslake, ed., Academic, New York, N. Y., 1965, pp. 44–109.

13 Carslaw, H. S., and Jaeger, J. C., *Conduction of Heat in Solids*, 2nd ed., Oxford University Press, Oxford, England, 1959, pp. 215–216.

14 Horton, T. E., and McDermit, J. H., "Design of a Specular Aspheric Surface to Uniformly Radiate a Flat Surface using a Non-uniform Collimated Radiation Source," JOURNAL OF HEAT TRANSFER, TRANS. ASME, Series C, Vol. 94, No. 4, Nov. 1972, pp. 453–458.

W. Z. BLACK
Associate Professor,
School of Mechanical Engineering,
Georgia Institute of Technology,
Atlanta, Ga.
Assoc. Mem. ASME

Optimization of the Directional Emission from V-Groove and Rectangular Cavities

Specially designed cavities are known to produce directional emissivities that have large variations with direction. Surfaces with large variations in radiative properties offer a means of controlling radiative exchange between surfaces. In this paper a measure of the directionality, or degree of focusing, is defined. Possible combinations of directionality and hemispherical emissivity are identified. Two limiting cases for the directional emissivity are discussed which provide collimation of emitted energy in directions which graze and are normal to the cavity opening area, respectively. For a given strength of emission these idealized situations provide maximum focusing of the emission pattern. A V-groove and a rectangular groove are selected as cavities which provide directional emissivities that approach the characteristics of the two limiting cases. Hemispherical emissivity and directionality results for both cavities are presented. Geometries and surface properties of both cavities are optimized to produce maximum focusing of emitted energy. Comparisons are made among the emission characteristics of the V-groove, rectangular groove, and the two idealized limiting cases.

Introduction

When thermal radiation is incident on a concave enclosure, multiple reflections from the surface cause the value for the ratio of absorbed to incident energy to exceed the absorptivity of the surface material itself. Similarly, the amount of energy emitted through an opening of an enclosure exceeds the energy which is emitted from an equal area of the surface material. This characteristic, often referred to as the cavity effect, suggests that the apparent radiative properties of an enclosure opening can be significantly altered by simply manipulating the geometric shape and the surface properties of the enclosure. In fact, by properly selecting the geometry of a cavity, an enclosure can be constructed which has radiative properties that approach those of a blackbody. Since the blackbody is the standard of comparison for radiating surfaces, it is only natural that there has been a great deal of interest in the absorption and emission properties of cavities. A review of absorptance and emittance of several of the more common cavity geometries is given in reference [1][1]. Surface emissivities for the most part have been limited to relatively high values in many studies in an attempt to achieve an apparent emissivity or absorptivity approaching unity. The surface of the enclosure is normally assumed to be a diffuse emitter and reflector, although recently some effort has been devoted to the determination of the directional absorptivity and emissivity of cavities with specularly reflecting surfaces [2].

In contrast to the abundance of information on the properties of enclosures to be used as strong emitters, very little has been reported on the directional characteristics of the emitted energy from enclosures. Just as repeated reflections from the side surfaces of an enclosure may enhance its emission characteristics, the reflections may also re-direct the energy into desired directions so that a cavity may yield an emission pattern which is highly collimated. A directional source of radiant energy acts like an infrared searchlight, and surfaces possessing this kind of emission behavior can have a large effect on the heat transfer between the various surfaces of a system. An illustration of this fact is provided by an experimental investigation [3] undertaken to determine what effect the distribution of emitted energy has on radiation heat-transfer rates. It was determined that collimated emission from a surface fabricated from specially designed cavities is capable of reducing the loss of radiation from two parallel plates by as much as 40 percent. This reduction represents a significant effect and indicates promise for the use of directional surfaces in controlling radiation heat-transfer rates.

The collimated emission pattern produced by a directional emitter can be used in practical applications to control radiative energy exchange between surfaces by directing the emission into desired paths. For example, a diffuse radiant heater placed on the ceiling of a high bay area would direct a significant portion of its emitted energy toward the walls of the structure. A much more effective and economical emission pattern for this heater would be one which produces a directional emissivity

[1] Numbers in brackets designate References at end of paper.

Contributed by the Heat Transfer Division for publication (without presentation) in the JOURNAL OF HEAT TRANSFER. Manuscript received by the Heat Transfer Division August 4, 1971. Paper No. 72-HT-L.

close to unity for those rays that are directed toward the work area on the floor and a directional emissivity close to zero for rays directed toward the walls.

A spacecraft radiator is another example of an application where the collimated energy from a directional enclosure would be desirable. If the radiator were designed to emit with a highly collimated emission pattern, it would be capable of adapting to the sizable variations in incident heat fluxes while still maintaining a close temperature control on the radiator surface. Excessive heat losses could be reduced by directing the radiator so that its emission would fall on other parts of the spacecraft. On the other hand, heat rejection could be enhanced by directing the radiator surface so that the collimated emission would be directed toward deep space. Other applications for collimated emitters, including the use of cavities with variable geometries as semi-active control systems, have been discussed by Clausen and Neu [4].

This paper discusses the design of a cavity not for its high emission or absorption capabilities, but for its directional emission characteristics. A parameter is defined which provides a measure of the focusing of any emission pattern. The problem of selecting the cavity geometry and surface properties so as to provide a directional emissivity which maximizes the collimating effect of the cavity is discussed. The emission pattern required for achieving the maximum collimation for a given strength of emission is presented. Two limiting cases are selected which represent the extremes in desired focused effect. The first is associated with focusing energy in a direction normal to the cavity opening area. The second provides emission focused at grazing angles relative to the cavity opening area. Two specially designed cavities are selected as enclosures which possess emission patterns that approach the two limiting cases. A V-groove is used as a cavity that focuses its emission in the normal direction, and a rectangular groove is used to obtain collimated emission focused in the grazing directions. Hemispherical emissivity and collimation data are presented for both of these cavity geometries. Geometrical parameters of the V-groove and rectangular groove for optimizing the directional effect are presented. Comparisons are made of the strength and collimation results for both the V-groove, the rectangular groove, and the two idealized limiting cases.

Directional Emission

The two factors that are of primary importance in the selection of a particular cavity for use as a directional source of radiant energy are the strength of emission and the degree of collimation. The strength of emission is measured by the hemispherical emissivity of the cavity. Assuming that the directional emissivity of a cavity is only a function of η, the angle between the normal to the plane covering the opening to the cavity and a ray leaving the cavity, the expression for the hemispherical emissivity is

$$\epsilon_h = \int_0^{\pi/2} \epsilon(\eta) \cos \eta d\eta \tag{1}$$

In this paper a limiting η angle, denoted as η_L, is defined which describes the degree of collimation provided by any cavity. The limiting η angle for cases where near-normal emission is desired is arbitrarily defined such that 90 percent of the energy leaving the cavity is enclosed between the angles $\pm\eta_L$. Thus

$$0.9\epsilon_h = \int_0^{\eta_L} \epsilon(\eta) \cos \eta d\eta \tag{2}$$

For cases where grazing emission is required, the degree of collimation can better be expressed in terms of a limiting η angle defined so that only 10 percent of the energy leaving the cavity is enclosed between the angles $\pm\eta_L$ or

$$0.1\epsilon_h = \int_0^{\eta_L} \epsilon(\eta) \cos \eta d\eta \tag{3}$$

Each emission pattern described by the $\epsilon(\eta)$ distribution possesses a unique combination of values for ϵ_h and η_L, but there are numerous $\epsilon(\eta)$ distributions with the same hemispherical emissivity that have different values of η_L. It is appropriate to determine the directional emissivity which, for a given hemispherical emissivity, will provide the strongest degree of collimation. In this paper two limiting cases of η_L are assumed to describe the desired focusing effect. A surface with the strongest collimation in the near-normal directions provides a limit for small values of η_L. For this case the appropriate definition of η_L is one which provides the strongest collimation in direction normal to the opening area. For grazing emission the objective is to produce an emission pattern which has a large value of η_L using equation (3) as the definition of η_L.

The problem now involves the selection of a directional emissivity so that, for a given hemispherical emissivity, the degree of collimation is maximized giving either a maximum or minimum value for η_L. The emission pattern which minimizes η_L for a given strength of emission is one for which $\epsilon(\eta)$ is unity for $0 \leq \eta \leq \eta_1$ and is zero for $\eta > \eta_1$ where η_1 is an arbitrary angle. This pattern is sketched in Fig. 1(a). For this emission pattern the hemispherical emissivity and directionality given by equations (1) and (2), respectively, are

$$\epsilon_h = \sin \eta_1$$

$$\eta_L = \sin^{-1}(0.9\epsilon_h)$$

The values of ϵ_h and η_L therefore depend only on the magnitude of η_1. These relations give the minimum value of η_L as a function of ϵ_h. The result is plotted and is labeled as the curve for maximum collimation in Fig. 1(b). The emission pattern with zero collimation is that of a diffuse surface. While there are emission patterns which possess larger values of η_L than those for a diffuse surface, they are ones for which the energy is focused into grazing angles. They are therefore not considered here where the purpose is to achieve near-normal collimation. As a result, the upper limit for η_L is assumed to be the value for a diffuse surface. The limiting η value for a diffuse surface is 64.2 deg regardless of the strength of emission. This particular η_L value is a result of the arbitrary choice of the constant 0.90 used in the definition of η_L. Based on this definition, all diffuse surface have only the single possible value of 64.2 deg for η_L. Directional surfaces, on the other hand, may have any value between 0 and 64.2 deg, but attempts to achieve smaller values of η_L require the expense of a corresponding decrease in ϵ_h.

Nomenclature

b = distance between the apex and base of V-groove
B = distance between apex and top of V-groove
$(b/B)_{opt}$ = depth ratio of a V-groove to obtain maximum focusing of emission
h = height of rectangular groove
w = width of rectangular groove
ϵ = emissivity
ϵ_b = emissivity of the base surface of the rectangular groove
ϵ_h = hemispherical emissivity
ϵ_s = emissivity of the side surfaces of the V-groove
$\epsilon(\eta)$ = directional emissivity
η = angle between a ray of energy leaving the cavity and the normal to the cavity opening
η_L = measure of directionality
η_1 = arbitrary η angle illustrated in Fig. 1(a)
η_2 = arbitrary η angle illustrated in Fig. 2(a)
θ = V-groove opening angle

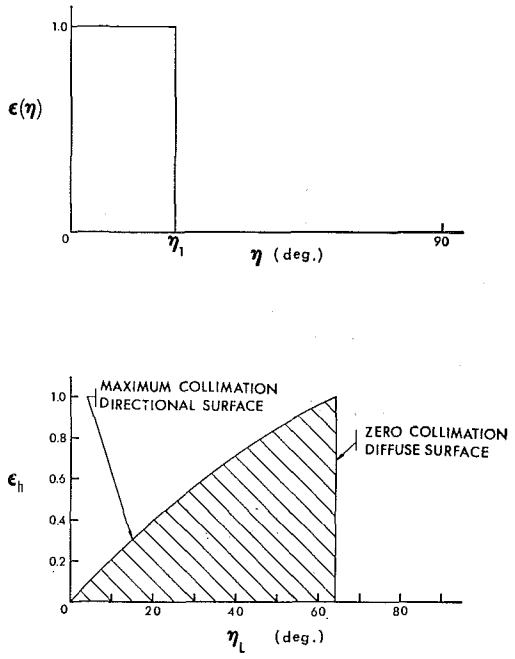

Fig. 1 Requirements for collimation normal to cavity opening; (a) directional emissivity for minimizing η_L for a given hemispherical emissivity; (b) possible combinations of strength and directionality

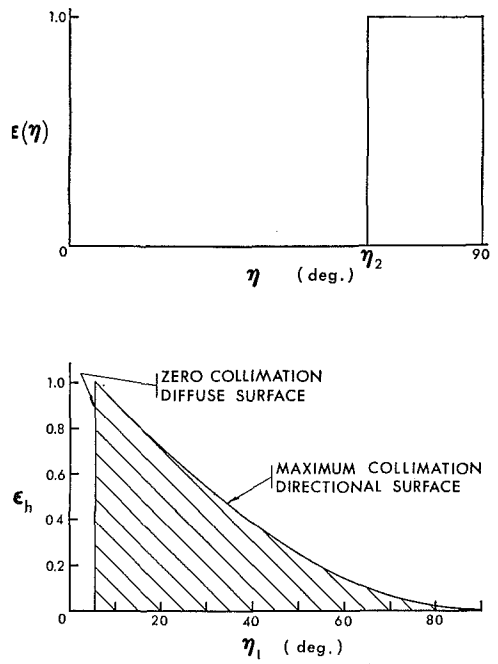

Fig. 2 Requirements for collimation grazing cavity opening; (a) directional emissivity for maximizing η_L for a given hemispherical emissivity; (b) possible combinations of strength and directionality

When the hemispherical emissivity is increased, the cavity becomes less directional in its emission pattern and the minimum possible value of η_L increases. In the limit the maximum emissivity is obtained with a black surface which is diffuse, having a directionality of $\eta_L = 64.2$ deg, thus yielding zero collimation. Those $\epsilon(\eta)$ distributions which are candidates for collimation in the near-normal directions possess ϵ_h and η_L values which lie inside the shaded area of Fig. 1(*b*). Points above the shaded region are not physically realizable, while points to the right of the shaded area are not of interest when normal collimation is desired.

If it is desired to design a cavity which emits a large percentage of energy at η angles approaching 90 deg, it is appropriate to achieve a large value of η_L according to the definition given in equation (3). The directional emissivity which maximizes η_L is one for which $\epsilon(\eta)$ is zero for $0 \leq \eta \leq \eta_2$ and unity for $\eta > \eta_2$ as shown in Fig. 2(*a*). The value of η_2 is arbitrary, but for each choice of η_2 the focusing of the emission pattern is maximized for the corresponding strength of emission. For this emission pattern the hemispherical emissivity and directionality given by equations (1) and (3), respectively, are

$$\epsilon_h = 1 - \sin \eta_2$$

$$\eta_L = \sin^{-1}(1 - 0.9\epsilon_h)$$

Possible combinations of ϵ_h and η_L providing for high values of η_L, using the grazing definition of η_L, equation (3), lie inside the shaded area in Fig. 2(*b*). Points above the shaded area are not physically realizable, while points to the left of the shaded area are not of interest. All diffuse surfaces have a value of η_L equal to 5.74 deg, a value which depends only on the arbitrary choice of the constant 0.1 used in the definition of η_L given by equation (3). The diffuse surface again is taken as the limiting case of zero collimation. The emission pattern shown in Fig. 2(*a*) yields the maximum value of η_L for any specified hemispherical emissivity, the result being indicated by the maximum collimation curve in Fig. 2(*b*). Note that attempts to increase η_L are eventually achieved only at the expense of decreasing ϵ_h. Conversely, if ϵ_h is increased toward unity the blackbody limit is eventually reached which yields zero collimation.

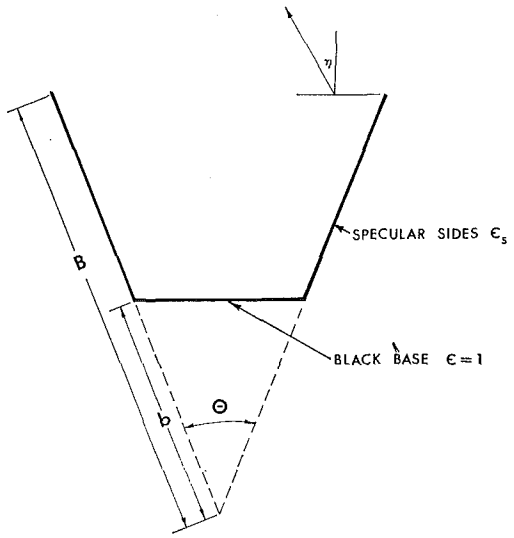

Fig. 3 V-groove geometry

Directional Cavities

V-Groove for Normal Emission. A V-groove cavity with a flat black base and specularly reflecting side surfaces is a source of energy that is strongly collimated in directions nearly normal to the cavity opening area [5]. The strength and distribution of emitted energy leaving the cavity are functions of the cavity geometry and the emissivity of the sides of the groove. The groove geometry is defined by the opening angle θ and the depth ratio b/B (Fig. 3). The groove is assumed to be infinitely long in the direction perpendicular to the plane of the figure. The side surfaces of the groove have emissivity ϵ_s. For the present study the emissivity of the V-groove was first found as a function of the angle leaving the groove and location across the opening area by using a ray-tracing, mirror-imaging technique. The values for the local directional emissivities were then integrated across the opening area to yield the directional emissivity as a function of the angle η. A brief description of the technique

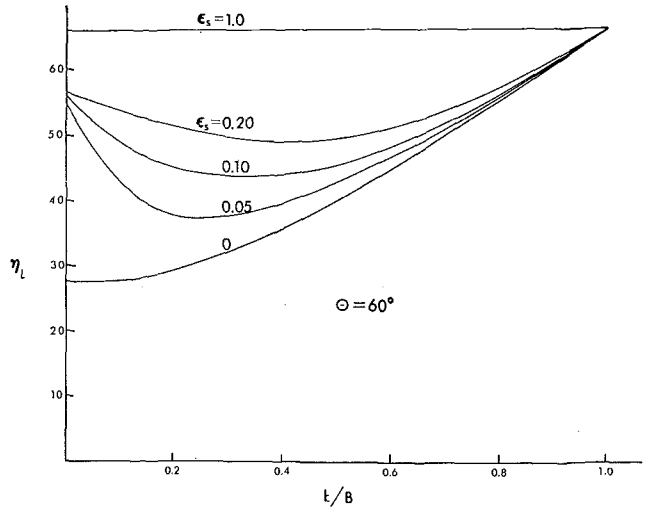

Fig. 4 Directionality for a 60-deg V-groove illustrating existence of an optimum depth

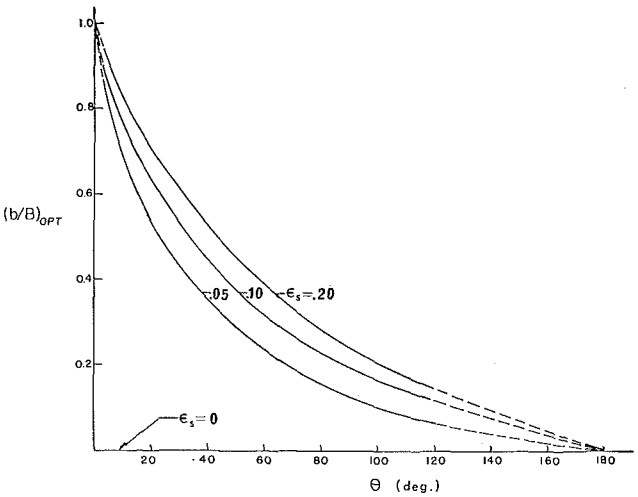

Fig. 5 V-groove optimum depth ratio corresponding to strongest normal emission

used to determine the directional emissivity of the V-groove may be found in reference [6]. A more detailed discussion, including detailed relationships for the local directional emissivity, may be found in reference [7]. For brevity the analysis is omitted here and only the results dealing with optimization of the directional effects are presented in this paper.

The specially designed V-groove is a rather interesting cavity geometry. Except for the idealized case of a groove with non-emitting side walls, deep cavities ($b/B \rightarrow 0$) are diffuse in their emission patterns because energy leaving the black base reflects numerous times before escaping the cavity opening. Shallow cavities ($b/B \rightarrow 1.0$) are also diffuse sources because the black base surface becomes large and it dominates the emission pattern. When the groove sides are emitters, there is a unique depth ratio between 0 and 1.0 for which the focusing of the emission pattern is strongest. The depth for which the focusing of the cavity emission is greatest is illustrated in Fig. 4 where η_L is plotted as a function of depth ratio for a V-groove with a 60 deg opening angle. Since the V-groove was selected as a geometry to provide strong emission in the near-normal directions, the condition which leads to a minimum value of η_L is considered desirable. The depth ratio for minimum η_L will therefore be referred to as the optimum depth ratio $(b/B)_{opt}$. The optimum depth ratio as shown in Fig. 4 is a rather weak function of the sidewall emissivity of the cavity, and it varies from about 0.25 to 0.40 for ϵ_s between 0.05 and 0.20. The directionality for cavities with non-emitting and black sides has also been plotted in Fig. 4 to provide a lower and upper limit for η_L. The cavity with black sides is simply a diffuse emitter. The η_L angle for this case is 64.2 deg regardless of the groove depth. On the other hand, the V-groove with non-emitting sides yields the most-collimated emission pattern. For a groove with non-emitting sides, the optimum depth ratio is zero, since the value for η_L continues to decrease as the depth of the groove is increased.

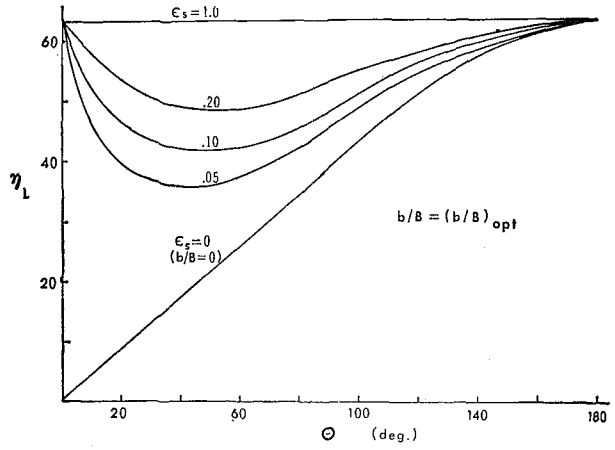

Fig. 6 V-groove directionality at optimum depth illustrating existence of optimum groove opening angle

Curves similar to those shown in Fig. 4 are typical of V-grooves with other opening angles. In fact, grooves having different θ values all exhibit optimum values for the depth ratio except for those possessing θ values close to 0 and 180 deg. As θ approaches either 0 or 180 deg, emission from the V-grooves becomes diffuse for all depth ratios, and the existence of an optimum depth ratio disappears. A plot of the optimum depth ratio as a function of groove angle for various sidewall emissivities is shown in Fig. 5. The curves are dashed for θ less than 5 and greater than 120 deg, indicating that no well-defined optimum depth ratio exists for these angles.

In addition to the unique depth that produces the maximum directional effect for a given θ value, there also exists a groove opening angle for which the emission pattern is strongest in its collimation. The existence of such an opening angle can be explained by the following reasoning. For small groove angles, reflections within the cavity are numerous and the cavity effect is dominant. The emission pattern as a result tends to be diffuse and the emissivity approaches unity regardless of the cavity depth. As the groove opening angle approaches 180 deg the cavity emission is dominated by the base surface which again yields a diffuse emission pattern and an emissivity close to one. At intermediate groove angles the emission pattern is focused as illustrated in Fig. 4. This reasoning suggests that there should be an optimum groove angle between 0 and 180 deg for which the collimating effect is strongest.

Figure 6 shows the variation of η_L as a function of θ with b/B taken to be the optimum depth ratio as indicated in Fig. 5. For the cavities with non-emitting side surfaces the depth ratio was always chosen to be zero so that the absolute minimum value of η_L was obtained. For cavities with emitting side surfaces the optimum groove opening angle indicated in Fig. 6 ranges from about 40 deg for $\epsilon_s = 0.05$ to about 55 deg for $\epsilon_s = 0.20$.

To verify the capability of the V-groove for producing a collimated emission pattern, the hemispherical emissivity is plotted in Fig. 7 as a function of the directionality for a groove angle of 40 deg. The limiting curve for minimum η_L of Fig. 1(*b*) is indicated as a dashed line in Fig. 7 to give an indication of the effectiveness of the 40-deg V-groove as compared with the ideal directional emitter. The minimum value for η_L is reached at the optimum depth ratio for the 40-deg groove indicated in

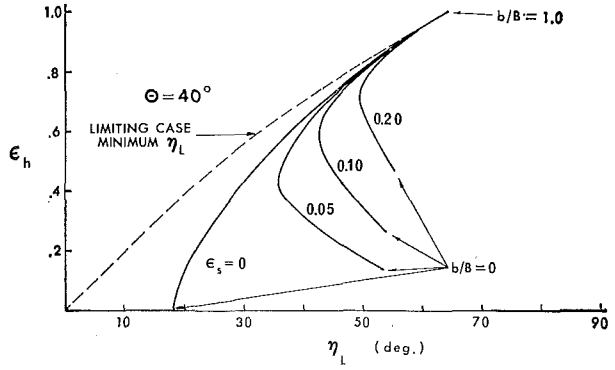

Fig. 7 Directionality and strength for a V-groove; comparison with limiting case

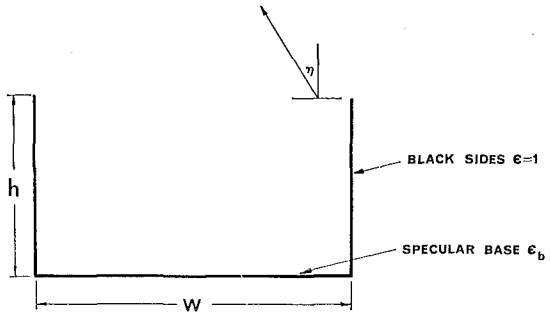

Fig. 8 Rectangular-groove geometry

Fig. 5. Figure 7 shows that a groove with non-emitting sides and a depth ratio of zero has the strongest focusing effect, but it also is weakest in terms of total emission.

Rectangular Groove for Grazing Emission. While the V-groove is a geometry particularly suited for collimated emission in the near-normal directions, a specially designed rectangular groove is capable of producing directional emission focused in directions which graze the cavity opening area [4]. This type of rectangular groove has a specularly reflecting base with emissivity ϵ_b and vertical side surfaces that are assumed to be black emitters. The depth of the cavity is h and the width between the vertical side surfaces is w (Fig. 8). The directional emissivity given in reference [4] for this type of cavity is

$$\epsilon(\eta) = 1 - (1 - \epsilon_b)\left[1 - 2\frac{h}{w}\tan\eta\right] \tag{4}$$

where η is limited by the equation

$$\eta \leq \tan^{-1}\left(\frac{1}{2h/w}\right) \tag{5}$$

The emissivity is unity for η angles above the limit of equation (5).

Representative curves of directional emissivity given by equations (4) and (5) are shown in Fig. 9. When $h/w = 0$ the emission pattern is diffuse with a hemispherical emissivity equal to the value of the base-surface emissivity. As the cavity becomes very deep the emission pattern again becomes diffuse with the hemispherical emissivity approaching unity. At intermediate values of h/w the directional effect of the groove's emission pattern increases and the strength of emission decreases as the cavity becomes shallower. Similar to the characteristics of the V-groove, there is a depth of the rectangular groove which will cause the collimation of the emission pattern to be maximized.

Expressions for the hemispherical emissivity of the rectangular groove may be obtained by substitution of equations (4) and (5) into equation (1). The resulting hemispherical emissivity for the rectangular groove is

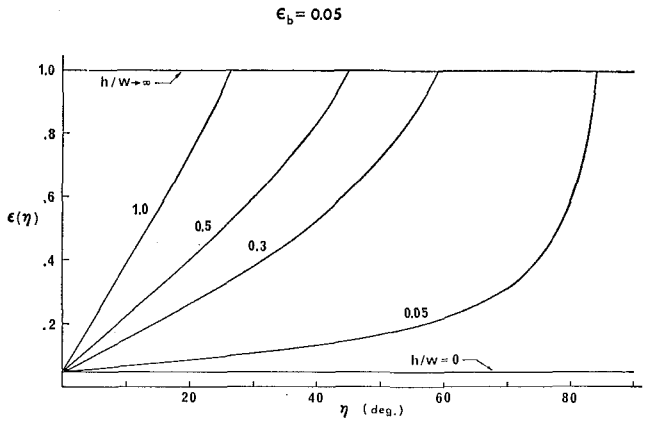

Fig. 9 Directional emissivity for the specially designed rectangular groove

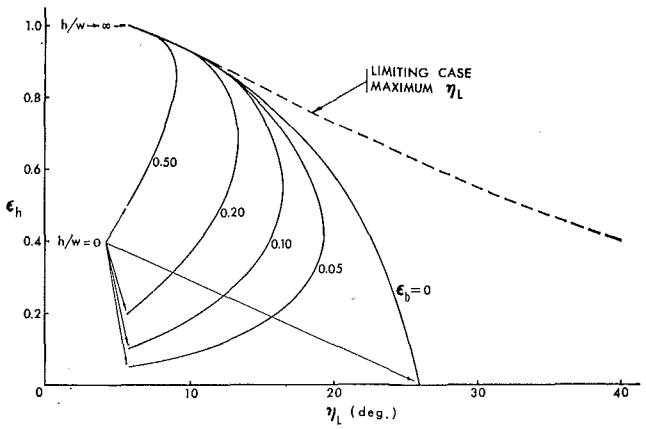

Fig. 10 Directionality and strength for the rectangular cavity; comparison with limiting case

$$\epsilon_h = 1 - (1 - \epsilon_b)[(4h^2/w^2 + 1)^{1/2} - 2h/w]$$

The value of η_L for the rectangular groove depends upon whether η_L is larger or smaller than the limit imposed by equation (5). If η_L is greater than the value of η given by equation (5), then the directionality is given by

$$\sin\eta_L = 0.1 + 0.9(1 - \epsilon_b)[(4h^2/w^2 + 1)^{1/2} - 2h/w]$$

If η_L is less than the value of η given in equation (5), then the directionality is given by the expression

$$\sin\eta_L - 2(h/w)\left(\frac{1 - \epsilon_b}{\epsilon_b}\right)\cos\eta_L = 0.1\left(\frac{1 - \epsilon_b}{\epsilon_b}\right) \times \left[\frac{1}{1 - \epsilon_b} - (4h^2/w^2 + 1)^{1/2} - 18h/w\right]$$

Both of these expressions for η_L yield the same result when $\eta_L = \tan^{-1}(w/2h)$.

Plots of the hemispherical emissivity and directionality for the rectangular groove as a function of base emissivity and groove depth are shown in Fig. 10. The curve for the limiting case of maximum η_L shown in Fig. 2(*b*) is also included in Fig. 10 so that the emission pattern of the rectangular groove can be compared with the one which provides the upper limit for η_L. The emission pattern is entirely diffuse ($\eta_L = 5.74$ deg) when the sides of the groove becomes vanishingly small ($h/w = 0$), with the exception of the case of the cavity with non-emitting base. The emission is diffuse regardless of base-surface emissivity as the groove becomes very deep ($h/w \to \infty$). At intermediate depths the value of η_L is always greater than 5.74 deg, indicating that the cavity produces an emission pattern that is more focused than that of a diffuse cavity. The maximum value of

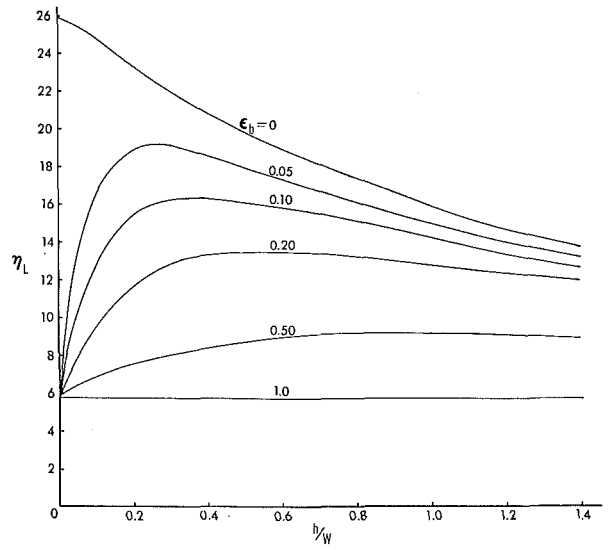

Fig. 11 Directionality of the rectangular cavity illustrating the existence of an optimum cavity depth

η_L for a cavity with an emitting base increases as the base emissivity decreases, indicating that the emission pattern for rectangular cavities becomes more collimated as the base emissivity is reduced. As long as the base surface is an emitter of radiant energy, there is a unique depth of the rectangular groove that gives an emission pattern with a maximum value of η_L. Since the rectangular groove was selected in order to provide a source of energy with a large portion of its energy leaving at grazing angles, the depth that produces a directional emissivity with a maximum value of η_L can be considered an optimum depth. Therefore, just as there was an optimum depth for the V-groove, there is also an optimum depth for the rectangular groove. The groove with the strongest collimation is one with a non-emitting base which is very shallow. This particular idealized cavity also has vanishing strength of emission, however, and cannot be fully achieved in reality.

The optimum depth for the rectangular groove is illustrated further in Fig. 11 where the directionality is shown as a function of the groove depth-to-width ratio for various values of ϵ_b. In general, rather shallow cavities with base emissivities close to zero have the strongest collimated emission. Note that for the idealized case of a non-emitting base, the value of η_L continues to increase as the groove becomes shallower, analogous to the behavior of the V-groove with non-emitting sidewalls.

Conclusions

Specially designed cavities with specularly reflecting surfaces can be used as sources of highly collimated emission or as absorbers that have large variations in directional absorptivity. A V-groove with flat black base and specular sides is a directional cavity that emits a large percentage of its energy in the near-normal directions. A properly designed rectangular groove with black sides and specular reflecting base is a directional cavity with a large percentage of its emitted energy leaving at grazing angles.

A limiting emission angle may be defined which is a convenient measure of the directionality or degree of collimation of any emission pattern. Two such limiting angles have been defined in this paper, one for cases of near-normal emission, equation (2), and one for grazing emission, equation (3). Possible combinations of strength and degree of collimation for both definitions are identified in Figs. 1 and 2.

An optimum depth of the V-groove exists which produces an emission pattern with the strongest collimation of emitted energy. The optimum depth ratio increases as the emissivity of the groove sides increases and as the groove opening angle decreases. The optimum depth values of all V-grooves are shown in Fig. 5.

An optimum V-groove opening angle exists which produces an emission pattern with the strongest collimation of emitted energy. For values of sidewall emissivity between 0.05 and 0.20, the optimum opening angle ranges between 40 and 60 deg as shown in Fig. 6.

An optimum depth of the rectangular groove exists that produces an emission pattern with the strongest collimation of emitted energy. For base emissivities of the rectangular groove between 0.05 and 0.20, the optimum depth-to-width ratio ranges between 0.25 and 0.90 as shown in Fig. 11.

References

1 Sparrow, E. M., "Radiant Emission, Absorption and Transmission Characteristics of Cavities and Passages," *NASA SP-55 Symposium on Thermal Radiation of Solids*, S. Katzoff, ed., 1965.

2 Lin, S. H., and Sparrow, E. M., "Radiant Interchange Among Curved Specularly Reflecting Surfaces—Application to Cylindrical and Conical Cavities," JOURNAL OF HEAT TRANSFER, TRANS. ASME, Series C, Vol. 87, No. 2, May 1965, pp. 299–307.

3 Black, W. Z., and Schoenhals, R. J., "An Experimental Study of Radiation Heat Transfer From Parallel Plates With Direction-Dependent Properties," JOURNAL OF HEAT TRANSFER, TRANS. ASME, Series C, Vol. 92, No. 4, Nov. 1970, pp. 610–615.

4 Clausen, O. W., and Neu, J. T., "The Use of Directionally Dependent Radiation Properties for Spacecraft Thermal Control," *Astronautica Acta*, Vol. 11, No. 5, Sept.–Oct. 1965, pp. 328–339.

5 Perlmutter, M., and Howell, J. R., "A Strongly Directional Emitting and Absorbing Surface," JOURNAL OF HEAT TRANSFER, TRANS. ASME, Series C, Vol. 85, No. 3, Aug. 1963, pp. 282–283.

6 Black, W. Z., and Schoenhals, R. J., "A Study of Directional Radiation Properties of Specially Prepared V-Groove Cavities," JOURNAL OF HEAT TRANSFER, TRANS. ASME, Series C, Vol. 90, No. 4, Nov. 1968, pp. 420–428.

7 Black, W. Z., "Radiative Heat Transfer Characteristics of Specially Designed V-groove Cavities," PhD thesis, Purdue University, Lafayette, Ind., Jan. 1968.

I. S. HABIB
Associate Professor,
Division of Engineering,
University of Michigan–Dearborn,
Dearborn, Mich.
Assoc. Mem. ASME

Solidification of a Semitransparent Cylindrical Medium by Conduction and Radiation

The effect of the radiative transport on the solidification rate and on the temperature distribution in a semitransparent cylindrical medium is investigated. The integral method is employed in the analysis, and results for the cases of absorbing, opaque, and nonparticipating media are presented. It is concluded that the radiative contribution to the process of phase change does have a significant effect on the solidification rate and on the temperature distribution in the solid phase.

Introduction

Engineering problems in which one material is transformed into another or into another phase with generation or absorption of heat continue to receive appreciable attention. Problems of this nature arise in areas such as melting or freezing of a solid, the progress of a temperature-dependent chemical reaction through a solid, the growing of vapor films, and others. The nonlinear nature of these problems requires in most cases numerical or approximate analytical techniques [1–3].[1]

Little study, if any, has been devoted to the solidification of semitransparent materials in which a substantial contribution to the process is due to the heat transfer by radiation. Such problems occur in the recrystallization of semitransparent solids accompanied by latent heat of recrystallization.

In an earlier study [4] we employed the integral method to study the effect of the radiative heat transfer on the solidification rate and on the temperature distribution in the solid phase of a semitransparent planar medium. We felt that in the majority of cases it is useful to have an approximate solution which can describe, however qualitatively, the phenomena under examination. The results for the planar medium showed that the radiative contribution to the process affects the solidification rate and the temperature distribution appreciably.

In the present study we extend the problem to investigate the effect of the radiative transport on the solidification rate and on the temperature distribution in a long cylindrical medium. The integral method is also used in the present analysis, and it is believed that in this way the significance of the radiative contribution to the process in cylindrical geometry can be well demonstrated.

Analysis

Figure 1 represents the problem considered, and it is the one-dimensional solidification of a semitransparent cylindrical homogeneous isotropic material with constant thermophysical and optical properties. A unique melt temperature T_1 is assumed to exist and the liquid phase is maintained at this temperature. The surface at $y = 0$ ($r = R_2$) is considered to be the cold wall at a constant temperature T_2. To reduce the complexities of the problem we assume the melt line and the cold boundary to be black surfaces. We note that in the study of a planar medium [4] the melt line and the cold boundary were not assumed black, and the effect of the emissivities was to slightly modify the solidification rate and the temperature distribution. No significant change in density occurs during solidification. The formulation given here is valid for the analogous melting problem with obvious modifications only.

[1] Numbers in brackets designate References at end of paper.

Contributed by the Heat Transfer Division and presented at the Winter Annual Meeting, New York, N. Y., November 26–30, 1972, of The American Society of Mechanical Engineers. Manuscript received by the Heat Transfer Division September 3, 1971. Paper No. 72-WA/HT-5.

Nomenclature

c = specific heat capacity
E = blackbody emissive power; E_1, E_2, emissive power of surfaces 1 and 2 respectively
E_n = exponential integral
$F(y', y, \gamma)$ = $[(R_2 - y')^2 - (R_2 - y)^2 \sin^2 \gamma]^{1/2}$
D_n = exponential integral function
k = thermal conductivity
n = index of refraction
q_r = radiative heat flux; $q_{r,0}$, radiative heat flux at $y = 0$; $q_{r,s}$, radiative heat flux at $y = s$
r = radius; R_2, exterior radius of cylinder
s = solid-liquid interface, "melt line"
t = time, integration variable
T = temperature
α = thermal diffusivity
λ = latent heat of freezing
ρ = density
σ = Stefan-Boltzmann constant
κ = absorption coefficient

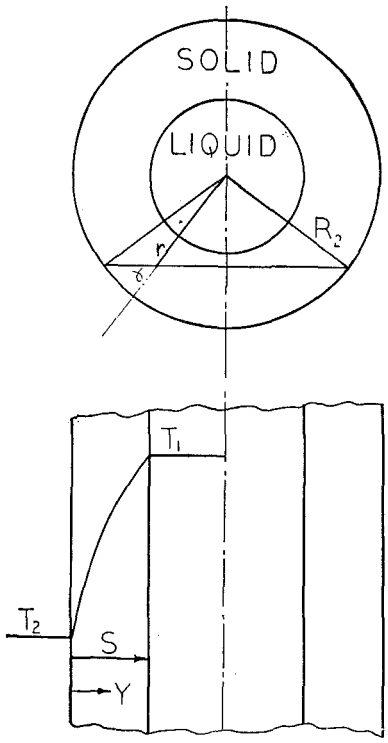

Fig. 1 The present model

The energy equation for the problem can be written in the form

$$\rho c \frac{\partial T}{\partial t} = \frac{1}{(R_2 - y)} \frac{\partial}{\partial y}\left[(R_2 - y)\left(k \frac{\partial T}{\partial y} - q_{r,y}\right)\right] \quad (1)$$

for $0 < y < s$

subject to the following conditions:

$$k \frac{\partial T}{\partial y} - q_{r,y} = \rho\lambda \frac{ds}{dt} \quad \text{at} \quad y = s \quad (2a)$$

$$T(0, t) = T_2 \quad (2b)$$

$$T(s, t) = T_1 \quad (2c)$$

where $y = R_2 - r$ and all other quantities are defined in the Nomenclature. Integrating equation (1) from $y = 0$ to $y = s$ using equation (2a) results in the following equation referred to as the heat-balance integral:

$$\left(\frac{\lambda}{c} + T_1\right)(R_2 - s)\frac{ds}{dt} = \frac{d\theta}{dt} + R_2\alpha\left(\frac{\partial T}{\partial y}\right)_{y=0} - \frac{R_2}{\rho c}(q_{r,y})_{y=0} \quad (3)$$

where

$$\theta = \int_0^s (R_2 - y)T(y, s)dy \quad (4)$$

In solving the heat-conduction problems with the integral method in rectangular geometry a polynomial approximation works well in representing the temperature profile. Lardner and Pohle [5] investigated the application of the integral method to the solution of the heat-conduction problems in regions with cylindrical and spherical symmetry and have shown that polynomial representation alone of the temperature profile would be inaccurate as an approximation. This is to be expected since the volume into which the heat flows does not remain the same for equal increments of r in the cylindrical and spherical coordinate systems; hence a modification in the assumed temperature profile is necessary. Lardner and Pohle suggested the following modifications for the temperature profiles.

In the cylindrical coordinate system the temperature profile may be chosen in the form

$$T = (\text{polynomial in } r)\cdot \ln r$$

and in the spherical coordinate system, the form

$$T = (\text{polynomial in } r)/r$$

In the present problem, if we let the temperature profile be represented by the form

$$T = \left(A + \frac{Br}{R_2}\right)\cdot \ln(r/R_2) + D \qquad 0 < r \leq R_2 \quad (5)$$

then three conditions are necessary to find the constants. Equations (2b) and (2c) are two conditions and the third is essentially equation (2a). But equation (2a) in its present form is not suitable because the coefficients in the polynomial would involve ds/dt. In turn, the heat-balance integral, equation (3), would involve the second derivative for $s(t)$, whereas there is only one initial condition for s, namely $s(0) = 0$. To avoid this difficulty we differentiate equation (2c) with respect to time

$$\frac{\partial T}{\partial y}\frac{ds}{dt} + \frac{\partial T}{\partial t} = 0 \quad (6a)$$

or

$$\frac{ds}{dt} = -\frac{\partial T/\partial t}{\partial T/\partial y} \quad (6b)$$

If we substitute equation (6b) in (2a) we obtain

$$\left(\frac{\partial T}{\partial y}\right)^2 = \left(\frac{q_{r,y}}{k}\right)\left(\frac{\partial T}{\partial y}\right) - \frac{\rho\lambda}{k}\frac{\partial T}{\partial t} \quad (7)$$

From the differential equation for the problem, equation (1), we substitute for $\partial T/\partial t$ in equation (7) and obtain the third required condition as

$$\left(\frac{\partial T}{\partial y}\right)^2_{y=s} = \left[\frac{q_{r,y}}{k}\frac{\partial T}{\partial y} - \frac{\lambda}{c}\frac{\partial^2 T}{\partial y^2} + \frac{\lambda}{c(R_2 - y)}\frac{\partial T}{\partial y} + \frac{\lambda}{kc}\frac{\partial}{\partial y}(q_{r,y}) - \frac{\lambda}{ck(R_2 - y)}q_{r,y}\right]_{y=s} \quad (8)$$

Introducing the variable y and using condition (2b) the temperature profile takes the form

$$T - T_2 = \left[A + B\frac{(R_2 - y)}{R_2}\right]\ln\left(\frac{R_2 - y}{R_2}\right) \quad \begin{matrix} 0 \leq y \leq s \\ s < R_2 \end{matrix} \quad (9)$$

Using equation (2c) and equation (8), A and B are then determined from the following expressions:

$$A = \frac{\delta - \sqrt{\delta^2 + 4\eta}}{2} \quad (10)$$

$$B = (\zeta - A)\left(\frac{R_2}{R_2 - s}\right) \quad (11)$$

and

$$\delta = \left[\frac{2Z_1^2\zeta - \frac{2Z_1\zeta}{R_2 - s} - \frac{1}{k(R_2 - s)}q_{r,y}\Big|_s + \frac{q_{r,y}}{k}\Big|_s Z_1 + Z_2}{\frac{1}{(R_2 - s)^2} - \frac{2Z_1}{(R_2 - s)} + Z_1^2}\right] \quad (12)$$

$$\eta = \left[\frac{\frac{\lambda}{kc}\frac{\partial}{\partial y}q_{r,y}\Big|_s - Z_1^2\zeta^2 - \frac{q_{r,y}}{k}\Big|_s Z_1\zeta - Z_2\zeta - \frac{\lambda}{kc(R_2 - s)}q_{r,y}\Big|_s}{\frac{1}{(R_2 - s)^2} - \frac{2Z_1}{(R_2 - s)} + Z_1^2}\right] \quad (13)$$

$$\zeta = \frac{T_1 - T_2}{\ln\left(\frac{R_2 - s}{R_2}\right)} \tag{14}$$

$$Z_1 = \left[\frac{1}{(R_2 - s)} + \frac{1}{(R_2 - s)} \ln\left(\frac{R_2 - s}{R_2}\right)\right] \tag{15}$$

$$Z_2 = \frac{\lambda}{c(R_2 - s)^2}\left[2 + \ln\left(\frac{R_2 - s}{R_2}\right)\right] \tag{16}$$

Radiative Heat Flux

In a cylindrical absorbing and emitting medium of index of refraction n bounded by black surfaces[2] the radiative heat flux for constant absorption coefficient and no scattering can be written in the form[3] [6, 14]

$$\frac{q_{r,y}}{4n^2/\pi} = \int_{\gamma=0}^{\gamma=\sin^{-1}\left(\frac{R_2-s}{R_2-y}\right)} \left\{\int_0^y [E(y') - E_2]\kappa \frac{(y' - R_2)}{F(y', y, \gamma)} \times D_2[\kappa\{F(y', y, \gamma) - (R_2 - y)\cos\gamma\}]dy' - \int_y^s [E(y') - E_1]\kappa \frac{(y' - R_2)}{F(y', y, \gamma)} D_2[\kappa\{(R_2 - y)\cos\gamma + F(y', y, \gamma)\}]dy'\right\} \cos\gamma d\gamma - \int_{\gamma=\sin^{-1}\left(\frac{R_2-s}{R_2-y}\right)}^{\pi/2} \times \left\{\int_0^y [E(y') - E_2]\kappa \frac{(y' - R_2)}{F(y', y, \gamma)} D_2[\kappa\{(R_2 - y)\cos\gamma + F(y', y, \gamma)\}]dy' + \int_y^s [E(y') - E_2]\kappa \frac{(y' - R_2)}{F(y', y, \gamma)} \times D_2[\kappa\{(R_2 - y)\cos\gamma - F(y, y', \gamma)\}]dy'\right\} \cos\gamma d\gamma - (E_1 - E_2)\left(\frac{R_2 - s}{R_2 - y}\right) \tag{17}$$

In equation (17) the exponential integral function $D_n(x)$ is defined by

$$D_n(x) \equiv \int_0^{\pi/2} (\cos^{n-1}\omega) \exp\left(\frac{-x}{\cos\omega}\right) d\omega = \int_0^1 \frac{\mu^{n-1}e^{-x/\mu}}{(1 - \mu^2)^{1/2}} d\mu \tag{18}$$

and it has the recurrence relation

$$D_n'(x) = -D_{n-1}(x) \qquad n > 1 \tag{19}$$

where $D_n'(x)$ is the derivative of $D_n(x)$ with respect to x. In a previous analysis [6] a formulation for the radiative heat flux in a cylindrical medium was carried out using the approximation

$$D_2(x) \approx ae^{-bx} \tag{20}$$

where a and b are arbitrary constants. Calculations were made using this approximation and a comparison between the approximate and the exact results was made. Excellent agreement was obtained for $a = 1$ and $b = 5/4$. We note that this approximation is similar to the well-known approximation used in the planar geometry for the exponential integral $E_2(x)$.

Employing the approximation given in equation (20) we obtain the following expression for the radiative heat flux:

$$\frac{q_{r,y}}{4n^2/\pi} = \int_{\gamma=0}^{\gamma=\sin^{-1}\left(\frac{R_2-s}{R_2-y}\right)} \left\{\int_0^y [E(y') - E_2]\kappa \frac{(y' - R_2)}{F(y', y, \gamma)} \times \exp[-b\kappa\{F(y', y, \gamma) - (R_2 - y)\cos\gamma\}]dy' - \int_y^s [E(y') - E_1]\kappa \frac{(y' - R_2)}{F(y', y, \gamma)} \exp[-b\kappa\{(R_2 - y)\cos\gamma + F(y', y, \gamma)\}]dy'\right\} \cos\gamma d\gamma - \int_{\gamma=\sin^{-1}\left(\frac{R_2-s}{R_2-y}\right)}^{\pi/2} \times \left\{\int_0^y [E(y') - E_2]\kappa \frac{(y' - R_2)}{F(y', y, \gamma)} \exp[-b\kappa\{(R_2 - y)\cos\gamma + F(y', y, \gamma)\}]dy' + \int_y^s [E(y') - E_2]\kappa \frac{(y' - R_2)}{F(y', y, \gamma)} \times \exp[-b\kappa\{(R_2 - y)\cos\gamma - F(y, y', \gamma)\}]dy'\right\} \cos\gamma d\gamma - (E_1 - E_2)\left(\frac{R_2 - s}{R_2 - y}\right) \tag{21}$$

Equations (3), (4), and (8) require that the radiative heat flux with its spatial and time derivatives be taken at $y = 0$ and at $y = s$. Performing these operations results in the following integral expression for the propagation of the solid–liquid interface with time:

$$t = \int_0^s \frac{\left[\beta - (R_2 - s)\left(\frac{\lambda}{c} + T_1\right)\right] ds}{\alpha(A + B) + R_2 \frac{q_{r,y}}{\rho c}\Big|_{y=0}} \tag{22}$$

in which we set $d\theta/dt = \beta(ds/dt)$ and

$$\beta = \left\{\int_0^s \frac{\partial}{\partial s} T(s, y)(R_2 - y)dy + T_1(R_2 - s)\right\} \tag{23}$$

In some previous studies [7–9] approximations to the propagation of the solid–liquid interface in opaque bodies were obtained by considering that the temperature in the frozen region follows that in a hollow cylinder in the steady state, namely

$$T(r, t) = -\frac{(T_1 - T_2)\ln(R_2 - y) + T_2 \ln(R_2 - s) - T_1 \ln R_2}{\ln\left(\frac{R_2}{R_2 - s}\right)} \tag{24}$$

If equation (24) is used in boundary condition (2a) the following expression results for the propagation of the solid–liquid interface:

$$t = \rho\lambda \int_0^s \frac{(R_2 - s)[\ln R_2 - \ln(R_2 - s)]ds}{k(T_1 - T_2) - (R_2 - s)[\ln R_2 - \ln(R_2 - s)]q_{r,s}} \tag{25}$$

This expression for opaque bodies yields the following known t vs. s relation:

$$\frac{-k(T_1 - T_2)t}{\rho\lambda} = \frac{(R_2 - s)^2}{2} \ln\left(\frac{R_2}{R_2 - s}\right) - \frac{1}{4}(2R_2 s - s^2) \tag{26}$$

Solution

The method of solution used in solving equation (22) is similar to the one we employed for the planar geometry [4]. Equation (22) requires that the radiative heat flux and its derivatives be determined first. That involves integration over the temperature distribution in the solid, which is unknown a priori, and

[2] In answer to a referee's comment we note that the emissivity of the solid–liquid interface depends upon the optical properties of the two phases. However, to include such a dependency in the analysis would result in a high degree of complexity while the objective in this paper is fundamentally to show the significance of the radiative transport in the process.

[3] In [6] the radiative heat flux in a cylindrical medium for nonblack boundaries is also presented.

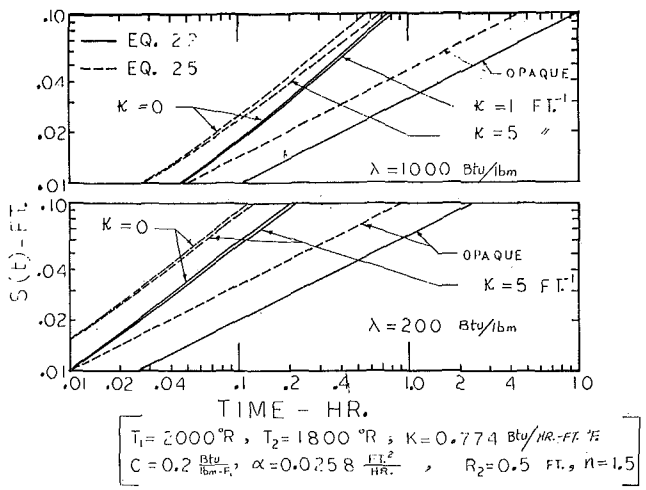

Fig. 2 Thickness of solid vs. time

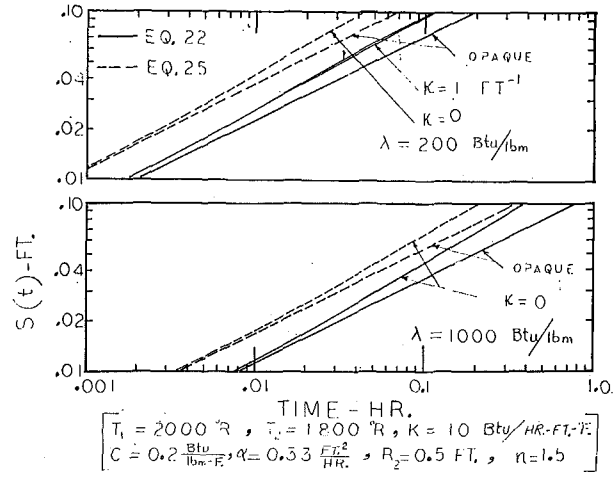

Fig. 3 Thickness of solid vs. time

demands values for A and B that reflect the effect of radiative transport at each value of s. The method of successive substitution, then, was used to determine A and B from equations (10)–(16). When the difference in the calculated values of A and B between two consecutive iterations was within 1 percent of the magnitude of each, the iteration was stopped and the values then obtained were considered satisfactory for the particular value of s. The method converged to the correct values of A and B very fast and in most cases did not require more than two iterations. With the correct values of A and B and the corresponding values for $q_{r,s}$, $q_{r,0}$, and $(dq_{r,y}/dy)|_s$, equation (22) was then integrated to obtain the value of time for that chosen s. The method was repeated for each prescribed value of s, resulting in the desired s vs. t curve and in the temperature distribution at each s.

Results and Conclusions

Figures 2 and 3 show the location of the solid–liquid interface as a function of time with and without the effects of radiation for four sets of conditions. Results for other thermophysical properties behaved in a similar fashion. It can be seen, as was shown in the planar problem, that the case of the nonparticipating medium,[4] $\kappa = 0$, represents an upper bound on the solidification rate, while the pure conduction base (opaque body) represents a lower bound. An increase in the radiation absorption in the medium shifts the solidification curve toward the pure conduction case. Results based upon the steady-state temperature distribution, equation (25), are also shown. Solidification rates obtained using the steady-state temperature distribution are lower for opaque and for radiating media than those obtained using the more exact integral method. We note however that for opaque materials in both methods the solidification rate is proportional to the square root of time, $s \sim \sqrt{t}$.

In Fig. 4 we see that the radiation phenomena appreciably affect the temperature distribution in the solid phase. For the present model the temperature distribution for a nonparticipating medium is higher than that for a pure conduction one. This might seem at first unusual; however, it should be emphasized that the solidification rate for $\kappa = 0$ is much higher than that for pure conduction. Increasing the absorption in the medium raises the temperature distribution further away from that of pure conduction. This can be attributed to a decrease in the net radiation loss by the medium to the boundary. The propagation rate of the interface and the temperature distribution in the solid phase for materials with high thermal diffusivities were little affected by the radiation contribution.[5]

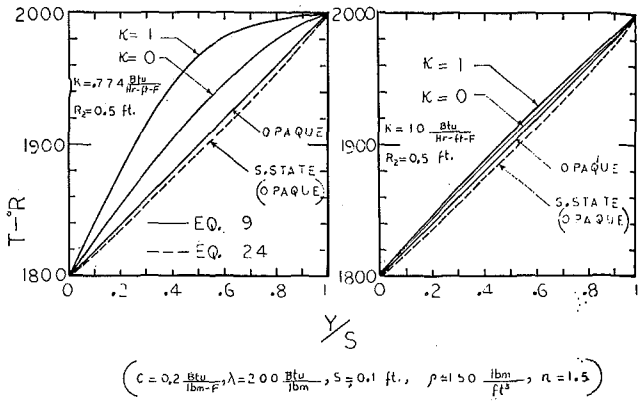

Fig. 4 Temperature distribution in solid

References

1 Goodman, T. R., "The Heat-Balance Integral and Its Application to Problems Involving a Change of Phase," TRANS. ASME, 1958, pp. 335–342.

2 Landau, H. E., "Heat Conduction in Melting Solid," *Q. Appl. Math.*, Vol. 18, 1950, p. 81.

3 Greif, R., and Kassem, A. E., "Heat Transfer in a Growing Vapor Film," *Z. Angew. Math. Phys.*, Vol. 19, No. 5, 1968, p. 824.

4 Habib, I. S., "Solidification of Semi-Transparent Materials by Conduction and Radiation," *International Journal of Heat and Mass Transfer*, Vol. 14, 1971, pp. 2161–2164.

5 Lardner, T. J., and Pohle, F. V., "Application of the Heat Balance Integral to Problems of Cylindrical Geometry," *Journal of Applied Mechanics*, Vol. 28, TRANS. ASME, Series E, Vol. 83, No. 2, June 1961, pp. 310–312.

6 Habib, I. S., and Greif, R., "Nongray Radiative Transport in a Cylindrical Medium," JOURNAL OF HEAT TRANSFER, TRANS. ASME, Vol. 92, No. 1, Feb. 1970, pp. 28–32.

7 Carslaw, H. S., and Jaeger, J. C., *Conduction of Heat in Solids*, Oxford, 1959.

8 Luikov, A. V., *Analytical Heat Diffusion Theory*, Academic, New York, N. Y., 1968.

[4] For a nonparticipating medium the radiative heat flux is constant for all values of s and reduces to the case of the gray concentric cylinder.

[5] With regard to the effect of the radiative transport on the freezing rate of water at 1 atm and 0 deg, we indicate that for water the value of the group $cT_1/\lambda\pi^{1/2}$ is small. Hence, according to [7] the approximate assumption of a temperature distribution based upon a steady state is quite satisfactory for predicting the freezing rate. Furthermore, in this case the solid phase is practically opaque to infrared radiation. Even if the radiative heat flux is significant its effect on the temperature profile is not large, as shown in Fig. 4 for materials with high thermal diffusivities. We note that the choice of the numerical values presented in this paper was made to include a wide spectrum of materials that undergo change of phase by vitrification or amorphous phase transition, crystallization, melting, and crystal–crystal transition.

9 Pekeris and Slichter, *J. Appl. Phys.*, Vol. 10, 1939, pp. 135–137.

10 Love, T. J., *Radiative Heat Transfer*, Charles E. Merrill Publ., 1968.

11 Sparrow, E. M., and Cess, R. D., *Radiation Heat Transfer*, Brooks/Cole, Belmont, Calif., 1966.

12 Chambré, P. L., "On the Dynamics of Phase Growth," *Quart. J. Mech. Appl. Math.*, Vol. 9, Pt. 2, 1956.

13 Elmas, M., "On the Solidification of a Warm Liquid Flowing Over a Cold Wall," *International Journal of Heat and Mass Transfer*, Vol. 13, 1970, pp. 1060–1062.

14 Chiba, Z., and Greif, R., University of California, Berkeley, private communication.

R. I. PEDROSO[1]
Professional Staff Member,
Philips Laboratories,
Briarcliff Manor, N. Y.
Assoc. Mem. ASME

G. A. DOMOTO
Associate Professor,
Department of Mechanical Engineering,
Columbia University,
New York, N. Y.
Assoc. Mem. ASME

Perturbation Solutions for Spherical Solidification of Saturated Liquids

A perturbation solution is obtained for outward and partial inward spherical solidification of a liquid initially at the freezing temperature. The constant-wall-temperature boundary condition is considered with the properties of the solidified material assumed as constants. A nonlinear transformation is applied to the sequence of partial sums in the perturbation solution to increase its range of applicability. For inward solidification it is found that the regular perturbation solution diverges for front positions close to the center. An Euler transformation and an overall energy balance are then used to obtain a modified series solution which is compared with numerical results.

Introduction

Solidification problems are of great practical importance. They are encountered in applications such as freezing foods, casting thermoplastics or metals, the formation of ice, in thermal storage devices for space vehicles, and during freezing of soil.

London and Seban [1][2] presented solutions for freezing rates in one-dimensional problems where the energy content of the solidified material was completely neglected. Kreith and Romie [2] assumed a constant freezing-front speed and obtained solutions through iterative approximations for one-dimensional geometries. Langford [3] obtained a solution assuming a nonlinear relation between first- and second-order time derivatives of the front position in spherical freezing. Longwell [4] used a graphical technique to obtain numerical values for one-dimensional freezing problems. Tao [5] applied a numerical method and presented the results in graphical form for inward solidification in the cylinder and sphere.

The present investigation applies a perturbation technique to solve for temperature distributions and freezing rates during spherical solidification. A perturbation technique to solve planar solidification problems was considered by Lock [6]. In his analysis both the temperature distribution and the freezing-front position were expanded in powers of a physical parameter which represented qualitatively the ratio of sensible to latent heat, the independent variables being time and position within the solidified material. This is in contrast to the technique presented in this paper where the front position replaces time as an independent variable and no need arises to expand the freezing-front position in a perturbation series.

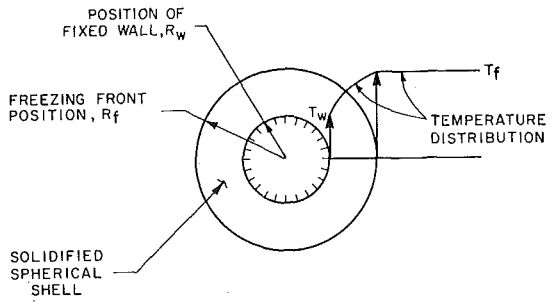

Fig. 1 One-dimensional spherical geometry shown for the case of outward solidification

The solutions obtained assume the fusion temperature and all thermal properties to remain constant. Further, the liquid is assumed to be at the fusion temperature. The solutions presented will also apply for melting problems if the liquid motion is neglected. The perturbation technique introduced in this paper can be applied to other boundary conditions and geometries.

Analysis

Regular Perturbation Solution—Outward and Partial Inward Solidification. The analysis deals with a one-dimensional spherical configuration as shown in Fig. 1. The heat flow within the frozen spherical shell is governed by the transient heat-conduction equation; since there is spherical symmetry and constant properties are assumed, this has the form

$$\frac{\partial T}{\partial t} = \frac{\alpha}{R}\frac{\partial^2 (RT)}{\partial R^2} \tag{1}$$

The constant temperatures at the fixed wall, T_w, and at the freezing front, T_f, yield the boundary conditions

$$T(t, R = R_w) = T_w \qquad T(t, R = R_f) = T_f \tag{2}$$

Since the temperature of the liquid is constant at

[1] Part of doctoral dissertation, Department of Mechanical Engineering, Columbia University, New York, N. Y.

[2] Numbers in brackets designate References at end of paper.

Contributed by the Heat Transfer Division for publication (without presentation) in the Journal of Heat Transfer. Manuscript received by the Heat Transfer Division December 8, 1971. Paper No. 72-HT-Q.

the freezing temperature, an energy balance at the interface yields

$$\frac{dR_f}{dt} = \frac{k}{\rho L}\frac{\partial T}{\partial R}\bigg|_{R=R_f} \tag{3}$$

We define the dimensionless quantities of physical parameter ϵ, temperature u, radial position r, freezing-front position r_f, and time τ as

$$\epsilon = C\frac{T_f - T_w}{L} \qquad u = \frac{T - T_w}{T_f - T_w} \qquad r = \frac{R}{R_w}$$

$$r_f = \frac{R_f}{R_w} \qquad \tau = k\frac{T_f - T_w}{\rho L R_w^2}\,t \tag{4}$$

The product of the specific heat of the solidified material C and the maximum temperature difference $T_f - T_w$ is an indication of the sensible heat in the solid. Therefore the physical parameter ϵ is a qualitative measure of the ratio of sensible to latent heat. Let the dimensionless freezing-front speed be

$$g = \frac{dr_f}{d\tau} \tag{5}$$

Substituting equations (4) into equations (1)–(3), changing variables $(t, r) \rightarrow (r_f, r)$, and substituting equation (5) yields the boundary-value problem in its normalized form

$$\begin{aligned} \epsilon g\frac{\partial u}{\partial r_f} &= \frac{1}{r}\frac{\partial^2(ru)}{\partial r^2} \\ u(r_f, r = r_f) &= 1 \\ u(r_f, r = 1) &= 0 \\ g &= \frac{\partial u}{\partial r}\bigg|_{r=r_f} \end{aligned} \tag{6}$$

The solution to equations (6) can be written in general as

$$u = u(r_f, r; \epsilon) \qquad g = g(r_f; \epsilon) \tag{7}$$

Expanding the dependence of u and g on ϵ in Taylor series about $\epsilon = 0$ yields the following perturbation series:

$$\begin{aligned} u(r_f, r; \epsilon) &= u_0(r_f, r) + \epsilon u_1(r_f, r) + \epsilon^2 u_2(r_f, r) + \ldots \\ g(r_f; \epsilon) &= g_0(r_f) + \epsilon g_1(r_f) + \epsilon^2 g_2(r_f) + \ldots \end{aligned} \tag{8}$$

Substituting equations (8) into (6) and equating coefficients of equal powers of ϵ yields

$$\begin{aligned} \frac{1}{r}\frac{\partial^2(ru_i)}{\partial r^2} &= \begin{cases} 0 & \text{for } i = 0 \\ \sum_{j=1}^{i} g_{j-1}\dfrac{\partial u_{i-j}}{\partial r_f} & \text{for } i \geq 1 \end{cases} \\ u_i(r_f, r = r_f) &= \begin{cases} 1 & \text{for } i = 0 \\ 0 & \text{for } i \geq 1 \end{cases} \\ u_i(r_f, r = 1) &= 0 \\ g_i &= \frac{\partial u_i}{\partial r}\bigg|_{r=r_f} \end{aligned} \tag{9}$$

The linear system of equations (9) was solved up to the second-order terms, yielding

$$\frac{u}{u_0} = 1 + \frac{1}{6}\left[1 - \left(\frac{r}{r_f}\right)^2 u_0^2\right]\frac{\epsilon}{r_f^2} - \left\{\frac{1}{36}\left[1 - \left(\frac{r}{r_f}\right)^2 u_0^2\right] + \frac{4r_f - 1}{120}\left[1 - \left(\frac{r}{r_f}\right)^4 u_0^4\right]\right\}\left(\frac{\epsilon}{r_f^2}\right)^2 \tag{10}$$

$$\frac{g}{g_0} = 1 - \frac{1}{3}\frac{\epsilon}{r_f} + \frac{1 + 6r_f}{45}\frac{\epsilon^2}{r_f^3} \tag{11}$$

where the zeroth-order terms are

$$u_0 = \frac{1 - \frac{1}{r}}{1 - \frac{1}{r_f}} \qquad g_0 = \frac{1}{r_f(r_f - 1)} \tag{12}$$

Equation (11) can be inverted and integrated to give

$$\tau = \frac{3(r_f - 1)^2 + 2(r_f - 1)^3}{6} + \frac{(r_f - 1)^2}{6}\epsilon - \frac{1}{45}\frac{(r_f - 1)^2}{r_f}\epsilon^2 \tag{13}$$

It is usually possible (because of the algebraic complexity) to calculate only the first few terms of the perturbation solution. However, if properly used, the first few terms of the solution will yield a large amount of information. This was the topic of a

Nomenclature

C = specific heat of solidified material
k = thermal conductivity of solidified material
L = latent heat of fusion
R = radial position in solidified material
R_f = radial position of freezing front
R_w = radial position of fixed (spherical) wall
T = temperature distribution in solidified material
T_f = freezing temperature
T_w = temperature at fixed (spherical) wall
t = time
α = thermal diffusivity of solidified material, $k/C\rho$
ρ = density of solidified material

Dimensionless quantities

K = function of ϵ introduced in equation (22)
K_i = value of K including the ith power of ξ in equations (24) and (25) and satisfying equation (26)
g = normalized freezing-front speed, $dr_f/d\tau$
g_i = coefficient of ϵ^i in the regular perturbation series for g
r = normalized radial position in solidified material, R/R_w
r_f = normalized freezing-front position, R_f/R_w
u = normalized temperature distribution in solidified material, $(T - T_w)/(T_f - T_w)$
u_i = coefficient of ϵ^i in the regular perturbation series for u
$u_i{}^t = \sum_{j=0}^{i} \epsilon^j u_j$, ith-order regular perturbation solution for u
u^* = value of u after nonlinear transformation is applied to u_0, $u_1{}^t$, and $u_2{}^t$
$\bar{u}_i$ = coefficient of ξ^i in the modified perturbation series for u
$\bar{u}_i{}^t = \sum_{j=0}^{i} \xi^j \bar{u}_j$, ith-order modified perturbation solution for u
ϵ = perturbation physical parameter, $C(T_f - T_w)/L$
η = $1/r_f$
ξ = $\eta/(K + \eta)$
τ = normalized time, $k(T_f - T_w)t/(\rho L R_w^2)$
τ_i = coefficient of ϵ^i in the regular perturbation series for $\tau(r_f)$
$\tau_i{}^t = \sum_{j=0}^{i} \epsilon^j \tau_j$, ith-order regular perturbation solution for $\tau(r_f)$
τ^* = value of τ after the nonlinear transformation is applied to τ_0, $\tau_1{}^t$, and $\tau_2{}^t$
$\bar{\tau}_i{}^t$ = normalized freezing time in the modified perturbation solution including the ith power of ξ in equations (24) and (25)

paper by Shanks [7] in which he considered a family of nonlinear sequence-to-sequence transformations. The transformations become most useful when the perturbation series is slowly convergent or divergent. Since in the above solutions, equations (10) and (13), only the first three terms have been calculated, it is only possible to apply the simplest of these transformations. For the normalized temperature distribution the result is

$$u^* = \frac{u_0u_1 - \epsilon(u_0u_2 - u_1^2)}{u_1 - \epsilon u_2} \tag{14}$$

which can be combined with equation (10) to obtain

$$\frac{u^*}{u_0} = \frac{1 + \frac{\epsilon}{r_f^2}\left\{\frac{1}{6} + \frac{4r_f - 1}{20}\left[1 + \left(\frac{r}{r_f}\right)^2 u_0^2\right] + \frac{1}{6}\left[1 - \left(\frac{r}{r_f}\right)^2 u_0^2\right]\right\}}{1 + \frac{\epsilon}{r_f^2}\left\{\frac{1}{6} + \frac{4r_f - 1}{20}\left[1 + \left(\frac{r}{r_f}\right)^2 u_0^2\right]\right\}} \tag{15}$$

The same nonlinear transformation can be applied to the terms in equation (13), yielding for the normalized time

$$\tau^* = \frac{1 - 3r_f^2 + 2r_f^3 + \epsilon\left[\frac{2}{15}\frac{1 - 3r_f^2 + 2r_f^3}{r_f} + (r_f - 1)^2\right]}{6 + \frac{4}{5}\frac{\epsilon}{r_f}} \tag{16}$$

The absolute values of the ratios of the first- and second-order terms to the quasi-steady-state temperature distribution reach their maximum values at the fixed wall ($r = 1$). The magnitudes of the first- and second-order corrections for both the temperature distribution (as r approaches one) and the freezing time reach their maximum values relative to the zeroth-order terms when r_f is at its minimum position. This will occur for outward solidification at the instant freezing begins. Hence it should be expected that the perturbation solution will be least accurate at this instant. For $|r_f - 1| \ll 1$ the perturbation solution for spherical solidification can be shown to be identical with that in the plane. Therefore a comparison with Neumann's [8] exact solution in the plane, for $(r - 1)/(r_f - 1) \ll 1$, will yield the maximum percentage errors in the temperature distributions and freezing times given above. These errors are shown in Table 1 and should represent upper bounds for the perturbation solution for outward solidification.

Modified Perturbation Solution—Inward Solidification. For inward solidification it can be seen from equations (10), (11), and (13) that the regular perturbation solutions will diverge for freezing-front positions near the center. Equations (10) and (11) can also be written as

$$\frac{u}{u_0} = 1 + \epsilon a_1\frac{1}{r_f} + \epsilon^2 a_3\frac{1}{r_f^3} \tag{17}$$

$$\frac{g}{g_0} = 1 + \epsilon b_1\frac{1}{r_f} + \epsilon^2 b_3\frac{1}{r_f^3} \tag{18}$$

where

$$a_1 = \frac{1/6}{r_f}\left[1 - \left(\frac{r}{r_f}\right)^2 u_0^2\right]$$

$$a_3 = -\frac{1}{r_f}\left\{\frac{1}{36}\left[1 - \left(\frac{r}{r_f}\right)^2 u_0^2\right] + \frac{4r_f - 1}{120}\left[1 - \left(\frac{r}{r_f}\right)^4 u_0^4\right]\right\} \tag{19}$$

$$b_1 = -\frac{1}{3} \qquad b_3 = \frac{1 + 6r_f}{45}$$

Note that as r_f approaches zero, u_0a_i and b_i $(i = 1, 3)$ remain finite quantities. The general form of the series (17) and (18) is

$$\beta = 1 + C_1\eta + C_3\eta^3 + C_5\eta^5 + \cdots \tag{20}$$

where

$$\eta = 1/r_f \tag{21}$$

and the quantities C_i are known functions of ϵ, r, and r_f. Equation (20) can be subjected to an Euler [9] transformation with a parameter $K = K(\epsilon)$ (which will be later determined from an overall energy balance), yielding

$$\beta = 1 + KC_1(1 + \xi)\xi + K(C_1 + K^2C_3)\xi^3 + K(C_1 + 3K^2C_3)\xi^4 + K(C_1 + 6K^2C_3 + K^4C_5)\xi^5 + \cdots \tag{22}$$

where

$$\xi = \frac{\eta}{K + \eta} \tag{23}$$

Note that ξ approaches one as r_f approaches zero. If equations (17) and (18) are transformed according to the general series equation (22), there results

$$\frac{u}{u_0} = 1 + Ka_1\epsilon(1 + \xi)\xi + K\epsilon(a_1 + K^2a_3\epsilon)\xi^3 + K\epsilon(a_1 + 3K^2a_3\epsilon)\xi^4 \tag{24}$$

$$\frac{g}{g_0} = 1 + Kb_1\epsilon(1 + \xi)\xi + K\epsilon(b_1 + K^2b_3\epsilon)\xi^3 + K\epsilon(b_1 + 3K^2b_3\epsilon)\xi^4 \tag{25}$$

An overall energy balance can be taken from the instant freezing begins to the moment that the center of the sphere freezes to obtain

$$\int_0^1 \frac{\left.\frac{\partial u}{\partial r}\right|_{r=1}}{g}\,dr_f + \epsilon\int_0^1 r^2u(r_f = 0, r)dr = \frac{1 + \epsilon}{3} \tag{26}$$

Table 1 Percentage errors in the regular perturbation solution for initial spherical solidification

		$\tau_i^t = \sum_{j=0}^{i} \epsilon^j\tau_j$	$u_i^t = \sum_{j=0}^{i} \epsilon^j u_j$		
λ	0.2	0.4	0.6	0.8	1
ϵ	0.0822	0.3564	0.9205	1.996	4.060
% τ_0	−2.639	−10.22	−21.78	−35.86	−50.74
% τ_1^t	0.0282	0.4481	2.222	6.807	15.93
% τ_2^t	−0.0011	−0.0588	−0.7238	−4.545	−20.16
% τ^*	−0.0007	−0.0358	−0.4019	−2.160	−7.489
% $u_0(r \to 1)$	−1.317	−5.087	−10.81	−17.79	−25.32
% $u_1^t(r \to 1)$	0.0341	0.5513	2.875	9.552	25.22
% $u_2^t(r \to 1)$	−0.0010	−0.0851	−1.113	−7.728	−39.76
% $u^*(r \to 1)$	−0.0001	−0.0205	−0.2129	−1.037	−3.208

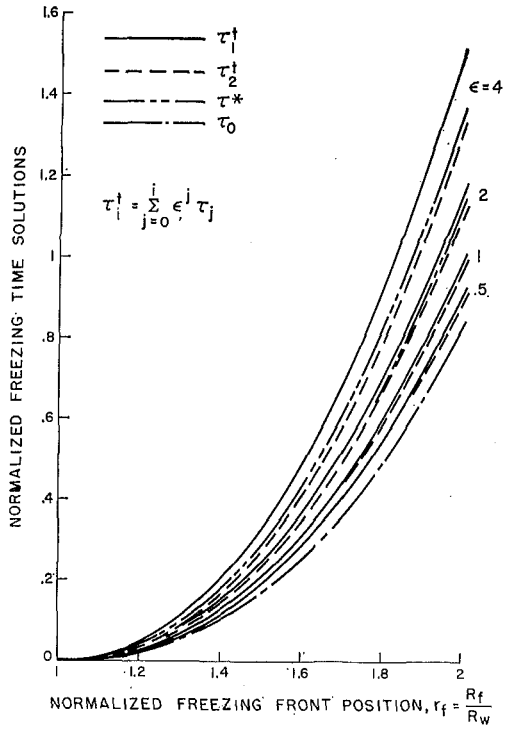

Fig. 2 Normalized freezing-time solutions in the regular perturbation series for outward solidification

Equations (24) and (25) can be truncated at powers of ξ of value less than four. Subsequent substitution into equation (26) will yield one equation to solve for the function $K = K(\epsilon)$. Define K_i to be the value of K including the ith power of ξ in equations (24) and (25) and satisfying equation (26). The resulting (transcendental) equation to solve for K_1 is

$$\frac{6 - (3 + 2\epsilon)K_1}{6K_1} \ln\left(1 + \frac{3K_1}{3 - \epsilon K_1}\right) = 1 - \frac{7}{40}\frac{\epsilon K_1^2}{3 - \epsilon K_1} \quad (27)$$

Define $\bar{\tau}_i{}^t$ to be the normalized freezing time in the modified perturbation solution including the ith power of ξ in equations (24) and (25). The solution including the zeroth- and first-order terms is

$$\bar{\tau}_1{}^t = \frac{\epsilon}{9K_1}[3 + (3 - \epsilon)K_1] \times \left[1 - r_f - \frac{3 - \epsilon K_1}{3K_1} \ln \frac{3 + (3 - \epsilon)K_1}{3 + (3r_f - \epsilon)K_1}\right] + \frac{3 - \epsilon}{6}(1 - r_f{}^2) - \frac{1 - r_f{}^3}{3} \quad (28)$$

It becomes progressively more difficult to perform analytically the integrations of the expressions yielding K_i and $\bar{\tau}_i{}^t$ for $i > 1$. It will be shown that for $\epsilon \leq 1$, $\bar{\tau}_1{}^t$ agrees well with the finite-difference numerical integration of the boundary-value problem. The solutions for K_i and $\bar{\tau}_i{}^t$ for $i > 1$ were obtained numerically using Simpson's rule with increments in freezing-front position of 0.025.

Define the ith-order modified perturbation solution for the normalized temperature distribution as

$$\bar{u}_i{}^t = \sum_{j=0}^{i} \xi^i \bar{u}_j \quad (29)$$

At the instant that the center of the sphere freezes, equation (24) yields

$$\bar{u}_i{}^t(r_f = 0, r = 0) = 1 \quad (30)$$

while for $r > 0$

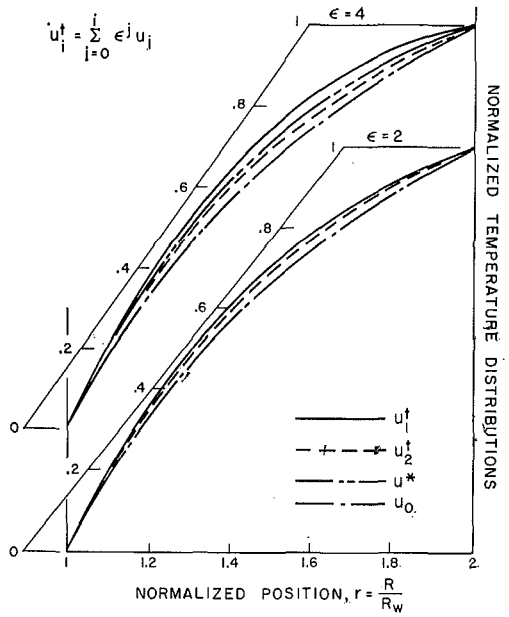

Fig. 3 Normalized temperature distributions in the regular perturbation series at a normalized freezing-front position $r_f = 2$

$$\bar{u}_0(r_f = 0, r) = 0$$

$$\bar{u}_1{}^t(r_f = 0, r) = \frac{\epsilon K_1}{6}(1 - r)(2 - r)$$

$$\bar{u}_2{}^t(r_f = 0, r) = \frac{\epsilon K_2}{3}(1 - r)(2 - r)$$

$$\bar{u}_3{}^t(r_f = 0, r) = \frac{\epsilon K_3}{2}(1 - r) \times \left[2 - r - \frac{\epsilon K_3{}^2}{180}(8 + 8r - 12r^2 + 3r^3)\right] \quad (31)$$

$$\bar{u}_4{}^t(r_f = 0, r) = \frac{2}{3}\epsilon K_4(1 - r) \times \left[2 - r - \frac{\epsilon K_4{}^2}{60}(8 + 8r - 12r^2 + 3r^3)\right]$$

By considering the limiting values of equations (31) as r approaches $+0$, one obtains the following conditions that must be satisfied in order for the temperature distribution to be between its values at the fixed wall and at the freezing front:

$$0 \leq K_1 \leq \frac{3}{\epsilon} \qquad 0 \leq K_2 \leq \frac{1.5}{\epsilon}$$

$$K_3\epsilon\left(1 - \frac{K_3{}^2\epsilon}{45}\right) \leq 1 \qquad \frac{4}{3}K_4\epsilon\left(1 - \frac{K_4{}^2\epsilon}{15}\right) \leq 1 \quad (32)$$

No multiple-valued solutions were found for K_1 and K_2 in the above ranges of physical importance. For certain values of ϵ there existed more than one K_3 and K_4 satisfying the above inequalities. In such cases the solutions chosen were the lowest positive values available.

Results and Discussion

Figure 2 shows the normalized freezing time obtained from the regular perturbation solution for outward solidification. Zeroth-, first-, and second-order solutions as well as nonlinear transformed solutions are shown for various values of ϵ. The first- and second-order terms are of opposite sign, suggesting that the exact solution will probably be found between the first- and second-order solutions. For initial solidification the transformed solution τ^*

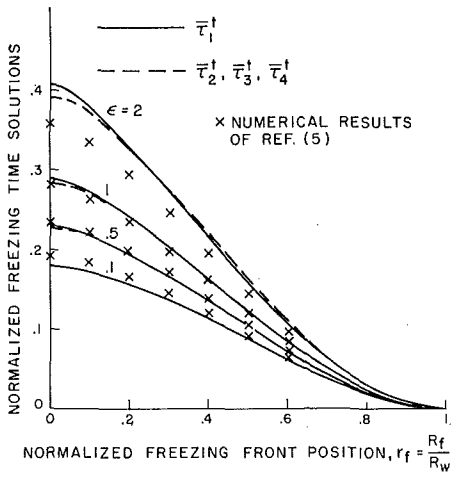

Fig. 4 Normalized freezing-time solutions in the modified perturbation series for inward solidification

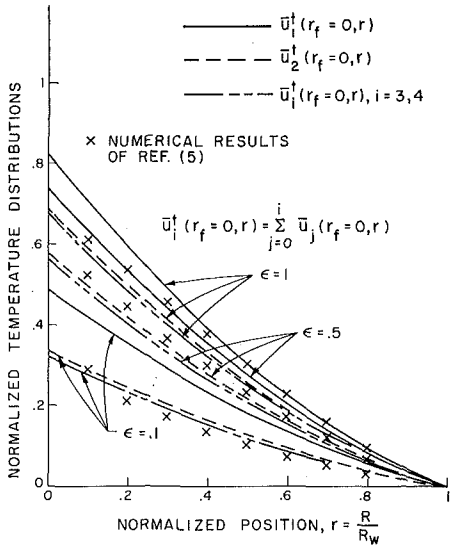

Fig. 5 Normalized temperature distributions in the modified perturbation series at the instant of freezing to the center

was found (see Table 1) to be more accurate than the second-order solution $\tau_2{}^t$. It is also expected that τ^* will be more accurate than $\tau_2{}^t$ for other front positions. The values for τ^* are always found to be between those of $\tau_1{}^t$ and $\tau_2{}^t$. For clarity, the curves for τ^* in the cases of $\epsilon = 0.5$ and 1 are not shown.

The normalized temperature distributions at a front position $r_f = 2$ are shown in Fig. 3. The exact solution probably lies between $u_1{}^t$ and $u_2{}^t$. The values for u^* are always found to be between those of $u_1{}^t$ and $u_2{}^t$. For clarity, the curve for u^* is not shown in the case of $\epsilon = 2$. For $r_f \gg 1$ the first- and second-order terms will approach zero and the temperature distribution approaches the quasi-steady-state solution.

The values of K in the modified perturbation solution for inward solidification were calculated from equations (26) and/or (27) and are listed in Table 2. The values of K decrease in magnitude with increasing ϵ and with increasing number of terms in the modified series solution. If this condition did not exist, then equations (24) and (25) could become divergent series.

The modified series solutions for freezing times are shown in Fig. 4. The values for $\bar{\tau}_2{}^t$, $\bar{\tau}_3{}^t$, and $\bar{\tau}_4{}^t$ were sufficiently close to warrant no graphical distinction. There is good agreement with the regular perturbation solutions over their ranges of applicability. The modified series solutions agree closely for $\epsilon = 0.5$ and 1 with the freezing times calculated numerically in [5]. The results from [5] appear to be a little high for $\epsilon = 0.1$. For large values of ϵ the modified series solution including four terms appears to be inaccurate in describing freezing rates. The disagreement with the values from [5] becomes significant for $\epsilon = 2$. This failure in the modified series solutions for large values of ϵ probably stems from the inadequacy of the linear system of equations (9) to describe solidification processes when the effect of the specific heat in the solidified material becomes very important relative to the latent heat of fusion.

The modified series solutions for the temperature distribution at the instant of freezing to the center as given by equations (31) are shown in Fig. 5. The values for $\bar{u}_3{}^t(r_f = 0, r)$ and $\bar{u}_4{}^t(r_f = 0, r)$ were sufficiently close to warrant no graphical distinction. Numerical values from [5] for positions $r \geq 0.1$ are also shown. The modified series solution yields temperature distributions with a point of singularity at the center of the sphere and should therefore be inaccurate in its vicinity. For freezing-front positions away from the center there is no point of singularity and the accuracy of the temperature distributions should improve. For front positions far from the center it is also possible to obtain the temperature distribution from the regular perturbation solution.

Table 2 Values of the parameter K satisfying the overall energy balance for complete inward solidification, equations (26) and/or (27)

ϵ	K_1	K_2	K_3	K_4
0.1	14.96	5.084	3.395	2.643
0.2	9.099	3.279	2.175	1.674
0.3	6.699	2.504	1.655	1.266
0.4	5.350	2.054	1.355	1.032
0.5	4.474	1.754	1.156	0.8774
0.6	3.854	1.537	1.013	0.7669
0.7	3.391	1.372	0.9038	0.6832
0.8	3.030	1.241	0.8176	0.6173
0.9	2.741	1.135	0.7476	0.5638
1	2.503	1.046	0.6894	0.5195
2	1.351	0.5988	0.3952	0.2968
3	0.9287	0.4237	0.2801	0.2102

References

1 London, A. L., and Seban, R. A., "Rate of Ice Formation," TRANS. ASME, Vol. 65, 1943, p. 771.

2 Kreith, F., and Romie, F. E., "A Study of the Thermal Diffusion Equation with Boundary Conditions Corresponding to Solidification or Melting of Materials Initially at the Fusion Temperature," *Proc. Phys. Soc.*, Vol. 68B, 1955, p. 277.

3 Langford, D., "The Freezing of Spheres," *International Journal of Heat and Mass Transfer*, Vol. 9, 1966, p. 827.

4 Longwell, P. A., "A Graphical Method for Solution of Freezing Problems," *AIChE Journal*, Vol. 4, No. 1, 1958, p. 53.

5 Tao, L. C., "Generalized Numerical Solutions of Freezing a Saturated Liquid in Cylinders and Spheres," *AIChE Journal*, Vol. 13, No. 1, 1967, p. 165.

6 Lock, G. S. H., "On the Use of Asymptotic Solutions to Plane Ice-Water Problems," *J. Glaciol.*, Vol. 8, 1969, p. 285.

7 Shanks, D., "Non-linear Transformations of Divergent and Slowly Convergent Sequences," *Jour. of Math. and Phys.*, Vol. 34, 1955, p. 1.

8 Carslaw, H. S., and Jaeger, J. C., *Conduction of Heat in Solids*, Oxford University Press, London, England, 1959, p. 285.

9 Van Dyke, M., *Perturbation Methods in Fluid Mechanics*, Academic, New York, N. Y., 1964, p. 32.

N. WEBER
Senior Development Engineer,
Westinghouse Hanford,
Richland, Wash.

R. E. POWE
Assistant Professor.
Assoc. Mem. ASME

E. H. BISHOP
Professor and Department Head.
Mem. ASME

J. A. SCANLAN
Professor.
Mem. ASME

Mechanical Engineering Department,
Montana State University,
Bozeman, Mont.

Heat Transfer by Natural Convection between Vertically Eccentric Spheres

Natural convection to a cooled sphere from an enclosed, vertically eccentric, heated sphere is described in this paper. Water and two silicone oils were utilized in conjunction with four different combinations of sphere sizes and six eccentricities for each of these combinations. Both heat-transfer rates and temperature profiles are presented. The effect of a negative eccentricity (inner sphere below center of outer sphere) on the temperature distribution was an enhancement of the convective motion, while a positive eccentricity tended to stabilize the flow field and promote conduction rather than convection. As for concentric spheres, a multicellular flow pattern was postulated to explain the thermal field observed for the largest inner sphere utilized. In all cases the heat-transfer rates were increased by moving the inner sphere to an eccentric position, and the utilization of a conformal-mapping technique to transform the eccentric spheres to concentric spheres enabled the application of existing empirical correlations for concentric spheres to the eccentric-sphere data. It is significant to note that this technique yields a single correlation equation, in terms of only k_{eff}/k and a modified Rayleigh number, which is valid for an extremely wide range of diameter ratios, eccentricities, Rayleigh numbers, and Prandtl numbers.

Introduction

Although the accurate prediction of natural-convection heat transfer within enclosed spaces is becoming increasingly important and more studies are appearing each year, knowledge in this area is still rather limited. Such information is important in several practical applications including the design of nuclear-reactor in-pile experiments, spent-fuel shipping containers, and reactor cores for thermal safety during emergency power-off situations. Apart from these and other practical considerations there remains unresolved the question of the interaction between the hydrodynamic and the thermal effects, especially under the unusual stability conditions associated with enclosures. As a first step in the study of this problem several relatively simple geometries, including rectangular cavities, concentric cylinders, and concentric spheres, have been investigated both experimentally and analytically.

The first investigations utilizing the spherical geometry [1–3][1] concentrated on an experimental determination of temperature profiles, heat-transfer rates, and flow patterns for air as the test fluid. By using diameter ratios ranging from 1.10 to 3.14, Grashof numbers based on gap thickness ranging from 2×10^4 to 3.6×10^6 were obtained. In addition an analytical solution for natural convection between concentric spheres at low Rayleigh numbers has been presented by Mack and Hardee [4]. This solution consists of the expansion of the temperature and stream functions in power series of the Rayleigh number and the evaluation of the first three terms in each of these series for a Prandtl number approximately equal to that of air.

More recently, heat-transfer and temperature-profile results have been obtained for a greatly extended Prandtl-number range by Scanlan, Bishop, and Powe [5]. Water and two silicone oils were utilized and the resulting data were combined with the previous air data to yield an overall Prandtl-number range of 0.7 to 4148. For relative gap widths $(r_o - r_i)/r_i$ between 0.09 and 1.81, it was found that the heat-transfer results, both for each fluid individually and for all the data combined, could be correlated simply in terms of k_{eff}/k and a Rayleigh number.

The purpose of the present study is to extend the previous results to include the case of eccentric spheres, where the eccentricity is parallel to the gravity vector and along the vertical diameter. An experimental study of the natural convection of fluids contained between a cooled outer sphere 24.9 cm in diameter and heated inner spheres with diameters ranging from 11.4 cm to 22.8 cm is discussed, and temperature profiles and heat-transfer data are presented. Water and silicone oils were utilized as the fluid in the gap to yield Prandtl numbers ranging from 4.7 to 4148. The results are combined with those of previous experimental investigations to yield detailed descriptions of the temperature profiles and an extremely general correlation equation for the heat-transfer data over a very wide range of Prandtl numbers, Rayleigh numbers, relative gap widths, and eccentricity ratios $e/(r_o - r_i)$.

[1] Numbers in brackets designate References at end of paper.

Contributed by the Heat Transfer Division and presented at the Winter Annual Meeting, New York, N. Y., November 26–30, 1972, of The American Society of Mechanical Engineers. Manuscript received by the Heat Transfer Division July 20, 1971. Paper No. 72-WA/HT-2.

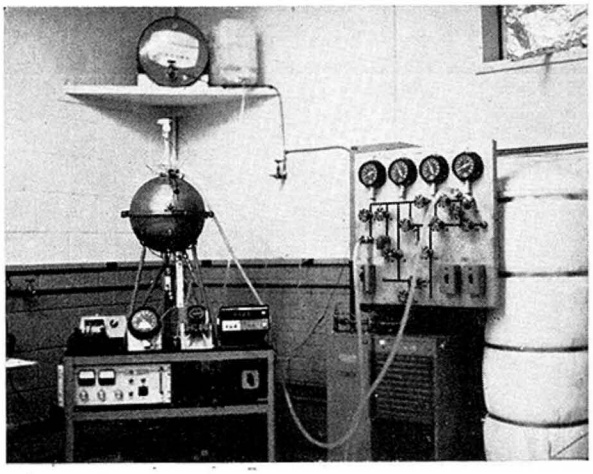

Fig. 1 Heat-transfer apparatus

Apparatus and Procedure

The heat-transfer apparatus shown in Fig. 1 consisted basically of a heated inner sphere and a cooled outer sphere, both enclosed within a spherical water jacket. The outer stainless-steel sphere, which was 24.9 cm ID, was used in conjunction with four copper inner spheres having outer diameters of 22.8, 17.8, 13.9, and 11.4 cm. These were supported in the outer sphere by a 1.27-cm-dia stainless-steel stem which was insulated on its lateral surface; a screw-type adjustment on this support stem allowed positioning of the inner sphere to any desired vertical location within the outer sphere.

An isothermal inner-sphere surface was achieved by internally condensing Freon-11 vapor. The surface temperature could be varied by changing the power input to electrical heaters which were submerged below the Freon liquid level. Since it has previously been established that this method of heating provides an isothermal surface [1], the surface temperature was measured by four thermocouples located at 90-deg intervals around the horizontal equator of the sphere. A small stainless-steel tube extended through the support stem for pressure measurements within the inner sphere and for venting during Freon charging operations.

The outer sphere and the water jacket were each composed of two stainless-steel hemispheres joined by an external flange and sealed with an O-ring to facilitate disassembly. Thermocouple-probe guides were attached to the outer surfaces of both the outer sphere and the water jacket. The outer sphere was supported within the water jacket by a removable stainless-steel spacer.

The water utilized to maintain the outer sphere at a constant temperature was provided by a closed supply system, shown in Fig. 1, consisting of two commercial water chillers, a centrifugal pump, and a 25-gal insulated storage tank. Water from this system was introduced at the base of the water jacket and withdrawn at the top through manifold systems. The outer-sphere temperature, which was taken to be the average of the inlet and outlet water temperatures, could be varied by adjusting the temperature level on the chillers.

Temperature profiles within the space between the two spheres were obtained by using thermocouple probes made of 24-gauge copper and constantan wires inserted through 15-gauge stainless-steel support tubes. The wires were fused together to form small thermocouple junctions and then sealed to the tubes at both ends with an epoxy cement. Each support tube was attached to a micrometer probing mechanism which could advance the probe and indicate its position to within 0.003 cm. The micrometer probing mechanism attached to the probe located along the upper vertical axis was also used for determining the exact location of the inner sphere. Previous work [1–3] had indicated that for concentric spheres under steady conditions the flow is axisymmetric, and it was hypothesized that this would also be the case for eccentric spheres. Thus five thermocouple probes were placed in a common vertical plane through the center of the spheres. These probes were spaced at 40-deg intervals beginning with the probe on the upward vertical axis, $\Phi = 0$ deg.

A total of approximately 1100 heat-transfer runs were conducted with water, Dow Corning 200 fluid–20 CS, and Dow Corning 200 fluid–350 CS in the gap. The Dow Corning 200 fluids are silicone-base fluids, and the 20 CS and 350 CS designations refer to the kinematic viscosity in centistokes at 25 deg C. Henceforth these fluids will be referred to as 20 and 350 fluids.

For each of the inner spheres utilized, and for each value of the eccentricity, five to 15 different values of temperature difference between the two spheres were established by controlling the power input to the heaters. The natural-convection heat-transfer rate q is the difference between the power input to the electrical heaters and the heat loss due to the supporting stem. Since the stem was well insulated on its lateral surface, convection from the stem was considered to be negligible and the total stem loss was taken to be due to conduction. Calculations showed that this loss was less than 1 percent of the total power input for the largest ΔT and the largest negative eccentricity ratio.

In general, heat-transfer rates and temperature profiles were obtained for six values of eccentricity ratio, $e/(r_0 - r_i) = \pm 0.25, \pm 0.5, \pm 0.75$, for each size inner sphere. Additional data for a zero eccentricity ratio (concentric spheres) were not obtained, but the current information was combined with previously available data for concentric spheres [5] to yield extremely general correlations. The ranges of the independent variables considered are shown in Table 1.

Before obtaining either heat-transfer or temperature-profile data, sufficient time was allowed for establishment of steady-

Table 1 Ranges of independent variables for water, 20 fluid, and 350 fluid

Variable	Minimum value	Maximum value
r_0	12.45 cm	12.45 cm
r_i	5.7 cm	11.4 cm
T_i	4 deg C	83 deg C
T_0	0 deg C	4 deg C
$e/(r_0 - r_i)$	−0.75	+0.75

Nomenclature

C_p = constant-pressure specific heat
e = eccentricity measured positive upward as defined in Fig. 4
g = local gravitational acceleration
Gr = Grashof number, $g\beta L^3\Delta T/\nu^2$
k = thermal conductivity
k_{eff} = effective fluid thermal conductivity, $qL/(4\pi\Delta T R_i r_0)$
L = gap thickness between concentric spheres, $r_0 - R_i$
Nu = Nusselt number based on inner-sphere radius, $q/(4\pi r_i k\Delta T)$
Pr = Prandtl number, ν/α
q = natural-convection heat-transfer rate
r, R, ξ = radii, see Fig. 4
Ra_L = Rayleigh number, Gr·Pr
Ra* = modified Rayleigh number, $g\beta L^4\Delta T/(\nu\alpha R_i)$
T = temperature
w = complex plane containing mapped concentric spheres, $u + iv$
z = complex plane containing eccentric spheres, $x + iy$
α = thermal diffusivity
β = thermal-expansion coefficient
ΔT = temperature difference between spheres, $T_i - T_0$
ν = kinematic viscosity
Φ = angular coordinate measured from upward vertical axis

Subscripts

i = refers to inner sphere
m = indicates mean value
0 = refers to outer sphere

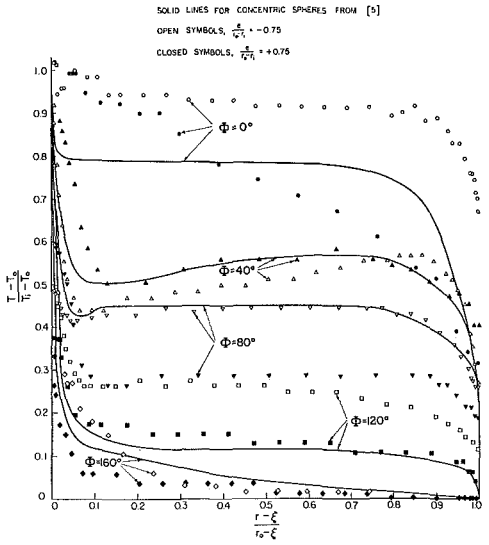

Fig. 2 Variation of temperature profiles with eccentricity for water, $r_0/r_i = 1.787$

state conditions. Temperature traverses were made utilizing the thermocouple probes at three temperature differences (small, intermediate, large) for each inner sphere, test fluid, and eccentricity ratio.

Temperature Distributions

Profiles of temperature T as a function of radial position r were obtained at selected values of ΔT and angular position Φ for each size inner sphere and at each eccentricity e for the three test fluids utilized. As with concentric spheres [5], the behavior of the temperature profiles was found to follow consistent general trends for all except the largest size inner sphere. For all values of eccentricity, temperature fluctuations, interpreted as the result of unsteady flow, occurred for the largest values of ΔT, and only profiles for which no such fluctuations occurred are presented herein. The general shape of the temperature profiles was found to be relatively independent of ΔT, as was first observed for concentric spheres [1, 5].

The effects of both positive and negative eccentricities on the temperature profiles are shown in Fig. 2, where the solid lines represent concentric-sphere profiles from [5]. In the current investigations a unicellular-type flow pattern, perhaps of either the crescent-eddy or the kidney-shaped-eddy type, is indicated for all degress of eccentricity. Near the bottom of the gap, at the Φ = 160-deg position, the fluid is relatively stagnant and eccentricity has little effect on the temperature profiles. In fact for a positive eccentricity the fluid appears to remain relatively stagnant all the way up to the Φ = 80-deg position. At the Φ = 0-deg location the temperature exceeds the concentric-sphere value near the inner surface and is less than the concentric-sphere value near the outer sphere, possibly indicating the existence of a large corner eddy near the inner-sphere surface. For negative eccentricities the temperature at a given position was generally larger than the corresponding value for concentric spheres, except near Φ = 40 deg and Φ = 80 deg where the two values were approximately the same.

In order to conserve space, additional temperature-profile plots will not be presented; however, the same general trends as described above were observed for all spheres used and for all test fluids. The basic flow patterns obtained for eccentric spheres, as hypothesized from the temperature profiles, appeared to remain essentially unchanged from those of concentric spheres, although some slight modifications did occur. These included an enhancement of the convective motion by negative eccentricities, while flow stabilization as well as a large corner eddy appeared to be promoted by positive eccentricities. The same conclusions resulted for even the largest inner sphere utilized, where the existence of a multicellular flow pattern was postulated in order to explain the behavior of the temperature profiles for both concentric and eccentric situations.

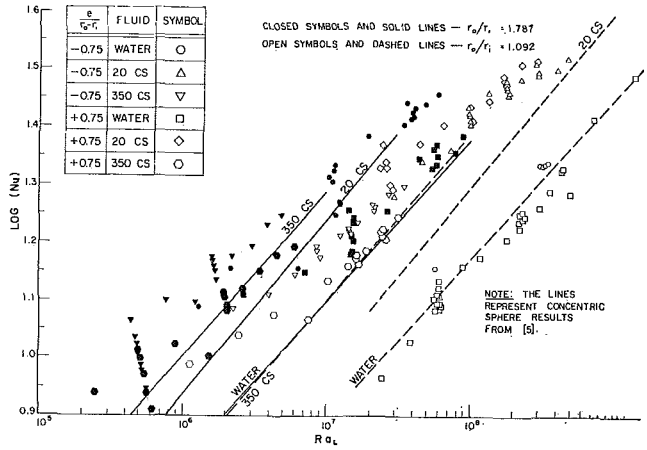

Fig. 3 Effect of eccentricity on heat-transfer rates

Heat-transfer Results

Heat-transfer results for eccentricities and radius ratios at the extremes of the ranges under consideration, as well as for all test fluids, are shown in Fig. 3. The solid lines in this figure represent the concentric-sphere equations for individual fluids developed by Scanlan, Bishop, and Powe [5] for a radius ratio of 1.787, while the dashed lines represent the corresponding equations for a radius ratio of 1.092. As would be expected on this type of plot, both the radius ratio and the Prandtl number significantly affect the heat-transfer results for both concentric and eccentric configurations. However it is somewhat surprising to note that for a given radius ratio and test fluid the heat transfer may be increased by moving the inner sphere either upward or downward from the concentric position. In general this was found to be true for all cases studied in the current investigation, even though the temperature profiles and probably the flow patterns are somewhat different for positive and negative eccentricities. This tends to confirm the relative insensitivity of the overall heat transfer to the detailed thermal and flow fields for natural convection in enclosed spaces as found in our previous work.

The customary use of dimensional analysis indicates the following functional relationship for concentric spheres, see, e.g., Ipsen [6]:

$$k_{\text{eff}}/k = F[(r_0 - r_i)/r_i, \text{Gr}, \text{Pr}, g\beta(r_0 - r_i)/C_p, \beta\Delta T] \quad (1)$$

It has previously been found that the last two parameters on the right-hand side of this equation are usually not of importance in free-convection processes and thus may be eliminated. The inclusion of one additional independent variable, eccentricity, results in the following functional relationship:

$$k_{\text{eff}}/k = F[(r_0 - r_i)/r_i, \text{Gr}, \text{Pr}, e/(r_0 - r_i)] \quad (2)$$

An attempt could be made to find a correlation equation of the form of (2), although this process would be complicated somewhat by the inclusion of the additional parameter.

The current geometry suggests a different approach, however. If a suitable mapping function can be found, then conformal-mapping techniques can be utilized to transform the eccentric spheres to concentric spheres. An attempt can then be made to utilize existing concentric-sphere correlations for the eccentric-sphere data. Such an approach was taken, and it should be emphasized that this technique provides merely an empirical correlation method—no attempt was made to examine the manner in which the governing equations and boundary conditions were transformed by the mapping function. The pertinent coordinate

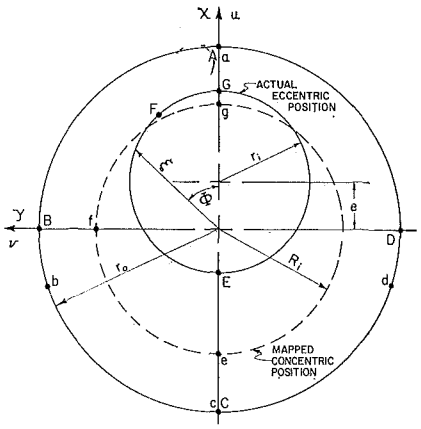

Fig. 4 Schematic defining nomenclature and coordinate system for eccentric spheres

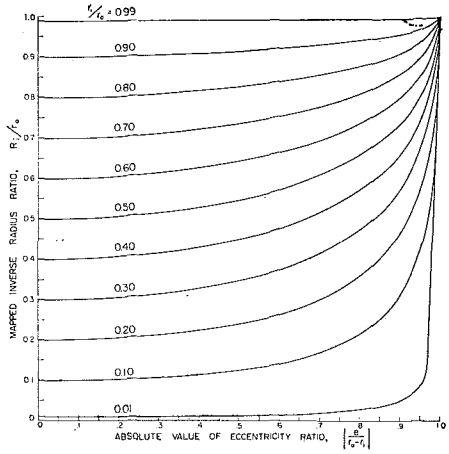

Fig. 5 Mapped inverse radius ratio as a function of eccentricity ratio for different radius ratios

systems for using this approach are shown in Fig. 4. In this figure the unmapped positions are denoted with capital letters while the corresponding mapped locations are denoted with lower-case letters. If the plane of this figure is taken to be the z plane, with

$$z = x + iy \tag{3}$$

then it is found that the eccentric spheres can be mapped into concentric spheres in the w plane, with

$$w = u + iv \tag{4}$$

through use of the mapping function

$$w = \frac{r_0(az - r_0)}{ar_0 - z} \tag{5}$$

where a, b, and c are given by

$$a = \frac{1 + bc + \sqrt{(1 - b^2)(1 - c^2)}}{b + c} \qquad b = \frac{e + r_i}{r_0} \qquad c = \frac{e - r_i}{r_0} \tag{6}$$

The mapped concentric spheres in the w plane are also shown in Fig. 4. It may be observed that the radius of the outer sphere is invariant under the transformation, while the radius of the inner sphere becomes

$$R_i = \frac{r_0(b - c)}{1 - bc + \sqrt{(1 - b^2)(1 - c^2)}} \tag{7}$$

Thus, in order to determine whether this mapping technique does correlate the heat-transfer data, the actual inner-sphere radius r_i may be replaced by the mapped radius R_i and an attempt made to utilize existing correlation equations to predict the data. This mapped radius is shown in graphical form in Fig. 5. It is encouraging to note that the mapping function yields the same inner-sphere radius for both positive and negative eccentricities.

The foregoing mapping technique also suggests a temperature upon which to base fluid properties for calculating the parameters appearing in existing correlation equations. It has previously been found [5] for concentric spheres that rather simple correlations result if fluid properties are based on a volume-weighted mean temperature, obtained by considering the fluid from the inner sphere to a mean radius to be at temperature T_i, while the fluid from the mean radius to r_0 is at temperature T_0. It is extremely difficult to find an equivalent temperature for eccentric spheres which can be evaluated simply, but the mapping technique suggests using a volume-weighted mean temperature similar to that of the concentric case and given by

$$T_m = \frac{(R_m^3 - R_i^3)T_i + (r_0^3 - R_m^3)T_0}{r_0^3 - R_i^3} \tag{8}$$

where

$$R_m = \frac{R_i + r_0}{2} \tag{9}$$

Henceforth all fluid properties will be based on this temperature.

Heat-transfer Data Correlation

As mentioned previously, heat-transfer results were obtained for four different sphere combinations and for six eccentricity ratios with each set of spheres. Each of these tests was conducted with three different fluids: water, 20 fluid, and 350 fluid. The conformal-mapping techniques were then utilized to map the eccentric spheres into concentric spheres, and the appropriate parameters, including conductivity ratio k_{eff}/k, Rayleigh number Ra_L, Prandtl number Pr, and gap–radius ratio L/R_i, were calculated using the mapped sphere sizes. An attempt was then made to utilize the empirical equations previously developed by Scanlan, Bishop, and Powe [5] for concentric spheres to correlate the eccentric-sphere data, and this section will be concerned with comparisons between these equations and the present data.

Scanlan et al. [5] found that the data for each fluid individually were best correlated by equations of the form

$$k_{\text{eff}}/k = \gamma \text{Ra}_L^{\zeta}(L/R_i)^{\eta} \tag{10}$$

and the empirical constants which they obtained are given in Table 2. Also included in this table is a comparison of the deviations encountered in using these equations for concentric spheres and mapped eccentric spheres.

Although equation (10) best fits the data for each individual fluid, it may be observed that η is relatively small, and Scanlan et al. [5] found that only a slight loss in apparent accuracy was

Table 2 Empirical constants and deviations for equation (10) for eccentric and concentric spheres

Fluid	Water	20 CS	350 CS
γ	0.078	0.072	0.104
ζ	0.279	0.305	0.288
η	0.155	0.124	0.110
Average % deviation (concentric spheres)	13.4	6.0	5.3
Average % deviation (eccentric spheres)	12.7	12.8	10.7
% of data within ±20% of equation (concentric spheres)	79.6	97.9	97.5
% of data within ±20% of equation (eccentric spheres)	77.0	75.9	87.8

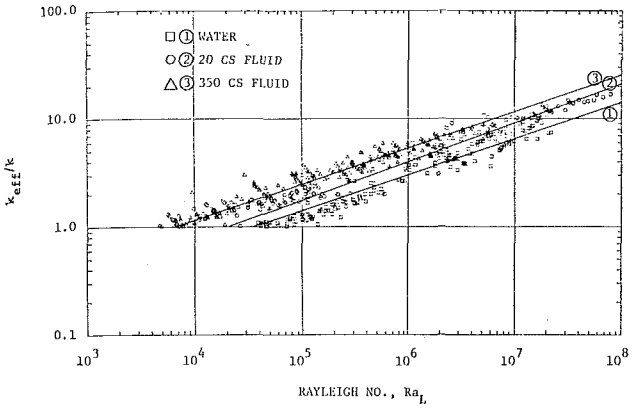

Fig. 6 Comparison of concentric-sphere correlations with mapped eccentric-sphere data for individual fluids

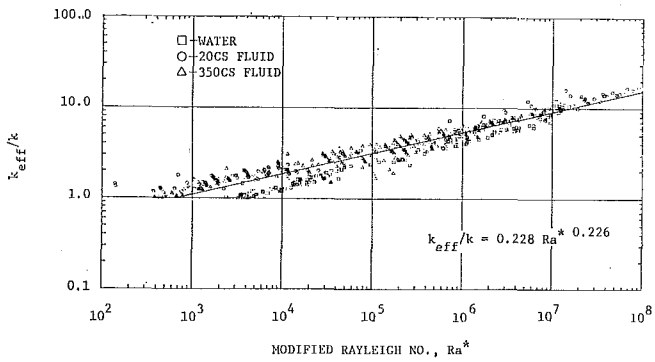

Fig. 7 Comparison of overall concentric-sphere correlation with mapped eccentric-sphere data

incurred by utilizing equations of the form

$$k_{\text{eff}}/k = \gamma \text{Ra}_L^{\zeta} \tag{11}$$

The empirical constants which they obtained for this equation are given in Table 3 together with a comparison of the deviations for concentric and mapped eccentric spheres. These equations are shown plotted with the mapped eccentric data in Fig. 6.

From Fig. 6 it is evident that no single equation of the form of equation (11) will suitably correlate the data for all of the test fluids. However, it was found by Scanlan et al. [5] that all of their concentric-sphere data could be correlated satisfactorily by the equation

$$k_{\text{eff}}/k = 0.202\text{Ra}_L^{0.228}(L/R_i)^{0.252}\text{Pr}^{0.029} \tag{12}$$

with an average deviation of 13.7 percent, while a comparison of the mapped eccentric data with this equation indicates an average deviation of 15.6 percent.

The exponent on Prandtl number in equation (12) is extremely small, while the exponents on Rayleigh number and gap–radius ratio are nearly equal. Thus Scanlan et al. [5] found that all their concentric-sphere data could be correlated by the single equation

$$k_{\text{eff}}/k = 0.228(\text{Ra}^*)^{0.226} \tag{13}$$

with an average deviation of 15.6 percent, while 76 percent of the data were within ±20 percent of values predicted by the equation. The Rayleigh number utilized in equation (13) is a modified form of the Rayleigh number defined as the product of Ra_L and L/R_i. Equation (13) is shown plotted with the mapped eccentric data in Fig. 7, and an error analysis indicated that these data are represented to within an average deviation of 18.2 percent by equation (13), while 67.6 percent of the data are within ±20 percent of the values predicted by the equation.

It is significant to note from the foregoing results that all of the empirical equations which have previously been utilized for predicting heat-transfer rates by natural convection between concentric spheres can also be used to predict natural-convection heat-transfer rates between eccentric spheres with reasonable accuracy if the actual inner-sphere radius is merely replaced with that obtained from the conformal mapping, equation (7). In the nomenclature of the current paper, these equations can be written as

$$k_{\text{eff}}/k = \gamma \text{Ra}_L^{\zeta} \tag{14a}$$

where the constants and ranges of validity are shown in Table 4.

The equation fitting all of the data is given by

$$k_{\text{eff}}/k = 0.228(\text{Ra}^*)^{0.226} \tag{14b}$$

for $1.2 \times 10^2 < \text{Ra}^* < 1.1 \times 10^9$ and $0.7 < \text{Pr} < 4148$. All of the foregoing equations are restricted to $0.09 \leq (r_o - r_i)/r_i \leq 1.81$, $-0.75 \leq e/(r_o - r_i) \leq 0.75$, and fluid properties evaluated at T_m. As in [5] the use of the overall equation (14*b*) is recommended in cases where the other equations (14*a*) are not specifically applicable.

Table 3 Empirical constants and deviations for equation (11) for eccentric and concentric spheres

Fluid	Water	20 CS	350 CS
γ	0.033	0.031	0.056
ζ	0.328	0.353	0.330
Average % deviation (concentric spheres)	15.7	7.1	6.5
Average % deviation (eccentric spheres)	16.7	13.9	10.6
% of data within ±20% of equation (concentric spheres)	71.4	98.6	98.6
% of data within ±20% of equation (eccentric spheres)	63.7	75.9	86.4

Conclusion

This paper presents the results of an experimental investigation of natural convection between eccentric spheres, where the eccentricity is parallel to the gravity vector. Water and two silicone oils were utilized as the test fluids for four combinations of sphere sizes and for six values of the eccentricity ratio for each of these sphere combinations. Information regarding both heat-transfer rates and temperature distributions is presented.

Temperature distributions are presented, and as would probably be expected it was found that a negative (downward) eccentricity tends to enhance the convective motion in the space between the spheres, while a positive eccentricity produces a tendency toward pure conduction, although this situation was certainly never fully achieved. As in the case of concentric spheres the thermal map was observed to be relatively independent of temperature difference between the two spheres. Temperature inversions, believed to be caused by the high rate of angular convection of heat relative to the radial transport, were observed for a variety of test conditions. The multicellular flow pattern which has previously been postulated to explain the temperature distribution between concentric spheres with a small gap spacing was also found to yield a plausible explanation for the thermal field obtained using the largest inner sphere considered in the current investigation.

Table 4 Heat-transfer correlation equations for individual fluids

$\text{Pr}_{\min}$	$\text{Pr}_{\max}$	$\text{Ra}_{L\,\min}$	$\text{Ra}_{L\,\max}$	γ	ζ
0.7	0.7	1.4×10^4	2.5×10^6	0.117	0.276
4.7	12.1	2.4×10^4	5.4×10^8	0.033	0.328
148	336	2.4×10^4	9.7×10^7	0.031	0.353
1954	4148	1.3×10^3	5.6×10^6	0.056	0.330

A conformal-mapping technique was developed to transform the eccentric spheres to concentric spheres, and it was found that the empirical equations previously developed for concentric spheres could be used to predict the heat transfer in the mapped eccentric spheres even though the governing differential equations may not have been transformed in an invariant manner. In the transformation the outer-sphere diameter was invariant, while the inner-sphere diameter was changed. This mapped inner diameter was then utilized for calculating the reference temperature, on which all fluid properties were based, as well as the various parameters which appear in the existing correlations for concentric spheres. The application of these existing correlations to the mapped eccentric-sphere data then indicated that these equations could indeed be utilized for the eccentric spheres, both for each fluid individually and for all the data combined. It is significant to note that an overall heat-transfer correlation which does not involve explicit use of Pr, L/r_i, or $c/(r_0 - r_i)$ was obtained even though large variations in these parameters were considered in the investigation.

To the best of the authors' knowledge the results described herein represent the only currently available information concerning natural-convection heat transfer between eccentric spheres. This work concentrated on obtaining heat-transfer rates and temperature profiles, and future work should be directed toward a determination of the more detailed effects which occur in the flow field for wide variations in the independent variables.

Acknowledgment

The work described in this paper was supported by the Atomic Energy Commission under contract AT(45-1)-2214 and the National Science Foundation under grant GK-31908.

References

1 Bishop, E. H., Mack, L. R., and Scanlan, J. A., "Heat Transfer by Natural Convection Between Concentric Spheres," *International Journal of Heat and Mass Transfer*, Vol. 9, 1966, pp. 649–662.

2 Bishop, E. H., Kolflat, R. S., Mack, L. R., and Scanlan, J. A., "Convective Heat Transfer Between Concentric Spheres," *Proceedings of the 1964 Heat Transfer and Fluid Mechanics Institute*, Stanford University Press, Stanford, Calif., 1964, pp. 69–80.

3 Bishop, E. H., Kolflat, R. S., Mack, L. R., and Scanlan, J. A., "Photographic Studies of Convection Patterns Between Concentric Spheres," *Society of Photo-Optical Instrumentation Engineers Journal*, Vol. 3, 1964–1965, pp. 47–49.

4 Mack, L. R., and Hardee, H. C., "Natural Convection Between Concentric Spheres at Low Rayleigh Numbers," *International Journal of Heat and Mass Transfer*, Vol. 11, 1968, pp. 387–396.

5 Scanlan, J. A., Bishop, E. H., and Powe, R. E., "Natural Convection Heat Transfer Between Concentric Spheres," *International Journal of Heat and Mass Transfer*, Vol. 13, 1970, pp. 1857–1872.

6 Ipsen, D. C., *Units, Dimensions, and Dimensionless Numbers*, McGraw-Hill, New York, N. Y., 1960.

J. QUINTIERE
U. S. Department of Commerce,
National Bureau of Standards,
Washington, D. C.

W. K. MUELLER
Professor,
Department of Mechanical Engineering,
New York University,
New York, N. Y.
Mem. ASME

An Analysis of Laminar Free and Forced Convection between Finite Vertical Parallel Plates

Approximate analytical solutions are presented for constant-property laminar free- and forced-convection flows between finite vertical parallel plates. For free convection, the thermal boundary conditions considered include the thermally symmetric channel with uniform wall temperature or step change in wall temperature and the unsymmetric channel with uniform but unequal wall temperatures. For forced convection and combined free and forced convection, the thermally symmetric and uniform thermal boundary condition is considered. Where possible, results are compared with available numerical and experimental results. Particular attention is given to heat-transfer results, which cover a wide range of Rayleigh and Prandtl numbers. For combined convection the heat-transfer results are related to the impressed pressure difference and flow rate.

I Introduction

COMBINED free- and forced-convection flows have been studied extensively (see Ostrach [1][1] and Chato [2] for general reviews), yet questions still remain to be answered on the subject. The present study introduces a new approximate method for analyzing laminar natural convection in finite vertical ducts. There is a need for flexible analytical methods that can provide good design heat-transfer information over a wide range of conditions. It is intended that this new method will help to fulfill that need. In particular, the class of problems to be considered is that of heat transfer to a fluid between two parallel vertical heated plates. Fluid from constant-temperature (T_∞) surroundings enters the channel at the bottom and discharges into the surroundings at the top. If a fan exists in the channel a forced-convection flow is superimposed on the buoyancy-induced flow.

In general a finite-length channel introduces mathematical difficulties which preclude the possibility of an exact solution to the governing equations. For this reason the limiting case of a very long channel or the assumption of fully developed flow has been made to simplify the problem and to permit exact mathematical solutions. Solutions of this type, for a variety of thermal boundary conditions and duct cross-sectional geometries, are presented in the literature by Ostrach [3–5] and other investigators [6–9]. These exact solutions are of limited value since the conditions over which they are valid are not always expressed in terms of a well-defined range of parameters. To be useful these limiting solutions must be complemented with experimental results or more complete solutions arrived at numerically or approximately. Thus the solution for fully developed flow must be complemented with some information on the developing-flow problem. Indeed the situation of fully developed flow may never be realized in finite channel flow, hence a knowledge of developing flow is essential.

Analytical studies of combined free- and forced-convection flows have usually treated free convection as a secondary effect. One early effort by Martinelli and Boelter [10] used the method of Leveque [11] to analyze flow in a short heated section of a long vertical duct. Later Rosen and Hanratty [12] used an approximate integral method to reconsider this same problem in more detail. They also pointed out from experimental observations that the results of Martinelli and Boelter included a range of values where flow inversions would occur, thus curtailing the range of applicability of these results. Scheele and Hanratty [13] and Lawrence and Chato [14], who examined the flow-stability problem more closely, found that transition to turbulent flow always occurred following an inflection in the velocity profile. Although an inflection point would always be expected in pure free convection, the flow in their studies was dominated by forced convection. Recent efforts to consider free- and forced-convection developing flow in a semi-infinite vertical duct include an approximate solution by Savkar [15] and a numerical solution by Zeldin and Schmidt [16].

The problem of developing natural convection between parallel plates was first studied by Elenbaas [17]. Examining air flowing between isothermal plates, he determined average heat-transfer coefficients and correlated the Nusselt number over a wide range of Rayleigh numbers. Sobel, Landis, and Mueller [18] experimentally examined the same problem except with a uniform-

[1] Numbers in brackets designate References at end of paper.

Contributed by the Heat Transfer Division and presented at the Winter Annual Meeting, New York, N. Y., November 26–30, 1972, of THE AMERICAN SOCIETY OF MECHANICAL ENGINEERS. Manuscript received by the Heat Transfer Division February 24, 1972. Paper No. 72-WA/HT-3.

heat-flux wall condition. Using boundary-layer-type equations Bodoia and Osterle [19] obtained a numerical solution to Elenbaas' problem. They imposed a uniform entrance velocity and matched pressure to its local hydrostatic ambient value at the entrance and exit of the channel. The numerical solution was terminated when the center-line fluid velocity reached zero [20]. Sanders [21] numerically solved a similar problem after introducing some approximations for terms in his governing equations. It is noteworthy that his heat-transfer results agree within ±10 percent with the results obtained from a slug-flow model for the energy equation. Novotny [22] presented fluid-temperature data over the first two-thirds of a channel with isothermal walls. For high Rayleigh numbers he found that the measured temperature profiles agreed with those predicted by single-vertical-plate theory. More recent experimental data for velocity and temperature in air at low Grashof numbers ($0.83 \leq \mathrm{Gr}^* \leq 8.0$) have been presented by Currie and Newman [23]. Flow-rate results are in good agreement with those of Bodoia and Osterle, and heat-transfer results follow those of Elenbaas. The only previous analytical approach to developing natural convection between vertical plates was given by Engel [24] and Engel and Mueller [25]. Their approach consisted of an integral method followed with an asymptotic expansion in 1/Pr to make the equations tractable. Their results for average Nusselt number are compared to Bodoia and Osterle [20] up to $\mathrm{Ra}^* = 2700$ where the deviation reaches 16 percent.

Additional numerical solutions have been presented for pure natural convection in finite vertical ducts. Dyer and Fowler [26] extended the work of [20] to include an initial unheated section followed by a constant-temperature-wall section. They also concluded that the initial velocity profile has no significant effect on the average heat-transfer and flow results. Dyer [27] also considered this problem experimentally. Dyer noticed that with an inlet restriction it is possible to have the flow from the bottom channel entrance supplemented by an open-thermosiphon effect at the top exit. Kageyama and Izumi [28] solved the vertical-circular-duct problem by a numerical technique for the wall conditions of constant temperature and constant heat flux.

The lack of analytical work done on developing natural convection in ducts motivated the present study. A method more flexible than the alternative integral method was sought. Furthermore, all previous[2] formulations of this problem specified a hydrostatic ambient pressure at the channel entrance, while the actual pressure must be lower since the fluid has been accelerated from rest. The possible importance of this factor also deserves investigation.

The present method is based upon a slug-flow linearization of the governing equations. This method has been used with success by Targ [30], Sparrow et al. [31–32], and Williams [33] for the isothermal-entrance-region problem. It is expected that it will be appropriate for the natural-convection case since it is accurate at large Reynolds numbers, corresponds to Sanders' results with the slug-flow energy equation, and reflects the unimportance of the momentum convective terms found by Engel and Mueller.

All problems considered will have a uniform channel wall temperature, except that a step change in wall temperature from an unheated to a heated wall condition and different temperatures at both walls will also be examined. In all cases the approximate solutions derived for small Rayleigh numbers converge to the exact fully developed solutions.

II Governing Equations

The governing equations for two-dimensional steady flow in channels have been well established and will not be derived here. A rigorous derivation is available in [36]. Basically, the Boussinesq assumption has been introduced, boundary-layer flow applies, and all properties are constant but evaluated at an appropriate temperature [34]. For the system shown in Fig. 1 the dimensionless groups θ, u, v, x, y, Gr, and Pr as defined in the nomenclature yield the governing set of equations in terms of dimensionless variables as

Continuity

$$\frac{\partial u}{\partial x} + \frac{\partial v}{\partial y} = 0 \tag{1a}$$

X-momentum

$$u\frac{\partial u}{\partial x} + v\frac{\partial u}{\partial y} = \frac{1}{\mathrm{Gr}}\left(\theta + \frac{\partial^2 u}{\partial y^2}\right) - \frac{\partial p_v}{\partial x} \tag{1b}$$

[2] Very recent work presented by Aihara [29] has investigated this factor in a numerical solution.

Nomenclature

a = channel width
b = channel half-width, $b = a/2$
c_p = specific heat at constant pressure
g = gravitational body force per unit mass
Gr = Grashof number, $b^4g\beta(T_w - T_\infty)/L\nu^2$
Gr* = Grashof number, $a^4g\beta(T_w - T_\infty)/L\nu^2$
$h(X)$ = average heat-transfer coefficient up to position X defined in equation (20)
k = thermal conductivity
L = channel length
L_H = heated channel length
Nu = Nusselt number, hb/k
Nu* = Nusselt number, ha/k
p_v = dimensionless pressure defect, $P_v/\rho_\infty U_R{}^2$
$p_{v_0}{}'$ = dimensionless initial pressure defect, $P_{v_0}b^4/\rho_\infty L^2\alpha^2$
P = pressure
P_v = pressure defect, $p + \rho_\infty gX$
Pr = Prandtl number, ν/α
$q_w(X)$ = heat flux from wall to fluid at position X
Ra = Rayleigh number, GrPr
Ra* = Rayleigh number, Gr*Pr
T = temperature
u = dimensionless vertical velocity component, U/U_R
$u_0{}'$ = Graetz number, (U_0b/ν) Pr (b/L)
U = vertical velocity component
U_R = reference velocity, see sections II, IIIA, $b^2g\beta(T_w - T_\infty)/\nu$
U_R = reference velocity, see section IIIB, $a^2g\beta(T_w - T_\infty)/\nu$
v = dimensionless horizontal velocity component, see section IIIA, VL/bU_R
v = dimensionless horizontal velocity component, see section IIIB, VL/aU_R
V = horizontal velocity component
x = dimensionless vertical coordinate, X/L
X, Y = vertical coordinate, horizontal coordinate
y = dimensionless horizontal coordinate, see sections II, IIIA, Y/b
y = dimensionless horizontal coordinate, see section IIIB, Y/a
α = thermal diffusivity
α_n = defined by equation (12)
β = coefficient of volume expansion, $-\frac{1}{\rho}\left(\frac{\partial\rho}{\partial T}\right)_P$
β_n = defined by equation (13)
γ = dimensionless cold-wall temperature, $(T_{w_0} - T_\infty)/(T_{w_1} - T_\infty)$
δ_n = defined by equation (26)
ξ = dimensionless independent variable, see section IIIA, $x/U_0\mathrm{Gr}$, section IIIB, $x/U_0\mathrm{Gr}^*$
ν = kinematic viscosity
θ = dimensionless temperature, $(T - T_\infty)/(T_{w\max} - T_\infty)$
ρ = density

Subscripts

0 = initial condition or hot wall in section IIIB
1 = cold wall in section IIIB
∞ = ambient condition
w = wall condition

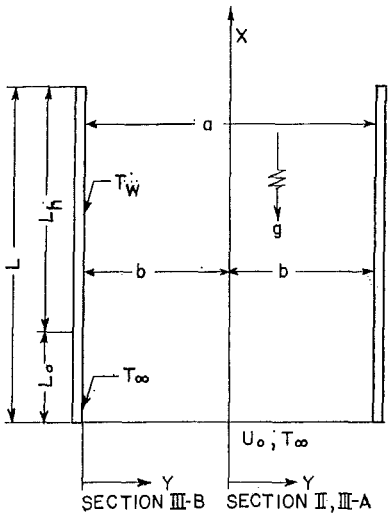

Fig. 1 Channel coordinate system

Y-momentum

$$\frac{\partial p_v}{\partial y} = 0 \tag{1c}$$

Energy

$$u\frac{\partial \theta}{\partial x} + v\frac{\partial \theta}{\partial y} = \frac{1}{\mathrm{GrPr}}\frac{\partial^2 \theta}{\partial y^2} \tag{1d}$$

The wall boundary conditions considered are zero velocity and prescribed surface temperature. The conditions at $x = 0$ are more difficult. Here it is assumed that both the temperature and the velocity are constant, with values T_∞ and U_0 respectively. The assumption of constant velocity is best justified by the results of Dyer and Fowler [26]. It is also necessary to specify the pressure at $x = 0$. In all other theoretical studies [19, 20, 24–28] the pressure defect P_v was taken to be zero at the inlet, neglecting the acceleration of the fluid to the channel inlet. The correct initial condition, given by application of Bernoulli's equation, should be

$$P_v = -\frac{\rho_\infty U_0^2}{2} \tag{2}$$

The effect of this condition on the results will be considered in the examples below. At the channel exit the pressure defect has been specified as zero, i.e.,

$$P_v = 0 \qquad \text{at} \qquad X = L \tag{3}$$

which is in agreement with previous theoretical studies and corresponds to parallel streamlines in the emerging flow. This condition is required to establish a value for the inlet flow which is a dependent quantity.

Finally, an integral continuity condition, from equation (1a) and wall boundary conditions,

$$\int_{-b}^{b} UdY = 2bU_0 \tag{4}$$

is added. This additional equation becomes mathematically necessary because the y-momentum equation has been essentially eliminated. Equation (4) with (1a), (1b), and (1d) provides four independent relationships to allow determination of the four unknown variables u, v, P_v, and θ.

III Approximate Method and Examples

A Symmetrically Heated Channel with Specified Wall Temperature. In this section, the method of solution will be developed and applied to the problem of a symmetrically heated channel with a prescribed wall temperature. The coordinate system of Fig. 1 applies as well as equations (1) and (4). To arrive at a tractable problem, the energy and momentum convective terms will be linearized as follows:

$$u\frac{\partial}{\partial x} + v\frac{\partial}{\partial y} \equiv u_0\frac{\partial}{\partial x} \tag{5}$$

where u_0 is the dimensionless entrance velocity which must later be determined from the solution. By introducing a new independent variable $\xi = x/u_0\mathrm{Gr}$ the linearized governing equations become

X-momentum

$$\frac{\partial u}{\partial \xi} = \theta + \frac{\partial^2 u}{\partial y^2} - \frac{1}{u_0}\frac{dp_v}{d\xi} \tag{6a}$$

Energy

$$\mathrm{Pr}\frac{\partial \theta}{\partial \xi} = \frac{\partial^2 \theta}{\partial y^2} \tag{6b}$$

Mass balance

$$\int_0^1 udy = u_0 \tag{6c}$$

The constraint conditions required by (6) are

$$x = 0: \qquad u = u_0 \qquad \theta = 0 \qquad p_v = p_{v0} \tag{7a}$$

$$x = 1: \qquad p_v = 0 \tag{7b}$$

$$y = 0: \qquad \frac{\partial u}{\partial y} = 0 \qquad \frac{\partial \theta}{\partial y} = 0 \tag{7c}$$

$$y = 1: \qquad u = 0 \qquad \theta = f(\xi) \tag{7d}$$

In the following analysis various values of p_{v0} will be considered. Setting $p_{v0} = 0$ conforms to previous works [19, 20, 24–28] and permits a comparison of results. Setting $p_{v0} = -u_0^2/2$ follows from equation (2) as the correct condition for pure free convection. Finally, setting p_{v0} above its corresponding free-convection value results in combined free and forced convection.

Although the governing equations have been linearized the solution is not straightforward. Using Laplace transforms [36] in the solution procedure it still is necessary to introduce specific wall temperature functions $f(\xi)$. Although general variations in the wall temperature could be considered, results are presented here for only two examples, a uniform wall temperature and a step change in the wall temperature.

For the uniform wall temperature

$$f(\xi) = 1 \tag{8}$$

and for the step change

$$f(\xi) = \begin{cases} 0 & \xi < \xi_0 \equiv L_0/L\ \mathrm{Gr}\ u_0 \\ 1 & \xi > \xi_0 \end{cases} \tag{9}$$

The solution for each case follows, with intermediate details shown in [36].

Constant-Wall-Temperature Case

$$\theta(\xi, y) = 1 + 2\sum_{n=1}^{\infty}\frac{(-1)^n}{\beta_n}e^{-\frac{\beta_n^2}{\mathrm{Pr}}\xi}\cos(\beta_n y) \tag{10a}$$

$$\frac{p_v(\xi) - p_{v0}}{u_0} = -u_0\left[\left(3\xi + \frac{1}{5}\right) - 2\sum_{n=1}^{\infty}\frac{e^{-\alpha_n^2\xi}}{\alpha_n^2}\right]$$

$$+ \left(\xi - \frac{2}{5}\mathrm{Pr}\right) + \frac{2}{(\mathrm{Pr}-1)}\left\{\sum_{n=1}^{\infty}\frac{e^{-\alpha_n^2\xi}}{\alpha_n^4} - \sum_{n=1}^{\infty}\frac{\tan(\alpha_n\sqrt{\mathrm{Pr}})}{\sqrt{\mathrm{Pr}}\,\alpha_n^5}\right.$$

$$\times e^{-\alpha_n^2\xi} - \sum_{n=1}^{\infty} \frac{\sqrt{\Pr}\, e^{-\frac{\beta_n^2}{\Pr}\xi}}{\beta_n^3\left[\frac{\beta_n}{\sqrt{\Pr}} - \tan\left(\frac{\beta_n}{\sqrt{\Pr}}\right)\right]}\Bigg\} \quad (10b)$$

$$u(\xi, y) = u_0\left\{\frac{3}{2}(1 - y^2) - 2\sum_{n=1}^{\infty}\frac{e^{-\alpha_n^2\xi}}{\alpha_n^2}\left[1 - \frac{\cos(\alpha_n y)}{\cos(\alpha_n)}\right]\right\}$$

$$+ \frac{2}{(\Pr - 1)}\Bigg\{\sum_{n=1}^{\infty}\left[\frac{\tan(\sqrt{\Pr}\,\alpha_n)}{\sqrt{\Pr}\,\alpha_n^5} - \frac{1}{\alpha_n^4}\right]\left[1 - \frac{\cos(\alpha_n y)}{\cos(\alpha_n)}\right]$$

$$\times e^{-\alpha_n^2\xi} + \sum_{n=1}^{\infty}\frac{\sqrt{\Pr}\, e^{-\frac{\beta_n^2}{\Pr}\xi}\left[1 - \frac{\cos\left(\frac{\beta_n}{\sqrt{\Pr}}y\right)}{\cos\frac{\beta_n}{\sqrt{\Pr}}}\right]}{\beta_n^3\left[\frac{\beta_n}{\sqrt{\Pr}} - \tan\frac{\beta_n}{\sqrt{\Pr}}\right]}$$

$$+ \sum_{n=1}^{\infty}\frac{\Pr(-1)^n e^{-\frac{\beta_n^2}{\Pr}\xi}\cos(\beta_n y)}{\beta_n^3}\Bigg\} \quad (10c)$$

Step-Change-in-Wall-Temperature Case

$$\theta(\xi, y) = \eta(\xi - \xi_0)\left[1 + 2\sum_{n=1}^{\infty}\frac{(-1)^n}{\beta_n}e^{-\frac{\beta_n^2}{\Pr}\xi}\cos(\beta_n y)\right] \quad (11)$$

The solutions for u and p_v are lengthy, and have been omitted in the interest of brevity. The interested reader is referred to [36]. α_n and β_n are given by

$$\alpha_n = \tan(\alpha_n) \qquad n = 1, 2, \ldots \quad (12)$$

where $\alpha_n \neq 0$, and

$$\beta_n = \left(\frac{2n - 1}{2}\right)\pi \qquad n = 1, 2, \ldots \quad (13)$$

In order to complete the solution the parameter u_0 must be determined as a function of independent parameters. This is accomplished by applying condition (7*b*) to equations (10*b*) and (11*b*). An explicit solution for u_0 is not possible, but it is convenient to introduce

$$u_0' = u_0\mathrm{Ra}$$

which permits an explicit solution for Ra, i.e.,

$$\mathrm{Ra} = \mathrm{Ra}\left(u_0', \Pr, \frac{L_H}{L}\right) \quad (14)$$

The quantity u_0' is in fact the Graetz number, represented in this case as

$$u_0' = \left(\frac{b}{L}\right)\left(\frac{U_0 b}{\nu}\right)(\Pr) \quad (15)$$

To improve upon the linearized solution an alternative method will be used to determine the u_0 relationship. From the original governing equations (1) the momentum equation can be integrated over the channel half-width and combined with the continuity equation to yield

$$\frac{dp_v}{dx} = \frac{1}{\mathrm{Gr}}\int_0^1\left(\theta + \frac{\partial^2 u}{\partial y^2}\right)dy - \frac{d}{dx}\int_0^1 u^2 dy \quad (16)$$

Further integration from 0 to x results in

$$p_v(x) - p_{v_0} = \frac{1}{\mathrm{Gr}}\int_0^x\int_0^1\left(\theta + \frac{\partial^2 u}{\partial y^2}\right)dydx + u_0^2 - \int_0^1 u^2 dy \quad (17)$$

This relationship, which is exact, represents an alternative method for determining the pressure where the terms on the right-hand side can be evaluated from the linearized solution, e.g., equations (10) or (11). A corresponding relationship derived from the linearized momentum equation is

$$p_v(x) - p_{v_0} = \frac{1}{\mathrm{Gr}}\int_0^x\int_0^1\left(\theta + \frac{\partial^2 u}{\partial y^2}\right)dydx \quad (18)$$

Letting $\tilde{p}_v$ denote the solution obtained by using equation (17) and letting all other terms denote the linearized solution, it can be seen that

$$\tilde{p}_v(x) = p_v(x) + u_0^2 - \int_0^1 u^2 dy \quad (19)$$

The inlet velocity u_0 can now be determined from the results of equation (19). These results for p_v and u_0 will be referred to as the "iterative solution" as opposed to the "linear solution" given by equation (10*b*).

A similar procedure will be used to obtain heat-transfer results. The average Nusselt number up to any location X is defined as

$$\mathrm{Nu}_x \equiv \frac{bh(x)}{k} = \frac{b}{k}\frac{\int_0^X q_w(X)dX}{L_H(T_w - T_\infty)} = \frac{L}{L_H}\int_0^x\left(\frac{\partial\theta}{\partial y}\right)_{y=1}dx \quad (20)$$

For the entire channel length

$$\mathrm{Nu} \equiv \frac{hb}{k} = \frac{L}{L_H}\int_0^1\left(\frac{\partial\theta}{\partial y}\right)_{y=1}dx \quad (21)$$

Thus

$$\mathrm{Nu} = \mathrm{Nu}\left(\mathrm{Ra}, \Pr, \frac{L_H}{L}\right) \quad (22)$$

can be determined from the "linear solution". This may be improved by accounting for the nonlinear convective terms by integrating the energy equation (1) over the channel half-width and then over the length of the channel. It follows from equation (21) that

$$\mathrm{Nu} = \left(\frac{L}{L_H}\right)\mathrm{GrPr}\int_0^1 (u\theta)_{x=1}dy \quad (23)$$

Equation (23) constitutes an alternative method for deriving relationship (22), and will again be referred to as the "iterative solution" for Nu. The integrals in equations (19) and (23) are easily evaluated numerically and are presented in graphical form.

B Unsymmetrically Heated Channel with Specified Wall Temperature. Here the thermal boundary conditions of uniform, but unequal, wall temperatures are selected for illustration with the constraint that $T_w \geq T_\infty$. As before, a uniform inlet velocity will be prescribed.

The notation used in this section is identical to that of section A except that the reference frame is shifted so that y is measured from one of the walls (see Fig. 1) and the full channel width $a = 2b$ is used in place of b as the reference length.

The governing equations remain as equations (6) with $\xi = x/U_0\mathrm{Gr}^*$ and $\mathrm{Gr}^* = g\beta(T_w - T_\infty)a^4/L\nu^2$. The constraint conditions at $x = 0$ and $x = 1$ remain as equations (7*a*) and (7*b*). At the walls the new conditions are

$$y = 0: \qquad u = 0 \qquad \theta = 1 \quad (24a)$$

and

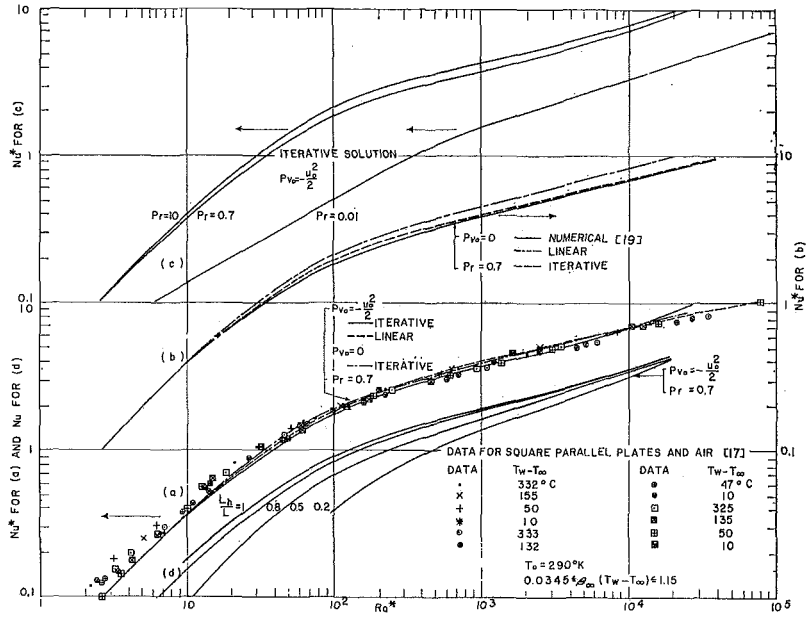

Fig. 2 Nusselt number as a function of Rayleigh number for the symmetric channel; (a) comparison of analytical with experimental results, (b) comparison of analytical with numerical results, (c) Prandtl-number effect, (d) effect of unheated entrance length

$$y = 1: \quad u = 0 \quad \theta = \gamma \quad (0 \leq \gamma \leq 1) \tag{24b}$$

The solution, obtained by the application of Laplace transforms, becomes

$$\theta(\xi, y) = (\gamma - 1)y + 1 + 2 \sum_{n=1}^{\infty} \frac{(-1)^n e^{-\frac{\delta_n^2}{\mathrm{Pr}}\xi}}{\delta_n} \times \{\gamma \sin(\delta_n y) + \sin[\delta_n(1 - y)]\} \tag{25}$$

with α_n and β_n given by equations (12) and (13), respectively, where

$$\delta_n = n\pi \qquad n = 1, 2, \ldots \tag{26}$$

u_0 is determined by the integral-equation method as given in equation (19). The heat-transfer results are evaluated as

$$\mathrm{Nu}_0^* = -\int_0^1 \left(\frac{\partial\theta}{\partial y}\right)_{y=0} dx = \frac{h_0 a}{k} \tag{27a}$$

and

$$\mathrm{Nu}_1^* = \int_0^1 \left(\frac{\partial\theta}{\partial y}\right)_{y=1} dx = \frac{h_1 a}{k} \tag{27b}$$

Here again the u and p_v results have been omitted for brevity, cf. [36].

IV Results and Discussion

In order to assess the accuracy of the present solution, the results were first compared with existing numerical solutions using the compatible zero inlet pressure defect. Experimental results were compared for both inlet pressure conditions, and solutions were generated for the non-zero pressure condition [36]. Some of these results will be presented here.

For pure free convection with constant wall temperature a comparison with the numerical solution of Bodoia and Osterle [19] is given in Fig. 2(*b*) for average Nusselt numbers. The "iterative solution" does agree very closely with the numerical solution except at moderate Rayleigh numbers where it exceeds the numerical result by approximately 5 percent. Apparently the iterative procedure which attempts to account for the nonlinear convective terms is successful in improving the approximate solution at high Rayleigh numbers. The "linear solution," while

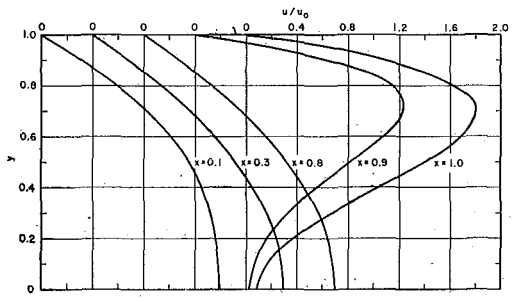

Fig. 3 Dimensionless velocity as a function of position for a step-heated symmetrical channel, $L_H/L = 0.2$, Pr = 0.70, Ra = 7218, $p_{v0} = -u_0^2/2$

maintaining the proper solution character, does overestimate the numerical result by 20 percent at most. In addition, comparison of local results with Bodoia and Osterle [19] (only available at a very low Rayleigh number) displayed excellent agreement with the present results [36].

The effect of the inlet pressure defect on the results is displayed in Fig. 2(*a*) along with the experimental results of Elenbaas [17]. Two factors should be pointed out in comparing the results to the data of Elenbaas. Firstly, the data are for square plates open at the sides, which introduces a three-dimensional edge effect. Secondly, the fluid properties essentially were evaluated at the wall temperature. Correcting for the edge effect [18] and evaluating properties at the average temperature [19] result in a downward shift of the data in the low-Rayleigh-number range. Hence, overall, the iterative solution for the non-zero inlet pressure condition best satisfies the data. Recent numerical results by Aihara [29] (not shown) appear to be at most 5 percent below this iterative solution for non-zero pressure defect. The upward inflection of this curve beyond $\mathrm{Ra}^* = 10^4$ must be looked upon as a possible weakness of the present method. Finally, it is recognized that the inlet pressure condition does have a significant effect on the heat-transfer results above $\mathrm{Ra}^* = 10$.

The average Nusselt-number results for the unheated-entrance-length example are shown in Fig. 2(*d*) with Rayleigh number based on heated length L_H. Where comparison could be made with the numerical results (for $p_{v0} = 0$) of Dyer and Fowler, the approximate solution was found to agree within 2 percent [36]. Figure 3 shows local velocity variations for one set of conditions when heating occurs only for the last fifth of the channel length

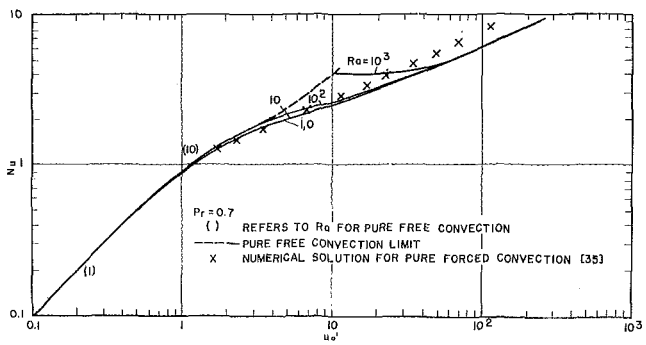

Fig. 4 Nusselt number as a function of Graetz and Rayleigh numbers for combined free and forced convection in the fully heated symmetrical channel

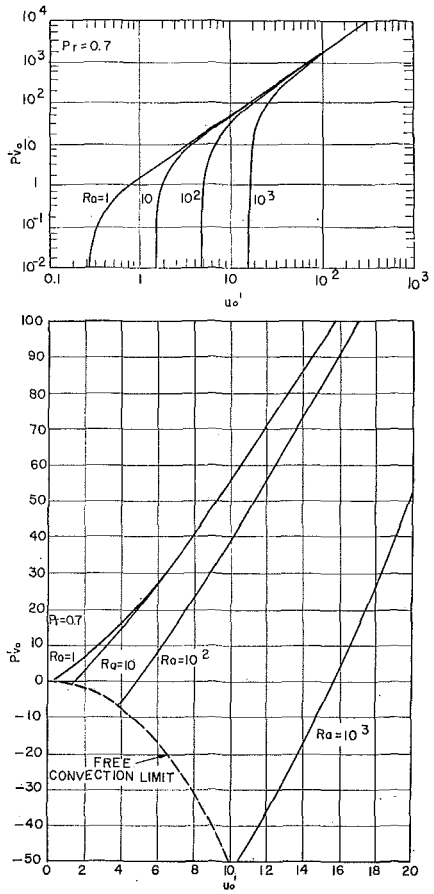

Fig. 5 Dimensionless pressure defect as a function of Graetz and Rayleigh numbers for combined free and forced convection in the fully heated symmetrical channel

($x \geq 0.8$). In the unheated section the flow approaches the fully developed state as indicated by the parabolic profile shape. The temperature of the short heated section is sufficient to cause a rapid distortion in this flow as indicated by its boundary-layer-like character. Not only does this figure dramatize the effect of the interacting mechanisms occurring, it also illustrates the ability of this solution technique to cope with such drastic changes in the flow pattern.

Figure 2(*c*) displays the effect of Prandtl number on the results for a uniformly heated channel. Although an extensive probe was not made for the effect of Pr, it is observed that heat-transfer coefficients for most gases and liquids will be weakly affected by Pr, whereas the effect of Pr will be significant for liquid metals.

Calculations for the Graetz flow parameter u_0' produced an unexpected maximum value as Ra was increased for $p_{v_0} = -u_0^2/2$. (No maximum occurred for the $p_{v_0} = 0$ case.) For

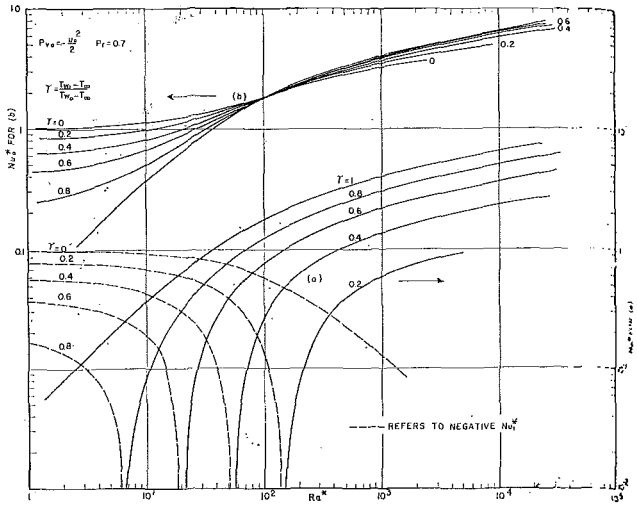

Fig. 6 Nusselt number as a function of Rayleigh number for the unsymmetrically heated uniform-temperature channel; (*a*) cold wall, (*b*) hot wall

example this occurred at approximately Ra = 2500 for the uniformly heated channel. It was discovered that when this maximum flow occurred the velocity profile indicated the beginning of downward flow at the center of the channel exit. Since boundary-layer-type equations would not be valid for this flow behavior, no solution results were presented beyond the "critical" Rayleigh number corresponding to the flow maximum. It is interesting to speculate about the physical significance of this flow behavior. Previous studies in free-forced convection [12–14] observed that flow inversions or inflections in the velocity profile do precede turbulent flow. Also, Dyer [27] noticed that for restricted channel entrances flow reversals did occur at the channel exit under certain conditions. It is not known whether this predicted flow pattern is a result of the assumptions contained in the present method or is a result of physical mechanisms indicating the limit of laminar boundary flow.

When the inlet pressure is arbitrarily specified the problem becomes that of combined free and forced convection. For this case, Fig. 4 displays the Nusselt number and Fig. 5 the initial pressure as functions of the Graetz and Rayleigh numbers. The latter figure is useful in selecting a proper fan for cooling purposes since the required fan pressure increase is given by

$$\Delta P_{\text{fan}} = P_{v_0} + \frac{\rho_\infty U_0^2}{2} = \frac{\rho_\infty L^2 \alpha^2}{b^4}\left(p_{v_0}' + \frac{u_0'^2}{2}\right)$$

In Fig. 4 the numerical solution for pure forced convection of Mercer et al. [35] is at most 13 percent above the present results at high u_0'; however, they report that their results exceed the results of others by 7 percent.

Figure 6 displays the average free-convection Nusselt number for the hot and cold walls of the unsymmetric-heating case. Although no other results exist for this case to permit a check of the solution, they possess the proper physical behavior and do converge to the exact solution for the case of fully developed flow (Ra → 0). Since the Nusselt number is defined as positive for heat transfer from the wall, at low Rayleigh numbers the cold wall actually receives heat from the fluid and a negative Nusselt number results.

V Conclusions

It has been demonstrated that the present method leads to accurate results for a number of examples over a wide range of conditions. The technique should also be useful in other cases, especially when overall heat-transfer results are desired. Finally, the effect of the pressure inlet condition has been examined and has been found to have a significant effect on heat transfer and

flow behavior at high Rayleigh numbers. The significance of the predicted flow-inversion phenomenon and its possible relation to turbulence should be examined in future studies.

References

1 Ostrach, S., "Laminar Flows with Body Forces," in: *Theory of Laminar Flows*, F. K. Moore, ed., Princeton University Press, Princeton, N. J., 1964.

2 Chato, J. C., "Combined Free and Forced Convection Flows in Channels," in: *Lectures on Advanced Heat Transfer*, B. T. Chao, ed., University of Illinois Press, 1968.

3 Ostrach, S., "Laminar Natural-Convection Flow and Heat Transfer of Fluids with and without Heat Sources in Channels with Constant Wall Temperatures," NACA TN, Dec. 1952.

4 Ostrach, S., "Combined Natural and Forced Convection Heat Transfer of Fluids with and without Heat Sources in Channels with Linearly Varying Wall Temperature," NACA TN 3141, Apr. 1954.

5 Ostrach, S., "Unstable Convection in Vertical Channels with Heating from Below Including Effects of Heat Sources and Frictional Heating," NACA TN 3458, July 1955.

6 Hallman, T. M., "Combined Forced and Free-Laminar Heat Transfer in Vertical Tubes With Uniform Internal Heat Generation," TRANS. ASME, Vol. 78, 1956, pp. 1831–1841.

7 Ostroumov, G. A., "Free Convection under Conditions of the Internal Problem," NACA TN 1407, 1958.

8 Lauber, T. S., and Welsh, A. U., "Natural Convection Heat Transfer Between Vertical Flat Plates with Uniform Heat Flux," *Proceedings of the Third International Heat Transfer Conference*, Vol. II, Aug. 1966, pp. 126–131.

9 Tao, L. N., "On Combined Free and Forced Convection Channels," JOURNAL OF HEAT TRANSFER, TRANS. ASME, Series C, Vol. 82, No. 3, Aug. 1960, pp. 233–238.

10 Martinelli, R. C., and Boelter, L. M. K., "The Analytical Prediction of Superimposed Free and Forced Viscous Convection in a Vertical Pipe," *Publs. Eng.*, University of California, Berkeley, Vol. 5, No. 2, 1942, pp. 23–58.

11 Leveque, M. A., "Transmissions de chaleur par Convection," *Annales des Mines*, Vol. 13, Sec. 12, 1928, pp. 201–300.

12 Rosen, E. M., and Hanratty, T. J., "Use of a Boundary-Layer Theory to Predict the Effect of Heat Transfer on the Laminar-Flow Field in a Vertical Tube with a Constant Wall Temperature," *AIChE Journal*, Vol. 7, No. 1, Mar. 1961, pp. 112–123.

13 Scheele, G. F., and Hanratty, T. J., "Effect of Natural Convection on Stability of Flow in a Vertical Pipe," *Journal of Fluid Mechanics*, Vol. 14, 1962, pp. 244–258.

14 Lawrence, W. T., and Chato, J. C., "Heat-Transfer Effects on the Developing Laminar Flow Inside Vertical Tubes," JOURNAL OF HEAT TRANSFER, TRANS. ASME, Series C, Vol. 88, No. 2, May 1966, pp. 214–222.

15 Savkar, S. D., "Developing Forced and Free Convective Flows Between Two Semi-Infinite Parallel Plates," *Proceedings of the Fourth International Heat Transfer Conference*, NC 3.8, Aug. 1970.

16 Zeldin, B., and Schmidt, F. W., "Developing Flow with Combined Forced–Free Convection in an Isothermal Vertical Tube," JOURNAL OF HEAT TRANSFER, TRANS. ASME, Series C, Vol. 94, No. 2, May 1972, pp. 211–223.

17 Elenbaas, W., "Heat Dissipation of Parallel Plates by Free Convection," *Physica*, Vol. 9, No. 1, 1942, pp. 1–28.

18 Sobel, R., Landis, F., and Mueller, W. K., "Natural Convection Heat Transfer in Short Vertical Channels Including the Effects of Stagger," *Proceedings of the Third International Heat Transfer Conference*, Vol. II, Aug. 1966, pp. 121–125.

19 Bodoia, J. R., and Osterle, J. F., "The Development of Free Convection Between Heated Vertical Plates," JOURNAL OF HEAT TRANSFER, TRANS. ASME, Series C, Vol. 84, No. 1, Feb. 1962, pp. 40–44.

20 Bodoia, J. R., "The Finite Difference Analysis of Confined Viscous Flows," PhD thesis, Carnegie Institute of Technology, Pittsburgh, Pa., 1959.

21 Sanders, V. D., "Steady State Laminar Free Convection Between Smooth Vertical Parallel Plates," in: *Heat Transfer, Thermodynamics and Education*, McGraw-Hill, New York, N. Y., 1964, pp. 295–318.

22 Novotny, J. L., "Laminar Free Convection Between Finite Vertical Parallel Plates," in: *Progress in Heat and Mass Transfer*, Vol. 2, T. F. Irvine, Jr., ed., Pergamon Press, New York, N. Y., 1969, pp. 13–22.

23 Currie, I. G., and Newman, W. A., "Natural Convection Between Isothermal Vertical Surfaces," *Proceedings of the Fourth International Heat Transfer Conference*, NC 2.7, Aug. 1970.

24 Engel, R. K., "The Development of Natural Convection of Vertical Flat Plates and in Vertical Channels," PhD thesis, New York University, New York, N. Y., 1965.

25 Engel, R. K., and Mueller, W. K., "An Analytical Investigation of Natural Convection in Vertical Channels," ASME Paper No. 67-HT-16.

26 Dyer, J. R., and Fowler, J. H., "The Development of Natural Convection in a Partially-Heated Vertical Channel Formed by Two Parallel Surfaces," *Mech. and Chem. Engrg. Trans. MC2*, Institution of Engineers (Australia), Vol. 1, May 1966, pp. 12–16.

27 Dyer, J. R., "The Development of Laminar Natural-Convective Flow in a Vertical Duct of Circular Cross-Section That Has a Flow Restriction at the Bottom," *Proceedings of the Fourth International Heat Transfer Conference*, NC 2.8, Aug. 1970.

28 Kageyama, M., and Izumi, R., "Natural Convection in a Vertical Circular Tube," *Bulletin of the JSME*, Vol. 13, No. 57, 1970, pp. 382–394.

29 Aihara, T., "The Effect of the Entrance Boundary Conditions on Free Convection between Vertical Parallel Plates," part 1, presented at the 9th Heat Transfer Symposium of Japan, Hiroshima, May, 1972.

30 Targ, in: *Dynamics of Viscous Incompressible Fluids*, by N. A. Slezkin, Gostekhizdat, Moscow, U.S.S.R., 1955.

31 Sparrow, E. M., Lundgren, T. S., and Lin, S. H., "Slip Flow in the Entrance Region of a Parallel Plate Channel," *Proceedings of the 1962 Heat Transfer and Fluid Mechanics Institute*, University of Washington, Seattle, Wash., June 1962, pp. 223–238.

32 Sparrow, E. M., Lin, S. H., and Lundgren, T. S., "Flow Development in the Hydrodynamic Entrance Region of Tubes and Ducts," *The Physics of Fluids*, Vol. 7, No. 3, Mar. 1964, pp. 338–347.

33 Williams, F. A., "Linearized Analysis of Constant-Property Duct Flows," *Journal of Fluid Mechanics*, Vol. 34, 1968, pp. 241–261.

34 Sparrow, E. M., and Gregg, J. L., "The Variable Fluid-Property Problem in Free Convection," TRANS. ASME, Vol. 80, 1958, pp. 879–886.

35 Mercer, W. E., Pearce, W. M., and Hitchcock, J. E., "Laminar Forced Convection in the Entrance Region Between Parallel Flat Plates," JOURNAL OF HEAT TRANSFER, TRANS. ASME, Series C, Vol. 89, No. 3, Aug 1967, pp. 251–257.

36 Quintiere, J. G., "An Analysis of Natural Convection Between Finite Vertical Parallel Plates," doctoral thesis, New York University, New York, N. Y., Sept. 1970.

P. H. OOSTHUIZEN
Associate Professor.

R. HART
Research Assistant.

Department of Mechanical Engineering,
Queen's University,
Kingston, Ontario, Canada

A Numerical Study of Laminar Combined Convective Flow over Flat Plates

The boundary-layer equations for combined forced- and free-convective flow over flat plates have been numerically solved using a simple implicit finite-difference scheme. The method of analysis has been developed for flow over plates for which either the surface temperature distribution or the surface heat-flux distribution is arbitrarily specified. Both assisting flow, in which the longitudinal component of the buoyancy force is in the same direction as the forced flow, and opposing flow, in which it is opposite in direction to the forced flow, have been considered. Numerical results have been obtained for plates having a uniform temperature and a uniform heat-flux distribution, and for fluids with Prandtl numbers of 0.7, 3, and 10.

Introduction

In studying fluid flow over heated surfaces it is usual to neglect the effects of the buoyancy forces when a forced velocity exists. Under some circumstances, however, such an assumption is not justifiable, the buoyancy forces considerably modifying the flow field and hence the heat-transfer rate from the surface despite the presence of the forced velocity. Such flows are termed combined, or mixed forced- and free-convective flows. The present note describes a numerical study of such combined convective flow over a flat surface aligned with the forced flow. Both the case where the surface temperature is specified and the case where the surface heat flux is specified are considered.

Several analytical studies of combined convective flow over vertical plane surfaces with a uniform surface temperature are available. Sparrow and Gregg [1][1] and Szewczyk [2] derived series solutions about the purely forced-convective solution in terms of a parameter characterizing the relative importance of the buoyancy forces. These solutions are only applicable when the buoyancy effects are small. Merkin [3] obtained a complete solution to the problem for a Prandtl number of 1 by using a combination series expansion and numerical solution. Attempts have also been made to analyze the problem using integral-equation methods [4, 5] but it can be shown that the accuracy of these analyses must be in doubt. Lloyd and Sparrow [6] analyzed the assisting-flow case, i.e., where the buoyancy forces are in the same direction as the forced flow, using a local-similarity method.

Analysis

The present study is concerned with combined convective flow over a plate which is set at an angle ϕ to the vertical, with the forced flow parallel to the surface of the plate. The analysis is based on the use of the boundary-layer equations, it being assumed that the fluid properties are constant except for the density change with temperature which leads, as a result of the gravitational potential, to the buoyancy force. In order to obtain results in as general a way as possible, these boundary-layer equations are expressed in terms of suitable dimensionless variables. Separate schemes are used for the cases where the surface temperature and where the surface heat flux are specified.

Consider first the case of flow over a plate with a specified surface temperature distribution. Using the set of dimensionless variables denoted by a bar, these being essentially the same as those used in the integral-equation analysis of [4], the boundary-layer equations become

$$\frac{\partial \bar{u}}{\partial \bar{x}} + \frac{\partial \bar{v}}{\partial \bar{y}} = 0 \tag{1}$$

$$\bar{u}\frac{\partial \bar{u}}{\partial \bar{x}} + \bar{v}\frac{\partial \bar{u}}{\partial \bar{y}} = \frac{\partial^2 \bar{u}}{\partial \bar{y}^2} \pm \bar{T} \tag{2}$$

$$\bar{u}\frac{\partial \bar{T}}{\partial \bar{x}} + \bar{v}\frac{\partial \bar{T}}{\partial \bar{y}} = \frac{1}{P_r}\frac{\partial^2 \bar{T}}{\partial \bar{y}^2} \tag{3}$$

The $\pm$ sign on the buoyancy term in equation (2) arises because of the way in which G is defined. The upper sign applies in assisting flow, i.e., where the longitudinal component of the buoyancy force is in the same direction as the forced velocity, while the lower sign applies in opposing flow.

In terms of the dimensionless variables, the boundary conditions on this set of equations are

$$\bar{y} = 0: \quad \bar{u} = \bar{v} = 0 \quad \bar{T}_w = \bar{T}_w(\bar{x}) \tag{4}$$

[1] Numbers in brackets designate References at end of paper.

Contributed by the Heat Transfer Division and presented at the Winter Annual Meeting, New York, N. Y., November 26–30, 1972, of The American Society of Mechanical Engineers. Manuscript received by the Heat Transfer Division October 19, 1971. Paper No. 72-WA/HT-4.

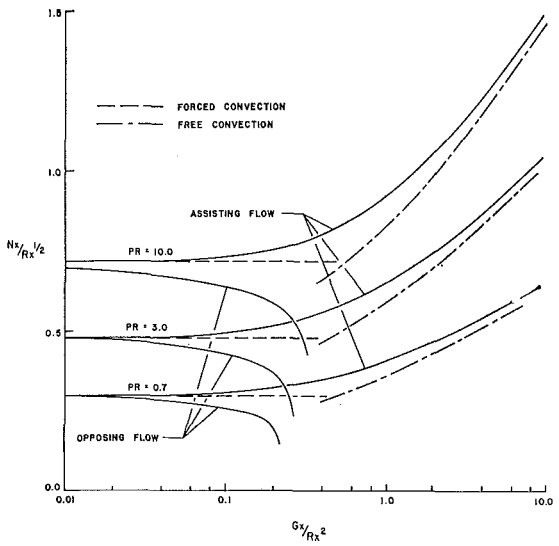

Fig. 1 Heat-transfer results for assisting and opposing flow over a uniform-temperature surface

$$\bar{y} \text{ large:} \qquad \bar{u} \to 1 \qquad \bar{T} \to 0$$

where

$$\bar{T}_w = (T_w - T_1)/(T_{wr} - T_1) \tag{5}$$

is a known function of $\bar{x}$, T_w being the local wall temperature.

Equations (1), (2), and (3) constitute the set of three equations in the three variables $\bar{u}$, $\bar{v}$, and $\bar{T}$ which must be solved in the specified-surface-temperature case.

Next consider the case of flow over a plate with a specified surface heat-flux distribution. In this case the set of variables denoted by an asterisk is used. In terms of these variables the boundary-layer equations become

$$\frac{3}{2}\frac{\partial u^*}{\partial x^*} + \frac{\partial v^*}{\partial y^*} + \frac{y^*}{4x^*}\frac{\partial u^*}{\partial y^*} = 0 \tag{6}$$

$$\frac{3}{2}u^*\frac{\partial u^*}{\partial x^*} + v^*\frac{\partial u^*}{\partial y^*} + \frac{u^*y^*}{4x^*}\frac{\partial u^*}{\partial y^*} = \frac{\partial^2 u^*}{\partial y^{*2}} \pm T^* \tag{7}$$

$$\frac{3}{2}u^*\frac{\partial T^*}{\partial x^*} + \frac{u^*T^*}{2x^*} + v^*\frac{\partial T^*}{\partial y^*} + \frac{u^*y^*}{4x^*}\frac{\partial T^*}{\partial y^*} = \frac{1}{P_r}\frac{\partial^2 T^*}{\partial y^{*2}} \tag{8}$$

The upper and lower signs on the buoyancy term in equation (7) again apply in assisting and opposing flow respectively.

In terms of the dimensionless variables, the boundary conditions become

$$y^* = 0: \qquad u^* = v^* = 0 \qquad q_w^* = q_w^*(x^*) \tag{9}$$

$$y^* \text{ large:} \qquad u^* \to 1 \qquad T^* \to 0$$

where

$$q_w^* = q_w/q_{wr} \tag{10}$$

is a known function of x^*, q_w being the local heat-transfer rate from the surface.

The wall boundary condition on heat transfer is utilized in obtaining the solution for T^* by noting that

$$q_w^* = -x^{*1/2}\left.\frac{\partial T^*}{\partial y^*}\right|_{y^*=0} \tag{11}$$

Therefore an alternative way of expressing the wall boundary condition on heat flux is

$$y^* = 0: \qquad -\partial T^*/\partial y^* = q_w^*(x^*)/x^{*1/2} \tag{12}$$

Equations (6), (7), and (8) constitute the set of three governing equations in the three variables u^*, v^*, and T^* in the specified-surface-heat-flux case.

The above sets of simultaneous partial differential equations have been solved using a forward-marching implicit finite-difference scheme. The scheme used is very straightforward and details will not be given here since it has been described in detail elsewhere [7].

It should be noted that since $\bar{x}$ and x^* depend on the longitudinal component of the buoyancy force, they both become zero when ϕ is 90 deg, i.e., when the plate is horizontal. Of course at all values of ϕ except zero there is in fact a component of the buoyancy force at right angles to the surface which leads to a pressure change across the boundary layer and a consequent pressure gradient along the plate within the boundary layer. At ϕ equal to 90 deg this is the only effect of the buoyancy force on the flow. The effects of this normal component were considered in [7] where it was shown that its effect will in most circumstances be important only relative to the effect of the longitudinal component when ϕ is very close to 90 deg and at Reynolds numbers that are much lower than those at which the longitudinal component of the buoyancy force becomes important at angles of ϕ different from 90 deg. For these reasons the effect of the normal component of the buoyancy force was not considered in the present work.

Results and Discussion

The sets of equations presented above apply when either the wall temperature distribution or the wall heat-flux distribution is arbitrarily prescribed. However, calculations have been carried out only for the uniform-wall-temperature and uniform-wall-heat-flux cases, i.e., for $\bar{T}_w = 1$ and $q_w^* = 1$. The main results have been obtained for Prandtl numbers of 0.7, 3, and 10.

The predicted variation of $N_x/R_x^{1/2}$ with $\bar{x}$ for the uniform-temperature case for the three Prandtl numbers is shown in Fig. 1. Also shown are curves giving the solutions for the limit-

Nomenclature

$G = |\beta g(T_{wr} - T_1)\cos\phi/\nu^2|$
G_x = Grashof number, $|\beta g(T_{wr} - T_1)\cos\phi\, x^3/\nu^2|$
$G^* = |\beta g q_{wr}\cos\phi/\nu^2 k|(\nu/u_1)^{5/2}$
G_x^* = modified Grashof number, $|\beta g q_{wr} x^4\cos\phi/\nu^2 k|$
k = coefficient of conductivity
N_x = local Nusselt number
P_r = Prandtl number
q_w = local heat-transfer rate at wall
q_{wr} = reference heat-transfer rate at wall
$R = u_1/\nu$
R_x = Reynolds number, $u_1 x/\nu$
T = temperature
T_1 = free-stream temperature
T_w = wall temperature
T_{wr} = reference wall temperature
$\bar{T} = (T - T_1)/(T_{wr} - T_1)$
$T^* = (T - T_1)kR_x^{1/2}/q_{wr}x$
u = velocity component in x direction
u_1 = free-stream velocity
$\bar{u} = u/u_1$
$u^* = u/u_1 = \bar{u}$
v = velocity component in y direction

$$\bar{v} = \frac{v}{u_1}\frac{R^{3/2}}{\bar{x}^{1/2}} = \frac{v}{u_1}\frac{R_x^{1/2}}{\bar{x}^{1/2}}$$

$$v^* = \frac{v}{u_1}\left(\frac{R_x}{G^*x^{3/2}}\right)^{1/2} = \frac{v}{u_1}\frac{R_x^{1/2}}{x^{*1/2}}$$

x = coordinate measured along surface
$\bar{x} = xG/R^2 = G_x/R_x^2$
$\bar{x}_1 = T_w^*\bar{x}$
$x^* = G^*x^{3/2} = G_x^*/R_x^{5/2}$
y = coordinate measured normal to surface
$\bar{y} = y(G/R)^{1/2} = (yR_x^{1/2}/x)\bar{x}^{1/2}$

$$y^* = \frac{y}{x}(R_xG^*x^{3/2})^{1/2} = \frac{y}{x}R_x^{1/2}x^{*1/2}$$

β = coefficient of cubical expansion
ν = kinematic viscosity
ρ = density
ϕ = angle relative to vertical

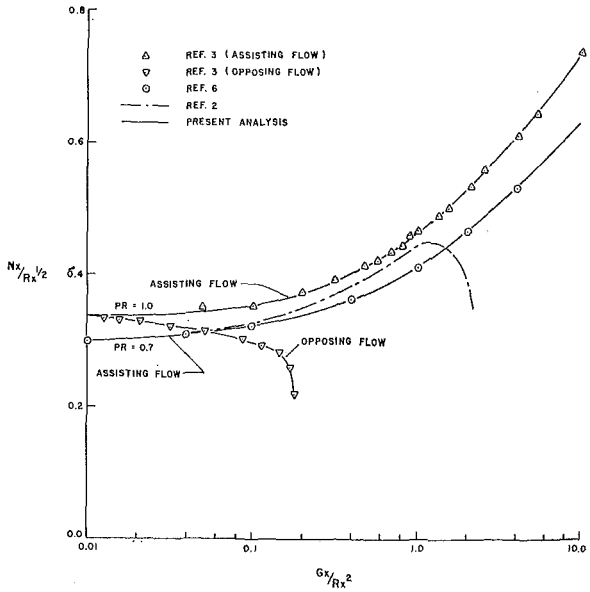

Fig. 2 Comparison of present results for assisting flow over an isothermal surface with some previous analytical results

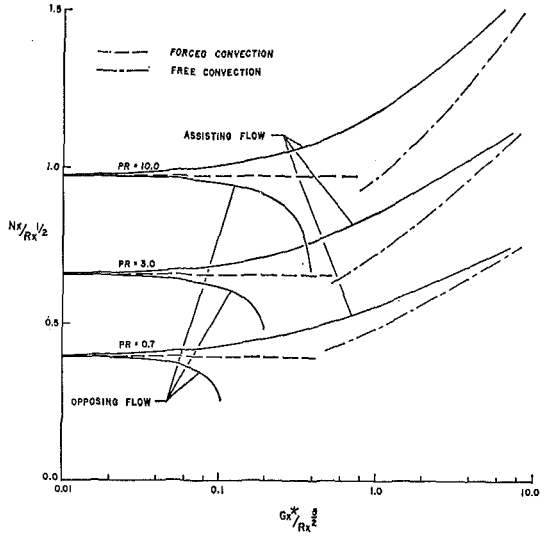

Fig. 3 Heat-transfer results for assisting and opposing flow over a surface with a uniform heat-transfer rate

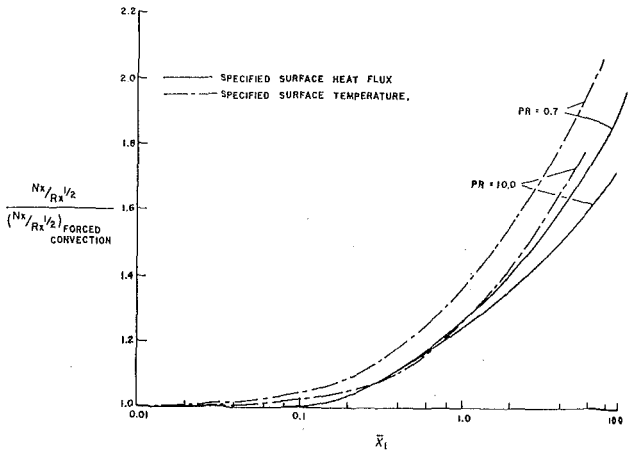

Fig. 4 Comparison of results for assisting flow over surfaces with a uniform temperature and a uniform heat-transfer rate

ing cases of purely forced and purely free convection. The forced-convection solution has the form

$$N_x/R_x^{1/2} = F_0 \tag{13}$$

where F_0 is a function of the Prandtl number alone, whose values can be deduced from [8], for example. The free-convection solution has the form

$$N_x/G_x^{1/4} = F_r \tag{14}$$

where F_r is also a function of the Prandtl number alone, whose values can be deduced from [9]. For the present purposes equation (14) is of course rewritten as

$$N_x/R_x^{1/2} = F_r\bar{x}^{1/4} \tag{15}$$

In assisting flow the results show that at small values of $\bar{x}$ the heat-transfer rate tends to that given by the purely forced-convection equation, while at large values of $\bar{x}$ it tends to that given by the purely free-convection equation.

In opposing flow it will be seen that at small values of $\bar{x}$ the heat-transfer rate tends, of course, to the forced-convection value given by equation (13). However, at large values of $\bar{x}$ in opposing flow there must exist a buoyancy-force-controlled flow adjacent to the surface which is in the opposite direction to the outer forced flow. At small values of $\bar{x}$, however, the entire flow is in the direction of the forced velocity. Thus in opposing flow there exists what is effectively a separation point at which the reversed flow first occurs. The present analysis, which is based on a forward-marching solution of the boundary-layer equation, cannot be applied beyond this "separation" point, and the calculations were therefore terminated at this point where the wall shearing stress becomes zero.

As discussed in the Introduction, several analyses of combined convective flow over a vertical isothermal surface are available. The present results have therefore been compared with the results of some of these analyses in Fig. 2. The series solution of Szewczyk [2] only applies at small values of $\bar{x}$ where it is in good agreement with the present results. Lloyd and Sparrow's [6] results cover a wider range of values of $\bar{x}$ and throughout this range are in excellent agreement with the present results. A comparison with the complete solution for a Prandtl number of 1 given by Merkin [3] is also shown. The agreement is very good.

Results for the uniform-surface-heat-flux case, for a range of variables similar to those considered for the uniform-surface-temperature case, are given in Fig. 3. These results exhibit the same basic features as those for the uniform-surface-temperature case which were discussed above. The limiting solution for purely forced convection which has the form

$$N_x/R_x^{1/2} = F_{oq} \tag{16}$$

where F_{oq} is a function of the Prandtl number alone and whose value can be deduced from [8], is shown in Fig. 3. The limiting solution for purely free convection is also given in the figure. It can be arranged in the form

$$N_x/R_x^{1/2} = F_{rq}x^{*1/5} \tag{17}$$

where the values of F_{rq}, which depends on the Prandtl number alone, can be deduced from [10].

In order to compare more directly the results for the uniform-temperature and uniform-heat-flux cases for assisting flow, an $\bar{x}$ based on the local value of the wall temperature can be defined in the uniform-heat-flux case such that

$$\bar{x}_1 = \left|\beta g(T_w - T_1)\cos\phi\, x/u_1^2\right| = \bar{x}T_w \tag{18}$$

Since in the uniform-surface-heat-flux case

$$T_w - T_1 = T_w{}^*q_{wr}x/kRe_x^{1/2}$$

it follows that in this case

$$\bar{x}_1 = \left|\frac{\beta g T_w{}^* q_{wr}\cos\phi\, x^4}{k\nu^2 R_x^{5/2}}\right| = T_w{}^*x^* \tag{19}$$

Using equation (19) the uniform-heat-flux results have been replotted in the form of $N_x/R_x^{1/2}$ against $\bar{x}_1$ in Fig. 4. The variation of $N_x/R_x^{1/2}$ with $\bar{x}$ for the uniform-surface-temperature case has also been plotted in this figure for comparison.

Conclusions

A simple numerical method for analyzing combined forced- and free-convective flow over a plane surface having either a specified surface temperature distribution or a specified surface heat-flux distribution has been developed.

Results have been obtained for a range of variables that is wider than that covered in previous analyses of the flow over a vertical surface with a uniform surface temperature, and in addition results have been obtained for the uniform-surface-heat-flux case.

Acknowledgments

The work described in the present report was part of a study sponsored by the McLaughlin Science Fund at Queen's University and the National Research Council of Canada under grant number A5573. The use of computer facilities provided by Queen's University is also gratefully acknowledged.

References

1 Sparrow, E. M., and Gregg, J. L., "Buoyancy Effects in Forced-Convection Flow and Heat Transfer," *Journal of Applied Mechanics*, Vol. 26, TRANS. ASME, Series E, Vol. 81, No. 1, Mar. 1959, pp. 133–134.

2 Szewczyk, A. A., "Combined Forced and Free-Convection Laminar Flow," JOURNAL OF HEAT TRANSFER, TRANS. ASME, Series C, Vol. 86, No. 4, Nov. 1964, pp. 501–507.

3 Merkin, J. H., "The Effect of Buoyancy Forces on the Boundary-Layer Flow over a Semi-infinite Vertical Flat Plate in a Uniform Free Stream," *Journal of Fluid Mechanics*, Vol. 35, 1969, p. 439.

4 Acrivos, A., "Combined Laminar Free- and Forced-Convection Heat Transfer in External Flows," *AIChE Journal*, Vol. 4, 1958, p. 285.

5 Oosthuizen, P. H., "A Note on the Combined Free and Forced Convective Laminar Flow over a Vertical Isothermal Plate," *South African Mech. Eng.*, Vol. 15, 1965, p. 8.

6 Lloyd, J. R., and Sparrow, E. M., "Combined Forced and Free Convection Flow on Vertical Surfaces," *International Journal of Heat and Mass Transfer*, Vol. 13, 1970, p. 434.

7 Oosthuizen, P. H., and Hart, R., "A Numerical Study of Laminar Combined Convective Flow over Flat Plates," Report 4/71, Queen's University Thermal and Fluid Sciences Group, Aug. 1971.

8 Kays, W. M., *Convective Heat and Mass Transfer*, McGraw-Hill, New York, N. Y., 1966.

9 Ede, A. J., "Advances in Free Convection," in: *Advances in Heat Transfer*, Vol. 4, J. P. Hartnett and T. F. Irvine, eds., Academic, New York, N. Y., 1967, p. 6.

10 Sparrow, E. M., and Gregg, J. L., "Laminar Free Convection From a Vertical Plate With Uniform Surface Heat Flux," TRANS. ASME, Vol. 78, 1956, pp. 435–440.

H. MIYAZAKI
Research Assistant,
Department of Mechanical Engineering,
University of Minnesota,
Minneapolis, Minn.

Combined Free- and Forced-Convective Heat Transfer and Fluid Flow in Rotating Curved Rectangular Tubes

A theoretical study is presented for combined free- and forced-convective heat transfer and fluid flow in curved rectangular tubes rotating about an axis through the center of curvature of the tube. The analysis is performed under the conditions that the flow is thermally and hydrodynamically fully developed, and the axial wall heat flux is uniform with a peripherally uniform wall temperature. The governing equations are solved numerically, and effects of the aspect ratio, radius ratio, Prandtl number, a nondimensional parameter representing the effects of Coriolis forces, Grashof number, and Dean number on the flow and heat-transfer characteristics are presented for velocity and temperature distributions, streamlines and isotherms, local and mean friction factors f and Nusselt numbers Nu. *The effects of the first two geometrical parameters are minor. However, an increase in the last three force parameters enhances both f and* Nu *greatly. An effect characteristic of the Coriolis forces is that they cause a great increase in f, while the enhancement of* Nu *is much less remarkable.*

Introduction

In recent years it has become increasingly important to incorporate some cooling system into the design of rotary machines such as gas turbines, electric generators, motors, etc. An improvement in the thermal efficiency of a gas turbine can be effectively achieved by increasing the gas temperature at the inlet of the turbine. However, since the maximum temperature at which present-day materials for rotor blades can insure reliable operation of a gas-turbine plant is approximately 850 deg C, if the inlet gas temperature exceeds this value some cooling device is essential. Schmidt first proposed that this problem be solved by the use of blades with holes drilled radially and filled with some cooling substance. It is expected that this gives an extremely effective cooling because the centrifugal acceleration can become of the order of 10^4 g. Many investigations of heat transfer inside these thermosiphon holes have been reported. These investigations were, however, conducted under the earth's gravitational field, which differs from the rotational field in the presence of Coriolis forces which induce a secondary flow in a plane perpendicular to the main flow.

Further, the employment of some cooling device for electric generators is also of great importance to protect the insulating materials surrounding conductors, which are usually resistant to a maximum temperature of 100 to 150 deg C for reliable long-range operation. As a coolant, air was first used. It was then replaced by pressurized hydrogen which has a larger thermal capacity. The cooling is effected by pumping a coolant through hollow passages located inside the conductors or through axially located holes in the rotor drum. The hydrogen-cooling method makes it possible to construct a generator with an output of up to 250,000 kw compared with a maximum output of 60,000 kw for an air-cooled generator. Recently it has been attempted to employ water, which is the most efficient coolant. Water-cooled generators have been constructed in various countries including the Soviet Union and Switzerland and put into operation, although there are some technical difficulties encountered in sealing, in balancing the rotor, and in meeting strength and insulation requirements. It is estimated that this type of cooling is capable of a maximum output of 750,000 kw.

As a rotating geometry, many configurations can be envisaged according to the shape and location of cooled components, i.e., (*a*) open thermosiphon, (*b*) closed thermosiphon, (*c*) straight tube rotating about a parallel axis, (*d*) straight tube rotating about a perpendicular axis, and (*e*) rotating curved tube. The first two, (*a*) and (*b*), are the configurations usually utilized for the cooling of gas-turbine blades. The first and the last three, (*a*), (*c*), (*d*), and (*e*), are the configurations encountered in cooling rotor drums and conductors of electric generators.

A remarkable characteristic of the flow and heat transfer in the system of rotational motion is the presence of centrifugal and Coriolis forces which induce a secondary flow in a plane perpendicular to the direction of main flow, resulting in three-dimensional flow and temperature fields. The secondary flow also arises when a tube is curved, and enhances significantly the pres-

Contributed by the Heat Transfer Division for publication (without presentation) in the Journal of Heat Transfer. Manuscript received by the Heat Transfer Division August 17, 1970. Paper No. 72-HT-N.

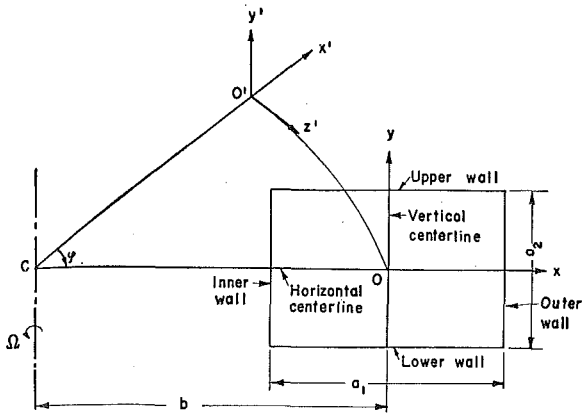

Fig. 1 Toroidal coordinate system

sure drops and heat-transfer rates. In spite of the great practical importance and academic interest, the flow and heat transfer in rotating configurations have not yet been sufficiently investigated, and little information is available for the design. Barua [1][1] has reported a theoretical analysis for fully developed flow in a straight tube with circular cross section rotating about a perpendicular axis, configuration (*d*). Morris [2] has presented the result of theoretical analysis for the asymptotic velocity and temperature distributions in configuration (*c*) solved by a series expansion in terms of the rotational Rayleigh number. Humphreys, Morris, and Barrow [3] also investigated experimentally the local and mean heat-transfer characteristics for air flowing turbulently in the entrance region of a circular duct revolving about a parallel axis. Mori and Nakayama [4] have solved the same problem by Pohlhausen's method, and have presented the pressure-drop and heat-transfer characteristics, which hold for a large angular velocity.

In contrast to the problem in a rotating system, the study of the flow and heat-transfer characteristics in curved stationary tubes has been fully made in conjunction with the application to heating and refrigerating plants. It was first treated theoretically by Dean [5, 6], who has solved the equations of flow by perturbation and has clarified that the flow field is controlled by the Dean number alone. Adler [7] made extensive measurements of velocity distributions and found that the boundary-layer approximation holds for large values of the Dean number. He also made a theoretical analysis by Pohlhausen's method, referring to the results of his measurements. Barua [8] solved the flow field by the same method, and later Mori and Nakayama [9, 10] reported the results of their theoretical analyses for both laminar and turbulent flows which are valid for large Dean numbers. Experimental investigations were made for turbulent flow and heat transfer by Ito [11], Seban and McLaughlin [12], Rogers and Mayhew [13], and others.

The investigation for the configuration (*e*) has been attempted by Ludwieg [14]. He has solved the boundary-layer equations by Pohlhausen's method for large values of the Dean number and rotational velocity for fully developed laminar flow in a square tube, and has obtained the friction factor which was verified by his experiment.

The object of the present analysis is to investigate theoretically the flow and heat-transfer characteristics in curved rectangular tubes rotating about an axis through the center of curvature, configuration (*e*). The governing equations are approximated by finite-difference schemes and solved by an iterative method under the conditions that the flow and temperature fields are fully developed and the wall heat flux is uniform with a peripherally uniform wall temperature. The results of computations are presented graphically for the temperature and velocity distributions, the streamlines and isotherms, and the local and mean Nusselt numbers and friction factors.

Theoretical Analysis

Figure 1 shows the coordinate system that is convenient in considering the motion of fluid through a tube of rectangular cross section coiled in the form of a circle. C is the axis of rotation, which is through the center of curvature of the circularly curved tube, and is perpendicular to the plane which contains the axis of the tube O'O. The sense of angular velocity is indicated by an arrow, while the fluid in the tube flows in the φ direction. The figure shows the cross section of a rectangular tube cut by a plane perpendicular to the axis of the tube O'O. For con-

[1] Numbers in brackets designate References at end of paper.

Nomenclature

a_1 = width of tube cross section
a_2 = height of tube cross section
a_h = hydraulic diameter $\equiv 2a_1a_2/(a_1 + a_2)$
A = aspect ratio $\equiv a_2/a_1$
b = radius of curvature
B = radius ratio $\equiv b/a_h$
C_1 = pressure gradient in the φ direction
C_2 = temperature gradient in the φ direction
f = friction factor
f_c = centrifugal acceleration $= b\Omega^2$
Gr_2 = Grashof number $\equiv \beta f_c \Delta t_2 a_h^3/\nu^2$
h = heat-transfer coefficient
k = thermal conductivity
K_1 = Dean number $\equiv a_h w_1/(\nu\sqrt{B})$
M = number of divisions in the X direction
N = number of divisions of the Y direction
Nu = Nusselt number $\equiv ha_h/k$
p = pressure
p' = modified pressure given by equation (3)
P = nondimensional pressure $\equiv p'/\rho(\nu/a_h)^2$
Pr = Prandtl number $\equiv \nu/\alpha$
Re = Reynolds number $\equiv a_h w_m/\nu$
Ro = nondimensional parameter representing the magnitude of the Coriolis force $\equiv a_h^2\Omega/\nu$
s = arc length of tube axis $= b\varphi$
t = temperature
Δt_2 = representative temperature $\equiv \mathrm{Pr} a_h C_2$
T = nondimensional temperature $\equiv (t_w - t)/\Delta t_2$
u, v, w = velocity components in the x, y, and φ directions respectively
U, V, W = nondimensional velocity components in the X, Y, and φ directions respectively $\equiv a_h u/\nu$, $a_h v/\nu$, and w/w_1
w_1 = representative velocity in the φ direction $\equiv a_h^2 C_1/\mu$
x, y, φ = toroidal coordinates
x', y', z' = cartesian coordinates
X, Y, φ = nondimensional toroidal coordinates $\equiv x/a_h$, y/a_h, φ
X', Y' = nondimensional coordinates $\equiv x'/a_1$, y'/a_1
α = thermal diffusivity
β = volume-expansion coefficient
δ = prescribed error for the iterative process
ϵ = ratio of mesh sizes $\equiv \Delta X/\Delta Y$
ζ = vorticity
η = quantity in the equation for the relaxation parameter ω
μ = viscosity
ν = kinematic viscosity
ρ = density
Ψ = nondimensional stream function
ω = relaxation parameter
Ω = angular velocity

Subscripts

b = bulk mean
l = local
m = mean
s = stationary straight rectangular tube
w = wall

venience of analysis the toroidal coordinate system x, y, φ is introduced instead of the cartesian coordinate system x', y', z'. The angle φ is measured from an arbitrary fixed point O′ on the axis of the tube. To facilitate the explanation, each side of the tube wall is termed the inner, outer, upper, or lower wall as shown in Fig. 1. The horizontal and vertical centerlines are also shown.

The flow is assumed to be laminar, and with the exception of density the physical properties are taken to be constant. The axial velocity is so low that there is no energy dissipation due to friction, and no heat source is present within the cooling fluid. The gravitational force is neglected compared with the centrifugal force due to rotation. The rotational acceleration is ordinarily of the order of 10^3 to 10^4 g for the rotary machines with which we are concerned, so that the elimination of the gravitational-force term apparently causes no significant error. The detailed derivation of the governing equations which describe the aforementioned physical model is given in [15]. The equations are, however, essentially three-dimensional and intractable, so we simplify them by assuming that the flow is both thermally and hydrodynamically fully developed. The pressure gradient in the axial direction is constant, i.e., $\partial p/\partial s = -C_1$. For the constant wall heat flux per unit length of tube considered here, the axial temperature gradient is also constant, i.e., $\partial t/\partial s = C_2$.

Further, we must incorporate the buoyancy-force term. If the fluid density is constant, the centrifugal force does not make any contribution to the motion of the fluid, since it is balanced by a pressure gradient in the x direction. If, however, there is a density gradient owing to temperature variation, the centrifugal force becomes locally nonuniform and gives rise to a fluid motion in the form of a buoyancy force. The density variation is usually small enough to be ignored in all terms except in the term of the buoyancy force. It varies approximately linearly with temperature as

$$\rho = \rho_w + \rho_w\beta(t_w - t) \approx \rho_w + \rho\beta(t_w - t) \tag{1}$$

since $\rho_w \approx \rho$. Strictly speaking, the volume-expansion coefficient β is a function of temperature, and its dependence is not necessarily negligible for water. However, it was found in [15] that the differences of f and Nu between the cases of variable and constant volume-expansion coefficients were approximately 0.6 and 2 percent respectively. This discrepancy is tolerable for the purpose of industrial application so that the volume-expansion coefficient is taken to be constant here for simplicity. Therefore, using equation (1), the rotational centrifugal force per unit volume is expressed in the form

$$\rho(b + x)\Omega^2 = \rho_w\left(1 + \frac{x}{b}\right)f_c + \rho\left(1 + \frac{x}{b}\right)f_c\beta(t_w - t) \tag{2}$$

Finally we introduce the modified pressure p' such that

$$p' = p - \rho_w\left(x + \frac{x^2}{2b}\right)f_c \tag{3}$$

With these aforementioned relations, we obtain the simplified governing equations, since all the velocity components and temperature are independent of φ

$$\frac{\partial}{\partial x}\{(b + x)u\} + \frac{\partial}{\partial y}\{(b + x)v\} = 0 \tag{4}$$

$$u\frac{\partial u}{\partial x} + v\frac{\partial u}{\partial y} - \frac{w^2}{b + x} - 2\Omega w - \left(1 + \frac{x}{b}\right)f_c\beta(t_w - t) = -\frac{1}{\rho}\frac{\partial p'}{\partial x} - \nu\frac{\partial}{\partial y}\left(\frac{\partial v}{\partial x} - \frac{\partial u}{\partial y}\right) \tag{5}$$

$$u\frac{\partial v}{\partial x} + v\frac{\partial v}{\partial y} = -\frac{1}{\rho}\frac{\partial p'}{\partial y} + \nu\frac{1}{b + x}\frac{\partial}{\partial x}\left\{(b + x)\left(\frac{\partial v}{\partial x} - \frac{\partial u}{\partial y}\right)\right\} \tag{6}$$

$$u\frac{\partial w}{\partial x} + v\frac{\partial w}{\partial y} + \frac{uw}{b + x} - 2\Omega u = \frac{1}{\rho}\frac{b}{b + x}C_1 + \nu\left\{\frac{\partial^2 w}{\partial x^2} + \frac{1}{b + x}\frac{\partial w}{\partial x} - \frac{w}{(b + x)^2} + \frac{\partial^2 w}{\partial y^2}\right\} \tag{7}$$

$$u\frac{\partial t}{\partial x} + v\frac{\partial t}{\partial y} + w\frac{b}{b + x}C_2 = \alpha\left(\frac{\partial^2 t}{\partial x^2} + \frac{1}{b + x}\frac{\partial t}{\partial x} + \frac{\partial^2 t}{\partial y^2}\right) \tag{8}$$

which are subject to the boundary conditions at the wall

$$u = v = w = 0 \qquad t = t_w \tag{9}$$

In order to nondimensionalize the governing equations we introduce the following nondimensional variables into equations (4)–(8)

$$U = \frac{a_h u}{\nu} \qquad V = \frac{a_h v}{\nu} \qquad W = \frac{w}{w_1} \qquad P = \frac{p'}{\rho(\nu/a_h)^2}$$

$$T = \frac{t_w - t}{\Delta t_2} \qquad X = \frac{x}{a_h} \qquad Y = \frac{y}{a_h} \tag{10}$$

Furthermore, we attempt to modify the nondimensionalized governing equations to facilitate the numerical procedure. First the equation of continuity is identically satisfied by the stream function

$$U = \frac{1}{1 + X/B}\frac{\partial\Psi}{\partial Y} \qquad V = -\frac{1}{1 + X/B}\frac{\partial\Psi}{\partial X} \tag{11}$$

Next we insert the vorticity

$$\zeta = \frac{\partial V}{\partial X} - \frac{\partial U}{\partial Y} \tag{12}$$

into equations (11) to give

$$\frac{\partial^2\Psi}{\partial X^2} - \frac{1}{B(1 + X/B)}\frac{\partial\Psi}{\partial X} + \frac{\partial^2\Psi}{\partial Y^2} = -\left(1 + \frac{X}{B}\right)\zeta \tag{13}$$

In the present analysis the pressure distribution is irrelevant, so the pressure terms are eliminated from the equations of momentum in the X and Y directions and the equation of vorticity is obtained

$$\frac{\partial^2\zeta}{\partial X^2} + \frac{1}{B(1 + X/B)}\frac{\partial\zeta}{\partial X} - \frac{1}{B^2(1 + X/B)^2}\zeta + \frac{\partial^2\zeta}{\partial Y^2} = U\frac{\partial\zeta}{\partial X} + V\frac{\partial\zeta}{\partial Y} - \frac{U}{B(1 + X/B)}\zeta + \frac{2K_1^2}{1 + X/B}W\frac{\partial W}{\partial Y} + 2\sqrt{B}K_1\mathrm{Ro}\frac{\partial W}{\partial Y} + \mathrm{Gr}_2\left(1 + \frac{X}{B}\right)\frac{\partial T}{\partial Y} \tag{14}$$

After some rearrangements, the equations of axial momentum and energy are given by

$$\frac{\partial^2 W}{\partial X^2} + \frac{1}{B(1 + X/B)}\frac{\partial W}{\partial X} - \frac{1}{B^2(1 + X/B)^2}W + \frac{\partial^2 W}{\partial Y^2} = U\frac{\partial W}{\partial X} + V\frac{\partial W}{\partial Y} + \frac{UW}{B(1 + X/B)} + \frac{2\mathrm{Ro}}{\sqrt{B}K_1}U - \frac{1}{1 + X/B} \tag{15}$$

$$\frac{\partial^2 T}{\partial X^2} + \frac{1}{B(1 + X/B)}\frac{\partial T}{\partial X} + \frac{\partial^2 T}{\partial Y^2} = \mathrm{Pr}\left(U\frac{\partial T}{\partial X} + V\frac{\partial T}{\partial Y}\right) - \frac{\sqrt{B}K_1}{1 + X/B}W \tag{16}$$

Equations (11) and (13) to (16) constitute the system of equations to be solved. The flow and temperature fields are either symmetric or antisymmetric about the X axis, so that it suffices to consider only the upper half of the tube cross section for analysis.

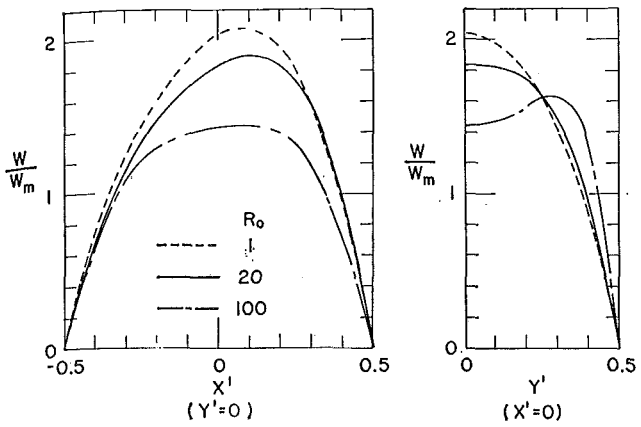

Fig. 2 Variation of axial-velocity distribution with Ro; $A = 1.0$, $B = 50$, $Pr = 0.7$, $Gr_2 = 10^3$, $K_1 = 100$

It is readily found that U, W, and T are symmetric, while V, Ψ, and ζ are antisymmetric, and therefore the boundary conditions (9) are reduced to

$$U = V = \Psi = \frac{\partial \Psi}{\partial X} = W = T = 0 \quad \text{at} \quad X = \pm\frac{1}{4}\left(1 + \frac{1}{A}\right)$$

$$\text{for} \quad 0 \leq Y \leq \frac{1}{4}(1 + A) \quad (17)$$

$$U = V = \Psi = \frac{\partial \Psi}{\partial Y} = W = T = 0 \quad \text{at} \quad Y = \frac{1}{4}(1 + A)$$

$$\text{for} \quad -\frac{1}{4}\left(1 + \frac{1}{A}\right) \leq X \leq \frac{1}{4}\left(1 + \frac{1}{A}\right) \quad (18)$$

$$\frac{\partial U}{\partial Y} = \frac{\partial W}{\partial Y} = \frac{\partial T}{\partial Y} = 0 \quad \text{at} \quad Y = 0$$

$$V = \Psi = \zeta = 0$$

$$\text{for} \quad -\frac{1}{4}\left(1 + \frac{1}{A}\right) \leq X \leq \frac{1}{4}\left(1 + \frac{1}{A}\right) \quad (19)$$

The governing equations are solved by finite-difference methods. The stability of a difference scheme largely depends on how the nonlinear inertia terms are approximated. The difference scheme employed here is the modified one-sided difference scheme utilized by Spalding, Runchal, and Wolfshtein [16]. Their scheme is based on the idea that the first derivatives in the inertia terms are approximated by the forward difference for non-positive velocity and by the backward difference for non-negative velocity, so that the stability criterion is unconditionally satisfied. A detailed description of the numerical solution is given in [15].

The vorticity at the walls is unknown, so it should be computed from some other dependent variables. For this purpose it is usual to use the relation between the vorticity and the stream function, equation (13). The approximation of wall vorticity is known to have a significant effect on the stability of the solution, and some approximation formulas have been devised. The Dorfman-Romanenko method [17] is employed in the present analysis.

Since the governing equations are nonlinear and the coefficients in finite-difference equations comprise unknowns, an iterative method should be utilized. The iteration was made in the order of Ψ, ζ, W, T, U, and V. The overrelaxation method was employed to accelerate the convergence. The relaxation parameter ω was computed by $\omega = 2(1 + \sqrt{1 - \eta})/\eta$ with $\eta = (\cos \pi/M + \cos \pi/N)/2$. Since overrelaxation impairs the stability of the iterative process for vorticity, underrelaxation was applied to it. The underrelaxation parameter was varied from 0.15 to 0.5 according to the magnitude of the nondimensional parameters. The iterations were terminated when the relative error of solutions became less than some preassigned small quantity δ. It was found in the preliminary computations that $M = 24$, $N = 12$, and $\delta = 0.001$ were the reasonable values from the viewpoint of accuracy and economy of computer time. However, in the computations for $Pr \geq 5$, $Ro \geq 100$, $Gr_2 \geq 10^4$, and $K_1 \geq 300$, the number of divisions was increased to $M = 36$ and $N = 18$ with $\delta = 0.001$. The solutions diverged for values of the parameters larger than $Pr = 6$, $Ro = 300$, $Gr_2 = 3 \times 10^4$, and $K_1 = 10^3$, with $M = 36$ and $N = 18$.

Results and Discussion

The characteristics of flow and heat transfer in rotating curved rectangular tubes are governed by the six nondimensional parameters A, B, Pr, Ro, Gr_2, and K_1. The parameter Ro involves the angular velocity and indicates the effects of the Coriolis force, which is, however, usually represented by the Rossby number. The Rossby number indicates the relative importance of the inertia to the Coriolis force, while Ro is the ratio of the Coriolis force to the viscous force. The parameter Ro is adopted here instead of the conventional Rossby number because the increase in Ro implies the growth of the Coriolis force, and its effects are more readily conceivable. These parameters are coupled with and affect each other, so that the effects of the parameters on the flow and heat-transfer characteristics are complicated and are not the mere superposition of individual effects, allthough the interactions between the parameters are indirect compared with the direct effects of each individual parameter.

There are many nondimensional parameters, and to know the effects of one of these parameters on flow and heat-transfer characteristics, not only that parameter but also the rest of the parameters should be varied, because their effects are interrelated and the effects of a single parameter differ for different values of the others. Therefore, computations are required for an extremely large number of cases to grasp the entire effect. However, this requires an extremely long computation time, so that, considering the economy, computations were performed by giving the parameters the standard values $A = 1.0$, $B = 50$, $Pr = 0.7$, $Ro = 20$, $Gr_2 = 10^3$, and $K_1 = 100$. To see the effects of one parameter, the rest were fixed at the standard values. The results of the computations consist of the axial-velocity and temperature distributions along the vertical and horizontal centerlines, the streamlines and isotherms, the local friction factors and Nusselt numbers, and the mean friction factors and Nusselt numbers. It is a lengthy process to describe the effects of all the parameters on the flow and heat-transfer characteristics. The descriptions here will be confined to the effects of Ro alone, except those on the mean friction factor and Nusselt number, provided that the effects of A and Pr on the mean characteristics are eliminated. For the complete presentation and descriptions of the results see [15].

The distributions of axial velocity and temperature along the horizontal centerline (left figure) and the vertical centerline (right figure) are illustrated in Figs. 2 and 3 respectively in nondimensional form with the mean values W/W_m and T/T_b against the nondimensional coordinates X' and Y'. The dotted, solid, and one-dotted lines indicate the curves for Ro = 1, 20, and 100 respectively. The Coriolis forces have a peculiar effect in that they flatten considerably the axial-velocity distribution in the central region of the tube cross section, while their effect on the temperature profile is negligible. The Coriolis forces have both x and φ components. Those due to rotation are $2\Omega w$ (x component) and $-2\Omega u$ (φ component), while that due to curvature is $-uw/(b + x)$ (φ component). In the central region where the x component of the secondary-flow velocity u is positive, the φ components of the Coriolis forces act such that they push back the main flow in the negative φ direction. The x component eventually has the same effect. A large w produces a strong

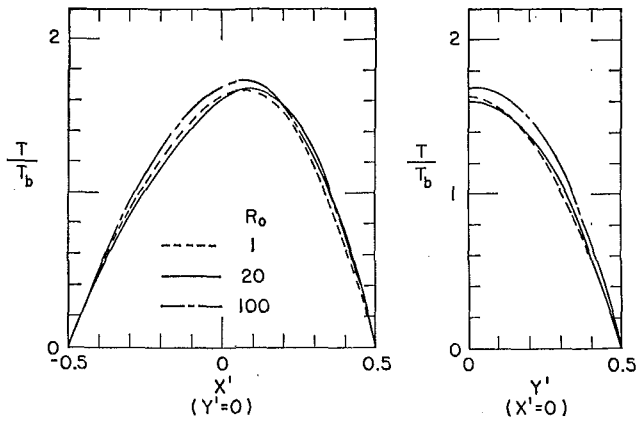

Fig. 3 Variation of temperature distribution with Ro; $A = 1.0$, $B = 50$, $Pr = 0.7$, $Gr_2 = 10^3$, $K_1 = 100$

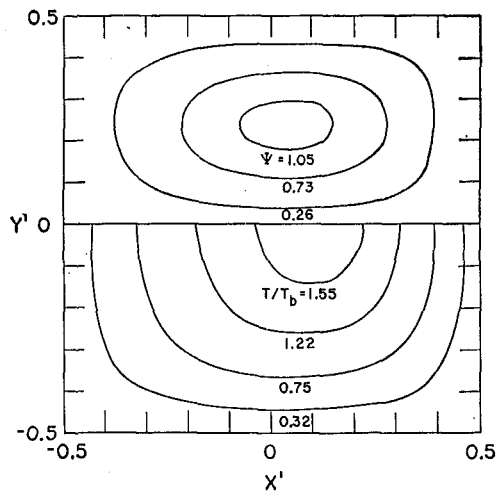

Fig. 4 Streamlines and isotherms for standard values of parameters; $A = 1.0$, $B = 50$, $Pr = 0.7$, $Ro = 20$, $Gr_2 = 10^3$, $K_1 = 100$

secondary flow which results in a large braking force, and consequently w decreases. A central core where the uniform secondary current flows in the x direction is thus formed, and the axial-velocity distribution possesses a wide flat part at the center. However, when w decreases owing to the increase in the braking force, the x component of the Coriolis force decreases. It follows that the corresponding secondary flow becomes weak and the braking force is reduced. It is seen, therefore, that the Coriolis forces always act so as to restore a system to some equilibrium state. This restoring property is typical of these forces. On the other hand, in the vicinity of the upper wall the velocity component u is negative and the gradient of w with respect to x is positive at $x = 0$. This occurs because the maximum point of w is shifted toward the outer wall by the secondary current. The φ component of the Coriolis force and the inertia force $-u\partial w/\partial x$ act in the positive φ direction. Therefore the velocity profile along the vertical centerline becomes such that for large Ro it increases toward the upper wall, attains its maximum value where the secondary-current velocity is highest, and then decreases in the close neighborhood of the upper wall due to the predominant viscous force there.

As Ro increases, the secondary flow is intensified. It does not mean, however, that the secondary-flow velocity in the central core is large, because the area through which the secondary current flows is widened to a greater extent. This result is derived as follows. In the equation of axial momentum (15) the viscous-dissipation term on the left-hand side and the first inertia term on the right-hand side are negligible because the axial-velocity distribution is flat in the central region. Since the Y component of the secondary-flow velocity V is negligible, the second inertia term also vanishes. We consider here the case of Coriolis forces sufficiently large to decelerate the main flow so that the third term of the Coriolis force due to curvature can be ignored compared with the Coriolis-force term due to rotation. Accordingly the force balance between the Coriolis force and the pressure force holds,

$$\frac{2\mathrm{Ro}}{\sqrt{B}K_1}U - \frac{1}{1+X/B} = 0$$

from which we obtain U

$$U = \frac{1}{1+X/B}\cdot\frac{\sqrt{B}K_1}{2\mathrm{Ro}}$$

U, therefore, decreases with Ro.

Since both U and V are small in the central core for large Ro, convection by the secondary current is negligible. The heat convected in the axial direction is consequently supplied mainly by conduction, and as Ro increases more heat is transferred to the axial flow by conduction. The axial-velocity distribution on the horizontal centerline and accordingly the convected heat in the axial direction are almost symmetric about the origin so that the heat transferred by conduction should also be symmetric. In other words the temperature distribution tends to be symmetric or less skewed as Ro increases. In the vicinity of the upper wall the conducted heat is carried away by both the axial and the secondary flows. In the central core the secondary-flow velocity is small so that the heat conduction is still significant there. This implies that the temperature should continue to increase toward the center. The temperature distribution on the vertical centerline becomes, therefore, as illustrated in Fig. 3, and is not similar to the velocity distribution. It is also less sensitive to the variation of Ro than the velocity distribution. The buoyancy force due to rotation and the centrifugal force due to curvature induce a strong secondary flow which deforms both the velocity and the temperature distributions. However, the Coriolis force influences the flow field through two mechanisms, i.e., the secondary flow and the braking force, while the heat transfer is enhanced solely by the secondary flow, which is relatively weak, as mentioned previously. Therefore the modification of the temperature distribution due to Ro is small compared with that of the velocity distribution.

As Ro increases, a broad central core is formed with a uniform secondary current which flows from the inner wall to the outer wall. The returning current is therefore confined to a very thin layer next to the wall where the velocity gradient is significant. The viscosity is relevant only in this thin layer, its effect being negligible in the central core so that it becomes feasible to make the boundary-layer approximation for large Ro. It also holds true for large Gr_2 and K_1.

The streamlines and isotherms were obtained by interpolation from the distributions of the stream function and the temperature respectively. These are shown in Fig. 4 for the standard values of the parameters, i.e., Ro = 20, and in Fig. 5 for Ro = 100. The three streamlines are drawn so that they pass the points $Y' \approx 0.05$, 0.14, or 0.4 on the vertical centerline, and the four isotherms are illustrated for $T/T_b = 0.3$, 0.7, 1.0, and 1.5. Since they are symmetric about the horizontal centerline, the streamlines and isotherms are illustrated in the upper and lower halves respectively of the cross section. The axis of rotation is located on the left of the cross section so that the secondary circular current flows counterclockwise.

It is seen in Fig. 4 that the center of circulation is shifted toward the outer wall owing to the induced secondary current. It is of great interest, however, that the increase in Ro results in the reduction of flow rate in the central core because a wide area of uniform secondary flow is created, as explained earlier. The center of circulation is shifted toward the upper wall where streamlines are dense and the secondary current is relatively strong. For Ro = 20 the point of maximum temperature is

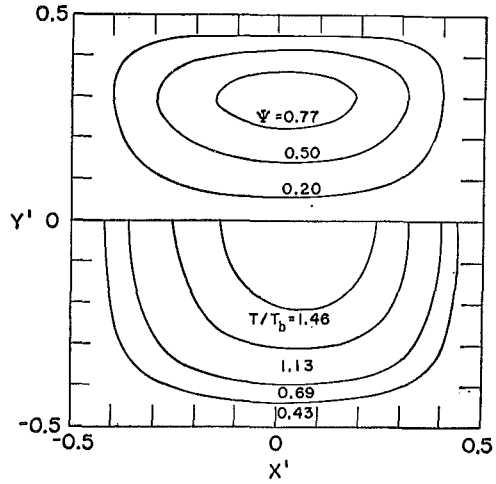

Fig. 5 Streamlines and isotherms for Ro = 100; A = 1.0, B = 50, Pr = 0.7, $Gr_2 = 10^3$, K_1 = 100

shifted toward the outer wall. The temperature gradient decreases at the inner wall, while it becomes steep at the outer wall. For Ro = 100, however, the point of maximum temperature returns to the center because of the weakening of the secondary current in the central region, and a steep temperature gradient due to the high secondary-current velocity is seen at the lower wall.

The product of the local friction factor times the Reynolds number, and the local Nusselt number at the wall, are plotted in Fig. 6 for Ro = 1, 20, and 100 in the order of the upper half of the inner wall, the upper wall, and the upper half of the outer wall. They are shown on the basis of those for a stationary straight rectangular tube to facilitate the understanding of variations. As Ro increases, the wide central core is formed where the secondary current is directed in the X' direction with a uniform and relatively small velocity. This uniform current impinges on the outer wall so that the local friction factor there is constant over a wide region of the wall. The velocity of the returning secondary current, confined to a narrow passage next to the upper wall, is somewhat high. The inertia and Coriolis forces enhance the main flow and the gradient of the axial velocity increases. Consequently the friction factor attains an extremely large value at the upper wall. Since the secondary flow is weak and the axial velocity is almost symmetric about $X' = 0$, the variation of the friction factor at the inner wall is similar to that at the outer wall. However, the effect of Ro on the heat transfer is different. The temperature distribution is not altered very much by the Coriolis forces because of the relatively weak secondary flow. Accordingly the effect on the Nusselt number is not so marked. It is relatively large at the outer wall, and its increase at the upper wall is not as great as that of the friction factor.

Figure 7 is the result of the computation for the mean friction factor and Nusselt number illustrated by the solid and dotted lines respectively. They are plotted in the form of $f \cdot \mathrm{Re}/(f_s \cdot \mathrm{Re})$ and $\mathrm{Nu}/\mathrm{Nu}_s$ respectively against the radius ratio B. B was varied from 5 to 500. Since the effect of B is concentrated on the centrifugal-force term, it can be reduced by the choice of the Dean number instead of the Reynolds number, as shown in the figure. The friction factor and the Nusselt number, however, increase slightly with an increase in B, because a fixed K_1 implies an increase in the axial velocity and accordingly the temperature difference, which causes a large buoyancy force.

Figure 8 is the mean friction factor and Nusselt number plotted against Ro, which was varied from 1 to 100. The effect of the Coriolis forces is largely dependent on the configuration of the rotating system. In the flow and heat transfer in a circular tube rotating about a parallel axis which has been solved analytically by Mori and Nakayama [4], the Coriolis-force terms are not involved in the axial component of momentum equations. They

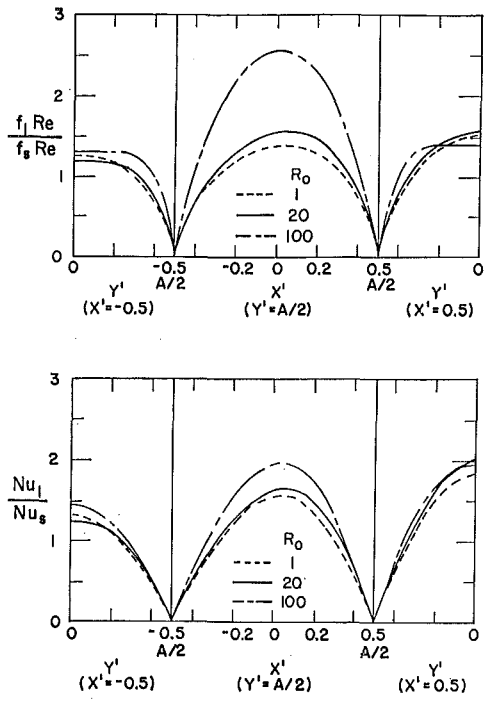

Fig. 6 Variation of local friction factor and Nusselt number with Ro; A = 1.0, B = 50, Pr = 0.7, $Gr_2 = 10^3$, K_1 = 100

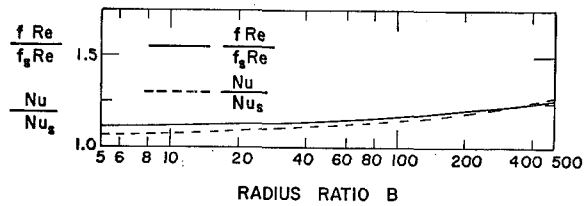

Fig. 7 Mean friction factor and Nusselt number versus B; A = 1.0, Pr = 0.7, Ro = 20, $Gr_2 = 10^3$, K_1 = 100

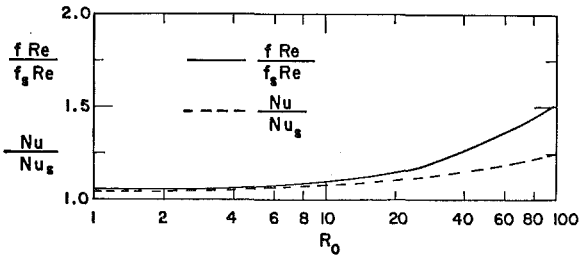

Fig. 8 Mean friction factor and Nusselt number versus Ro; A = 1.0, B = 50, Pr = 0.7, $Gr_2 = 10^3$, K_1 = 100

affect only the velocity components of secondary flow, which are usually smaller than the axial velocity, so that the effect of the Coriolis forces in this configuration is minor. Since in their analysis the axial velocity and the angular-velocity vector are in the same sense, the Coriolis forces impair the secondary flow induced by the rotational buoyancy force when the wall is heated. Therefore both f and Nu decrease with the increase in Ro. Moreover the relative effect of the Coriolis forces decreases with the increase in Re, because they have no direct effect on the axial velocity which does not affect the velocity components of secondary flow. This is substantiated by the experiment conducted by Humphreys, Morris, and Barrow [3] with the exception that f and Nu increase with the increase of Ro because it seems that the axial velocity and the angular-velocity vector are in the opposite sense. In the present configuration the Coriolis forces act not only on the secondary flow but also on the axial velocity, and thus enhance secondary flow, so that they exercise significant effects on both f and Nu. If the fluid is at rest, there will be no

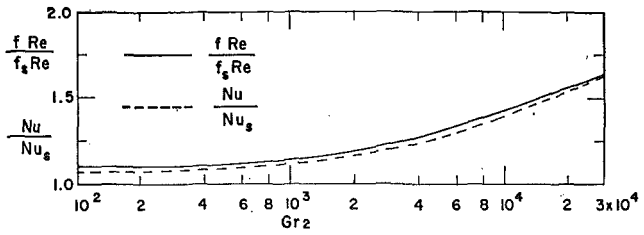

Fig. 9 Mean friction factor and Nusselt number versus Gr_2; $A = 1.0$, $B = 50$, Pr = 0.7, Ro = 20, $K_1 = 100$

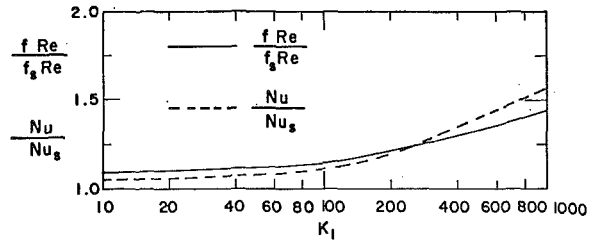

Fig. 10 Mean friction factor and Nusselt number versus K_1; $A = 1.0$, $B = 50$, Pr = 0.7, Ro = 20, $Gr_2 = 10^3$

resistance against the secondary flow. Therefore there are no critical values at which the effects of the secondary-flow-inducing forces start to appear. Actually, however, they are substantially negligible up to some values of the nondimensional force parameters. Since the walls of the tube have a direct influence on the rise of the secondary flow, the so-called threshold values of the parameters are largely dependent on the geometry of tube cross section. For Ro < 10 the effect is negligible. As Ro tends to zero, $f \cdot \mathrm{Re}/(f_s \cdot \mathrm{Re})$ and $\mathrm{Nu}/\mathrm{Nu}_s$ do not approach unity because there are some contributions by the buoyancy and centrifugal forces. For Ro > 10, f increases rapidly, and the extrapolation shows that $f \cdot \mathrm{Re}/(f_s \cdot \mathrm{Re})$ is proportional to $\mathrm{Ro}^{1/5}$. According to Ludwieg's analysis [14] $f \cdot \mathrm{Re}/(f_s \cdot \mathrm{Re})$ is proportional to $\mathrm{Ro}^{1/2}$ for large Ro. The increase in Nu is less remarkable, and it is shown by the extrapolation of the curve that $\mathrm{Nu}/\mathrm{Nu}_s$ is proportional to $\mathrm{Ro}^{1/12}$.

Figure 9 shows the mean friction factor and Nusselt number against Gr_2, which is varied from 100 to 3×10^4. The effect of Gr_2 becomes remarkable at $Gr_2 \approx 10^3$ where both f and Nu increase at almost the same rate as Gr_2 in the range of Gr_2 computed. However, it is seen that there is a trend for Nu to increase more rapidly for large Gr_2. The extrapolation of the curves shows that $f \cdot \mathrm{Re}/(f_s \cdot \mathrm{Re})$ and $\mathrm{Nu}/\mathrm{Nu}_s$ are proportional to $Gr_2^{1/6}$ and $Gr_2^{1/5}$ respectively. According to Mori and Nakayama's analysis [4] for a circular tube rotating about a parallel axis, they are approximately proportional to $Gr_2^{1/9}$ and $Gr_2^{1/7}$ respectively for large Gr_2.

Figure 10 shows the mean friction factor and Nusselt number against K_1, which is varied from 10 to 10^3. The centrifugal force begins to exercise a marked effect at $K_1 \approx 100$, and the rate of increase of f is different from that of Nu. This indicates that there are interactions between the secondary-flow-inducing forces, and therefore their total effects cannot be represented by the mere sum of the effects of each single force. The extrapolation shows that $f \cdot \mathrm{Re}/(f_s \cdot \mathrm{Re})$ and $\mathrm{Nu}/\mathrm{Nu}_s$ vary porportionally to $K_1^{1/10}$ and $K_1^{1/6}$ respectively, while both of them increase with $K_1^{1/2}$ for large K_1 in the case of a stationary curved circular tube according to Mori and Nakayama's analysis [10].

Conclusions

The problem treated in the present investigation is the flow and heat transfer in curved rectangular tubes rotating about an axis through the center of curvature. The flow and heat-transfer characteristics are determined by the six nondimensional parameters A, B, Pr, Ro, Gr_2, and K_1. The results of computations are presented for the axial-velocity and temperature fields, the local friction factors and Nusselt numbers, and the mean friction factors and Nusselt numbers. Because of excessive length, the presentation of results is confined to the effects of Ro alone on the flow and heat-transfer characteristics, except those on the mean f and Nu. However, the effects of A and Pr on the mean f and Nu are abbreviated.

The formation and intensity of secondary flow are characteristic of each parameter. Both an increase and decrease in A impair the secondary flow, because a narrow cross section causes a greater resistance against it. It is somewhat intensified by the increase in B, since the axial velocity and accordingly the centrifugal and Coriolis forces are increased by it. Pr exercises practically no effect, although the intensity of the secondary flow tends to decrease very slightly. Ro creates a broad central core where a uniform and rather weak secondary current flows, but a rather strong returning current arises in the immediate vinicity of the upper and lower walls. The effect of Gr_2 is somewhere between those of Ro and K_1, and the secondary flow is strong not only in the central region but also in the neighborhood of the upper and lower walls. K_1 induces a strong current along the horizontal centerline, which, however, decreases rapidly toward the upper or lower wall.

The friction factor f and the Nusselt number Nu are also affected characteristically by the parameters. Their increase is most remarkable when $A = 1$. As A deviates from unity, however, the secondary flow is suppressed, so that the mean f and Nu approach those for a stationary straight tube. They are raised as B increases, but its effect is minor because its greatest effect is involved in the centrifugal force in terms of K_1. Pr has no substantial effect on f, while Nu is significantly increased. On the contrary, Ro causes a great increase in f, but Nu is much less enhanced. Their increase due to Gr_2 is gradual. However, it has an advantageous characteristic in that it tends to make more contribution to the enhancement of heat transfer than flow friction. K_1 also possesses the same advantage, and raises more rapidly both f and Nu than does Gr_2.

Since the tube wall exercises a resistant force against the secondary flow, its rise and intensity depend largely on the geometrical shape of the tube cross section. It is apparent, therefore, that the threshold values of the nondimensional force parameters at which their effects commence to be considerable are different according to the tube cross section. For the rectangular tube with $A = 1$ the threshold values are Ro ≈ 10, $Gr_2 \approx 10^3$, and $K_1 \approx 100$.

Acknowledgment

The author wishes to thank the University of Minnesota Computer Center for the grant of computation time on the CDC 6600 computer.

References

1 Barua, S. N., "Secondary Flow in a Rotating Straight Pipe," *Proceedings of the Royal Society*, Series A, Vol. 227, 1954, pp. 133–139.

2 Morris, W. D., "Laminar Convection in a Heated Vertical Tube Rotating about a Parallel Axis," *Journal of Fluid Mechanics*, Vol. 21, No. 3, 1965, pp. 453–464.

3 Humphreys, J. F., Morris, W. D., and Barrow, H., "Convection Heat Transfer in the Entry Region of a Tube which Revolves about an Axis Parallel to Itself," *International Journal of Heat and Mass Transfer*, Vol. 10, 1967, pp. 333–347.

4 Mori, Y., and Nakayama, W., "Forced Convective Heat Transfer in a Straight Pipe Rotating about a Parallel Axis (1st Report, Laminar Region)," *International Journal of Heat and Mass Transfer*, Vol. 10, 1967, pp. 1179–1194.

5 Dean, W. R., "Note on the Motion of Fluid in a Curved Pipe," *Philosophical Magazine*, Vol. 4, No. 20, 1927, pp. 208–223.

6 Dean, W. R., "The Stream Line Motion of Fluid in a Curved Pipe," *Philosophical Magazine*, Vol. 5, No. 30, 1928, pp. 673–695.

7 Adler, M., "Strömung in Gekrümmten Rohren," *Zeitschrift der Angewandte Mathematik und Mechanik*, Vol. 14, 1934, pp. 257–275.

8 Barua, S. N., "On Secondary Flow in Stationary Curved Tubes," *Quarterly Journal of Mechanics and Applied Mathematics*, Vol. 16, 1963, pp. 61–77.

9 Mori, Y., and Nakayama, W., "Study on Forced Convective Heat Transfer in Curved Pipes (1st Report, Laminar Region)," *International Journal of Heat and Mass Transfer*, Vol. 8, 1965, pp. 67–82.

10 Mori, Y., and Nakayama, W., "Study on Forced Convective Heat Transfer in Curved Pipes (2nd Report, Turbulent Region)," *International Journal of Heat and Mass Transfer*, Vol. 10, 1967, pp. 37–59.

11 Ito, H., "Friction Factors for Turbulent Flow in Curved Pipes," *Journal of Basic Engineering*, TRANS. ASME, Series D, Vol. 81, No. 2, June 1959, pp. 133–134.

12 Seban, R. A., and McLaughlin, E. F., "Heat Transfer in Tube Coils with Laminar and Turbulent Flow," *International Journal of Heat and Mass Transfer*, Vol. 6, 1963, pp. 387–395.

13 Rogers, G. F. C., and Mayhew, Y. R., "Heat Transfer and Pressure Loss in Helically Coiled Tubes with Turbulent Flow," *International Journal of Heat and Mass Transfer*, Vol. 7, 1964, pp. 1207–1216.

14 Ludwieg, H., "Die Ausgebildete Kanalströmung in einem Rotierenden System," *Ingenieur-Archiv*, Vol. 19, 1959, pp. 77–85.

15 Miyazaki, H., "Combined Free and Forced Convective Heat Transfer and Fluid Flow in Rotating Curved Tubes," MS thesis, University of Minnesota, Minneapolis, Minn., 1970.

16 Spalding, D. B., Runchal, A. K., and Wolfshtein, M., "Solutions of the Equations for the Transport of Vorticity, Heat and Mass for Two-Dimensional Flows with and without Recirculation," Imperial College, Mechanical Engineering Department, SF/TN/2, 1967.

17 Dorfman, L. A., and Romanenko, U. B., "Flow of Viscous Fluid in Cylindrical Vessel with Rotating Cover" (in Russian), *AH CCCP, Mechanics of Fluid and Gas*, No. 5, 1966, pp. 63–69.

G. J. HWANG
Department of Power Mechanical Engineering, National Tsing Hua University, Hsinchu, Taiwan, China

K. C. CHENG
Department of Mechanical Engineering, University of Alberta, Edmonton, Alberta, Canada

Convective Instability in the Thermal Entrance Region of a Horizontal Parallel-Plate Channel Heated from Below

An investigation is carried out to determine the conditions marking the onset of longitudinal vortex rolls due to buoyant forces in the thermal entrance region of a horizontal parallel-plate channel where the lower plate is heated isothermally and the upper plate is cooled isothermally. Axial heat conduction is included in an analytical solution for the Graetz problem with fully developed laminar velocity profile. Linear-stability theory based on Boussinesq approximation is employed in the derivation of perturbation equations. An iterative procedure using high-order finite-difference approximation is applied to solve the perturbation equations and a comparison is made against the conventional second-order approximation. It is found that for $\mathrm{Pr} \geq 0.7$ *the flow is more stable in the thermal entrance region than in the fully developed region, but the situation is just opposite for small Prandtl number, say* $\mathrm{Pr} \leq 0.2$. *Graphical results for the critical Rayleigh numbers and the corresponding disturbance wavenumbers are presented for the case of* $\mathrm{Pe} \rightarrow \infty$ *with Prandtl number as a parameter and the case of air* ($\mathrm{Pr} = 0.7$) *with Peclet number as a parameter in the range of dimensionless axial distance from the entrance between* $x = 0.001$ *and* 4×10^{-1}.

Introduction

The classical Bénard problem on thermal instability of a layer of fluid enclosed between two infinite horizontal plates heated from below has been studied extensively in the past and various extensions of the problem have been reported in the literature.

Recently the onset of longitudinal vortex rolls due to buoyant forces for fully developed laminar forced convection between two infinite horizontal parallel plates with a constant axial temperature gradient and at different or identical temperature levels at the upper and lower plates was studied theoretically by Nakayama, Hwang, and Cheng [1][1] and confirmed experimentally by Akiyama, Hwang, and Cheng [2]. The thermal-instability problem considered in [1] is characterized by a nonlinear basic temperature profile and in this respect is similar to the problem studied by Sparrow, Goldstein, and Jonsson [3] where the thermal instability in a horizontal fluid layer is caused by a nonlinear basic temperature profile due to uniform internal heat generation.

It is true that the critical Rayleigh numbers reported in [1] are useful in estimating the onset of instability in practical problems; however, the assumption of fully established basic temperature profile is fulfilled only if the channel is very long. In practice the ratio of length to hydraulic diameter is usually moderate, and the thermal entrance region is of practical interest. The need for extending the thermal-instability problem reported in [1] to the thermal entrance region is obvious.

The purpose of this investigation is to determine the conditions marking the onset of longitudinal vortex-type secondary flow for a hydrodynamically fully developed but thermally developing region of the horizontal parallel-plate channel where the lower plate is heated isothermally and the upper plate is cooled isothermally. The problem under consideration can be regarded as the Bénard problem with fully developed laminar flow superimposed. Furthermore, the vortex rolls with axes parallel to the basic flow direction may be regarded as an infinitely elongated form of the Bénard convection cells. Knowledge of the onset of instability is required in the practical design problem since the solution of the classical Graetz problem will not be valid after the secondary flow sets in.

Theoretical Analysis

Graetz Problem for Fully Developed Laminar Flow between Horizontal Parallel Plates. Consideration is given to a Graetz problem which deals with a steady fully developed laminar flow of an incompressible viscous fluid with constant properties in a horizontal parallel-plate channel, Fig. 1. The fluid temperature is constant and equal to the wall temperature T_0 for $x' \leq 0$, see Fig. 1, except

[1] Numbers in brackets designate References at end of paper.

Contributed by the Heat Transfer Division for publication (without presentation) in the Journal of Heat Transfer. Manuscript received by the Heat Transfer Division September 15, 1971. Paper No. 72-HT-P.

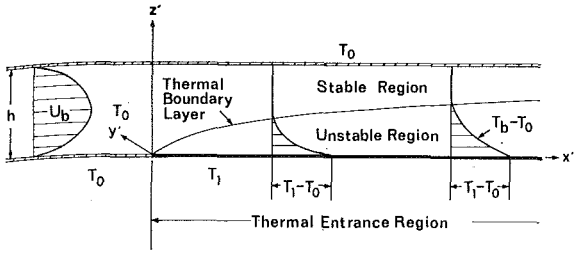

Fig. 1 Coordinate system for fully developed laminar flow in thermal entrance section of a horizontal parallel-plate channel

that at some axial position $x' = 0$ there is a step change in the lower-wall temperature to a higher value T_1 with the upper-wall temperature still maintained at the uniform temperature T_0.

Referring to the coordinate system shown in Fig. 1, the fully developed velocity profile in the unperturbed state is

$$U_b = 6U_m[(z'/h) - (z'/h)^2] = U_m\phi_u \tag{1}$$

where U_m is the mean velocity and $\phi_u = 6[(z'/h) - (z'/h)^2]$ is a dimensionless quantity representing a basic velocity-profile function. The temperature distribution for $x' > 0$ is determined by solving the following equation expressing energy conservation for a fluid:

$$6U_m\left[\left(\frac{z'}{h}\right) - \left(\frac{z'}{h}\right)^2\right]\frac{\partial T_b}{\partial x'} = \kappa\left(\frac{\partial^2 T_b}{\partial z'^2} + \frac{\partial^2 T_b}{\partial x'^2}\right) \tag{2}$$

By introducing dimensionless variables $z = z'/h$, $x = x'/(h\ \mathrm{Pe})$, and $\phi_\theta = (T_b - T_0)/(T_1 - T_0)$ and a parameter $\mathrm{Pe} = U_m h/\kappa$, the following normalized equation results:

$$6(z - z^2)\frac{\partial \phi_\theta}{\partial x} = \frac{\partial^2 \phi_\theta}{\partial z^2} + \frac{1}{\mathrm{Pe}^2}\frac{\partial^2 \phi_\theta}{\partial x^2} \tag{3}$$

The boundary conditions are

$$\phi_\theta(0, z) = \phi_\theta(\infty, z) - (1 - z) = \phi_\theta(x, 0) - 1 = \phi_\theta(x, 1) = 0 \quad \text{for} \quad x > 0 \tag{4}$$

It is noted that the first term $\partial^2\phi_\theta/\partial z^2$ on the right-hand side of equation (3) represents the heat conducted from the lower plate and the term $6(z - z^2)\partial\phi_\theta/\partial x$ represents the heat convected in the main flow direction. The remaining term in equation (3), $(1/\mathrm{Pe}^2)\partial^2\phi_\theta/\partial x^2$, signifies the conduction effect in the main flow direction. The solution of equation (3) with the associated boundary conditions (4) is given in the Appendix for Pe = 10, 20, 30, 50, 100, and ∞.

According to the recent works by Hennecke [4] and Hsu [5] for the exact analysis of low-Peclet-number thermal-entry-region heat transfer based on the rigorous boundary condition of $\phi_\theta(-\infty, z) = 0$, the heat conducted upstream of $x = 0$ is found to be significant only for the extremely small Peclet-number regime. However, the upstream conduction effect [5] in the adiabatic section of the channel will not be considered for the present work in order to limit the scope of the investigation. It should be mentioned that a step change in wall temperature (temperature discontinuity) assumed at the entrance in the formulation of the classical Graetz problem is seldom met in practice. Consequently the exact solution of the present problem with the upstream conduction effect right near the entrance is believed to be of theoretical interest only. Furthermore, for the extremely small Peclet-number regime the possibility exists that the transverse rolls may appear first under certain circumstances.

Perturbation Equations

In the thermal entrance region under consideration a nonlinear basic temperature distribution $T_b - T_0$ in the vertical direction exists near the lower plate, see Fig. 1, and eventually the distribution becomes linear when the temperature is fully developed. Within the thermal boundary layer shown in Fig. 1 a top-heavy situation prevails and the onset of convection in the vertical direction is marked by the critical value of the Rayleigh number. The instability theory considers amall disturbances superimposed upon the basic flow, and both the disturbed and undisturbed flows are assumed to satisfy the Navier–Stokes equations of motion and the energy equation. For this purpose perturbations are now superimposed on the basic velocity and temperature fields as

$$U = U_b + u' \qquad V = v' \qquad W = w' \qquad T = T_b + \theta'$$
$$\text{and} \qquad P = P_b + p' \tag{5}$$

where V and W are velocity components in the y' and z' directions respectively, and P_b is the pressure in the unperturbed state. The above perturbation quantities are considered to be in the steady state [1, 2] and are functions of space variables x', y', and z' only. Introducing the nondimensional quantities $(x', y', z') = h(x^+, y^+, z^+)$, $(u', v', w') = (\nu/h)(u, v, w)$, $\theta' = (\Delta T)\theta$, $p' = (\rho\nu^2/h^2)p$ and parameters $\mathrm{Gr} = \beta g(T_1 - T_0)h^3/\nu^2$, $\mathrm{Pr} = \nu/\kappa$, $\mathrm{Re} = U_m h/\nu$, $\mathrm{Ra} = \mathrm{PrGr}$, $\mathrm{Pe} = \mathrm{PrRe}$, the following component perturbation equations in dimensionless form are obtained after linearization involving a few manipulations:

Nomenclature

a = wavenumber, $2\pi h/\lambda$
c = amplification or damping factor, $c = 0$ on onset of instability
D = d/dz
G = mode shape function defined by equation (9)
Gr = Grashof number, $g\beta\Delta T h^3/\nu^2$
g = gravitational acceleration
h = distance between two infinite horizontal flat plates
P = pressure
Pe = Peclet number, Pr Re
Pr = Prandtl number, ν/κ
p = dimensionless pressure
Ra = Rayleigh number, $g\beta\Delta T h^3/\nu\kappa$
Re = Reynolds number, $U_m h/\nu$
T = temperature
T_b = basic temperature in unperturbed flow
T_0, T_1 = fixed upper- and lower-plate temperatures respectively
U, V, W = velocity components in x', y', and z' directions
U_b, U_m = basic velocity in unperturbed flow and mean basic velocity respectively
u, v, w = dimensionless velocity disturbances in x', y', and z' directions
u', v', w' = velocity disturbances in x', y', and z' directions
x, y, z = dimensionless cartesian coordinates
x', y', z' = cartesian coordinates
β = coefficient of thermal expansion
ΔT = temperature difference between two plates, $T_1 - T_0$
θ = dimensionless temperature disturbance
θ' = temperature disturbance
κ = thermal diffusivity
λ = wavelength of vortex rolls
ν = kinematic viscosity
ρ = density
ϕ_u = basic velocity-profile function
ϕ_θ = basic temperature-profile function
∇^2 = dimensionless three-dimensional Laplacian operator

Superscripts and Subscripts

$'$ = disturbance quantities or dimensional quantities
$*$ = critical value or a dimensionless variable
$+$ = dimensionless coordinate variables or amplitude of disturbance
b = basic quantities in unperturbed state

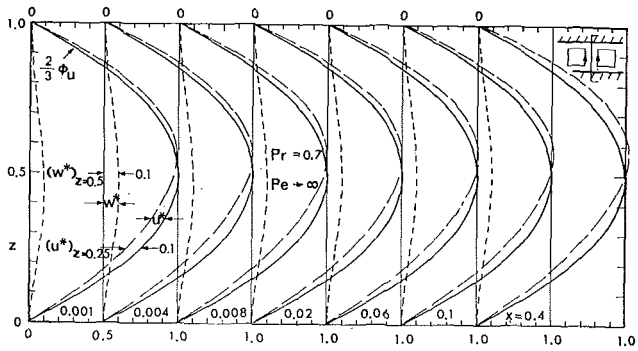

Fig. 2 Axial and vertical velocity perturbations at the onset of instability in the thermal entrance region of a horizontal parallel-plate channel

$$\mathrm{Re}\left(\phi_u \frac{\partial}{\partial x^+}\nabla^2 w - \frac{\partial^2 \phi_u}{\partial z^{+2}}\frac{\partial w}{\partial x^+}\right) = \nabla^2\nabla^2 w + \mathrm{Gr}\left(\frac{\partial^2}{\partial x^{+2}} + \frac{\partial^2}{\partial y^{+2}}\right)\theta \quad (6)$$

$$\mathrm{Re}\left(\phi_u \frac{\partial u}{\partial x^+} + w\frac{\partial \phi_u}{\partial z^+}\right) = -\frac{\partial p}{\partial x^+} + \nabla^2 u \quad (7)$$

$$\mathrm{Pr}\left(\mathrm{Re}\phi_u \frac{\partial \theta}{\partial x^+} + u\frac{\partial \phi_\theta}{\partial x^+} + w\frac{\partial \phi_\theta}{\partial z^+}\right) = \nabla^2\theta \quad (8)$$

where $\nabla^2 = \partial^2/\partial x^{+2} + \partial^2/\partial y^{+2} + \partial^2/\partial z^{+2}$.

The following characterization of the disturbance form serves also to demonstrate the region of interest in this study:

$$\begin{aligned} u &= u^+(z^+)G(x^+, y^+) \\ w &= w^+(z^+)G(x^+, y^+) \\ p &= p^+(z^+)G(x^+, y^+) \\ \theta &= \theta^+(z^+)G(x^+, y^+) \end{aligned} \quad (9)$$

where $G(x^+, y^+) = \exp(cx^+ + iay^+)$, c is the amplification factor denoting the degree of amplification or damping along the main flow direction, and $a = 2\pi h/(\text{wave length})$ is the wavenumber to be determined. Both quantities c and a are real for the present study involving the onset of longitudinal vortices. It should be noted that the perturbation quantities are taken to be "in the steady state" in this analysis since steady-state longitudinal vortices were observed to occur in the entrance region in earlier experiments [2]. After substituting the relations (9) into equations (6)–(8) and utilizing the condition of neutral stability or threshold of instability marked by $c = 0$, one obtains

$$(D^2 - a^2)^2 w^+ = a^2\,\mathrm{Gr}\,\theta^+ \quad (10)$$

$$(D^2 - a^2)u^+ = \mathrm{Re}\,w^+\frac{\partial \phi_u}{\partial z^+} \quad (11)$$

$$(D^2 - a^2)\theta^+ = \mathrm{Pr}\left(u^+\frac{\partial \phi_\theta}{\partial x^+} + w^+\frac{\partial \phi_\theta}{\partial z^+}\right) \quad (12)$$

where $D = d/dz$. In view of equation (3) for the basic temperature and previous related works [1, 2], it is convenient to use parameters Pr, Pe, and Ra instead of Pr, Re, and Gr which appear in the above set of equations. To achieve this end the new variables $w^+ = w^*$, $\theta^+ = \mathrm{Pr}\,\theta^*$, $u^+ = \mathrm{Re}\,u^*$, $z^+ = z$, and $x^+ = \mathrm{Pe}\,x$ are introduced. Then the following perturbation equations result:

$$(D^2 - a^2)^2 w^* = a^2\,\mathrm{Ra}\,\theta^* \quad (13)$$

$$(D^2 - a^2)u^* = w^*\frac{\partial \phi_u}{\partial z} \quad (14)$$

$$(D^2 - a^2)\theta^* = \frac{u^*}{\mathrm{Pr}}\frac{\partial \phi_\theta}{\partial x} + w^*\frac{\partial \phi_\theta}{\partial z} \quad (15)$$

The appropriate boundary conditions for the disturbances are

$$w^* = Dw^* = u^* = \theta^* = 0 \quad \text{at} \quad z = 0 \text{ and } 1 \quad (16)$$

It is instructive to note that the term $a^2\,\mathrm{Ra}\,\theta^*$ in equation (13) presents the effect of buoyancy forces which is balanced by the viscous term $(D^2 - a^2)^2 w^*$. In equation (14) the inertia force term $w^*\partial\phi_u/\partial z$ is caused by the coupled effect of upward disturbance velocity w^* and the vertical gradient of the basic velocity-profile function and is seen to be balanced by the viscous term $(D^2 - a^2)u^*$. Furthermore, in energy equation (15) there are two convective motions; one is the convective motion caused by velocity disturbance u^* and basic temperature gradient $\partial\phi_\theta/\partial x$ in the main flow direction, and the other is the convective motion caused by velocity disturbance w^* and basic temperature gradient $\partial\phi_\theta/\partial z$ in the vertical direction. These two convective terms are balanced by the conduction term $(D^2 - a^2)\theta^*$. The boundary conditions $w^* = u^* = \theta^* = 0$ indicate that the velocity and temperature disturbances vanish on the solid boundary, and the condition $Dw^* = 0$ follows by also applying the continuity equation.

In this investigation a minimum value of Rayleigh number and the corresponding wavenumber which permits a solution of the set of the disturbance equations satisfying the boundary conditions is sought.

Numerical Method of Solution Using High-Order Finite-Difference Approximation

Since the solution of equation (3) for the basic temperature distribution is available in a numerical form, a finite-difference method using iterative technique is chosen for the simultaneous solution of the disturbance equations (13)–(15). The details of the numerical solution will not be given here because of space limitation.

The high-order finite-difference approximation due to Thomas [6] in a study on the stability of plane Poiseuille flow is employed in the present investigation. The detailed derivation of the approximation is given by Chen [7] in a study on the hydrodynamic stability of developing flow in a parallel-plate channel. After extensive numerical experiment, a mesh size of $M = 40$ is used in all the computations to insure the accuracy for at least five significant figures.

Results and Discussion

Perturbed Velocity and Temperature Fields. Some insights into the physical mechanism of thermal instability for the present problem can be gained by a detailed study of the perturbed velocity and temperature fields. Fig. 2 shows the distribution of the velocity disturbances along the vertical section of the upward stream (see inset), u^* in the main flow direction, and w^* in the vertical direction, at representative axial positions x with the fully developed basic velocity profiles $2\phi_u/3$ superimposed for comparison for the case of Pr = 0.7 and Pe → ∞. Since the magnitudes of the disturbance quantities cannot be determined by using linear stability theory, the values of $u^* = 0.1$ at $z = 0.25$ and $w^* = 0.1$ at $z = 0.5$ are taken as reference values. Due to the fact that the unstable region prevails in the lower part of the channel, the relative magnitudes of the velocity disturbances are seen to be larger in the lower region $z \leq 0.5$ than those in the upper region $z \geq 0.5$. This trend becomes less pronounced as the axial distance x increases. For example at $x = 0.4$ the absolute values of the disturbances are almost symmetric with respect to the central plane $z = 0.5$. From this figure one can also say that the eye of the vortex roll is initially located in the lower region of the channel when x is small and gradually moves toward the center line $z = 0.5$ as x increases.

The distribution of the temperature disturbance θ^* along the vertical section of the upward stream is of considerable theoretical interest and is shown in Fig. 3 with the basic temperature profile

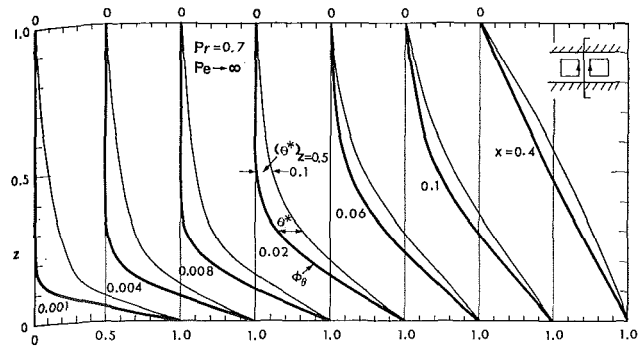

Fig. 3 Basic temperature-profile development and temperature perturbation at the onset of instability in the thermal entrance region of a horizontal parallel-plate channel

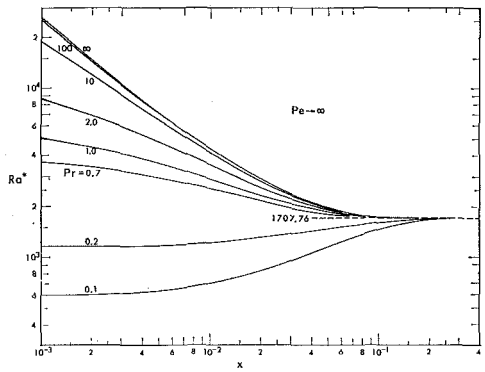

Fig. 4 Effect of Prandtl number on critical Rayleigh numbers marking the onset of instability for Pe → ∞

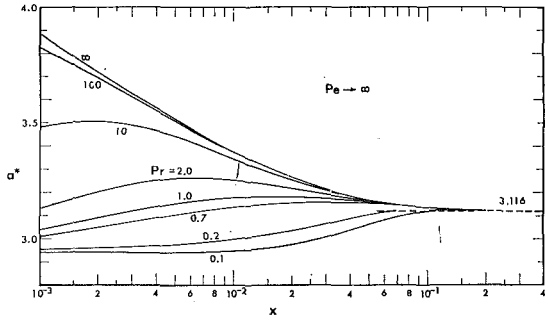

Fig. 5 Effect of Prandtl number on critical wavenumbers at the onset of instability for Pe → ∞

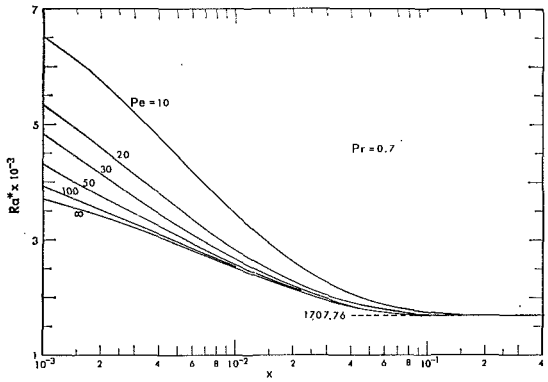

Fig. 6 Effect of Peclet number on critical Rayleigh numbers marking the onset of instability for air (Pr = 0.7)

ϕ_θ superimposed for comparison for the identical case, Pr = 0.7 and Pe → ∞, and identical axial positions as are shown in Fig. 2. Again the value of $\theta^* = 0.1$ at $z = 0.5$ is taken as the reference quantity. It is found that the maximum temperature disturbance is located in the range $0.1 \leq z \leq 0.5$ depending on the axial position x. This observation is of particular interest in experimental verification of the onset of longitudinal vortices by a transverse temperature-profile measurement for the small temperature fluctuations using a thermocouple probe [2].

Effects of Prandtl Number and Peclet Number on Critical Rayleigh Numbers Ra*. The Rayleigh numbers marking the onset of instability along the axial direction in the thermal entrance region of the parallel-plate channel are presented graphically in Fig. 4 for various Prandtl numbers for the case where the axial-conduction term is neglected (Pe → ∞) with $\phi_\theta(0, z) = 0$. In this figure both the entrance and Prandtl-number effects are of interest.

Referring to perturbation equations (13)–(15) it is seen that the flow field is destabilized by the term representing the vertical convective motion, $w^* \partial\phi_\theta/\partial z$, only when the Prandtl number approaches infinity. With thinner thermal boundary layer, see Figs. 1 and 3, the flow is more stable in the thermal entrance region than in the fully developed region. It is expected that as the axial distance x increases the basic temperature profile gradually approaches the linear temperature profile in the fully developed region and the critical Rayleigh number approaches a critical value of 1707.76 at $x \approx 0.1$. When the Prandtl number is finite the effect of convective motion in the main flow direction represented by the term $(u^*/\mathrm{Pr})\partial\phi_\theta/\partial x$ also destabilizes the flow. For small Prandtl number, say 0.1 or 0.2, the destabilizing effect due to the convective motion in the main flow direction predominates over the stabilizing effect of thinner thermal boundary layer and the flow is more unstable in the entrance region than in the fully developed region.

In Fig. 4, when Pr ≥ 0.7 the critical Rayleigh number decreases monotonically with increasing axial distance and finally approaches to a limiting value of 1707.76. On the other hand, when Pr < 0.2 the critical Rayleigh number increases monotonically along the axial distance and approaches the same limiting value from below. Thus a completely different trend is observed for the small-Prandtl-number case as opposed to the large-Prandtl-number case. This can be explained from the fact that as Pe → ∞, ϕ_θ is the same for all Prandtl numbers, but the effect of the axial-temperature-gradient term $(u^*/\mathrm{Pr})\partial\phi_\theta/\partial x$ increases as Pr decreases. As x increases, both effects diminish and eventually vanish completely when the temperature profile becomes linear and fully developed. All the curves for various Prandtl numbers are seen to approach a critical value of Ra* = 1707.76 at $x \approx 0.1 \sim 0.2$. The curve for Pr = 100 is seen to be very close to the curve for Pr → ∞, and for practical purposes they may be regarded as identical. From this, one also sees the practical implication of large Prandtl number.

The interaction of the two opposing effects represented by the two extreme cases of Pr → ∞ and Pr → 0 in the thermal entrance region is noteworthy. The stabilizing effect in the form of thinner thermal boundary layer corresponds to the case of Pr → ∞ and the destabilizing effect in the form of convective motion in the axial direction corresponds to the other case of Pr → 0. When the Prandtl number is finite both effects are important in the thermal entrance region. It is well to note that when the basic temperature becomes linear and fully established, $\partial\phi_\theta/\partial x = 0$ and the perturbed equations (13)–(15) reduce to those for the classical Bénard problem. Under the condition of uniform but different wall temperatures the critical Rayleigh number remains Ra* = 1708 regardless of the presence of forced flow.

The critical wavenumbers of the disturbances corresponding to the critical Rayleigh numbers shown in Fig. 4 are presented graphically in Fig. 5. The variation of the critical wavenumber along the axial distance for different Prandtl numbers is of considerable interest. For Pr ≥ 100 the critical wavenumber decreases monotonically along the axial distance, but for the range $0.7 \leq \mathrm{Pr} \leq 10$ a maximum value for a^* exists. The location of the maximum value from the entrance increases as the Prandtl number decreases. For Pr = 0.1 the critical wavenumber does not seem to change up to $x = 0.01$, and then increases to the limiting value of 3.116 from below for the fully developed case

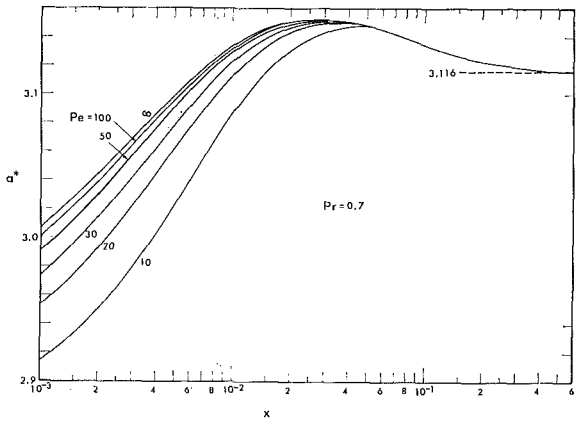

Fig. 7 Effect of Peclet number on critical wavenumbers at the onset of instability for air (Pr = 0.7)

at $x \approx 0.2$. All the curves are seen to approach the limiting value $a^* = 3.116$. The behavior of a^* in the thermal entrance region for Pr $\leq$ 10 shown in Fig. 5 is rather complicated and no physical explanation can be offered.

At this point it should be said that the experimental confirmation of the limiting critical values $Ra^* = 1708$ and $a^* = 3.116$ for the fully developed condition is reported in [2].

Consideration may next be given to the effect of Peclet number, representing the contribution of convective motion relative to that of axial conduction on the onset of instability. Fig. 6 presents the variation of the critical Rayleigh number along the axial distance for Pr = 0.7 with Peclet number as a parameter. Since the dimensionless axial distance x is defined as $x'/(h\text{Pe})$, the effect of Peclet number cannot readily be explained. Focusing one's attention to the curves for Pe = 10 and 100, one finds the critical Rayleigh number to be $Ra^* \approx 3400$ for Pe = 10 at $x = 0.01$ or $x'/h = 0.1$, and $Ra^* \approx 3900$ for Pe = 100 at $x = 0.001$ or $x'/h = 0.1$. This observation leads one to conclude that at a fixed axial position x' the effect of axial conduction is to increase the thermal boundary-layer thickness, which tends to destabilize the flow. The effect of Peclet number can better be seen if Ra^* is plotted against the variable x'/h instead of x. However, Fig. 6 has the advantage of conciseness and convenience in application. Practically speaking, the curve for Pe = 100 may be regarded as already approaching the asymptotic solution for Pe $\rightarrow \infty$, since the largest deviation is found to be about 5 percent at $x = 0.001$.

The effect of axial conduction is to increase the thermal boundary-layer thickness and decrease the axial temperature gradient. However, depending on the magnitude of Prandtl number, one factor dominates over the other. When Pr $\rightarrow \infty$ the increase of thermal boundary-layer thickness dominates and the axial conduction leads to destabilizing effect. When Pr $\rightarrow$ 0 the decrease of axial temperature gradient dominates and the axial conduction leads to stabilizing effect as can be seen from perturbation equation (15). Practically, the destabilizing effect of heat conduction appears for Pr $\geq$ 0.7 and the stabilizing effect of heat conduction appears for Pr $\leq$ 0.2. Fig. 6 shows that the critical Rayleigh number decreases monotonically along the axial distance and approaches the limiting value of 1707.76 from above. Although not presented here, the numerical results show that for Pr $\leq$ 0.2 the critical Rayleigh number increases monotonically along the axial distance and approaches the limiting value from below.

The role of wavenumber at the onset of instability is rather complicated, as can be seen from the perturbation equations (13)–(15). The wavenumber arises from the separation of variables, and the terms involving a^2 in the perturbation equations represent either the viscous term or the conduction term in the transverse direction y'. Fig. 7 shows the critical wavenumber distribution corresponding to the critical Rayleigh-number distribution shown in Fig. 6. It should be pointed out that the variation of a^* in the thermal entrance region is rather small for air (Pr = 0.7) with the maximum variation from $a^* = 3.116$ being about 6 percent for Pe = 10. In view of the complexity of the role of wavenumber at the onset of instability, no attempt will be made to explain the behavior of a^* shown in Fig. 7. Figs. 6 and 7 suggest that the results for Peclet number of order 100 already approach an asymptotic solution for Pe $\rightarrow \infty$, and this observation is important in understanding the physics and the practical implications of Pe $\rightarrow \infty$. In this respect the effect of Peclet number depends on the value of Prandtl number and large Peclet number does not necessarily wash out the buoyancy effect. For example with Pr $\geq$ 0.7 the secondary motion may appear at some downstream position as Peclet number increases, see Fig. 6. For Pr $\leq$ 0.2 the flow is more unstable in the entrance region. One also notes that the results neglecting axial conduction (Pe $\rightarrow$ 0) serve as an important asymptotic solution as demonstrated clearly in Figs. 6 and 7.

Concluding Remarks

1 The onset of steady longitudinal vortices in the thermal entrance region of a horizontal parallel-plate channel heated from below is approached by an efficient iterative technique based on high-order finite-difference approximation [6, 7]. For the case with Pe $\rightarrow \infty$ the critical Rayleigh number decreases monotonically along the axial distance from the entrance for large-Prandtl-number fluids, whereas the critical Rayleigh number increases monotonically along the axial distance for small-Prandtl-number fluids. At the end of the thermal entrance region the temperature profile becomes fully established (linear temperature distribution) and a limiting value of $Ra^* = 1707.76$ which is independent of Prandtl number is approached. The thermal entrance length x for small-Prandtl-number fluid is longer than that for large-Prandtl-number fluid.

2 The completely different effects of axial heat conduction on thermal instability appear depending on the magnitude of Prandtl number. For Pr $\geq$ 0.7, the increase of thermal boundary-layer thickness due to axial conduction tends to destabilize the flow. On the other hand, for Pr $\leq$ 0.2 the decrease of the axial temperature gradient due to axial conduction tends to stabilize the flow. The thermal entrance length x depends on Peclet number and is longer for lower Peclet number.

3 The convergence of the numerical solution is assured by the excellent agreement between the limiting values of $Ra^* = 1707.76$ and $a^* = 3.116$ for the present problem and those of the Bénard problem. The present problem can be considered as an extension of the Bénard problem with fully developed laminar flow superimposed. The experimental confirmation for the limiting case with $Ra^* = 1707.76$ is given in [2].

4 The instability problem for the present parallel-plate channel in inclined configuration making an angle of ϕ with respect to the vertical is of considerable practical interest. Under the assumption that the free-convection effect from side walls on the basic velocity and temperature profiles is negligible, such as in the central region of a rectangular channel with large aspect ratio [2], the results presented in this study can be applied to the inclined parallel-plate channel by simply replacing Ra^* by $Ra^* \sin\phi$ for the case of large-Prandtl-number fluid only.

5 The results of experiments on the onset of longitudinal vortices in fully developed laminar convection between horizontal plates [2] suggest that the present thermal instability problem can arise in a horizontal rectangular channel with a large aspect ratio, say near the order of 10. This information may be of interest in practical application.

6 The onset of longitudinal vortex rolls is sought in this analysis since they are observed experimentally even at Re $\approx$ 4.7 [2]. The region of interest for this study is discussed in [1]. In contrast, the transverse rolls may have priority of occurrence when the Reynolds number is extremely small. However, the finite dimension in the transverse direction for most practical applications may prevent the occurrence of transverse rolls.

Acknowledgment

This work was supported by the National Research Council of Canada through grant NRC A-1655.

References

1 Nakayama, W., Hwang, G. J., and Cheng, K. C., "Thermal Instability in Plane Poiseuille Flow," JOURNAL OF HEAT TRANSFER, TRANS. ASME, Series C, Vol. 92, No. 1, Feb. 1970, pp. 61–68.

2 Akiyama, M., Hwang, G. J., and Cheng, K. C., "Experiments on the Onset of Longitudinal Vortices in Laminar Forced Convection Between Horizontal Plates," JOURNAL OF HEAT TRANSFER, TRANS. ASME, Series C, Vol. 93, No. 4, Nov. 1971, pp. 335–341.

3 Sparrow, E. M., Goldstein, R. J., and Jonsson, V. K., "Thermal Instability in a Horizontal Fluid Layer: Effect of Boundary Conditions and Nonlinear Temperature Profile," *Journal of Fluid Mechanics*, Vol. 18, 1964, pp. 513–528.

4 Hennecke, D. K., "Heat Transfer by Hagen-Poiseuille Flow in the Thermal Development Region with Axial Conduction," *Wärme- und Stoffübertragung*, Vol. 1, 1968, pp. 177–184.

5 Hsu, C. J., "An Exact Analysis of Low Peclet Number Thermal Entry Region Heat Transfer in Transversely Nonuniform Velocity Fields," *AIChE Journal*, Vol. 17, 1971, pp. 732–740.

6 Thomas, L. H., "The Stability of Plane Poiseuille Flow," *Physical Review*, Vol. 91, 1953, pp. 780–783.

7 Chen, T. S., "Hydrodynamic Stability of Developing Flow in a Parallel-Plate Channel," PhD thesis, University of Minnesota, Minneapolis, Minn., 1966.

8 Lundberg, R. E., McCuen, P. A., and Reynolds, W. C., "Heat Transfer in Annular Passages. Hydrodynamically Developed Laminar Flow with Arbitrarily Prescribed Wall Temperatures or Heat Fluxes," *International Journal of Heat and Mass Transfer*, Vol. 6, 1963, pp. 495–529.

APPENDIX

Solution of the Graetz Problem with Axial Heat Conduction

Reference is made to equation (3) for basic temperature and the boundary conditions (4). In order to obtain the homogeneous boundary conditions at $z = 0$ and 1 and faster convergence of a power-series solution, the following transformations are introduced:

$$z = z_1 + \tfrac{1}{2}$$
$$\phi_\theta = \tfrac{1}{2} - z_1 + H \tag{17}$$

Substituting equation (17) into equations (3) and (4) one obtains

$$6\left(\frac{1}{4} - z_1^2\right)\frac{\partial H}{\partial x} = \frac{\partial^2 H}{\partial z_1^2} + \frac{1}{\mathrm{Pe}^2}\frac{\partial^2 H}{\partial x^2} \tag{18}$$

$$H(0, z_1) + \tfrac{1}{2} - z_1 = H(\infty, z_1) = H(x, -\tfrac{1}{2}) = H(x, \tfrac{1}{2}) = 0 \tag{19}$$

Applying the method of separation of variables, the solution of ϕ_θ can be written as

$$\phi_\theta = \frac{1}{2} - z_1 + H = \frac{1}{2} - z_1 + \sum_{n=1}^{\infty} C_n Z_n(z_1) \exp(-\gamma_n^2 x) \tag{20}$$

where the constants γ_n^2 are the eigenvalues and the functions $Z_n(z_1)$ are the eigenfunctions of the boundary-value problem

$$Z_n'' + (\gamma_n^4/\mathrm{Pe}^2 + \tfrac{3}{2}\gamma_n^2)Z_n - 6\gamma_n^2 z_1^2 Z_n = 0 \tag{21}$$

$$Z_n(-\tfrac{1}{2}) = Z_n(\tfrac{1}{2}) = 0 \tag{22}$$

The coefficients C_n, $n = 1, 2, 3, \ldots$, are evaluated by considering the boundary condition at $x = 0$ and the orthogonality of the eigenfunctions. The result is

$$C_n = \frac{\displaystyle\int_{-1/2}^{1/2} H(0, z_1)(2\gamma_n^2/\mathrm{Pe}^2 + \tfrac{3}{2} - 6z_1^2)Z_n dz_1}{\displaystyle\int_{-1/2}^{1/2} (2\gamma_n^2/\mathrm{Pe}^2 + \tfrac{3}{2} - 6z_1^2)Z_n^2 dz_1} \tag{23}$$

The eigenfunctions Z_n of equation (21) are obtained by using a power-series solution as

$$Z_n = \sum_{m=0}^{\infty} A_m z_1^m$$

The solution is found to be accurate up to 12 significant figures. The corresponding eigenvalues γ_n^2 are determined by employing the secant method with an error less than the order of 10^{-8}. The calculated eigenvalues γ_n^2 for various Peclet numbers are listed in Table 1. A comparison of the first four eigenvalues for the case of $\mathrm{Pe} \to \infty$ from this work with those listed in [8] shows excellent agreement confirming the accuracy of the numerical results.

Table 1 Calculated eigenvalues γ_n^2

n	Pe = ∞	Pe = 100	Pe = 50	Pe = 30	Pe = 20	Pe = 10
1	7.540701 7.540	7.536377	7.523465	7.493206	7.435475	7.151305
2	35.96191 35.95	35.84704	35.51094	34.76111	33.45733	28.61544
3	85.72609 85.73	85.03635	83.09086	79.08866	72.99041	55.82801
4	156.8283 156.8	154.4649	148.1291	136.3370	120.6686	84.97557
5	249.2664	243.2531	228.1029	202.7741	173.0479	114.9146
6	363.0394	350.3295	320.4783	275.6037	228.2296	145.2647
7	498.1466	474.4884	422.9615	352.9115	285.1895	175.8672
8	654.5878	614.4478	533.6113	433.4291	343.3533	206.6406
9	832.3629	768.9026	650.8537	516.3153	402.3772	237.5365
10	1031.472	936.5684	773.4427	601.0005	462.0415	268.5232
11	1251.914	1116.215	900.4027	687.0872	522.1974	299.5793
12	1493.690	1306.689	1030.971	774.2891	582.7395	330.6894
13			1164.550	862.3944	643.5908	361.8423
14			1300.663	951.2417	704.6934	393.0298
15						424.2455
16						455.4846
17						486.7436

Note: The eigenvalues with four figures are from reference [8].

S. W. CHURCHILL
Carl V. S. Patterson Professor of Chemical Engineering.

H. OZOE[1]
Graduate Student.

School of Chemical Engineering, University of Pennsylvania, Philadelphia, Pa.

Correlations for Laminar Forced Convection with Uniform Heating in Flow over a Plate and in Developing and Fully Developed Flow in a Tube

Asymptotic solutions for $\mathrm{Pr} \to 0$ *and* $\mathrm{Pr} \to \infty$ *and numerical solutions for intermediate* Pr *were obtained for a uniformly heated flat plate. The method of Churchill and Usagi was utilized to construct a simple correlation for these values. The same method was used to develop simple correlations for plug flow and fully developed flow in a uniformly heated tube. These correlations were in turn combined to develop correlations for the available experimental data and computed values for developing flow in a uniformly heated tube. Derivations and test calculations in which convection normal to the wall was neglected reveal that this error is significant but insufficient to explain all of the discrepancies in the computed values.*

Introduction

THE SUBJECT of laminar forced convection from uniformly heated surfaces has received considerably less attention than forced convection from surfaces with a uniform wall temperature. A preliminary examination of the available experimental data and theoretical solutions revealed various discrepancies for both developing and fully developed flow in tubes. Supplementary solutions were therefore derived and computed for flow over a flat plate with the intent of using these results as a criterion for resolving the discrepancies. Partial success was achieved. The concurrent development by Churchill and Usagi [1][2] of a method for constructing simple empirical correlations then provided a far more powerful method of evaluating and correlating the results for both flat plates and tubes, and this investigation was completely reshaped in that form.

Solutions for a Flat Plate

Mathematical Model. The solution obtained by Blasius [2] for the laminar portion of flow over a flat plate can be summarized as follows:

$$u = u_0\varphi'(\eta)/2 \tag{1}$$

$$v = (\nu u_0/x)^{1/2}[\eta\varphi'(\eta) - \varphi(\eta)]/2 \tag{2}$$

Howarth [3] computed and tabulated values of $\varphi(\eta)$ and $\varphi'(\eta)$. For small values of η this function is represented well by the series

$$\varphi(\eta) = \frac{A\eta^2}{2!} - \frac{A^2\eta^5}{5!} + \frac{11A^3\eta^8}{8!} - \frac{375A^4\eta^{11}}{11!} + \dots \tag{3}$$

A value of 1.32824 for A has been calculated by Goldstein [4]. For large η

$$\varphi(\eta) \to 2(\eta - 0.860385) \tag{4}$$

The corresponding temperature field can be represented by the following energy balance which assumes constant physical properties, negligible dissipation, and the usual simplifications of boundary-layer theory:

$$u\frac{\partial T}{\partial x} + v\frac{\partial T}{\partial y} = \alpha\frac{\partial^2 T}{\partial y^2} \tag{5}$$

The boundary conditions are

$$T = T_0 \qquad \text{for } x < 0 \quad \text{and for} \quad y \to \infty \tag{6}$$

$$j = -k(\partial T/\partial y) \qquad \text{at } y = 0, \quad x > 0 \tag{7}$$

Solutions. $\mathrm{Pr} \to 0$. For the limiting case of $\mathrm{Pr} \to 0$ the temperature profile develops primarily in the region beyond the momentum boundary layer in which $u \cong u_0$. Equation (5) then reduces to

[1] Currently with the Department of Industrial and Mechanical Engineering, Okayama University, Okayama, Japan.

[2] Numbers in brackets designate References at end of paper.

Contributed by the Heat Transfer Division and presented at the Winter Annual Meeting, New York, N. Y., November 26–30, 1972, of THE AMERICAN SOCIETY OF MECHANICAL ENGINEERS. Manuscript received by the Heat Transfer Division November 24, 1971. Paper No. 72-WA/HT-14.

$$u_0 \frac{\partial T}{\partial x} = \alpha \frac{\partial^2 T}{\partial y^2} \tag{8}$$

Equation (8) with boundary conditions (6) and (7) is equivalent to the well-known problem of transient conduction in a semi-infinite region [5] with x/u_0 substituted for t. The solution can be expressed in terms of a heat-transfer coefficient as follows:

$$\mathrm{Nu}_x = (\pi \mathrm{Re}_x \mathrm{Pr})^{1/2}/2 = 0.886(\mathrm{Re}_x \mathrm{Pr})^{1/2} \tag{9}$$

Pr → ∞. For the limiting case of Pr → ∞ the development of the temperature profile occurs very near the wall where only the first term in equation (3) needs to be considered. Making this simplification and then applying the method of Hellums and Churchill [6] permits reduction of equations (5), (6), and (7) to

$$\psi'' + (Y^2/2)\psi' - Y\psi = 0 \tag{10}$$

$$\psi' = -1 \quad \text{at} \quad Y = 0 \tag{11}$$

$$\psi \to 0 \quad \text{as} \quad Y \to \infty \tag{12}$$

This boundary-value problem was solved numerically by the Runge–Kutta method, guessing values of ψ at $Y = 0$. The value of $\psi(0, \infty)$ for which $\psi(Y, \infty) \to 0$ as $Y \to \infty$ was calculated to be 1.18535. Hence

$$\mathrm{Nu}_x = [A^{1/3}/2\psi(0, \infty)]\mathrm{Re}_x^{1/2}\mathrm{Pr}^{1/3} = 0.464\mathrm{Re}_x^{1/2}\mathrm{Pr}^{1/3} \tag{13}$$

General Pr. Application of the method of Hellums and Churchill in the general case yields

$$\psi'' + \theta\psi' - \theta'\psi = 0 \tag{14}$$

Boundary conditions (11) and (12) are still applicable. This problem was solved for a series of values of Pr by the same method used for equation (10). In these calculations equation (3) was used for $\eta \leq 1.6$, equation (4) for $\eta \geq 3.0$, and the values tabulated by Howarth were interpolated for $1.6 < \eta < 3.0$. For $\mathrm{Pr} \geq 10$, equation (3) was sufficient since $\psi(Y, \mathrm{Pr})$ becomes negligibly small before $\eta = Y/(A\mathrm{Pr})^{1/3}$ exceeds 1.6.

The heat-transfer rates indicated by these computations can be expressed in the convenient form

$$\mathrm{Nu}_x = [A^{1/3}/2\psi(0, \mathrm{Pr})]\mathrm{Re}_x^{1/2}\mathrm{Pr}^{1/3} = 0.464\mathrm{Re}_x^{1/2}\mathrm{Pr}^{1/3} f(\mathrm{Pr}) \tag{15}$$

Values of $\psi(0, \mathrm{Pr})$ and $f(\mathrm{Pr}) = \psi(0, \infty)/\psi(0, \mathrm{Pr})$ are given in Table 1. It may be noted that $f(\mathrm{Pr})$ is only a slight function of Pr for $\mathrm{Pr} > 1$. The agreement of $\psi(0, 10^3)$ with the asymptotic value for Pr → ∞ to five significant figures is a confirmation of the accuracy of the numerical calculations.

Pr → ∞, v = 0. The effect of neglecting convection normal to the plate in the limiting case of Pr → ∞ can be evaluated by dropping the $v(\partial T/\partial y)$ term and again using only the first term of equation (3). Dimensional analysis then leads to

$$\psi'' + Y^2\psi' - Y\psi = 0 \tag{16}$$

The boundary-value problem represented by equations (16), (11), and (12) has the same mathematical form as the approximate representation utilized by Sellars et al. [7], Bird [8], and Bird et al. [9] for the temperature field in fully developed laminar flow in a tube following the application of a uniform heat flux [3, 4]. A solution may be obtained by dividing equation (16) by Y, differentiating with respect to Y, and introducing the additional boundary condition

Table 1 Computed values

Pr	$\psi(0, \mathrm{Pr})$	$f(\mathrm{Pr}) = \frac{\psi(0, \infty)}{\psi(0, \mathrm{Pr})}$	$[1 + (0.0207/\mathrm{Pr})^{2/3}]^{-1/4}$	$\psi^*(0, \mathrm{Pr})$	$f^*(\mathrm{Pr}) = \frac{\psi^*(0, \infty)}{\psi^*(0, \mathrm{Pr})}$
∞	1.18535	1.0000	1.0000	1.06509	1.0000
10^3	1.18536	1.0000	0.9998	1.065	1.000
10^2	1.18547	0.9999	0.9991	1.065	1.000
10	1.8662	0.9989	0.996	1.066	0.999
1	1.19752	0.9898	0.982	1.079	0.987
10^{-1}	1.27147	0.9323	0.928	1.172	0.909
10^{-2}	1.5268	0.7764	0.786	1.463	0.728
10^{-3}	2.0537	0.5772	0.585	2.020	0.527
10^{-4}	2.9222	0.4056	0.408	2.90	0.367

Nomenclature

A = constant = 1.32824
D = tube diameter, ft
$f(\mathrm{Pr}) = \psi(0, \infty)/\psi(0, \mathrm{Pr})$
$f^*(\mathrm{Pr}) = \psi^*(0, \infty)/\psi^*(0, \mathrm{Pr})$
$\mathrm{Gz} = \pi D^2 u_m/4\alpha x$ = Graetz number
$h_x = j/(T_w - T_0)$ = local heat-transfer coefficient for a flat plate, Btu/hr-ft²-deg F
$h_D = j/(T_w - T_m)$ = local heat-transfer coefficient for a tube, Btu/hr-ft²-deg F
j = heat-flux density at wall, Btu/hr-ft²
$J_0(\beta)$ = Bessel function of zero order
k = thermal conductivity, Btu/hr-ft-deg F
n = arbitrary exponent in equation (19)
$\mathrm{Nu}_x = h_x x/k = jx/(T_w - T_0)k$ = local Nusselt number on flat plate
$\mathrm{Nu}_D = h_D D/k = jD/(T_w - T_m)k$ = local Nusselt number in tube
$\mathrm{Pr} = \nu/\alpha$ = Prandtl number
$\mathrm{Re}_x = xu_0/\nu$ = local Reynolds number for flat plate
$\mathrm{Re}_D = Du_m/\nu$ = Reynolds number in tube
T = temperature, deg F
T_0 = inlet temperature, deg F
T_m = mixed-mean temperature, deg F
T_w = local wall temperature, deg F
u = local velocity in x direction, ft/hr
u_m = mean velocity in tube, ft/hr
u_0 = free-stream velocity far from plate, ft/hr
v = local velocity in y direction, ft/hr
$w(z)$ = any function
$w(0)$ = asymptotic behavior of function for $z \to 0$
$w(\infty)$ = asymptotic behavior of function for $z \to \infty$
$W = w(z)/w(0)$ for increasing and $w(\infty)/w(z)$ for decreasing power of z
x = distance along flat plate or tube wall, ft
y = distance normal to flat plate or tube wall, ft
$Y = (A\mathrm{Pr})^{1/3}\eta = (A\mathrm{Pr})^{1/3}y(u_0/x\nu)^{1/2}/2$
z = any independent variable
$Z = w(\infty)/w(0)$ for increasing and $w(0)/w(\infty)$ for decreasing power of z
α = thermal diffusivity, ft²/hr
β_n = roots of equation (24)
$\gamma(^2/_3) = \int_0^\infty z^{-1/3}e^{-z}dz = 1.358$
$\eta = y(u_0/x\nu)^{1/2}/2$
$\theta(Y, \mathrm{Pr}) = (\mathrm{Pr}^2/A)^{1/3}\{\varphi[Y/(A\mathrm{Pr})^{1/3}]\}$
ν = kinematic viscosity, ft²/hr
ρ = density, lb/ft³
$\varphi(\eta)$ = velocity distribution function in Blasius solution, see equations (1) and (2)
$\psi(Y, \mathrm{Pr}) = k(T - T_0)(A\mathrm{Pr})^{1/3}(u_0/x\nu)^{1/2}/2j$
$\psi^*(Y, \mathrm{Pr}) = \psi(Y, \mathrm{Pr})$ for $v = 0$

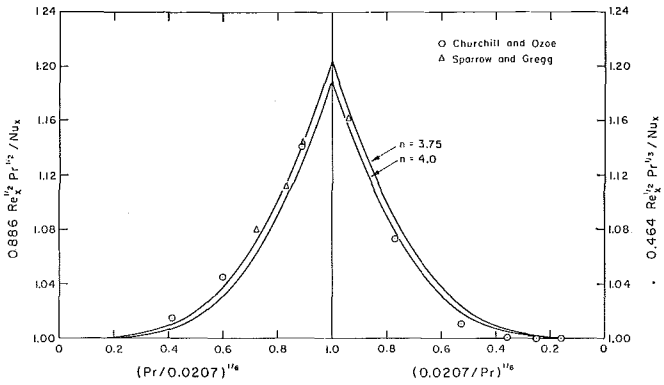

Fig. 1 Correlation for the effect of Pr on forced convection in laminar flow over a uniformly heated plate

$$\psi' \to 0 \qquad \text{as} \qquad Y \to \infty \tag{17}$$

The solution yields $\psi(0, \infty) = 3^{1/3}/\gamma(2/3) = 1.06509$, thus giving a heat-transfer rate 11.2 percent greater than the solution of the complete equation.

General Pr, v = 0. Dropping the $v(\partial T/\partial x)$ term leads to

$$\psi'' + Y\theta'\psi' - \theta'\psi = 0 \tag{18}$$

in place of equation (14). Numerical solution by the Runge–Kutta method yielded the values included in Table 1 under the headings $\psi^*(0, \text{Pr})$ and $f^*(\text{Pr})$.

Results. The percentage overestimate of Nu which results from neglecting the normal-convective term decreases from 11.3 percent to 10.9 percent at Pr = 1 and then more rapidly to 4.4 percent at Pr = 0.01, and of course to zero as Pr → 0. Ulrichson and Schmitz [10] calculated only a 6 percent overestimate for Pr = 0.7 in a tube, indicating that their computations may not have extended far enough upstream. Since normal convection carries energy away from the wall, a solution which neglects this term might be expected to underestimate rather than overestimate the heat-transfer coefficient. However, as explained by Ulrichson and Schmitz, the resulting disappearance of some of the heat flux supplied at the wall when the normal velocity is neglected has a greater effect. Since the neglect of normal convection does not produce a significant simplification in the boundary-value problem for Pr > 0, this approximation does not appear to have any justification for the flat plate.

The agreement to four significant figures between $\psi^*(0, \infty)$ and $\psi^*(0, 10^3)$ constitutes a check on the accuracy of the numerical integration, since the asymptotic value for Pr → ∞ was obtained from previously tabulated functions rather than by numerical integration. Sparrow and Gregg [11] solved the equivalent of equation (14) for Pr = 0.003, 0.006, 0.01, and 0.03 and compared their results with the asymptotic solution for Pr → 0. These values are compared with those computed herein in the next section. Other solutions appear to be based on integral or other approximate models.

Correlation for a Flat Plate

Churchill and Usagi [1] suggested the construction of correlations in the form

$$W = [1 + Z^n]^{1/n} \tag{19}$$

Since the dependence of Nu_x on Pr in this instance decreases from the 1/2 power to the 1/3 power as Pr increases, the corresponding trial correlation is

$$0.886\text{Re}_x^{1/2}\text{Pr}^{1/2}/\text{Nu}_x = [1 + (\text{Pr}/0.0207)^{n/6}]^{1/n} \tag{20}$$

The values computed herein as well as those computed by Sparrow and Gregg [11] are plotted in Fig. 1 in the form suggested by Churchill and Usagi. The curve corresponding to $n = 4$ represents the computed values within about 1 percent, although a slightly higher value of say 4.5 would yield an even better representation for Pr > 0.0207 and a slightly lower value of say 3.5 an even better representation for Pr < 0.0207. Comparison of equation (20) with $n = 4$ and equation (15) indicates that the empirical approximation for $f(\text{Pr})$ is $[1 + (0.0207/\text{Pr})^{2/3}]^{-1/4}$. Values of this term are compared in Table 1.

Asymptotic Solutions for Inlet of a Tube in Developing Flow

The above solutions and correlations for the flat plate can be used to develop asymptotic solutions for the inlet region of a uniformly heated tube in developing flow insofar as the velocity field for the flat plate is applicable, i.e., insofar as acceleration of the fluid in the core of the tube owing to the development of the momentum boundary layer can be neglected.

For forced convection inside a tube the dimensionless flow rate is usually expressed in terms of Re_D or Gz and the dimensionless heat-transfer rate in terms of Nu_D, since this latter quantity is a function only of Gz for developing flow with Pr = 0 and for fully developed flow at all Pr. The heat-transfer coefficient is ordinarily expressed in terms of the mixed-mean temperature rather than the inlet temperature. Lipkis [12] suggested that recxpression of the Lévêque solution for the onset of heating following a step in a wall temperature in fully developed flow in a tube in terms of the mixed-mean temperature would extend its range of applicability to smaller Gz. The equivalent form of equation (20) with $n = 4$ is

$$\text{Nu}_D = \text{Gz}^{1/2}/\{[1 + (\text{Pr}/0.0207)^{2/3}]^{1/4} - \pi\text{Gz}^{-1/2}\} \tag{21}$$

The Gz term in the denominator has the effect of increasing Nu_D. For large Pr the correction becomes less than 5 percent for $\text{Gz} > 1075/\text{Pr}^{1/3}$. In the limiting case of Pr → 0 the dependence on Gz in the denominator of equation (21) does not become less than 5 percent until Gz exceeds 3950. Thus the difference between correlations based on T_0 and T_m may be significant even in the inlet region. The applicability of equation (21) is obviously limited to $\text{Gz} > \pi^2/[1 + (\text{Pr}/0.0207)^{2/3}]^{1/2}$ by the singularity in the denominator. This singularity arises from boundary condition (6) for $y \to \infty$ which is not valid for the pipe as Gz → 0.

As discussed in the next section, the series solution of Worsøe-Schmidt [13] for large Gz and fully developed flow reveals that the effect of curvature, which is neglected in equation (21), is to reduce Nu_D. This effect more than compensates for the increase due to the use of the mixed-mean temperature. Lipkis [12] and Munakata [14] previously noted but did not explain the same discrepancy for uniform wall temperature. The effect of curvature would be expected to be less in developing flow. Pending the development of an analytical solution for developing flow corresponding to the Worsøe-Schmidt solution for fully developed flow, or of numerical solutions in which the various simplifications are evaluated, it therefore seems reasonable to drop the Gz term in the denominator of equation (21) to obtain the following better lower bound:

$$\text{Nu}_D = \text{Gz}^{1/2}/[1 + (\text{Pr}/0.0207)^{2/3}]^{1/4} \tag{22}$$

Correlations for Fully Developed and Plug Flow in a Tube

The series solutions for plug and fully developed flow converge satisfactorily for moderate values of Gz. The asymptotic solutions for Gz → ∞ are valid only for very large Gz owing to the neglect of curvature, but the perturbation solution of Worsøe-Schmidt [13] is satisfactory for the intervening range for fully developed flow and an equivalent expansion could be derived for plug flow. Empirical correlations for these processes, however, still have a justification if they are simpler to use and if they are sufficiently accurate for practical purposes. Furthermore, a correlation for fully developed flow is of direct use in the derivation of a correlation for developing flow.

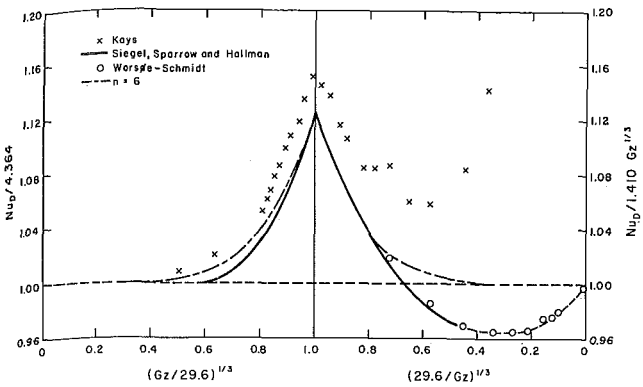

Fig. 2 Correlation for forced convection in fully developed laminar flow through a uniformly heated tube based on an asymptotic solution of Sellars, Tribus, and Klein

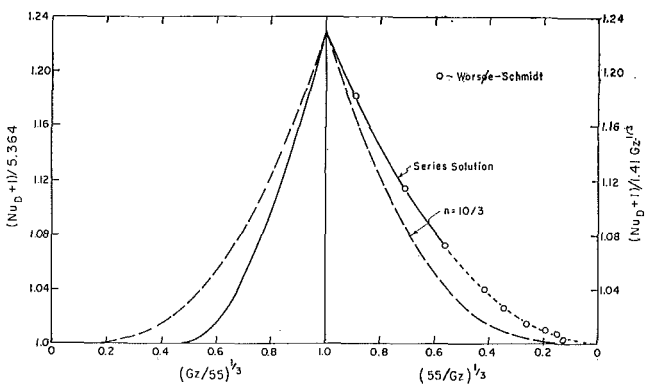

Fig. 3 Correlation for forced convection in fully developed laminar flow through a uniformly heated tube based on the Worsøe-Schmidt solution

Plug Flow. Plug flow may be applicable for solids and under other special circumstances. However it is primarily of interest for fluids as a bounding solution for $\mathrm{Pr} \to 0$. A solution for plug flow can be constructed from the solution discussed by Carslaw and Jaeger [5] for conduction in a heated cylinder and is

$$\mathrm{Nu}_D = 8 \Big/ \left(1 - 8 \sum_{n=1}^{\infty} e^{-\pi\beta_n^2/\mathrm{Gz}}/\beta_n^2\right) \tag{23}$$

where β_n are the roots of

$$J_0(\beta) = 0 \tag{24}$$

Equation (23) indicates that the asymptotic solution for $\mathrm{Gz} \to \infty$ is $\mathrm{Nu}_D = 8$. Equation (21) with $\mathrm{Pr} = 0$ can be shown to be an asymptotic solution for plug flow for $\mathrm{Gz} \to \infty$. However the singularity at $\mathrm{Gz} = \pi^2/[1 + (\mathrm{Pr}/0.0207)^{2/3}]^{1/2}$, which is irrelevant for large Gz, would persist in a combined expression for all Gz. Equation (22) with $\mathrm{Pr} = 0$ may be a more appropriate bounding solution in any event because of the compensating effect of neglecting curvature. The resulting trial solution is

$$\mathrm{Nu}_D/8 = [1 + (\mathrm{Gz}/64)^{n/2}]^{1/n} \tag{25}$$

A plot in the form suggested by Churchill and Usagi of the values computed from equation (23) reveals that the best overall value of n is 2.0, producing the simple correlation

$$\mathrm{Nu}_D = (64 + \mathrm{Gz})^{1/2} \tag{26}$$

The series in equation (23) actually converges very rapidly as contrasted with the equivalent solutions for fully developed flow. Indeed the first term in the series provides a better approximation than equation (26) for $\mathrm{Gz} < 64$. Furthermore equation (21) with $\mathrm{Pr} = 0$ provides just as good an approximation as equation (26) for $\mathrm{Gz} > 400$. Hence equation (26) has value only by virtue of its simplicity and its applicability over the entire range of Gz.

Fully Developed Flow. Prior Work. Sellars et al. [7] obtained a series solution for a step in heat-flux density in fully developed laminar flow in a tube by integration of the Graetz solution for a step in wall temperature and computed the coefficients for the first three terms in the series. Siegel et al. [15] derived this same solution directly from the differential energy balance and computed the first seven terms. Kays [16] integrated the differential energy balance numerically for fully developed flow for $4 < \mathrm{Gz} < 628$ in order to test his computational procedure for developing flow. He asserted that his results for a step in uniform wall temperature agreed with the series solution to within 2 percent and implied an equivalent accuracy for other boundary conditions.

Sellars et al. also presented an asymptotic solution for large Gz analogous to the Lévêque solution for uniform wall temperature which can be reexpressed as

$$\mathrm{Nu}_D = 1.410\ \mathrm{Gz}^{1/3} \tag{27}$$

Bird [8] and Bird et al. [9] rederived this equation more directly and in greater detail and showed that it can be reinterpreted as a solution for certain non-Newtonian models. (The expression for the temperature field in the derivation is incorrectly written as $k(T - T_0)/qR^2$ on page 309, but is correct on page 364 of [9].) This asymptotic solution is based on the difference between the wall and the inlet temperatures.

Worsøe-Schmidt [13] derived a series solution which represents a perturbation on this asymptotic solution and extends its applicability to lower Gz. His solution reveals that equation (27) is not a lower bound for the general solution as has sometimes been asserted or implied. Worsøe-Schmidt attributes the error in equation (27) primarily to the neglect of the effect of curvature and the use of a linearized approximation for the velocity profile near the wall. Churchill and Balzhiser [17] have shown that the radial heat-flux density goes through a maximum near the wall in fully developed flow due to the predominance of the effect of curvature relative to longitudinal transfer. Their equation (11) demonstrates quantitatively how this effect reduces Nu_D. Analysis of the derivation of equation (27) indicates that linearization of the velocity profile increases Nu_D. This effect is thus in the same direction but is probably small with respect to the effect of curvature. The error due to the use of the inlet temperature is in the opposite direction. This partial compensation of errors gives equation (27) more credence than it deserves. The Worsøe-Schmidt solution which corrects for all three errors should now be used generally in place of equation (27) and in place of the extension derived by Bird.

Empirical Correlations. Equation (27) was first combined with $\mathrm{Nu} = 4.364$ to construct a correlation in the hope that its limitations might not be significant in this particular usage. The resulting trial expression is

$$\mathrm{Nu}_D/4.364 = [1 + (\mathrm{Gz}/29.6)^{n/3}]^{1/n} \tag{28}$$

A curve representing the series solution, with values computed by Worsøe-Schmidt for his series and values computed by Kays by numerical integration, is plotted in the suggested form in Fig. 2. The seven coefficients and eigenvalues computed by Siegel et al. are sufficient only for $(29.6/\mathrm{Gz})^{1/3} > 0.45$ ($\mathrm{Gz} < 325$) as indicated. Fortunately the solution of Worsøe-Schmidt appears to be valid for $\mathrm{Gz} > 325$. The swing of this combined solution below unity for $(29.6/\mathrm{Gz})^{1/3} < 0.666$ ($\mathrm{Gz} > 100$) is due to the failure of equation (27) to provide a lower bound. The values computed by Kays are self-consistent and only about 2 percent high for $\mathrm{Gz} < 30$, but the deviations become erratic and much greater for larger Gz, presumably owing to the use of too large a grid size for that region. An advantage of the coordinates of Fig. 2 is that these deviations which would hardly be distinguishable in a plot of log Nu_D versus log Gz are shown very clearly: $n = 6$ represents the series solution within 1 percent for $\mathrm{Gz} < 90$ and is in error a maximum of only 3.5 percent for larger Gz.

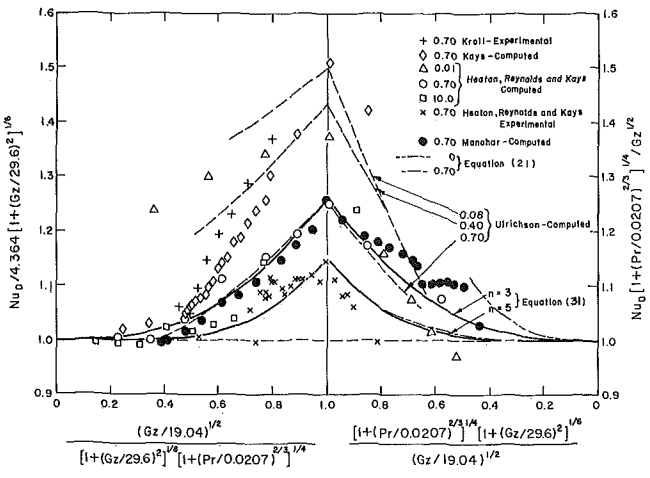

Fig. 4 Correlation for forced convection in developing laminar flow through a uniformly heated tube for all Pr

The first-order correction of the Worsøe-Schmidt solution including correction for the mixed-mean temperature can be approximated closely as

$$\mathrm{Nu}_D = 1.41\,\mathrm{Gz}^{1/3} - 1.00 \tag{29}$$

This approximation corresponds to a tangent at $29.6/\mathrm{Gz} = 0$ to the curve representing the solution of Worsøe-Schmidt in Fig. 2. $\mathrm{Nu}_D = 4.364$ can be combined with equation (29) to yield the trial solution

$$(\mathrm{Nu}_D + 1)/5.364 = [1 + (\mathrm{Gz}/55)^{n/3}]^{1/n} \tag{30}$$

The corresponding plot is shown in Fig. 3. Some dissymmetry is evident: $n = {}^{10}/_{3}$ represents the solution closely at $\mathrm{Gz} = 55$ but is in error as much as 3.5 percent for small Gz and as much as 2.5 percent for large Gz. The choice of equation (28) or (30) depends on the application. For example equation (30) may be preferable to equation (28) as an asymptotic solution for developing flow for large Gz since it is a lower bound, whereas equation (28) is not.

Developing Flow in a Tube

An exact analytical solution for a developing velocity field in a tube has not yet been derived. Hence solutions for forced convection have either utilized an approximate analytical solution or a numerical solution for the flow field. Apparently neither an analytical solution nor a general empirical correlation has been developed for convection. A simple correlation of the various values obtained by numerical integration would appear to be of value. This has been the principal objective of this work. Unfortunately the various sets of computed values are not in agreement, so that a prerequisite to the development of a reliable correlation is the critical evaluation of the computed values.

Prior Work. Kays [16] presented results obtained by numerical integration of the differential energy balance for developing flow in a uniformly heated tube for $\mathrm{Pr} = 0.7$ and $\mathrm{Gz} \leqq 785$. He utilized the approximate analytical solution for the longitudinal velocity field derived by Langhaar [18] and neglected radial convection. His solution agrees closely with the experimental data of Kroll for $\mathrm{Gz} < 180$ as reported by Tribus and Klein [19].

Heaton et al. [20] subsequently presented tabulated values of an approximate integral solution for the inlet region of an annulus with a uniform heat-flux density at the wall, including the limiting case of an empty tube, and reported values of Nu_D for $\mathrm{Pr} = 0.01$, 0.7, and 10 and Gz up to 983. The solution takes convection normal to the wall into account on the average. The same authors [21] presented experimental data for Gz up to 983.

Ulrichson and Schmitz [10] integrated the differential energy balance numerically for $\mathrm{Pr} = 0.7$. They too used the longitudinal velocity field of Langhaar but calculated the radial velocity field from the continuity equation and hence took radial convection into account. Their results agree closely with the solution of Heaton et al. for $\mathrm{Gz} < 1000$ but are somewhat above their experimental data. From test calculations in which radial convection was neglected, they conclude that this simplification results in a 6 percent overestimate of Nu_D near the entrance. They further conclude that the earlier values of Kays are significantly in error on the high side because of the use of too large a grid size. (The abscissas of the figures in [10] should be labeled $x/4\mathrm{Re}_r\mathrm{Pr}$, which is equivalent to $x/D\mathrm{Re}_D\mathrm{Pr}$ in the nomenclature of this paper, rather than $4x/\mathrm{Re}_D\mathrm{Pr}$.) Ulrichson [22] presented additional results for $\mathrm{Pr} = 0.08$ and 0.4.

Manohar [23] integrated the differential mass and momentum balances as well as the energy balance numerically. He concludes that the values of Nu_D computed by Ulrichson and Schmitz are slightly low for large Gz because of their use of an approximate solution for the velocity field, and agrees with their assessment of the values computed by Kays. Manohar presents only curves, but the computer printout of the calculations has been generously provided for use in this work.

Development of an Expression for Correlation. Combination of equation (28) with $n = 6$ and equation (22) yields the test expression

$$\frac{\mathrm{Nu}_D}{4.364[1 + (\mathrm{Gz}/29.6)^2]^{1/6}} = \left[1 + \left(\frac{\mathrm{Gz}/19.04}{[1 + (\mathrm{Pr}/0.0207)^{2/3}]^{1/2}[1 + (\mathrm{Gz}/29.6)^2]^{1/3}}\right)^{n/2}\right]^{1/n} \tag{31}$$

This expression proves to be surprisingly successful even though equation (28) is not a true lower bound.

Arbitrarily adding 1.0 to the left side of equation (22) to correct for the net effect of curvature and the use of the inlet temperature makes it compatible in form with equation (30). Combining this expression with equation (30) with $n = {}^{10}/_{3}$ yields

$$\frac{\mathrm{Nu}_D + 1}{5.364[1 + (\mathrm{Gz}/55)^{10/9}]^{9/10}} = \left[1 + \left(\frac{\mathrm{Gz}/28.8}{[1 + (\mathrm{Pr}/0.0207)^{2/3}]^{1/2}[1 + (\mathrm{Gz}/55)^{10/9}]^{3/5}}\right)^{n/2}\right]^{1/n} \tag{32}$$

This equation, which is based on a better lower bound, also proves successful for correlation.

Equations (31) and (32) appear to be somewhat ungainly, but they are probably the simplest possible expressions which converge to the chosen asymptotic solutions for both large and small Pr and Gz. Thus for any n they approach the chosen correlations for fully developed flow as $\mathrm{Pr} \to \infty$, they approach the chosen asymptotic solution for the inlet region as $\mathrm{Gz} \to \infty$, they approach the upper bounding solution for plug flow as $\mathrm{Pr} \to 0$ for large Gz, and they approach $\mathrm{Nu}_D = 4.364$ as $\mathrm{Gz} \to 0$.

Evaluation of Computed and Experimental Values. The computed values of Kays, Heaton et al., and Manohar (selected) and the experimental values of Kroll and Heaton et al. are plotted in Fig. 4 in the form suggested by equation (31). The computed values of Ulrichson are represented by curves since tabulated values are not available. The computed values of Manohar, Ulrichson, and Heaton et al. for $\mathrm{Pr} = 0.7$ are in general agreement, although the values of Manohar which are the latest and presumably most accurate show considerable scatter for large Gz. The computed values of Heaton et al. for $\mathrm{Pr} = 10$ and for $\mathrm{Pr} = 0.01$ and large Gz are also in accord. The experimental values of Heaton et al. are generally 10 percent below the computed values. The computed values of Kays and the experimental values of Kroll deviate increasingly and significantly on

the high side as Gz increases. The agreement between the results of these two early investigations was apparently fortuitous and gave them false credence. The computed values of Ulrichson for Pr = 0.04 and 0.8 and of Heaton et al. for Pr = 0.01 are very high for small Gz but appear to be approaching the presumably more reliable values as Gz increases.

Final Correlations. It appears that $n = 3$ is a reasonable choice to represent the computed values in Fig. 4. If complete confidence could be placed in the experimental values of Heaton et al., $n = 5$ would be a better choice. However, in view of the agreement of the several independent theoretical solutions it is probable that the experimental values are in slight error on the low side. It should be emphasized that the choice of coordinates in Fig. 4 exaggerates the deviations. The maximum difference between the curves for $n = 3$ and $n = 5$ is only 10 percent and is completely negligible at both large and small Gz. Indeed even the most extreme values in Fig. 4 do not differ from the curve for $n = 3$ by much more than 25 percent. It is somewhat surprising that the computed values for large Gz do not fall slightly below unity as they do in Fig. 2, since this plot has the same theoretical limitation. It may be that more accurate values for larger Gz would.

The alternative correlation suggested by equation (32) is shown in Fig. 5 in which only the sets of values which are deemed to be most reliable are plotted. A value of $n = 5/2$ appears to represent these values remarkably well. A few values fall slightly below unity for small Gz, and the values of Heaton et al. for Pr = 0.01 are again far above the others for low Gz.

Evaluation of Asymptotic Solutions for the Inlet. Equation (21) is plotted in Figs. 4 and 5 for Pr = 0 and 0.7. The fact that equation (21) for Pr = 0.7 falls below the correlation implies that the effect of the acceleration of the velocity in the core exceeds the effect of curvature, and conversely for Pr → 0. Equation (21) apparently has a far more limited range of applicability than Gr > 1000 Pr, the limit inferred from the Langhaar solution. This conclusion is critically dependent on the validity of the correlations derived in Figs. 4 and 5 and might be modified by additional computed values for large Gz and Pr.

Discussion and Conclusions

Flat Plate. The values computed herein and the values previously computed by Sparrow and Gregg are in good agreement and are correlated within 1 percent for all Pr by equation (20) with $n = 4$. The neglect of convection normal to the wall results in a maximum overestimate of Nu_x of 11.3 percent.

Tube–Plug Flow. Equation (26) represents the series solution to within 10 percent for all Gz. However the series solution converges very rapidly and the first term in the series is an even better approximation than equation (26) for Gz < 64. Equation (21), which is based on the correlation for the flat plate, with Pr = 0 represents the series solution even better than equation (26) for Gz > 400.

Tube–Fully Developed Flow. The series solution of Worsøe-Schmidt reveals that the Lévêque-type solution of Sellars et al. is not a lower bound for large Gz, owing to the neglect of curvature. The extension of this solution to certain non-Newtonian fluids by Bird is correspondingly in error. The neglect of curvature more than compensates for the error arising from the use of the inlet temperature in place of the mixed-mean temperature by both Sellars et al. and Bird. Equation (29) is a first-order approximation of the Worsøe-Schmidt solution for uniform heating.

The seven coefficients and eigenvalues computed for the Graetz-type solution by Siegel et al. are sufficient only for Gz < 325. However the Worsøe-Schmidt solution is satisfactory for all higher Gz. The overall solution is represented within 3.5 percent for all Gz by equation (28) with $n = 6$ and within 1 percent for Gz < 90. The computed values of Kays are only about 2 percent high for Gz < 30 but are as much as 14 percent in error for higher Gz. The overall solution is also represented within 3.5 percent for all Gz by equation (30) with $n = 10/3$. This equation is based on the Worsøe-Schmidt solution rather than on the Lévêque-type solution.

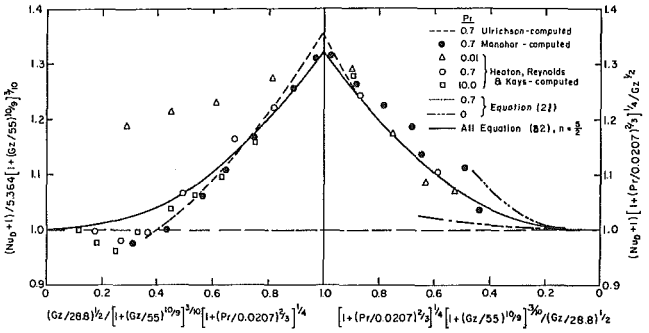

Fig. 5 Modified correlation for forced convection in developing laminar flow through a uniformly heated tube for all Pr

Tube–Developing Flow. The computed values of Heaton et al. for Pr = 0.7 and 10, of Ulrichson and Schmitz for Pr = 0.7, and of Manohar for Pr = 0.7 are represented within about 5 percent for all Gz by equation (31) with $n = 3$ and even better by equation (32) with $n = 5/2$. These equations also approach the chosen asymptotic solutions for both large and small Gz and Pr. Additional precise values for large Gz and large Pr are still needed to test the correlations critically in that range.

The computed values of Ulrichson for Pr = 0.08 and 0.4 and of Heaton et al. for Pr = 0.01 are increasingly in error on the high side as Gz decreases. The experimental values of Heaton et al. for Pr = 0.7 appear to be about 10 percent low.

The computed values of Kays and the experimental values of Kroll are in seriously increasing error as Gz increases. The apparently fortuitous agreement between these two sets of values gave them early false credence. Kays' solution deviates from the others more than can be accounted for by his neglect of convection normal to the wall. The additional error is presumably due to the use of too large a grid size. Most current books on heat transfer present curves based on this pioneering work which is now seen to be in error.

Equation (21), which is an asymptotic solution for large Gz based on the flat-plate solution, would be expected to be high because curvature is neglected and low because acceleration of the fluid in the core is neglected. Comparison with the correlations for developing flow suggests that the former effect is predominant for Pr → 0 and the latter for Pr → ∞.

The solutions and correlations presented herein all neglect longitudinal conduction and variations in the physical properties with temperature. McMordie and Emery [24] indicate that the former effect is significant only for very small Pr and only in the very inlet. Rosenberg and Hellums [25] indicate that the latter effect may be quite significant.

Plots such as Figs. 1–5 reveal the scatter of the computed and experimental points far more clearly than conventional log–log plots. Equations (20), (22), (26), (28), (30), (31), and (32) with the appropriate exponents are not only more convenient for calculations than the series or numerical solutions which they represent, but are more convenient and accurate to use than log–log plots. Hence this conventional graphical form may have outlived its usefulness for the presentation of data and solutions for convective heat transfer.

References

1 Churchill, S. W., and Usagi, R., "A General Expression for the Correlation of Rates of Transfer and Other Phenomena," *AIChE Journal*, Vol. 18, 1972, pp. 1121–1128.

2 Blasius, H., "Grenzschichten in Flüssigkeiten mit kleiner Reibung," *Z. Math. Phys.*, Vol. 56, 1908, pp. 1–37.

3 Howarth, L., "On the Solution of the Laminar Boundary Layer Equations," *Proceedings of the Royal Society*, London, Series A, Vol. 164, 1938, pp. 547–579.

4 Goldstein, S., "Concerning Some Solutions of the Boundary Layer Equations in Hydrodynamics," *Proc. Camb. Phil. Soc.*, Vol. 26, 1930, pp. 1–30.

5 Carslaw, H. S., and Jaeger, J. C., *Conduction of Heat in Solids*, 2nd ed., Oxford at the Clarendon Press, 1959.

6 Hellums, J. D., and Churchill, S. W., "Simplification of the Mathematical Description of Boundary and Initial Value Problems," *AIChE Journal*, Vol. 10, 1964, pp. 110–114.

7 Sellars, J. R., Tribus, M., and Klein, J. S., "Heat Transfer to Laminar Flow in a Round Tube or Flat Conduit—The Graetz Problem Extended," TRANS. ASME, Vol. 78, 1956, pp. 441–448.

8 Bird, R. B., "Zur Theorie des Wärmeübergangs an nicht-Newtonsche Flüssigkeiten bei laminarer Rohrströmung," *Chemie-Ing. Tech.*, Vol. 31, 1959, pp. 569–572.

9 Bird, R. B., Stewart, W. E., and Lightfoot, E. N., *Transport Phenomena*, Wiley, New York, N. Y., 1960, pp. 308–309, 363–364.

10 Ulrichson, D. L., and Schmitz, R. A., "Laminar Flow Heat Transfer in the Entrance Region of Circular Tubes," *International Journal of Heat and Mass Transfer*, Vol. 8, 1965, pp. 253–258.

11 Sparrow, E. M., and Gregg, J. L., "Details of Exact Low Prandtl Number Boundary-Layer Solutions for Forced and Free Convection," NASA Memo 2-27-59 E, Washington, D. C., Feb. 1959.

12 Lipkis, R. P., discussion of paper by W. M. Kays, "Numerical Solutions for Laminar-Flow Heat Transfer in Circular Tubes," TRANS. ASME, Vol. 77, 1955, pp. 1272–1273.

13 Worsøe-Schmidt, P. M., "Heat Transfer in the Thermal Entrance Region of Circular Tubes and Annular Passages with Fully Developed Laminar Flow," *International Journal of Heat and Mass Transfer*, Vol. 10, 1967, pp. 541–551.

14 Munakata, T., "A Calculation on Laminar Heat Transfer in Tube," *Chemical Engineering*, Tokyo, Vol. 26, 1962, p. 1085–1088.

15 Siegel, R., Sparrow, E. M., and Hallman, T. M., "Steady Laminar Heat Transfer in a Circular Tube with Prescribed Wall Heat Flux," in: *Applied Science Research*, Section A, Vol. 7, 1958, pp. 386–392.

16 Kays, W. M., "Numerical Solutions for Laminar-Flow Heat Transfer in Circular Tubes," TRANS. ASME, Vol. 77, 1955, pp. 1265–1274.

17 Churchill, S. W., and Balzhiser, R. E., "The Radial Heat Flux," *Chemical Engineering Symposium Series No. 29*, Vol. 55, 1959, pp. 127–135.

18 Langhaar, H. L., "Steady Flow in the Transition Length of a Straight Tube," *Journal of Applied Mechanics*, Vol. 9, TRANS. ASME, Vol. 64, No. 2, June 1942, pp. A-55-58.

19 Tribus, M., and Klein, J., "Forced Convection from Nonisothermal Surfaces," in: *Heat Transfer—A Symposium*, University of Michigan Press, Ann Arbor, Mich., 1953, pp. 211–235.

20 Heaton, H. S., Reynolds, W. C., and Kays, W. M., "Heat Transfer in Annular Passages. Simultaneous Development of Velocity and Temperature Fields in Laminar Flow," *International Journal of Heat and Mass Transfer*, Vol. 7, 1964, pp. 763–781.

21 Heaton, H. S., Reynolds, W. C., and Kays, W. M., "Heat Transfer with Laminar Flow in Concentric Annuli with Constant Heat Flux and Simultaneously Developing Velocity and Temperature Distributions," Report No. AHT-5, Thermosciences Div., Department of Mechanical Engineering, Stanford University, Stanford, Calif., July 1962.

22 Ulrichson, D. L., MS thesis, University of Illinois, Urbana, Ill., 1963.

23 Manohar, R., "Analysis of Laminar Flow Heat Transfer in the Entrance Region of Circular Tubes," *International Journal of Heat and Mass Transfer*, Vol. 12, 1969, pp. 15–22.

24 McMordie, R. K., and Emery, A. F., "A Numerical Solution for Laminar-Flow Heat Transfer in Circular Tubes With Axial Conduction and Developing Thermal and Velocity Fields," JOURNAL OF HEAT TRANSFER, TRANS. ASME, Series C, Vol. 89, No. 1, Feb. 1967, pp. 11–16.

25 Rosenberg, D. E., and Hellums, J. D., "Flow Development and Heat Transfer in Variable Viscosity Fluids," in: *Industrial and Engineering Chemistry Fundamentals*, Vol. 4, 1965, pp. 417–421.

LLOYD H. BACK
Member, Technical Staff,
Jet Propulsion Laboratory,
California Institute of Technology,
Pasadena, Calif.
Mem. ASME

Non-isothermal Laminar Flow of Gases through Cooled Tubes[1]

Numerical solutions of the laminar-flow equations in differential form are presented for gas flows through cooled tubes. For nearly isothermal flow there is good agreement with available experimental data, as is also found for the case of a large amount of wall cooling. This correspondence along with a check on the satisfaction of the global momentum and energy constraints allowed an appraisal of the effect of wall cooling on flow through tubes. In general, the effect of wall cooling was to decrease the wall friction and the change in pressure along tubes, but the average heat-transfer coefficient did not vary much.

I Introduction

In a recent investigation [1][2] numerical solutions of the laminar-flow equations in differential form were described and compared to experimental measurements for a very high temperature argon gas flow through the entrance region of an externally cooled tube. The ratio of the wall to inlet enthalpy $H_w = H_w'/H_{ti}'$ was about 0.05. Good agreement was found between the measured and calculated wall heat flux and internal flow and thermal distributions. The pressure was found experimentally to be nearly uniform along the flow in the entrance region (actually increased slightly) as the gas decelerated along the tube while cooling. This behavior is unlike more familiar laminar flow through tubes with no heat transfer in which acceleration occurs in the core flow in the entrance region and there is a pressure drop, e.g., see the survey in [2] and other investigations [3–11].

The present investigation was undertaken to provide information on gas flows through tubes over a wide range of wall cooling spanning the highly cooled to the nearly adiabatic condition. The analysis accounts for the variation of properties across the flow and involves the numerical solution of the laminar-flow equations in differential form. Of specific interest are the internal flow and thermal distribution, pressure variation, wall shear-stress and heat-flux distributions along the flow, and how these quantities are influenced by the amount of wall cooling. Such an investigation apparently has not been reported in the literature for gases flowing through cooled tubes over this wide range of wall cooling. Most of the previous heat-transfer investigations apply to situations where the amount of wall cooling (or heating) is sufficiently small so that property variation is negligible, e.g., [12–15]. The few analyses, e.g., [16, 17], that have been made for a significant amount of wall cooling (or heating) are discussed in Section III in connection with the present results. These latter analyses differ from the present analysis in that the inlet profiles were chosen therein to be nonuniform, presumably because of a relatively long uncooled (or unheated) portion of tube upstream [16] or because of the effects of gas heating upstream [17]. The present analysis accounts for the simultaneous growth of both the velocity and the thermal layers in the inlet region, since the axial velocity and the total enthalpy profiles were taken to be uniform at the tube inlet.

The analysis is briefly described (Section II), a discussion of the numerical calculations and applicability of the results follows (Section III), and then the results are presented (Section IV). The results of the calculations and the comparisons to experimental data are shown graphically.

II Analysis

A brief description of the analysis is given to indicate the differential form of the conservation equations that is considered, the spirit of the calculation scheme, and the global conservation equations which also must be satisfied by the numerical calculations. Details of the finite-difference formulation are given in [1].

For steady axisymmetric laminar flow the conservation equations that are taken to describe the flow through a stationary tube are as follows:

continuity

$$\frac{\partial}{\partial z}(\rho' w') + \frac{1}{r}\frac{\partial}{\partial r}(r\rho' u') = 0 \tag{1}$$

axial momentum

[1] This work presents the results of one phase of research carried out in the Propulsion Research and Advanced Concepts Section of the Jet Propulsion Laboratory, California Institute of Technology, under contract NAS7-100, sponsored by the National Aeronautics and Space Administration.

[2] Numbers in brackets designate References at end of paper.

Contributed by the Heat Transfer Division of The American Society of Mechanical Engineers and presented at the AIChE-ASME Heat Transfer Conference, Denver, Colo., August 6–9, 1972. Manuscript received by the Heat Transfer Division May 14, 1971. Paper No. 72-HT-45.

$$\rho' w' \frac{\partial w'}{\partial z} + \rho' u' \frac{\partial w'}{\partial r} = -\frac{dp'}{dz} + \frac{1}{r}\frac{\partial}{\partial r}\left(r\mu' \frac{\partial w'}{\partial r}\right) \quad (2)$$

total energy

$$\rho' w' \frac{\partial H_t'}{\partial z} + \rho' u' \frac{\partial H_t'}{\partial r} = \frac{1}{r}\frac{\partial}{\partial r}\left(rk' \frac{\partial T'}{\partial r}\right) + \frac{1}{r}\frac{\partial}{\partial r}\left(rw'\mu' \frac{\partial w'}{\partial r}\right) \quad (3)$$

In these equations where the primes refer to dimensional quantities, w' and u' are the axial and radial velocity components in the z and r directions, respectively, and the total enthalpy is

$$H_t' = H' + \frac{(w')^2 + (u')^2}{2} \quad (4)$$

In this form of the momentum and energy equations, the important viscous stress is taken to be the shear stress in the axial direction, $\tau' = \mu' \partial w'/\partial r$, the important heat flux that in the radial direction, $q' = -k' \partial T'/\partial r$, and the pressure is taken to be uniform across the flow so that p' is a function of z only. The analysis accounts for variable properties across the flow, radial convection, and viscous dissipation. A perfect gas is considered

$$p' = \rho' R T' \quad (5)$$

with a viscosity–temperature relation described empirically as

$$\mu' \propto (T')^{\omega} \quad (6)$$

The Prandtl number $\mathrm{Pr} = \mu' c_p'/k'$ is presumed to be invariable with temperature. The distributions of axial velocity and of enthalpy are taken to be prescribed at the tube inlet, and the tube wall is taken to be impermeable and at a specified temperature dictated by external cooling so that the enthalpy distribution along the wall is known.

The system of equations was written in terms of nondimensional independent and dependent variables as given in [1]. By expressing the nondimensional version of equations (2) and (3) in finite-difference form, the numerical solution was carried out in the axial direction z because of the parabolic form of the equations. The calculation scheme consisted of using equations (2) and (3) to directly solve for the axial velocities and total enthalpies across the flow at the $z + \Delta z$ location from the known values at the prior $z - \Delta z$ and z locations by a method of successive iterations. The equation of state, viscosity relation, and total enthalpy were used to express p', ρ', μ', and H' or T' in terms of w' and H_t'. Radial velocities were obtained by integration of the continuity equation across the flow. The pressure distribution was calculated along the flow by using the mass-flow constraint which in nondimensional form is

$$I_{mi} - I_m = 0 \quad \text{where} \quad I_m = \int_0^1 \rho w \zeta d\zeta; \qquad \zeta = \frac{r}{r_w} \quad (7)$$

in conjunction with an averaged axial-momentum equation involving a balance between the axial convective acceleration and the pressure gradient. In this method, the pressure was adjusted so that the axial velocity was forced to satisfy the mass-flow constraint, which indeed must be the case.

The numerical formulation allows for variable radial and axial increments. The radial increment can be chosen to become progressively smaller as the wall is approached where gradients are larger. Without this provision the wall shear and heat flux cannot be obtained accurately with a reasonable number of radial increments for gas flows with an appreciable amount of wall cooling [1].

In addition to satisfying the mass-flow constraint, the integral form of the conservation equations (2) and (3), i.e., momentum and energy, should be satisfied. In nondimensional form these are

$$I_{M_i} - I_M = -\tfrac{1}{2}\Delta P + I_\tau \quad (8)$$

$$I_{H_i} - I_H = I_q \quad (9)$$

where the momentum and enthalpy integrals and pressure-change parameter are

$$I_M = \int_0^1 \rho w^2 \zeta d\zeta$$

$$I_H = \int_0^1 \rho w H_t \zeta d\zeta; \qquad \Delta P = \frac{p_i' - p'}{\rho_i'(w_i')^2} \quad (10)$$

and the shear-stress and heat-flux integrals are

Nomenclature

A_s = surface area of tube
c_f = friction coefficient, equation (12)
c_p' = specific heat at constant pressure
D = tube diameter
g = gravitational force per unit mass
$\tilde{h}$ = average heat-transfer coefficient based on log mean temperature difference
H' = static enthalpy
H_w = wall to inlet total enthalpy ratio, H_w'/H_{t_i}'
H_t' = total enthalpy, equation (4)
H_t = dimensionless total enthalpy, H_t'/H_{t_i}'
I_m, I_M, I_H = mass, momentum, and enthalpy integrals, equations (7) and (10)
I_τ, I_q = shear-stress and heat-flux integrals, equation (11)
k' = thermal conductivity
L = tube length
$\dot{m}$ = mass flow rate
Nu_D = Nusselt number, equation (12)
p' = static pressure
Pr = Prandtl number
ΔP = pressure-change parameter, equation (10)
q' = heat flux, $q' = -k' \dfrac{\partial T'}{\partial r}$
r = radial distance
r_w = tube radius
R = gas constant
Re_{D_i} = Reynolds number based on diameter, $\mathrm{Re}_{D_i} = \rho_i' w_i' D/\mu_i'$
T' = static temperature
T_w = wall to inlet temperature ratio, T_w'/T_i'
u' = radial velocity component
w' = axial velocity component
w = dimensionless velocity, w'/w_i'
z = axial distance
γ = specific-heat ratio
δ^* = boundary-layer displacement thickness
ζ = dimensionless radial distance, $\zeta = r/r_w$
μ' = viscosity
ν' = kinematic viscosity
ρ' = density
ρ = dimensionless density, ρ'/ρ_i'
τ' = shear stress, $\tau' = \mu' \dfrac{\partial w'}{\partial r}$
χ = dimensionless axial coordinate, $\dfrac{z}{D}\dfrac{1}{\mathrm{Re}_{D_i}}$
χ_L = dimensionless tube-length coordinate, $\dfrac{L}{D}\dfrac{1}{\mathrm{Re}_{D_i}}$
ω = exponent of viscosity–temperature relation

Subscripts

e = exit condition
i = inlet condition
ℓ = condition along tube centerline
w = condition at tube wall

Superscripts

$'$ = dimensional quantity
$\bar{}$ = average value across flow
$\tilde{}$ = average value for length of tube

$$I_\tau = \frac{1}{r_w \rho_i' (w_i')^2} \int_0^z \tau_w' dz = 2 \int_0^\chi \left(\frac{c_f}{2} \mathrm{Re}_{D_i} \right) d\chi$$

$$I_q = \frac{1}{r_w \rho_i' w_i' H_{t_i}'} \int_0^z q_w' dz = 2(1 - H_w) \int_0^\chi \mathrm{Nu}_D d \left(\frac{\chi}{\mathrm{Pr}} \right) \quad (11)$$

The friction coefficient c_f, the Nusselt number Nu_D, and the dimensionless axial coordinate χ are defined as follows:

$$\frac{c_f}{2} = \frac{\tau_w'}{\rho_i' (w_i')^2} \qquad \mathrm{Nu}_D = \frac{q_w'}{(H_{t_i}' - H_w')} \frac{D \, \mathrm{Pr}}{\mu_i'}$$

$$\chi = \frac{z}{D} \frac{1}{\mathrm{Re}_{D_i}} \quad (12)$$

These global constraints are important in determining if solutions have actually been obtained, since there are errors in the finite-difference approximations that depend upon mesh size and there are numerical round-off errors to a lesser extent. An attempt was made in [1] to satisfy these global relations at each axial step, but the scheme was unstable. Consequently, it is important to check that the global constraints are indeed satisfied before the results can be judged to be reliable. These relations are referred to in Section IV.

III Numerical Calculations and Applicability of Results

Calculations were made for a relatively low-speed flow through a tube at constant temperature with $H_w = 0.04$, 0.5, and 0.99. Values of the Prandtl number, viscosity-temperature exponent, and specific-heat ratio, typical of many gases, are shown in Table 1 along with the Mach numbers at the tube inlet. Table 1 also contains information on the number of radial increments used between the centerline and the wall, the radial increment at the wall, and the extent of the calculations in terms of the axial coordinate χ_L. For a moderately cooled tube ($H_w = 0.5$) the calculations extended to a relatively large value of χ_L for which the flow was nearly fully developed. Since the calculations were more difficult to make with a large amount of wall cooling ($H_w = 0.04$) and consumed a longer computation time, they extended to a smaller value of χ_L. For a nearly isothermal flow ($H_w = 0.99$) the calculations were carried out to a value of χ_L to establish a reference datum to appraise the effect of wall cooling and to compare to available experimental data. The calculations were made with a UNIVAC 1108 computer.

Axial-velocity and total-enthalpy profiles were taken to be uniform at the tube inlet. Of various inlet profiles that are found in practice, including those for abrupt entrances where flow separation, reattachment, and subsequent development occur, the uniform-flow condition was felt to be a plausible choice in order to calculate the flow and the thermal development farther downstream. The precise nature of the inlet condition which is usually unknown in most applications tends to be less important in determining the pressure drop (or rise), frictional loss, and heat transfer for the entire tube as the length-to-diameter ratio increases. Numerical calculations with other inlet conditions appear in [16, 17]. The case of entering cubic velocity and linear enthalpy profiles was treated in [17] for a severely cooled tube ($T_w = 0.05$). In [16] a relatively long uncooled (or unheated) portion of the tube was presumed to exist upstream so that the entering velocity profile where wall cooling (or heating) began was taken to be parabolic. Calculations were carried out in [16] for one wall cooling condition ($T_w = 0.5$) and wall heating conditions ($T_w = 2$ and 5) as well as for various uniform wall heat-flux conditions.

In the calculations the Reynolds number based on inlet conditions Re_{D_i} was chosen as 500. The results, however, are presented in terms of dimensionless variables that should lead to negligible error if they are applied to higher Reynolds-number flows. This is so because by a different choice of dimensionless

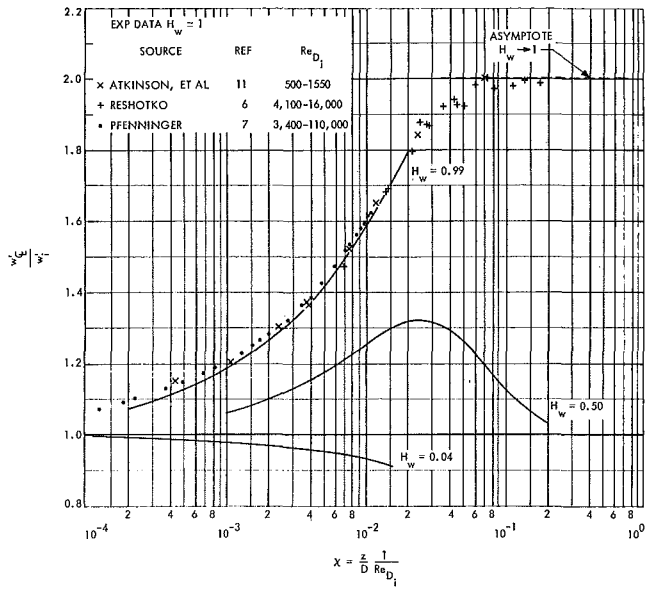

Fig. 1 Effect of wall cooling on the centerline velocity distribution along the flow

independent and dependent variables [16] than used in [1], the system of equations can be written in a form in which they depend upon the parameters M_i, Pr, ω, and γ along with H_w and the shape of the inlet profiles for the situation where the contribution of the radial velocity component to the kinetic energy in the total enthalpy expression equation (4) is negligible, i.e., $(u')^2/2 \ll (w')^2/2$. Experience has indicated that this is usually the case unless the Reynolds number is relatively small.

Utilization of the present results for much lower Reynolds-number flows, i.e., smaller ratio of inertia to viscous flows, is less clear since normal viscous stresses and axial heat conduction, not included in this analysis, begin to become important as indicated by constant-property calculations, e.g., see [18–24]. Although variable-property calculations apparently have not been carried out, the constant-property calculations indicate that axial heat conduction should not be significant provided that the Peclet number $\mathrm{Re}_{D_i}\mathrm{Pr}$ is on the order of 50 and larger. It should be noted in this regard that the calculation of variable- or constant-property internal flows at relatively low Reynolds numbers for which the equations (including the radial-momentum equation) are elliptic are more difficult to make in a meaningful way because of the need to specify realistic conditions either at or upstream of the tube inlet.

The question of free-convection effects also arises. This depends upon tube orientation and the magnitude of the gravitational forces relative to the viscous forces. For a variable-property flow this ratio of forces can be written in terms of a modified Grashof number and Reynolds number

$$\frac{\rho' g}{\mu' w'/D^2} = \left(\frac{gD^3}{\nu'^2} \right) \frac{1}{w'D/\nu'} = \frac{\mathrm{Gr}_D}{\mathrm{Re}_D}$$

Calculations in [16] for upward flow through a vertical tube with a uniform heat flux along its length indicated that the influence of buoyancy was not significant for values of $\mathrm{Gr}_D/\mathrm{Re}_D$ up to about 50. For other tube orientations, e.g., horizontal, variable-property calculations apparently have not been carried out for gases to appraise the importance of buoyancy effects. This would entail the inclusion of the radial- and circumferential-momentum equations in the system of equations. Of note is that the effect of free convection is less in gases at high temperatures, since $\mathrm{Gr}_D/\mathrm{Re}_D \propto 1/T^{1+\omega}$. In particular, the effect of free convection was not believed to be significant for a very high temperature gas flow by inference from the good agreement between the calculated and measured wall heat fluxes [1].

To apply the calculations to the flow of specific gases, sufficient

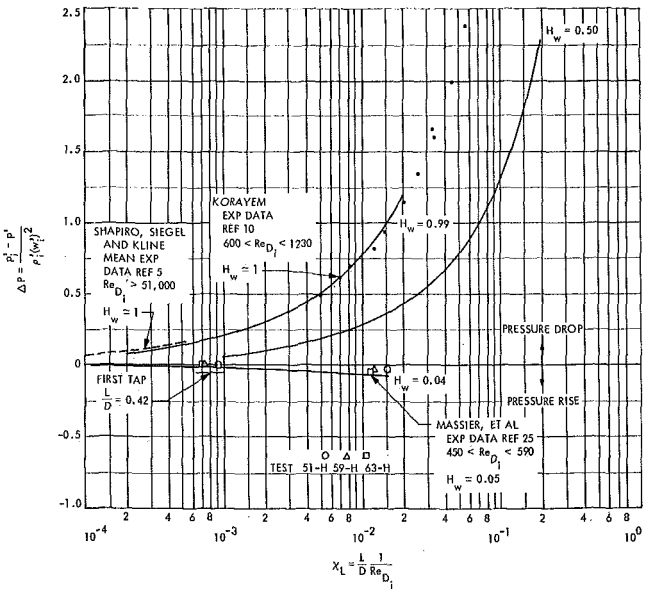

Fig. 2 Effect of wall cooling on the pressure changes along the flow

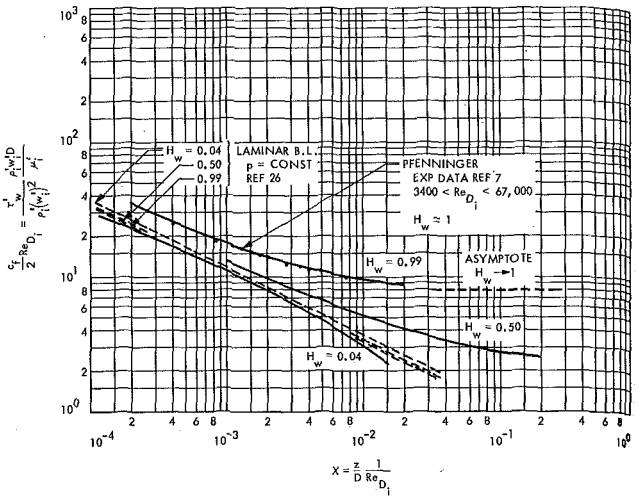

Fig. 3 Local wall friction along the flow

information must be available to determine the range of temperatures and pressures for which dissociation, ionization, radiation, and rarefaction effects are not important, since these effects are not accounted for in the analysis.

IV Results

The results of the calculations and comparisons to available experimental data are shown in Figs. 1–9. The global features of the flow with a negligible amount of wall cooling ($H_w = 0.99$) are evident in Figs. 1–4. As the shear layer grew in thickness and eventually extended to the centerline along the tube, the core flow accelerated (Fig. 1), the pressure dropped (Fig. 2), the local shear stress shown in terms of the friction group decreased (Fig. 3), and consequently so did the average shear stress (Fig. 4). There is reasonable agreement between the present calculations that display these familiar trends and the relatively small amount of experimental data with negligible wall cooling that is shown in Figs. 1–4 and summarized in Table 2. In the inlet region, measured centerline velocities (Fig. 1) and pressures (Fig. 2) are larger than calculated. This may be partially caused by the finite thickness of the shear layer at the inlet of the tubes. These tubes were preceded by contraction sections. Farther along the tubes there is better agreement between the calculated and measured centerline velocities and pressures. The calculated local shear stress also agrees well with the measurements by Pfenninger [7]. Of note is that laminar flow was maintained at rather large Reynolds numbers in the experimental investigations of Shapiro, Siegel, and Kline [5], Reshotko [6], and Pfenninger because of the stabilizing effect of acceleration on disturbances in the contraction sections and also in the inlet region of the tubes. Reshotko and Pfenninger also used screens upstream to minimize disturbances. On the other hand, the experimental data of Kays and London [4] (Fig. 4) were obtained in a tube with an abrupt inlet where flow separation, reattachment, and development occurred downstream. However, the length-to-diameter ratios of the tubes were sufficiently large (Table 1) so that there still is good agreement between the average shear stresses inferred from the measurements and those calculated (Fig. 4).

With a large amount of wall cooling ($H_w = 0.04$) the core flow decelerated (Fig. 1) and the pressure rose (Fig. 2) in the inlet region of the tube. The pressure measurements by Massier, Back, and Roschke [25] (Table 2) indicated a relatively small pressure rise (Fig. 2) although the predicted rise is more than observed experimentally. This discrepancy is partially caused by the location of the first pressure tap in the tube inlet region being downstream of the actual inlet. Nevertheless, there is an entirely different behavior in a highly cooled flow compared to a nearly isothermal flow. The available pressure measurements, although admittedly few, support the predicted trends. Heat-transfer measurements described in [25] were found to be in good agreement in [1] with the predicted values that are shown in Fig. 5. These heat-transfer measurements are not shown again herein on a local basis, but instead are shown on an overall basis subsequently.

The check on the global momentum and energy constraints is shown in Fig. 6. The check was very good for a moderately cooled tube ($H_w = 0.5$) and is considered to be satisfactory for a highly cooled tube. For a nearly isothermal flow the check was not as good just downstream of the inlet, although farther downstream the discrepancy is small. For example, for a nearly isothermal flow at a Reynolds number of 500 the respective differences between the average shear stress for tubes with an L/D of 1 and 10 are 10 percent and 1.8 percent as obtained by using the calculated local shear stress or the shear-stress integral inferred from the momentum balance.

Fig. 6 also indicates the momentum changes and energy losses in the flow. These relations apply as well to tubes of given lengths, i.e., $\chi = \chi_L$.

The general agreement with available measurements and the satisfactory check with the global constraints warrant a more specific look at the effect of wall cooling indicated by the calculations.

The predicted development of the velocity and enthalpy-

Table 1 Information on numerical calculations

H_w	Pr	ω	γ	M_i	No. of radial increments	$\Delta\xi_w$ radial increment at wall	No. of axial steps	χ_L axial coordinate
0.99	$\frac{2}{3}$	$\frac{3}{4}$	$\frac{5}{3}$	0.1	20	0.01	...	0.02
0.50	0.7	0.7	1.4	0.1	20	0.04	7600	0.2
0.04	$\frac{2}{3}$	$\frac{3}{4}$	$\frac{5}{3}$	0.076	40	0.0025	4030	0.016

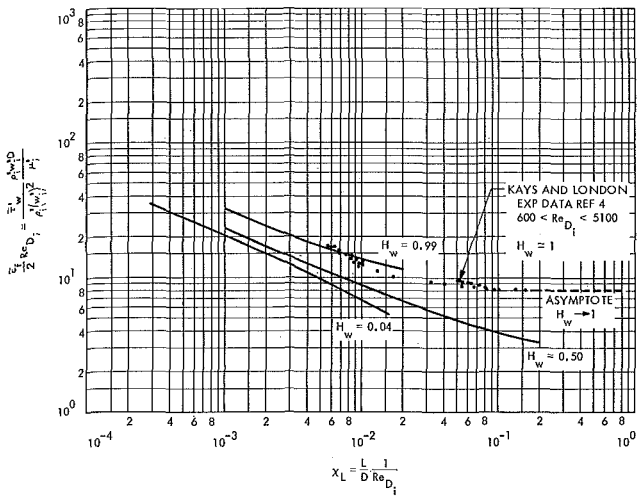

Fig. 4 Wall friction for entire tube

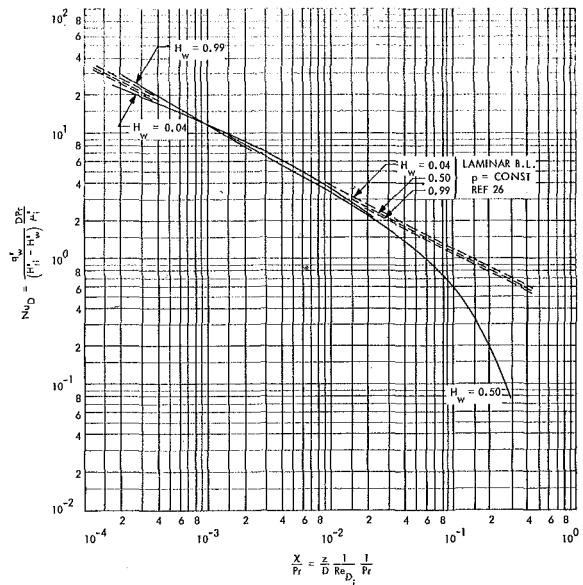

Fig. 5 Local heat transfer along the flow

difference profiles along a moderately cooled tube ($H_w = 0.5$) is shown in Fig. 7. The profiles became less steep near the wall as the shear and thermal layers grew along the tube wall; consequently, the shear stress (Fig. 3) and heat flux (Fig. 5) decreased. The shear and thermal layers extended to the centerline at an axial location of $\chi \simeq 0.01$. At this location the centerline velocity exceeded the inlet velocity by about 25 percent, so that similar to a nearly isothermal flow the shear layer grew in an acceleration region, but the acceleration was less (Fig. 1). Farther along the tube at a location of $\chi = 0.025$, the centerline velocity reached a peak value and then the flow along the centerline decelerated because of cooling and the attendent increase in the density of the gas (Fig. 6). In the deceleration region the velocity profiles did not develop a point of inflection; hence the flow would still be more stable to small disturbances. Of note is that at the largest value of $\chi = 0.2$ where the flow was nearly fully developed, e.g., see Figs. 3 and 6, the centerline velocity was about the same as the inlet value. The enthalpy-difference profiles depict the loss of energy by heat transfer to the wall (Fig. 5).

The development of the profiles along the tube is not shown for a nearly isothermal or a highly cooled flow. For example, see [8] for predicted velocity profiles for an isothermal flow and [1] for predicted velocity and enthalpy profiles for a highly cooled flow, that include comparisons to measurements.

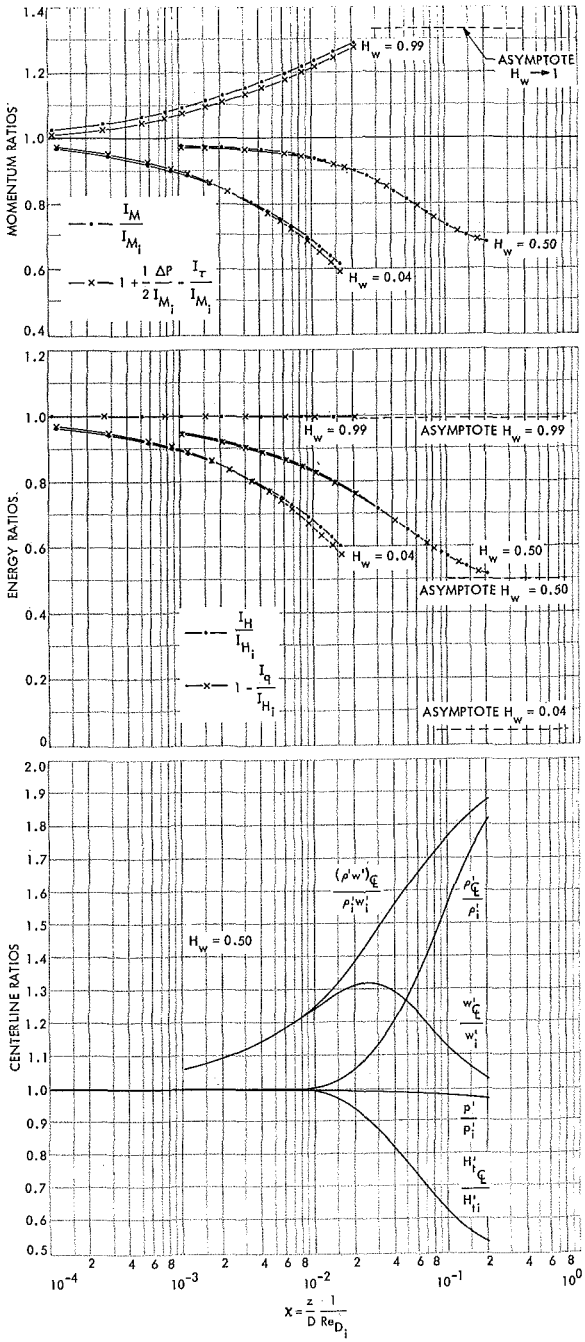

Fig. 6 Momentum and energy ratios along the flow with wall cooling; and centerline distributions along the flow in particular for moderate cooling, $H_w = 0.50$

The influence of wall cooling on the velocity and mass-flux profiles is shown in Fig. 7 at a particular axial location, $\chi = 0.01$. Near the wall the velocity profile was steeper for a highly cooled flow than for a nearly isothermal flow, but it was less steep for a moderately cooled flow, presumably because of the smaller magnitude of the velocity in the core region compared to a nearly isothermal flow. However, the local shear stress (Fig. 3) became progressively smaller with the amount of wall cooling, i.e., as H_w decreased, because of the lower viscosities at the wall.

The mass-flux profiles determined the basic flow field. Because of the increase in the density of a gas in the region of a cooled wall, the mass flux was larger, and in particular for a highly cooled wall exceeded the mass flux in the core region. In this case the flow along the centerline decelerated starting from the inlet of the tube (Fig. 1). With moderate cooling the mass flux in the region near the wall was also larger than for a

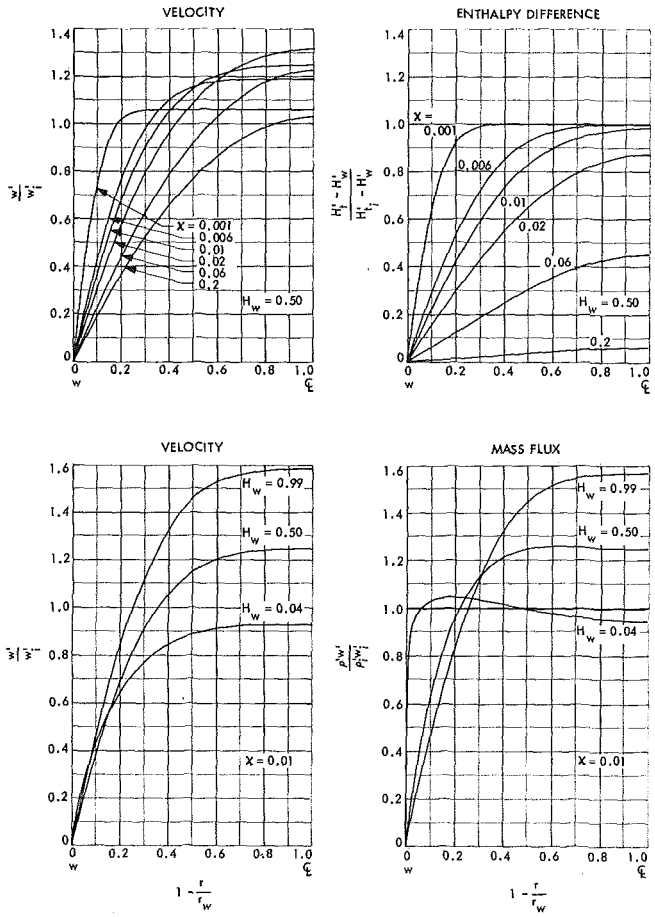

Fig. 7 Velocity and enthalpy profiles across the flow of various axial locations χ for moderate cooling, H_w = 0.50; and effect of wall cooling on the velocity and mass-flux profiles across the flow at χ = 0.01

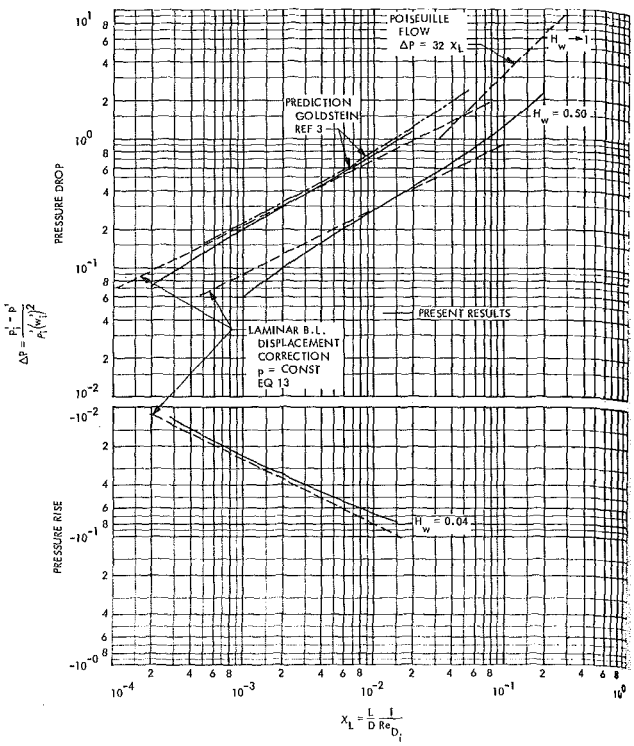

Fig. 8 Pressure changes along the flow

nearly isothermal flow, and therefore the centerline velocities were lower. Even for this case the eventual increase in gas density in the core region farther along the tube leads to flow deceleration along the centerline.

The mass-flux deficit in the shear layer in the inlet region also determined the kind of pressure variation there (Fig. 8). Application of the inviscid form of the momentum equation in the core-flow region and utilization of the continuity equation give the following expression for the pressure change for a low-speed flow where the displacement thickness δ^* is small compared to the radius of the tube:

$$\Delta P = 2(\delta^*/r_w) \tag{13}$$

Estimates from equation (13) are shown in Fig. 8 based on the

Table 2 Experimental data

Source	Ref.	Fluid	H_w	Re_{D_i}	D in.	$\frac{L}{D}$	Inlet configuration	Measurements
Kays and London (1952)*	4	air	~1	600 to 2,500	0.231	80	abrupt inlet	average wall shear stress; average heat transfer with wall heating; see [12]
Shapiro, Siegel, and Kline (1954)	5	air	~1	51,000 to 113,000	1.25	48	contraction section upstream	pressure drop
Kays (1955)	12	air	~1.25	600 to 2,500	less than 0.25	42 to 80	abrupt inlet	heat transfer with wall heating
Reshotko (1958)	6	air	~1	4,100 7,600 16,000	2.02	110 to 670	contraction section upstream, with screens	velocity profiles; local pressure drop
Pfenninger (1961)	7	air	~1	3,400 to 110,000	2.0	250 to 350	contraction section upstream, with screens	velocity profiles; local wall shear stress obtained from velocity profiles
Korayem (1965)	10	water–sugar solution, Newtonian	~1	600 to 1,230	0.93	5 to 38	contraction section upstream	velocity profiles; pressure drop
Atkinson, Kemblowski, and Smith (1967)	11	water	~1	500 to 1,550	1.0	48	series of brass gauzes in tube	velocity profiles
Massier, Back, and Roschke (1969)	25	high-temperature argon	0.039 to 0.055	450 to 590	1.95	7	contraction section upstream	pressure drop; velocity and enthalpy profiles; local and average heat transfer

* Other data reported by Kays and London are for L/D = 16, 35, and 100; Re_{D_i} from 640 to 5100.

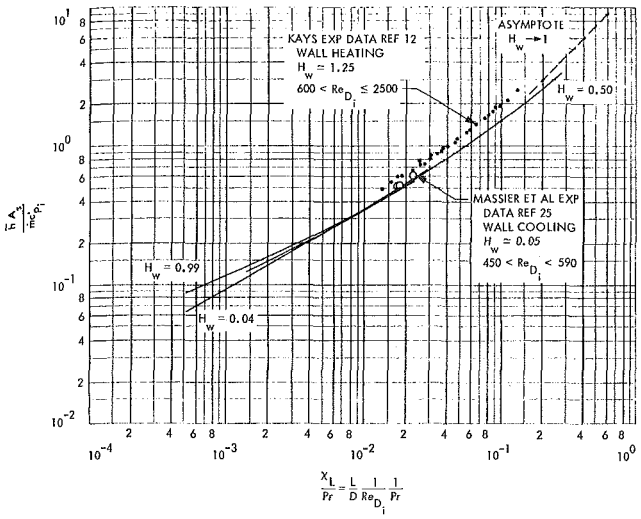

Fig. 9 Average heat-transfer group for entire tube

growth of a low-speed laminar boundary layer with constant free-stream velocity, i.e., p = const, along a cooled surface [26]. These estimates are too high for a nearly isothermal and a moderately cooled flow. This difference may be attributable to the accuracy of the tube flow calculations just downstream of the inlet and to the fact that flow acceleration occurred in this region which would decrease the displacement thickness, e.g., see [27]. Nevertheless, on an overall basis, the estimates from equation (13) indicate the magnitude of the pressure variation just downstream of the inlet. Of note is that Fig. 8 is a logarithmic representation. The actual magnitudes of the rather small pressure changes for tubes with small values of χ_L are better seen in the linear vertical representation of Fig. 2.

The amount of wall cooling significantly influenced the magnitude of the local shear stress in the inlet region (Fig. 3). Whereas rather small differences are estimated from laminar-boundary-layer theory for a constant-free-stream-velocity flow over a cooled surface, the tube flow calculations indicate larger differences and an opposite effect of wall cooling. This is believed to occur because with wall cooling velocity differences across the flow are less and the smaller core flow accelerations or decelerations would increase the shear stress less than in a nearly isothermal flow, e.g., see [27, 28] for laminar-boundary-layer calculations.

The local heat flux in nondimensional form in terms of the Nusselt number (Fig. 5) is insensitive to the amount of wall cooling and thus acceleration or deceleration in the inlet region. This trend is also consistent with laminar-boundary-layer calculations [27, 28].

Of significant importance is the reduction in the shear stress with the amount of wall cooling as seen in Fig. 3 on a local basis and in Fig. 4 on an average basis. Hence the frictional drag would be less and the mechanical energy losses would be smaller than for an isothermal flow. As an example, for a fully developed isothermal flow the friction group $\frac{c_f}{2}\mathrm{Re}_{D_i}$ is 8, whereas for a moderately cooled flow the asymptotic value of $\frac{c_f}{2}\mathrm{Re}_{D_i}$ is about 2.5. Correspondingly, the pressure change is also less since application of the momentum equation in the fully developed region gives a relationship between the pressure change and the friction group when the inlet effects have become insignificant

$$\Delta P = 4\left(\frac{c_f}{2}\mathrm{Re}_{D_i}\right)\chi_L$$

For a moderately cooled flow, $\Delta P \simeq 10\chi_L$, while for Poiseuille flow ($H_w = 1$), $\Delta P = 32\chi_L$, see Fig. 8. Of note is that eventually the pressure must drop along a highly cooled tube that is sufficiently long so that the flow becomes fully developed, i.e., where there is essentially no heat transfer to the wall. In general, the asymptotic value for the friction group is

$$\frac{c_f}{2}\mathrm{Re}_{D_i} = 4\left(\frac{\mu_w'}{\mu_i'}\right)\left(\frac{w_\ell'}{w_i'}\right)$$

and the asymptotic velocity profile is parabolic

$$\frac{w'}{w_i'} = \frac{w_\ell'}{w_i'}(1 - \zeta^2)$$

The calculated velocity profile shown in Fig. 7 at $\chi = 0.2$ for a moderately cooled tube is very nearly parabolic, consistent with the expected behavior. Of course, numerical calculations must be carried out to determine the centerline velocity before the asymptotic values for the friction group and the pressure change are specified explicitly.

To facilitate the use of the results in heat-transfer applications, an average heat-transfer coefficient $\bar{h}$ was calculated based on the log mean temperature difference. The results are shown in Fig. 9 in terms of the heat-transfer group

$$\frac{\bar{h}A_s}{\dot{m}c_{p_i}'}$$

A_s is the surface area of the tube and $\dot{m}$ is the mass flow rate. In this representation $\bar{h}$ can be obtained from the ordinate in Fig. 9 given the inlet conditions, i.e., $\dot{m}$, c_{p_i}', Re_{D_i}, and tube length in terms of L/D. It is also a simple matter to calculate the length of tube required to cool a gas to a given exit temperature $\bar{T}_e'$ with specified inlet and wall temperatures and inlet conditions. For example, for a specified thermal "effectiveness," $\epsilon = \dfrac{T_i' - \bar{T}_e'}{T_i' - T_w'}$, the heat-transfer group is known from an energy balance (typical heat-exchanger calculation with the average heat-transfer coefficient based on the log mean temperature difference and one fluid (surface) at a uniform temperature)

$$\frac{\bar{h}A_s}{\dot{m}c_{p_i}'} = \ln\left[\frac{1}{1-\epsilon}\right] \tag{14}$$

Therefore, the tube length in L/D can be obtained from the abscissa in Fig. 9 and the known inlet conditions. For the other situation where the exit temperature is to be calculated for a given tube length and specified inlet and wall temperatures and inlet conditions, χ_L is known and the heat-transfer group can be obtained from Fig. 9. Equation (14), when rewritten as follows, is then used to calculate ϵ and thus $\bar{T}_e'$

$$\epsilon = 1 - \exp\left(-\frac{\bar{h}A_s}{\dot{m}c_{p_i}'}\right)$$

Representations that involve the Nusselt number and the Reynolds number with properties evaluated at some average or "bulk" condition are difficult to use.

The heat-transfer group shown in Fig. 9 did not vary much with wall cooling, a trend also consistent with measurements that extended over a large range of H_w from the wall heating condition $H_w \simeq 1.25$ (Kays [12]) to a highly cooled wall, $H_w \simeq 0.05$ [25]. This trend was also observed experimentally by Kays and Nicoll [29] for air flow through a cooled tube (T_w from 0.85 to 0.56) at Reynolds numbers Re_D from 950 to 1400, but with a relatively long uncooled length of tube upstream (L/D = 64) so that the entering velocity profile was probably parabolic where cooling began. The asymptotic value for the heat-transfer group shown in Fig. 9 was obtained from the expression

$$\frac{\bar{h}A_s}{\dot{m}c_{p_i}'} = 4\left(\frac{\bar{h}D}{k_i'}\right)\left(\frac{\chi_L}{\mathrm{Pr}}\right)$$

by taking $\bar{h}D/k_i' = 3.65$ for $H_w \to 1$. The average or "bulk" enthalpy for the flows considered can be obtained from Fig. 6 since

$$\frac{I_H}{I_{Hi}} = \frac{\overline{H_t'}}{H_{t_i}'}$$

Note that the abscissa in Fig. 6 is χ, not χ/Pr as it is in Figs. 5 and 9.

V Summary and Conclusions

Numerical solutions of the laminar-flow equations have been presented for gas flows through tubes for a wide range of wall cooling from nearly adiabatic conditions to wall-to-gas enthalpy ratios as low as 0.04. The large changes in properties that occur across the flow for the highly cooled conditions were taken into account in the analysis.

The flow field was found to be strongly influenced by heat transfer. Because of the increase in the density of a gas in the region of a cooled wall, the mass flux in this region as $H_w \to 0$ exceeded that in the core. Correspondingly, the flow along the centerline decelerated in the inlet region. With moderate wall cooling, $H_w = 0.5$, the mass flux in the wall region was also larger than for a nearly isothermal flow, $H_w \to 1$, and consequently the centerline velocities were lower. Even for this case, the eventual increase in gas density in the core region farther along the tube led to flow deceleration along the centerline because of cooling.

Smaller pressure changes and wall friction were found with cooling. The pressure drop was less because of the smaller mass-flux deficit in the shear flow. For the case of a highly cooled wall there was a pressure rise in the inlet region instead. Of significance is the reduction in shear stress with the amount of wall cooling since the frictional drag would be less and the mechanical energy losses would be smaller than for an isothermal flow. With wall cooling the shear stress is reduced because velocity differences across the flow are less and the smaller core-flow accelerations or decelerations would increase the shear stress less than in a nearly isothermal flow.

The average heat-transfer coefficient for tubes did not vary much with wall cooling primarily because of the insensitivity of the heat flux (when normalized by the driving potential for heat transfer) to the amount of wall cooling and thus acceleration or deceleration in the inlet region.

The general agreement between the calculations and available measurements and the satisfactory check of the global constraints indicate that reliable predictions can be made of quantities of engineering importance, i.e., pressure drop (or rise), frictional losses, and heat transfer, for the flow of gases through cooled tubes.

Acknowledgment

The author expresses his gratitude to Mr. M. Diethelm of JPL for programming and carrying out the numerical calculations on a digital computer.

References

1 Back, L. H., "Very High Temperature Laminar Flow of a Gas through the Entrance Region of a Cooled Tube–Numerical Calculations and Experimental Results," *International Journal of Heat and Mass Transfer*, Vol. 15, No. 5, May 1972, pp. 1001–1021.

2 Christiansen, E. B., and Lemmon, H. E., "Entrance Region Flow," *AIChE Journal*, Vol. 11, No. 6, Nov. 1965, pp. 995–999.

3 Goldstein, S., *Modern Developments in Fluid Dynamics*, Vol. I, Oxford University Press, 1938, p. 307.

4 Kays, W. M., and London, A. L., "Convective Heat-Transfer and Flow-Friction Behavior of Small Cylindrical Tubes—Circular and Rectangular Cross Sections," TRANS. ASME, Vol. 74, 1952, pp. 1179–1189.

5 Shapiro, A. H., Siegel, R., and Kline, S. J., "Friction Factor in the Laminar Entry Region of a Smooth Tube," *Proceedings of the Second U. S. National Congress of Applied Mechanics*, P. M. Naghdi, ed., ASME, New York, N. Y., 1954, pp. 733–741.

6 Reshotko, E., "Experimental Study of the Stability of Pipe Flow, I—Establishment of an Axially Symmetric Poiseuille Flow," Progress Report No. 20-364, Jet Propulsion Laboratory, Pasadena, Calif., Oct. 1958.

7 Pfenninger, W., "Boundary Layer Suction Experiments with Laminar Flow at High Reynolds Numbers in the Inlet Length of a Tube by Various Suction Methods," *Boundary Layer and Flow Control*, Vol. 2, Lachmann, G. V., ed., 1961, Pergamon Press, Elmsford, N. Y., pp. 961–980.

8 Sparrow, E. M., Lin, S. H., and Lundgren, T. S., "Flow Development in the Hydrodynamic Entrance Region of Tubes and Ducts," *Physics of Fluids*, Vol. 7, No. 3, Mar. 1964, pp. 338–347.

9 Hornbeck, R. W., "Laminar Flow in the Entrance Region of a Pipe," *Appl. Sci. Res.*, Vol. 13, Sec. A, No. 2–3, Dec. 1964, pp. 224–232.

10 Korayem, A. Y., "Non-Isothermal Laminar Flow of Non-Newtonian Fluids in the Entrance Region of a Pipe," PhD thesis, University of California, Davis, Calif., 1965 (data reported by McKillop, A. A., Harper, J. C., Bader, H. J., and Korayem, A. Y., "Variable Viscosity Entrance-Region Flow of Non-Newtonian Liquids," *International Journal of Heat and Mass Transfer*, Vol. 13, May 1970, pp. 901–909); also private communication with A. A. McKillop.

11 Atkinson, B., Kemblowski, Z., and Smith, J. M., "Measurements of Velocity Profile in Developing Liquid Flows," *AIChE Journal*, Vol. 13, No. 1, Jan. 1967, pp. 17–20.

12 Kays, W. M., "Numerical Solutions for Laminar-Flow Heat Transfer in Circular Tubes," TRANS. ASME, Vol. 77, 1955, pp. 1265–1274.

13 Hornbeck, R. W., "An All-Numerical Method for Heat Transfer in the Inlet of a Tube," ASME Paper No. 65-WA/HT-36.

14 Ulrichson, D. L., and Schmitz, R. A., "Laminar-Flow Heat Transfer in the Entrance Region of Circular Tubes," *International Journal of Heat and Mass Transfer*, Vol. 8, No. 2, Feb. 1965, pp. 253–258.

15 Manohar, R., "Analysis of Laminar-Flow Heat Transfer in the Entrance Region of Circular Tubes," *International Journal of Heat and Mass Transfer*, Vol. 12, No. 1, Jan. 1969, pp. 15–22.

16 Worsoe-Schmidt, P. M., and Leppert, G., "Heat Transfer and Friction for Laminar Flow of Gas in a Circular Tube at High Heating Rate," *International Journal of Heat and Mass Transfer*, Vol. 8, 1965, pp. 1281–1301.

17 Incropera, F. P., and Leppert, G., "Laminar Flow Heat Transfer from an Argon Plasma in a Circular Tube," *International Journal of Heat and Mass Transfer*, Vol. 10, Dec. 1967, pp. 1861–1873.

18 Schneider, P. J., "Effect of Axial Fluid Conduction on Heat Transfer in the Entrance Regions of Parallel Plates and Tubes," TRANS. ASME, Vol. 79, 1957, pp. 765–773.

19 Wang, Y. L., and Longwell, P. A., "Laminar Flow in the Inlet Section of Parallel Plates," *AIChE Journal*, Vol. 10, No. 3, May 1964, pp. 323–329.

20 Simuni, L. M., "Motion of a Viscous Incompressible Fluid in a Plane Pipe," *Vychisl. Mate. i Mate. Fiz.*, Vol. 5, No. 6, 1965, pp. 1138–1141 (translation by Lockheed Missiles & Space Co., Sunnyvale, Calif., available as NASA-STAR N-66-18422).

21 Vrentas, J. S., Duda, J. C., and Bargeron, K. G., "Effect of Axial Diffusion of Vorticity in Flow Development in Circular Conduits: Part I, Numerical Solutions," *AIChE Journal*, Vol. 12, No. 5, Sept. 1966, pp. 837–844.

22 Hennecke, D. K., "Heat Transfer by Hagen–Poiseuille Flow in the Thermal Development Region with Axial Conduction," *Wärme und Stoffübertragung*, Vol. 1, 1968, pp. 177–184.

23 Friedmann, M., Gillis, J., and Liron, N., "Laminar Flow in a Pipe at Low and Moderate Reynolds Numbers," *Appl. Sci. Res.*, Vol. 19, No. 6, Nov. 1968, pp. 426–438.

24 Schmidt, F. W., and Zeldin, B., "Laminar Flows in Inlet Sections of Tubes and Ducts," *AIChE Journal*, Vol. 15, No. 4, July 1969, pp. 612–614.

25 Massier, P. F., Back, L. H., and Roschke, E. J., "Heat Transfer and Laminar Boundary-Layer Distributions in an Internal Subsonic Gas Stream at Temperatures Up to 13,900 Deg R," JOURNAL OF HEAT TRANSFER, TRANS. ASME, Series C, Vol. 91, No. 1, Feb. 1969, pp. 83–90.

26 Back, L. H., "Effects of Severe Surface Cooling and Heating on the Structure of Low Speed, Laminar Boundary Layer Gas Flows with Constant Free-Stream Velocity," TR 32-1301, Jet Propulsion Laboratory, Pasadena, Calif., 1968.

27 Back, L. H., "Acceleration and Cooling Effects in Laminar Boundary Layers—Subsonic, Transonic and Supersonic Speeds," *AIAA Journal*, Vol. 8, No. 4, Apr. 1970, pp. 794–802.

28 Cohen, C. B., and Reshotko, E., "Similar Solutions for the Compressible Laminar Boundary Layer with Heat Transfer and Pressure Gradient," NACA R-1293, 1956.

29 Kays, W. M., and Nicoll, W. B., "Laminar Flow Heat Transfer to a Gas With Large Temperature Differences," JOURNAL OF HEAT TRANSFER, TRANS. ASME, Series C, Vol. 85, No. 4, Nov. 1963, pp. 329–338.

D. SOMOGYI
Engineering Consultant.

H. H. YEN
Senior Staff Engineer.

Sperry Rand Space Support Div., Huntsville, Ala.

An Approximate Analysis of the Diffusing Flow in a Self-controlled Heat Pipe[1]

Constant-density two-dimensional axisymmetric equations are presented for the diffusing flow of a class of self-controlled heat pipes. The analysis is restricted to the vapor space. Condensation of the vapor is related to its mass fraction at the wall by the gas kinetic formula. The Karman–Pohlhausen integral method is applied to obtain approximate solutions. Solutions are presented for a water heat pipe with neon control gas.

Introduction

THE FORMULATION of an analytical model for the performance of a heat pipe was first developed by Cotter [1].[2] He derived the governing equations for the processes taking place and indicated capillary- and incipient-boiling limits of operation. A number of modifications to this theory have been proposed by various investigators. For the case of incompressible vapor flow and zero gravity, Cotter's meniscus boundary conditions have been modified by Ernst [2] who assumed that the pressure equality between liquid and vapor occurs at the interface between condenser and evaporator sections. Various alternative expressions for the pressure drop in the gas and liquid have been suggested. Busse [3] treated laminar vapor flow in a cylindrical heat pipe for constant heat addition and removal by solving the Navier–Stokes equation through a fourth-power polynomial approximation for the axial-velocity profile. Haskin [4] considered a heat pipe with an adiabatic section where the pressure drop was found by assuming Poiseuille flow. Brosens [5] used Poiseuille flow throughout the pipe. For high vapor velocities Levy [6] analyzed a one-dimensional compressible vapor flow decoupled from the liquid phase and predicted a choking limit. Many other models exist for the description of the flow and are valid in various regions of applicability.

It was demonstrated by Grover et al. [7] that if a heat pipe contains a noncondensible gas it is driven to the end of the condenser. There it forms a stagnant zone the length of which is proportional to the mass of the gas and its mean temperature and inversely proportional to the pressure. The result is an effective shortening of the condenser, thus reducing the total axial heat-transfer capability of the heat pipe. If the axial heat flux is increased the pressure increases correspondingly and the gas zone contracts to allow more of the condenser to become operative again. The converse is also true when the heat flux is decreased. Cotter first noted that this feature might be extremely useful in certain applications. Katzoff [8] suggested that one possible technique to accomplish thermal control with the heat pipe serving as a variable thermal conductor is to intentionally introduce an inert gas into the vapor space. Bienert [9] showed that control is improved by the use of large inert-gas reservoirs. He further indicated that it is advantageous to keep the reservoir at the temperature of the evaporator through intimate contact to reduce temperature fluctuations. Bienert, however, assumed a perfect interface between the vapor and the inert gas. This may or may not be a good approximation depending on certain parameters. A number of investigators have experimented with inert-gas-controlled heat pipes. Among the most recent investigations is that reported by Marcus and Fleischman [10]. Their analysis also considered a perfect interface. Based on their experimental results, however, they concluded that diffusion and axial conduction played a strong part in determining the actual diffused region and controllability.

To date no theoretical analysis of the flow in a heat pipe has been presented that includes the mutual diffusion between the vapor and the inert gas. The object of the present investigation is to study the theoretical behavior of the diffusing flow and its effect on the self-control capability. The analysis is restricted to the vapor space and completely decoupled from the liquid flow in the wick. Only incompressible and isothermal flow fields are treated in a cylindrical heat pipe. The control-gas concept is the hot non-wicked reservoir.

Flow Equations

The determination of the effect of the inert gas diffusion on the self-control capability of a heat pipe is a complex problem. The thermodynamic-state variables in the heat pipe are coupled to those in the inert-gas chamber. A complete evaluation would involve the study of a flow field with evaporation or condensation, convection, and diffusion in an irregular geometry. The problem

[1] This investigation was supported by the National Aeronautics and Space Administration under contract NAS8-20055. Technical monitoring was by D. Counter, S&E-ASTR-MA, Marshall Space Flight Center, Huntsville, Ala.

[2] Numbers in brackets designate References at end of paper.

Contributed by the Heat Transfer Division for publication (without presentation) in the JOURNAL OF HEAT TRANSFER. Manuscript received by the Heat Transfer Division April 26, 1971. Paper No. 72-HT-M.

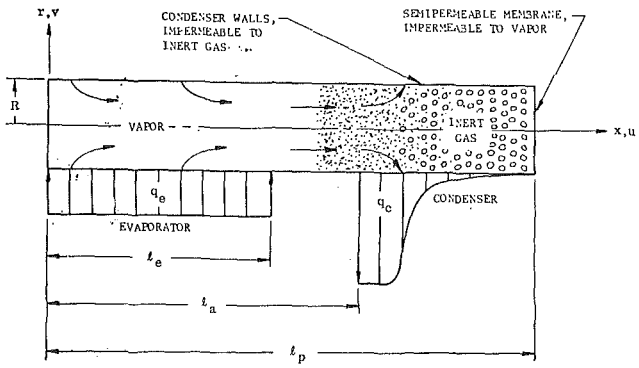

Fig. 1 Heat-pipe inert-gas diffusion model

is simplified by treating the decoupled system shown in Fig. 1. The heat-pipe vapor space is separated from the inert-gas chamber by a semipermeable membrane which is impermeable to the working-fluid vapor. The interaction is determined by a number of iterations on the common parameters of the final solutions.

The analysis considers only the vapor space and ignores the effects of the liquid flow in the wick. This restriction is justified if it is assumed that only those geometries are treated which satisfy an overall heat-pipe design analysis. This study refers specifically to the cylindrical heat pipe whose design is presented in [11]. This is a high-performance water heat pipe designed to transfer a heat load of approximately 640 Btu/hr at 190 deg F. Total length is 38 in. with a diameter of 0.75 in. Heat is added uniformly over a 24-in. length; the adiabatic as well as the condenser lengths are 7 in. The wick consists of sintered metal of high thermal conductivity diffusion-bonded to the wall with an inner diameter of 0.433 in. The design analysis consisted of a one-dimensional model with a perfect vapor–inert-gas interface.

In the operating regime of this heat pipe the axial-flow Reynolds number $\mathrm{Re}_a \leq 1000$; hence the flow is laminar. Furthermore, if only vapor–inert-gas combinations of equal molecular weights are considered, density and temperature gradients generally experienced in a heat pipe have second-order effects on the primary flow parameters. Equal molecular weights also imply uniform mixture viscosity if the collision diameters are similarly equivalent. Then for constant density and viscosity, isothermal flow, and negligible body forces the equations of conservation of mass, species, and momentum in axisymmetric cylindrical coordinates are

$$\frac{\partial u}{\partial x} + \frac{1}{r}\frac{\partial}{\partial r}(rv) = 0 \tag{1}$$

$$u\frac{\partial C_2}{\partial x} + v\frac{\partial C_2}{\partial r} = D_{12}\frac{\partial^2 C_2}{\partial x^2} + D_{12}\frac{1}{r}\frac{\partial}{\partial r}\left(r\frac{\partial C_2}{\partial r}\right) \tag{2}$$

$$u\frac{\partial u}{\partial x} + v\frac{\partial u}{\partial r} = -\frac{1}{\rho}\frac{\partial p}{\partial x} + \nu\left[\frac{\partial^2 u}{\partial x^2} + \frac{1}{r}\frac{\partial}{\partial r}\left(r\frac{\partial u}{\partial r}\right)\right] \tag{3}$$

$$u\frac{\partial v}{\partial x} + v\frac{\partial v}{\partial r} = -\frac{1}{\rho}\frac{\partial p}{\partial r} + \nu\left[\frac{\partial^2 v}{\partial x^2} + \frac{\partial^2 v}{\partial r^2} + \frac{\partial}{\partial r}\left(\frac{v}{r}\right)\right] \tag{4}$$

If the global-continuity equation (1) is used, then only one of the species-conservation equations needs to be included, in this case that of the inert gas (2).

Due to the geometry and the behavior of some of the state variables in the operating regime of the heat pipe, boundary-layer-type approximations may be made. For this purpose the following dimensionless variables are defined:

$$u^* = \frac{\pi R^2 \rho h_{12}}{Q_e}u \tag{5a}$$

$$v^* = \frac{2\pi R(l_p - l_a)\rho h_{12}}{Q_e}v \tag{5b}$$

$$p^* = \frac{\pi^2 R^4 \rho h_{12}^2}{Q_e^2}p \tag{5c}$$

$$x^* = \frac{x}{l_p} \qquad x^* = \frac{x}{R} \quad \text{for} \quad C_2 \text{ and } v \tag{5d}$$

$$r^* = \frac{r}{R} \tag{5e}$$

The reference velocity used to nondimensionalize u is the maximum axial velocity based on the constant density ρ. The density ρ is based on the operating temperature and pressure in the inert-gas chamber at maximum heat load. The reference radial velocity is the condensing-mixture velocity at full heat load with full condenser surface available. The reference pressure is based on the reference axial velocity in the usual manner. It should be noted that the isothermal assumption inherently implies negligible sensible heats and that the heat transfer is entirely accomplished by the vapor convection of latent heat of condensation. The axial distance is normalized by l_p, except in the consideration of the mass fraction C_2 and the radial velocity v, where R is used. This is due to the fact that for a useful interface to exist sharp axial gradients must be allowed in C_2 as well as v, which is inversely proportional to C_2.

Use of the dimensionless quantities transforms the governing equations to the following form:

$$\frac{\partial u^*}{\partial x^*} + \frac{l_p}{2(l_p - l_a)}\frac{1}{r^*}\frac{\partial}{\partial r^*}(r^* v^*) = 0 \tag{6}$$

Nomenclature

a_c, b_c, c_c = constants in equation (22b)
a_u, b_u, c_u = constants in equation (22a)
C = mass fraction
D_{12} = binary diffusion coefficient
h_{12} = latent heat
j = integer
K_p = constant in equation (34)
K_s = sink conductance
K_t = constant in equation (34)
l_a = length of evaporator and adiabatic section
l_e = length of evaporator
l_p = length of heat pipe
m_2 = mass of inert gas in heat pipe
m_c = total mass of inert gas
N_a = $l_a/\Delta x$
N_e = $l_e/\Delta x$
N_p = $l_p/\Delta x$
p = pressure
p_1 = partial pressure of vapor
p_v = vapor pressure of liquid
q_c = condenser heat flux
q_e = evaporator heat flux
Q_e = total heat load
r = radial coordinate
R = radius of heat-pipe vapor chamber
R_g = gas constant of vapor
T_l = liquid temperature
T_v = vapor temperature
u = axial velocity
v = radial velocity
V_c = inert-gas-chamber volume
x = axial coordinate
$O(\ )$ = order of
α = condensation coefficient
ξ = dummy variable
μ = viscosity
ν = kinematic viscosity
ρ = density

Subscripts

1 = vapor
2 = inert gas
0 = value at center of pipe
r = value at wall
m = maximum

Superscripts

(i) = iteration step
$*$ = dimensionless variable
$'$ = first derivative
$''$ = second derivative

$$u^* \frac{\partial C_2}{\partial x^*} + \frac{R}{2(l_p - l_a)} v^* \frac{\partial C_2}{\partial r^*} = \left(\frac{\pi R \rho D_{12} h_{12}}{Q_e}\right)\left[\frac{\partial^2 C_2}{\partial x^{*2}} + \frac{1}{r^*}\frac{\partial}{\partial r^*}\left(r^* \frac{\partial C_2}{\partial r^*}\right)\right] \quad (7)$$

$$u^* \frac{\partial u^*}{\partial x^*} + \frac{l_p}{2(l_p - l_a)} v^* \frac{\partial u^*}{\partial r^*} = -\frac{\partial p^*}{\partial x^*} + \left(\frac{\pi l_p h_{12} \mu}{Q_e}\right)\left[\left(\frac{R}{l_p}\right)^2 \frac{\partial^2 u^*}{\partial x^{*2}} + \frac{1}{r^*}\frac{\partial}{\partial r^*}\left(r^* \frac{\partial u^*}{\partial r^*}\right)\right] \quad (8)$$

$$\frac{R}{2(l_p - l_a)} u^* \frac{\partial v^*}{\partial x^*} + \frac{R^2}{4(l_p - l_a)^2} v^* \frac{\partial v^*}{\partial r^*} = -\frac{\partial p^*}{\partial r^*} + \left(\frac{\pi R^2 h_{12} \mu}{2(l_p - l_a) Q_e}\right)\left[\frac{\partial^2 v^*}{\partial x^{*2}} + \frac{\partial^2 v^*}{\partial r^{*2}} + \frac{\partial}{\partial r^*}\left(\frac{v^*}{r^*}\right)\right] \quad (9)$$

The order of magnitude of the dimensionless coefficients in each equation is evaluated in view of the parameter values given in [11]. Although these parameters apply specifically to the referenced heat-pipe system, the order-of-magnitude analysis will in general hold for heat pipes of similar length-to-diameter ratios. Using these typical parameters it can be shown that

$$\frac{l_p}{2(l_p - l_a)} = \mathrm{O}(1) \quad (10a)$$

$$\frac{\pi R \rho D_{12} h_{12}}{Q_e} = \mathrm{O}(1) \quad (10b)$$

$$\frac{\pi l_p h_{12} \mu}{Q_e} = \mathrm{O}(1) \quad (10c)$$

$$\frac{R}{2(l_p - l_a)} \ll 1 \quad (10d)$$

$$\frac{R}{l_p} \ll 1 \quad (10e)$$

$$\frac{\pi R^2 h_{12} \mu}{2(l_p - l_a) Q_e} \ll 1 \quad (10f)$$

It is important to note that the reference radial velocity is based on the full condenser length available. However, as the vapor–inert-gas interface is displaced toward the evaporator due to reduced sink temperature, the effective condenser length $l_p - l_a$ is shortened. The reference radial velocity should be based on this reduced condenser length. However, only in the extreme case, when the interface is within a distance of $R/2$ of the entrance to the condenser, will the orders of magnitude of (10*a*), (10*d*), and (10*f*) be affected significantly. This case is eliminated from consideration in this investigation. Retaining only terms of O(1), the governing equations, when written in dimensional coordinates again, become

$$\frac{\partial u}{\partial x} + \frac{1}{r}\frac{\partial}{\partial r}(rv) = 0 \quad (11)$$

$$u \frac{\partial C_2}{\partial x} = D_{12} \frac{\partial^2 C_2}{\partial x^2} + D_{12} \frac{1}{r}\frac{\partial}{\partial r}\left(r \frac{\partial C_2}{\partial r}\right) \quad (12)$$

$$u \frac{\partial u}{\partial x} + v \frac{\partial u}{\partial r} = -\frac{1}{\rho}\frac{dp}{dx} + \frac{\nu}{r}\frac{\partial}{\partial r}\left(r \frac{\partial u}{\partial r}\right) \quad (13)$$

The boundary conditions that must be satisfied are

$$x = 0: \quad u = 0 \quad v = 0 \quad \frac{\partial C_2}{\partial x} = 0 \quad (14a)$$

$$x = l_p: \quad u = 0 \quad v = 0 \quad \frac{\partial C_2}{\partial x} = 0 \quad (14b)$$

$$r = 0: \quad \begin{cases} u = u_0 \\ \dfrac{\partial u}{\partial r} = 0 \end{cases} \quad v = 0 \quad \begin{cases} C_2 = C_{20} \\ \dfrac{\partial C_2}{\partial r} = 0 \end{cases} \quad (14c)$$

$$r = R: \quad u = 0 \quad v = f(q_e, C_{2r}) \quad C_2 = C_{2r} \quad (14d)$$

The functional relationship in (14*d*) is to be established from the gas kinetic formula for condensation. The pressure gradient may be eliminated from equation (13) by noting that p is independent of r. Then the equation may be evaluated at $r = 0$ to obtain an expression for dp/dx as

$$-\frac{1}{\rho}\frac{dp}{dx} = u_0 \frac{du_0}{dx} - \lim_{r \to 0}\left[\frac{\nu}{r}\frac{\partial}{\partial r}\left(r \frac{\partial u}{\partial r}\right)\right] \quad (15)$$

Momentum and Concentration Integrals

To obtain solutions, the Karman–Pohlhausen integral method, common in boundary-layer analysis, is applied. In the usual application of this technique integration is carried out across the boundary layer using assumed profiles for the dependent variables. Thereby the partial differential equations are reduced to ordinary differential equations with the boundary-layer thickness as one of the dependent variables. In the present analysis the final variables will be the axial velocity at the pipe centerline, u_0, and the mass fraction of the inert gas at the wall, C_{2r}.

To apply the method, equations (12) and (13) are multiplied by r and integrated with respect to r from 0 to R. Making use of the boundary conditions and equation (15), these integrals become

$$\int_0^R ru \frac{\partial C_2}{\partial x} dr = D_{12} \int_0^R r \frac{\partial^2 C_2}{\partial x^2} dr + D_{12} R \left(\frac{\partial C_2}{\partial r}\right)_{r=R} \quad (16)$$

$$\int_0^R ru \frac{\partial u}{\partial x} dr + \int_0^R rv \frac{\partial u}{\partial r} dr = \frac{R^2 u_0}{2}\frac{du_0}{dx} - \frac{R^2}{2}\lim_{r \to 0}\left[\frac{\nu}{r}\frac{\partial}{\partial r}\left(r \frac{\partial u}{\partial r}\right)\right] + \nu R \left(\frac{\partial u}{\partial r}\right)_{r=R} \quad (17)$$

The radial velocity v can be eliminated from equation (17) by applying the continuity equation. Multiplying equation (11) by r and integrating with respect to r from any point r to R yields

$$rv = Rv_r + \int_r^R r \frac{\partial u}{\partial x} dr \quad (18)$$

When this is substituted into the second integrand in equation (17) and integration performed by parts, the integral becomes

$$\int_0^R rv \frac{\partial u}{\partial r} dr = -Rv_r u_0 - u_0 \int_0^R r \frac{\partial u}{\partial x} dr + \int_0^R ru \frac{\partial u}{\partial x} dr \quad (19)$$

Substituting this back into equation (17), the concentration and momentum integrals become

$$\int_0^R ru \frac{\partial C_2}{\partial x} dr - D_{12} \int_0^R r \frac{\partial^2 C_2}{\partial x^2} dr = D_{12} R \left(\frac{\partial C_2}{\partial r}\right)_{r=R} \quad (20)$$

$$2\int_0^R ru \frac{\partial u}{\partial x} dr - u_0 \int_0^R r \frac{\partial u}{\partial x} dr - Rv_r u_0 - \frac{R^2 u_0}{2}\frac{du_0}{dx} = -\frac{R^2}{2}\lim_{r \to 0}\left[\frac{\nu}{r}\frac{\partial}{\partial r}\left(r \frac{\partial u}{\partial r}\right)\right] + \nu R \left(\frac{\partial u}{\partial r}\right)_{r=R} \quad (21)$$

Application of Karman–Pohlhausen Method

To apply the Karman–Pohlhausen method it is necessary to assume a form for the distribution of velocity and concentration across the pipe. The simplest polynomial expressions that satisfy the required boundary conditions are the following quadratic forms:

$$u(x, r) = u_0(x)\left(1 - \frac{r^2}{R^2}\right) \tag{22}$$

$$C_2(x, r) = C_{20}(x)\left(1 - \frac{r^2}{R^2}\right) + C_{2r}(x)\frac{r^2}{R^2} \tag{23}$$

By assuming profiles separately for $u(x, r)$ and $C_2(x, r)$, the interaction between convection and diffusion takes place in the mean instead of locally. This is consistent with the boundary-layer-type approximation for heat pipes that has ratios of $R/l_p \ll 1$. The assumed profile for velocity is the usual parabolic form for fully developed laminar flow in a pipe. The actual flow in the evaporator and condenser is dynamically equal to pipe flow with injection or suction through a porous wall. This has been studied by Yuan and Finkelstein [12], and their results indicate that for the low radial Reynolds numbers encountered here, $\mathrm{Re}_r = 2.4$, the velocity profile is close to the parabolic shape. Weissberg [13] analyzed laminar flow in the entrance region of a porous pipe. His results are given in terms of two parameters, Re_r and ζ, a dimensionless axial coordinate. For the heat pipe under consideration $\zeta = 0.6$ for all conditions of heat load up to the design limit. For the operating conditions characterized by these parameters there is only small variation from the parabolic profile. Although in the interface region Re_r decreases rapidly so that Weissberg's analysis is not strictly applicable, it is expected that as ζ approaches unity the profile approaches parabolic. A similar argument is assumed to apply to the concentration profile.

Upon substituting the assumed profiles, equations (22) and (23), into the concentration and momentum integrals, equations (20) and (21), and performing the integrations over r, the following nonlinear ordinary differential equations result:

$$u_0' = -\frac{12}{5}\frac{v_r}{R} \tag{24}$$

$$3D_{12}C_{20}'' + 3D_{12}C_{2r}'' - 2u_0C_{20}' - u_0C_{2r}' + \frac{24D_{12}}{R^2}(C_{2r} - C_{20}) = 0 \tag{25}$$

Note that the radial velocity at the wall, v_r, is the forcing function for the system. It can be evaluated in terms of the boundary conditions by considering the heat balance. In the evaporator this velocity is directly proportional to the heat flux, which is a constant, and is independent of the concentration. Since the sensible heat is neglected, the heat balance in this section can be expressed as

$$(\rho_1 v_1)_r h_{12} = q_e \tag{26}$$

For a binary mixture

$$\rho v_r = (\rho_1 v_1 + \rho_2 v_2)_r$$

But $(v_2)_r = 0$, so that from equation (26)

$$v_r = \frac{q_e}{\rho h_{12}} \tag{27}$$

In the adiabatic section there is no heat transfer, that is, $v_r = 0$. In the condenser section the phenomenon is more complex, since in a self-controlled heat pipe the heat rejection is a function of axial location and depends on the mass fraction itself. The condenser heat flux can be expressed in terms of the condensed-liquid temperature T_l, which also is a function of location, and a sink temperature T_s, which is a constant.

$$q_c = K_s(T_l - T_s) \tag{28}$$

The sink conductance K_s generally depends on T_l as well as T_s. The present sink design, however, consists of laminar flow of water through a coil of tubing wrapped around the condenser. Temperature rise of the cooling water is negligible. In this case K_s can be considered to be constant. Replacement of q_e by q_c in equation (27) yields an expression for v_r that is valid in the condenser.

$$v_r = \frac{K_s}{\rho h_{12}}(T_l - T_s) \tag{29}$$

The new unknown introduced, T_l, can be related to the mass fraction at the wall, C_{2r}, by employing the kinetic formula for condensation (or evaporation) which can be expressed as

$$\frac{q_c}{h_{12}} = \frac{\alpha}{\sqrt{2\pi R_g T_l}}(p_1 - p_v)_{r=R} \tag{30}$$

The partial pressure of the vapor, p_1, can be written in the form

$$p_1 = \rho R_g T_v(1 - C_2) \tag{31}$$

At this point it is recalled that the flow field is considered to be isothermal. It is recognized that this is not consistent with the assumption of constant density and the perfect-gas equation of state since an axial pressure variation is allowed which is the prime driving force for vapor transport. However, the range of T_v is limited here to relatively small values, whereas C_2 may take on values between zero and unity. Hence p_1 is determined mostly by C_2, and T_v may be taken to be a constant. The vapor pressure of the liquid is a complicated function of the liquid temperature T_l. Over a relatively small range of T_l, $T_s \leq T_l \leq T_v$, the functional relationship can be approximated by an exponential for mathematical convenience as

$$p_{v1} = K_p \exp(K_t T_l) \tag{32}$$

where K_p and K_t are taken to be constants and depend on the working fluid under consideration. Combination of equations (28), (30), (31), and (32) results in the following relation between T_l and C_{2r}:

$$\frac{\alpha h_{12}}{\sqrt{2\pi R_g T_l}}[\rho R_g T_v(1 - C_{2r}) - K_p \exp(K_t T_l)] = K_s(T_l - T_s) \tag{33}$$

In this form no solution for T_l is possible. To facilitate the analysis the following expansions are made:

$$\frac{1}{\sqrt{T_l}} = \frac{1}{\sqrt{T_s}}\left[1 - \frac{T_l - T_s}{2T_s} + \mathrm{O}\left(\frac{T_l - T_s}{T_s}\right)^2\right] \tag{34}$$

$$\exp(K_t T_l) = \exp(K_t T_s)\{1 + K_t(T_l - T_s) + \mathrm{O}[K_t(T_l - T_s)]^2\} \tag{35}$$

If $T_l - T_s$ is limited to small values such that $K_t(T_l - T_s) = \mathrm{O}(0.1)$, the higher order terms in the expansions may be neglected. Substitution of the truncated series into equation (33) yields a quadratic expression for $T_l - T_s$.

$$\left[\frac{\alpha h_{12}K_pK_t \exp(K_tT_s)}{2T_s\sqrt{2\pi R_gT_s}}\right](T_l - T_s)^2 - \left\{\frac{\alpha h_{12}K_pK_t \exp(K_tT_s)}{\sqrt{2\pi R_gT_s}} + \frac{\alpha h_{12}[\rho R_gT_v(1 - C_{2r}) - K_p \exp(K_tT_s)]}{2T_s\sqrt{2\pi R_gT_s}} + K_s\right\}(T_l - T_s) + \left\{\frac{\alpha h_{12}[\rho R_gT_v(1 - C_{2r}) - K_p \exp(K_tT_s)]}{\sqrt{2\pi R_gT_s}}\right\} = 0 \tag{36}$$

For the heat pipe under consideration the coefficients in this equation have different orders of magnitude. Using the parameters of [11] again

$$\frac{\alpha h_{12}K_pK_t \exp(K_tT_s)}{2T_s\sqrt{2\pi R_gT_s}} = \mathrm{O}(10^{-3}) \tag{37a}$$

$$\frac{\alpha h_{12}K_pK_t \exp(K_tT_s)}{\sqrt{2\pi R_gT_s}} = \mathrm{O}(1) \tag{37b}$$

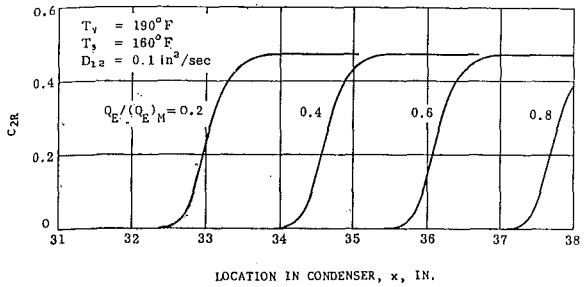

Fig. 2 Inert-gas mass fraction at the wall as a function of location in the condenser for various heat loads

$$\frac{\alpha h_{12}[\rho R_g T_v(1 - C_{2r}) - K_p \exp(K_t T_s)]}{2T_s\sqrt{2\pi R_g T_s}} = O(10^{-2}) \quad (37c)$$

$$\frac{\alpha h_{12}[\rho R_g T_v(1 - C_{2r}) - K_p \exp(K_t T_s)]}{\sqrt{2\pi R_g T_s}} = O(10^{-5}) \quad (37d)$$

$$K_s = O(10^{-4}) \quad (37e)$$

$$T_l - T_s = O(10) \quad (37f)$$

Then an approximate solution, as determined by the most significant terms, is given by

$$T_l - T_s = \frac{\rho R_g T_v(1 - C_{2r})}{K_p K_t \exp(K_t T_s)} - \frac{1}{K_t} \quad (38)$$

Substituting this for $T_l - T_s$ in equation*(29), v_r in the condenser section becomes

$$v_r = \frac{K_s}{\rho h_{12}}\left[\frac{\rho R_g T_v(1 - C_{2r})}{K_p K_t \exp(K_t T_s)} - \frac{1}{K_t}\right] \quad (39)$$

The radial velocity at the wall has thus been expressed in terms of the mass fraction at the wall, C_{2r}. The mass fraction at the center, C_{20}, can be related to C_{2r} by considering the mass transfer at the wall. Mass balance requires that

$$\rho v_r = \frac{\rho D_{12}}{C_{2r}}\left(\frac{\partial C_2}{\partial r}\right)_{r=R} \quad (40)$$

Differentiating equation (23) with respect to r and evaluating the derivative at $r = R$

$$\left(\frac{\partial C_2}{\partial r}\right)_{r=R} = \frac{2}{R}(C_{2r} - C_{20}) \quad (41)$$

Solving equations (40) and (41) for C_{20}

$$C_{20} = \left(1 - \frac{R}{2D_{12}} v_r\right) C_{2r} \quad (42)$$

The terms in equations (24) and (25) have now been reduced to functions of C_{2r}. These two equations can be combined into one by integrating (24) as

$$u_0 = -\frac{12}{5R}\int_0^x v_r(\xi)d\xi \quad (43)$$

and using equations (27), (39), and (42) in the appropriate sections of the heat pipe. After substitution, differentiation, and rearrangement, the final governing equations for the three sections, respectively, become

for $0 \le x \le l_e$

$$\left(\frac{5RD_{12}\rho h_{12}}{8q_e}\right) C_{2r}'' + \left(\frac{3D_{12}\rho h_{12} - Rq_e}{4D_{12}\rho h_{12} - Rq_e}\right) xC_{2r}' + \left(\frac{5D_{12}\rho h_{12}}{4D_{12}\rho h_{12} - Rq_e}\right) C_{2r} = 0 \quad (44a)$$

for $l_e \le x \le l_a$

$$C_{2r}'' + \left(\frac{6q_e l_e}{5RD_{12}\rho h_{12}}\right) C_{2r}' = 0 \quad (44b)$$

for $l_a \le x \le l_p$

$$\left[6D_{12} - \frac{3RK_sR_gT_v}{2h_{12}K_pK_t\exp(K_tT_s)} + \frac{3RK_s}{2\rho h_{12}K_t} + \frac{3RK_sR_gT_v}{h_{12}K_pK_t\exp(K_tT_s)} C_{2r}\right] C_{2r}'' + \frac{3RK_sR_gT_v}{h_{12}K_pK_t\exp(K_tT_s)}(C_{2r}')^2 + \left\{\frac{12q_el_e}{5R\rho h_{12}} + \frac{12K_s}{5R\rho h_{12}}\int_{l_a}^{x}\left[\frac{\rho R_gT_v(1 - C_{2r})}{K_pK_t\exp(K_tT_s)} - \frac{1}{K_t}\right]d\xi\right\} \times \left\{2C_{2r}'\left[\frac{3}{2} - \frac{RK_sR_gT_v}{2D_{12}h_{12}K_pK_t\exp(K_tT_s)} + \frac{RK_s}{2D_{12}\rho h_{12}K_t} + \frac{RK_sR_gT_v}{D_{12}h_{12}K_pK_t\exp(K_tT_s)} C_{2r}\right]\right\} + \frac{24D_{12}}{R^2} C_{2r} \times \left[\frac{RK_sR_gT_v}{2D_{12}h_{12}K_pK_t\exp(K_tT_s)}(1 - C_{2r}) - \frac{RK_s}{2D_{12}\rho h_{12}K_t}\right] = 0 \quad (44c)$$

The boundary conditions that remain to be satisfied after transformation are:

$$x = 0: \quad C_{2r}' = 0 \quad (45a)$$

$$x = l_p: \quad C_{2r}' = 0 \qquad C_{2r} = 1 - \frac{K_p \exp(K_t T_s)}{\rho R_g T_v} \quad (45b)$$

The requirement on C_{2r} is a result of the condition that $v = 0$ at $x = l_p$, equation (14*b*), and is obtained by setting equation (39) to zero. It is a statement of overall heat balance and that the mixture is in equilibrium with the liquid at the end of the condenser.

Inert-Gas-Chamber Interaction

Up to this point it has been assumed that the operating pressure and temperature levels are unaffected by the presence of inert gas in the heat-pipe vapor space. To estimate this effect it is necessary to obtain the total amount of inert gas diffused into the pipe. This is given by

$$m_2 = 2\pi\rho\int_0^R\int_0^{l_p} rC_2 dx dr$$

Using equations (22), (23), (27), (39), and (42) for C_2, this can be written in the form

$$m_2 = \pi R^2\rho\left(1 - \frac{Rq_e}{4D_{12}\rho h_{12}}\right)\int_0^{l_e} C_{2r}d\xi + \pi R^2\rho\int_{l_e}^{l_a} C_{2r}d\xi + \pi R^2\rho\int_{l_a}^{l_p}\left\{1 - \frac{1}{2}\left[\frac{RK_sR_gT_v}{2D_{12}h_{12}K_pK_t\exp(K_tT_s)} - \frac{RK_s}{2D_{12}\rho h_{12}K_t} - \frac{RK_sR_gT_v}{2D_{12}h_{12}K_pK_t\exp(K_tT_s)} C_{2r}\right]\right\} C_{2r}d\xi \quad (46)$$

For the hot non-wicked reservoir the pressure and temperature in the inert-gas chamber are equal to those in the heat pipe itself, and the equation of state can be written as

$$p = \frac{(m_c - m_2)R_g}{V_c} T_v$$

This equation should be satisfied by p and T_v at all times. In this analysis it is used as an iterative correction by writing the equation as

$$p^{(i)} = \frac{(m_c - m_2^{(i-1)})}{V_c} T_v^{(i)} \quad (47)$$

That is, m_2 is always based on the previous solutions of C_{2r}. Since p and T_v are not far from equilibrium at any time, the exponential approximation of equation (32) is applicable

$$p^{(i)} = K_p \exp (K_t T_v^{(i)})$$

or approximately

$$p^{(i)} = K_p \exp (K_t T_v^{(i-1)})[1 + K_t(T_v^{(i)} - T_v^{(i-1)})] \quad (48)$$

Combining equations (47) and (48) and solving for $T_v^{(i)}$

$$T_v^{(i)} = \frac{T_v^{(i-1)} - \frac{1}{K_t}}{1 - \frac{(m_c - m_2^{(i-1)})R_g}{V_c K_p K_t \exp (K_t T_v^{(i-1)})}} \quad (49)$$

The iteration is continued until the changes in $T_v^{(i)}$ and $p^{(i)}$ become negligible. At this point the pressure p, axial velocity u_0, radial velocity v_r, and centerline mass fraction C_{20} are obtained directly from equations (15), (43), (27), (39), and (42) respectively.

Numerical Solution

The equations (44) describe the behavior of C_{2r} in the heat pipe. In the evaporator and adiabatic sections they are linear differential equations. In the condenser it is a nonlinear integro-differential equation to which no analytic solution is possible. A computer program using the finite-difference technique is therefore employed here. Using simple central and forward differences, the equations become

for $0 \leq x \leq l_e \qquad j = 2, 3, \ldots, N_e$

$$C_{2r}^{j+1} = 2C_{2r}^{j} - C_{2r}^{j-1} - \frac{8q_e}{5RD_{12}\rho h_{12}}\left[\frac{3D_{12}\rho h_{12} - Rq_e}{4D_{12}\rho h_{12} - Rq_e}(j+1)(\Delta X)^2 \times (C_{2r}^{j} - C_{2r}^{j-1}) + \frac{5D_{12}\rho h_{12}}{4D_{12}\rho h_{12} - Rq_e}(\Delta X)^2 C_{2r}^{j}\right] \quad (50a)$$

for $l_e \leq x \leq l_a \qquad j = N_e, \ldots, N_a$

$$C_{2r}^{j+1} = 2C_{2r}^{j} - C_{2r}^{j-1} - \frac{6q_e l_e}{5RD_{12}\rho h_{12}}(\Delta X)(C_{2r}^{j} - C_{2r}^{j-1}) \quad (50b)$$

for $l_a \leq x \leq l_p \qquad j = N_a, \ldots, N_p$

$$C_{2r}^{j+1} = 2C_{2r}^{j} - C_{2r}^{j-1} + \frac{(\Delta X)^2}{6D_{12} + \frac{3RK_s}{2K_t\rho h_{12}}\left(1 - \frac{\rho R_g T_v}{K_p \exp (K_t T_s)}\right) + \frac{3RK_s R_g T_v}{K_p K_t h_{12} \exp (K_t T_s)} C_{2r}^{j}} \times \left\{-\frac{3RK_s R_g T_v}{K_p K_t h_{12} \exp (K_t T_s)}\frac{1}{(\Delta X)^2}(C_{2r}^{j} - C_{2r}^{j-1})^2 - \left[\frac{24q_e l_e}{5R\rho h_{12}} + \frac{24K_s R_g T_v}{5RK_p K_t h_{12} \exp (K_t T_s)}(\Delta X)\sum_{i=N_a}^{j}(1 - C_{2r}^{j}) - \frac{24K_s}{5RK_t\rho h_{12}}(\Delta X)(j + 1 - N_a)\right]\left[\frac{RK_s R_g T_v}{D_{12}K_p K_t h_{12} \exp (K_t T_s)}\frac{1}{(\Delta X)}(1 - C_{2r}^{j})(C_{2r}^{j} - C_{2r}^{j-1}) - \left(\frac{3}{2} + \frac{RK_s R_g T_v}{2D_{12}K_p K_t h_{12} \exp (K_t T_s)} + \frac{RK_s}{2D_{12}K_t\rho h_{12}}\right)\frac{1}{(\Delta X)}(C_{2r}^{j} - C_{2r}^{j-1})\right] + \frac{24D_{12}}{R^2}C_{2r}^{j}\left[\frac{RK_s}{2D_{12}\rho h_{12}K_t} - \frac{RK_s R_g T_v}{2D_{12}h_{12}K_p K_t \exp (K_t T_s)}(1 - C_{2r}^{j})\right]\right\} \quad (50c)$$

In this formulation, this is a mixed initial-boundary-value problem. The slopes are zero at both ends of the heat pipe and the magnitude of the mass fraction is known at the end $x = l_p$. At the initial point $x = 0$ the magnitude of the mass fraction is unknown and an iteration is required, that is, with an assumed initial magnitude and zero slope the integration is carried to the end point, and if the required conditions are not met an indicated correction on the initial assumption is made. However, for typical conditions in an operating heat pipe the inert-gas mass fraction is so close to zero away from the interface region that even the use of double precision results in fast divergence. Therefore the initial point has to be shifted toward the interface. This shift results in an additional complication in that at the new initial point neither the slope nor the magnitude is known. The solution now requires double iteration. The error in equations (52) grows rapidly, but sufficient accuracy is available with the computer so that the end boundary conditions can be satisfied with an acceptable deviation.

Results and Discussion

To illustrate the method of analysis and the effect of diffusion on heat-pipe performance, the computer program was applied to the configuration selected in [11]. The present analysis pertains only to water as the working fluid, an operating temperature level T_v of 190 deg F, and a design heat load $(Q_e)_m$ of 640 Btu/hr. Since the analytical model assumes equal molecular weights for the vapor and control gas, neon would be a good choice.

The variation of the inert-gas mass fraction at the wall, C_w, with location in the heat pipe, x, is shown in Fig. 2 for a number of heat-load ratios $Q_e/(Q_e)_m$, a sink temperature of $T_s = 160$ deg F, and a diffusion coefficient $D_{12} = 0.1$ in.^{2}/sec. The shapes of the curves are completely similar for all of the heat loads shown, and are equally spaced. The diffused region extends over a length of about 1.25 in. The equilibrium value at the end of the pipe for the case considered in this work depends only on the sink temperature, which for $T_s = 160$ deg F is 0.471. It can be observed that at the heat-load ratio of 0.8 the equilibrium value has not been reached at the end of the pipe. According to the mathematical model no solution exists in this case with the semipermeable membrane and the constant pressure and temperature assumed in the convective-diffusion analysis. The physical significance in the absence of the membrane is that diffusion of the vapor into the inert-gas chamber would take place, raising the pressure level and readjusting the equilibrium situation. Therefore diffusion has the effect of limiting the maximum heat-transport capability of the heat pipe.

It should be noted here that the accuracy of this solution is limited to relatively small values of $K_t(T_v - T_s)$, due to the series approximation of equation (35). This also implies lower values for the equilibrium inert-gas mass fraction $C_{2r}(l_p)$. Therefore, in the absence of the semipermeable membrane a sufficiently large amount of vapor would diffuse into the inert-gas chamber before the establishment of equilibrium. This in turn would raise the operating pressure level and counteract the small pressure drop normally expected in the self-controlled heat pipe when the heat load is lowered. The effect of vapor in the inert-gas chamber is not accounted for in the analysis outlined here; hence only large values of $T_v - T_s$ can be compared with the actual physical situation where no semipermeable membrane is used. However, the influence of the diffusion on the real heat pipe can be determined by the present analysis even though strict accuracy is only obtained for small values of $K_t(T_v - T_s)$. The trends

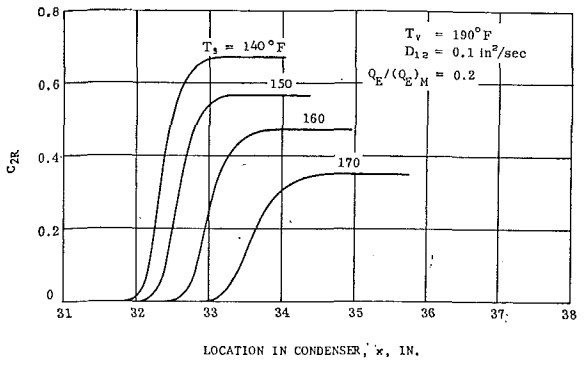

Fig. 3 Effect of sink temperature T_s on the vapor–inert-gas interface

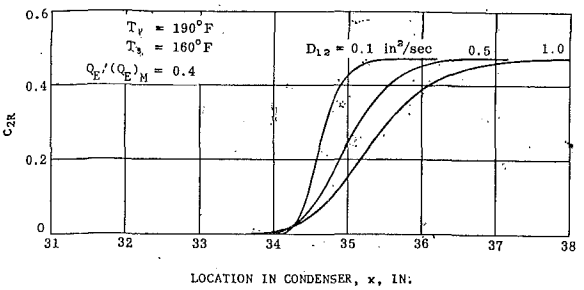

Fig. 4 Vapor–inert-gas interface as affected by diffusion

predicted here must be the same, with some error in the location of the vapor–inert-gas interface.

The effect of sink temperature T_s on the vapor–inert-gas interface is shown in Fig. 3. Lowering the sink temperature has the effect of reducing the width of the interface diffuse region. At T_s = 170 deg F the interface width is about 1.50 in., while at 140 deg F it reduces to about 1.0 in. Lowering sink temperature has the additional effects of raising equilibrium mass fraction of the inert gas at the end of the pipe, $C_{2r}(l_p)$, and of shifting the interface toward the evaporator end. The shift and narrowing of the interface is due to the higher rate of condensation to the colder liquid in the wick. Therefore, indications are that the colder sink temperatures minimize the effects of diffusion.

The effect of diffusion coefficient on the interface is shown in Fig. 4. As is expected, an inert gas with a higher diffusion coefficient exhibits a more diffuse interface with an accompanying reduction in the maximum heat-transfer capacity. Actually, at the operating temperature level of T_v = 190 deg F the diffusion coefficient does not vary as much as is indicated in the figure. At lower temperature levels, however, the value of D_{12} can increase considerably, since it is inversely proportional to density. Low-density effects are encountered during start-up of a heat pipe, indicating the requirement for a thorough transient analysis with diffusion.

Figure 5 illustrates the difference in value of the inert-gas mass fraction at the pipe wall and at the pipe centerline. The concentration gradients are of the same order in the axial and radial directions. Therefore, as postulated, both are significant in the description of the interface profile, and the two-dimensional approach seems warranted.

Figure 6 shows the self-control performance of the heat pipe with diffusion for various sink temperatures. It should be recalled that this was obtained by neglecting the possibility of the presence of working-fluid vapor in the inert-gas chamber. The drop in the operating-temperature level is less than about 3 deg F for the lowest sink temperature considered, T_s = 140 deg F, for all heat-load ratios. The dashed line indicates the maximum heat-load ratio as reduced by the diffusion. Finally, based on this analysis, it can be concluded that for the water heat pipe considered with neon control gas the diffusion does not impair the self-control feature. It does reduce the total heat-load capacity somewhat depending on the sink temperature.

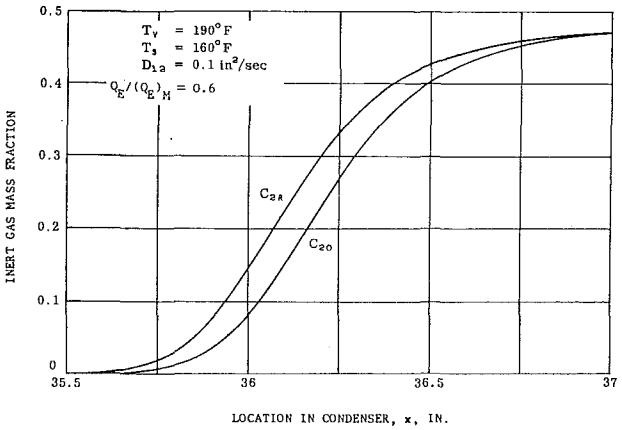

Fig. 5 Comparison of inert-gas mass fractions at the wall and center for a typical case

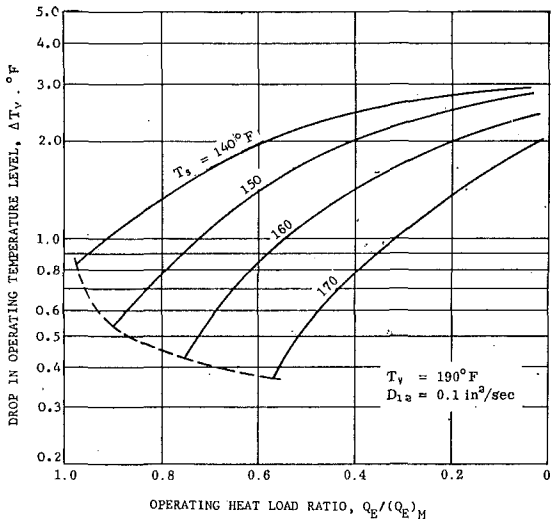

Fig. 6 Self-control performance of the heat pipe with diffusion for various sink temperatures

A heat pipe with the configuration analyzed here has been fabricated, but testing has not progressed to the point where comparison with prediction can be made. Valuable data have been reported by Kirkpatrick and Marcus [14] for a heat pipe that was similarly controlled by a hot reservoir. However, no direct comparison with their results is possible due to two major differences. The first is the nonlinear cooling by radiation of a finned condenser in contrast to the constant conductance of the water cooling coils. The second is that the temperature differences between evaporator and sink are larger than is allowable in the present analysis due to the approximations of the functions in equations (34) and (35).

References

1 Cotter, T. P., "Theory of Heat Pipes," Los Alamos Science Laboratory Report L.A.-3246-MS, 1965.

2 Ernst, D. M., "Evaluation of Theoretical Heat Pipe Performance," Thermionic Conversion Specialist Conference, Palo Alto, Calif., Oct. 30–Nov. 1, 1967.

3 Busse, C. A., "Pressure Drop in the Vapor Phase of Long Heat Pipes," Thermionic Conversion Specialist Conference, Palo Alto, Calif., Oct. 30–Nov. 1, 1967.

4 Haskin, W. L., "Cryogenic Heat Pipe," Air Force Flight Dynamics Laboratory Technical Report AFFDL-TR-66-228, June 1967.

5 Brosens, P. J., "Thermionic Converter with Heat Pipe Radiator," Advances in Energy Conversion Engineering Conference, Aug. 1967.

6 Levy, E. K., "Theoretical Investigation of Heat Pipes Operating at Low Vapor Pressures," Aviation and Space: Progress and Prospects Annual Aviation and Space Conference, June 1968.

7 Grover, G. M., Cotter, T. P., and Erickson, G. F., "Structures of Very High Thermal Conductance," *Journal of Applied Physics*, Vol. 35, 1964.

8 Katzoff, S., "Heat Pipes and Vapor Chambers for Thermal Control of Spacecraft," AIAA Thermophysics Specialist Conference, AIAA 67-310, Apr. 10, 1967.

9 Bienert, W., "Heat Pipes for Temperature Control," Fourth Intersociety Energy Conversion Engineering Conference, Washington, D. C., Sept. 22–26, 1969.

10 Marcus, B. D., and Fleischman, G. L., "Steady-State and Transient Performance of Hot Reservoir Gas-Controlled Heat Pipes," ASME Paper No. 70-HT/SpT-11.

11 Somogyi, D., "Heat Pipe Design Analysis for the NASA 2-KW Fuel Cell, Phase A," Sperry Rand Report SP-205-0341, Apr. 23, 1970.

12 Yuan, S. W., and Finkelstein, A. B., "Laminar Pipe Flow With Injection and Suction Through a Porous Wall," TRANS. ASME, Vol. 78, 1956, pp. 719–724.

13 Weissberg, H. L., "Laminar Flow in the Entrance Region of a Porous Pipe," *The Physics of Fluids*, Vol. 2, No. 5, Sept. 1959.

14 Kirkpatrick, J. P., and Marcus, B. D., "A Variable Conductance Heat Pipe Flight Experiment," AIAA Paper No. 71-411, Apr. 1971.

C. S. LANDRAM
Sandia Laboratories,
Livermore, Calif.
Mem. ASME

Heat Transfer during Vessel Discharge: Mean and Fluctuating Gas Temperature

A gas, discharging from its container through an orifice to the atmosphere, is shown to experience a temperature history that is strongly dependent upon the heat transfer from the container wall. Using a quasi-steady free-convection model for the instantaneous conductance between the wall and gas, a satisfactory correlation results between experimental and analytical mean gas-temperature response during discharge. For the special case of choked orifice flow and constant wall temperature, the mean temporal temperature of the gas remaining within the vessel is shown to depend upon just two parameters. The onset of the oscillating component of gas temperature is shown to occur at times which correspond to the dramatic growth of the diffusional thermal boundary layer on the wall, and this finding is in agreement with the Malkus theory of turbulence. The relative size of the temperature oscillations during discharge is shown to reach a maximum at the time when the scale of dimensionless temperature, a parameter essentially dependent on the instantaneous mean gas temperature, is a maximum.

Introduction

There are many practical applications in which a compressed gas is allowed to discharge from a vessel through an orifice into another region of lower pressure [1–3].[1] The wall-to-gas heat-transfer mechanism, which controls the mean temporal temperature of the gas within the vessel, has been identified as free convection [4]. However, apparently no prior study has validated the application of a quasi-steady free-convection model during discharge, especially when the fluctuations in the gas temperature are included.

In the present study, both the mean and fluctuating gas-temperature components were considered. In determining the mean gas-temperature response, three factors were included which were not previously addressed. First, the dependence of the mean gas temperature on the unchoking of the flow was determined. Second, effects of wall-temperature change were included and assessed. Third, variation in the gas properties, i.e., density, viscosity, and thermal conductivity, were considered as an integral part in assessing the validity of the free-convection model. Examination of the fluctuating component of the gas temperature revealed several significant findings. First, the onset of the fluctuations was found to correspond to the rapid growth of the thermal-diffusional layer on the wall of the vessel, which is in accord with the theory of Malkus [5]. Second, the developed fluctuating component of temperature was found to correlate with certain mean parameters which have previously been introduced for the problem of the steady heating of a gas from below [6]. Third, under certain conditions the fluctuating component of gas temperature has a significant effect on the mean value.

The experimental apparatus, consisting of a cylindrical vessel with an orifice at one end, was operated for initial gas pressures in the range 70 to 370 atm. Two gases, nitrogen and helium, were discharged. Under these operating conditions, a systematic study could be made of both the mean and fluctuating gas-temperature components and their influences on the discharge process.

Formulation

Mean Gas-Temperature Response. Consider a vessel of wall thickness L, mass M_w, and specific-heat capacity c_w containing a gas initially at pressure p_0 where both the wall and the gas are initially at the same temperature T_0. Beginning at time $t = 0$ the gas is allowed to exit from the vessel through the orifice of area A_1 into the surroundings maintained at atmospheric pressure. In seeking the temperature response of the gas remaining within the vessel owing to heat transfer, the temporal gas temperature is assumed to be uniformly distributed throughout the entire volume V of the container.

The energy equation applied to the control volume represented by the volume V is given by

$$\frac{M_w}{m_0} c_w T_0 \left(\frac{\partial v_w}{\partial x^+}\right)_{x^+=0} = -\frac{pV}{\bar{m}m_0}\frac{d\bar{m}}{d\tau} + \bar{m}\frac{du}{d\tau} \qquad (1)$$

[1] Numbers in brackets designate References at end of paper.

Contributed by the Heat Transfer Division and presented at the Winter Annual Meeting, Washington, D. C., November 28–December 2, 1971, of The American Society of Mechanical Engineers. Manuscript received by the Heat Transfer Division August 9, 1971; revised manuscript received May 30, 1972. Paper No. 71-WA/HT-32.

The experimental data discussed in subsequent sections were obtained under conditions where ideal-gas behavior could be assumed. Hence, using the equations of state for an ideal gas allows equation (1) to be written as

$$\frac{M_w c_w}{m_0 R}\left(\frac{\partial v_w}{\partial x^+}\right)_{x^+=0} = -\bar{T}\frac{d\bar{m}}{d\tau} + \frac{\bar{m}}{(\gamma-1)}\frac{d\bar{T}}{d\tau} \tag{2}$$

Two additional specifications are required before a solution to equation (2) can be obtained. One of these is the wall-temperature gradient $(\partial v_w/\partial x^+)_0$. To obtain this gradient, the heat-conduction equation within the wall, $0 < x^+ < 1$, must be solved; that is

$$\frac{\partial^2 v_w}{\partial x^{+2}} = \frac{\partial v_w}{\partial \tau} \tag{3}$$

subject to the initial condition $v_w = 1$ when $\tau = 0$, and to the boundary conditions on which discussion is deferred.[2]

The second specification needed to solve equation (2) is the mass rate of flow, $-d\bar{m}/d\tau$. The flow is choked ($\mathbf{M}_1 = 1$) for times $0 < \tau < \tau_c$

$$\tau_c = \tau_{\text{REF}}\left[\left(\frac{p_0}{p_{\text{ATM}}}\right)^{\frac{\gamma-1}{2\gamma}}\sqrt{\frac{2}{\gamma+1}} - 1\right] \tag{4a}$$

$$\tau_{\text{REF}} = \frac{\alpha_w}{L^2}\frac{V}{A_1}\frac{2/\sqrt{\gamma g R T_0}}{(\gamma-1)\left(\frac{2}{\gamma+1}\right)^{\gamma/(\gamma-1)}\sqrt{1+\frac{\gamma-1}{2}}} \tag{4b}$$

and unchoked for times $\tau > \tau_c$, during which time the exit-orifice Mach number is given by

$$\mathbf{M}_1^2 = \frac{2}{\gamma-1}\left[\left(\frac{p_0}{p_{\text{ATM}}}\bar{m}\bar{T}\right)^{\frac{\gamma-1}{\gamma}} - 1\right] \tag{5}$$

With $\mathbf{M}_1 = 1$ for $0 < \tau < \tau_c$ and $\mathbf{M}_1$ given by equation (5) for $\tau > \tau_c$, the mass rate of flow is specified by

$$-\frac{d\bar{m}}{d\tau} = \left(\frac{2}{\gamma-1}\right)\frac{\bar{m}\sqrt{\bar{T}}}{\tau_{\text{REF}}}\mathbf{M}_1\left[\frac{1+\left(\frac{\gamma-1}{2}\right)}{1+\left(\frac{\gamma-1}{2}\right)\mathbf{M}_1^2}\right]^{\frac{\gamma+1}{2(\gamma-1)}} \tag{6}$$

Finally, the boundary conditions for equation (3) must be considered. Taking a free-convection heat-transfer coefficient h_0 on the outer surface of the wall (at $x^+ = 1$)

$$\frac{\partial v_w}{\partial x^+} + \frac{h_0 L}{k_w}(v_w - 1) = 0, \quad x^+ = 1 \tag{7}$$

At the wall–gas interface, where $x^+ = 0$, a quasi-steady (turbulent) free-convective heat-transfer coefficient $h(\tau)$ was taken:

$$\frac{h(\tau)D_{ch}}{k_g} = c\left[\frac{gD_{ch}^3\text{Pr}}{\nu^2(\tau)}[v_w(0,\tau) - \bar{T}]/\bar{T}\right]^n \tag{8}$$

The gaseous thermal conductivity k_g and kinematic viscosity ν are given by the instantaneous values below:

$$k_g/k_{g0} = \sqrt{\bar{T}} \qquad \nu/\nu_0 = \sqrt{\bar{T}}/m$$

where k_{g0} and ν_0 are initial values of those properties, respectively. If this (turbulent) free-convective coefficient $h(\tau)$ is to suffice in describing the model, the values for the constants c and n in equation (8) should be: (a) independent of time during any one discharge and (b) insensitive to the initial conditions of pressure, temperature, volume, or type of gas. The values of c and n, determined by correlating analytical and experimental results, were found to be 0.105 and $^1/_3$, respectively, over a wide range of initial gas pressures for the two gases; thus both criteria were adequately met (see Discussion of Results for further details). Note that for the value of $n = {}^1/_3$ the characteristic dimension D_{ch} in equation (8) is eliminated, and thus the results of this analysis do not depend upon the shape of the container. The boundary condition at $x^+ = 0$ is thus given by

$$\frac{\partial v_w}{\partial x^+} + \frac{h(\tau)L}{k_w}(\bar{T} - v_w) = 0, \quad x^+ = 0 \tag{9}$$

With the initial conditions $v_w = \bar{T} = \bar{m} = 1$ at the time $\tau = 0$, equations (1)–(9) completely formulate the problem. The

[2] Equation (3) is written for planar walls, although it still has validity for curved walls if the wall thickness is small compared to the characteristic vessel size.

Nomenclature

A_1 = effective discharge area of orifice
c = constant in equation (8) found to be 0.105
c_v = specific heat capacity at constant volume for gas within vessel
c_w = specific heat capacity of vessel wall
D_{ch} = characteristic vessel size, approximately $2Z$
g = acceleration due to gravity
$h(\tau)$ = temporal mean heat-transfer coefficient at wall–gas interface
h_0 = heat-transfer coefficient on outer wall of vessel
k = thermal conductivity
L = vessel wall thickness
$\bar{m}$ = mass of gas remaining within vessel normalized to initial mass
$\mathbf{M}_1$ = Mach number at discharge (orifice) area
M_w = mass of vessel wall
n = exponent in equation (8) found to be $^1/_3$
p = pressure of gas within vessel
Pr = Prandtl number of gas
$Q = c\alpha\left(\frac{g\text{Pr}}{\nu^2}\right)^n\left(\frac{v_w(0,\tau) - \bar{T}}{\bar{T}}\right)^{1+n}$
R = gas constant
Ra_δ = Rayleigh number, $\frac{g\delta^3\text{Pr}}{\nu^2}\left(\frac{v_w(0,\tau) - \bar{T}}{\bar{T}}\right)$
t = time after initiation of discharge
t_{REF} = defined by equation (4b)
$\bar{T}$ = gas temperature within vessel normalized to initial value
u = mean gas internal energy
$u_0 = (\alpha g Q)^{1/4}$
$v_w = v_w(x^+, \tau)$ = wall temperature normalized to initial gas temperature
V = vessel internal volume
x^+ = coordinate measured into vessel wall from gas–wall interface normalized to wall thickness
Z = distance from wall to temperature sensors, 0.87 in. = radius of cylinder
$Z_0 = (\alpha^3/gQ)^{1/4}$
α = thermal diffusivity of the gas
γ = ratio of specific-heat capacities for the gas
τ = Fourier number, $\alpha_w t/L^2$
ν = kinematic viscosity of the gas
ρ = density of gas
$\theta_0 = [Q^3/(\alpha g)]^{1/4}$
$\theta_{0\,\max}$ = maximum of the function θ_0 in time
$\omega = t/t_{\text{REF}}$

Subscripts

0 = initial conditions of the gas
ATM = conditions in discharge reservoir
c = choked conditions
w = properties of the wall
g = temporal gas properties within vessel
1 = refers to thermocouple closest to the orifice along axis of cylinder
2 = refers to thermocouple farthest from the orifice along axis of cylinder

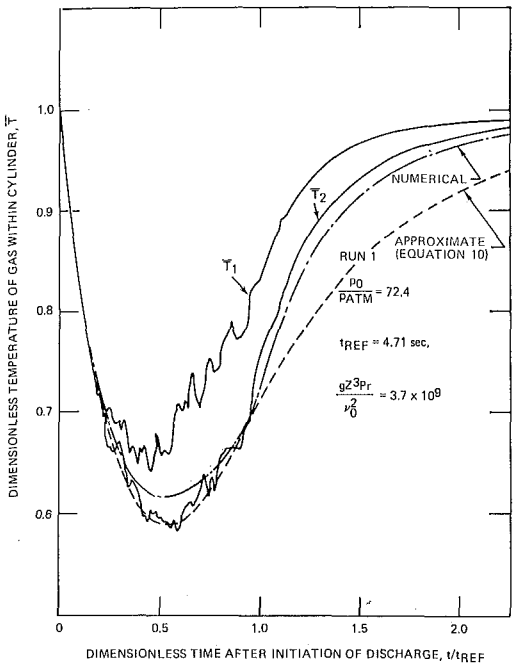

Fig. 1(*a*) Nitrogen temperature response within vessel; solid curves are data measured at two locations along axis of cylinder; broken curve is the mean predicted response for $c = 0.105$, $n = 1/3$

method of solution is that of [8], with particular details described in [9]. The results for three particular cases are shown in Figs. 1(*a*), 2(*a*), and 3(*a*).

With the recognition that $\bar{m}$ depends only weakly upon $\bar{T}$, it is possible to decouple equations (2) and (6) in calculating $\bar{T}$. If in addition a constant wall temperature is taken, $M_w c_w/(m_0 R) \gg 1$, and choked-orifice flow is taken, a closed-form solution for $\bar{T}$ follows:

$$\bar{T} = \frac{e^{-AI_1(\gamma,\omega)}}{(1+\omega)^2}\left[1 + AI_2(A,\gamma,\omega)\right] \tag{10}$$

where

$$A = (\gamma - 1)\tau_{REF}\frac{M_w c_w}{m_0 R}\, C\, \frac{k_{g0}}{k_w}\left(\frac{gL^3 \mathrm{Pr}}{\nu_0^2}\right)^{1/3} \tag{11}$$

$$I_1 = \int_0^{\omega} \zeta(\omega',\gamma)\, d\omega' \tag{12}$$

$$I_2 = \int_0^{\omega} (1+\omega')^2 \zeta(\omega',\gamma)\, \exp\left[A\int_0^{\omega'} \zeta(\omega'',\gamma) d\omega''\right] d\omega' \tag{13}$$

$$\zeta^3 = \omega(2+\omega)/(1+\omega)^{(\gamma-3)/(\gamma-1)} \tag{14}$$

The results of equation (10) were found to be in excellent agreement with the exact solution for times less than the time for the flow to unchoke. Further discussion is deferred regarding the constraints leading to equation (10).

Onset of Fluctuating Component of Gas Temperature. Figures 1(*a*), 2(*a*), and 3(*a*) show that the fluctuating components of the gas temperature within the container begin at times corresponding approximately to $t/t_{REF} = 0.2$, 0.3, and 0.4, respectively. Thereafter, they grow and have the same general character as the fluctuations reported for the case of the steady heating of a gas from below (for example, see [5]). As the mean gas temperature approaches $\bar{T} = 1$, the fluctuations appear to diminish in size until the oscillations are no longer discernible. The Malkus theory of turbulence [5] describes the onset and existence of these fluctuations as the detachment of columns of hot gas from the edge of the conduction layer on the wall and the erosion of these rising columns by contact with the surrounding cooler gas.

If the Malkus theory has validity for the present case, one can

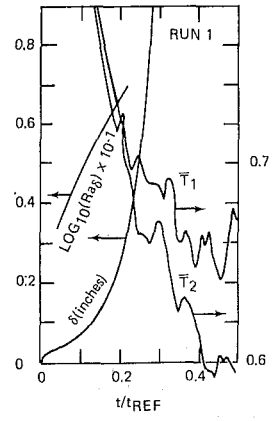

Fig. 1(*b*) Wall growth of thermal diffusion layer δ for nitrogen and the correspondence to the onset of fluctuations

anticipate that there should be some correspondence between the onset of fluctuations and the size of the conduction layer which grows on the wall of the container below the sensors. In fact, the growth of the thermal layer on the wall (determined below) will be shown to be dramatic at times that correspond to the onset of temperature fluctuations.

Assuming the curvature of the wall slight and a one-dimensional thermal-diffusional-layer growth, the conductive boundary layer is described by the following:

$$\frac{\partial}{\partial y}\left(k_g \frac{\partial f}{\partial y}\right) - \rho c_v \frac{\partial f}{\partial t} = \rho c_v \frac{d\bar{T}}{dt} \tag{15}$$

where the term on the right-hand side represents a temporal heat sink within the diffusional layer as a consequence of discharge. The coordinate y is the distance measured from the wall into the diffusional layer and f is the excess temperature $1 - T/T_0$ within the layer. Since the objective is to determine the diffusional-layer thickness prior to the onset of fluctuations, the presence of heat transfer outside the diffusional layer can be neglected because the terms on the right-hand side of equation (1) can be shown to dominate the term representing heat transfer in equation (1). Hence, for early times (approximately less than about $0.2\, t_{REF}$), it can be shown from equations (2) and (6) that

$$\bar{T} = \frac{1}{(1 + t/t_{REF})^2} \qquad 0 < \frac{t}{t_{REF}} < 0.2 \tag{16}$$

$$\frac{p}{p_0} = \frac{1}{(1 + t/t_{REF})^{2\gamma/(\gamma-1)}} \qquad 0 < \frac{t}{t_{REF}} < 0.2 \tag{17}$$

If the pressure is assumed to be uniform throughout the diffusional layer, and the variation of gas conductivity with temperature is considered, equation (15) becomes

$$\frac{k_0}{\rho_0 c_v}\frac{\partial}{\partial y}\left(\sqrt{1-f}\,\frac{\partial f}{\partial y}\right) - \frac{\dfrac{\partial f}{\partial t} - \dfrac{2/t_{REF}}{(1 + t/t_{REF})^3}}{(1 + t/t_{REF})^{2\gamma/(\gamma-1)}(1-f)} = 0 \tag{18}$$

The boundary conditions are given by

$$f = 0, \text{ all } y, \text{ when } t = 0 \tag{19a}$$

$$f = 0, \text{ all } t, \text{ when } y = 0 \tag{19b}$$

$$1 - f \to \bar{T}, \text{ all } t, \text{ as } y \to \infty \tag{19c}$$

Since the growth of the thermal diffusional layer is sought, an approximate method [8] which introduces a diffusional-layer thickness has been chosen to solve equation (18). The profile

$$\frac{f}{f_1} = 2\frac{y}{\delta}\left(1 - \frac{1}{2}y/\delta\right)$$

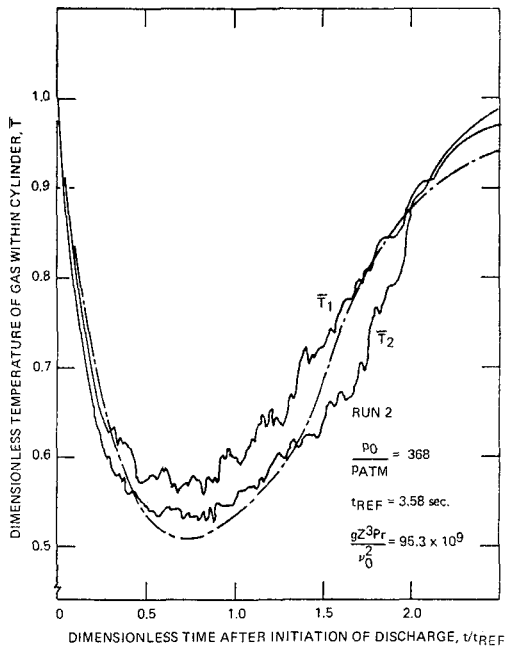

Fig. 2(a) Nitrogen temperature response within vessel; solid curves are data measured at two locations along axis of cylinder; broken curve is the mean predicted response for $c = 0.105$, $n = 1/3$

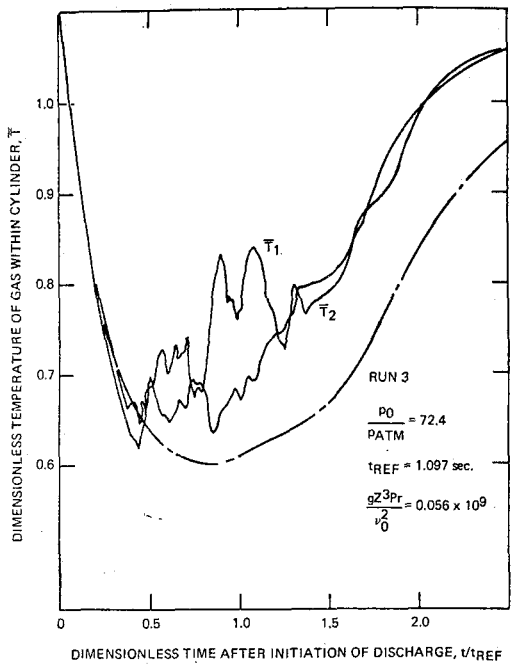

Fig. 3(a) Helium temperature response within vessel; solid curves are data measured at two locations along axis of cylinder; broken curve is the mean predicted response for $c = 0.105$, $n = 1/3$

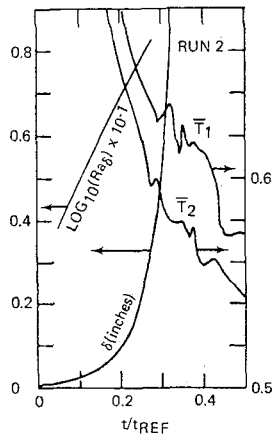

Fig. 2(b) Wall growth of the thermal diffusion layer δ for nitrogen and the correspondence to the onset of fluctuations

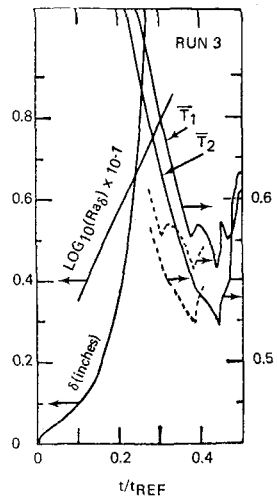

Fig. 3(b) Wall growth of the thermal diffusion layer δ for helium and the correspondence to the onset of fluctuations; the dotted curves correct for the time lag, $\Delta\omega \cong 0.06$, in measuring $\bar{T}_1$ and $\bar{T}_2$ owing to cellular movement between wall and sensor

with

$$f_1 = \frac{(2 + t/t_{REF})t/t_{REF}}{(1 + t/t_{REF})^2}$$

satisfies the constraints of equations (19b) and (19c). Using equation (18), integrally averaged over δ, then gives

$$\frac{d\delta^2}{d\omega} = 12\frac{k_0 t_{REF}}{\rho_0 c_v}(1+\omega)^{\frac{2\gamma}{\gamma-1}}\left[1 - \left(\frac{2}{3} - \frac{f_1}{5}\right)f_1\right] + 8\delta^2\left\{\frac{\left[1 + \frac{(2+\omega)\omega}{(1+\omega)^6}\right](1+\omega)^5}{(2+\omega)} - \frac{3}{2}\frac{1}{\omega(2+\omega)(1+\omega)}\right\} \quad (20)$$

Equation (20) is linear in δ^2 and therefore may be solved using quadrature. For the cases shown in Figs. 1(a), 2(a), and 3(a), $\delta = \delta(t)$ was calculated, and the results are shown in Figs. 1(b), 2(b), and 3(b), respectively. For very early times (approximately $0 < t/t_{REF} < 0.01$), $\delta^2 = 4(k_0/\rho_0 c_v)t$, but near the times when the fluctuations become discernible (of order of $t/t_{REF} = 0.2$), δ^2 grows roughly according to $(1 + t/t_{REF})^5$.

Developed Fluctuating Component of Gas Temperature. Once the temperature fluctuations have developed, it is desirable to determine the mean quantities upon which they depend. For the problem of the steady heating of a gas from below, it has been shown (see, for example, [5]) that three mean quantities suffice to describe the root-mean-square of the fluctuations, $\overline{\Delta T^2}^{1/2}$. In terms of the previously introduced mean temporal quantities, these are a scale of length Z_0, velocity u_0, and dimensionless temperature θ_0, this latter scale being independent of pressure for $n = 1/3$.

In the problem of the steady heating of a gas from below [6], the root-mean-square of the temperature fluctuations, nondimensionalized by $T_0\bar{T}\theta_0$, did correlate with the parameter Z/Z_0, where Z was the distance between sensor and heated surface. No such correlation existed for the present case of transient heating (by virtue of discharge). However, the parameter θ_0 behaved in time similar to the relative size of the fluctuating component of temperature: that is, θ_0 in both early and late times was found to be small, and in the intermediate times at-

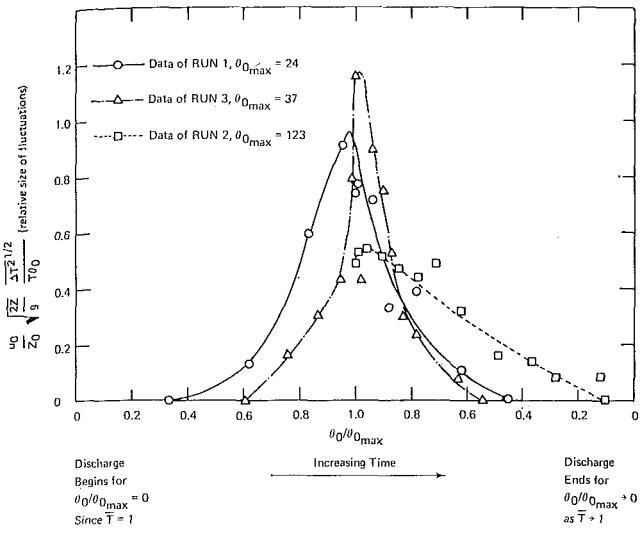

Fig. 4 Fluctuating temperature and its correlation with the mean parameter $\theta_0/\theta_{0\ max}$

tained a maximum very near the time when the fluctuations were found to be most severe. Additionally, the fluctuating temperature data from Figs. 1(*a*), 2(*a*), and 3(*a*) could be nondimensionalized according to the grouping

$$\frac{u_0}{Z_0}\sqrt{\frac{2Z}{g}}\frac{\overline{\Delta T^2}^{1/2}}{T_0\bar{T}\theta_0}$$

where $\sqrt{2Z/g}$ is the time for a particle of hot gas at the wall to travel under constant acceleration g to the sensor a distance Z from the wall. Hence, Fig. 4 was constructed and the above ordinate was plotted as a function of $\theta_0/\theta_{0\ max}$.

Experimental Apparatus

The apparatus consisted of a cylindrical vessel which discharged the two gases, nitrogen or helium, through an exit orifice at one end of the cylinder to the atmosphere. Two burst discs, located downstream of the orifice, acted as a rapidly opening valve to initiate the discharge. The cylindrical vessel, whose axis was perpendicular to the gravity field, was instrumented with two 0.001-in. copper–constantan thermocouples and a pressure gauge. One of the thermocouple junctions (T_1) was positioned within the cylinder at an axial position 1.575 in. from the orifice and the other (T_2) at an axial position 2.515 in. from the orifice: the distance between the orifice and opposite end wall of the cylinder was 4.145 in. Further details on the design and construction of the apparatus are given in [7].

The effective orifice discharge area A_1 appearing in equation (4*b*) was obtained by the use of the early-time solutions given by equations (16) and (17) as substituted into equation (6). Equation (6) was then integrated in early times, and the mass within the tank resulting from this calculation was set equal to the mass remaining as a result of the equation of state using measured pressure and mean temperature data. This procedure, valid for times less than about $0.5t_{REF}$, gave effective discharge exit areas which were substantially constant in these early times. For times later than about $0.5t_{REF}$, the same effective orifice discharge area was used as was found in the early times, the basis for this assumption being estimates from the results of Deckker and Chang [1].

Discussion of Results

Mean Gas Temperature. Three different experimental runs were considered, and the results for each of these runs are shown in Figs. 1(*a*), 1(*b*) (run 1); Figs. 2(*a*), 2(*b*) (run 2); and Figs. 3(*a*), 3(*b*) (run 3). Nitrogen was discharged in runs 1 and 2; run 1 was for a pressure ratio $p_0/p_{ATM} = 72.4$, while for run 2, $p_0/p_{ATM} = 368$. In run 3, helium was discharged at the pressure ratio $p_0/p_{ATM} = 72.4$ to give an experimental range of conditions for t_{REF} and also to give greater oscillations than in runs 1 and 2. The conditions for runs 1, 2, and 3 (shown in Figs. 1(*a*), 2(*a*), and 3(*a*), respectively) assured a turbulent free-convective mechanism throughout the minimum of mean gas temperature, $gZ^3\beta\ (\Delta T/\nu^2) > 10^8$.

The predicted mean temperatures, the broken curves shown in Figs. 1(*a*), 2(*a*), and 3(*a*), were obtained using the values for c and n in equation (9) of 0.105 and $1/3$, respectively. The experimental temperatures $\bar{T}_1$ and $\bar{T}_2$ reproduced in Figs. 1(*a*), 2(*a*), and 3(*a*) are shown for the two axial locations along the cylinder axis. Apparently there was a tendency for $\bar{T}_1$ to read consistently higher than $\bar{T}_2$, evidently as a result of axial position with respect to the orifice location. Both the mean and fluctuating components of $\bar{T}_1$ and $\bar{T}_2$ were found to be repeatable when any given run was repeated using the same initial conditions.

The value of $c = 0.105$ was chosen so that the mean of the experimental history of $\bar{T}_2$ matched the predicted response, since $\bar{T}_2$, farther from the orifice than $\bar{T}_1$, was thought to best represent the bulk temperature of the gas. For runs 1 and 2, as shown in Figs. 1(*a*) and 2(*a*), there was good agreement between the predicted and experimental mean temperatures at all times. For run 3, as shown in Fig. 3(*a*), the fluctuations in $\bar{T}_1$ were much larger than those observed for runs 1 and 2, and difficulty was experienced in interpreting a mean temperature response. However, it does appear that the predicted mean temperature response of Fig. 3(*a*) for helium underestimates the mean experimental values. This could be a consequence of the large magnitude of the fluctuations interfering to such an extent that the experimental mean temperature rises above its predicted value.

The unchoking of the flow must be accounted for to obtain the mean gas-temperature response in later times, as shown in Fig. 1(*a*). Equation (10) should not be used when $t > t_c$.

For the experimental data of runs 1, 2, and 3, the ratio of wall thermal capacitance to initial gas thermal capacitance, $M_w c_w/(m_0 R)$, was equal to 356, 70, and 353, respectively. The wall temperature was found to be essentially constant under these conditions. It was determined that the above parameter for the thermal-capacitance ratio had to be smaller than about 10 to cause a 10 percent or more change in the wall temperature.

An additional computation was performed to determine the accuracy of the approximate result given by equation (10). It was found that pressure ratios p_0/p_{ATM} greater than about 15 gave mean gas temperatures within about 10 percent of the coupled (actual) solution.

Fluctuating Gas Temperature. The temperature measurements for $\bar{T}_1$ and $\bar{T}_2$ are shown on an enlarged scale in Figs. 1(*b*), 2(*b*), and 3(*b*) for runs 1, 2, and 3, respectively. Superimposed on these figures are the calculated thermal diffusional layer δ from equation (20) and the Rayleigh number Ra_δ. As shown, the growth of δ in time is very rapid, and in Figs. 1(*b*) and 2(*b*) the fluctuations appear at the same time that δ begins to grow rapidly. However, in Fig. 3(*b*) (helium) the onset of fluctuations as directly read from the thermocouples appears to lag the rapid growth of δ. Upon further study of Fig. 3(*b*) it was noted that the abscissa t/t_{REF} for helium had a different reference time than did the nitrogen data, Figs. 1(*b*) and 2(*b*), and therefore a cellular-type movement for the helium data of run 3 from the wall to the sensor, located a distance $Z = 0.87$ in. from the wall, would take a longer dimensionless time t/t_{REF} to reach the sensor than would the nitrogen data of runs 1 and 2. In fact, if the correction is made for the time lag of a particle to travel from the wall to the sensor under constant acceleration g, then the onset of fluctuations appears to correspond more closely with the rapid growth of δ for the helium data of Fig. 3(*b*), see the dotted curves. (For the nitrogen data, the time-lag correction was found to be negligible.) At the point where oscillations are first discernible, the Rayleigh number Ra_δ, which is based

upon δ, appears to be the same for all three runs, about 10^8. Since the results of Figs. 1(b), 2(b), and 3(b) show a strong correspondence between the wall diffusion layer and the onset of fluctuations, the results of Townsend [6] appear to have validity even for transient heat transfer of the type discussed herein.

In Fig. 4 the relative size of the fluctuations is plotted as a function of the scale of logarithmic temperature. The data are seen to fall nearly symmetrically about the line $\theta_0/\theta_{0\,max} = 1$, giving substantiation to this mean correlating quantity. Since the dependence of θ_0 on mean gas temperature is $\theta_0 \sim [v_w(0, \tau) - \bar{T}]/\bar{T}$, and since θ_0 is independent of gas pressure, it may be concluded that during discharge the relative fluctuation size is governed primarily by the difference between wall and mean gas temperatures. The scaling parameter used for the ordinate of Fig. 4 appears to adequately group the fluctuation size for the data considered.

References

1 Deckker, B. E. L., and Chang, Y. F., "Transient Effects in the Discharge of Compressed Air From a Cylinder Through an Orifice," *Journal of Basic Engineering*, TRANS. ASME, Series D, Vol. 90, No. 3, Sept. 1968, pp. 333–342.

2 Ulrich, R. D., Wirtz, D P., and Nunn, R. H., "Transient Heat Transfer in Closed Containers After Gas Injection," JOURNAL OF HEAT TRANSFER, TRANS. ASME, Series C, Vol. 91, No. 3, Aug. 1969, pp. 461–463.

3 Murphy, J. S., Rannie, D., and Timson, G. W., "Stagnation Temperature Control in Blowdown Wind Tunnels," *Journal of the Aero/Space Sciences*, Vol. 25, No. 11, 1958, p. 691.

4 Tyler, B. J., and Tuck, A. F., "Heat Transfer to a Gas from a Spherical Enclosure: Measurements and Mechanism," *International Journal of Heat and Mass Transfer*, Vol. 10, No. 21, 1967, p. 251.

5 Malkus, W. V. R., "Discrete Transitions in Turbulent Convection," *Proc. Roy. Soc. A*, Vol. 225, 1954a, p. 185.

6 Townsend, A. A., "Temperature Fluctuations over a Heated Horizontal Surface," *Journal of Fluid Mechanics*, Vol. 5, 1959, p. 209.

7 Dodge, P. R., and Peterson, T. G., "The Blowdown of a Cylindrical Volume to Atmosphere," Sandia Laboratories Internal Report, 1969.

8 Goodman, T. R., "The Heat-Balance Integral and Its Application to Problems Involving a Change of Phase," TRANS. ASME, Vol. 80, 1958, pp. 335–342.

9 Landram, C. S., Sandia Laboratories Report SCL-DC-710048, May 1971.

CHIEN FAN
Research Specialist,
Aeromechanics Department,
Lockheed Missiles & Space Co.,
Huntsville, Ala.

Heat Transfer and Forces on Concave Surfaces in a Free Molecular Flow

A Monte Carlo modeling technique is described for mathematically simulating free molecular flows over a concave spherical surface and a concave cylindrical surface of finite length. The half-angle of the surfaces may vary from 0 to 90 deg, and the incident flow may have an arbitrary speed ratio and an arbitrary angle of attack. Partial diffuse reflection and imperfect energy accommodation for molecules colliding with the surfaces are also considered. Results of heat transfer, drag, and lift coefficients are presented for a variety of flow conditions. The present Monte Carlo results are shown to be in very good agreement with certain available theoretical solutions.

Introduction

ALTHOUGH THE subject of free molecule flow over simple convex bodies has been extensively investigated and relevant theories well developed, the problem of free molecule flow over concave bodies, such as a spherical surface or a cylindrical segment, is relatively unexplored. This is primarily due to the difficulties involved in analyzing the complicated multiple inter-surface reflections for a concave flow. Previous studies pertaining to this subject were all based on the simplified assumptions that the flow is hyperthermal (thermal motion neglected) and that the molecule–surface interaction is perfectly diffuse [1–7].[1] A notable exception is, however, the recently reported work of Stewart [8], in which the author made theoretical calculations of non-hyperthermal (arbitrary speed) flow *along* an infinitely long, diffusely reflecting, concave cylindrical surface. The condition of imperfect energy accommodation for the gas particles colliding with a surface was considered in most of the concave-flow studies. But the possible effects of molecular shielding are not treated except in two of the above-mentioned papers. Sparrow et al. [5] considered shielding effects in a study of hyperthermal flow over concave cylindrical surfaces of infinite length. Wimberly [7] also made investigations of shielding effects for hyperthermal flow over a hemispherical cavity.

This paper is concerned with the heat-transfer and aerodynamic-force characteristics on concave spherical and concave cylindrical surfaces in a free molecule flow. The usual limiting assumptions of hyperthermal flow and diffuse reflection have been removed. The effects of molecular shielding are included in the analysis. The length of the cylindrical surface is considered to be finite. The problems are solved by the application of a Monte Carlo simulation technique which was developed through a series of previous studies of various molecular flow problems [9–13]. The results of this study have applications in such areas as the design of high-altitude air collectors and in analyzing space-vehicle concave surfaces.

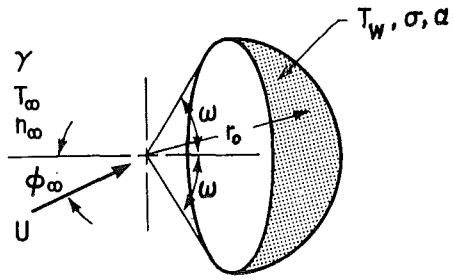

Fig. 1 Schematic of flow over a concave spherical surface

Description of the Problems

The two problems considered in this study are shown schematically in Figs. 1 and 2. A highly rarefied gas flows steadily and uniformly with a mass velocity **U** and an angle of attack ϕ_∞ over a concave spherical or a concave cylindrical surface which has a radius of curvature r_0 and a half-angle ω. The cylindrical surface has a length l, and the flow is considered to be normal to its axis. Both ϕ_∞ and ω may take on any value between 0 to 90 deg. The gas particles have a molecular mass m and a ratio of specific heats γ. The free stream is maintained at a temperature T_∞ and a number density n_∞. It is assumed that n_∞ is sufficiently low that the effect of intermolecular collisions in the vicinity of the body is negligible and a free molecule flow analysis is valid.

The temperature of the bodies is assumed to be kept at a constant value T_w. Maxwell's reflection coefficient σ and Knudsen's energy accommodation coefficient α are used to account for partial diffuse reflection and imperfect thermal accommodation for

[1] Numbers in brackets designate References at end of paper.

Based on a paper contributed by the Heat Transfer Division and presented at the Winter Annual Meeting, Washington, D. C., November 28–December 2, 1971, of THE AMERICAN SOCIETY OF MECHANICAL ENGINEERS as Paper No. 71-WA/HT-17. Manuscript received by the Heat Transfer Division August 2, 1971; revised manuscript received February 14, 1972.

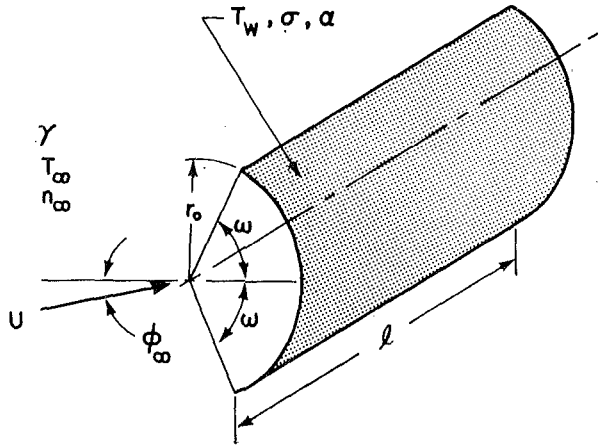

Fig. 2 Schematic of flow over a concave cylindrical surface

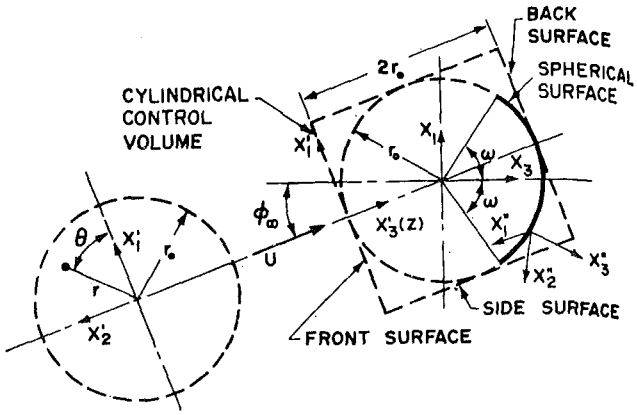

Fig. 3 The cylindrical control volume enclosing the concave spherical surface

the molecules colliding with the surface. The extreme cases of totally diffuse reflection with perfect energy accommodation ($\sigma = \alpha = 1.0$) and completely specular reflection without energy accommodation ($\sigma = \alpha = 0$) are also considered. It is assumed, as usual, that the probability distribution of the molecular velocities in the free stream is drifting Maxwellian.

Monte Carlo Simulation Procedure

To start the Monte Carlo simulation of molecular motion, it is necessary first to construct a control volume which completely encloses the body. The control volume constructed for the spherical surface is in the form of an imaginary cylinder as shown in Fig. 3. A rectangular parallelepiped control volume is chosen for the concave cylindrical body. The surfaces of the control volumes are used as the starting locations for the trajectories of sample molecules, which are mathematically simulated, one at a time, on a high-speed digital computer by means of random numbers. The selection of the control volume for a given problem is very critical to the Monte Carlo simulation of the problem. An appropriate choice of the control volume would not only simplify the calculations but also minimize the computation time.

For the present selections, the surfaces of the control volumes are either perpendicular or parallel to the free-stream velocity; thus the calculations for the position and velocity of the starting sample molecules are greatly simplified.

Consider first the flow over the concave spherical surface. A body-centered cartesian coordinate system $x_1x_2x_3$ and three local coordinate systems $x_1'x_2'x_3'$, $r\theta z$, and $x_1''x_2''x_3''$ are defined in Fig. 3 for later calculation purposes. The body-centered coordinates have their origin located at the center of curvature of the spherical body. The origin of $x_1'x_2'x_3'$ axes coincides with the center of the front surface of the control volume. The cylindrical coordinate system $r\theta z$ is an alternate system for $x_1'x_2'x_3'$ (z axis coincides with x_3' axis). The site of a molecule–surface collision will be chosen as the origin of $x_1''x_2''x_3''$ coordinates. The x_3'' axis will always be an outer normal of the spherical surface. The x_1'' axis will be perpendicular to the x_1 axis and will always make an acute angle with the x_2 axis. These coordinate systems are all right-handed.

The Monte Carlo calculations of the problem begin now by simulating a molecule (by calculating its trajectory and velocity) as it enters the control volume by means of uniformly distributed random numbers. The random numbers are generated by a congruential multiplicative random number generator [14] as

Nomenclature

A = projected area of body, $A = \pi r_0^2 \sin^2 \omega$ for the concave spherical surface, $A = 2r_0 l \sin \omega$ for the concave cylindrical surface
c_{ij} = cosine of the angle between x_i'- and x_j-axes; $i = 1, 2, 3$ and $j = 1, 2, 3$
C_D = drag coefficient defined by equation (13)
C_L = lift coefficient defined by equation (14)
C_Q = heat transfer coefficient defined by equation (12)
E_i = kinetic energy of an incident molecule
E_r = energy of a molecule reflected from the body
E_w = energy of a molecule if it is in thermal equilibrium with the body
f = velocity distribution function of the molecules crossing a surface
f_r, f_θ, f_z = marginal velocity distribution functions with respect to a set of cylindrical coordinates $r\theta z$
F_D = total drag force
F_L = total lift force
k = Boltzmann constant
l = length of the concave cylindrical surface
m = mass of a molecule
$\mathbf{M}_i$ = momentum of an incident molecule
n_∞ = number density in free stream
n_0 = sample number density in free stream
N = sample size or total number of molecules generated on the surfaces of a control volume
q_f = sample flux generated at the front surface of a control volume
Q = total amount of heat transferred to a body per unit time
r_0 = radius of curvature of the concave bodies
R_i = ith uniformly distributed pseudo-random number in the interval of 0 and 1; $i = 1, 2, \ldots, 2^{33}$
S = speed ratio, $S = U/v_m$
T_r = temperature of a molecule reflected from wall
T_w = temperature of body
T_∞ = temperature of gas in free stream
u_i = direction cosines of $\mathbf{V}_d$ with respect to $x_1x_2x_3$ axes; $i = 1, 2, 3$
$\mathbf{U}$ = mass velocity of gas in free stream
$\mathbf{v}$ = thermal velocity of a molecule
v_m = most probable thermal speed of a molecule in free stream, $v_m = (2kT_\infty/m)^{1/2}$
$\mathbf{V}_d$ = velocity of a diffusely reflected molecule
$\mathbf{V}_i$ = resultant or incident velocity of a molecule
α = energy accommodation coefficient, $0 \leq \alpha \leq 1.0$
γ = ratio of specific heats of gas
σ = Maxwell's reflection coefficient or tangential momentum accommodation coefficient, $0 \leq \sigma \leq 1.0$
ϕ_∞ = angle of attack, $0 \leq \phi_\infty \leq \pi/2$
ω = half-angle of the concave bodies, $0 \leq \omega \leq \pi/2$

follows:

$$N_{i+1} = 5^7 N_i \pmod{2^{35}} \qquad i = 0, 1, 2, \ldots \tag{1a}$$

$$R_{i+1} = 2^{-35} N_{i+1} \tag{1b}$$

where N_0 is an initial random number which could be any odd integer. The R_1, R_2, R_3, etc. are uniformly distributed pseudo-random numbers in the interval of 0 and 1 with a period 2^{33}.

For a sample molecule simulated at the front surface of the control volume (see Fig. 3), the position of the molecule with respect to the $x_1'x_2'x_3'$ axes is calculated in terms of random numbers, such that its positional distribution will be completely uniform.

Next, a thermal velocity vector for the sample molecule is randomly selected according to the assumed Maxwellian velocity distribution of the molecules crossing the surface. The relationships of the thermal velocity components in cylindrical coordinates (v_r, θ, v_z) and the random numbers can be derived using random-variable theory as follows:

$$v_r/v_m = [\ln (1/R_1)]^{1/2} \tag{2a}$$

$$\theta = 2\pi R_2 \tag{2b}$$

$$\{\exp (-v_z^2/v_m^2) + \pi^{1/2} S[1 - \text{erf } (v_z/v_m)]\}/\chi(S) = R_3 \tag{2c}$$

where v_m is the most probable thermal speed of the molecules in the free stream and the function $\chi(S)$ is defined by

$$\chi(S) = \exp (-S^2) + \pi^{1/2} S(1 + \text{erf } S) \tag{2d}$$

A brief derivation of these equations is given in the Appendix of reference [17]. Note that v_z is only implicitly related to the random number R_3 by equation (2c). An explicit relationship can, however, be developed for any S of interest by a least-squares curve fitting of a polynomial in terms of R_3. For example, a seventh-degree polynomial fit for $S = 5.0$ is

$$v_z/v_m = -3.16689 + 8.04001\eta - 12.39235\eta^2 + 11.70761\eta^3 - 1.16134\eta^4 - 6.01112\eta^5 + 4.20561\eta^6 - 0.88090\eta^7 \tag{3}$$

where $\eta = [\ln (1/R_3)]^{1/4}$.

After the thermal velocity of the molecule is computed, it is added vectorially to the mass velocity $\mathbf{U}$ to give the resultant velocity $\mathbf{V}_i$.

The total kinetic energy and momentum of this molecule may now be calculated as [15]

$$E_i = \frac{1}{2} m V_i^2 + \frac{5 - 3\gamma}{2(\gamma - 1)} kT_\infty \tag{4}$$

and

$$\mathbf{M}_i = m\mathbf{V}_i \tag{5}$$

The last term in equation (4) represents the vibrational and rotational modes of energy for polyatomic gases.

At this time, a determination is made as to whether this molecule will hit or miss the body. In the latter case, a new molecule is simulated on either the front, back, or side surface of the control volume. The number of molecules simulated on each surface of the control volume is made proportional to the molecular flux through that surface. The procedures of simulation of a sample molecule on the back surface are the same as those described above, except that the flow is away from the surface, and consequently a negative S value should be used. For a molecule simulated on the side surface of the control volume, its positional distribution is again taken to be uniform.

The equations for calculating the magnitude and polar angles of a sample molecule as it crosses the side surface of the control volume may be derived as [16]

$$v/v_m = \{\ln [1/(R_4 \cdot R_5)]\}^{1/2} \tag{6a}$$

$$\phi' = \sin^{-1} (R_6^{1/2}) \tag{6b}$$

$$\theta' = 2\pi R_7 \tag{6c}$$

where ϕ' and θ' represent the colatitude and longitude with respect to an inner normal and a tangent line drawn at the point at which the molecule is simulated. The resultant velocity of the molecule is again the vectorial sum of $\mathbf{v}$ and $\mathbf{U}$. Both energy and momentum of this molecule are calculated as above.

When a molecule hits either the concave or the convex side of the body, the site of collision is first determined and the coordinates $x_1''x_2''x_3''$ established (see Fig. 3), and then the molecule is assumed to be reflected or reemitted according to Maxwell's surface-collision model. That is, a fraction σ of all the molecule–surface collisions is reflected diffusely according to Lambert's cosine law, while the remainder is reflected specularly.

A specular reflection causes no change in the components of velocity which are tangential to the body surface, and the normal component is reversed in direction but unchanged in magnitude. There is no energy or tangential momentum (shear force) transfer for this type of collision. The normal momentum transfer (pressure force) is equal to twice the incident normal momentum.

The velocity distribution of the diffusely reemitted molecules is assumed to be Maxwellian at a temperature T_r which depends on the wall temperature T_w and the energy accommodation coefficient α.

The magnitude of velocity V_d of the diffusely reemitted molecules can be calculated by [10, 12]

$$V_d = \left(\frac{2kT_r}{m}\right)^{1/2} \left(\ln \frac{1}{R_8 R_9}\right)^{1/2} \tag{7}$$

with

$$T_r = \frac{2(\gamma - 1)}{\gamma + 1} \left(\frac{\sigma - \alpha}{\sigma}\right) \frac{E_i}{k} + \frac{\alpha}{\sigma} T_w \tag{7a}$$

It is emphasized that the quantities σ and α are treated as overall phenomenological averages and are considered to be known a priori.

The direction cosines of $\mathbf{V}_d$ with respect to $x_1''x_2''x_3''$ axes may be calculated by

$$u_{1d}'' = R_{10}^{1/2} \cos (2\pi R_{11}) \tag{8a}$$

$$u_{2d}'' = R_{10}^{1/2} \sin (2\pi R_{11}) \tag{8b}$$

$$u_{3d}'' = \pm (1 - R_{10})^{1/2} \tag{8c}$$

where, in the last equation, a positive value is taken for a convex-side collision and a negative value for concave-side collision.

The direction cosines of $\mathbf{V}_d$ with respect to $x_1x_2x_3$ axes may be obtained through the following coordinate transformation:

$$u_{id} = c_{ji} u_{jd}'' \quad (i, j = 1, 2, 3) \tag{9}$$

where c_{ji} is the cosine of the angle between the positive x_j'' and x_i axes. The nine components of the direction cosine matrix $[c_{ij}]$ were derived in reference [12].

At this time, the energy and momentum transfer to the body due to this collision are computed and recorded as

$$\Delta Q = E_i - E_r \tag{10}$$

$$\Delta \mathbf{M} = \mathbf{M}_i - m\mathbf{V}_d \tag{11}$$

where m is again the mass of a molecule.

If the collision occurs on the convex side of the body, the reflected molecule will be lost in space, and the simulation of a new molecule is in order. But if the collision occurs on the concave side of the body, further intersurface collisions are possible. The trajectory of the diffusely or specularly reflected molecule is continually traced, and momenta and energy exchanges for further collisions are again computed and recorded, until the molecule finally moves out of the control volume. After that, a new molecule is again simulated on one of the surfaces of the control volume, and the calculation is repeated.

The Monte Carlo calculation procedure used for the flow over the concave cylindrical surface is the same as that described

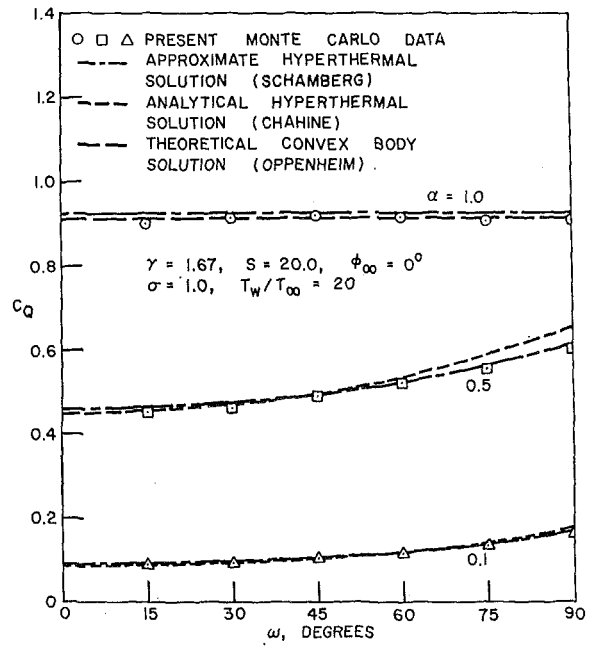

Fig. 4 Heat transfer coefficient vs. half-angle for a concave spherical surface for different values of energy accommodation coefficient

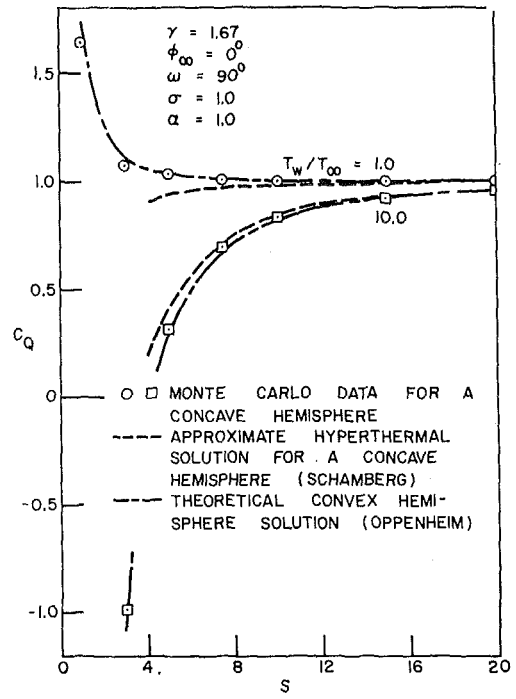

Fig. 5 Heat transfer coefficient vs. speed ratio for different values of wall-to-gas temperature ratio

above, the only difference being the geometry of the body and the shape of the control volume. This brings up an important point; namely, a Monte Carlo method can be applied to problems with more complex geometries without undue difficulties.

The Monte Carlo calculation of a molecular flow problem is completed when a sufficiently large number of molecules is sampled and when the energy and momentum exchanges for all collisions are tallied. The statistical results of heat transfer rate, drag force, and lift force may be calculated in terms of heat transfer, drag, and lift coefficients which are defined, respectively, as follows:

$$C_Q = \frac{Q/A}{(1/2)n_0 m U^3} \tag{12}$$

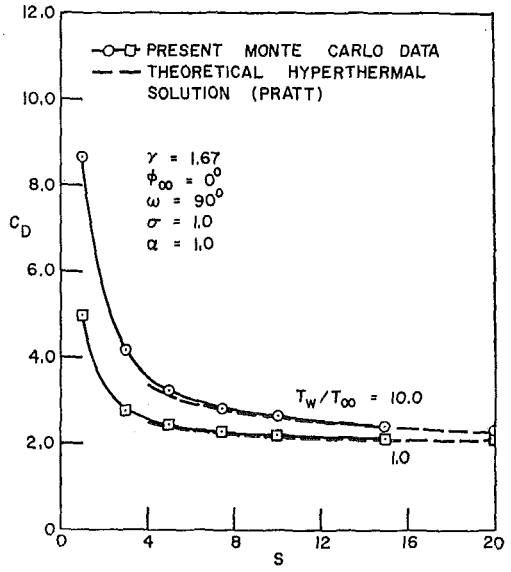

Fig. 6 Drag coefficient for a concave hemisphere vs. speed ratio for different values of wall-to-gas temperature ratio

$$C_D = \frac{F_D/A}{(1/2)n_0 m U^2} \tag{13}$$

$$C_L = \frac{F_L/A}{(1/2)n_0 m U^2} \tag{14}$$

In the above equations, A is the projected area of body ($A = \pi r_0^2 \sin^2 \omega$ for the concave spherical surface, $A = 2r_0 l \sin \omega$ for the concave cylindrical surface), Q is the total rate of heat transferred to a body on both sides, and F_D and F_L are the drag and lift forces (momentum rates) acting respectively in the direction of and normal to the mass velocity **U**. The quantity n_0 appearing in the denominator of the above equations is the sample number density in the free stream, which may be calculated from the sample flux q_f, at the front surface of the control volume as

$$n_0 = \frac{2\pi^{1/2} q_f}{v_m \chi(S)} \tag{15}$$

where the function $\chi(S)$ was defined by equation (2*d*).

Table 1 Monte Carlo calculated C_Q for a concave spherical surface and a long concave cylindrical surface compared with other analytical solutions; $S = 20.0$, $\phi_\infty = 0$ deg, $T_w/T_\infty = 20.0$, $\sigma = 1.0$, $\gamma = 1.67$, $N = 10{,}000$

		C_Q					
		Chahine's Analytical Hyperthermal Solution*		Schamberg's Approximate Hyperthermal Solution‡		Present Monte Carlo Results	
α	ω (deg)	Spherical Surface	Cylindrical Surface†	Spherical Surface	Cylindrical Surface†	Spherical Surface	Cylindrical Surface†
0.1	0	0.090	0.090	0.092	0.092	—	—
	15	0.091	0.092	0.094	0.094	0.092	0.102
	30	0.095	0.098	0.098	0.096	0.096	0.102
	45	0.105	0.104	0.106	0.108	0.104	0.104
	60	0.120	0.118	0.120	0.109	0.117	0.111
	75	0.146	0.136	0.138	0.119	0.136	0.120
	90	0.178	0.158	0.168	0.132	0.166	0.135
0.5	0	0.450	0.450	0.462	0.462	—	—
	15	0.455	0.452	0.467	0.466	0.455	0.464
	30	0.468	0.458	0.480	0.473	0.465	0.462
	45	0.490	0.477	0.499	0.495	0.491	0.479
	60	0.535	0.504	0.529	0.504	0.522	0.493
	75	0.594	0.527	0.567	0.528	0.555	0.518
	90	0.652	0.562	0.617	0.555	0.603	0.543
1.0	0	0.900	0.900	0.925	0.925	—	—
	15	0.900	0.900	0.925	0.925	0.900	0.900
	30	0.900	0.900	0.925	0.925	0.910	0.913
	45	0.900	0.900	0.925	0.925	0.917	0.897
	60	0.900	0.900	0.925	0.925	0.913	0.904
	75	0.900	0.900	0.925	0.925	0.906	0.907
	90	0.900	0.900	0.925	0.925	0.908	0.909

*Reproduced from Figs. 4 and 7 of Ref. 2.
‡Calculated with Eq. (21) of Ref. 6.
†Infinite length.
‡$l/r_0 = 20.0$.

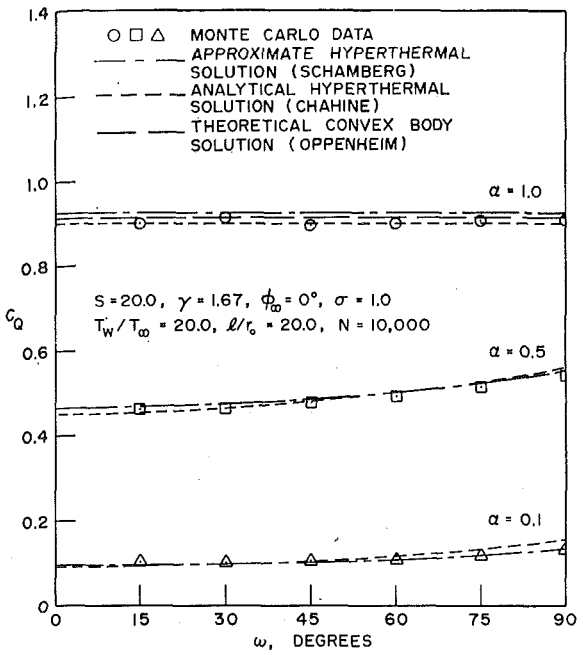

Fig. 7 Heat transfer coefficient vs. half-angle for a long concave cylindrical surface for different values of energy accommodation coefficient

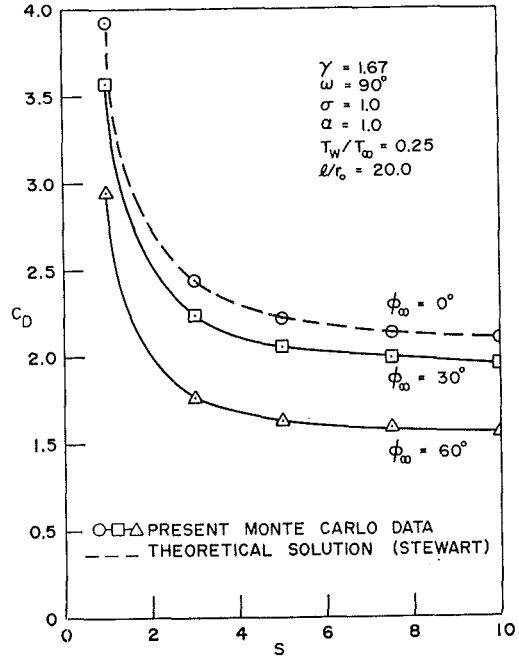

Fig. 8 Drag coefficient vs. speed ratio for a long concave cylindrical surface for different values of angle of attack

Discussion of Results

Two separate Monte Carlo computer programs were developed. A large amount of data was obtained for many possible combinations of the flow parameters γ, S, ϕ_∞, ω, T_w/T_∞, α, σ, and l/r_0. The calculations were carried out on an IBM 7094 digital computer using a sample size of 10,000 to 20,000 molecules. The computation time required for each flow case is approximately 1 to 2 min. Probable errors for the statistical results are estimated (by comparing various Monte Carlo data with known exact solutions) to be less than 3 percent.

Some typical results of heat transfer, drag, and lift coefficients are presented in Tables 1, 2, and 3, and in Figs. 4–8. Table 1 shows the Monte Carlo calculated results of heat transfer coefficient C_Q for both concave spherical and cylindrical surfaces for a near-hyperthermal flow ($S = 20.0$) compared with analytical hyperthermal solutions obtained by Chahine [2] and Schamberg [6]. In Table 2, the Monte Carlo data of C_Q, C_D, and C_L are tabulated for various values of speed ratio S. Since $\phi_\infty = 0$, C_L should be equal to zero. The data of C_L are shown in Table 2 to be close to zero. The minor variation from zero merely reflects the random fluctuation. The data tabulated in Table 3 show the effects of molecule-sample size on the accuracy of the Monte Carlo calculated results.

The results of C_Q for a concave spherical surface tabulated in Table 1 are also plotted in Fig. 4. Good agreement is observed between the present Monte Carlo data and the analytical solutions from other sources, except that Chahine's results are seen to be somewhat too high for the cases of large concavity ($\omega \geq 60$ deg). This discrepancy is perhaps due to minor errors introduced in Chahine's formulation of his momentum and energy balance equations (see Pratt [3], Sparrow et al. [5], and Schamberg [6]). The Monte Carlo results of C_Q for concave surfaces with $\alpha = 1.0$ are also shown to be in excellent agreement with corresponding theoretical convex-body solutions by Oppenheim [15]. This is because for concave surfaces with $\alpha = 1.0$ and a uniform wall temperature, multiple collisions have no effect on heat transfer; and, for a convex surface, multiple collisions are not possible (see also Fan [11]).

In Fig. 5, C_Q for a concave hemisphere is plotted as a function of S for two different values of T_w/T_∞. The dotted and center-lined curves were calculated from references [6, 15] (using their equations 21 and 2.15, respectively). As expected, the Monte Carlo results for a concave hemisphere lie very close to Oppenheim's theoretical convex-hemisphere solutions for nearly all values of S (since $\alpha = 1.0$). It is also expected that Schamberg's hyperthermal solutions agree with the Monte Carlo results only at large speed ratios, but not for small ones.

The results of C_D for a concave hemisphere are shown plotted in Fig. 6 as a function of speed ratio for two different values of

Table 2 Monte Carlo calculated C_Q, C_D, and C_L for a concave hemisphere and a finite-length concave cylindrical half-surface; $\gamma = 1.67$, $\phi_\infty = 0$ deg, $\omega = 90$ deg, $\alpha = 1.0$, $\sigma = 1.0$, $T_w/T_\infty = 0.25$, $N = 10{,}000$

S	C_Q		C_D		C_L	
	Spherical Surface	Cylindrical Surface*	Spherical Surface	Cylindrical Surface*	Spherical Surface	Cylindrical Surface*
1.0	3.526	3.364	4.106	3.968	0.006	-0.006
3.0	1.269	1.226	2.502	2.393	0.009	-0.001
5.0	1.094	1.091	2.250	2.230	0.001	0.003
7.5	1.037	1.038	2.144	2.137	0.001	-0.001
10.0	1.027	1.024	2.116	2.100	-0.002	0.002
15.0	1.014	1.005	2.077	2.052	-0.002	-0.000
20.0	1.007	1.004	2.051	2.042	0.001	-0.001

* $\ell/r_0 = 4.0$ for the cylindrical surface.

Table 3 Effects of sample size on the accuracy of Monte Carlo calculated results; $S = 20.0$, $\phi_\infty = 0$ deg, $T_w/T_\infty = 20.0$, $\omega = 90$ deg, $\alpha = 1.0$, $\sigma = 1.0$, $\gamma = 1.67$

Sample Size N	C_Q		C_D		C_L	
	Spherical Surface	Cylindrical Surface*	Spherical Surface	Cylindrical Surface*	Spherical Surface	Cylindrical Surface*
100	0.8969	0.8958	2.405	2.400	-0.0025	0.0198
200	0.8949	0.8679	2.403	2.313	-0.0086	0.0342
500	0.9003	0.8912	2.417	2.344	-0.0183	-0.0009
1000	0.9104	0.8936	2.438	2.363	-0.0036	-0.0051
2000	0.9122	0.9053	2.430	2.405	0.0091	0.0080
5000	0.9116	0.9060	2.438	2.400	0.0029	-0.0061
10000	0.9082	0.9091	2.430	2.400	-0.0024	0.0037
20000	0.9076	0.9076	2.421	2.407	-0.0025	-0.0016
50000	0.9055	0.9074	2.417	2.404	0.0015	0.0005
Exact Sol.	0.9062‡	0.9062†	2.418‡	2.409†	0	0

* $\ell/r_0 = 20.0$

‡ Calculated from Ref. 15

† Calculated from Ref. 4

wall-to-gas temperature ratio. The dotted curves are Pratt's theoretical hyperthermal solutions. It is observed that at large speed ratios, the Monte Carlo calculated results nearly coincide with the hyperthermal solution. As one would expect, however, this agreement begins to deteriorate at the lower speed ratios.

The results of C_Q for a long concave cylindrical surface ($l/r_0 = 20$) in a near-hyperthermal stream ($S = 20$) are given in Fig. 7, along with various analytical solutions from other sources. Similar observations can be noted as those given for Fig. 4.

Fig. 8 shows the results of drag coefficient for a long concave cylindrical surface as a function of speed ratio for different angles of attack. The dotted curve in Fig. 8 was reproduced from Stewart's paper [8]. Excellent agreement is again observed between the present Monte Carlo results and the theoretical solutions. Other results of C_Q, C_D, and C_L for various flow conditions are available.

Conclusions

A Monte Carlo modeling technique is developed and applied to the calculation of free molecule flow over concave spherical and cylindrical surfaces. The results indicate the following: (1) A relatively large number of flow and physical parameters can be analyzed using the present Monte Carlo calculation scheme; (2) solutions having a high degree of accuracy (error less than 3 percent) can be obtained utilizing a moderate sample size (10,000 to 20,000 molecules); and (3) computation time is not excessive (1 to 2 min on an IBM 7094 computer).

Acknowledgment

This work was supported by NASA Marshall Space Flight Center under contract NAS8-20082.

References

1 Cohen, I. M., "Free Molecule Flow over Non-Convex Bodies," *ARS Journal*, Vol. 30, No. 8, Aug. 1960, pp. 770–772.

2 Chahine, M. T., "Free Molecule Flow over Non-Convex Surfaces," in: *Rarefied Gas Dynamics*, L. Talbot, ed., Academic Press, New York, N. Y., 1961, pp. 209–230.

3 Pratt, M. J., "Concave Surfaces in Free Molecule Flow," *AIAA Journal*, Vol. 1, No. 7, 1963, pp. 1716–1717.

4 Pratt, M. J., "The Free-Molecule Flow Characteristics of Concave Surfaces," Note No. 155, The College of Aeronautics, Cranfield, England, June 1963.

5 Sparrow, E. M., et al., "Heat Transfer and Forces for Free-Molecule Flow on a Concave Cylindrical Surface," JOURNAL OF HEAT TRANSFER, TRANS. ASME, Series C, Vol. 86, No. 1, Feb. 1964, pp. 1–11.

6 Schamberg, R., "On Concave Bodies in Free Molecule Flow," P-3164-1, The Rand Corp., Santa Monica, Calif., Aug. 1967.

7 Wimberly, C. R., "Convective Heating of a Yawed Concave Hemisphere in Free Molecule Flow," *AIAA Journal*, Vol. 6, No. 12, Dec. 1968, pp. 2420–2422.

8 Stewart, J. D., "Free-Molecular Drag for Flow Along a Concave Cylindrical Surface," *AIAA Journal*, Vol. 7, No. 8, Aug. 1969, pp. 1530–1537.

9 Fan, C., "Aerodynamic Forces and Heat Transfer on Shielded Flat Plates in a Free Molecule Flow," in: *Rarefied Gas Dynamics*, L. Trilling and H. Y. Wachman, eds., Academic Press, New York, N. Y., 1969, Vol. I, pp. 551–560.

10 Fan, C., and Robertson, S. J., "Monte Carlo Solutions of Mass, Momentum and Energy Transfer for Free Molecule and Near-Free Molecule Flow Through Circular Tubes," in: *Rarefied Gas Dynamics*, L. Trilling and H. Y. Wachman, eds., Academic Press, New York, N. Y., 1969, Vol. I, pp. 655–666.

11 Fan, C., "Monte Carlo Calculation of Free Molecule Flow over Concave Spherical Surfaces," *AIAA Journal*, Vol. 7, No. 9, 1969, pp. 1803–1805.

12 Fan, C., "Monte Carlo Calculations of Energy and Momentum Transfer for Concave Spherical Surfaces in a Free Molecule Flow," LMSC-HREC A791833, Lockheed Missiles & Space Co., Huntsville, Ala., Sept. 1968.

13 Fan, C., and Robertson, S. J., "The Velocity Distribution Functions and Their Monte Carlo Random Number Relations for a Maxwellian Gas Stream Flowing Across a Surface," LMSC-HREC A784406, Lockheed Missiles & Space Co., Huntsville, Ala., July 1967.

14 Hull, T. E., and Dobell, A. R., "Random Number Generators," *SIAM Review*, Vol. 4, 1962, pp. 230–254.

15 Oppenheim, A. K., "Generalized Theory of Convective Heat Transfer in a Free Molecule Flow," *J. Aeron. Sci.*, Vol. 20, 1953, pp. 49–58.

16 Perlmutter, M., "Monte Carlo Solution for the Characteristics of Highly Rarefied Ionized Gas Flowing Through a Channel with a Transverse Magnetic Field," in: *Rarefied Gas Dynamics*, J. H. deLeeuw, ed., Academic Press, New York, N. Y., Vol. II, 1966, pp. 1–21; also NASA TND-2211, 1964.

17 Fan, C., "Heat Transfer and Forces on Concave Surfaces in Free Molecule Flow," ASME Paper No. 71-WA/HT-17.

R. C. EBERHART
Senior Research Member,
Institute of Medical Science,
Presbyterian Hospital,
San Francisco, Calif.

M. JACKSON
NIH Bioengineering Trainee.

G. J. TREZEK
Associate Professor,
Mem. ASME

Thermal Systems Division,
Department of Mechanical Engineering,
University of California,
Berkeley, Calif.

Application of a Heat-Transfer Model to Determine Regional Blood Flow Rate

The temporal patterns of central and skin temperature may provide important predictive and diagnostic information during the recovery period from major surgery. Experimentally it is found that large changes in toe temperature occur at a predictable time, early in the postoperative period. These changes reflect cardiovascular dynamics and are related to modern concepts of thermoregulation. In order to explore the contribution of time-varying blood flow to heat transfer, a heat-transfer model was applied to the great toe. This model allowed prediction of toe blood flow rate from measurements of the central and skin temperatures. Experimental verification of the analytically determined blood flow rates was made using a modified technique of venous occlusion plethysmography.

Introduction

THE CLINICIAN has long utilized skin temperature as a qualitative measure of blood flow. Correspondingly, research workers have developed energy balances in which the temperature gradient of the skin is proportional to blood flow [1–3].[1] Such models are not rigorous and yet provide reasonable results, given the uncertainties of anatomy and thermal properties and errors in skin temperature measurement [4]. Regional and whole-body thermal models have been developed. It has been possible to include many details of physiological heat transfer in the more sophisticated of these models [5], but as yet there has been no solution which adequately characterizes the regulation of convective heat flux in the cardiovascular system [6].

Recently the skin temperature of the great toe was applied to predict the entire cardiac output for the clinically significant problem of shock [7]. Moreover the toe measurement was also shown on statistical grounds to predict with some accuracy the recovery from shock. These results have provoked interest which leads to a more detailed analysis of the relation between blood flow and skin temperature.

Large and sudden changes in skin temperature occur at times of clinical significance, and recent advances in understanding of the thermoregulatory control system [8] may allow the rational interpretation of these changes. According to modern concepts of thermoregulation, a diffuse network of peripheral cold receptors and a concentrated warm receptor pool, in the anterior region of the hypothalamus, provide the sensory basis for thermal control. Via as yet unspecified pathways these signals reach a thermoregulatory control center located in the posterior hypothalamus. Comparison with a temperature set point is made at that site and signals are developed through multiple pathways which lead to heat production or heat loss by a number of mechanisms (shivering, vasoconstriction, sweating, vasodilation, behavioral responses).

In the case of rewarming following open-heart surgery, body heat is conserved during the first postoperative hours by vasoconstriction in response to low hypothalamic and skin temperatures. Metabolic heat production and shutdown of skin heat-rejection mechanisms provide for increasing central temperature until the set point is reached. At that time a strong vasodilation takes place, warm blood flows to the hands and feet, and skin temperature rises significantly (3 to 10 deg C). Absence of this response suggests one or more of the following problems: aberration of the thermal homeostatic control function, peripheral vascular disease, or weak heart function. A strong correlation exists between absence of the response and morbidity and mortality. A study of 140 patients showed absence of the normal thermal response in 47 cases: 18 of these 47 patients ultimately died and 12 others developed severe early postoperative complications [9]. Only five of the cases with normal thermal response died; these occurred, with one exception, due to arrythmia two weeks or later postoperatively.

A more intensive study of postoperative hemodynamics was undertaken in order to explore the basis of these results. This study provided an opportunity to apply a detailed heat-transfer model to the indirect computation of regional blood flow, in the context of the general postoperative course of cardiac-surgery patients.

In the following, two typical cases (I and II) with few postoperative complications will be presented and discussed in general, and with particular reference to the central- and skin-temperature responses. A case involving significant postoperative complication (III) will also be presented and discussed. The

[1] Numbers in brackets designate References at end of paper.

Contributed by the Heat Transfer Division and presented at the Winter Annual Meeting, Washington, D. C., November 28–December 2, 1971, of THE AMERICAN SOCIETY OF MECHANICAL ENGINEERS. Manuscript received by the Heat Transfer Division August 11, 1971; revised manuscript received March 22, 1972. Paper No. 71-WA/HT-38.

heat-transfer model will be applied to predict toe blood flow, and the results will be compared to those from the venous-occlusion plethysmography technique.

Methods and Materials

Patients who have undergone open-heart surgery at Pacific Medical Center are monitored through the early recovery period by a computer-based system developed by IBM Corp. in conjunction with the Institute of Medical Sciences. This system has been described in detail [10] and provides measurements every 10 min of the hemodynamic, respiratory, and thermal parameters listed in Table 1. Semiautomatic measurements were also performed, every hour or at more frequent intervals, of arteriovenous oxygen-content difference, cardiac output by Fick technique or dye-dilution technique [11]. Parenteral fluid administration, blood loss, and urine output were recorded every half hour, and drugs were recorded as administered. The patients were supine throughout the period of observation, which generally lasted through the first six to 12 postoperative hours. Preoperative diagnosis and the findings at cardiac catheterization were included in the record.

Thermistor thermometers (Yellow Springs Instruments) were attached to the pads of both great toes by sections of perforated tape. These and a rectal thermistor probe were interfaced with the patient monitoring system. Ambient temperature was measured at half-hour intervals.

Water-bath calibrations were performed for 14 skin thermistors against an ASTM 49C thermometer in the 27 to 40 deg C range. The reference thermometer had been calibrated against melting-point solutions. The calibration curves were linear. The range of slopes was 0.94 to 1.02 ($\sigma = 0.011$), with offsets at 30 deg C varying from 0 to 1.10 deg C ($\sigma = 0.59$ deg C). These thermistors were utilized at random from day to day. The YSI skin thermistors leave much to be desired in terms of size (0.63 cm diameter, 0.25 cm thick) and thermal inertia. They were found, however, to be robust, and the mode of attachment was practical in view of the exigencies of the recovery-room situation.

In addition to the toe and rectal temperatures, tympanic-membrane temperatures were obtained with a Radiation Systems, Inc. model A 3591-01 tympanic thermometer. Tympanic-membrane temperatures were obtained at 20-min intervals during the course of the experiment and recorded manually. This was accomplished by inserting the probe in the external acoustic meatus and gently bringing the probe to rest on the tympanum. The probe was removed following each measurement.

Blood flow rates in the great toe were measured by a modification of Whitney's method of venous-occlusion plethysmography [12]. The technique assumes the venous return from the toe may be occluded, without affecting inflow, such that rate of change of circumference of the toe is proportional to flow at the instant of occlusion. The many details of technique and analysis are discussed in a series of papers in the physiological literature [13].

Analytical Model

In order to more fully understand the circulatory mechanisms which have been previously discussed, the bio heat equation was used to model the heat-transfer process in the great toe. This analytical expression, which has been successfully used in prior biological heat-transfer studies, is based on the fact that the heat-transfer mechanism in tissue must not only account for conduction but also heat addition or removal by blood supply and metabolic heat-generation. Thus for cylindrical coordinates and constant properties

$$\rho c \frac{\partial T}{\partial t} = \frac{k}{r} \frac{\partial}{\partial r}\left(r \frac{\partial T}{\partial r}\right) + \dot{m}_b c_b (T_b - T) + S_m \qquad (1)$$

where S_m is the contribution from metabolic heat-generation and the quantity $\dot{m}_b c_b (T_b - T)$ represents the heat exchange between the blood and tissue. Both the physical and analytical implications of the terms in equation (1) have received prior attention [14]. Also, in applying the relation to the great toe, two assump-

Table 1 Physiologic parameters monitored by the IBM Institute of Medical Science patient monitoring system

Hemodynamic parameters

Arterial pressure: systolic, diastolic, mean
Left atrial pressure: mean
Central venous pressure: mean
Pulse rate: from pressure
Heart rate: from EKG
Cardiac output: Fick and dye-dilution techniques

Respiratory parameters

Respiratory rate
Tidal volume and minute volume
Lung compliance
Work of inspiration
Frictional airway resistance
Oxygen consumption
Carbon dioxide production
Inspired oxygen concentration
End-expired oxygen and carbon dioxide concentrations

Thermal parameters

Rectal and skin [2] temperatures

Blood gas, urine, clinical chemistry data, plus nurse's notes are entered into the record via a bedside interactive terminal

Nomenclature

a = parabolic profile parameter, deg C/cm²
c = medium heat capacity, cal/gm-deg C
c_b = heat capacity of blood, cal/gm-deg C
$\dot{m}_b$ = blood flow rate, ml/cm³-sec
k = medium thermal conductivity, cal/cm-sec-deg C
K = gage calibration constant, cm/mv
G = grid baseline (circumference), cm
ΔE = voltage change of plethysmograph, v
t = time, sec
r = radial coordinate, cm
r_0 = radius for assumed cylindrical toe geometry, cm
R = nondimensional radius (r/r_0)
S_m = metabolic heat generation, cal/cm³
T = temperature, deg C
T_c = temperature at $r = 0$, deg C
T_i = ambient temperature, deg C
T_b = blood inlet temperature to toe, deg C
T_0 = $T_b + S_m/\dot{m}_b c_b$, deg C
V = $T - T_i$, deg C
V_0 = $T_b - T_i + S_m/\dot{m}_b c_b$, deg C
h = nondimensional heat-transfer coefficient (Hr_0/k)
H = surface heat-transfer coefficient, cal/sec-cm²-deg C
I_0, I_1 = modified Bessel function of the first kind
J_0, J_1 = Bessel function of the first kind
u_m = eigenvalues of $u_m J_1(u_m) - hJ_0(u_m) = 0$
α = thermal diffusivity, cm²/sec
β = blood flow parameter ($\dot{m}_b c_b r_0^2/k$)
ρ = medium density, gm/cm³
MAP = mean arterial pressure, mm Hg
CVP = central venous pressure, cm H_2O
CO = cardiac output, l/min
TPR = total peripheral resistance, dyne-sec/cm⁵
HR = heart rate from EKG, 1/sec
PR = pulse rate from pressure curve, 1/sec
OUP = oxygen consumption, ml/min

tions must be noted. First, the heat-transfer process through the toe is assumed to be in the radial direction, which implies the model of an infinite cylinder. Experimental evidence of the similarity of temperature responses of thermistors placed near the ventrum and the tip of a great toe during a patient's rewarming imply that this is reasonable. Second, the perfusion $\dot{m}_b$ is assumed to be uniform over the cross section of the toe.

Equation (1) can be cast into a more convenient analytical form by introducing the following quantities:

$$T_0 = T_b + S_m/\dot{m}_b c_b \qquad V = T - T_i$$

$$R = r/r_0 \qquad V_0 = T_b - T_i + S_m/\dot{m}_b c_b$$

so that

$$\frac{\partial^2 V}{\partial R^2} + \frac{1}{R}\frac{\partial V}{\partial R} - \frac{r_0^2}{\alpha}\frac{\partial V}{\partial t} - \beta V = -\beta V_0 \tag{2}$$

where $\beta = \dot{m}_b c_b r_0^2/k$ and can be considered as a blood flow parameter. Equation (2) is solved by standard methods for symmetry of the temperature profile at the center line ($\partial V/\partial R = 0$ at $R = 0$) and convective heat transfer from the surface of the toe; that is,

$$\text{at} \quad R = 1 \qquad \frac{\partial V}{\partial R} = -hV \qquad \text{where} \qquad h = Hr_0/k$$

The solution is

$$V = V_0\left[1 - \frac{hI_0(\sqrt{\beta}R)}{\sqrt{\beta}I_1(\sqrt{\beta}) + hI_0(\sqrt{\beta})}\right] - 2\beta h V_0 \sum_{m=1}^{\infty} \frac{e^{-(\alpha/r_0^2)(u_m^2+\beta)t}\, J_0(u_m R)}{(u_m^2 + \beta)(h^2 + u_m^2)J_0(u_m)} \tag{3}$$

u_m is given by $u_m J_1(u_m) - hJ_0(u_m) = 0$.

The solution of equation (3) is valid at all R, but the surface temperature is of principal interest in this case. It can be obtained by evaluating equation (3) where h, V_0, and β are invariant with time. Knowing the values of the heat-transfer coefficient at the surface of the toe and the temperature of the incoming blood T_b, agreement between the analytical and experimental surface temperatures will result when the proper value of $\dot{m}_b$ is selected. However, as will be further elaborated, treating $\dot{m}_b$ as a step function with time will yield surface temperature profiles which are not in agreement with experimental observations. Equation (3) can be extended for variable blood flow rate by employing an iterative procedure. Specifically, a test value of $\dot{m}_b$ is chosen and held constant over a time interval, typically 500 sec for the range of experimental variables being considered. The criterion on $\dot{m}_b$ is that computed surface temperature be within 0.1 deg C of measured temperature. At each interval a new approximate initial condition which is a parabolic form of the temperature profile, namely $V = T_c - ar^2$, is generated and used as the initial condition for the particular time interval. The parabola is an excellent fit to the computed temperature distribution. With this modification equation (3) becomes

$$V = V_0\left[1 - \frac{hI_0(\sqrt{\beta}R)}{\sqrt{\beta}I_1(\sqrt{\beta}) + hI_0(\sqrt{\beta})}\right] + \sum_{m=1}^{\infty} A_m J_0(u_m R) e^{-(\alpha/r_0^2)(u_m^2+\beta)t} \tag{4}$$

where

$$A_m = \frac{2hT_c(u_m^2 + \beta) - 2hV_0\beta - 2ah(1 - 4/u_m^2)(u_m^2 + \beta) - 4a(u_m^2 + \beta)}{(u_m^2 + \beta)(h^2 + u_m^2)J_0(u_m)}$$

The infinite series has a rapid rate of convergence so that only five or six terms are required to yield a value of temperature within 10^{-7}.

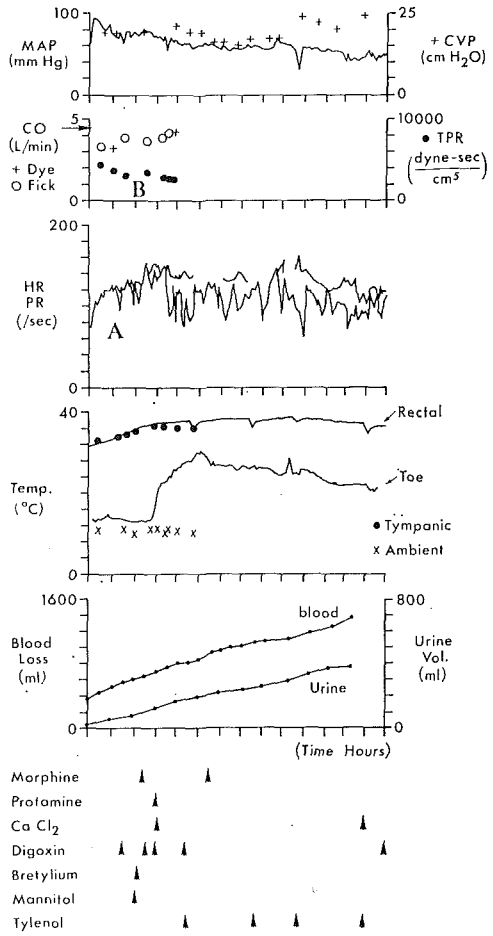

Fig. 1 Summary of clinically measured variables, case I

Case Studies

Case Study I. Figure 1 presents a general record of the first 12 postoperative hours of a mitral-valve-replacement patient. The mean arterial pressure (MAP) was typical for this type of patient, showing an initially high value which declined and stabilized in the first four postoperative hours. Atrial fibrillation was observed at the second postoperative hour (A) by the decrement between heart rate (HR) and pulse rate (PR), and was treated with Digoxin. An initial blood loss was corrected by administration of Protamine and infusion of blood. The bleed and arrythmia caused an initially low cardiac output (CO) below the preoperative value. Total peripheral resistance (TPR), defined as systemic pressure drop divided by cardiac output, declined at a steady rate, modified only by the transient vasoconstrictive effect of Bretylium (B). Urine output was on the low side of normal, although improved by administration of Mannitol. Blood gases and respiratory data were normal.

Turning to the temperature data, normal steady increases in rectal and tympanic-membrane temperatures were observed in the first hours, accompanied by a normal slight decline in toe skin temperature. Tympanic-membrane temperatures stabilized at the third postoperative hour, in conjunction with a strong increase in toe temperature. This rewarming pattern is typical in all features for patients with uneventful recoveries.

The toe pattern may not be called a normal response, however, as there were several drugs with cardiovascular activity given in the hour preceding the onset of the toe rewarming. Following the

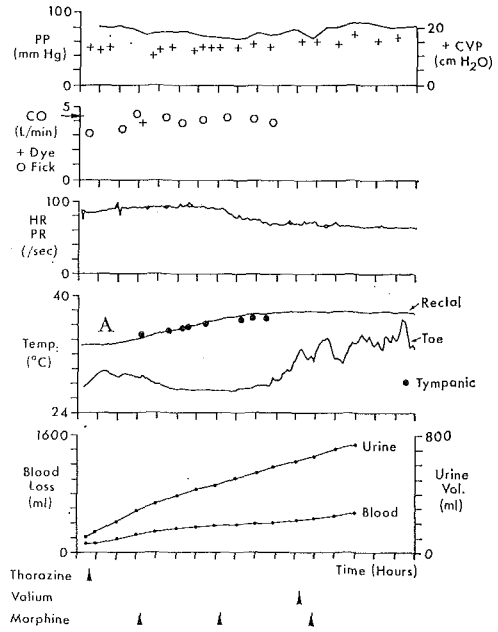

Fig. 2 Summary of clinically measured variables, case II

initial rise the course of the toe temperature was affected by Tylenol, fluid balance, and ambient conditions. The postoperative course of this patient was uneventful following this initial period.

Case Study II. A second mitral-valve-replacement case is presented in Fig. 2. A strong pulse pressure (PP defined as systolic–diastolic), stable heart rate, and stable central venous pressure (CVP) characterize the first postoperative hours. An initially low cardiac output responds to the vasodilational effect of Thorazine at the first postoperative hour; thereafter it was stable, equal to the preoperative value at cardiac catheterization. Bleeding rate was low and urine output initially high, becoming normal later in recovery. Oxygen consumption was initially low, but rose steadily in the first hours. There was no evidence from blood gas data of impaired lung function. The low oxygen consumption correlates with an initially low rectal temperature. Rectal temperature did not begin to rise until the patient was covered (except his feet) with warmed blankets (A). Despite the initial low core temperature, the patient was awake and alert and did not exhibit visible shivering. Toe temperature rose initially due to the legs being covered with warm blankets, but then exhibited a characteristic decline in conjunction with rising rectal temperature. The patient did not reach a steady tympanic-membrane temperature until the tenth postoperative hour. The rise in toe temperature was strong, but slightly delayed. Recovery of this patient was good, despite the strong initial hypothermia.

Case Study III. This patient (see Fig. 3) exhibited symptoms of diabetes and peripheral vascular disease preoperatively, and was operated for coronary artery disease, receiving two aorto-coronary grafts. Postoperatively the mean arterial pressure was elevated and the patient appeared pale and vasoconstricted. Lidocaine was used to treat postoperative atrial fibrillation (which is evidenced by the heart-rate/pulse-rate decrement). This appeared to be unsuccessful, and Digitalis therapy, which had been initiated during surgery, was reinstituted in the fourth postoperative hour. A moderate bleed, primarily from the left chest drain, was balanced by blood administration. Urine output increased in response to apparent renal vasodilation with administration of Thorazine, but then declined to low-normal rate. Cardiac output was low initially and increased slowly as the physician sought to correct arrythmia, bleeding, and vasoconstriction. Total peripheral resistance was initially high (A) and responded to the vasodilational action of Thorazine, but stabilized at a still elevated level. Oxygen consumption (OUP) was normal, but this was accomplished at the expense of a large A–V difference of blood oxygen content, and in the face of an inefficient alveolar ventilation.

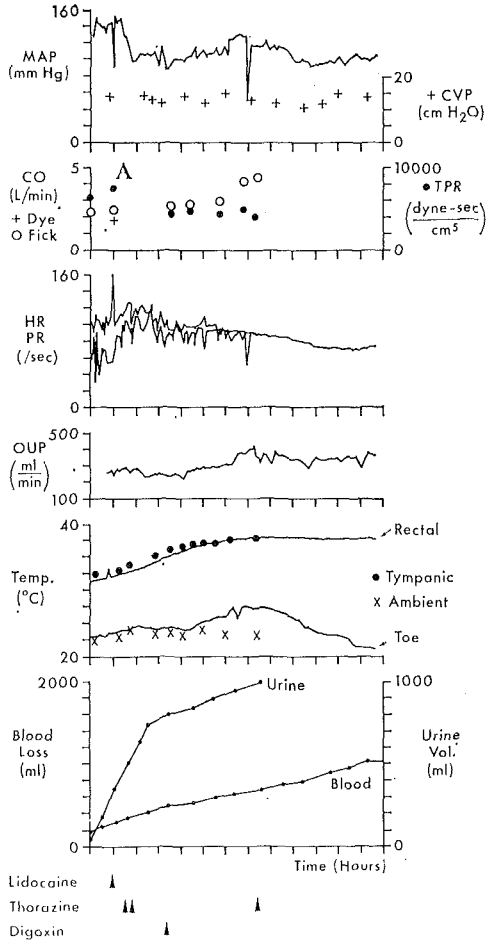

Fig. 3 Summary of clinically measured variables, case III

Rectal temperature was quite low initially but increased steadily, lagging tympanic-membrane temperature approximately one hour. Toe temperature rose in response to warm blankets covering the legs (not the feet). The tympanic-membrane temperature stabilized midway in the fifth hour and a weak response was seen in both toes. At the beginning of the seventh hour, a 1 deg C step in toe temperature took place, in synchrony with increased oxygen consumption, cardiac output, urine output, and increased mean arterial pressure. No single therapeutic measure correlates with the sudden improvement. A combination of improved circulating volume and cumulative effects of Digoxin might explain these changes in status. In any event, the improvement was transitory. Vasoconstriction was countered again with Thorazine, which caused a decrease in central venous pressure but also a drop in toe temperature. The patient was seen through a difficult early recovery period, but suffered cardiac arrest on the sixth postoperative day, declined in status, and died five days later.

Results

Parametric-Model Evaluation. Equation (3) was evaluated for a range of β in order to obtain the response of the surface temperature to variations in the blood flow. The blood flow rate is treated as a step function at time zero. The effects are shown in Fig. 4 for typical values of blood inlet temperature ($T_0 = 37$), heat-transfer coefficient ($H = 1.355 \times 10^{-4}$ cal/sec-cm²-deg C), and geometry. It is important to note that the analytical toe temperature profiles do not necessarily resemble those of a typical rewarming

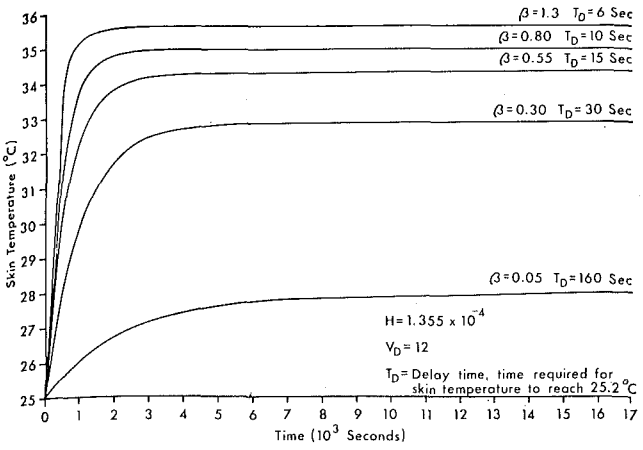

Fig. 4 Skin temperature response curves for the step changes in blood flow rate with constant heat-transfer coefficient and blood inlet temperature

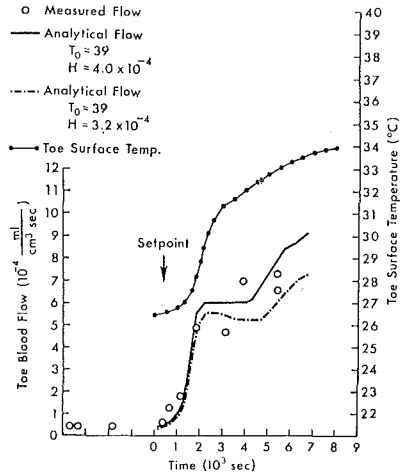

Fig. 5 Comparison of analytical and experimental blood flow rates, case I

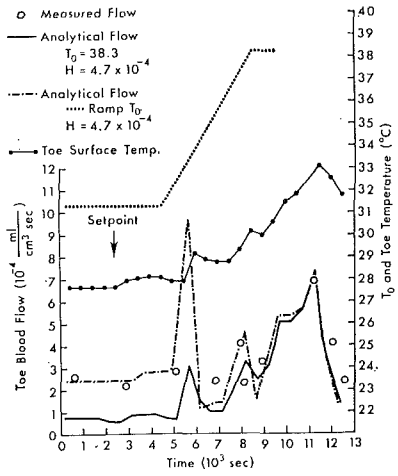

Fig. 6 Comparison of analytical and experimental blood flow rates, case II

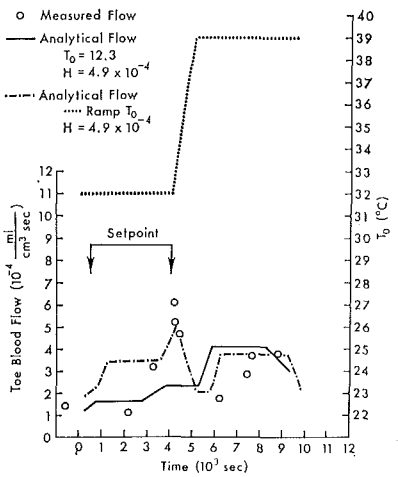

Fig. 7 Comparison of analytical and experimental blood flow rates, case III

pattern (cf. case II, Fig. 2, where the knee of the curve is less sharply defined). Based on this evidence the analytical model was modified to treat a variable blood flow rate, and equation (4) was used for comparison with experimental data.

Blood Flow. The analytical and experimental toe blood flows and the experimental temperatures are shown for case I in Fig. 5. Blood inlet temperature was assumed to be 39 deg C, which is the rectal temperature. Agreement with experimentally determined blood flow rates is achieved for values of the heat-transfer coefficient between 3.2 and 4.0 $\times$ 10^{-4} cal/sec-cm²-deg C, which are in the range of expected values for the particular experimental condition (T_{ambient} = 25 deg C). The analytically determined blood flow rates follow the trends of increasing and stabilizing surface temperature. The tympanic-membrane temperature stabilized at the time indicated by the arrow in the figure. According to the thermoregulation theory discussed in the Introduction, a chain of events culminating in peripheral vasodilation and increased blood flow to the toes would occur soon after stabilization of tympanic temperature.

The blood flow comparisons for case II are given in Fig. 6. The analytical blood flow is computed with inlet temperature assumed equal to rectal temperature and a heat-transfer coefficient of 4.7 $\times$ 10^{-4} cal/sec-cm²-deg C. The detailed agreement of predicted and observed blood flow is not as good as for the previous case. Trends are reproduced, but a decrement at the early times is apparent. A heat-transfer coefficient of 6.3 $\times$ 10^{-4} increases flow by only 0.1 $\times$ 10^{-4} ml/cm³-sec at t = 1000, while increasing flow by 2 $\times$ 10^{-4} ml/cm³-sec at t = 11,500. Clearly the response is skewed by such a change in heat-transfer coefficient. It is not unreasonable in the light of clinical experience that blood inlet temperature to the toes should fall below rectal temperature in the initial stages of rewarming. This was tested by applying a ramp function to the toe inlet temperature profile. As seen in Fig. 6 the experimental–analytical comparison is greatly improved.

Results from case III are presented in Fig. 7. A smaller increase in temperature and lower specific blood flows, in general, were observed for this terminal case. Stabilization of tympanic-membrane temperature was not as sharply defined as in other cases, indeed there may have been an adjustment of the set point within the period indicated in Fig. 7. A strong increase in experimental blood flow is observed at the end of this period. This would be in agreement with the thermoregulatory-response theory. However, this pulse is unsupported by the skin-temperature-derived blood flow for constant inlet temperature. A second increase in flow obtained at 6000 sec, which is reflected in the analytical results; this second rise corresponds to the transient improvement in status of the patient at the sixth postoperative hour (see Case Studies). A ramp inlet temperature profile was tried in order to improve the experimental–analytical comparison. As in case II the ramp function provided a better fit to the experimental data than did the case of constant inlet temperature.

Discussion

Although the model accounts for metabolic heat-generation, cf. $S_m/\dot{m}_b c_b$, this term has been explicitly assumed to be small compared to the blood inlet temperature. The model assumes a

homogeneous isotropic medium, and the thermal properties used are those for water [15]. In general, for constant values of blood inlet temperature and surface heat-transfer coefficient, analytical values of the blood flow rates are determined when the analytically computed surface temperature matches the experimentally measured surface temperature. Under the experimental conditions of constant ambient temperature and a quiet patient, large variations in surface heat-transfer coefficient are unlikely.

Case I gives good agreement between theory and experiment, whereas in cases II and III the model (with constant blood inlet temperature) predicts lower values of the blood flow rate during early times in the rewarming pattern. In this instance the model appears to be dominated by the trends established by the surface temperature profile. There is an observable pattern between changes in measured blood flow and skin temperature, and the model on this basis correctly predicts the trends in the blood flow rate.

In cases II and III there is a delay between stabilization of central temperature and onset of the toe response. This may be indicative of sluggish flow and increased residence time in the peripheral bed. Cold limbs were observed in both these cases and it is therefore reasonable that heat loss occurred prior to blood entry into the capillary network of the toe. This provides a rationale for application of a time-varying blood inlet temperature.

Several ramp-function inlet temperature distributions were modelled in order to obtain the best fit with the plethysmographic data. Beginning the ramp at the time the set point was achieved did not provide the best agreement. The time durations of the "best-fit" ramps were quite different for the two cases (4000 and 1000 sec). Ramp height was also chosen for best-fit results. More clinical data and experience in application of the model will be necessary before rules can be developed for construction of the inlet temperature function. It is clear, however, that a time-varying inlet temperature substantially improves the agreement of the model with measured blood flow rate.

The maximum measured values of toe blood flow in cases I and II were 12.3 and 7.0 $\times$ 10^{-4} ml/cm^3-sec respectively. Skin blood flow has been estimated at 20 $\times$ 10^{-4} ml/cm^3-sec [16] Finger and toe blood flow rates have been measured by water plethysmographs with values around 50 $\times$ 10^{-4} ml/cm^3-sec [13]. Agreement with literature values was not really expected, since the patients considered in this study have weak hearts and have undergone the trauma of surgery.

Our data suggest that there is no correlation between cardiac output and toe temperature in the early recovery period following cardiac surgery. This is in contrast to the results of Joly et al. [7] for patients in shock. It should be noted that cardiovascular status in shock is quite different than in early surgical recovery. Hence the results are not necessarily inconsistent.

The detailed responses and interactions of multiple-organ systems are not well understood, particularly so in states of disease. One therefore approaches correlations of physiological parameters with caution. The physician must manage the cardiac patient in spite of such difficulties, and places emphasis on pump function and those indicators of pump function which he can measure. It is therefore a curious but potentially significant fact that a rise in toe temperature of 3 deg C or less, at the stabilization of central temperature, should correlate with mortality and morbidity. The hypothesis outlined in the Introduction may be amplified in light of the data presented herein. When toe skin temperature is lower than 27 deg C, and hypothalamic temperature is below the set point, impulses from cold receptors in the toe do not lead to peripheral vasodilation. Once the set point is achieved, as evidenced by stabilized tympanic-membrane temperature, a vasomotor response takes place leading to a steady increase in blood flow above a basal level of 1 to 3 $\times$ 10^{-4} ml/cm^3-sec. This is accompanied by an increase of 3 to 10 deg C in toe temperature. The case exhibiting a transient increase in toe blood flow was unable to sustain this perfusion. Why was peripheral flow not maintained? The peripheral vasodilation is assumed to occur in two steps. First, vasoconstrictor tone must be released; this is assumed to be under control of the thermoregulator/vasomotor system. Next, a force is required to open the peripheral bed; this is assumed to be provided by pressure impulses transmitted down the arterial tree. If cardiac output is low and vasoconstriction continues in the arterial/arteriolar net upstream of the toes (which may involve a multiplicity of collateral pathways), the critical opening pressure cannot be initiated or maintained. The control in this case is transferred to vasomotor action at an as yet unspecified site. The initial flow to the toes is dictated by the need to lose heat in order to maintain central temperature at the set point. The results indicate that in the hierarchy of vasomotor controls this is a less significant requirement. As such, and in the light of the predictability of the onset of toe blood flow, the physician has a tool for the early warning of cardiovascular dysfunction.

Conclusions

The analytical model predicts reasonable values of time-varying toe blood flow. Including a physiologically reasonable time-varying blood inlet temperature in the model provides good agreement with blood flow measured by venous-occlusion plethysmography.

Experimental measurements of the flow following peripheral rewarming are lower than those reported in the literature for normal subjects. There is no correlation between toe temperature and cardiac output in early recovery from cardiac surgery.

Heat convection predominates in the bulk of this tissue. The model, which had previously been verified in a conduction-dominated tissue, is validated for this situation.

Acknowledgments

This research was supported in part by USPHS grant 5P01-He06311 and in part as a joint study project with IBM Corp. The cooperation of Dr. John Osborn and the staff at Pacific Medical Center is gratefully acknowledged. The work was also supported in part by USPHS NINDS grant 2R01-NS 08236-03.

References

1 Burton, A. C., *Journal of Nutrition*, Vol. 7, 1934, p. 481.

2 Felder, D., et al., "Relationship in the Toe of Skin Surface Temperature to Mean Blood Flow Measured with a Plethysmograph," *Clinical Science*, 1954, pp. 251–256.

3 Richardson, P. D. J., and Whitelaw, J. H., "Transient Heat Transfer in Human Skin," *J. Franklin Institute*, Vol. 286, 1968, p. 169.

4 Stoll, A. M., "Techniques and Uses of Skin Temperature Measurements, Thermography and Its Clinical Applications," *Ann. N. Y. Academy of Science*, Vol. 121, 1964, pp. 49–56.

5 Wissler, E. H., "A Mathematical Model of the Human Thermal System," in: *Chemical Engineering in Medicine*, E. F. Leonard, ed., AIChE, Vol. 62, 1966, pp. 65–78.

6 Fan, L. T., "A Review on Mathematical Models of the Human Thermal System," *IEEE Transactions on Bio-Medical Engineering*, BME-18, 1971, pp. 218–234.

7 Joly, H. R., and Weil, M. H., "Temperature of the Great Toe as an Indication of the Severity of Shock," *Circulation*, Vol. 39, 1969, p. 131.

8 Benzinger, T. H., "Heat Regulation: Homeostasis of Central Temperature in Man," *Physiological Reviews*, Vol. 49, 1969, p. 671.

9 Eberhart, R. C., "Peripheral Temperature and Cardiac Output in the Postoperative Heart Patient," *Annual Conference on Engineering in Medicine and Biology*, Vol. 23, 1970, p. 34.

10 Osborn, J. J., et al., "Computation for Quantitative On-Line Measurements in an Intensive Care Ward," *Computers in Biomedical Research*, Vol. 3, 1969, pp. 207–237.

11 Eberhart, R. C., Shenker, M., and Radke, W. A., "On Line Measurement of Cardiac Output," in: *Society of Engineering Science Symposium*, Washington University, St. Louis, Mo., Nov. 1969.

12 Whitney, R. J., "The Measurement of Volume Changes in Human Limbs," *Journal of Physiology*, Vol. 121, 1953, pp. 1-27.
13 Wolstenholme, G. E. W., and Freeman, J. S., eds., "Peripheral Circulation in Man," in: *Ciba Foundation Symposium*, Little, Brown and Co., 1954.
14 Trezek, G. J., and Jewett, D. L., "Nodal Network Simulation of Transient Temperature Fields from Cooling Sources in Anesthetized Brain," *IEEE Transactions on Bio-Medical Engineering*, Oct. 1970, pp. 281-286.
15 Cooper, T. E., and Trezek, G. J., "Correlation of Thermal Properties of Some Human Tissue with Water Content," *Aerospace Medicine*, Vol. 42, No. 1, Jan. 1971, pp. 24-27.
16 Ganong, W. F., *Review of Medical Physiology*, 3rd ed., Lange Medical Publications, Los Altos, Calif., 1967.

journal of heat transfer

technical briefs

This section consists of contributions of 1500 words or less (about 5 double-spaced typewritten pages, including figures). Technical briefs will be reviewed and approved by the specific division's reviewing committee prior to publication. After approval such contributions will be published as soon as possible, normally in the next issue of the journal.

An Experimental Study of Combined Forced- and Free-Convective Heat Transfer from Flat Plates to Air at Low Reynolds Numbers

P. H. OOSTHUIZEN[1] and M. BASSEY[2]

Introduction

MEAN heat-transfer rates from thin flat plates aligned with a forced velocity have been measured under such conditions that the effects of the buoyancy forces cannot be ignored, i.e., in the region of combined- or mixed-convective flow. A number of analytical studies of this problem have, of course, been undertaken, see, for example, [1, 2].[3] However, these studies have all been based on the use of the boundary-layer equations, while the range of variables covered by the present tests is such that the boundary-layer approximations are not applicable. The range of variables is also different from those covered in previous experimental studies [3, 4].

Apparatus

The tests were carried out in an open-return wind tunnel with an 8- × 4-in. working section. The test plates consisted of 0.001-in-thick platinum ribbons which were mounted on the center line of the wind tunnel and spanned the 8-in. width of the tunnel as shown in Fig. 1. The plates were clamped between aluminum blocks on the walls of the tunnel, and these blocks had screw adjustments which allowed the ribbons to be kept taut and aligned with the flow. Four ribbons were used, these having lengths L as defined in Fig. 1 of 0.125, 0.25, 0.5, and 1 in.

The entire wind tunnel was mounted on a frame which could be pivoted on a horizontal axis parallel to the test plates. In this way the air stream and the test plates could be set at any angle α to the vertical. Results are reported here for angles α of 0 deg, i.e., for assisting flow, and 180 deg, i.e., for opposing flow.

The plates were heated by passing a d-c current through them. The power dissipated was then obtained by measuring the current passing through the plate and the voltage drop across the entire plate. Some of the heat generated was, of course, conducted from the plate to the clamping blocks, and in order to calculate the heat-transfer rate a correction for this end loss had to be made. This was done by calculating the end loss using a one-dimensional fin-type analysis. In no case did the end loss so found exceed 10 percent of the total heat generated in the plate. The adequacy of this method of determining the end loss was confirmed by repeating some of the tests with voltage taps attached to the plates at a distance of 1 in. from each clamping block, thus allowing the heat generated over the central portion of the plate to be found and eliminating the need to apply an end-loss correction.

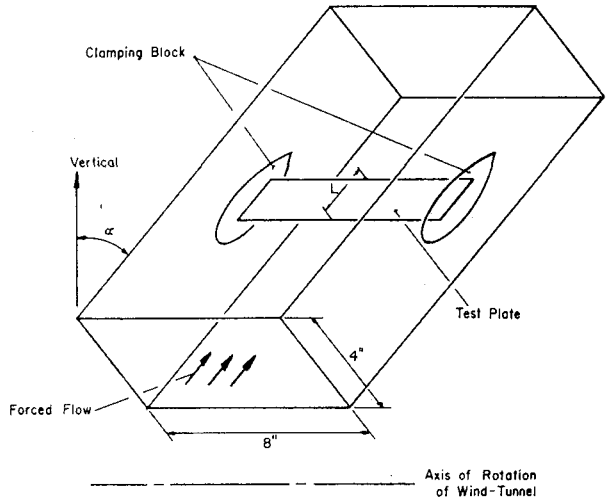

Fig. 1 Arrangement of test plates in wind tunnel

The mean temperature of the plates was determined by calculating their resistance from the voltage and current readings and using their measured resistance in the unheated state and their measured temperature coefficient of resistance.

In the present study the heat-transfer rate from the surface of the plates to the air was not uniform due to internal heat conduction. An order-of-magnitude analysis suggests, in fact, that a uniform-surface-temperature condition was more nearly simulated than a uniform-surface-heat-flux condition.

The velocity of the air in the wind tunnel could be varied between 0 and about 1 fps. The velocity was measured using a DISA low-velocity anemometer. Because of the low velocities used in the present work, the boundary layers on the walls of the tunnel were relatively thick and the velocity was not uniform across the width of the plate. In all cases the Reynolds numbers used to describe the results are based on the average velocity. In no case did this differ by more than 5 percent from the centerline velocity.

Results and Discussion

In combined convection

$$N_L = \text{function } (R_L, G_L, \text{Pr}, \alpha) \tag{1}$$

where $N_L = \bar{h}L/k$ is the mean Nusselt number, $G_L = \beta g(\bar{T}_w - T_\infty)L^3/\nu^2$ is the mean Grashof number, Pr is the Prandtl number, and α is the angle of the plate to the vertical. $\bar{T}_w$ is, of course, the mean plate temperature which is also used in determining the mean heat-transfer coefficient $\bar{h}$.

In the present tests, Pr remained effectively constant. As previously mentioned, measurements were undertaken at $\alpha = 0$ and

[1] Associate Professor, Department of Mechanical Engineering, Queen's University, Kingston, Ontario, Canada.
[2] Research Assistant, Department of Mechanical Engineering, Queen's University, Kingston, Ontario, Canada. Assoc. Mem. ASME.
[3] Numbers in brackets designate References at end of technical brief.
Contributed by the Heat Transfer Division of THE AMERICAN SOCIETY OF MECHANICAL ENGINEERS. Manuscript received by the Heat Transfer Division April 10, 1972.

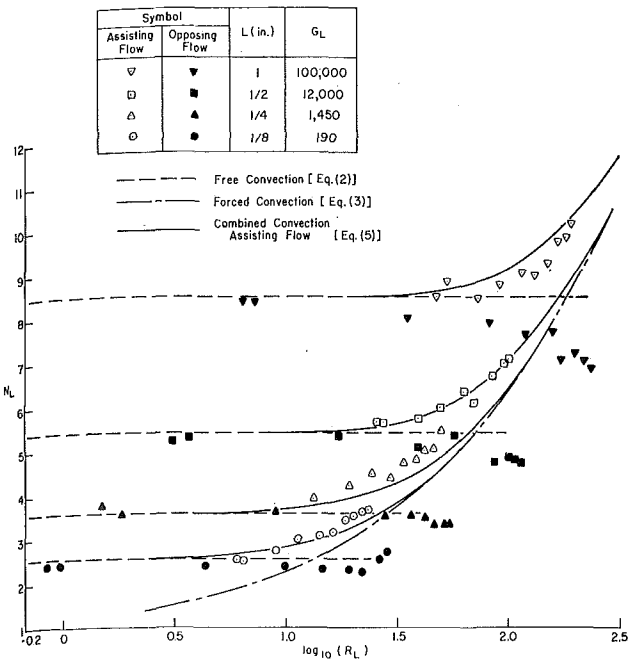

Fig. 2 Variation of Nusselt number with Reynolds number for various Grashof numbers in assisting and opposing flow

180 deg. At each of these values of α, measurements were made at a series of different velocities and a series of different plate temperatures. Results will, however, only be reported here for a mean plate temperature of 120 deg F above ambient. This temperature difference corresponds to Grashof numbers of approximately 190, 1450, 12,000, and 10^5 for the 0.125-, 0.25-, 0.5-, and 1-in. plates respectively. The variation of N_L with R_L for each of the plates for these values of G_L for assisting and opposing flow is shown in Fig. 2. Fluid properties have been evaluated at the mean film temperature.

Also shown in Fig. 2 are the variations of N_L for the limiting cases of purely free convection and purely forced convection. The variation in purely free convection was obtained by carrying out tests at zero velocity, the results so obtained being well fitted by the equation

$$N_{L\,\text{free}} = 1 + 0.42 G_L^{0.25} \tag{2}$$

The tests did not extend to velocities which were high enough to determine the variation in purely forced convection with the same degree of confidence, but the following equation appears to give an adequate representation:

$$N_{L\,\text{forced}} = 0.4 + 0.59 R_L^{0.5} \tag{3}$$

At large values of R_L this equation reduces, effectively, to $N_{L\,\text{forced}} = 0.59 R_L^{0.5}$, the result given by boundary-layer theory.

From Fig. 2 it will be seen that in the combined-convection region in assisting flow the heat-transfer rate is higher than in either purely forced or purely free convection. In opposing flow, however, as R_L increases, the heat-transfer rate drops below the purely free-convective rate, and at higher values of R_L it drops below the purely forced-convective rate. It then passes through a minimum, and had tests been carried out at higher values of R_L it would then have risen toward the purely forced-convection variation.

In [5] it was shown that the results for assisting combined-convective heat transfer from cylinders could be correlated using an equation of the form

$$N_L = (N_{L\,\text{free}}{}^4 + N_{L\,\text{forced}}{}^4)^{0.25} \tag{4}$$

This equation was obtained by considering the similar forms of the purely forced- and purely free-convection correlation equations. Equations (2) and (3) for the flat plate do not show this similarity, but equation (4) will here be regarded as purely empirical and assumed also to apply to flat-plate assisting flow. Substituting equations (2) and (3) into equation (4) gives

$$N_L = R_L^{0.5}\left[\left\{\frac{1}{R_L^{0.5}} + 0.42\left(\frac{G_L}{R_L^2}\right)^{0.25}\right\}^4 + \left\{\frac{0.4}{R_L^{0.5}} + 0.59\right\}^4\right]^{0.25} \tag{5}$$

At large values of R_L this gives $N_L/R_L^{0.5}$ = function (G_L/R_L^2) as predicted by boundary-layer theory.

A comparison between equation (5) and the experimental results for assisting flow is shown in Fig. 2, and the agreement will be seen to be reasonably good.

Acknowledgment

This work was supported by the National Research Council of Canada under grant number A5573.

References

1 Lloyd, J. R., and Sparrow, E. M., "Combined Forced and Free Convection Flow over Vertical Surfaces," *International Journal of Heat and Mass Transfer*, Vol. 13, 1970, p. 434.

2 Merkin, J. H., "The Effect of Buoyancy Forces on the Boundary Layer Flow over a Semi-infinite Vertical Flat Plate in a Uniform Free Stream," *Journal of Fluid Mechanics*, Vol. 35, 1969, p. 439.

3 Kliegel, J. R., "Laminar Free and Forced Convective Heat Transfer from a Vertical Flat Plate," PhD thesis, University of California, Berkeley, Calif., 1959.

4 Oosthuizen, P. H., and Hart, R., "An Experimental Study of Combined Convective Heat Transfer from a Flat Plate to Air," Report 6/71, Thermal and Fluid Sciences Group, Department of Mechanical Engineering, Queen's University, Kingston, Ontario, Canada, 1971.

5 Jackson, T. W., and Yen, H. H., "Combining Forced and Free Convective Equations to Represent Combined Heat-Transfer Coefficients for a Horizontal Cylinder," JOURNAL OF HEAT TRANSFER, TRANS. ASME, Series C, Vol. 93, No. 2, May 1971, pp. 247–248.

Effect of Buoyancy on Forced Convection in a Two-dimensional Wall Jet along a Vertical Wall

J. W. YANG[1] and R. D. PATEL[2]

Introduction

IT IS known that the heat-transfer rates in wall jets are an order of magnitude higher than those usually associated with gaseous heat-transfer media. However, in wall jet flow, the forced convection decreases rapidly due to the decay of jet velocity as it expands along the solid wall. In turbulent wall jets, the heat-transfer rate reaches a maximum at a short distance from the nozzle exit and then decreases sharply with the increase of distance from the nozzle exit [1].[3] For laminar wall jets, the heat-transfer rate exhibits a monotonic decrease with the distance [2]. Akfirat [2] has shown that the jet flow is of laminar type at Reynolds numbers less than 190. The Reynolds number is based on the nozzle width and the jet velocity at the nozzle exit.

[1] Associate Professor, Department of Mechanical Engineering, State University of New York at Buffalo, Buffalo, N. Y. Mem. ASME.

[2] Graduate Student, Department of Mechanical Engineering, State University of New York at Buffalo, Buffalo, N. Y.

[3] Numbers in brackets designate References at end of technical brief.

Contributed by the Heat Transfer Division of THE AMERICAN SOCIETY OF MECHANICAL ENGINEERS. Manuscript received by the Heat Transfer Division May 10, 1972.

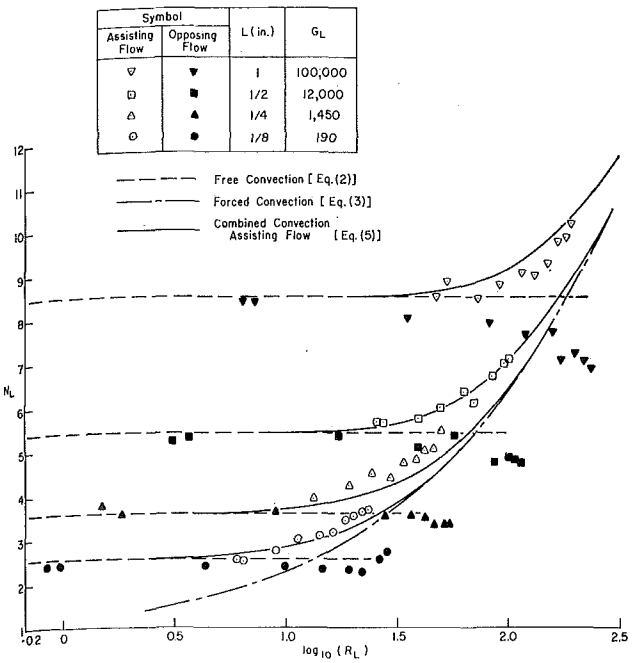

Fig. 2 Variation of Nusselt number with Reynolds number for various Grashof numbers in assisting and opposing flow

180 deg. At each of these values of α, measurements were made at a series of different velocities and a series of different plate temperatures. Results will, however, only be reported here for a mean plate temperature of 120 deg F above ambient. This temperature difference corresponds to Grashof numbers of approximately 190, 1450, 12,000, and 10^5 for the 0.125-, 0.25-, 0.5-, and 1-in. plates respectively. The variation of N_L with R_L for each of the plates for these values of G_L for assisting and opposing flow is shown in Fig. 2. Fluid properties have been evaluated at the mean film temperature.

Also shown in Fig. 2 are the variations of N_L for the limiting cases of purely free convection and purely forced convection. The variation in purely free convection was obtained by carrying out tests at zero velocity, the results so obtained being well fitted by the equation

$$N_{L\,\text{free}} = 1 + 0.42 G_L^{0.25} \tag{2}$$

The tests did not extend to velocities which were high enough to determine the variation in purely forced convection with the same degree of confidence, but the following equation appears to give an adequate representation:

$$N_{L\,\text{forced}} = 0.4 + 0.59 R_L^{0.5} \tag{3}$$

At large values of R_L this equation reduces, effectively, to $N_{L\,\text{forced}} = 0.59 R_L^{0.5}$, the result given by boundary-layer theory.

From Fig. 2 it will be seen that in the combined-convection region in assisting flow the heat-transfer rate is higher than in either purely forced or purely free convection. In opposing flow, however, as R_L increases, the heat-transfer rate drops below the purely free-convective rate, and at higher values of R_L it drops below the purely forced-convective rate. It then passes through a minimum, and had tests been carried out at higher values of R_L it would then have risen toward the purely forced-convection variation.

In [5] it was shown that the results for assisting combined-convective heat transfer from cylinders could be correlated using an equation of the form

$$N_L = (N_{L\,\text{free}}{}^4 + N_{L\,\text{forced}}{}^4)^{0.25} \tag{4}$$

This equation was obtained by considering the similar forms of the purely forced- and purely free-convection correlation equations. Equations (2) and (3) for the flat plate do not show this similarity, but equation (4) will here be regarded as purely empirical and assumed also to apply to flat-plate assisting flow. Substituting equations (2) and (3) into equation (4) gives

$$N_L = R_L^{0.5}\left[\left\{\frac{1}{R_L^{0.5}} + 0.42\left(\frac{G_L}{R_L^2}\right)^{0.25}\right\}^4 + \left\{\frac{0.4}{R_L^{0.5}} + 0.59\right\}^4\right]^{0.25} \tag{5}$$

At large values of R_L this gives $N_L/R_L^{0.5}$ = function (G_L/R_L^2) as predicted by boundary-layer theory.

A comparison between equation (5) and the experimental results for assisting flow is shown in Fig. 2, and the agreement will be seen to be reasonably good.

Acknowledgment

This work was supported by the National Research Council of Canada under grant number A5573.

References

1 Lloyd, J. R., and Sparrow, E. M., "Combined Forced and Free Convection Flow over Vertical Surfaces," *International Journal of Heat and Mass Transfer*, Vol. 13, 1970, p. 434.

2 Merkin, J. H., "The Effect of Buoyancy Forces on the Boundary Layer Flow over a Semi-infinite Vertical Flat Plate in a Uniform Free Stream," *Journal of Fluid Mechanics*, Vol. 35, 1969, p. 439.

3 Kliegel, J. R., "Laminar Free and Forced Convective Heat Transfer from a Vertical Flat Plate," PhD thesis, University of California, Berkeley, Calif., 1959.

4 Oosthuizen, P. H., and Hart, R., "An Experimental Study of Combined Convective Heat Transfer from a Flat Plate to Air," Report 6/71, Thermal and Fluid Sciences Group, Department of Mechanical Engineering, Queen's University, Kingston, Ontario, Canada, 1971.

5 Jackson, T. W., and Yen, H. H., "Combining Forced and Free Convective Equations to Represent Combined Heat-Transfer Coefficients for a Horizontal Cylinder," JOURNAL OF HEAT TRANSFER, TRANS. ASME, Series C, Vol. 93, No. 2, May 1971, pp. 247–248.

Effect of Buoyancy on Forced Convection in a Two-dimensional Wall Jet along a Vertical Wall

J. W. YANG[1] and R. D. PATEL[2]

Introduction

IT IS known that the heat-transfer rates in wall jets are an order of magnitude higher than those usually associated with gaseous heat-transfer media. However, in wall jet flow, the forced convection decreases rapidly due to the decay of jet velocity as it expands along the solid wall. In turbulent wall jets, the heat-transfer rate reaches a maximum at a short distance from the nozzle exit and then decreases sharply with the increase of distance from the nozzle exit [1].[3] For laminar wall jets, the heat-transfer rate exhibits a monotonic decrease with the distance [2]. Akfirat [2] has shown that the jet flow is of laminar type at Reynolds numbers less than 190. The Reynolds number is based on the nozzle width and the jet velocity at the nozzle exit.

[1] Associate Professor, Department of Mechanical Engineering, State University of New York at Buffalo, Buffalo, N. Y. Mem. ASME.

[2] Graduate Student, Department of Mechanical Engineering, State University of New York at Buffalo, Buffalo, N. Y.

[3] Numbers in brackets designate References at end of technical brief.

Contributed by the Heat Transfer Division of THE AMERICAN SOCIETY OF MECHANICAL ENGINEERS. Manuscript received by the Heat Transfer Division May 10, 1972.

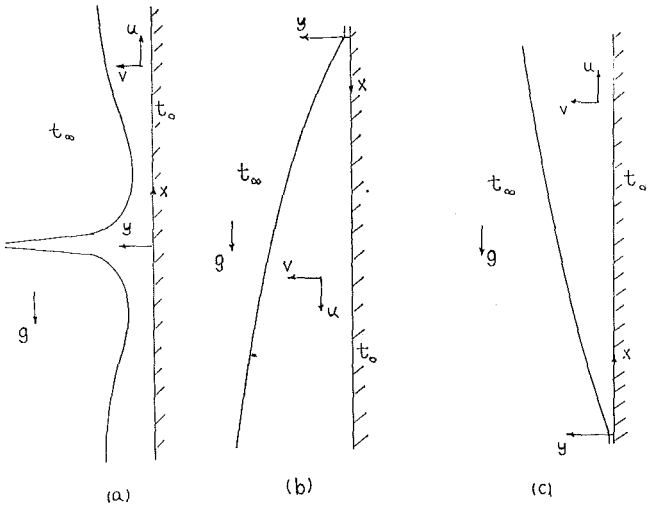

Fig. 1 Physical model and coordinates

It is for the low-speed laminar wall jet that the buoyancy effect is expected to be significant in the region downstream of the jet nozzle. The analysis of mixed natural and forced convection in a two-dimensional wall jet along a vertical isothermal wall is presented in this note.

Analysis

Several possible physical models are illustrated in Fig. 1. Sketch (*a*) represents an impinging jet and sketches (*b*) and (*c*) show wall jets along or opposite to the gravitational field. For the impinging jet, studies [1, 2] have shown that away from the impinging region the flow is essentially a wall jet. The jet flows can be designated as aiding flows and opposing flows according to the flow direction being parallel or opposite to the buoyancy force. For the case of upward jet flow, it is required to have $t_w > t_\infty$ for aiding flow and $t_w < t_\infty$ for opposing flow. The above criteria will be interchanged for jets flowing downward. For laminar, steady, and constant-property jet flow, the conservation equations, in dimensionless form, are

$$\frac{\partial U}{\partial X} + \frac{\partial V}{\partial Y} = 0 \tag{1}$$

$$U\frac{\partial U}{\partial X} + V\frac{\partial U}{\partial Y} = \frac{\partial^2 U}{\partial Y^2} \pm \frac{g\beta\nu(t_w - t_\infty)\theta}{U_m{}^3} \tag{2}$$

$$U\frac{\partial \theta}{\partial X} + V\frac{\partial \theta}{\partial Y} = \frac{1}{\Pr}\frac{\partial^2 \theta}{\partial Y^2} \tag{3}$$

and

$$U = u/U_m \qquad V = v/U_m \qquad Y = yU_m/\nu$$
$$\theta = (t - t_\infty)/(t_w - t_\infty) \qquad X = xU_m/\nu$$

where x and y denote distance along and normal to the wall; u and v are the corresponding velocity components; U_m is a constant reference velocity related to the exterior momentum flux [3]; t is the static temperature; and ν, g, β, and Pr are the kinematic viscosity, gravity force, coefficient of thermal expansion, and Prandtl number, respectively. The last term on the right side of equation (2) denotes the buoyancy force due to the temperature difference. The positive sign refers to the upward flow and negative sign to the downard flow. The boundary conditions are

$$U(0) = 0 \qquad V(0) = 0 \qquad \theta(0) = 1$$
$$U(\infty) = 0 \qquad \theta(\infty) = 0 \tag{4}$$

To solve the above equations, the reduced velocity f and temperature θ are expanded in series

$$f(\eta, \zeta) = f_0(\eta) + \zeta f_1(\eta) + \zeta^2 f_2(\eta) + \ldots \tag{5}$$

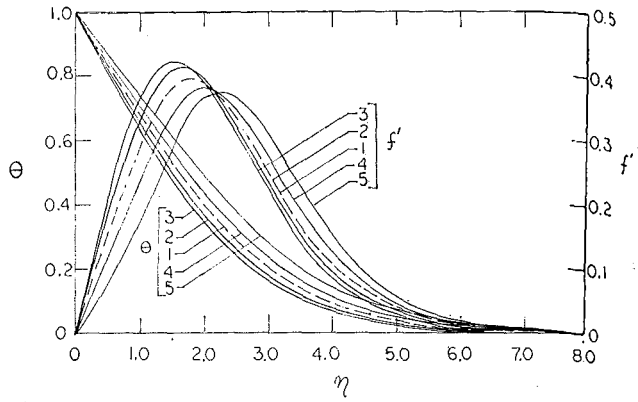

Fig. 2 Representative temperature and velocity profiles; (1) no buoyancy force; adding flow: (2) $\zeta = 0.125$, (3) $\zeta = 0.25$; opposing flow: (4) $\zeta = 0.125$, (5) $\zeta = 0.25$

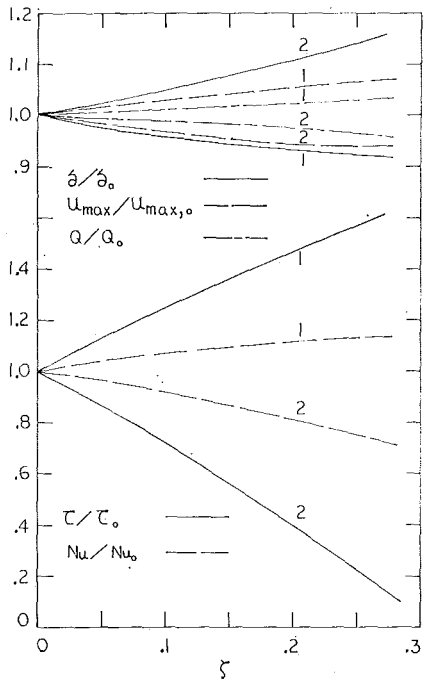

Fig. 3 Ratios of Nusselt number, wall shear stress, volume flow rate, maximum velocity, and jet width at Pr = 0.7; (1) adding flow; (2) opposing flow

$$\theta(\eta, \zeta) = \theta_0(\eta) + \zeta\theta_1(\eta) + \zeta^2\theta_2(\eta) + \ldots \tag{6}$$

where the Glauert transformations [3] have been modified as

$$\eta = YX^{-3/4}/4 \qquad \psi = X^{1/4}f(\eta, \zeta) \qquad \zeta = \frac{64g\beta(t_w - t_\infty)x^3}{U_m\nu}$$
$$= 64\ \mathrm{Gr}/\mathrm{Re}$$

Using the above transformations and the proposed velocity and temperature variables, equations (1)–(3) are reduced to a set of ordinary differential equations governing the functions f_i and θ_i ($i = 0, 1, 2, \ldots$). The solution of these ordinary differential equations provides the approximations of the present problem.

Discussion of Results

Numerical solutions were obtained for the first three approximations at Pr = 0.7. Representative graphs of temperature and velocity profiles are shown in Fig. 2. It is seen that in aiding flow the buoyancy force acts like a favorable pressure gradient and the flow is accelerated in the inner region near the wall. The acceleration increases the temperature gradient at the wall which results a higher heat-transfer rate. On the other hand, the jet

becomes narrower with the increase of the buoyancy effect. The width of the jet δ is defined such that $u = {}^1/_2 u_{max}$ at $y = \delta$. These effects are reversed in the opposing flow as indicated in Fig. 2. The effect of buoyancy on the wall jet is indicated in Fig. 3 by the ratio of the local Nu and τ in the presence of buoyancy to that of Nu_0 and τ_0 in the absence of buoyancy. It is noted that the shear stress and the heat-transfer rate increase with the buoyancy in aiding flow and decrease in opposing flow. However, the effect on the shear stress is much stronger than that on the heat-transfer rate. At $\zeta = 0.25$, the wall shear stress decreases 77 percent in opposing flow and increases 57 percent in aiding flow due to the buoyancy force. For the same value of ζ, the reduction of heat-transfer rate is 25 percent in opposing flow and the increase is only 13 percent in aiding flow.

The volume flow rate in a wall jet is known to increase in the downstream direction due to the entrainment of fluid particles by friction. The effects of buoyancy on volume flow rate, maximum velocity, and the jet width are also illustrated in Fig. 3. In general, the buoyancy effect is significant only at higher values of ζ.

References

1 Gardon, R., and Akfirat, J. C., "Heat Transfer Characteristics of Impinging Two-Dimensional Air Jets," JOURNAL OF HEAT TRANSFER, TRANS. ASME, Series C, Vol. 88, No. 1, Feb. 1966, pp. 101–108.

2 Akfirat, J. C., "Transfer of Heat from an Isothermal Flat Plate to a Two-Dimensional Wall Jet," *Proceedings of 3rd International Heat Transfer Conference*, Vol. 2, 1966, pp. 274–279.

3 Glauert, M. B., "The Wall Jet," *Journal of Fluid Mechanics*, Vol. 1, 1956, pp. 625–642.

Free Convection at a Vertical Plate with Uniform Flux Condition in Non-Newtonian Power-Law Fluids

T. Y. W. CHEN[1] and D. E. WOLLERSHEIM[2]

THE recent work by Selman and Newman [1][3] can be extended to include non-Newtonian fluids by applying a technique similar to that developed by Acrivos [2] for non-Newtonian laminar free convection with an isothermal boundary condition.

Under the same assumption as that of [1, 2], the governing partial differential equations are transformed to ordinary differential equations using the following substitutions:[4]

$$\zeta = \frac{y}{L}\frac{\mathrm{Gr}_C^{1/(N+4)}\,\mathrm{Pr}_C^{N/(3N+2)}}{\left[(3N+2)\dfrac{x}{L}\right]^{N/(3N+2)}} \tag{1}$$

$$\theta = \frac{t - t_\infty}{\dfrac{qL}{k}}\frac{\mathrm{Gr}_C^{1/(N+4)}\,\mathrm{Pr}_C^{N/(3N+2)}}{\left[(3N+2)\dfrac{x}{L}\right]^{N/(3N+2)}} \tag{2}$$

$$u = \frac{\left[(3N+2)\dfrac{x}{L}\right]^{(N+2)/(3N+2)} f'}{\left(\dfrac{k}{g\beta q L^2}\right)^{1/2}\mathrm{Gr}_C^{1/[2(N+4)]}\mathrm{Pr}_C^{(N+2)/(3N+2)}} \tag{3}$$

$$v = \frac{N}{\left[(3N+2)\dfrac{x}{L}\right]^{N/(3N+2)}} \times \frac{\zeta f' - \dfrac{2(N+1)}{N} f}{\left(\dfrac{k}{g\beta q L^2}\right)^{1/2}\mathrm{Gr}_C^{3/[2(N+4)]}\,\mathrm{Pr}_C^{2(N+1)/(3N+2)}} \tag{4}$$

where Gr_C and Pr_C are the generalized Grashof number and generalized Prandtl number defined as

$$\mathrm{Gr}_C = \left(\frac{\rho}{m}\right)^2 L^4 \left(\frac{g\beta q}{k}\right)^{2-N} \tag{5}$$

$$\mathrm{Pr}_C = \frac{\rho c_p}{k}\left(\frac{m}{\rho}\right)^{5/(N+4)} L^{2(N-1)/(N+4)} \left(\frac{g\beta q}{k}\right)^{3(N-1)/(N+4)} \tag{6}$$

in which m and N are the consistency index and the power-law fluid index defined from an empirical shear-stress–strain-rate relationship known as the characteristic equation of power-law fluids

$$\tau = m\left|\frac{\partial u}{\partial y}\right|^{N-1}\frac{\partial u}{\partial y} \tag{7}$$

The set of coupled ordinary differential equations, namely the equation of motion and the equation of thermal energy, becomes

$$\theta + \frac{d}{d\zeta}(f'')^N = 0 \tag{8}$$

$$\theta'' + 2(N+1)f\theta' - Nf'\theta = 0 \tag{9}$$

The boundary conditions in the inner (diffusion) region are

$$f'(0) = f(0) = \theta'(0) + 1 = f''(\infty) = \theta(\infty) = 0$$

where primes denote differentiation with respect to ζ.

Equations (8) and (9) and their boundary conditions have been solved using the procedure of Nachtsheim and Swigert [3] to find the starting values for the fourth-order Runge–Kutta numerical integration scheme. These starting values are given in Table 1.

The local temperature difference $t_0 - t_\infty$ and the local shear stress τ_0 at the plate are

$$t_0 - t_\infty = \left[(3N+2)\frac{x}{L}\right]^{N/(3N+2)}\frac{qL}{k}\frac{\theta(0)}{\mathrm{Gr}_C^{1/(N+4)}\,\mathrm{Pr}_C^{N/(3N+2)}} \tag{10}$$

$$\tau_0 = \left[\frac{Pm^{1/N}}{L}\frac{f''(0)}{\left[(3N+2)\dfrac{x}{L}\right]^{N/(3N+2)}}\right]^N \mathrm{Gr}_C^{N/(N+4)}\,\mathrm{Pr}_C^{N^2/(3N+2)} \tag{11}$$

where

$$P = \left[\frac{m}{\rho}L^{N+2}\left(\frac{g\beta q}{k}\right)^{N+1}\right]^{1/(N+4)}\left[\frac{(3N+2)\dfrac{x}{L}}{\mathrm{Pr}_C}\right]^{(N+2)/(3N+2)}$$

On any given surface along the vertical plate, equation (10) indicates $t_0 - t_\infty$ is proportional to $x^{N/(3N+2)}$. Thus the variation of the wall temperature with distance along the wall is

Table 1 Numerical values of dimensionless temperature difference, shear stress, and average heat-transfer parameter

			$\overline{\mathrm{Nu}}/\mathrm{Gr}_A^{1/[2(N+1)]}\mathrm{Pr}_A^{N/(3N+1)}$		
			Uniform Flux	Uniform Temperature	
N	$f''(0)$	$\theta(0)$	present work	Acrivos [2]	Chen [7]
0.1	5.0558	1.3188	0.6063	0.60	0.6246
0.5	1.1145	1.3026	0.6176	0.63	0.6212
1.0	0.811846	1.1474	0.6697	0.67	0.6703
1.5	0.7497	1.0286	0.7013	0.71	0.6998

[1] Engineer, York Division Engineering Department, Borg-Warner Corp., York, Pa. Assoc. Mem. ASME.

[2] Associate Professor, Department of Mechanical and Aerospace Engineering, University of Missouri, Columbia, Mo.

[3] Numbers in brackets designate References at end of technical brief.

[4] Notation is that of [1] except as noted.

Contributed by the Heat Transfer Division of THE AMERICAN SOCIETY OF MECHANICAL ENGINEERS. Manuscript received by the Heat Transfer Division July 3, 1972.

becomes narrower with the increase of the buoyancy effect. The width of the jet δ is defined such that $u = {}^1/_2 u_{max}$ at $y = \delta$. These effects are reversed in the opposing flow as indicated in Fig. 2. The effect of buoyancy on the wall jet is indicated in Fig. 3 by the ratio of the local Nu and τ in the presence of buoyancy to that of Nu_0 and τ_0 in the absence of buoyancy. It is noted that the shear stress and the heat-transfer rate increase with the buoyancy in aiding flow and decrease in opposing flow. However, the effect on the shear stress is much stronger than that on the heat-transfer rate. At $\zeta = 0.25$, the wall shear stress decreases 77 percent in opposing flow and increases 57 percent in aiding flow due to the buoyancy force. For the same value of ζ, the reduction of heat-transfer rate is 25 percent in opposing flow and the increase is only 13 percent in aiding flow.

The volume flow rate in a wall jet is known to increase in the downstream direction due to the entrainment of fluid particles by friction. The effects of buoyancy on volume flow rate, maximum velocity, and the jet width are also illustrated in Fig. 3. In general, the buoyancy effect is significant only at higher values of ζ.

References

1 Gardon, R., and Akfirat, J. C., "Heat Transfer Characteristics of Impinging Two-Dimensional Air Jets," JOURNAL OF HEAT TRANSFER, TRANS. ASME, Series C, Vol. 88, No. 1, Feb. 1966, pp. 101–108.

2 Akfirat, J. C., "Transfer of Heat from an Isothermal Flat Plate to a Two-Dimensional Wall Jet," *Proceedings of 3rd International Heat Transfer Conference*, Vol. 2, 1966, pp. 274–279.

3 Glauert, M. B., "The Wall Jet," *Journal of Fluid Mechanics*, Vol. 1, 1956, pp. 625–642.

Free Convection at a Vertical Plate with Uniform Flux Condition in Non-Newtonian Power-Law Fluids

T. Y. W. CHEN[1] and D. E. WOLLERSHEIM[2]

THE recent work by Selman and Newman [1][3] can be extended to include non-Newtonian fluids by applying a technique similar to that developed by Acrivos [2] for non-Newtonian laminar free convection with an isothermal boundary condition.

Under the same assumption as that of [1, 2], the governing partial differential equations are transformed to ordinary differential equations using the following substitutions:[4]

$$\zeta = \frac{y}{L}\frac{\mathrm{Gr}_C^{1/(N+4)}\,\mathrm{Pr}_C^{N/(3N+2)}}{\left[(3N+2)\dfrac{x}{L}\right]^{N/(3N+2)}} \tag{1}$$

$$\theta = \frac{t - t_\infty}{\dfrac{qL}{k}}\frac{\mathrm{Gr}_C^{1/(N+4)}\,\mathrm{Pr}_C^{N/(3N+2)}}{\left[(3N+2)\dfrac{x}{L}\right]^{N/(3N+2)}} \tag{2}$$

$$u = \frac{\left[(3N+2)\dfrac{x}{L}\right]^{(N+2)/(3N+2)} f'}{\left(\dfrac{k}{g\beta q L^2}\right)^{1/2}\mathrm{Gr}_C^{1/[2(N+4)]}\mathrm{Pr}_C^{(N+2)/(3N+2)}} \tag{3}$$

$$v = \frac{N}{\left[(3N+2)\dfrac{x}{L}\right]^{N/(3N+2)}} \times \frac{\zeta f' - \dfrac{2(N+1)}{N} f}{\left(\dfrac{k}{g\beta q L^2}\right)^{1/2}\mathrm{Gr}_C^{3/[2(N+4)]}\,\mathrm{Pr}_C^{2(N+1)/(3N+2)}} \tag{4}$$

where Gr_C and Pr_C are the generalized Grashof number and generalized Prandtl number defined as

$$\mathrm{Gr}_C = \left(\frac{\rho}{m}\right)^2 L^4 \left(\frac{g\beta q}{k}\right)^{2-N} \tag{5}$$

$$\mathrm{Pr}_C = \frac{\rho c_p}{k}\left(\frac{m}{\rho}\right)^{5/(N+4)} L^{2(N-1)/(N+4)} \left(\frac{g\beta q}{k}\right)^{3(N-1)/(N+4)} \tag{6}$$

in which m and N are the consistency index and the power-law fluid index defined from an empirical shear-stress–strain-rate relationship known as the characteristic equation of power-law fluids

$$\tau = m\left|\frac{\partial u}{\partial y}\right|^{N-1}\frac{\partial u}{\partial y} \tag{7}$$

The set of coupled ordinary differential equations, namely the equation of motion and the equation of thermal energy, becomes

$$\theta + \frac{d}{d\zeta}(f'')^N = 0 \tag{8}$$

$$\theta'' + 2(N+1)f\theta' - Nf'\theta = 0 \tag{9}$$

The boundary conditions in the inner (diffusion) region are

$$f'(0) = f(0) = \theta'(0) + 1 = f''(\infty) = \theta(\infty) = 0$$

where primes denote differentiation with respect to ζ.

Equations (8) and (9) and their boundary conditions have been solved using the procedure of Nachtsheim and Swigert [3] to find the starting values for the fourth-order Runge–Kutta numerical integration scheme. These starting values are given in Table 1.

The local temperature difference $t_0 - t_\infty$ and the local shear stress τ_0 at the plate are

$$t_0 - t_\infty = \left[(3N+2)\frac{x}{L}\right]^{N/(3N+2)}\frac{qL}{k}\frac{\theta(0)}{\mathrm{Gr}_C^{1/(N+4)}\,\mathrm{Pr}_C^{N/(3N+2)}} \tag{10}$$

$$\tau_0 = \left[\frac{Pm^{1/N}}{L}\frac{f''(0)}{\left[(3N+2)\dfrac{x}{L}\right]^{N/(3N+2)}}\right]^N \mathrm{Gr}_C^{N/(N+4)}\,\mathrm{Pr}_C^{N^2/(3N+2)} \tag{11}$$

where

$$P = \left[\frac{m}{\rho}L^{N+2}\left(\frac{g\beta q}{k}\right)^{N+1}\right]^{1/(N+4)}\left[\frac{(3N+2)\dfrac{x}{L}}{\mathrm{Pr}_C}\right]^{(N+2)/(3N+2)}$$

On any given surface along the vertical plate, equation (10) indicates $t_0 - t_\infty$ is proportional to $x^{N/(3N+2)}$. Thus the variation of the wall temperature with distance along the wall is

Table 1 Numerical values of dimensionless temperature difference, shear stress, and average heat-transfer parameter

			$\overline{\mathrm{Nu}}/\mathrm{Gr}_A^{1/[2(N+1)]}\mathrm{Pr}_A^{N/(3N+1)}$		
			Uniform Flux	Uniform Temperature	
N	$f''(0)$	$\theta(0)$	present work	Acrivos [2]	Chen [7]
0.1	5.0558	1.3188	0.6063	0.60	0.6246
0.5	1.1145	1.3026	0.6176	0.63	0.6212
1.0	0.811846	1.1474	0.6697	0.67	0.6703
1.5	0.7497	1.0286	0.7013	0.71	0.6998

[1] Engineer, York Division Engineering Department, Borg-Warner Corp., York, Pa. Assoc. Mem. ASME.

[2] Associate Professor, Department of Mechanical and Aerospace Engineering, University of Missouri, Columbia, Mo.

[3] Numbers in brackets designate References at end of technical brief.

[4] Notation is that of [1] except as noted.

Contributed by the Heat Transfer Division of THE AMERICAN SOCIETY OF MECHANICAL ENGINEERS. Manuscript received by the Heat Transfer Division July 3, 1972.

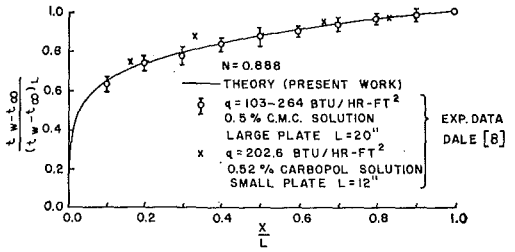

Fig. 1 Comparison between predicted wall temperature variation $(t_0 - t_\infty)/(t_0 - t_\infty)_L$ along plate surface and experimental results for $N = 0.888$

$$\frac{t_0 - t_\infty}{(t_0 - t_\infty)_L} = \left(\frac{x}{L}\right)^{N/(3N+2)} \tag{12}$$

where L is the length of surface for which the flow is laminar. Note that equation (12) is the same as the exact solution for Newtonian flow derived by Sparrow and Gregg [4] when N equals 1. It indicates the rate of increase of the wall temperature is greater near $x = 0$, and the variation increases as N decreases.

It is interesting to observe, as has been discovered in [4] for Newtonian fluids, the relationship between the uniform-wall-temperature case and the uniform-surface-heat-flux case. If we define a mean heat-transfer coefficient $\bar{h}$ as

$$\bar{h} = \frac{q}{(t_0 - t_\infty)_{L/2}}$$

the mean Nusselt number $\overline{\mathrm{Nu}}$ is then obtained from equations (5), (6), and (12)

$$\overline{\mathrm{Nu}} = \left(\frac{2}{3N+2}\right)^{N/(3N+2)} \frac{\mathrm{Gr}_C^{1/(N+4)}\,\mathrm{Pr}_C^{N/(3N+2)}}{\theta(0)} \tag{13}$$

Furthermore, we may redefine the generalized Prandtl number and the generalized Grashof number for the uniform-surface-heat-flux case in the same manner as Acrivos [2] for the case of uniform wall temperature.

$$\mathrm{Gr}_A = \left(\frac{\rho}{m}\right)^2 L^{2+N}[g\beta(\overline{t_0 - t_\infty})_L]^{2-N} \tag{14}$$

$$\mathrm{Pr}_A = \frac{\rho c_p}{k}\left(\frac{m}{\rho}\right)^{2/(1+N)} [L\beta g(\overline{t_0 - t_\infty})_L]^{3(N-1)/[2(N+1)]} L^{(1-N)/(1+N)} \tag{15}$$

Equation (13) can be rearranged to obtain

$$\frac{\overline{\mathrm{Nu}}}{\mathrm{Gr}_A^{1/[2(N+1)]}\mathrm{Pr}_A^{N/(3N+1)}} = \left[\frac{\left(\frac{2}{3N+2}\right)^N}{[\theta(0)]^{3N+2}}\right]^{1/(3N+1)} \tag{16}$$

Equation (16) is compared with the results for a uniform-temperature plate for various power-law fluid indices in Table 1. The agreement of the values of $\overline{\mathrm{Nu}}/\mathrm{Gr}_A^{1/[2(N+1)]}\mathrm{Pr}_A^{N/(3N+1)}$ evaluated using $(t_0 - t_\infty)_{L/2}$ for the uniform-heat-flux case with those for the uniform-wall-temperature case verifies the point made by Sparrow and Gregg, and is extended now to include non-Newtonian fluids. This has been recently applied with success in correlating the experimental data of Emery et al. [5].

Finally, the present theoretical work is compared with the experimental data reported very recently by Dale and Emery [6] in Figs. 1 and 2. Further details regarding the present work may be found in [7].

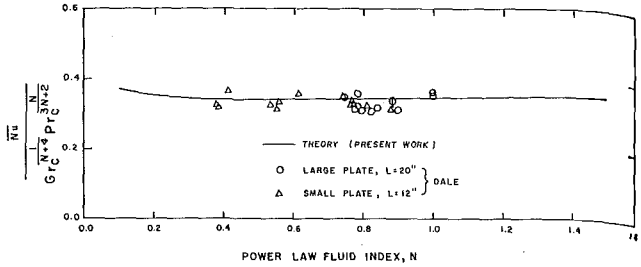

Fig. 2 Comparison of average heat-transfer parameters using: $\overline{\mathrm{Nu}} = \frac{1}{L}\int_0^L \frac{hx}{k}\,dx$ and experiments

References

1 Selman, J. R., and Newman, J., "High Sc Limit of Free Convection at a Vertical Plate With Uniform Flux Condition," JOURNAL OF HEAT TRANSFER, TRANS. ASME, Series C, Vol. 93, No. 4, Nov. 1971, pp. 465–466.

2 Acrivos, A., "A Theoretical Analysis of Laminar Natural Convection Heat Transfer to Non-Newtonian Fluids," *AIChE Journal*, Vol. 6, 1960, pp. 584–590.

3 Nachtsheim, P. R., and Swigert, P., "Satisfaction of Asymptotic Boundary Conditions in the Numerical Solution of Boundary-Layer Equations," NASA TMX-52118, 1965.

4 Sparrow, E. M., and Gregg, J. L., "Laminar Free Convection From a Vertical Plate With Uniform Surface Heat Flux," TRANS. ASME, Vol. 78, 1956, pp. 435–440.

5 Emery, A. F., Chi, H. W., and Dale, J. D., "Free Convection Through Vertical Plane Layers of Non-Newtonian Power Law Fluids," JOURNAL OF HEAT TRANSFER, TRANS. ASME, Series C, Vol. 93, No. 2, May 1971, pp. 164–171.

6 Dale, J. D., and Emery, A. F., "The Free Convection of Heat from a Vertical Plate to Several Non-Newtonian 'Pseudoplastic' Fluids," JOURNAL OF HEAT TRANSFER, TRANS. ASME, Series C, Vol. 94, No. 1, Feb. 1972, pp. 64–72 (see also Dale, J. D., PhD thesis, University of Washington, Seattle, Wash., 1969).

7 Chen, T. Y. W., PhD thesis, University of Missouri-Columbia, 1971.

High-Prandtl-Number Free Convection for Uniform Surface Heat Flux

S. ROY[1]

Nomenclature

C = dimensional constant, equation (1)
F = velocity function, equations (5) and (6)
f = nondimensional stream function, equation (1)
g = acceleration due to gravity
Gr_x^* = local Grashof number, $g\beta q x^4/(k\nu^2)$
k = thermal conductivity
Nu_x = local Nusselt number, equation (14)
q = constant surface heat flux
t = temperature
u, v = velocity components along x and y directions
x, y = coordinates along and normal to plate
β = coefficient of thermal expansion of fluid
γ = constant, equation (6)
η = similarity variable, equation (1)
ζ = transformed similarity variable, equations (5) and (6)
θ = nondimensional temperature, equation (1)
Φ = nondimensional transformed temperature in inner layer, equation (5)
ν = kinematic viscosity
ψ = dimensional stream function, equation (1)
σ = Prandtl number, equation (3)

Subscripts

ω = wall conditions

[1] Research Fellow, Department of Mechanical Engineering, University of Aston, Birmingham, U. K.

Contributed by the Heat Transfer Division of THE AMERICAN SOCIETY OF MECHANICAL ENGINEERS. Manuscript received by the Heat Transfer Division May 8, 1972.

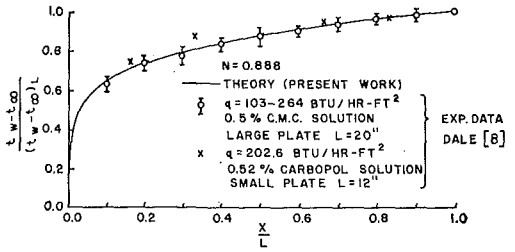

Fig. 1 Comparison between predicted wall temperature variation $(t_0 - t_\infty)/(t_0 - t_\infty)_L$ along plate surface and experimental results for $N = 0.888$

$$\frac{t_0 - t_\infty}{(t_0 - t_\infty)_L} = \left(\frac{x}{L}\right)^{N/(3N+2)} \tag{12}$$

where L is the length of surface for which the flow is laminar. Note that equation (12) is the same as the exact solution for Newtonian flow derived by Sparrow and Gregg [4] when N equals 1. It indicates the rate of increase of the wall temperature is greater near $x = 0$, and the variation increases as N decreases.

It is interesting to observe, as has been discovered in [4] for Newtonian fluids, the relationship between the uniform-wall-temperature case and the uniform-surface-heat-flux case. If we define a mean heat-transfer coefficient $\bar{h}$ as

$$\bar{h} = \frac{q}{(t_0 - t_\infty)_{L/2}}$$

the mean Nusselt number $\overline{\mathrm{Nu}}$ is then obtained from equations (5), (6), and (12)

$$\overline{\mathrm{Nu}} = \left(\frac{2}{3N+2}\right)^{N/(3N+2)} \frac{\mathrm{Gr}_C^{1/(N+4)}\,\mathrm{Pr}_C^{N/(3N+2)}}{\theta(0)} \tag{13}$$

Furthermore, we may redefine the generalized Prandtl number and the generalized Grashof number for the uniform-surface-heat-flux case in the same manner as Acrivos [2] for the case of uniform wall temperature.

$$\mathrm{Gr}_A = \left(\frac{\rho}{m}\right)^2 L^{2+N}[g\beta(\overline{t_0 - t_\infty})_L]^{2-N} \tag{14}$$

$$\mathrm{Pr}_A = \frac{\rho c_p}{k}\left(\frac{m}{\rho}\right)^{2/(1+N)}[L\beta g(\overline{t_0 - t_\infty})_L]^{3(N-1)/[2(N+1)]}L^{(1-N)/(1+N)} \tag{15}$$

Equation (13) can be rearranged to obtain

$$\frac{\overline{\mathrm{Nu}}}{\mathrm{Gr}_A^{1/[2(N+1)]}\mathrm{Pr}_A^{N/(3N+1)}} = \left[\frac{\left(\frac{2}{3N+2}\right)^N}{[\theta(0)]^{3N+2}}\right]^{1/(3N+1)} \tag{16}$$

Equation (16) is compared with the results for a uniform-temperature plate for various power-law fluid indices in Table 1. The agreement of the values of $\overline{\mathrm{Nu}}/\mathrm{Gr}_A^{1/[2(N+1)]}\mathrm{Pr}_A^{N/(3N+1)}$ evaluated using $(t_0 - t_\infty)_{L/2}$ for the uniform-heat-flux case with those for the uniform-wall-temperature case verifies the point made by Sparrow and Gregg, and is extended now to include non-Newtonian fluids. This has been recently applied with success in correlating the experimental data of Emery et al. [5].

Finally, the present theoretical work is compared with the experimental data reported very recently by Dale and Emery [6] in Figs. 1 and 2. Further details regarding the present work may be found in [7].

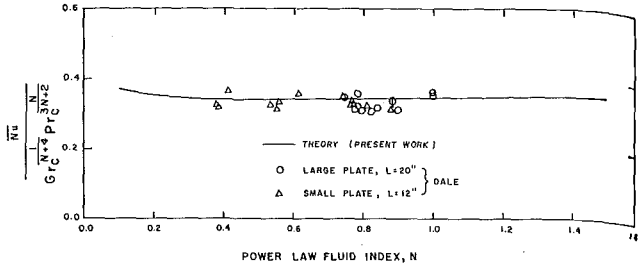

Fig. 2 Comparison of average heat-transfer parameters using: $\overline{\mathrm{Nu}} = \frac{1}{L}\int_0^L \frac{hx}{k}\,dx$ and experiments

References

1 Selman, J. R., and Newman, J., "High Sc Limit of Free Convection at a Vertical Plate With Uniform Flux Condition," JOURNAL OF HEAT TRANSFER, TRANS. ASME, Series C, Vol. 93, No. 4, Nov. 1971, pp. 465–466.

2 Acrivos, A., "A Theoretical Analysis of Laminar Natural Convection Heat Transfer to Non-Newtonian Fluids," *AIChE Journal*, Vol. 6, 1960, pp. 584–590.

3 Nachtsheim, P. R., and Swigert, P., "Satisfaction of Asymptotic Boundary Conditions in the Numerical Solution of Boundary-Layer Equations," NASA TMX-52118, 1965.

4 Sparrow, E. M., and Gregg, J. L., "Laminar Free Convection From a Vertical Plate With Uniform Surface Heat Flux," TRANS. ASME, Vol. 78, 1956, pp. 435–440.

5 Emery, A. F., Chi, H. W., and Dale, J. D., "Free Convection Through Vertical Plane Layers of Non-Newtonian Power Law Fluids," JOURNAL OF HEAT TRANSFER, TRANS. ASME, Series C, Vol. 93, No. 2, May 1971, pp. 164–171.

6 Dale, J. D., and Emery, A. F., "The Free Convection of Heat from a Vertical Plate to Several Non-Newtonian 'Pseudoplastic' Fluids," JOURNAL OF HEAT TRANSFER, TRANS. ASME, Series C, Vol. 94, No. 1, Feb. 1972, pp. 64–72 (see also Dale, J. D., PhD thesis, University of Washington, Seattle, Wash., 1969).

7 Chen, T. Y. W., PhD thesis, University of Missouri-Columbia, 1971.

High-Prandtl-Number Free Convection for Uniform Surface Heat Flux

S. ROY[1]

Nomenclature

C = dimensional constant, equation (1)
F = velocity function, equations (5) and (6)
f = nondimensional stream function, equation (1)
g = acceleration due to gravity
Gr_x^* = local Grashof number, $g\beta q x^4/(k\nu^2)$
k = thermal conductivity
Nu_x = local Nusselt number, equation (14)
q = constant surface heat flux
t = temperature
u, v = velocity components along x and y directions
x, y = coordinates along and normal to plate
β = coefficient of thermal expansion of fluid
γ = constant, equation (6)
η = similarity variable, equation (1)
ζ = transformed similarity variable, equations (5) and (6)
θ = nondimensional temperature, equation (1)
Φ = nondimensional transformed temperature in inner layer, equation (5)
ν = kinematic viscosity
ψ = dimensional stream function, equation (1)
σ = Prandtl number, equation (3)

Subscripts

ω = wall conditions

[1] Research Fellow, Department of Mechanical Engineering, University of Aston, Birmingham, U. K.

Contributed by the Heat Transfer Division of THE AMERICAN SOCIETY OF MECHANICAL ENGINEERS. Manuscript received by the Heat Transfer Division May 8, 1972.

∞ = conditions at large distance from plate surface
1 = inner layer
2 = outer layer

Introduction

FREE-CONVECTIVE heat transfer to a high-Prandtl-number fluid from a heated semi-infinite flat vertical surface has been studied by many, including LeFevre [1],[2] Stewartson and Jones [2], Kuiken [3], Roy [4, 5], Eshghy [6], and Selman and Newman [7]. Of these, the first six dealt with isothermal surfaces. Particularly, [3–6] presented results in which the Prandtl number occurred explicitly; [7] provided solutions for the uniform-heat-flux boundary conditions for infinite Prandtl number.

We shall in this communication study the uniform-heat-flux case by the double-boundary-layer method described in detail by Roy [5]. We shall present results in series in powers of $\sigma^{-1/2}$ and compare them with the exact results of Sparrow and Gregg [8] and the approximate ones of Sparrow [9] obtained on application of the Karman–Pohlhausen integral method.

Mathematical Formulation

Sparrow and Gregg [8] obtained similarity solutions of the boundary-layer equations for the conservation of mass, momentum, and energy in the following form:

$$u = \frac{\partial\psi}{\partial y} \qquad v = -\frac{\partial\psi}{\partial x} \qquad \eta = Cy/x^{1/5}$$
$$\psi = 5\nu C x^{4/5} f(\eta) \qquad t_\infty - t = \frac{qx^{1/5}}{kC}\theta(\eta) \qquad C = \left(\frac{g\beta q}{5k\nu^2}\right)^{1/5} \tag{1}$$

where f and θ satisfy the coupled ordinary nonlinear differential equations

$$f''' + 4ff'' - 3(f')^2 - \theta = 0 \tag{2}$$
$$\theta'' + \sigma(4f\theta' - f'\theta) = 0 \tag{3}$$

subject to the boundary conditions

$$f(0) = f'(0) = 0 \qquad \theta'(0) = 1$$
$$f' \to 0 \qquad \theta \to 0 \qquad \text{as} \qquad \eta \to \infty \tag{4}$$

Inner and Outer Layers

For large values of σ the whole boundary layer can be divided into two regions: one of thickness $O(\sigma^{-1/5})$ in which the temperature difference is brought to zero and one of thickness $O(\sigma^{3/10})$ in which the velocity parallel to the surface is brought to zero again. It has been shown already that in the case of isothermal surfaces these thicknesses are $O(\sigma^{-1/4})$ and $O(\sigma^{1/4})$ respectively. We shall deal with these layers separately, call them the inner and outer layers, and introduce different transformations suitable for each as follows:

Inner layer:

$$\zeta_1 = \sigma^{1/5}\eta$$
$$f(\eta) = \sigma^{-4/5}F_1(\zeta_1) \tag{5}$$
$$\theta(\eta) = \sigma^{-1/5}\Phi_1(\zeta_1)$$

Outer layer:

$$\zeta_2 = \gamma\sigma^{-3/10}\eta$$
$$f(\eta) = \gamma\sigma^{-3/10}F_2(\zeta_2) \tag{6}$$
$$\theta(\eta) = 0$$

where γ is a constant to be specified suitably later. The functions F_1, Φ_1, and F_2 satisfy the equations

$$F_1''' - \Phi_1 + \sigma^{-1}\{4F_1F_1'' - 3(F_1')^2\} = 0 \tag{7}$$
$$\Phi_1'' + 4F_1\Phi_1' - F_1'\Phi_1 = 0 \tag{8}$$

and

$$F_2''' + 4F_2F_2'' - 3(F_2')^2 = 0 \tag{9}$$

In the above, a prime denotes differentiation with respect to the appropriate variable ζ_1 or ζ_2. Also, it should be noted that the boundary conditions at $\eta = \infty$ are redundant for F_1 and those at $\eta = 0$ are so for F_2. Further, the equations (7)–(9) suggest that series solutions in some negative powers of σ exist. The appropriate series and the boundary conditions at $\zeta_1 = \infty$ and at $\zeta_2 = 0$ are determined by matching the inner solutions for large values of ζ_1 with the outer solutions for small values of ζ_2. Proceeding up to terms $O(\sigma^{-1})$, they are obtained to be

$$F_1 = \sum_{i=0}^{2} \sigma^{-i/2}F_{1i}$$
$$\Phi_1 = \sum_{i=0}^{2} \sigma^{-i/2}\Phi_{1i} \tag{10}$$
$$F_2 = \sum_{i=0}^{2} \sigma^{-i/2}F_{2i}$$

and

$$F_{10}''(\infty) = 0$$
$$F_{20}(0) = 0$$
$$F_{20}'(0) = 1 \qquad [\text{assuming } \gamma^2 = \lim_{\zeta_1\to\infty} F_{10}'(\zeta_1)]$$
$$F_{11}''(\infty) = \gamma^3 F_{20}''(0)$$
$$F_{21}(0) = \lim_{\zeta_1\to\infty}\left[\frac{1}{\gamma}F_{10}(\zeta_1) - \gamma\zeta_1\right]$$
$$F_{21}'(0) = \lim_{\zeta_1\to\infty}\left[\frac{1}{\gamma^2}F_{11}'(\zeta_1) - \gamma\zeta_1 F_{20}''(0)\right] \tag{11}$$
$$F_{12}''(\infty) = \gamma^3 \lim_{\zeta_1\to\infty}[F_{21}''(0) + 3\gamma\zeta_1]$$
$$F_{22}(0) = \lim_{\zeta_1\to\infty}\left[\frac{1}{\gamma}F_{11}(\zeta_1) - \zeta_1 F_{21}'(0) - \frac{1}{2}\gamma^2\zeta_1^2 F_{20}''(0)\right]$$
$$F_{22}'(0) = \lim_{\zeta_1\to\infty}\left[\frac{1}{\gamma^2}F_{12}'(\zeta_1) - \gamma\zeta_1 F_{21}''(0) - \frac{3}{2}\gamma^2\zeta_1^2\right]$$

The rest of the boundary conditions are

$$F_{1j}(0) = F_{1j}'(0) = F_{2j}'(\infty) = \Phi_{10}'(0) - 1$$
$$= \Phi_{11}'(0) = \Phi_{12}'(0) = \Phi_{1j}(\infty) = 0 \tag{12}$$

For the details of matching see Roy [5].

Solutions

The nine equations obtained from (7)–(10) and subject to the boundary conditions (11) and (12) are solved numerically on an electronic computer and the following results are obtained:

$$\gamma = 0.663902$$
$$F_{10}''(0) = 0.811546 \qquad \Phi_{10}(0) = -1.147565$$
$$F_{11}''(0) = -0.173879 \qquad \Phi_{11}(0) = -0.226844$$
$$F_{12}''(0) = 0.134655 \qquad \Phi_{12}(0) = 0.030392$$
$$F_{20}(0) = 0.0 \qquad F_{20}'(0) = 1.0 \qquad F_{20}''(0) = -1.837319 \tag{13}$$
$$F_{21}(0) = -0.300701 \qquad F_{21}'(0) = 0.732916$$
$$F_{21}''(0) = -1.399446 \qquad F_{22}(0) = -0.311263$$
$$F_{22}'(0) = 0.804204 \qquad F_{22}''(0) = -1.578787$$

Heat Transfer

The corresponding Nusselt number has been defined by Sparrow and Gregg [8] as

$$\mathrm{Nu}_x = qx/[k(t_w - t_\infty)] \tag{14}$$

With the help of (1), (5), (10), and (13) we have equation (14) reduced to

[2] Numbers in brackets designate References at end of technical brief.

$$(\sigma \mathrm{Gr}_x^*/5)^{1/5} = \mathrm{Nu}_x(1.1476 + 0.2268\sigma^{-1/2} - 0.0304\sigma^{-1}) \quad (15)$$

In Table 1 we compare our results with those of Sparrow and Gregg [8] and Sparrow [9] for $\sigma = 1, 10, 100$, the three large Prandtl numbers dealt with by Sparrow and Gregg [8].

References

1 LeFevre, E. J., "Laminar Free Convection from a Vertical Surface," *Proceedings of Ninth International Congress of Applied Mechanics*, Vol. 4, 1956, pp. 168–173.

2 Stewartson, K., and Jones, L. T., "The Heated Vertical Plate at High Prandtl Number," *Journal of the Aeronautical Sciences*, Vol. 24, 1957, pp. 379–380.

3 Kuiken, H. K., "An Asymptotic Solution for Large Prandtl Number Free Convection," *Journal of Engineering Mathematics*, Vol. 2, 1968, pp. 355–371.

4 Roy, S., "A Note on Natural Convection at High Prandtl Numbers," *International Journal of Heat and Mass Transfer*, Vol. 12, 1969, pp. 239–241.

5 Roy, S., "Double-Boundary-Layer Concept in Free Convection at High Prandtl Numbers," *Indian Journal of Physics*, Vol. 44, 1970, pp. 488–494.

6 Eshghy, S., "Free Convection Layers at Large Prandtl Numbers," *ZAMP*, Vol. 22, 1971, pp. 275–292.

7 Selman, J. R., and Newman, J., "High Sc Limit of Free Convection at a Vertical Plate With Uniform Flux Condition," JOURNAL OF HEAT TRANSFER, TRANS. ASME, Series C, Vol. 93, No. 4, Nov. 1971, pp. 465–466.

8 Sparrow, E. M., and Gregg, J. L., "Laminar Free Convection From a Vertical Plate With Uniform Surface Heat Flux," TRANS. ASME, Vol. 78, 1956, pp. 435–440.

9 Sparrow, E. M., "Laminar Free Convection on a Vertical Plate with Prescribed Non-Uniform Wall Heat Flux or Prescribed Non-Uniform Wall Temperature," NACA TN 3508.

Table 1 Dimensionless temperature difference, shear stress, and Nusselt number for different values of Prandtl number

	σ	$-\theta(0)$	$f''(0)$	$\mathrm{Nu}_x(\mathrm{Gr}_x^*)^{-1/4}$
	1	1.34402	0.77232	0.53927
Roy	10	0.76741	0.30655	0.94444
	100	0.46576	0.12608	1.55607
	1	1.35740	0.72196	0.53395
[8]	10	0.76746	0.30639	0.94439
	100	0.46566	0.12620	1.55645
	1	...	...	0.54792
[9]	10	...	...	0.96181
	100	...	...	1.54553

Finite-Element Method Applied to Heat Conduction in Solids with Nonlinear Boundary Conditions

R. E. BECKETT[1] and S.-C. CHU[2]

By use of an implicit iteration technique, the finite-element method applied to the heat-conduction problems of solids is no longer restricted to the linear heat-flux boundary conditions, but is extended to include nonlinear radiation–convection boundary conditions. The variation of surface temperatures within each time increment is taken into account; hence a rather large time-step size can be assigned to obtain transient heat-conduction solutions without introducing instability in the surface temperature of a body.

Introduction

SINCE Zienkiewicz and Cheung [1][3] and Wilson and Nickell [2] used the finite-element method to solve steady and transient heat-conduction problems, the application of this method to heat-transfer analysis for solids has attracted considerable attention. However, very little work has been done on the finite-element method for a solid with nonlinear radiation–convection heat-flux boundary conditions. Recently, Richardson and Shum [3] discussed the application of the finite-element method to the solution of heat-conduction problems involving nonlinear radiation boundary conditions. However, in their analysis the contribution due to radiation and convection was calculated entirely from the information available at one time step earlier, rather than from consideration of the variation of surface temperatures between each time increment. This modification, in which the effect of radiation is considered, introduces a source of instability in the surface temperature; therefore a small time-increment size is necessary to keep it under control. The purpose of this investigation is to extend the finite-element method to heat conduction in solids with nonlinear boundary conditions so that surface temperature can be varied within each time increment.

Analysis

The variational principles introduced by Gurtin [4] and applied by Wilson and Nickell [2] are used in this investigation. The details of the analysis will not be repeated. However, some main assumptions and results will be reviewed for the convenience of the reader.

The region of interest is divided into a finite number M of subregions with a finite number P of nodal points. The temperature at any position within the element m can be expressed in terms of nodal-point temperatures of a complete finite-element system by the matrix equation[4]

$$\theta_m(\mathbf{x}, t) = \langle b_m(\mathbf{x}) \rangle \{\theta(t)\} \quad (1)$$

Differentiation of equation (1) with respect to the spatial coordinates gives a column vector of temperature gradients

$$\{\theta_{m,i}(\mathbf{x}, t)\} = [a_m(\mathbf{x})]\{\theta(t)\} \quad (2)$$

Substituting equations (1) and (2) into a functional proposed by Gurtin [4] gives the generating functional for the complete finite-element system in the form of a summation over all M elements

$$\Omega_t = \sum_{m=1}^{M} \left[\int \frac{1}{2} \left\{ \rho_m c_m \theta_m^* \theta_m + \theta_{m,i}^* \overset{m}{k}_{ij}^* \theta_{m,j} - 2\rho_m^* p_m^* \theta_m - 2\rho_m c_m \theta_0^* \theta_m \right\} (\mathbf{x}, t) dV_m - \int \left\{ \overset{m}{\hat{Q}}_i n_i^* \theta_m \right\} (\mathbf{x}, t) dS_m \right] \quad (3)$$

Performing the first variation of equation (3) and noting that the resulting expression must vanish for an arbitrary variation $\delta\theta_i$ results in

$$[C]\{\theta(t)\} + [K]^*\{\theta(t)\} = [C]\{\theta(t - \Delta t)\} + \{Q(t)\} \quad (4)$$

in which the heat-capacity matrix $[C]$, the conductivity matrix $[K]$, and the thermal-force vector $\{Q(t)\}$ are defined in [2, 3].

If linear variation of temperature within each time increment $(t - \Delta t, t)$ is assumed to be valid, then equation (4) becomes

$$\left([C] + \frac{\Delta t}{2} [K] \right) \{\theta(t)\} = \left([C] - \frac{\Delta t}{2} [K] \right) \{\theta(t - \Delta t)\} + \{F\} \quad (5)$$

where the vector $\{F\}$ can be determined by substitution of the linear variational temperature expression into the thermal-force vector $\{Q_m(t)\}$ which is defined in [2, 3].

---

[1] Director, Weapons Laboratory (WECOM), Rock Island, Ill. Mem. ASME.

[2] Mechanical Engineer, Research Directorate, Weapons Laboratory (WECOM), Rock Island, Ill. Assoc. Mem. ASME.

[3] Numbers in brackets designate References at end of technical brief.

Contributed by the Heat Transfer Division of THE AMERICAN SOCIETY OF MECHANICAL ENGINEERS. Manuscript received by the Heat Transfer Division September 14, 1972.

[4] All notations in this technical brief are the same as in [2, 4] except those which are defined here.

$$(\sigma \mathrm{Gr}_x^*/5)^{1/5} = \mathrm{Nu}_x(1.1476 + 0.2268\sigma^{-1/2} - 0.0304\sigma^{-1}) \quad (15)$$

In Table 1 we compare our results with those of Sparrow and Gregg [8] and Sparrow [9] for $\sigma = 1, 10, 100$, the three large Prandtl numbers dealt with by Sparrow and Gregg [8].

References

1 LeFevre, E. J., "Laminar Free Convection from a Vertical Surface," *Proceedings of Ninth International Congress of Applied Mechanics*, Vol. 4, 1956, pp. 168–173.

2 Stewartson, K., and Jones, L. T., "The Heated Vertical Plate at High Prandtl Number," *Journal of the Aeronautical Sciences*, Vol. 24, 1957, pp. 379–380.

3 Kuiken, H. K., "An Asymptotic Solution for Large Prandtl Number Free Convection," *Journal of Engineering Mathematics*, Vol. 2, 1968, pp. 355–371.

4 Roy, S., "A Note on Natural Convection at High Prandtl Numbers," *International Journal of Heat and Mass Transfer*, Vol. 12, 1969, pp. 239–241.

5 Roy, S., "Double-Boundary-Layer Concept in Free Convection at High Prandtl Numbers," *Indian Journal of Physics*, Vol. 44, 1970, pp. 488–494.

6 Eshghy, S., "Free Convection Layers at Large Prandtl Numbers," *ZAMP*, Vol. 22, 1971, pp. 275–292.

7 Selman, J. R., and Newman, J., "High Sc Limit of Free Convection at a Vertical Plate With Uniform Flux Condition," JOURNAL OF HEAT TRANSFER, TRANS. ASME, Series C, Vol. 93, No. 4, Nov. 1971, pp. 465–466.

8 Sparrow, E. M., and Gregg, J. L., "Laminar Free Convection From a Vertical Plate With Uniform Surface Heat Flux," TRANS. ASME, Vol. 78, 1956, pp. 435–440.

9 Sparrow, E. M., "Laminar Free Convection on a Vertical Plate with Prescribed Non-Uniform Wall Heat Flux or Prescribed Non-Uniform Wall Temperature," NACA TN 3508.

Table 1 Dimensionless temperature difference, shear stress, and Nusselt number for different values of Prandtl number

	σ	$-\theta(0)$	$f''(0)$	$\mathrm{Nu}_x(\mathrm{Gr}_x^*)^{-1/4}$
	1	1.34402	0.77232	0.53927
Roy	10	0.76741	0.30655	0.94444
	100	0.46576	0.12608	1.55607
	1	1.35740	0.72196	0.53395
[8]	10	0.76746	0.30639	0.94439
	100	0.46566	0.12620	1.55645
	1	...	...	0.54792
[9]	10	...	...	0.96181
	100	...	...	1.54553

Finite-Element Method Applied to Heat Conduction in Solids with Nonlinear Boundary Conditions

R. E. BECKETT[1] and S.-C. CHU[2]

By use of an implicit iteration technique, the finite-element method applied to the heat-conduction problems of solids is no longer restricted to the linear heat-flux boundary conditions, but is extended to include nonlinear radiation–convection boundary conditions. The variation of surface temperatures within each time increment is taken into account; hence a rather large time-step size can be assigned to obtain transient heat-conduction solutions without introducing instability in the surface temperature of a body.

Introduction

SINCE Zienkiewicz and Cheung [1][3] and Wilson and Nickell [2] used the finite-element method to solve steady and transient heat-conduction problems, the application of this method to heat-transfer analysis for solids has attracted considerable attention. However, very little work has been done on the finite-element method for a solid with nonlinear radiation–convection heat-flux boundary conditions. Recently, Richardson and Shum [3] discussed the application of the finite-element method to the solution of heat-conduction problems involving nonlinear radiation boundary conditions. However, in their analysis the contribution due to radiation and convection was calculated entirely from the information available at one time step earlier, rather than from consideration of the variation of surface temperatures between each time increment. This modification, in which the effect of radiation is considered, introduces a source of instability in the surface temperature; therefore a small time-increment size is necessary to keep it under control. The purpose of this investigation is to extend the finite-element method to heat conduction in solids with nonlinear boundary conditions so that surface temperature can be varied within each time increment.

Analysis

The variational principles introduced by Gurtin [4] and applied by Wilson and Nickell [2] are used in this investigation. The details of the analysis will not be repeated. However, some main assumptions and results will be reviewed for the convenience of the reader.

The region of interest is divided into a finite number M of subregions with a finite number P of nodal points. The temperature at any position within the element m can be expressed in terms of nodal-point temperatures of a complete finite-element system by the matrix equation[4]

$$\theta_m(\mathbf{x}, t) = \langle b_m(\mathbf{x}) \rangle \{\theta(t)\} \quad (1)$$

Differentiation of equation (1) with respect to the spatial coordinates gives a column vector of temperature gradients

$$\{\theta_{m,i}(\mathbf{x}, t)\} = [a_m(\mathbf{x})]\{\theta(t)\} \quad (2)$$

Substituting equations (1) and (2) into a functional proposed by Gurtin [4] gives the generating functional for the complete finite-element system in the form of a summation over all M elements

$$\Omega_t = \sum_{m=1}^{M} \left[\int \frac{1}{2} \left\{ \rho_m c_m \theta_m^* \theta_m + \theta_{m,i}^* {}^m k_{ij}^* \theta_{m,j} - 2\rho_m^* p_m^* \theta_m - 2\rho_m c_m \theta_0^* \theta_m \right\}^m (\mathbf{x}, t) dV_m - \int \left\{ \hat{Q}_i n_i^* \theta_m \right\}^m (\mathbf{x}, t) dS_m \right] \quad (3)$$

Performing the first variation of equation (3) and noting that the resulting expression must vanish for an arbitrary variation $\delta\theta_i$ results in

$$[C]\{\theta(t)\} + [K]^*\{\theta(t)\} = [C]\{\theta(t - \Delta t)\} + \{Q(t)\} \quad (4)$$

in which the heat-capacity matrix $[C]$, the conductivity matrix $[K]$, and the thermal-force vector $\{Q(t)\}$ are defined in [2, 3].

If linear variation of temperature within each time increment $(t - \Delta t, t)$ is assumed to be valid, then equation (4) becomes

$$\left([C] + \frac{\Delta t}{2}[K]\right)\{\theta(t)\} = \left([C] - \frac{\Delta t}{2}[K]\right)\{\theta(t - \Delta t)\} + \{F\} \quad (5)$$

where the vector $\{F\}$ can be determined by substitution of the linear variational temperature expression into the thermal-force vector $\{Q_m(t)\}$ which is defined in [2, 3].

---

[1] Director, Weapons Laboratory (WECOM), Rock Island, Ill. Mem. ASME.

[2] Mechanical Engineer, Research Directorate, Weapons Laboratory (WECOM), Rock Island, Ill. Assoc. Mem. ASME.

[3] Numbers in brackets designate References at end of technical brief.

Contributed by the Heat Transfer Division of THE AMERICAN SOCIETY OF MECHANICAL ENGINEERS. Manuscript received by the Heat Transfer Division September 14, 1972.

[4] All notations in this technical brief are the same as in [2, 4] except those which are defined here.

In [2, 3] equation (5) is written in the form

$$\left([C] + \frac{\Delta t}{2}[K]\right)\{\theta(t)\} = \left([C] - \frac{\Delta t}{2}[K]\right)\{\theta(t-\Delta t)\} + \frac{\Delta t}{2}\{Q(t)\} + \frac{\Delta t}{2}\{Q(t-\Delta t)\} \quad (6)$$

This is true only if the boundary conditions are linear. If nonlinear boundary conditions are involved, the thermal-force vector is difficult to separate into the two thermal-force vectors at two discrete times $t - \Delta t$ and t.

Nonlinear Heat Transfer at the Surface

Since linearity is fundamental to Gurtin's variational principle, to consider the radiation–convection boundary condition, the following expression for surface heat flux was assumed to be valid:

$$q = R(\theta_R{}^3 + \theta_R{}^2\theta + \theta_R\theta^2 + \theta^3)^*(\theta_R - \theta) + H^*(\theta_C - \theta) \quad (7)$$

where R and H are constants related to the effects of radiation and convection at the surface, respectively. The surface with temperature θ is exposed to radiation (temperature θ_R) and convection (temperature θ_C).

The inclusion of radiation–convection boundary condition, equation (7), leads to the following form of the element thermal-force matrix:

$$\begin{aligned}\{Q_m\} = &-\frac{R_m}{5}\Delta t\,([\theta^4(t-\Delta t) + \theta^3(t-\Delta t)\theta(t) \\ &+ \theta^2(t-\Delta t)\theta^2(t) + \theta(t-\Delta t)\theta^3(t) + \theta^4(t)]) \\ &\times \int_{S_m}\langle d_m\rangle^T\langle d_m\rangle\langle d_m\rangle^T\langle d_m\rangle\langle d_m\rangle^T dS_m \\ &-\frac{H_m}{2}\Delta t([\theta(t-\Delta t) + \theta(t)])\int_{S_m}\langle d_m\rangle^T\langle d_m\rangle dS_m \\ &+ \int_{S_m}\theta_R{}^{4*}R_m\langle d_m\rangle^T dS_m + \int_{S_m}\theta_C{}^*H_m\langle d_m\rangle^T dS_m \\ &+ \int_{V_m}\rho_m{}^*p_m\langle b_m\rangle^T dV_m + \int_{S_m}\hat{Q}_j{}^m n_j\langle b_m\rangle^T dS_m \quad (8)\end{aligned}$$

and

$$\{F\} = \sum_{m=1}^{M}\{Q_m\} \quad (9)$$

From equations (8) and (9) one knows that the thermal-force vector $\{F\}$ cannot be separated into two vectors that include the information at times $t - \Delta t$ and t, respectively, since $\theta(t - \Delta t)$ and $\theta(t)$ are coupled in the first term of equation (8).

Substituting equations (8) and (9) into equation (5) results in the following equation for the finite-element system:

$$\begin{aligned}&\frac{\Delta t}{5}[A](\{\theta_t{}^4\} + \{\theta_{t-\Delta t}\theta_t{}^3\} + \{\theta^2{}_{t-\Delta t}\theta_t{}^2\} + \{\theta^3{}_{t-\Delta t}\theta_t\}) \\ &+ \left([C] + \frac{\Delta t}{2}[K] + \frac{\Delta t}{2}[H]\right)\{\theta_t\} = \left([C] - \frac{\Delta t}{2}[K] \right. \\ &\left. + \frac{\Delta t}{2}[H]\right)\{\theta_{t-\Delta t}\} + \frac{\Delta t}{5}[A]\{\theta^4{}_{t-\Delta t}\} + \{G(t)\} \quad (10)\end{aligned}$$

where

$$[A] = \sum_{m=1}^{M}[A_m] \qquad [H] = \sum_{m=1}^{M}[H_m]$$

$$\{G(t)\} = \sum_{m=1}^{M}\{G_m(t)\} \quad (11)$$

Each of the m-subscripted matrices represents the result of the appropriate integration over the mth element, e.g.

$$[A_m] = \int_{S_m} R_m\langle d_m\rangle^T\langle d_m\rangle\langle d_m\rangle^T\langle d_m\rangle\langle d_m\rangle^T dS_m$$

$$[H_m] = \int_{S_m} H_m\langle d_m\rangle^T\langle d_m\rangle dS_m \quad (12)$$

and

$$\{G_m(t)\} = \int_{V_m}\rho_m{}^*p_m\langle b_m\rangle dV_m + \int_{S_m}\theta_C{}^*H_m\langle d_m\rangle^T dS_m + \int_{S_m}\theta_R{}^{4*}R_m\langle d_m\rangle^T dS_m + \int_{S_m}\sum_{m}^{m}\hat{Q}_i n_i\langle b_m\rangle^T dS_m$$

It should be emphasized that equation (10) represents a set of nonlinear algebraic equations of nodal-point temperatures for the complete finite-element system which can be solved by the direct iteration technique used in [5]. This method has been proved [6] to be absolutely convergent and the order of convergence is quadratic. The detailed discussion of the convergence, the speed of convergence, and truncation errors of this method will not be presented here; however, they can be found in [6]. In the subsequent transient-temperature problems, if the initial temperature distribution is assumed to be an estimated solution, then a satisfactory solution can be obtained with only two or three iterations for each time increment. If the maximum difference of solutions for two successive iterations is less than a specified limit ϵ, say $\pm 10^{-6}$, the solution is considered to be suitable for all calculations in the following examples.

Examples

To illustrate the solution technique on a transient heat-conduction problem of a solid subjected to nonlinear boundary conditions, a plane slab of thickness $2L$ ($0 \le x \le 2L$) through which heat is exchanged with a radiating and convecting environment is considered. The initial temperature of the slab is assumed to be uniform with value θ_0. The radiation–convection boundary conditions are assumed to be

$$q = \Gamma(\theta_R{}^{*4} - \theta_W{}^{*4}) + B(\theta_C{}^* - \theta_W{}^*) \quad \text{at} \quad \eta = 0 \quad \eta = 2 \quad (13)$$

The solution for $\theta^*(\eta, \tau)$ depends upon the four parameters Γ, B, $\theta_R{}^*$, and $\theta_C{}^*$. In this investigation the decision was made to consider $\theta_R{}^* = \theta_C{}^* = 0$ and to vary Γ and B. Hence the results obtained by the present approach can be compared with those of the solution by Haji-Sheikh and Sparrow [7] based on the same input data.

The finite-element solution was obtained by use of a step-by-step technique. For each time increment $\Delta\tau$, an implicit iteration process [5] was used to solve equations (10). A variable time-step size was chosen. A value of $\Delta\tau = 0.001$ was chosen initially. After $\tau = 0.02$, $\Delta\tau$ was increased to 0.0025. After $\tau = 0.2$, $\Delta\tau$ was increased to 0.01. After $\tau = 0.4$, $\Delta\tau$ was increased to 0.025. After $\tau = 1.0$, $\Delta\tau$ was increased to 0.05. The magnitude of $\Delta\tau$ was increased with time since the change in the surface temperature decreases with an increase in time. The temperature history at the surface and at the center plane of the slab obtained by the present method and by the probability method is provided in Fig. 1 for $B = 1.0$ and $\Gamma = 0$, 1, and 4.0. Excellent agreement has been found, as shown in Fig. 1, between the present results and those of Haji-Sheikh and Sparrow obtained by use of the Monte Carlo method.

A comparison of the surface temperature predicted by use of the Richardson and Shum approach [3] and by use of the present method for a slab ($B = 1.0$, $\Gamma = 1.0$) with total elapsed time of one unit exposed to radiation and convection cooling is also shown in Fig. 1 by the dash-and-dot line and by the dash line,

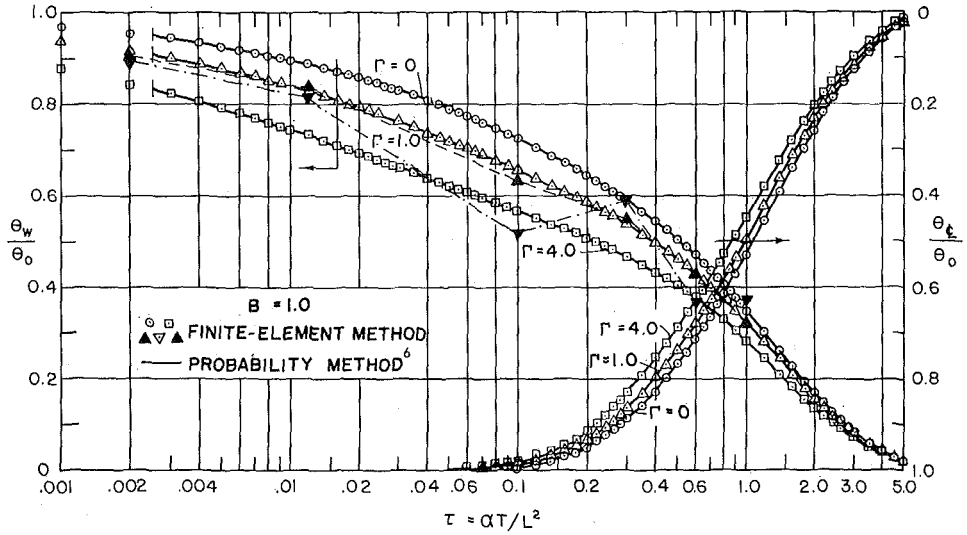

Fig. 1 Transient temperature results for a slab with radiation–convection boundary conditions

respectively. The time-increment sequence (in that order) $\Delta\tau_1 = 0.002$, $\Delta\tau_2 = 0.010$, $\Delta\tau_3 = 0.088$, $\Delta\tau_4 = 0.10$, $\Delta\tau_5 = 0.20$, $\Delta\tau_6 = 0.30$, and $\Delta\tau_7 = 0.40$ (note that $\sum_{i=1}^{7} \Delta\tau_i = 1.0$) was used to compute temperature distribution so that the total elapsed dimensionless time equals one unit. The difference between the solutions presented by the open and solid upright triangles is due to different time-increment sizes used to obtain solutions. The solution presented by open upright triangles can be considered closer to the exact solution since smaller time increments, as indicated, were used. However, the difference of those two solutions is insignificant for practical engineering problems. This points out that with the present method a satisfactory solution can be predicated even with large time increments. Since no iterative correction procedure is involved for the computing of temperatures in the Richardson and Shum method, the larger error introduced by use of their method may be due to the calculation of the contribution of radiation and convection at the surface based entirely on the surface temperature at one time step earlier (e.g., at $\Delta\tau = 0.012$) rather than on consideration of the variation of surface temperatures between each time step (e.g., between time interval $\Delta\tau = [0.012, 0.1]$).

An alternative explicit successive-substitution iteration technique [8] was also used to obtain the transient temperature distribution of the plane slab subjected to radiation–convection boundary conditions as mentioned previously. With this approach, the new computed surface temperature was used to estimate the contribution of radiation and convection on the surface of the slab. The detail discussion of this explicit iteration technique will not be presented here; however, it can be found in [8]. For comparison of the results obtained by use of both the explicit and the implicit iteration techniques presented in this investigation, the spatial coordinates of all nodal points were assigned as the same. Hence the size of banded matrices formulated by use of both methods is the same and so with almost the same required core storage space. Various time-step sizes are considered. Both the explicit and the implicit solutions are considered to be satisfactory if the maximum difference of results for two successive iterations is less than $\epsilon = \pm 10^{-4}$. A comparison of the number of iterations required to obtain a satisfactory solution by use of explicit and implicit methods for various time-step sizes and various Γ and B is given in Table 1.

From Table 1 the following conclusions are obtained:

1 The speed of convergence of the explicit iteration technique not only strongly depends upon the size of time increment $\Delta\tau$ but also strongly depends upon the values of Γ and B. However, the size of time increment $\Delta\tau$ and the values of Γ and B do not much affect the speed of convergence of the implicit iteration technique.

2 The speed of convergence of the implicit iteration technique is much faster than the speed of convergence of the explicit iteration technique. The implicit iteration technique used here has been proved [6] to be quadratically convergent; in other words, the number of correct decimal places is doubled at each iteration.

3 The implicit iteration technique used in this investigation is always convergent [6] even with large time-increment size (e.g., $\Delta\tau = 0.5$). Of course, if large time increments are used, the result will not converge to the exact solution.

Conclusions

With the use of iteration techniques, the finite-element method is extended to solid heat conduction with nonlinear heat-flux (radiation–convection) boundary conditions. The speed of convergence of the implicit method is faster than that of the explicit method. This may be due to the fact that the implicit method requires iteration of temperatures not only at the surfaces but also at all nodal points in the solid. The disadvantage of applying the implicit iteration method is that it is more difficult to program than the explicit iteration method; however, an experienced programmer can readily reduce the complexity of programming.

References

1 Zienkiewicz, O. C., and Cheung, Y. K., *The Finite-Element Method in Structural and Continuum Mechanics*, McGraw-Hill, New York, N. Y., 1967.

2 Wilson, E. L., and Nickell, R. E., "Application of the Finite Element Method to Heat Conduction Analysis," *Nuclear Engineering and Design*, Vol. 4, 1966, pp. 276–286.

3 Richardson, P. D., and Shum, Y. M., "Use of Finite Element Methods in Solution of Transient Heat Conduction Problems," ASME Paper No. 69-WA/HT-36.

Table 1 Comparison of the number of iterations required in the computing of temperatures of a plane slab at the end of the first time increment starting at $\tau = 0$

	$\Gamma = 1.0, B = 0.2$		$\Gamma = 2.0, B = 0.2$		$\Gamma = 4.0, B = 0.2$	
$\Delta\tau$	Explicit method	Implicit method	Explicit method	Implicit method	Explicit method	Implicit method
0.002	5	3	8	3	16	4
0.005	7	3	13	4	43	4
0.01	9	4	20	4	50*	4
0.05	20	4	50*	5	50*	5
0.10	33	4	50*	5	50*	5
0.20	50*	5	50*	5	50*	6
0.30	50*	5	50*	5	50*	6
0.40	50*	5	50*	5	50*	6
0.50	50*	5	50*	5	50*	6

* After 50 iterations, the convergence criterion ($\epsilon = \pm 10^{-4}$) still not reached.

4 Gurtin, N. E., "Variational Principles for Linear Initial Value Problems," *Quarterly of Applied Mathematics*, Vol. 22, 1964, pp. 252–256.
5 Chu, S. C., "Piecewise Polynomials and the Partition Method for Nonlinear Ordinary Differential Equations," *Journal of Engineering Mathematics*, Vol. 4, No. 1, Jan. 1970, pp. 65–76.
6 Henrici, P., *Discrete Variable Methods in Ordinary Differential Equations*, John Wiley & Sons, New York, N. Y., 1965.
7 Haji-Sheikh, A., and Sparrow, E. M., "The Solution of Heat Conduction Problems by Probability Methods," JOURNAL OF HEAT TRANSFER, TRANS. ASME, Series C, Vol. 89, No. 3, May 1967, pp. 121–131.
8 Chu, S. C., and Yalamanchili, R. V. S., "Application of the Finite-Element Method to Heat-Transfer Problems," Part I and Part II, Technical Reports, AD 726370 and AD 726371, U. S. Army Weapons Command, 1971.

Conductive Shape Factors for a Circular Cylinder Centered in a Rectangular Slab Having One and Two Adiabatic Surfaces

E. I. GRIGGS,[1] D. R. PITTS,[2] and A. B. GOYAL[3]

Introduction

MANY practical heat-transfer problems pertain to heat conduction between two isothermal surfaces through an intervening medium posing a variable cross-sectional area to the heat flow. For such cases, the influence of variable geometry is commonly included in a conductive shape factor defined by

$$q = Sk\Delta T \tag{1}$$

Many configurations have previously been investigated and typical shape factors are reported in [1-4].[4]

In this note, attention is directed to the case of a circular cylinder centered in a rectangular slab, Fig. 1(*a*). For this arrangement with both the inner and outer surfaces at constant but different temperatures, an expression for the shape factor has been obtained by means of conformal mapping and reported by Balcerzak and Raynor [1] as

$$S = \frac{2\pi}{\ln \frac{4a}{\pi r} - 2K} \tag{2}$$

where K is a function of the ratio b/a. Two variations of this arrangement which are considered in this note include the case where one side of the rectangle is adiabatic and the case where two opposing sides are adiabatic. Shape factors for the first variation apply directly to a symmetrical half of the arrangement shown in Fig. 1(*b*), while those for the second variation apply directly to a symmetrical section of the arrangement shown in Fig. 1(*c*). Results for the two variations may be useful in estimating heat-transfer rates for situations such as that shown in Fig. 1(*d*), provided some caution is exercised since the geometrical dividing line between the two cylinders at an end is not a precise line of thermal symmetry.

[1] Associate Professor, Department of Mechanical Engineering, Tennessee Technological University, Cookeville, Tenn. Assoc. Mem. ASME.
[2] Professor, Department of Mechanical Engineering, Tennessee Technological University, Cookeville, Tenn. Mem. ASME.
[3] Graduate Student, Department of Mechanical Engineering, Tennessee Technological University, Cookeville, Tenn.
[4] Numbers in brackets designate References at end of technical brief.

Contributed by the Heat Transfer Division of THE AMERICAN SOCIETY OF MECHANICAL ENGINEERS. Manuscript received by the Heat Transfer Division February 29, 1972.

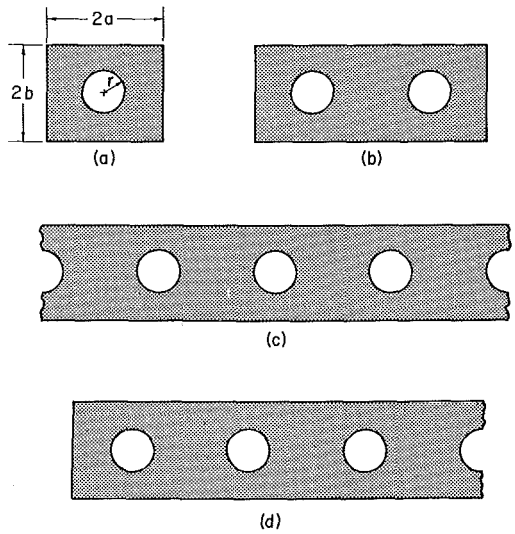

Fig. 1 Configurations of a homogeneous rectangular slab containing heated or cooled tubes

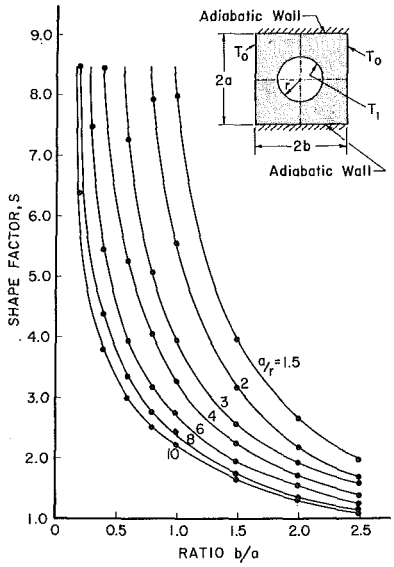

Fig. 2 Conductive shape factors for a rectangular section containing a heated or cooled tube—two sides isothermal and two sides adiabatic

Computations and Results

A symmetrical section of Fig. 1(*a*) was isolated for numerical study. In the first variation considered with one wall adiabatic and the other three isothermal, this amounted to a half-section. For the second variation with two opposing walls isothermal and the other two adiabatic, this corresponded to a quarter-section. In each case, the selected section was subdivided into a square-grid network.

Appropriate finite-difference equations relating nodal-point temperatures to those of adjacent points were formulated as presented in the conduction literature. For those nodal points adjacent to the interior curved boundary, use was made of fractional nodal spacings in accordance with the technique outlined in [5]. A suitably small grid spacing, using from 288 to 2560 grid points for the symmetrical section analyzed, was chosen to insure accuracy of the numerical solution for each configuration. Computations were carried out using an IBM 360/40 digital computer.

The integrity of the numerical technique was ascertained by computing shape factors for the range of ratios a/r and b/a of this study corresponding to the case of all four surfaces isothermal. These numerical predictions agreed in each case within 2 percent of the exact solution given by equation (2), and this is

4 Gurtin, N. E., "Variational Principles for Linear Initial Value Problems," *Quarterly of Applied Mathematics*, Vol. 22, 1964, pp. 252–256.
5 Chu, S. C., "Piecewise Polynomials and the Partition Method for Nonlinear Ordinary Differential Equations," *Journal of Engineering Mathematics*, Vol. 4, No. 1, Jan. 1970, pp. 65–76.
6 Henrici, P., *Discrete Variable Methods in Ordinary Differential Equations*, John Wiley & Sons, New York, N. Y., 1965.
7 Haji-Sheikh, A., and Sparrow, E. M., "The Solution of Heat Conduction Problems by Probability Methods," JOURNAL OF HEAT TRANSFER, TRANS. ASME, Series C, Vol. 89, No. 3, May 1967, pp. 121–131.
8 Chu, S. C., and Yalamanchili, R. V. S., "Application of the Finite-Element Method to Heat-Transfer Problems," Part I and Part II, Technical Reports, AD 726370 and AD 726371, U. S. Army Weapons Command, 1971.

Conductive Shape Factors for a Circular Cylinder Centered in a Rectangular Slab Having One and Two Adiabatic Surfaces

E. I. GRIGGS,[1] D. R. PITTS,[2] and A. B. GOYAL[3]

Introduction

MANY practical heat-transfer problems pertain to heat conduction between two isothermal surfaces through an intervening medium posing a variable cross-sectional area to the heat flow. For such cases, the influence of variable geometry is commonly included in a conductive shape factor defined by

$$q = Sk\Delta T \tag{1}$$

Many configurations have previously been investigated and typical shape factors are reported in [1-4].[4]

In this note, attention is directed to the case of a circular cylinder centered in a rectangular slab, Fig. 1(*a*). For this arrangement with both the inner and outer surfaces at constant but different temperatures, an expression for the shape factor has been obtained by means of conformal mapping and reported by Balcerzak and Raynor [1] as

$$S = \frac{2\pi}{\ln \frac{4a}{\pi r} - 2K} \tag{2}$$

where K is a function of the ratio b/a. Two variations of this arrangement which are considered in this note include the case where one side of the rectangle is adiabatic and the case where two opposing sides are adiabatic. Shape factors for the first variation apply directly to a symmetrical half of the arrangement shown in Fig. 1(*b*), while those for the second variation apply directly to a symmetrical section of the arrangement shown in Fig. 1(*c*). Results for the two variations may be useful in estimating heat-transfer rates for situations such as that shown in Fig. 1(*d*), provided some caution is exercised since the geometrical dividing line between the two cylinders at an end is not a precise line of thermal symmetry.

[1] Associate Professor, Department of Mechanical Engineering, Tennessee Technological University, Cookeville, Tenn. Assoc. Mem. ASME.
[2] Professor, Department of Mechanical Engineering, Tennessee Technological University, Cookeville, Tenn. Mem. ASME.
[3] Graduate Student, Department of Mechanical Engineering, Tennessee Technological University, Cookeville, Tenn.
[4] Numbers in brackets designate References at end of technical brief.

Contributed by the Heat Transfer Division of THE AMERICAN SOCIETY OF MECHANICAL ENGINEERS. Manuscript received by the Heat Transfer Division February 29, 1972.

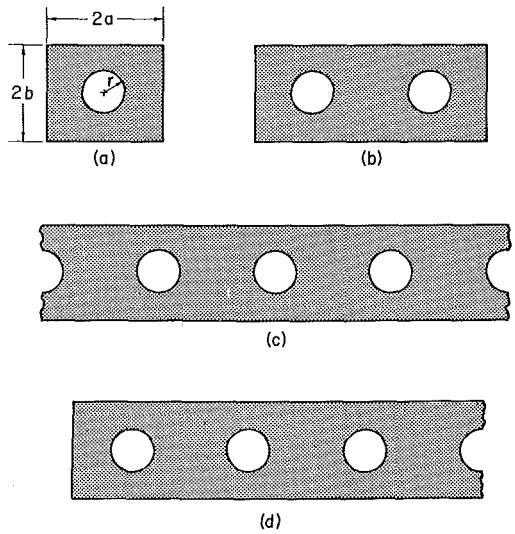

Fig. 1 Configurations of a homogeneous rectangular slab containing heated or cooled tubes

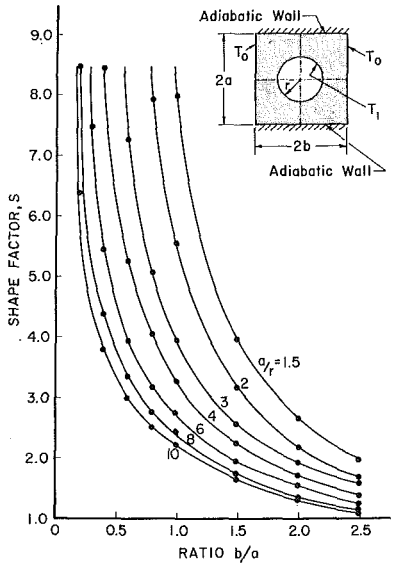

Fig. 2 Conductive shape factors for a rectangular section containing a heated or cooled tube—two sides isothermal and two sides adiabatic

Computations and Results

A symmetrical section of Fig. 1(*a*) was isolated for numerical study. In the first variation considered with one wall adiabatic and the other three isothermal, this amounted to a half-section. For the second variation with two opposing walls isothermal and the other two adiabatic, this corresponded to a quarter-section. In each case, the selected section was subdivided into a square-grid network.

Appropriate finite-difference equations relating nodal-point temperatures to those of adjacent points were formulated as presented in the conduction literature. For those nodal points adjacent to the interior curved boundary, use was made of fractional nodal spacings in accordance with the technique outlined in [5]. A suitably small grid spacing, using from 288 to 2560 grid points for the symmetrical section analyzed, was chosen to insure accuracy of the numerical solution for each configuration. Computations were carried out using an IBM 360/40 digital computer.

The integrity of the numerical technique was ascertained by computing shape factors for the range of ratios a/r and b/a of this study corresponding to the case of all four surfaces isothermal. These numerical predictions agreed in each case within 2 percent of the exact solution given by equation (2), and this is

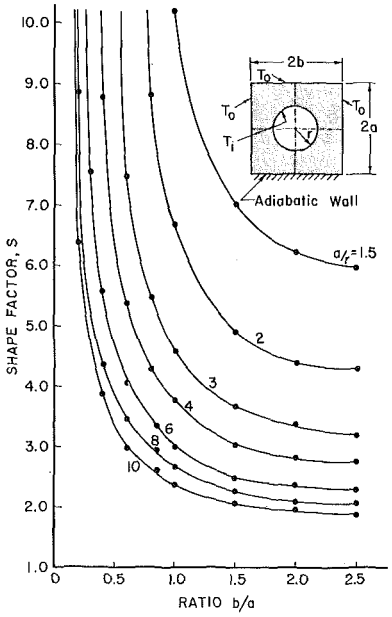

Fig. 3 Conductive shape factors for a rectangular section containing a heated or cooled tube—three sides isothermal and one side adiabatic

considered to be indicative of the accuracy of the results reported herein. The results are summarized in Figs. 2 and 3, where the indicated "points" in these figures correspond to specific numerical computations.

References

1 Balcerzak, M. J., and Raynor, S., "Steady State Temperature Distribution and Heat Flow in Prismatic Bars with Isothermal Boundary Conditions," *International Journal of Heat and Mass Transfer*, Vol. 3, 1961, pp. 113–125.

2 Faulkner, R. C., and Andrews, R. V., "Shape Factors in Multipipe Systems," *AIChE Journal*, Vol. 1, 1955, pp. 559–561.

3 Murthy, M. L., and Ramchandranan, A., "Shape Factor in Conduction Heat Transfer," *British Chemical Engineering*, Vol. 12, No. 5, 1967, pp. 730–731.

4 Sunderland, J. E., and Johnson, K. R., "Shape Factors for Heat Conduction through Bodies with Isothermal or Convective Boundary Conditions," *Trans. ASHRAE*, Vol. 70, 1964, pp. 237–241.

5 Schneider, P. J., *Conduction Heat Transfer*, Addison-Wesley, Reading, Mass., 1955, pp. 138–162.

Separated-Variables Solution for Steady Temperatures in Rectangles with Broken Boundary Conditions[1]

R. B. KELMAN[2] and C. A. KOPER, JR.[3]

Introduction and Background

ANALYTIC formulas for steady temperatures in rectangles with broken boundary conditions are obtained. These results supplement standard formulas for corresponding continuous boundary-value problems, e.g., [1, pp. 166, 435; 2, pp. 101, 182].[4] In dimensionless coordinates (ξ, η) the rectangle is $0 < \xi < 1$ and $0 < \eta < \beta$ (this includes the semi-infinite rectangle for which $\beta = \infty$). The temperature T satisfies Laplace's equation and the boundary conditions

$$\left[h_{11}T - k_{11}\frac{\partial T}{\partial \eta}\right]_{\eta=0} = f_{11}(\xi) \qquad 0 < \xi < \gamma \tag{1}$$

$$\left[h_{12}T - k_{12}\frac{\partial T}{\partial \eta}\right]_{\eta=0} = f_{12}(\xi) \qquad \gamma < \xi < 1 \tag{2}$$

$$\left[h_2T + k_2\frac{\partial T}{\partial \xi}\right]_{\xi=1} = 0 \qquad \left[h_4T - k_4\frac{\partial T}{\partial \xi}\right]_{\xi=0} = 0 \qquad 0 < \eta < \beta \tag{3}$$

where the constants ha/k are Biot numbers (a being a characteristic length) [2, p. 12], γ is a point between 0 and 1, and the functions f are given. If $\beta = \infty$, then T is bounded as $\eta \to \infty$, whereas if $\beta < \infty$, then

$$\left[h_3T + k_3\frac{\partial T}{\partial \eta}\right]_{\eta=\beta} = f_3(\xi) \qquad 0 < \xi < 1 \tag{4}$$

Note that $k = 0$ and $h = 0$ correspond, respectively, to boundary conditions of the first and second kind [2, p. 7]. For brevity, we exclude the case in which both h_2 and h_4 are zero. This case can be solved by slightly modifying the answers given here, cf. [1, pp. 18, 101].

The difficulty in finding T is due entirely to conditions (1) and (2), the "broken" or "discontinuous" boundary conditions, which correspond to a discontinuity in the differential boundary operator, i.e., the left-hand sides of (1) and (2), at $\xi = \gamma$. The continuity properties of the functions f are not important.

We separate variables to find a solution in ξ-eigenfunctions satisfying all the boundary conditions except along the base. The solution is fitted to the base boundary conditions by an integrated least-squares criterion [3, 4]. The procedure we use is related to the method of dual trigonometric series [5, 6] often used in continuum mechanics [7] and electrostatics [6, 8]. It is easier to apply than dual series since it involves no manipulation of special functions or use of integral equations, and for heat transfer has the advantage of applying to problems with boundary conditions of the third kind. Thus the present technique combines for the rectangle the principal advantage of dual series [6]—a neat eigenfunction solution—with the main advantages of integrated least-squares boundary fitting [3, 4]—the flexibility to handle all linear boundary conditions and computational simplicity.

A related problem is finding the temperature U which satisfies equations (1)–(4) modified as follows: the right-hand sides of (1), (2), and (4) are set equal to zero; the right-hand sides of the equations in (3) are replaced by given functions $f_2(\eta)$ and $f_4(\eta)$. In finding T there is a discontinuity in the differential boundary operator along an edge with a nonhomogeneous boundary condition, whereas in finding U the discontinuity is on an edge with a homogeneous boundary condition. One uses ξ-eigenfunctions for finding T and η-eigenfunctions for finding U. Since ξ and η do not enter either problem symmetrically, a very different method was used [9, 10] to find U than is used here to find T. This stands in sharp contrast to the case of continuous boundary operators for which, since ξ and η enter the problem symmetrically, solutions involving ξ-eigenfunctions are obtained from those involving η-eigenfunctions by simply interchanging ξ and η [1, 2].

Application of the Method

Separating variables in the usual fashion leads to the following solution for the semi-infinite rectangle:

$$T(\xi, \eta) = \sum_{n=1}^{\infty} a_n \sin(\lambda_n\xi + \phi_n)e^{-\lambda_n\eta} \tag{5}$$

[1] This work was supported in part by the Office of Naval Research under contract N00014-67-A-0299-0001 (task N0041-278).

[2] Professor, Department of Mathematics and Computer Science, Colorado State University, Ft. Collins, Colo.

[3] Graduate Student, Department of Civil Engineering, Colorado State University, Ft. Collins, Colo.

[4] Numbers in brackets designate References at end of technical brief.

Contributed by the Heat Transfer Division of THE AMERICAN SOCIETY OF MECHANICAL ENGINEERS. Manuscript received by the Heat Transfer Division June 6, 1972.

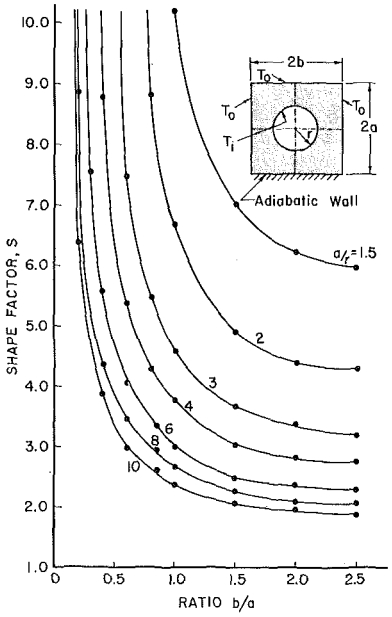

Fig. 3 Conductive shape factors for a rectangular section containing a heated or cooled tube—three sides isothermal and one side adiabatic

considered to be indicative of the accuracy of the results reported herein. The results are summarized in Figs. 2 and 3, where the indicated "points" in these figures correspond to specific numerical computations.

References

1 Balcerzak, M. J., and Raynor, S., "Steady State Temperature Distribution and Heat Flow in Prismatic Bars with Isothermal Boundary Conditions," *International Journal of Heat and Mass Transfer*, Vol. 3, 1961, pp. 113–125.

2 Faulkner, R. C., and Andrews, R. V., "Shape Factors in Multipipe Systems," *AIChE Journal*, Vol. 1, 1955, pp. 559–561.

3 Murthy, M. L., and Ramchandranan, A., "Shape Factor in Conduction Heat Transfer," *British Chemical Engineering*, Vol. 12, No. 5, 1967, pp. 730–731.

4 Sunderland, J. E., and Johnson, K. R., "Shape Factors for Heat Conduction through Bodies with Isothermal or Convective Boundary Conditions," *Trans. ASHRAE*, Vol. 70, 1964, pp. 237–241.

5 Schneider, P. J., *Conduction Heat Transfer*, Addison-Wesley, Reading, Mass., 1955, pp. 138–162.

Separated-Variables Solution for Steady Temperatures in Rectangles with Broken Boundary Conditions[1]

R. B. KELMAN[2] and C. A. KOPER, JR.[3]

Introduction and Background

ANALYTIC formulas for steady temperatures in rectangles with broken boundary conditions are obtained. These results supplement standard formulas for corresponding continuous boundary-value problems, e.g., [1, pp. 166, 435; 2, pp. 101, 182].[4] In dimensionless coordinates (ξ, η) the rectangle is $0 < \xi < 1$ and $0 < \eta < \beta$ (this includes the semi-infinite rectangle for which $\beta = \infty$). The temperature T satisfies Laplace's equation and the boundary conditions

$$\left[h_{11}T - k_{11}\frac{\partial T}{\partial \eta}\right]_{\eta=0} = f_{11}(\xi) \qquad 0 < \xi < \gamma \tag{1}$$

$$\left[h_{12}T - k_{12}\frac{\partial T}{\partial \eta}\right]_{\eta=0} = f_{12}(\xi) \qquad \gamma < \xi < 1 \tag{2}$$

$$\left[h_2T + k_2\frac{\partial T}{\partial \xi}\right]_{\xi=1} = 0 \qquad \left[h_4T - k_4\frac{\partial T}{\partial \xi}\right]_{\xi=0} = 0 \qquad 0 < \eta < \beta \tag{3}$$

where the constants ha/k are Biot numbers (a being a characteristic length) [2, p. 12], γ is a point between 0 and 1, and the functions f are given. If $\beta = \infty$, then T is bounded as $\eta \to \infty$, whereas if $\beta < \infty$, then

$$\left[h_3T + k_3\frac{\partial T}{\partial \eta}\right]_{\eta=\beta} = f_3(\xi) \qquad 0 < \xi < 1 \tag{4}$$

Note that $k = 0$ and $h = 0$ correspond, respectively, to boundary conditions of the first and second kind [2, p. 7]. For brevity, we exclude the case in which both h_2 and h_4 are zero. This case can be solved by slightly modifying the answers given here, cf. [1, pp. 18, 101].

The difficulty in finding T is due entirely to conditions (1) and (2), the "broken" or "discontinuous" boundary conditions, which correspond to a discontinuity in the differential boundary operator, i.e., the left-hand sides of (1) and (2), at $\xi = \gamma$. The continuity properties of the functions f are not important.

We separate variables to find a solution in ξ-eigenfunctions satisfying all the boundary conditions except along the base. The solution is fitted to the base boundary conditions by an integrated least-squares criterion [3, 4]. The procedure we use is related to the method of dual trigonometric series [5, 6] often used in continuum mechanics [7] and electrostatics [6, 8]. It is easier to apply than dual series since it involves no manipulation of special functions or use of integral equations, and for heat transfer has the advantage of applying to problems with boundary conditions of the third kind. Thus the present technique combines for the rectangle the principal advantage of dual series [6]—a neat eigenfunction solution—with the main advantages of integrated least-squares boundary fitting [3, 4]—the flexibility to handle all linear boundary conditions and computational simplicity.

A related problem is finding the temperature U which satisfies equations (1)–(4) modified as follows: the right-hand sides of (1), (2), and (4) are set equal to zero; the right-hand sides of the equations in (3) are replaced by given functions $f_2(\eta)$ and $f_4(\eta)$. In finding T there is a discontinuity in the differential boundary operator along an edge with a nonhomogeneous boundary condition, whereas in finding U the discontinuity is on an edge with a homogeneous boundary condition. One uses ξ-eigenfunctions for finding T and η-eigenfunctions for finding U. Since ξ and η do not enter either problem symmetrically, a very different method was used [9, 10] to find U than is used here to find T. This stands in sharp contrast to the case of continuous boundary operators for which, since ξ and η enter the problem symmetrically, solutions involving ξ-eigenfunctions are obtained from those involving η-eigenfunctions by simply interchanging ξ and η [1, 2].

Application of the Method

Separating variables in the usual fashion leads to the following solution for the semi-infinite rectangle:

$$T(\xi, \eta) = \sum_{n=1}^{\infty} a_n \sin(\lambda_n\xi + \phi_n)e^{-\lambda_n\eta} \tag{5}$$

[1] This work was supported in part by the Office of Naval Research under contract N00014-67-A-0299-0001 (task N0041-278).

[2] Professor, Department of Mathematics and Computer Science, Colorado State University, Ft. Collins, Colo.

[3] Graduate Student, Department of Civil Engineering, Colorado State University, Ft. Collins, Colo.

[4] Numbers in brackets designate References at end of technical brief.

Contributed by the Heat Transfer Division of THE AMERICAN SOCIETY OF MECHANICAL ENGINEERS. Manuscript received by the Heat Transfer Division June 6, 1972.

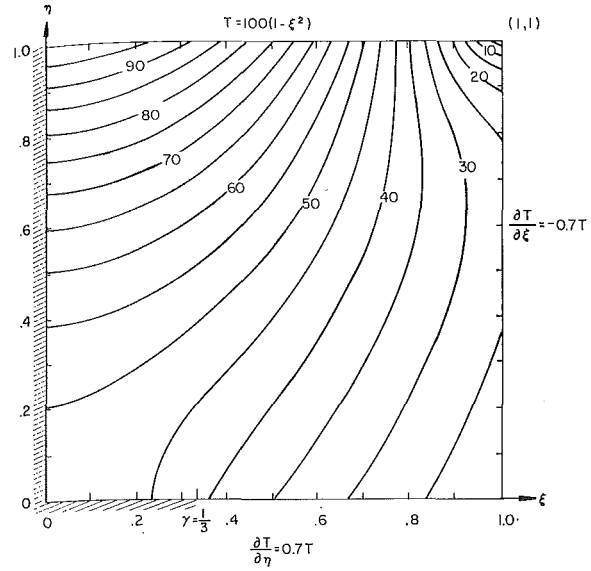

Fig. 1 Isotherms are displayed for an illustrative example in which T satisfies the boundary conditions shown along the sides of the square; the temperature increment between isotherms is 5; the break in boundary conditions along the base occurs at $\gamma = \frac{1}{3}$; to the left of γ the base is insulated, while to the right convective heat transfer occurs by Newtonian cooling

where λ_n is the nth positive root of

$$(k_2k_4\lambda^2 - h_2h_4)\tan\lambda = \lambda(h_2k_4 + h_4k_2) \tag{6}$$

and

$$\phi_n = \arctan(k_4\lambda_n/h_4) \tag{7}$$

This solution satisfies (3). To satisfy conditions (1) and (2) the $\{a_n\}$ are chosen to minimize the integrated least-squares deviation along the base, i.e.,

$$I = \int_0^\gamma \left(\left[k_{11}\frac{\partial T}{\partial\eta} + h_{11}T - f_{11}\right]_{\eta=0}\right)^2 d\xi + \int_\gamma^1 \left(\left[k_{12}\frac{\partial T}{\partial\eta} + h_{12}T - f_{12}\right]_{\eta=0}\right)^2 d\xi$$

To find the minimum we set $\partial I/\partial a_n = 0$ for $n = 1, 2, \ldots$, and obtain (after some straightforward algebra) the equations for $\{a_n\}$

$$\sum_{n=1}^{\infty} A_{pn}a_n = F_p \qquad p = 1, 2, \ldots, \tag{8}$$

where

$$F_p = (\lambda_p k_{11} + h_{11})\int_0^\gamma f_{11}(\xi)\sin(\lambda_p\xi + \phi_p)d\xi + (\lambda_p k_{12} + h_{12})\int_\gamma^1 f_{12}(\xi)\sin(\lambda_p\xi + \phi_p)d\xi \tag{9}$$

For conveniently expressing A_{pn} we introduce the notation $\lambda_{pn}^{\pm} = \lambda_p \pm \lambda_n$, $\phi_{pn}^{\pm} = \phi_p \pm \phi_n$, and

$$\delta_{pn} = \frac{\sin(\lambda_{pn}^-\gamma + \phi_{pn}^-) - \sin\phi_{pn}^-}{2\lambda_{pn}^-} - \frac{\sin(\lambda_{pn}^+\gamma + \phi_{pn}^+) - \sin\phi_{pn}^+}{2\lambda_{pn}^+} \qquad p \neq n$$

$$\delta_{pp} = \frac{1}{2}\left\{\gamma - \frac{\sin(2\lambda_p\gamma + 2\phi_p) - \sin 2\phi_p}{2\lambda_p}\right\}$$

$$\epsilon_{pn} = \frac{\sin(\lambda_{pn}^- + \phi_{pn}^-) - \sin(\lambda_{pn}^-\gamma + \phi_{pn}^-)}{2\lambda_{pn}^-} - \frac{\sin(\lambda_{pn}^+ + \phi_{pn}^+) - \sin(\lambda_{pn}^+\gamma + \phi_{pn}^+)}{2\lambda_{pn}^+} \qquad p \neq n$$

$$\epsilon_{pp} = \frac{1}{2}\left\{1 - \gamma - \frac{\sin(2\lambda_p + 2\phi_p) - \sin(2\lambda_p\gamma + 2\phi_p)}{2\lambda_p}\right\}$$

In this notation

$$A_{pn} = (\lambda_p k_{11} + h_{11})(\lambda_n k_{11} + h_{11})\delta_{pn} + (\lambda_p k_{12} + h_{12})(\lambda_n k_{12} + h_{12})\epsilon_{pn} \tag{10}$$

For the finite rectangle, T is found in exactly the same way. The answer here is

$$T(\xi,\eta) = \sum_{n=1}^{\infty}\{a_n[-\sinh\lambda_n\eta + \mu_n\cosh\lambda_n\eta] + G_n\cosh\lambda_n\eta\}\sin(\lambda_n\xi + \phi_n) \tag{11}$$

where $\mu_n = (h_3\tanh\lambda_n\beta + k_3\lambda_n)/(h_3 + k_3\lambda_n\tanh\lambda_n\beta)$,

$$G_n = \frac{4\lambda_n\,\mathrm{sech}\,\lambda_n\beta\int_0^1 f_3(\xi)\sin(\lambda_n\xi + \phi_n)d\xi}{(h_3 + k_3\lambda_n\tanh\lambda_n\beta)(2\lambda_n - \sin(2\lambda_n + 2\phi_n) + \sin 2\phi_n)}$$

and $\{a_n\}$ is the solution to (8) with

$$F_p = (h_{11}\mu_p + k_{11}\lambda_p)\int_0^\gamma f_{11}(\xi)\sin(\lambda_p\xi + \phi_p)d\xi + (h_{12}\mu_p + k_{12}\lambda_p)\int_\gamma^1 f_{12}(\xi)\sin(\lambda_p\xi + \phi_p)d\xi - \sum_{n=1}^{\infty} G_n[h_{11}(h_{11}\mu_p + k_{11}\lambda_p)\delta_{pn} + h_{12}(h_{12}\mu_p + k_{12}\lambda_p)\epsilon_{pn}] \tag{12}$$

$$A_{pn} = (h_{11}\mu_p + k_{11}\lambda_p)(h_{11}\mu_n + k_{11}\lambda_n)\delta_{pn} + (h_{12}\mu_p + k_{12}\lambda_p)(h_{12}\mu_n + k_{12}\lambda_n)\epsilon_{pn} \tag{13}$$

The nth-order approximation to T is found by truncating the series in (5), (8), and (11) at the nth term. For most applications, $n \leq 20$ suffices. Computations were performed on a CDC 6400 with a program written in FORTRAN IV. Our program generates on command isotherm curves which are automatically displayed on a cathode-ray tube and recorded on 35-mm film. Figure 1 was produced this way with $n = 20$. Little change was seen in these curves in going from the 20th- to the 100th-order approximation. We have obtained similar results for other examples.

In summary, integrated least-squares boundary fitting is an analytically simple and numerically effective procedure for extending separation-of-variables formulas to steady temperatures in rectangles with discontinuous boundary conditions.

References

1 Carslaw, H. S., and Jaeger, J. C., *Conduction of Heat in Solids*, 2nd ed., Oxford University Press, London, 1959.

2 Özisik, M. N., *Boundary Value Problems of Heat Conduction*, International Textbook Co., Scranton, Pa., 1968.

3 Williams, W., Parke, N. G., Moran, D. A., and Sherman, C. H., "Acoustic Radiation from a Finite Cylinder," *Journal of the Acoustical Society of America*, Vol. 36, 1964, pp. 2316–2322.

4 France, D. M., "Analytical Solution to Steady-State Heat-Conduction Problems With Irregularly Shaped Boundaries," JOURNAL OF HEAT TRANSFER, TRANS. ASME, Series C, Vol. 93, No. 4, Nov. 1971, pp. 449–454.

5 Kelman, R. B., and Koper, C. A., Jr., "Least Squares Approximations for Dual Trigonometric Series," to appear in the *Glasgow Mathematical Journal*.

6 Sneddon, I. N., *Mixed Boundary Value Problems in Potential Theory*, North-Holland Publishing Co., Amsterdam, 1966.

7 Sneddon, I. N., and Lowengrub, M., *Crack Problems in Classical Theory of Elasticity*, John Wiley & Sons, New York, N. Y., 1969.

8 Kiyono, T., and Shimasaki, M., "On the Solution of Laplace's Equation by Certain Dual Series Equations," *SIAM Journal on Ap-*

plied Mathematics, Vol. 21, 1971, pp. 245–257.
9 Kelman, R. B., "Harmonic Mixed Boundary-Value Problems in Composite Rectangular Domains," *Quarterly Journal of Mechanics and Applied Mathematics*, Vol. 23, 1970, pp. 549–566.
10 Schmitz, R. A., "Heat Flux Through a Strip-Heated Flat Plate," JOURNAL OF HEAT TRANSFER, TRANS. ASME, Series C, Vol. 92, No. 1, Feb. 1970, pp. 201–202.

A Numerical Solution of the Graetz Problem with Axial Conduction Included

F. H. VERHOFF[1] and D. P. FISHER[2]

Nomenclature

C_p = specific heat
k = thermal conductivity
K = constant of axial transformation
Nu = Nusselt number, $2Rq_w/[k(T_w - T_b)]$
Pe = Peclet number, $2\rho RuC_p/k$
q_w = heat flux at wall
r = radial dimension
R = pipe radius
T = temperature
T_b = bulk temperature
u = mean velocity
u_r = velocity
z = axial dimension
η = dimensionless axial dimension
θ = dimensionless temperature
ξ = dimensionless radial dimension
ρ = density

Introduction

THE familiar Graetz problem of laminar-flow heat transfer in a pipe has traditionally been solved by neglecting the effect of axial heat conduction because the mathematical problem is simplified from an elliptic equation with boundary conditions at infinity to a parabolic equation with this assumption. However, for low Peclet numbers the effect of conduction is significant; Hennecke [1][3] has presented numerical solutions with axial conduction included for constant-wall-temperature and uniform-heat-flux cases. By trial and error he approximated the boundary conditions at infinity. Hsu [2] has developed an exact solution to the uniform-wall-heat-flux case by a separation-of-variables technique. Petukhov and Tsvetkov [3] solved the constant-heat-flux case by using an approximate technique that Hsu found to contain considerable error. Jones [4] recently presented an analytical solution for the constant-wall-temperature case.

The solutions of these authors are complicated by the use of boundary conditions at infinity. This work presents a numerical solution that avoids the infinite boundary conditions. Constant-wall-temperature, uniform-heat-flux, and insulated constant-wall-temperature cases are all investigated; however, detailed results are given only for the case of flow from an insulated pipe into a constant-temperature pipe since these results (possibly more useful) are not as yet to be found in the literature.

[1] Assistant Professor, Department of Chemical Engineering, University of Notre Dame, Notre Dame, Ind.
[2] First Lieutenant, U. S. Air Force.
[3] Numbers in brackets designate References at end of technical brief.
Contributed by the Heat Transfer Division of THE AMERICAN SOCIETY OF MECHANICAL ENGINEERS. Manuscript received by the Heat Transfer Division March 6, 1972.

Relevant Equations

The equation for heat transfer to a laminarly flowing fluid in a tube can be written [5]

$$\frac{1}{r}\frac{\partial}{\partial r}\left(r\frac{\partial T}{\partial r}\right) + \frac{\partial^2 T}{\partial z^2} = \rho\frac{C_p}{k}u_r\frac{\partial T}{\partial z} \tag{1}$$

where u_r is the parabolic velocity profile. Various sets of boundary conditions are given below:

	Uniform heat flux	Constant wall temperature	Insulated constant temperature
$z = -\infty$	$T = T_0$	$T = T_0$	$T = T_0$
$z = +\infty$	$\frac{\partial T}{\partial z} = \frac{2q_w}{\rho C_p u R}$	$T = T_1$	$T = T_1$
$r = 0$	$\frac{\partial T}{\partial r} = 0$	$\frac{\partial T}{\partial r} = 0$	$\frac{\partial T}{\partial r} = 0$
$r = R, z < 0$	$\frac{\partial T}{\partial r} = 0$	$T = T_0$	$\frac{\partial T}{\partial r} = 0$
$r = R, z > 0$	$\frac{\partial T}{\partial r} = \frac{q_w}{k}$	$T = T_1$	$T = T_1$

(2)

The infinite boundary conditions can be eliminated by making a variable transformation of the form $\eta = \tan^{-1}z$.

Introducing the dimensionless variables

$$r = \xi R \qquad z = KR\tan\pi\eta \qquad \theta = \frac{T - T_0}{T_1 - T_0} \tag{3}$$

so that $\eta = \frac{1}{\pi}\tan^{-1}\frac{z}{KR}$ results in the following dimensionless equation:

$$\mathrm{Pe}\,(1-\xi^2)\frac{\cos^2\pi\eta}{\pi K}\frac{\partial\theta}{\partial\eta} = \frac{\partial^2\theta}{\partial\xi^2} + \frac{1}{\xi}\frac{\partial\theta}{\partial\xi} + \frac{1}{(K\pi)^2}\left[\cos^4\pi\eta\frac{\partial^2\theta}{\partial\eta^2} - 2\pi\cos^3\pi\eta\sin\pi\eta\frac{\partial\theta}{\partial\eta}\right] \tag{4}$$

Transformed boundary conditions for the constant-wall-temperature case and the insulated constant-temperature case were obtained and only contain zeros or ones.

	Constant wall temperature	Insulated constant temperature
$\eta = -0.5$	$\theta = 0$	$\theta = 0$
$\eta = +0.5$	$\theta = 1$	$\theta = 1$
$\xi = 0$	$\frac{\partial\theta}{\partial\xi} = 0$	$\frac{\partial\theta}{\partial\xi} = 0$
$\xi = 1, \eta < 0$	$\theta = 0$	$\frac{\partial\theta}{\partial\eta} = 0$
$\xi = 1, \eta > 0$	$\theta = 1$	$\theta = 1$

(5)

These results follow from the fact that $\frac{\partial\eta}{\partial z} = \frac{1}{\pi KR}\cos^2\pi\eta$, $\partial^2\eta/\partial z^2 = -2\pi\cos^3\pi\eta\sin\pi\eta/(\pi KR)^2$, and $\mathrm{Pe} = 2\rho RuC_p/k$.

Finite-Difference Technique

The finite-difference equations, which were an approximation of equation (4) with the boundary conditions, were developed

plied Mathematics, Vol. 21, 1971, pp. 245–257.
9 Kelman, R. B., "Harmonic Mixed Boundary-Value Problems in Composite Rectangular Domains," *Quarterly Journal of Mechanics and Applied Mathematics*, Vol. 23, 1970, pp. 549–566.
10 Schmitz, R. A., "Heat Flux Through a Strip-Heated Flat Plate," JOURNAL OF HEAT TRANSFER, TRANS. ASME, Series C, Vol. 92, No. 1, Feb. 1970, pp. 201–202.

A Numerical Solution of the Graetz Problem with Axial Conduction Included

F. H. VERHOFF[1] and D. P. FISHER[2]

Nomenclature

C_p = specific heat
k = thermal conductivity
K = constant of axial transformation
Nu = Nusselt number, $2Rq_w/[k(T_w - T_b)]$
Pe = Peclet number, $2\rho RuC_p/k$
q_w = heat flux at wall
r = radial dimension
R = pipe radius
T = temperature
T_b = bulk temperature
u = mean velocity
u_r = velocity
z = axial dimension
η = dimensionless axial dimension
θ = dimensionless temperature
ξ = dimensionless radial dimension
ρ = density

Introduction

THE familiar Graetz problem of laminar-flow heat transfer in a pipe has traditionally been solved by neglecting the effect of axial heat conduction because the mathematical problem is simplified from an elliptic equation with boundary conditions at infinity to a parabolic equation with this assumption. However, for low Peclet numbers the effect of conduction is significant; Hennecke [1][3] has presented numerical solutions with axial conduction included for constant-wall-temperature and uniform-heat-flux cases. By trial and error he approximated the boundary conditions at infinity. Hsu [2] has developed an exact solution to the uniform-wall-heat-flux case by a separation-of-variables technique. Petukhov and Tsvetkov [3] solved the constant-heat-flux case by using an approximate technique that Hsu found to contain considerable error. Jones [4] recently presented an analytical solution for the constant-wall-temperature case.

The solutions of these authors are complicated by the use of boundary conditions at infinity. This work presents a numerical solution that avoids the infinite boundary conditions. Constant-wall-temperature, uniform-heat-flux, and insulated constant-wall-temperature cases are all investigated; however, detailed results are given only for the case of flow from an insulated pipe into a constant-temperature pipe since these results (possibly more useful) are not as yet to be found in the literature.

[1] Assistant Professor, Department of Chemical Engineering, University of Notre Dame, Notre Dame, Ind.
[2] First Lieutenant, U. S. Air Force.
[3] Numbers in brackets designate References at end of technical brief.

Contributed by the Heat Transfer Division of THE AMERICAN SOCIETY OF MECHANICAL ENGINEERS. Manuscript received by the Heat Transfer Division March 6, 1972.

Relevant Equations

The equation for heat transfer to a laminarly flowing fluid in a tube can be written [5]

$$\frac{1}{r}\frac{\partial}{\partial r}\left(r\frac{\partial T}{\partial r}\right) + \frac{\partial^2 T}{\partial z^2} = \rho\frac{C_p}{k}u_r\frac{\partial T}{\partial z} \tag{1}$$

where u_r is the parabolic velocity profile. Various sets of boundary conditions are given below:

	Uniform heat flux	Constant wall temperature	Insulated constant temperature
$z = -\infty$	$T = T_0$	$T = T_0$	$T = T_0$
$z = +\infty$	$\frac{\partial T}{\partial z} = \frac{2q_w}{\rho C_p u R}$	$T = T_1$	$T = T_1$
$r = 0$	$\frac{\partial T}{\partial r} = 0$	$\frac{\partial T}{\partial r} = 0$	$\frac{\partial T}{\partial r} = 0$
$r = R, z < 0$	$\frac{\partial T}{\partial r} = 0$	$T = T_0$	$\frac{\partial T}{\partial r} = 0$
$r = R, z > 0$	$\frac{\partial T}{\partial r} = \frac{q_w}{k}$	$T = T_1$	$T = T_1$

(2)

The infinite boundary conditions can be eliminated by making a variable transformation of the form $\eta = \tan^{-1}z$.

Introducing the dimensionless variables

$$r = \xi R \qquad z = KR\tan\pi\eta \qquad \theta = \frac{T - T_0}{T_1 - T_0} \tag{3}$$

so that $\eta = \frac{1}{\pi}\tan^{-1}\frac{z}{KR}$ results in the following dimensionless equation:

$$\mathrm{Pe}\,(1-\xi^2)\frac{\cos^2\pi\eta}{\pi K}\frac{\partial\theta}{\partial\eta} = \frac{\partial^2\theta}{\partial\xi^2} + \frac{1}{\xi}\frac{\partial\theta}{\partial\xi} + \frac{1}{(K\pi)^2}\left[\cos^4\pi\eta\frac{\partial^2\theta}{\partial\eta^2} - 2\pi\cos^3\pi\eta\sin\pi\eta\frac{\partial\theta}{\partial\eta}\right] \tag{4}$$

Transformed boundary conditions for the constant-wall-temperature case and the insulated constant-temperature case were obtained and only contain zeros or ones.

	Constant wall temperature	Insulated constant temperature
$\eta = -0.5$	$\theta = 0$	$\theta = 0$
$\eta = +0.5$	$\theta = 1$	$\theta = 1$
$\xi = 0$	$\frac{\partial\theta}{\partial\xi} = 0$	$\frac{\partial\theta}{\partial\xi} = 0$
$\xi = 1, \eta < 0$	$\theta = 0$	$\frac{\partial\theta}{\partial\eta} = 0$
$\xi = 1, \eta > 0$	$\theta = 1$	$\theta = 1$

(5)

These results follow from the fact that $\frac{\partial\eta}{\partial z} = \frac{1}{\pi KR}\cos^2\pi\eta$, $\partial^2\eta/\partial z^2 = -2\pi\cos^3\pi\eta\sin\pi\eta/(\pi KR)^2$, and $\mathrm{Pe} = 2\rho RuC_p/k$.

Finite-Difference Technique

The finite-difference equations, which were an approximation of equation (4) with the boundary conditions, were developed

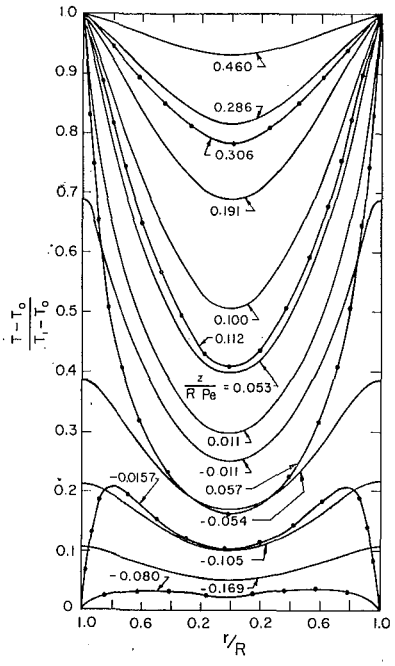

Fig. 1 Radial temperature profiles for various axial distances; insulated constant-temperature case (——) and constant-temperature case (—•—•—) both with Peclet number equal to 5

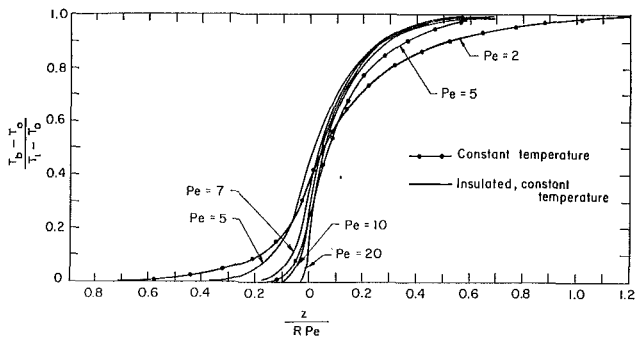

Fig. 2 Bulk temperature as a function of axial distance for constant-temperature and insulated constant-temperature cases

using the techniques given by Carnahan et al. [6]. The first derivatives were approximated with the central difference operator, and the second derivative also was approximated with an accuracy to the second order. The boundary condition at the center of the tube was handled in the usual way (see [6]). Other boundary conditions are straightforward.

The computer was programmed to solve this set of equations by the Gauss–Seidel iteration technique. The radial and axial directions were divided into grids with from 10 to 40 divisions. A good approximation to the equations was achieved for 10 radial divisions and 30 axial divisions. The transformation constant K was varied between 0.5 to 2.0; a satisfactory value was 1.0. Convergence was quite rapid and was terminated when the dimensionless temperature values changed less than 0.01 percent in an iteration.

Results

The constant-wall-temperature case was run for various values of the Peclet number; the radial temperature profiles with axial distance as a parameter were compared with those of Hennecke [1] and rather close agreement was observed. The Nusselt numbers obtained were also compared with those of Hennecke; good comparison was obtained for the downstream section but the results for the upstream numbers were slightly higher than those of Hennecke. The uniform-heat-flux case was also solved, and the results compared very well with those of Hennecke [1] and Hsu [2].

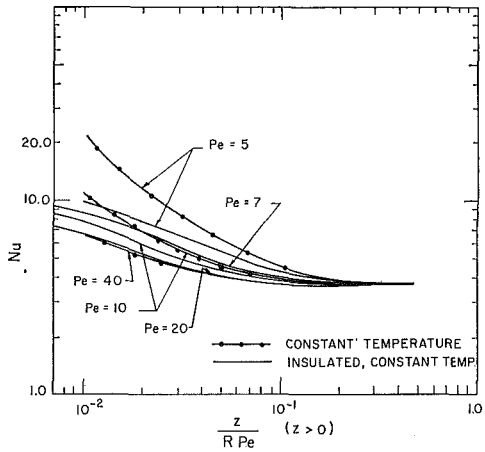

Fig. 3 Nusselt number as a function of downstream axial distance for insulated constant-temperature case

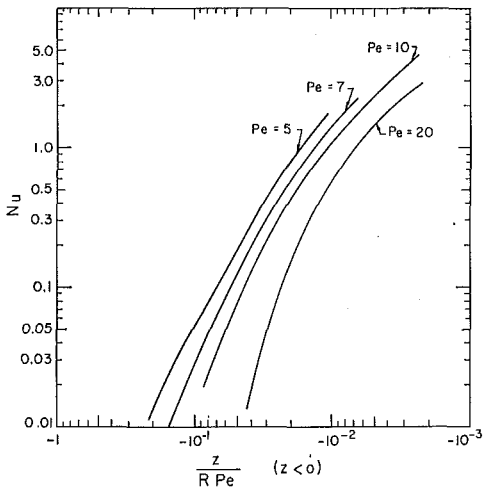

Fig. 4 Nusselt number as a function of upstream axial distance for insulated constant-temperature case

Figure 1 is a plot of radial temperature profile with axial distance as a parameter for the case of insulated upstream section and constant downstream temperature with the Peclet number equal to 5. The temperature profiles in the upstream section differ markedly from the constant-temperature case and this difference extends into the downstream section of the tube. The bulk temperatures as a function of downstream distance for the two cases and for different Peclet numbers are plotted in Fig. 2. The results of this study and those of Hennecke are essentially identical for the constant-temperature case, but these results differ significantly from those of the insulated case as can be seen from the graph.

Local Nusselt numbers for the insulated constant-temperature case were calculated from the defining equation. The Nusselt-number results as a function of axial distance for the insulated constant-temperature case are shown in Figs. 3 and 4 for various Peclet numbers. The entrance-region Nusselt numbers for this case are much lower than for the constant-temperature case. Thus the extra heat transfer expected in the entrance region would be much less for the insulated upstream case in comparison with the constant-temperature case.

Conclusions

The inverse-tangent transformation permits the conversion of the infinite boundaries for the Graetz problem into finite boundaries. The resulting equations are easily solved by finite-difference techniques. Results for the constant-temperature and uniform-heat-flux boundary conditions compared well with the results of Hennecke [1] and Hsu [2]. The insulated upstream and

constant-temperature downstream results are presented and indicate the bulk temperature and Nusselt numbers differ significantly from those of the constant-temperature case.

References

1 Hennecke, D. K., "Heat Transfer by Hagen-Poiseuille Flow in the Thermal Development Region with Axial Conduction," Wärme- und Stoffübertragung, Vol. 1, 1968, p. 177.

2 Hsu, C. J., "An Exact Analysis of Low Peclet Number Thermal *Entry Region Heat Transfer in Transversely Nonuniform Velocity* Fields," *AIChE Journal*, Vol. 17, 1971, p. 732.

3 Petukhov, B. S., and Tsvetkov, F. F., "Raschet Temperature pri Lammarnom Techcci Zhidkosti v. Turbakly v. Oblasti Malykh Chisel Pekle," *Inzhenerno-Fizechoskii Zhurnal*, Vol. 4, No. 3, 1961, p. 10.

4 Jones, A. S., "Extensions to the Solution of the Graetz Problem," *International Journal of Heat and Mass Transfer*, Vol. 14, 1971, p. 619.

5 Bird, R. B., Stewart, W. E., and Lightfoot, E. H., *Transport Phenomena*, John Wiley & Sons, New York, N. Y., 1960, p. 295.

6 Carnahan, B., Luther, H. A., and Wilkes, J. O., *Applied Numerical Methods*, John Wiley & Sons, New York, N. Y., 1969, chapter 7.

Variable-Property Turbulent Flow in a Horizontal Smooth Tube during Uniform Heating and Constant Surface-Temperature Cooling

J. ZUCCHETTO[1] and R. S. THORSEN[2]

DURING the investigation of friction and heat-transfer behavior in turbulent swirl flow of air with both heating and cooling [1],[3] it was evident that existing correlations for turbulent convection in circular tubes which adequately accounted for temperature-dependent properties were not available over the entire range of temperatures investigated. This was particularly true for the case of cooling, i.e., the case of a hot gas and a cold surface. It therefore became necessary to independently establish Nusselt-number correlations for both heating and cooling to serve as a base line for comparison with the twisted-strip-induced swirl-flow results.

The results for uniform heating are briefly repeated here since they are somewhat obscured by the emphasis on swirl flow in [1] and because some of the equipment used in the present cooling study, e.g., orifice flowmeter and reverse-flow adiabatic mixing chambers, were calibrated and used in the heating experiments. The constant-property Nusselt-number correlation, denoted by subscript 0 and obtained from low-heat-flux data, was

$$Nu_0 = 0.021\ Re^{0.8}Pr^{0.4} \quad \text{(heating, uniform heat flux)} \quad (1)$$

Equation (1) is in agreement with results reported by McEligot et al. [2] and Kays [3].

At large heat fluxes, and therefore large differences between the local surface temperature T_s and bulk temperature T_B, the effect of temperature-dependent properties is important and the Nusselt number can be correlated according to

$$Nu = Nu_0(T_s/T_B)^{-a} \quad (2)$$

In equation (2) the temperatures are measured on an absolute scale. In [1] values of T_s/T_B ranging from 1 to 1.9 were considered and a least-squares error fit of the data indicated a value of $a = 0.32$. As reported by both Kays and Jackson [4], the analytic results of Deissler and Eian [5] correspond to $a = 0.34$. For the experimental Reynolds-number range of 18,000 to 215,000 the results reported in [1] are therefore seen to be in agreement with [5].

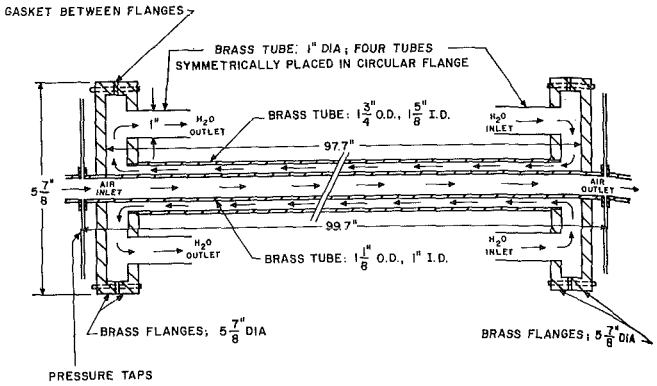

Fig. 1 Schematic of test section

For the cooling experiments reported in [1], two factors contribute to the uncertainty of the no-swirl Nusselt-number correlation reported. First the range of T_s/T_B was not very great and second the test section L/D ratio was only 36. This was adequate for the swirl-flow experiments but the question of thermal-entrance-length effects was left unresolved for the case of no-swirl cooling. These two uncertainties motivated the study reported herein. The horizontal brass test section used is shown schematically in Fig. 1. Copper-constantan thermocouples (30-gage) were used to measure the water temperature and surface temperature of the test section. The air inlet and exit bulk temperatures were measured in reverse-flow adiabatic mixing chambers. The air flow rate was measured using an orifice flowmeter and was heated to temperatures up to 700 deg F prior to entering the test section. The maximum Mach number encountered was 0.34 but was generally much less. Further details of the experimental facility are reported in [6].

Results

The test-section surface temperature was measured with nine copper–constantan thermocouples attached at various axial and circumferential positions on the tube. For the entire range of experiments the surface temperature T_s varied from 39 to 62 deg F depending on water-supply conditions. However, in no case was there a temperature variation of more than 4 deg F between thermocouples, confirming that a uniform-temperature boundary condition was achieved. The total heat-transfer rate from the flowing air, $\dot{Q}$, was calculated from the measured mass flow rate and bulk temperature change from inlet to exit with the constant-pressure specific heat evaluated at the arithmetic-mean bulk temperature. In order to maintain isothermal wall conditions the water flow rate was maximized. This resulted in very small changes in the bulk temperature of the water and precluded an accurate energy balance. However, the flowmeter had been separately calibrated as had been the mixing chambers during the heating runs reported in [1]. There a heat balance was possible, and $\dot{Q}$ calculated as described above was generally found to be well within 4 percent of the value predicted from the heat balance.

By removing the exit mixing chamber a traversing thermocouple could be attached to the end of the test sections. Vertical and horizontal traverses were made and they revealed complete symmetry with respect to the tube axis. No circumferential asymmetry due to superimposed free convection was detectable [6]. The heat-transfer coefficient was therefore calculated according to

[1] Graduate Student, University of Florida, Gainesville, Fla.

[2] Associate Professor, Mechanical Engineering Department, New York University, New York, N. Y. Mem. ASME.

[3] Numbers in brackets designate References at end of technical brief.

Contributed by the Heat Transfer Division of THE AMERICAN SOCIETY OF MECHANICAL ENGINEERS. Manuscript received by the Heat Transfer Division April 4, 1972.

constant-temperature downstream results are presented and indicate the bulk temperature and Nusselt numbers differ significantly from those of the constant-temperature case.

References

1 Hennecke, D. K., "Heat Transfer by Hagen-Poiseuille Flow in the Thermal Development Region with Axial Conduction," Wärme- und Stoffübertragung, Vol. 1, 1968, p. 177.

2 Hsu, C. J., "An Exact Analysis of Low Peclet Number Thermal *Entry Region Heat Transfer in Transversely Nonuniform Velocity* Fields," *AIChE Journal*, Vol. 17, 1971, p. 732.

3 Petukhov, B. S., and Tsvetkov, F. F., "Raschet Temperature pri Lammarnom Techcci Zhidkosti v. Turbakly v. Oblasti Malykh Chisel Pekle," *Inzhenerno-Fizechoskii Zhurnal*, Vol. 4, No. 3, 1961, p. 10.

4 Jones, A. S., "Extensions to the Solution of the Graetz Problem," *International Journal of Heat and Mass Transfer*, Vol. 14, 1971, p. 619.

5 Bird, R. B., Stewart, W. E., and Lightfoot, E. H., *Transport Phenomena*, John Wiley & Sons, New York, N. Y., 1960, p. 295.

6 Carnahan, B., Luther, H. A., and Wilkes, J. O., *Applied Numerical Methods*, John Wiley & Sons, New York, N. Y., 1969, chapter 7.

Variable-Property Turbulent Flow in a Horizontal Smooth Tube during Uniform Heating and Constant Surface-Temperature Cooling

J. ZUCCHETTO[1] and R. S. THORSEN[2]

DURING the investigation of friction and heat-transfer behavior in turbulent swirl flow of air with both heating and cooling [1],[3] it was evident that existing correlations for turbulent convection in circular tubes which adequately accounted for temperature-dependent properties were not available over the entire range of temperatures investigated. This was particularly true for the case of cooling, i.e., the case of a hot gas and a cold surface. It therefore became necessary to independently establish Nusselt-number correlations for both heating and cooling to serve as a base line for comparison with the twisted-strip-induced swirl-flow results.

The results for uniform heating are briefly repeated here since they are somewhat obscured by the emphasis on swirl flow in [1] and because some of the equipment used in the present cooling study, e.g., orifice flowmeter and reverse-flow adiabatic mixing chambers, were calibrated and used in the heating experiments. The constant-property Nusselt-number correlation, denoted by subscript 0 and obtained from low-heat-flux data, was

$$Nu_0 = 0.021\ Re^{0.8}Pr^{0.4} \quad \text{(heating, uniform heat flux)} \quad (1)$$

Equation (1) is in agreement with results reported by McEligot et al. [2] and Kays [3].

At large heat fluxes, and therefore large differences between the local surface temperature T_s and bulk temperature T_B, the effect of temperature-dependent properties is important and the Nusselt number can be correlated according to

$$Nu = Nu_0(T_s/T_B)^{-a} \quad (2)$$

In equation (2) the temperatures are measured on an absolute scale. In [1] values of T_s/T_B ranging from 1 to 1.9 were considered and a least-squares error fit of the data indicated a value of $a = 0.32$. As reported by both Kays and Jackson [4], the analytic results of Deissler and Eian [5] correspond to $a = 0.34$. For the experimental Reynolds-number range of 18,000 to 215,000 the results reported in [1] are therefore seen to be in agreement with [5].

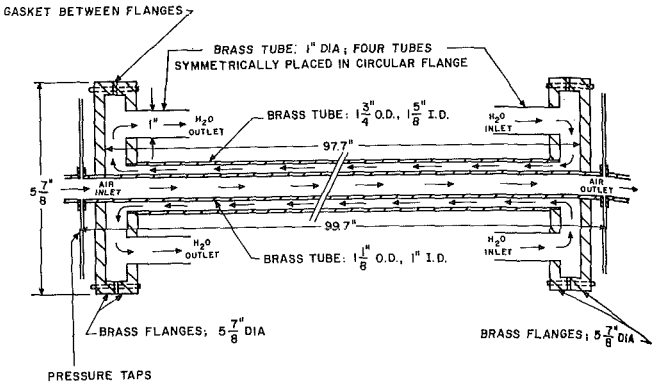

Fig. 1 Schematic of test section

For the cooling experiments reported in [1], two factors contribute to the uncertainty of the no-swirl Nusselt-number correlation reported. First the range of T_s/T_B was not very great and second the test section L/D ratio was only 36. This was adequate for the swirl-flow experiments but the question of thermal-entrance-length effects was left unresolved for the case of no-swirl cooling. These two uncertainties motivated the study reported herein. The horizontal brass test section used is shown schematically in Fig. 1. Copper-constantan thermocouples (30-gage) were used to measure the water temperature and surface temperature of the test section. The air inlet and exit bulk temperatures were measured in reverse-flow adiabatic mixing chambers. The air flow rate was measured using an orifice flowmeter and was heated to temperatures up to 700 deg F prior to entering the test section. The maximum Mach number encountered was 0.34 but was generally much less. Further details of the experimental facility are reported in [6].

Results

The test-section surface temperature was measured with nine copper–constantan thermocouples attached at various axial and circumferential positions on the tube. For the entire range of experiments the surface temperature T_s varied from 39 to 62 deg F depending on water-supply conditions. However, in no case was there a temperature variation of more than 4 deg F between thermocouples, confirming that a uniform-temperature boundary condition was achieved. The total heat-transfer rate from the flowing air, $\dot{Q}$, was calculated from the measured mass flow rate and bulk temperature change from inlet to exit with the constant-pressure specific heat evaluated at the arithmetic-mean bulk temperature. In order to maintain isothermal wall conditions the water flow rate was maximized. This resulted in very small changes in the bulk temperature of the water and precluded an accurate energy balance. However, the flowmeter had been separately calibrated as had been the mixing chambers during the heating runs reported in [1]. There a heat balance was possible, and $\dot{Q}$ calculated as described above was generally found to be well within 4 percent of the value predicted from the heat balance.

By removing the exit mixing chamber a traversing thermocouple could be attached to the end of the test sections. Vertical and horizontal traverses were made and they revealed complete symmetry with respect to the tube axis. No circumferential asymmetry due to superimposed free convection was detectable [6]. The heat-transfer coefficient was therefore calculated according to

[1] Graduate Student, University of Florida, Gainesville, Fla.

[2] Associate Professor, Mechanical Engineering Department, New York University, New York, N. Y. Mem. ASME.

[3] Numbers in brackets designate References at end of technical brief.

Contributed by the Heat Transfer Division of THE AMERICAN SOCIETY OF MECHANICAL ENGINEERS. Manuscript received by the Heat Transfer Division April 4, 1972.

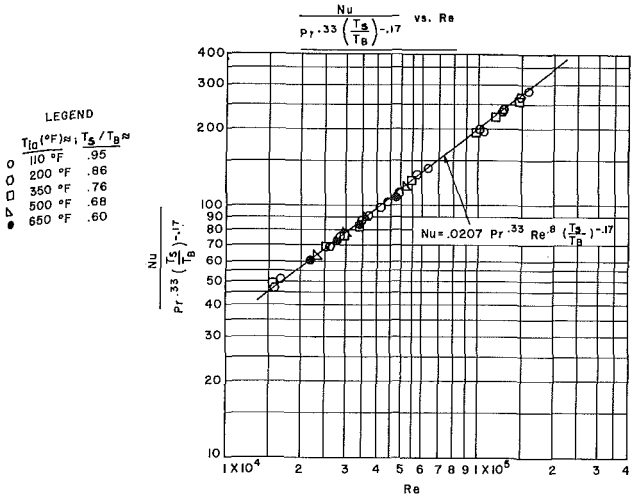

Fig. 2 Heat-transfer results for uniform surface-temperature cooling—correction for property variations

$$h = \frac{\dot{Q}}{A(\Delta T)_{LM}} \tag{3}$$

where $(\Delta T)_{LM}$ is the logarithmic-mean temperature difference between the air and the tube surface. The area A in equation (3) was computed on the basis of the inside diameter of the test section and an adjusted length. The adjusted length consists of the test-section length exposed to the cooling water, i.e., 97.7 in. as shown in Fig. 1, plus a correction to account for cooling that takes place between the upstream and downstream mixing chambers and the end of the test-section flanges. The physical length involved was 4 in. at each end. Since these 4-in. end "fins" were not isothermal, an effectiveness had to be determined to compute the equivalent isothermal lengths to be added to the 97.7-in. water-cooled length. Thus

$$A = \pi D(L + \eta_i L_i + \eta_e L_e) \tag{4}$$

In equation (4), D is the test-section inside diameter, L is the water-cooled length (97.7 in.), L_i and L_e are the lengths of the tubing joining the water-cooled section to the inlet and exit mixing chambers respectively, and η_i and η_e are the effectivenesses of these lengths evaluated using the insulated end condition. (This was consistent with the nature of the connection between the brass tube and mixing chambers and with measured temperatures along these "fins.") Since the effectivenesses in equation (4) depend on h, an iterative scheme was required to compute h from equations (3) and (4). Details of the data reduction are described in [6].

The constant-property diametral Nusselt-number correlation was obtained using the experimental data for $T_s/T_B \approx 0.95$. These results are shown as circles in Fig. 2 and showed good agreement with the relation

$$\mathrm{Nu}_0 = 0.0207\ \mathrm{Pr}^{0.33}\mathrm{Re}^{0.8} \quad \text{(cooling, } T_s = \text{constant)} \tag{5}$$

In the presence of large fluid-to-surface temperature differences, account must be taken of property variations by the relation

$$\mathrm{Nu} = \mathrm{Nu}_0 \left(\frac{T_s}{T_B}\right)^{-b} \tag{6}$$

In equation (6) the properties were evaluated at the average bulk temperature, i.e.,

$$T_B = T_s + (\Delta T)_{LM} \tag{7}$$

With decreasing values of T_s/T_B the experimental points were displaced farther above the curve corresponding to equation (5). A multiple regression analysis was therefore performed to determine the coefficient in equation (7), the Reynolds-number exponent, and b. Using all of the data in Fig. 2 resulted in

$$\mathrm{Nu} = 0.0207\ \mathrm{Pr}^{0.33}\ \mathrm{Re}^{0.8}\left(\frac{T_s}{T_B}\right)^{-0.17} \tag{8}$$

It is noted that the value $b = 0.17$ is somewhat larger than the value of 0.1 recommended by Kays [3] but agrees with the analytic results of Deissler and Eian [5] which correspond to a value of $b = 0.19$ for cooling [3].

Isothermal and diabatic friction factors were obtained and they compared well with the Karman–Nikuradse data for smooth tubes. No significant temperature-ratio effect could be found during cooling. This is in agreement with the recommendation of Kays [3].

References

1 Thorsen, R., and Landis, F., "Friction and Heat Transfer Characteristics in Turbulent Swirl Flow Subjected to Large Transverse Temperature Gradients," JOURNAL OF HEAT TRANSFER, TRANS. ASME, Series C, Vol. 90, No. 1, Feb. 1968, pp. 87–97.

2 McEligot, D. M., Magee, P. M., and Leppert, G., "Effect of Large Temperature Gradients on Convective Heat Transfer: The Downstream Region," JOURNAL OF HEAT TRANSFER, TRANS. ASME, Series C, Vol. 87, No. 1, Feb. 1965, pp. 67–76.

3 Kays, W. M., *Convective Heat and Mass Transfer*, McGraw-Hill, New York, N. Y., 1966, pp. 173, 263, 264.

4 Jackson, J. D., "A Theoretical Investigation into the Effects of Surface/Gas Temperature Ratio for Fully Developed Turbulent Flow of Air, Helium and Carbon Dioxide in Smooth Circular Tubes," A.R.C. 22, 784, F.M. 3084 (Great Britain), Apr. 1961, ASTIA AD-269066.

5 Deissler, R. G., and Eian, C. S., "Analytical and Experimental Investigation of Fully Developed Turbulent Flow of Air in a Smooth Tube with Heat Transfer with Variable Fluid Properties," NACA TN 2629, Feb. 1952.

6 Zucchetto, J., "Variable Property Turbulent Flow in a Horizontal Smooth Tube with a Constant Wall Temperature Boundary Condition," MS thesis, Department of Mechanical Engineering, New York University, New York, N. Y., 1969.

Film-Cooling Effectiveness in the Presence of a Backward-facing Step

L. MATTHEWS and J. H. WHITELAW[1]

Introduction

THE influence of slot geometry on the effectiveness of film cooling has been shown to be of considerable importance both for two- and three-dimensional slot configurations and stems from the different flow conditions which a particular slot creates in the plane of its exit. The present paper is concerned with two-dimensional slots and extends the work of [1–3][2] to include measurements of the influence of a backward-facing step, located as shown in Fig. 1, on the downstream impervious-wall effectiveness.[3] Since the velocity ratio, density ratio, and lip-thickness-to-slot-height ratio are known to have significant influence, and also to be of practical importance, they are regarded as parameters.

The range of parameters investigated is particularly relevant

[1] Department of Mechanical Engineering, Imperial College of Science and Technology, London, England.

[2] Numbers in brackets designate References at end of technical brief.

[3] Defined as $\eta \equiv (m_W - m_G)/(m_C - m_G)$ where m is mass concentration of the injected gas and W, C, and G refer respectively to the impervious wall, the slot, and the free stream.

Contributed by the Heat Transfer Division of THE AMERICAN SOCIETY OF MECHANICAL ENGINEERS. Manuscript received by the Heat Transfer Division April 26, 1972.

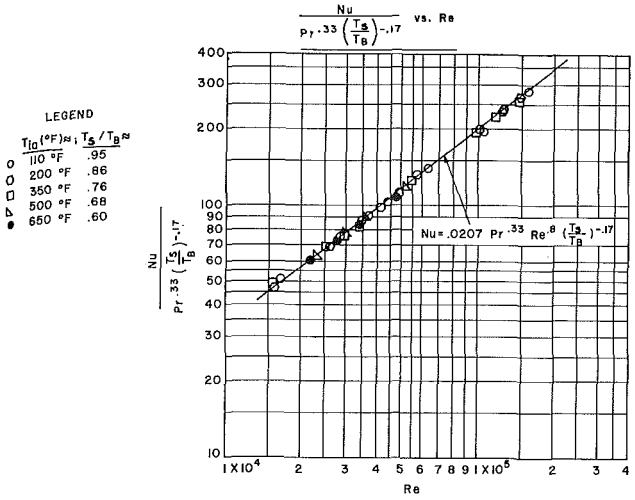

Fig. 2 Heat-transfer results for uniform surface-temperature cooling—correction for property variations

$$h = \frac{\dot{Q}}{A(\Delta T)_{LM}} \tag{3}$$

where $(\Delta T)_{LM}$ is the logarithmic-mean temperature difference between the air and the tube surface. The area A in equation (3) was computed on the basis of the inside diameter of the test section and an adjusted length. The adjusted length consists of the test-section length exposed to the cooling water, i.e., 97.7 in. as shown in Fig. 1, plus a correction to account for cooling that takes place between the upstream and downstream mixing chambers and the end of the test-section flanges. The physical length involved was 4 in. at each end. Since these 4-in. end "fins" were not isothermal, an effectiveness had to be determined to compute the equivalent isothermal lengths to be added to the 97.7-in. water-cooled length. Thus

$$A = \pi D(L + \eta_i L_i + \eta_e L_e) \tag{4}$$

In equation (4), D is the test-section inside diameter, L is the water-cooled length (97.7 in.), L_i and L_e are the lengths of the tubing joining the water-cooled section to the inlet and exit mixing chambers respectively, and η_i and η_e are the effectivenesses of these lengths evaluated using the insulated end condition. (This was consistent with the nature of the connection between the brass tube and mixing chambers and with measured temperatures along these "fins.") Since the effectivenesses in equation (4) depend on h, an iterative scheme was required to compute h from equations (3) and (4). Details of the data reduction are described in [6].

The constant-property diametral Nusselt-number correlation was obtained using the experimental data for $T_s/T_B \approx 0.95$. These results are shown as circles in Fig. 2 and showed good agreement with the relation

$$\mathrm{Nu}_0 = 0.0207\ \mathrm{Pr}^{0.33}\mathrm{Re}^{0.8} \quad \text{(cooling, } T_s = \text{constant)} \tag{5}$$

In the presence of large fluid-to-surface temperature differences, account must be taken of property variations by the relation

$$\mathrm{Nu} = \mathrm{Nu}_0 \left(\frac{T_s}{T_B}\right)^{-b} \tag{6}$$

In equation (6) the properties were evaluated at the average bulk temperature, i.e.,

$$T_B = T_s + (\Delta T)_{LM} \tag{7}$$

With decreasing values of T_s/T_B the experimental points were displaced farther above the curve corresponding to equation (5). A multiple regression analysis was therefore performed to determine the coefficient in equation (7), the Reynolds-number exponent, and b. Using all of the data in Fig. 2 resulted in

$$\mathrm{Nu} = 0.0207\ \mathrm{Pr}^{0.33}\ \mathrm{Re}^{0.8}\left(\frac{T_s}{T_B}\right)^{-0.17} \tag{8}$$

It is noted that the value $b = 0.17$ is somewhat larger than the value of 0.1 recommended by Kays [3] but agrees with the analytic results of Deissler and Eian [5] which correspond to a value of $b = 0.19$ for cooling [3].

Isothermal and diabatic friction factors were obtained and they compared well with the Karman–Nikuradse data for smooth tubes. No significant temperature-ratio effect could be found during cooling. This is in agreement with the recommendation of Kays [3].

References

1 Thorsen, R., and Landis, F., "Friction and Heat Transfer Characteristics in Turbulent Swirl Flow Subjected to Large Transverse Temperature Gradients," JOURNAL OF HEAT TRANSFER, TRANS. ASME, Series C, Vol. 90, No. 1, Feb. 1968, pp. 87–97.

2 McEligot, D. M., Magee, P. M., and Leppert, G., "Effect of Large Temperature Gradients on Convective Heat Transfer: The Downstream Region," JOURNAL OF HEAT TRANSFER, TRANS. ASME, Series C, Vol. 87, No. 1, Feb. 1965, pp. 67–76.

3 Kays, W. M., *Convective Heat and Mass Transfer*, McGraw-Hill, New York, N. Y., 1966, pp. 173, 263, 264.

4 Jackson, J. D., "A Theoretical Investigation into the Effects of Surface/Gas Temperature Ratio for Fully Developed Turbulent Flow of Air, Helium and Carbon Dioxide in Smooth Circular Tubes," A.R.C. 22, 784, F.M. 3084 (Great Britain), Apr. 1961, ASTIA AD-269066.

5 Deissler, R. G., and Eian, C. S., "Analytical and Experimental Investigation of Fully Developed Turbulent Flow of Air in a Smooth Tube with Heat Transfer with Variable Fluid Properties," NACA TN 2629, Feb. 1952.

6 Zucchetto, J., "Variable Property Turbulent Flow in a Horizontal Smooth Tube with a Constant Wall Temperature Boundary Condition," MS thesis, Department of Mechanical Engineering, New York University, New York, N. Y., 1969.

Film-Cooling Effectiveness in the Presence of a Backward-facing Step

L. MATTHEWS and J. H. WHITELAW[1]

Introduction

THE influence of slot geometry on the effectiveness of film cooling has been shown to be of considerable importance both for two- and three-dimensional slot configurations and stems from the different flow conditions which a particular slot creates in the plane of its exit. The present paper is concerned with two-dimensional slots and extends the work of [1–3][2] to include measurements of the influence of a backward-facing step, located as shown in Fig. 1, on the downstream impervious-wall effectiveness.[3] Since the velocity ratio, density ratio, and lip-thickness-to-slot-height ratio are known to have significant influence, and also to be of practical importance, they are regarded as parameters.

The range of parameters investigated is particularly relevant

[1] Department of Mechanical Engineering, Imperial College of Science and Technology, London, England.

[2] Numbers in brackets designate References at end of technical brief.

[3] Defined as $\eta \equiv (m_W - m_G)/(m_C - m_G)$ where m is mass concentration of the injected gas and W, C, and G refer respectively to the impervious wall, the slot, and the free stream.

Contributed by the Heat Transfer Division of THE AMERICAN SOCIETY OF MECHANICAL ENGINEERS. Manuscript received by the Heat Transfer Division April 26, 1972.

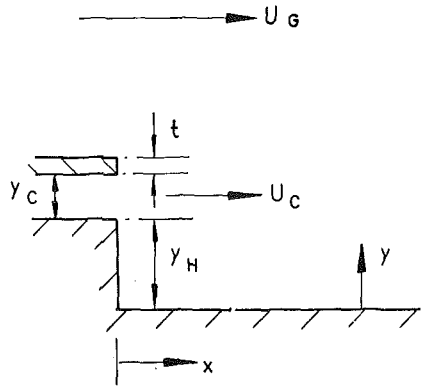

Fig. 1 Flow configuration

to the cooling of gas-turbine combustion-chamber walls. In practice, cooling rings result in three-dimensional flows, but, with improving design, tend toward configurations which result, at very short distances from the slot exit, in two-dimensional flows. Thus, the two-dimensional limitation of the present work implies that the results conform to the optimum effectiveness for prescribed values of the parameters specified above.

Equipment

The experiments were carried out in the wind tunnel previously described in [4] with a free-stream velocity of 60 fps and a slot height of $^1/_4$ in. The two-dimensionality of the flow had previously been checked, but, because separation regions are particularly sensitive to three-dimensional effects, the two-dimensionality of the reattachment line was confirmed visually for the largest step height of $^1/_2$ in. A mixture of mineral oil and titanium dioxide was used for the surface-flow visualization and resulted in reattachment lines which were parallel to the slot exit to within 5 percent of the distance from the slot exit over the central 15-in. section of the tunnel.

The experimental techniques were modified from those described in [1–4]. The mass concentration of either a tracer gas (helium) in air or Arcton 12 in air was measured after drawing samples through static-pressure holes in the base plate of the wind tunnel. The need for rapid, on-line concentration measurements precluded the use of the chromatographic technique used earlier.

Since only two-component mixtures were employed, the chromatograph was replaced by a sensitive katharometer (Servomex MK 158) which combined sensitivity with stability, low internal volume, and the ability to sustain high flow rates. The katharometer consisted of two chambers, each of 1.6×10^{-4} in.^{3} internal volume and containing a matched pair of platinum filaments. The two sets of filaments formed a Wheatstone bridge and were supplied with constant voltage by an external unit with zeroing and signal-attenuation controls. The balance voltage, which resulted from one set of filaments being exposed to a gas of composition different from the reference gas, was scanned continuously by a data logger and recorded on punched tape. The flow rate of both streams was regulated by matched needle valves and measured on matched rotameters and the katharometer and preheating coils were located in a thermostatically controlled oven; these precautions insured that the balance voltage was a function of concentration alone.

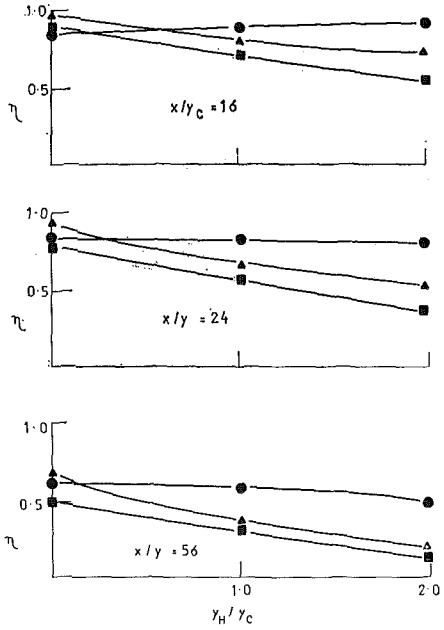

Fig. 3 Effect of step height on film-cooling effectiveness: ρ_C/ρ_G = 2, t/y_C = 1/8; $\rho_C U_C/\rho_G U_G$ = for ●, 2.0; for ▲, 1.0; for ■ 0.7

The katharometer was calibrated for mixtures of Arcton 12 in air and for helium in air by injecting samples of known concentration. The Arcton-12 calibration was nonlinear and that for helium was linear for volume concentrations of less than 1 percent. Air was used as the reference gas in these calibrations.

To measure values of wall concentration, samples were induced from the static-pressure holes through equal lengths of hypodermic tubing to a fluidics-type selector valve which permitted any one of 10 sample lines to be switched to the katharometer. The flow was induced by a vacuum pump, and a choked orifice

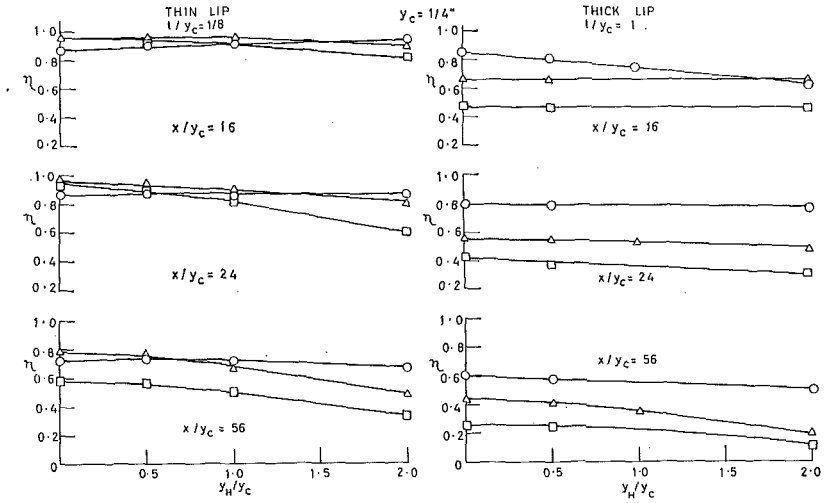

Fig. 2 Effect of step height on film-cooling effectiveness: ρ_C/ρ_G = 1; $\rho_C U_C/\rho_G U_G$ = for ○, 2.0; for △, 1.0; for □, 0.7

between the pump and the katharometer insured that the flow was steady. This arrangement permitted measurements of mass concentration to a precision of ±1 percent and with a response time of less than 2 sec.

Results and Discussion

The measured values of impervious-wall effectiveness are shown in Figs. 2 and 3. Figure 2 indicates the influence of the backward-facing step for three velocity ratios, for three downstream distances, and for two values of the lip-thickness-to-slot-height ratio. The measurements shown in Fig. 2 were obtained using a tracer of helium gas in the slot flow, and they conform, therefore, to uniform density. It is clear that in the case of the thin lip the decrease in effectiveness with step height is greatest for the lower velocity ratios; the maximum decrease in effectiveness corresponds to approximately 15 percent of unity for a step-height-to-slot-height ratio of 2. For the case of the thick lip, the highest velocity ratio resulted in the greatest decrease in effectiveness close to the slot exit; this trend is reversed with downstream distance and at x/y_C of 56; the largest decrease in effectiveness was recorded with the lower velocity ratios.

Figure 3 presents measurements corresponding to the thin lip and for a density ratio of 2. These results were obtained by injecting a mixture of Arcton 12 and air through the slot exit and they relate particularly to gas-turbine combustor practice where similar density ratios are encountered. It is clear that the influence of the step height is considerable; for example, a decrease in effectiveness of 50 percent was recorded at x/y_C of 16 for the lowest blowing rate and for a step-height-to-slot-height ratio of 2. The measurements with a density ratio of 2 were not reported with the thick-lip geometry because it was anticipated that the influence of the step height would be less in this case.

The measurements of Figs. 2 and 3 may be replotted against downstream distance, and for the case of the thin lip and uniform density they indicate that the separation region immediately downstream of the step causes a maximum in the effectiveness curve at the reattachment line. Upstream of the reattachment line the effectiveness drops to a minimum. In contrast, the measurements obtained at a density ratio of 2 decrease monotonically.

References

1 Kacker, S. C., and Whitelaw, J. H., "The Effect of Slot Height and Slot-Turbulence Intensity on the Effectiveness of the Uniform Density, Two-Dimensional Wall Jet," JOURNAL OF HEAT TRANSFER, TRANS. ASME, Series C, Vol. 90, No. 4, Nov. 1968, pp. 469–475.

2 Pai, B. R., and Whitelaw, J. H., "The Influence of Density Gradients on the Effectiveness of Film Cooling," A.R.C., C.P. 1013, 1968.

3 Kacker, S. C., and Whitelaw, J. H., "An Experimental Investigation of the Influence of Slot-Lip Thickness on the Impervious-Wall Effectiveness of the Uniform-Density Two-Dimensional Wall Jet," *International Journal of Heat and Mass Transfer*, Vol. 12, 1969, pp. 1196.

4 Whitelaw, J. H., "An Experimental Investigation of the Two-dimensional Wall Jet," A.R.C., C.P. 942, 1967.

Heat Transfer through a Rankine Vortex

M. GHIL[1] **and A. SOLAN**[2]

THE object of this note is to present a closed-form solution for the heat transfer through a Rankine vortex. It turns out that for certain conditions, satisfied in many actual flow situations, this solution gives a square-root dependence of the Nusselt number on the Peclet number, irrespective of the details of the temperature boundary conditions. This result plays a role in the heat transfer from the rear of bluff bodies.

Consider a Rankine vortex, composed of a core of radius r_1 rotating in solid-body rotation with tangential velocity ωr and a potential-vortex outer flow with tangential velocity $\Gamma/(2\pi r)$. Assume that at a radius r_2 the temperature is prescribed, and it is required to calculate the heat transfer through the rotating vortex and to compare it with the heat transfer through a stationary fluid under the same boundary conditions. (The problem thus defined is an extension of the basic idea of Cole [1],[3] who considered only the two limiting cases of $r_1 = 0$ and $r_1 = r_2$.) The typical situation we shall have to deal with is that in which the heat enters through one half of the circumference and exits through the other half. In this situation we may think of the vortex as located between two regions of the flow field far away from each other, the one hot and the other cold. Due to the linearity of the problem it is possible to study each Fourier component of the temperature boundary condition separately, and, as will be seen, an interesting general result can be obtained even without specifying the details of the boundary condition.

The equations governing the temperature field are:

$$0 < r < r_1 \qquad \omega \frac{\partial T}{\partial \theta} = \alpha \left(\frac{\partial^2 T}{\partial r^2} + \frac{1}{r} \frac{\partial T}{\partial r} + \frac{1}{r^2} \frac{\partial^2 T}{\partial \theta^2} \right) \tag{1}$$

$$r_1 < r < r_2 \qquad \frac{\Gamma}{2\pi} \frac{1}{r^2} \frac{\partial T}{\partial \theta} = \alpha \left(\frac{\partial^2 T}{\partial r^2} + \frac{1}{r} \frac{\partial T}{\partial r} + \frac{1}{r^2} \frac{\partial^2 T}{\partial \theta^2} \right) \tag{2}$$

with the boundary conditions

$$\text{at} \quad r = r_2 \qquad T = f(\theta) = \sum_{n=1}^{\infty} C_n \cos n\theta + \sum_{n=1}^{\infty} D_n \sin n\theta \tag{3}$$

$$\text{at} \quad r = r_1 \qquad T(r_1 - 0) = T(r_1 + 0)$$

$$\left. \frac{\partial T}{\partial r} \right|_{r_1 - 0} = \left. \frac{\partial T}{\partial r} \right|_{r_1 + 0} \tag{4}$$

$$\text{at} \quad r = 0 \qquad |T| < \infty \tag{5}$$

After separation of variables, for equation (1) we obtain by standard manipulations the solution

$$0 \le r \le r_1 \qquad T(r, \theta) = \sum_{n=1}^{\infty} e_n J_n[(i^3 \omega n/\alpha)^{1/2} r] e^{in\theta} + \sum_{n=1}^{\infty} (-1)^n f_n J_n[(i\omega n/\alpha)^{1/2} r] e^{-in\theta} \tag{6}$$

where J_n are Bessel functions of the first kind. Similarly, for equation (2) we get

$$r_1 \le r \le r_2 \qquad T(r, \theta) = \sum_{n=1}^{\infty} (a_n r^{\mu} + b_n r^{-\mu}) e^{in\theta} + \sum_{n=1}^{\infty} (c_n r^{\bar{\mu}} + d_n r^{-\bar{\mu}}) e^{-in\theta} \tag{7}$$

where

$$\mu = \sqrt{n^2 + i\lambda n} = n^{1/2} (n^2 + \lambda^2)^{1/4} \exp\left(\frac{i}{2} \arctan \frac{\lambda}{n} \right) \tag{8}$$

$\bar{\mu}$ is the complex conjugate of μ, $\lambda = \Gamma/(2\pi\alpha)$, and $\arctan(\lambda/n)$ is

[1] Research Assistant, Faculty of Mechanical Engineering, Technion–Israel Institute of Technology, Haifa, Israel; presently at the Courant Institute of Mathematical Sciences, New York University, New York, N. Y.

[2] Associate Professor, Faculty of Mechanical Engineering, Technion–Israel Institute of Technology, Haifa, Israel. Assoc. Mem. ASME.

[3] Numbers in brackets designate References at end of technical brief.

Contributed by the Heat Transfer Division of THE AMERICAN SOCIETY OF MECHANICAL ENGINEERS. Manuscript received by the Heat Transfer Division March 1, 1972.

between the pump and the katharometer insured that the flow was steady. This arrangement permitted measurements of mass concentration to a precision of ±1 percent and with a response time of less than 2 sec.

Results and Discussion

The measured values of impervious-wall effectiveness are shown in Figs. 2 and 3. Figure 2 indicates the influence of the backward-facing step for three velocity ratios, for three downstream distances, and for two values of the lip-thickness-to-slot-height ratio. The measurements shown in Fig. 2 were obtained using a tracer of helium gas in the slot flow, and they conform, therefore, to uniform density. It is clear that in the case of the thin lip the decrease in effectiveness with step height is greatest for the lower velocity ratios; the maximum decrease in effectiveness corresponds to approximately 15 percent of unity for a step-height-to-slot-height ratio of 2. For the case of the thick lip, the highest velocity ratio resulted in the greatest decrease in effectiveness close to the slot exit; this trend is reversed with downstream distance and at x/y_C of 56; the largest decrease in effectiveness was recorded with the lower velocity ratios.

Figure 3 presents measurements corresponding to the thin lip and for a density ratio of 2. These results were obtained by injecting a mixture of Arcton 12 and air through the slot exit and they relate particularly to gas-turbine combustor practice where similar density ratios are encountered. It is clear that the influence of the step height is considerable; for example, a decrease in effectiveness of 50 percent was recorded at x/y_C of 16 for the lowest blowing rate and for a step-height-to-slot-height ratio of 2. The measurements with a density ratio of 2 were not reported with the thick-lip geometry because it was anticipated that the influence of the step height would be less in this case.

The measurements of Figs. 2 and 3 may be replotted against downstream distance, and for the case of the thin lip and uniform density they indicate that the separation region immediately downstream of the step causes a maximum in the effectiveness curve at the reattachment line. Upstream of the reattachment line the effectiveness drops to a minimum. In contrast, the measurements obtained at a density ratio of 2 decrease monotonically.

References

1 Kacker, S. C., and Whitelaw, J. H., "The Effect of Slot Height and Slot-Turbulence Intensity on the Effectiveness of the Uniform Density, Two-Dimensional Wall Jet," JOURNAL OF HEAT TRANSFER, TRANS. ASME, Series C, Vol. 90, No. 4, Nov. 1968, pp. 469–475.

2 Pai, B. R., and Whitelaw, J. H., "The Influence of Density Gradients on the Effectiveness of Film Cooling," A.R.C., C.P. 1013, 1968.

3 Kacker, S. C., and Whitelaw, J. H., "An Experimental Investigation of the Influence of Slot-Lip Thickness on the Impervious-Wall Effectiveness of the Uniform-Density Two-Dimensional Wall Jet," *International Journal of Heat and Mass Transfer*, Vol. 12, 1969, pp. 1196.

4 Whitelaw, J. H., "An Experimental Investigation of the Two-dimensional Wall Jet," A.R.C., C.P. 942, 1967.

Heat Transfer through a Rankine Vortex

M. GHIL[1] **and A. SOLAN**[2]

THE object of this note is to present a closed-form solution for the heat transfer through a Rankine vortex. It turns out that for certain conditions, satisfied in many actual flow situations, this solution gives a square-root dependence of the Nusselt number on the Peclet number, irrespective of the details of the temperature boundary conditions. This result plays a role in the heat transfer from the rear of bluff bodies.

Consider a Rankine vortex, composed of a core of radius r_1 rotating in solid-body rotation with tangential velocity ωr and a potential-vortex outer flow with tangential velocity $\Gamma/(2\pi r)$. Assume that at a radius r_2 the temperature is prescribed, and it is required to calculate the heat transfer through the rotating vortex and to compare it with the heat transfer through a stationary fluid under the same boundary conditions. (The problem thus defined is an extension of the basic idea of Cole [1],[3] who considered only the two limiting cases of $r_1 = 0$ and $r_1 = r_2$.) The typical situation we shall have to deal with is that in which the heat enters through one half of the circumference and exits through the other half. In this situation we may think of the vortex as located between two regions of the flow field far away from each other, the one hot and the other cold. Due to the linearity of the problem it is possible to study each Fourier component of the temperature boundary condition separately, and, as will be seen, an interesting general result can be obtained even without specifying the details of the boundary condition.

The equations governing the temperature field are:

$$0 < r < r_1 \qquad \omega \frac{\partial T}{\partial \theta} = \alpha \left(\frac{\partial^2 T}{\partial r^2} + \frac{1}{r} \frac{\partial T}{\partial r} + \frac{1}{r^2} \frac{\partial^2 T}{\partial \theta^2} \right) \tag{1}$$

$$r_1 < r < r_2 \qquad \frac{\Gamma}{2\pi} \frac{1}{r^2} \frac{\partial T}{\partial \theta} = \alpha \left(\frac{\partial^2 T}{\partial r^2} + \frac{1}{r} \frac{\partial T}{\partial r} + \frac{1}{r^2} \frac{\partial^2 T}{\partial \theta^2} \right) \tag{2}$$

with the boundary conditions

$$\text{at} \quad r = r_2 \qquad T = f(\theta) = \sum_{n=1}^{\infty} C_n \cos n\theta + \sum_{n=1}^{\infty} D_n \sin n\theta \tag{3}$$

$$\text{at} \quad r = r_1 \qquad T(r_1 - 0) = T(r_1 + 0)$$

$$\left. \frac{\partial T}{\partial r} \right|_{r_1 - 0} = \left. \frac{\partial T}{\partial r} \right|_{r_1 + 0} \tag{4}$$

$$\text{at} \quad r = 0 \qquad |T| < \infty \tag{5}$$

After separation of variables, for equation (1) we obtain by standard manipulations the solution

$$0 \le r \le r_1 \qquad T(r, \theta) = \sum_{n=1}^{\infty} e_n J_n[(i^3 \omega n/\alpha)^{1/2} r] e^{in\theta} + \sum_{n=1}^{\infty} (-1)^n f_n J_n[(i\omega n/\alpha)^{1/2} r] e^{-in\theta} \tag{6}$$

where J_n are Bessel functions of the first kind. Similarly, for equation (2) we get

$$r_1 \le r \le r_2 \qquad T(r, \theta) = \sum_{n=1}^{\infty} (a_n r^{\mu} + b_n r^{-\mu}) e^{in\theta} + \sum_{n=1}^{\infty} (c_n r^{\bar{\mu}} + d_n r^{-\bar{\mu}}) e^{-in\theta} \tag{7}$$

where

$$\mu = \sqrt{n^2 + i\lambda n} = n^{1/2} (n^2 + \lambda^2)^{1/4} \exp\left(\frac{i}{2} \arctan \frac{\lambda}{n} \right) \tag{8}$$

$\bar{\mu}$ is the complex conjugate of μ, $\lambda = \Gamma/(2\pi\alpha)$, and $\arctan(\lambda/n)$ is

[1] Research Assistant, Faculty of Mechanical Engineering, Technion–Israel Institute of Technology, Haifa, Israel; presently at the Courant Institute of Mathematical Sciences, New York University, New York, N. Y.

[2] Associate Professor, Faculty of Mechanical Engineering, Technion–Israel Institute of Technology, Haifa, Israel. Assoc. Mem. ASME.

[3] Numbers in brackets designate References at end of technical brief.

Contributed by the Heat Transfer Division of THE AMERICAN SOCIETY OF MECHANICAL ENGINEERS. Manuscript received by the Heat Transfer Division March 1, 1972.

the principal value of $\tan^{-1}(\lambda/n)$. Note that λ *is a Peclet number,* based on an arbitrary radius r and its corresponding velocity $\Gamma/(2\pi r)$ in the potential vortex, $\mathrm{Pe} = vr/\alpha = \Gamma/2\pi\alpha = \lambda$. As it turns out to be more convenient to work with complex quantities, to the physical real part of $T(r_2, \theta)$ in (3) an imaginary part is now added, which, thanks to the linearity of equations (1) and (2) in the temperature T, may be discarded in due time. The nth Fourier component of the complex boundary condition is then

$$T_n(r_2, \theta) = A_n e^{in\theta} + iB_n e^{-in\theta} \qquad n = 1, 2, \ldots \tag{9}$$

The constants in the solutions (6), (7) must then satisfy the following system of six linear equations for each n:

$$\begin{aligned}
a_n r_2^{\mu} + b_n r_2^{-\mu} &= A_n \\
c_n r_2^{\bar{\mu}} + d_n r_2^{-\bar{\mu}} &= iB_n \\
e_n J_n(i^{3/2}x_1) &= a_n r_1^{\mu} + b_n r_1^{-\mu} \\
(-1)^n f_n J_n(i^{1/2}x_1) &= c_n r_1^{\bar{\mu}} + d_n r_1^{-\bar{\mu}} \\
c_n \frac{d}{dr} J_n(i^{3/2}x_1) &= a_n \mu r_1^{\mu-1} - b_n \mu r_1^{-\mu-1} \\
(-1)^n f_n \frac{d}{dr} J_n(i^{1/2}x_1) &= c_n \bar{\mu} r_1^{\bar{\mu}-1} \\
&\quad - d_n \bar{\mu} r_1^{-\bar{\mu}-1}
\end{aligned} \qquad n = 1, 2, \ldots \tag{10}$$

where A_n, B_n are real; $a_n, b_n, c_n, d_n, e_n, f_n$ are complex; $x_1 = (\omega n/\alpha)^{1/2} r_1$; and

$$\begin{aligned}
J_n(i^{3/2}x) &= ber_n x + ibei_n x \\
J_n(i^{1/2}x) &= (-1)^n (ber_n x - ibei_n x)
\end{aligned} \tag{11}$$

with $ber_n x$, $bei_n x$ Kelvin functions of order n. Writing the system (10) in block matrix form, we invert it in two steps by partitioning to yield

$$\begin{aligned}
a_n &= r_1^{-\mu}\left(1 + \frac{\mu}{r_1}\frac{I_1}{I_2}\right)\Big/\Delta\alpha \cdot A_n \\
b_n &= -r_1^{\mu}\left(1 - \frac{\mu}{r_1}\frac{I_1}{I_2}\right)\Big/\Delta\alpha \cdot A_n \\
c_n &= -r_1^{-\bar{\mu}}\left(\frac{\bar{\mu}}{r_1} + \frac{\bar{I}_2}{\bar{I}_1}\right)\Big/\Delta\alpha_1 \cdot iB_n \\
d_n &= -r_1^{\bar{\mu}}\left(\frac{\bar{\mu}}{r_1} - \frac{\bar{I}_2}{\bar{I}_1}\right)\Big/\Delta\alpha_1 \cdot iB_n \\
e_n &= 2\frac{\mu}{r_1}\frac{1}{I_2 \cdot \Delta\alpha} \cdot A_n \\
f_n &= -2\frac{\bar{\mu}}{r_1}\frac{1}{\Delta\alpha_1 \cdot \bar{I}_1} \cdot iB_n
\end{aligned} \qquad n = 1, 2, \ldots \tag{12}$$

where

$$\begin{aligned}
I_1 &= J_n(i^{3/2}x_1) \\
I_2 &= \frac{d}{dr} J_n(i^{3/2}\sqrt{\omega n/\alpha}\, r)\Big|_{r=r_1} = i^{3/2}(\omega n/\alpha)^{1/2} J_n'(i^{3/2}x_1) \\
\Delta\alpha &= (r_2/r_1)^{\mu}\left(1 + \frac{\mu}{r_1}\frac{I_1}{I_2}\right) - (r_1/r_2)^{\mu}\left(1 - \frac{\mu}{r_1}\frac{I_1}{I_2}\right) \\
-\Delta\alpha_1 &= (r_2/r_1)^{\bar{\mu}}\left(\frac{\bar{\mu}}{r_1} + \frac{\bar{I}_2}{\bar{I}_1}\right) + (r_1/r_2)^{\bar{\mu}}\left(\frac{\bar{\mu}}{r_1} - \frac{\bar{I}_2}{\bar{I}_1}\right)
\end{aligned} \tag{13}$$

With (12) we may finally get down to our purpose of calculating the heat transfer through the Rankine vortex. Obviously the heat transfer will be obtained by integration of the radial derivative of the temperature along the "circumference" $r = r_2$ of the vortex between appropriate limits. For the typical situation in which the heat enters through half the circumference and exits through the other half, the heat flux is

$$q = k\int_{-\pi/2}^{\pi/2} \left.\frac{\partial T}{\partial r}\right|_{r_2} \cdot r_2 d\theta \tag{14}$$

Due to the linearity of the problem already mentioned, it is possible to study each Fourier component of the boundary condition (3) separately. The heat transfer corresponding to the nth cosine component

$$T(r_2, \theta) = C_n \cos n\theta \tag{15}$$

is then the real part of

$$q = 2k\frac{s(n)}{n}\mu(n)(a_n r_2^{\mu} - b_n r_2^{-\mu}) \tag{16}$$

where

$$s(n) = \begin{cases} 0 & n = 2k \\ 1 & n = 4k + 1 \\ -1 & n = 4k + 3 \end{cases} \tag{17}$$

(The heat flux corresponding to the sine components vanishes.) By referring now the heat transfer (16) to the heat transmitted through the same volume of fluid at rest ($\lambda = 0$) by conduction alone, $q_0 = 2ks(n)C_n$, we define a (complex) Nusselt number

$$\mathrm{Nu}_n = q/q_0 = \frac{\mu}{n}\,\frac{1 + r_*^{2\mu} + \dfrac{\mu}{(n\lambda)^{1/2}}\dfrac{J_n(i^{3/2}x_1)}{\dfrac{d}{dx}J_n(i^{3/2}x_1)}(1 - r_*^{2\mu})}{1 - r_*^{2\mu} + \dfrac{\mu}{(n\lambda)^{1/2}}\dfrac{J_n(i^{3/2}x_1)}{\dfrac{d}{dx}J_n(i^{3/2}x_1)}(1 + r_*^{2\mu})} \tag{18}$$

where $r_* = r_1/r_2$ is dimensionless. (This includes as a special case Cole's solution [1] for a potential vortex, $r_* = 0$ and $n = 1$, $q/q_0 = \sqrt{1 + i\lambda}$.) Though in general this appears to be a rather complicated function of the Peclet number $\mathrm{Pe} \equiv \lambda$ (recall that $\mu = \sqrt{n^2 + i\lambda n}$) and the core radius r_*, the interesting result is that for $r_* < 0.5$ and Peclet number $\mathrm{Pe} > 30n$ we have $|r_*^{2\mu}| < 0.01$, and, by taking the real part of (18), we obtain the very simple relation[4]

$$\mathrm{Nu}_n \cong \mathrm{Pe}^{1/2}/(2n)^{1/2} \tag{19}$$

The overall Nusselt number

$$\mathrm{Nu} = \frac{\sum_{n=1}^{\infty} (\mu/n)\cdot F(n, r_*, \mathrm{Pe})\cdot s(n)\cdot C_n}{\sum_{n=1}^{\infty} s(n)C_n} \tag{20}$$

where $F(n, r_*, \mathrm{Pe})$ denotes the second fraction on the right side of (18), then reduces to

$$\mathrm{Nu} = c\mathrm{Pe}^{1/2} \tag{21}$$

where the constant c depends on the temperature boundary condition. It may be seen that irrespective of the details of the boundary condition and of the vortex core radius, the Nusselt number is proportional to the square root of the Peclet number (i.e., the circulation/diffusivity ratio). Thus, although there

[4] As seen from equation (18), $|r_*^{2\mu}| \to 0$ insures $\mathrm{Nu}_n \to \mu/n$, if the ratio of the Bessel functions $J_n/[(d/dx)(J_n)]$ appearing in it stays bounded for all values of the parameters involved. This is indeed so (although the functions themselves diverge for large values of the arguments), as can easily be seen by using asymptotic expansions of the polar form of these functions (cf., e.g., Abramowitz and Stegun [2]).

will normally be difficulties in ascertaining the temperature distribution (3) at some radius r_2 by measurements or analysis, one may safely ignore its details and rely on the general square-root dependence on Pe, equation (20), leaving the numerical coefficient, which will have to express the averaging over all n's, to be determined experimentally in any given flow and heat-transfer configuration. Such square-root dependence can be applied, for instance, to correlate the heat transfer from the rear of bluff obstacles [3].

References

1 Cole, J. D., "Note on the Effect of Circulation in Heat Transfer," RM-1351, Rand Corp., Santa Monica, Calif., Sept. 1954.

2 Abramowitz, M., and Stegun, J. A., eds., *Handbook of Mathematical Functions, Appl. Math. Ser.*, Vol. 55, National Bureau of Standards, U. S. Government Printing Office, Washington, D. C., Mar. 1965.

3 Ghil, M., and Solan, A., "Heat and Mass Transfer through a Viscous Linear Vortex: A Model for Transport Phenomena from the Rear of Bluff Obstacles," Report TME-113, Faculty of Mechanical Engineering, Technion, Haifa, Israel, 1970.

journal of heat transfer

discussion

Unsteady Heat Transfer and Temperature for Stokesian Flow about a Sphere[1]

R. G. Watts.[2] Dr. Konopliv and Professor Sparrow are to be complimented on their elegant treatment of a very timely problem. Analytical solutions of the problem of transient heat transfer from a constant-temperature sphere to a fluid at a different temperature have now been presented for three important limiting cases. Chao and Chen [2][3] published a solution for the special case of large Reynolds number and small Peclet number. The present paper (first part) treats the case of small Reynolds number and large Peclet number. Choudhury and Drake [11] recently presented a solution for the case of Re $\ll$ 1 and Pe $<$ 1. The corresponding steady-state solutions have been given respectively by Watts [12], Acrivos and Goddard [9], and Acrivos and Taylor [4]. Judging from the dates of publication, the paper by Choudhury and Drake seems to have appeared while the present paper was in press. I suspect the authors would like to comment on its significance in relation to their own work.

I would like to discuss the relation between the results obtained by the authors and those presented by Choudhury and Drake, particularly as regards the range of validity of the authors' results and the approach to steady state.

The authors state that "During the conduction regime ($0 \leq \tau \leq 0.5$), the Nusselt-number results are unaffected by the thermal boundary-layer assumptions" and that "there is no Peclet-number limitation for $\tau < 0.5$." This is not true. When the Peclet number is large the steady-state Nusselt number is given approximately by $\mathrm{Nu}^* \simeq 0.922 + 0.991\ \mathrm{Pe}^{1/3}$ as stated by the authors and given in [9]. However, when Pe $<$ 1, $\mathrm{Nu}^* \simeq 2 + \mathrm{Pe}/2$ [4]. It is unlikely that the Nusselt number ever falls below 2, corresponding to pure conduction. Fig. 7 is a reproduction of Fig. 3 with appropriate steady-state results for Pe $<$ 1 sketched in. Clearly the authors' solution cannot be valid when $\tau < 0.5$ for all Pe because for small Pe their solution curve falls well below the steady-state values, except for very small values of τ. The limitation of Pe is shown more clearly in Fig. 8 where the authors' results for low Pe are compared to those of Choudhury and Drake. The *range* of validity of the authors' results evidently depends strongly on the Peclet number. For example, Fig. 8 indicates that when Pe = 0.5, their results are already far too low when $\tau = 0.05$.

The reason for this is most probably because when the Peclet number is small the thermal boundary layer thickens very rapidly, making the boundary-layer assumption invalid even for very small τ. The extent of the thermal boundary layer can be estimated from Fig. 4. If $\delta_T/r_0 = 0.5$ is taken to be an upper limit for the assumption of a thin thermal boundary layer, and if Pe = 0.5, then $(\delta_T/r_0)\ (^3/_4\ \mathrm{Pe})^{1/3} = 0.361$. Assuming the outer edge of the thermal boundary layer to be located where $(T_f^* - T_\infty)\ /\ (T_i - T_\infty) = 0.25$, we find that $\delta_T/r_0 = 0.5$ when $\tau \simeq 0.05$. The thermal-layer thickness is already quite large.

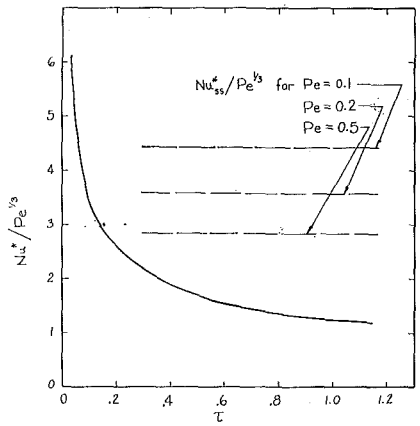

Fig. 7 Steady-state values for low Pe

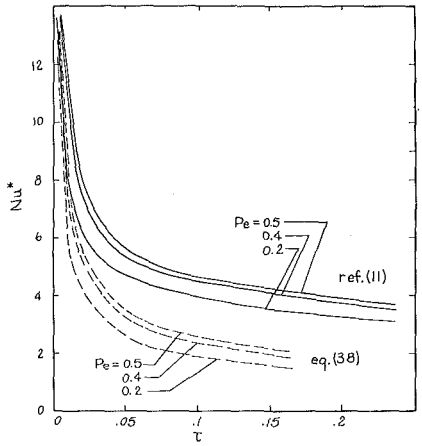

Fig. 8 Comparison of present results with those of Choudhury and Drake [11] for low Pe

Authors' Closure

The authors are grateful to Professor Watts for his interest in the article and for his kind remarks.

Equation (30) can be rewritten in a form which shows the explicit dependence of Nu* on Pe

$$\mathrm{Nu}^* = \frac{2}{\sqrt{\pi \mathrm{Fo}}} + \frac{19}{120\sqrt{\pi}}\ \mathrm{Pe\ Fo} + \mathrm{O}(\mathrm{Fo}^{11/2})$$

where Fo is the Fourier number. During the conduction regime

[1] By N. Konopliv and E. M. Sparrow, published in the Aug. 1972 issue of the JOURNAL OF HEAT TRANSFER, TRANS. ASME, Series C, Vol. 94, No. 3, pp. 266–272.

[2] Associate Professor, Department of Mechanical Engineering, Tulane University, New Orleans, La. Mem. ASME.

[3] Numbers in brackets designate References in the paper under discussion as well as Additional References at end of discussion.

(defined to be $0 \leq \tau \leq 0.5$), the Fourier number does not exceed $0.5/(3\text{Pe}/4)^{2/3}$. Consequently, the fractional deviation of Nu* from that of transient conduction does not exceed $19/(180 \cdot 2^{3/2})$ or 3.74 percent. We thus take issue with the challenge of Professor Watts that our statement that "there is no Peclet-number limitation for $\tau < 0.5$" is not true. It is true, keeping in mind that our study applies to large values of the Peclet number and as such should not necessarily be applicable to low values of the Peclet number.

The solution of Choudhury and Drake [11], when expressed in a form similar to the foregoing, is

$$\text{Nu}^* = \frac{2}{\sqrt{\pi \text{Fo}}} + 2 + \frac{19}{160\sqrt{\pi}} \text{Pe}^2 \text{Fo}^{5/2} + O(\text{Fo}^3)$$

If we utilize the conduction-regime criterion for this case to be that of the previous, then the fractional deviations of Nu* from that of pure conduction are also small. Clearly then, the Nusselt numbers within this regime differ uniformly by two, and Fig. 8 of Professor Watts shows this to be the case. However, in view of the implicit dependence of the abscissa on Pe, this figure shows an explicit dependence on Pe, whereas for all practical purposes Nu* depends *only* on Fo ($\tau \leq 0.5$): $\text{Nu}^* = 2/\sqrt{\pi \text{Fo}} + 2$ for $\text{Pe} < 1$ and $\text{Nu}^* = 2/\sqrt{\pi \text{Fo}}$ for $\text{Pe} \gg 1$.

In order to explain the aforementioned discrepancy, it is necessary to examine the nature of the physical processes involved and to explain the asymptotic solutions used in each of the limiting cases.

The $\text{Pe} < 1$ case, being conduction-dominated, exhibits nearly spherical isotherms around a sphere for the entire duration of the heat transfer, whereas for the $\text{Pe} \gg 1$ case this holds only during the initial stage, and with passage of time the isotherms are "carried away" from the sphere into the fluid in the direction of the fluid flow, exhibiting the maximum extent at steady state at the rear stagnation point.

The solution of Choudhury and Drake is derived in essence via the perturbation around the spherical isotherms and is applicable to all spherical coordinates, but our solution is not—it excludes the region in the proximity of the rear stagnation point where the thermal boundary layer as such may not exist. In fact, at $\phi = \pi$, $\theta^* = 0$ is the only admissible solution and consequently the local Nusselt number at that location is zero. A more detailed consideration (of steady-state heat transfer) by Shi and Newman [13] shows that the local Nusselt number there is not zero, but is 1.192. The contribution to the *total* surface heat transfer from this region is small, so that the boundary-layer assumption is justified over the entire surface of the sphere.

The authors were aware of the discrepancy of two due to steady-state conduction, a discrepancy which apparently led to the other comment of the discusser: that our statement is not true that "during the conduction regime ($0 \leq \tau \leq 0.5$), the Nusselt-number results are unaffected by the thermal boundary-layer assumptions." The comment is well taken but here also the statement applies only to the $\text{Pe} \gg 1$ case, so that the "pure conduction solution" is $\theta^* = \text{erfc}(\zeta/2\sqrt{\tau})$ and Nu* is indeed $2/\sqrt{\pi \text{Fo}}$.

Once again, the authors wish to express sincere thanks to Professor Watts for a rather detailed review of the first part of our paper.

Additional References

11 Choudhury, P. N., and Drake, D. G., "Unsteady Heat Transfer from a Sphere in a Low Reynolds Number Flow," *Quart. Journal of Mechanics and Appl. Math.*, Vol. 24, Pt. 1, 1971, pp. 23–36.

12 Watts, R. G., "The Effect of Curvature on Heat or Mass Transfer from an Isothermal Sphere," JOURNAL OF HEAT TRANSFER, TRANS. ASME, Series C, Vol. 94, No. 1, Feb. 1972, pp. 1–6.

13 Shi, P. H., and Newman, J., "Mass Transfer to the Rear of a Sphere in Stokes Flow," *International Journal of Heat and Mass Transfer*, Vol. 10, No. 12, 1967, pp. 1749–1756.

Correlations for Thermal Contact Conductance In Vacuo[1]

Paul W. O'Callaghan[2] and S. Douglas Probert.[3]

Since the compilation of data presented by Thomas and Probert, over 800 experimental values have been obtained for the thermal resistance of various contacts. Seven different specimen pairs (see Table 1), involving invar, aluminum, PTFE, aluminum oxide, quartz, and gold, were examined in high vacua [38].[4] The results are shown superimposed upon the previous data in Figs. 1 and 2. Each point on the figures is the arithmetic average of at least four independent determinations of resistance taken under constant applied loading. The exponents from each regression analysis are 0.63 and 0.66 respectively. All the data shown in Fig. 2 were subsequently replotted using the effective elastic modulus of the contact instead of the hardness M in the dimensionless loading factor. This modification, however, increased the scatter in the data, and so it was concluded that the hardness rather than the elastic modulus is the more significant parameter with respect to correlation of thermal-contact-resistance data. Further details concerning experimental technique may be found in [38, 39].

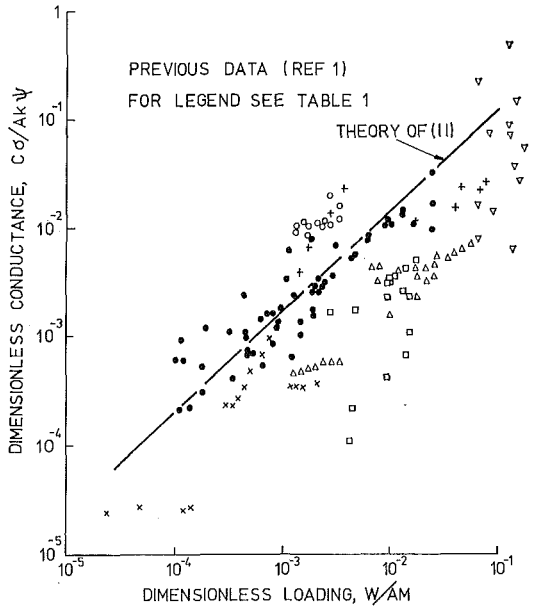

Fig. 1 Variation of the dimensionless conductance with dimensionless load for plastic contacts between flat isotropically rough surfaces

Additional References

38 O'Callaghan, P. W., "Some Aspects of Contacts between Solids," PhD thesis, University of Wales, 1971.

39 O'Callaghan, P. W., and Probert, S. D., "Prediction and Measurement of Thermal Contact Resistance," to be published.

[1] By T. R. Thomas and S. D. Probert, published in the August, 1972, issue of the JOURNAL OF HEAT TRANSFER, TRANS. ASME, Series C, Vol. 94, No. 3, pp. 276–281.

[2] Research Officer, School of Mechanical Engineering, Cranfield Institute of Technology, Bedford, England.

[3] Professor of Engineering Thermodynamics, Cranfield Institute of Technology, Bedford, England.

[4] Numbers in brackets designate Additional References at end of discussion.

(defined to be $0 \leq \tau \leq 0.5$), the Fourier number does not exceed $0.5/(3\mathrm{Pe}/4)^{2/3}$. Consequently, the fractional deviation of Nu* from that of transient conduction does not exceed $19/(180 \cdot 2^{3/2})$ or 3.74 percent. We thus take issue with the challenge of Professor Watts that our statement that "there is no Peclet-number limitation for $\tau < 0.5$" is not true. It is true, keeping in mind that our study applies to large values of the Peclet number and as such should not necessarily be applicable to low values of the Peclet number.

The solution of Choudhury and Drake [11], when expressed in a form similar to the foregoing, is

$$\mathrm{Nu}^* = \frac{2}{\sqrt{\pi \mathrm{Fo}}} + 2 + \frac{19}{160\sqrt{\pi}} \mathrm{Pe}^2 \mathrm{Fo}^{5/2} + O(\mathrm{Fo}^3)$$

If we utilize the conduction-regime criterion for this case to be that of the previous, then the fractional deviations of Nu* from that of pure conduction are also small. Clearly then, the Nusselt numbers within this regime differ uniformly by two, and Fig. 8 of Professor Watts shows this to be the case. However, in view of the implicit dependence of the abscissa on Pe, this figure shows an explicit dependence on Pe, whereas for all practical purposes Nu* depends *only* on Fo ($\tau \leq 0.5$): $\mathrm{Nu}^* = 2/\sqrt{\pi \mathrm{Fo}} + 2$ for $\mathrm{Pe} < 1$ and $\mathrm{Nu}^* = 2/\sqrt{\pi \mathrm{Fo}}$ for $\mathrm{Pe} \gg 1$.

In order to explain the aforementioned discrepancy, it is necessary to examine the nature of the physical processes involved and to explain the asymptotic solutions used in each of the limiting cases.

The $\mathrm{Pe} < 1$ case, being conduction-dominated, exhibits nearly spherical isotherms around a sphere for the entire duration of the heat transfer, whereas for the $\mathrm{Pe} \gg 1$ case this holds only during the initial stage, and with passage of time the isotherms are "carried away" from the sphere into the fluid in the direction of the fluid flow, exhibiting the maximum extent at steady state at the rear stagnation point.

The solution of Choudhury and Drake is derived in essence via the perturbation around the spherical isotherms and is applicable to all spherical coordinates, but our solution is not—it excludes the region in the proximity of the rear stagnation point where the thermal boundary layer as such may not exist. In fact, at $\phi = \pi$, $\theta^* = 0$ is the only admissible solution and consequently the local Nusselt number at that location is zero. A more detailed consideration (of steady-state heat transfer) by Shi and Newman [13] shows that the local Nusselt number there is not zero, but is 1.192. The contribution to the *total* surface heat transfer from this region is small, so that the boundary-layer assumption is justified over the entire surface of the sphere.

The authors were aware of the discrepancy of two due to steady-state conduction, a discrepancy which apparently led to the other comment of the discusser: that our statement is not true that "during the conduction regime ($0 \leq \tau \leq 0.5$), the Nusselt-number results are unaffected by the thermal boundary-layer assumptions." The comment is well taken but here also the statement applies only to the $\mathrm{Pe} \gg 1$ case, so that the "pure conduction solution" is $\theta^* = \mathrm{erfc}(\zeta/2\sqrt{\tau})$ and Nu* is indeed $2/\sqrt{\pi \mathrm{Fo}}$.

Once again, the authors wish to express sincere thanks to Professor Watts for a rather detailed review of the first part of our paper.

Additional References

11 Choudhury, P. N., and Drake, D. G., "Unsteady Heat Transfer from a Sphere in a Low Reynolds Number Flow," *Quart. Journal of Mechanics and Appl. Math.*, Vol. 24, Pt. 1, 1971, pp. 23–36.

12 Watts, R. G., "The Effect of Curvature on Heat or Mass Transfer from an Isothermal Sphere," JOURNAL OF HEAT TRANSFER, TRANS. ASME, Series C, Vol. 94, No. 1, Feb. 1972, pp. 1–6.

13 Shi, P. H., and Newman, J., "Mass Transfer to the Rear of a Sphere in Stokes Flow," *International Journal of Heat and Mass Transfer*, Vol. 10, No. 12, 1967, pp. 1749–1756.

Correlations for Thermal Contact Conductance In Vacuo[1]

Paul W. O'Callaghan[2] and S. Douglas Probert.[3]

Since the compilation of data presented by Thomas and Probert, over 800 experimental values have been obtained for the thermal resistance of various contacts. Seven different specimen pairs (see Table 1), involving invar, aluminum, PTFE, aluminum oxide, quartz, and gold, were examined in high vacua [38].[4] The results are shown superimposed upon the previous data in Figs. 1 and 2. Each point on the figures is the arithmetic average of at least four independent determinations of resistance taken under constant applied loading. The exponents from each regression analysis are 0.63 and 0.66 respectively. All the data shown in Fig. 2 were subsequently replotted using the effective elastic modulus of the contact instead of the hardness M in the dimensionless loading factor. This modification, however, increased the scatter in the data, and so it was concluded that the hardness rather than the elastic modulus is the more significant parameter with respect to correlation of thermal-contact-resistance data. Further details concerning experimental technique may be found in [38, 39].

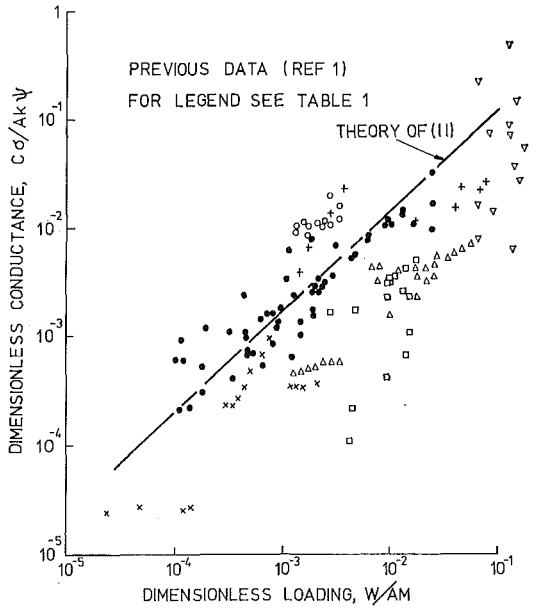

Fig. 1 Variation of the dimensionless conductance with dimensionless load for plastic contacts between flat isotropically rough surfaces

Additional References

38 O'Callaghan, P. W., "Some Aspects of Contacts between Solids," PhD thesis, University of Wales, 1971.

39 O'Callaghan, P. W., and Probert, S. D., "Prediction and Measurement of Thermal Contact Resistance," to be published.

[1] By T. R. Thomas and S. D. Probert, published in the August, 1972, issue of the JOURNAL OF HEAT TRANSFER, TRANS. ASME, Series C, Vol. 94, No. 3, pp. 276–281.

[2] Research Officer, School of Mechanical Engineering, Cranfield Institute of Technology, Bedford, England.

[3] Professor of Engineering Thermodynamics, Cranfield Institute of Technology, Bedford, England.

[4] Numbers in brackets designate Additional References at end of discussion.

Appendix

For the purposes of the present compilation, k, σ, ψ, $\bar{\rho}$, E^*, and λ were calculated respectively from

$$\frac{2}{k} = \frac{1}{k_1} + \frac{1}{k_2}$$

$$\sigma = (\sigma_1^2 + \sigma_2^2)^{1/2}$$

$$\psi = [(|\psi_1|^2 + |\psi_2|^2)/(\sigma_1^2 + \sigma_2^2)]^{1/2}$$

$$\frac{1}{\bar{\rho}} = \frac{1}{\bar{\rho}_1} + \frac{1}{\bar{\rho}_2}$$

$$\frac{1}{E^*} = \left(\frac{1 - \nu_1^2}{E_1}\right) + \left(\frac{1 - \nu_2^2}{E_2}\right)$$

and

$$\lambda = \frac{E^*}{M}\left(\frac{\sigma}{\bar{\rho}}\right)^{1/2}$$

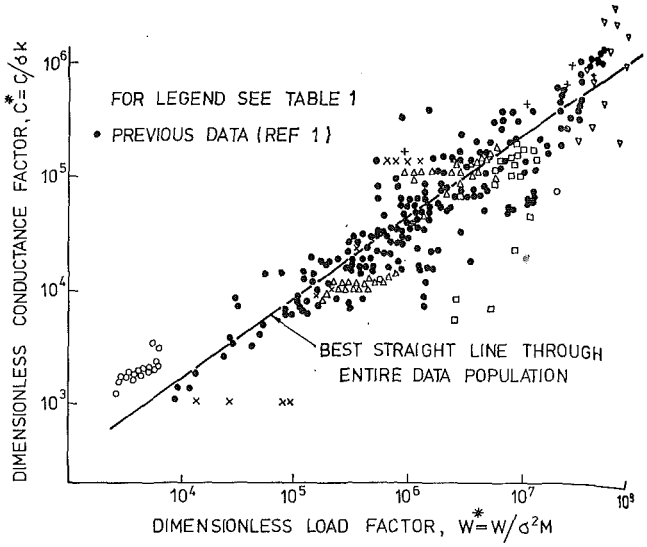

Fig. 2 Variation of dimensionless conductance with dimensionless load for contacts in vacuo

Table 1 The contacts considered

	Contact specification						
	invar to invar	invar to mica	aluminum to invar	rough invar to smooth invar	PTFE to invar	Al_2O_3 to invar	gold to quartz
Harmonic mean thermal conductivity, k ($Wm^{-1}K^{-1}$)	15.00	1.12	28.00	15.00	0.88	16.60	13.20
Effective rms roughness, σ† (10^{-6} m)	0.52	0.52	0.68	9.12	0.51	1.10	0.94
Effective mean absolute surface slope, ψ (mm^{-1})	302.00	300.00	339.00	25.60	3240*	3320	1980
Harmonic mean peak radius of curvature, $\bar{\rho}$ (10^{-6} m)	34.87	69.82	34.41	0.99	13.70*	10.45	2.20
Effective mean elastic modulus, E^* (10^8 Nm^{-2})	745	840	515	745	14.5	945	458
Plasticity index, λ	3.60	830.00	16.80	74.20	3.70*	10.30	14.40
Nominal contact area (mm^2)	163.00	166.00	168.00	169.00	168.00	162.00	125.00
Number of observations	47	30	86	98	59	139	96
Number used for correlations	11	7	18	22	13	17	17
Symbols on Figs. 1 and 2	×	+	□	○	▽	▲	△
Hardness of the softer contacting material, M (10^8 Nm^{-2})	30.3	1.0	4.3	30.3	0.6	30.3	6.4

* Where values of ψ or $\bar{\rho}$ of either of the contacting materials could not be assessed, estimates were made.
† All surfaces were nominally flat, i.e., the waviness undulations were of the order of the roughness.

Nongray Radiative Transport in a Cylindrical Medium[1]

Z. Chiba[2] and R. Greif.[2] In a study of the radiative transport in a cylindrical medium, Habib and Greif noted that their gray gas results differed from those obtained by Kesten [1].[3] The reason for this difference has been pointed out to us by Guy [2]. Equation (24) of Kesten is the correct result for the radiative flux, but in going to equation (27) an error appears to have been made. However, the numerical results of Kesten were apparently based on the correct equation (24), while Habib and Greif utilized the incorrect equation (27). Thus the numerical results presented by Kesten are correct and those by Habib and Greif are incorrect.

The question of the validity of the approximation

$$D_2(x) = \int_0^1 \frac{\mu e^{-x/\mu}\, d\mu}{(1 - \mu^2)^{1/2}} \approx e^{-5x/4} \qquad (1)$$

was therefore reexamined. Results obtained using equation (1) were *now* found to be in very good agreement with the gray gas calculations of Kesten (Chiba [3]). Expressions for the spectral radiative flux using equation (1) have also been obtained and are available in [3].

Additional References

1 Kesten, A. S., "Radiant Heat Flux Distribution in a Cylindrically Symmetric Nonisothermal Gas with Temperature-Dependent Absorption Coefficient," *Journal of Quantitative Spectroscopy and Radiation Transfer*, Vol. 8, Pergamon Press, 1968, pp. 419–434.
2 Guy, A. G., Pilkington Research and Development Laboratories, Lancashire, England, personal communication.
3 Chiba, Z., "The Study of Heat Transfer with Radiation to Gases in Turbulent Flow within Tubes," PhD dissertation, University of California, Berkeley, Calif., 1972.

[1] By I. S. Habib and R. Greif, published in the February, 1970, issue of the JOURNAL OF HEAT TRANSFER, TRANS. ASME, Series C, Vol. 92, No. 1, pp. 28–32.

[2] Department of Mechanical Engineering, University of California, Berkeley, Calif.

[3] Numbers in brackets designate Additional References at end of discussion.

Appendix

For the purposes of the present compilation, k, σ, ψ, $\bar{\rho}$, E^*, and λ were calculated respectively from

$$\frac{2}{k} = \frac{1}{k_1} + \frac{1}{k_2}$$

$$\sigma = (\sigma_1^2 + \sigma_2^2)^{1/2}$$

$$\psi = [(|\psi_1|^2 + |\psi_2|^2)/(\sigma_1^2 + \sigma_2^2)]^{1/2}$$

$$\frac{1}{\bar{\rho}} = \frac{1}{\bar{\rho}_1} + \frac{1}{\bar{\rho}_2}$$

$$\frac{1}{E^*} = \left(\frac{1 - \nu_1^2}{E_1}\right) + \left(\frac{1 - \nu_2^2}{E_2}\right)$$

and

$$\lambda = \frac{E^*}{M}\left(\frac{\sigma}{\bar{\rho}}\right)^{1/2}$$

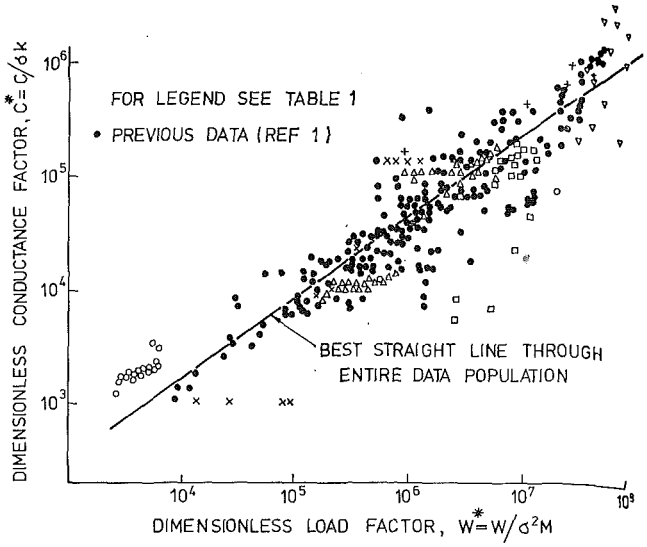

Fig. 2 Variation of dimensionless conductance with dimensionless load for contacts in vacuo

Table 1 The contacts considered

	Contact specification						
	invar to invar	invar to mica	aluminum to invar	rough invar to smooth invar	PTFE to invar	Al_2O_3 to invar	gold to quartz
Harmonic mean thermal conductivity, k ($Wm^{-1}K^{-1}$)	15.00	1.12	28.00	15.00	0.88	16.60	13.20
Effective rms roughness, σ† (10^{-6} m)	0.52	0.52	0.68	9.12	0.51	1.10	0.94
Effective mean absolute surface slope, ψ (mm^{-1})	302.00	300.00	339.00	25.60	3240*	3320	1980
Harmonic mean peak radius of curvature, $\bar{\rho}$ (10^{-6} m)	34.87	69.82	34.41	0.99	13.70*	10.45	2.20
Effective mean elastic modulus, E^* (10^8 Nm^{-2})	745	840	515	745	14.5	945	458
Plasticity index, λ	3.60	830.00	16.80	74.20	3.70*	10.30	14.40
Nominal contact area (mm^2)	163.00	166.00	168.00	169.00	168.00	162.00	125.00
Number of observations	47	30	86	98	59	139	96
Number used for correlations	11	7	18	22	13	17	17
Symbols on Figs. 1 and 2	×	+	□	○	▽	▲	△
Hardness of the softer contacting material, M (10^8 Nm^{-2})	30.3	1.0	4.3	30.3	0.6	30.3	6.4

* Where values of ψ or $\bar{\rho}$ of either of the contacting materials could not be assessed, estimates were made.
† All surfaces were nominally flat, i.e., the waviness undulations were of the order of the roughness.

Nongray Radiative Transport in a Cylindrical Medium[1]

Z. Chiba[2] and R. Greif.[2] In a study of the radiative transport in a cylindrical medium, Habib and Greif noted that their gray gas results differed from those obtained by Kesten [1].[3] The reason for this difference has been pointed out to us by Guy [2]. Equation (24) of Kesten is the correct result for the radiative flux, but in going to equation (27) an error appears to have been made. However, the numerical results of Kesten were apparently based on the correct equation (24), while Habib and Greif utilized the incorrect equation (27). Thus the numerical results presented by Kesten are correct and those by Habib and Greif are incorrect.

The question of the validity of the approximation

$$D_2(x) = \int_0^1 \frac{\mu e^{-x/\mu}\, d\mu}{(1 - \mu^2)^{1/2}} \approx e^{-5x/4} \qquad (1)$$

was therefore reexamined. Results obtained using equation (1) were *now* found to be in very good agreement with the gray gas calculations of Kesten (Chiba [3]). Expressions for the spectral radiative flux using equation (1) have also been obtained and are available in [3].

Additional References

1 Kesten, A. S., "Radiant Heat Flux Distribution in a Cylindrically Symmetric Nonisothermal Gas with Temperature-Dependent Absorption Coefficient," *Journal of Quantitative Spectroscopy and Radiation Transfer*, Vol. 8, Pergamon Press, 1968, pp. 419–434.
2 Guy, A. G., Pilkington Research and Development Laboratories, Lancashire, England, personal communication.
3 Chiba, Z., "The Study of Heat Transfer with Radiation to Gases in Turbulent Flow within Tubes," PhD dissertation, University of California, Berkeley, Calif., 1972.

[1] By I. S. Habib and R. Greif, published in the February, 1970, issue of the JOURNAL OF HEAT TRANSFER, TRANS. ASME, Series C, Vol. 92, No. 1, pp. 28–32.

[2] Department of Mechanical Engineering, University of California, Berkeley, Calif.

[3] Numbers in brackets designate Additional References at end of discussion.